ČESKÉ VYSOKÉ UČENÍ TECHNICKÉ
V PRAZE

Fakulta jaderná a fyzikálně inženýrská

Scintilační vlastnosti granátů $(Lu,Gd)_3(Al,Ga)_5O_{12}$:Ce a jejich optimalizace

Habilitační práce

Ing. Petr Průša, Ph.D.

Praha 2019

Obsah

Kapitola 1
Úvod

Objev paprsků X W.C. Röntgenem v roce 1895 [1], následovaný objevem radioaktivity H. Becquerelem v roce 1896 [2] vyvolal potřebu detekce ionizujícího záření. Již na počátku 20. století se, díky vynalezení spintariskopu W. Crookesem, scintilátory významně uplatnily při výzkumu jeho vlastností [3]. Spintariskop se scintilátorem na bázi ZnS využili např. H. Geiger a E. Marsden v laboratoři E. Rutherforda ke studiu rozptylu α částic na zlaté fólii [4]. Jejich experiment byl zásadním podnětem k přebudování modelu atomu a postulování existence malého atomového jádra, v němž je soustředěna naprostá většina hmotnosti jádra, a řídkého elektronového obalu. Tvůrcem tohoto tzv. planetárního modelu byl sám E. Rutherford.

Spintariskop sice přinesl několik zásadních objevů [5] [6], nicméně rozvoj plynových detektorů způsobil jeho postupné mizení z experimentální praxe a laboratoří. Bylo tomu tak především pro nemožnost vyhodnocení větších četností interakcí spintariskopem, jež byla dána nutností počítat scintilační záblesky pouhým okem, a subjektivitou měření. Snaha nahradit oko pozorovatele světlocitlivým přístrojem přinesla úspěch až v roce 1944. Tehdy Curran a Baker spojili scintilátor ZnS s fotonásobičem – sestavili tedy první scintilační detekční jednotku [7].

V několika následujících letech byly objeveny nové scintilátory, jmenovitě NaI:Tl [8], CsI:Tl [9] a antracen [10]. NaI:Tl je díky své cenové dostupnosti, přijatelné detekční účinnosti i energetické rozlišovací schopnosti stále nejpoužívanějším anorganickým scintilátorem. Přesto k němu existuje řada alternativ.

Jednou ze starších je BGO ($Bi_4Ge_3O_{12}$), scintilátor s velmi vysokým efektivním atomovým číslem Z_{eff} a značnou hustotou, s nímž lze i při malém detekčním objemu dosáhnout vysoké detekční účinnosti. Scintilátor BGO byl poprvé popsán v sedmdesátých letech [11].

Rozrůznění aplikací scintilátorů před koncem 20. století přineslo silný impulz k jejich výzkumu. Každá aplikace přinesla specifický soubor požadovaných vlastností, přičemž se ukázalo nemožným nalézt jeden jediný materiál, který by splňoval požadavky všech aplikací. Materiály jsou tak dnes do určité míry vyvíjeny pro potřeby jedné nebo několika málo aplikací. Uveďme si několik příkladů.

Scintilátory užívané ve výpočetní tomografii (CT – Computed tomography) musí vykazovat vysokou detekční účinnost pro záření X, emisi v oblasti citlivosti fotodiod, velmi nízký

afterglow, nízkou teplotní závislost odezvy, dobrou opracovatelnost a další [12] [13]. Za optimální scintilátor je v současné době považována keramika GOS (Gd_2O_2S – Gadolinium OxySulfite; též Gadox), dopantů je v ní možno použít několik [14] [15].

PET (Pozitronová emisní tomografie) vyžaduje dobrou energetickou rozlišovací schopnost, vysokou detekční účinnost, vynikající časovou rozlišovací schopnost a další [13]. State-of-the-art scintilátory pro PET jsou LSO:Ce (Lu_2SiO_5:Ce) a LYSO:Ce ($Lu_{2(1-x)}Y_{2x}SiO_5$:Ce) [13].

SPECT (Single Photon Emission Computed Tomography) skenery se v ideálním případě konstruují z krystalů značné velikosti s přijatelnou rozlišovací schopností, emisní vlnovou délkou vhodnou pro fotonásobiče a dobrou detekční účinností pro energie asi 200 keV. Především potřeba velké detekční plochy tvořené jedním krystalem a nízká cena spolurozhodly o tom, že dosud nejpoužívanějším materiálem pro SPECT skenery je NaI:Tl [13] [16].

Tématem předkládané habilitační práce jsou scintilátory na bázi granátů. Prvním takovým byl YAG:Ce ($Y_3Al_5O_{12}$:Ce) [17], objevený v roce 1967 a v 70. letech dále zkoumaný [18]. V dnešní době se používá např. k výrobě detektorů elektronů v elektronových mikroskopech [19]. Pro Čechy není bez zajímavosti, že této specifické tržní nice dominuje turnovská firma Crytur s.r.o [20].

V případě elektronového záření je nízké Z_{eff} výhodou a nízká hustota nepředstavuje problém, ovšem detekční účinnost YAG:Ce pro fotonové záření je nízká. Substitucí Y/Lu dostaneme materiál LuAG:Ce ($Lu_3Al_5O_{12}$:Ce), který má fotonovou detekční účinnosti podstatně lepší [21]. Bohužel tento materiál vykazuje významný podíl pomalých složek scintilační odezvy [22] [23] [24] [25] a, což úzce souvisí, světelný výtěžek výrazně pod teoretickým limitem [26] [27][1].

Příčina horších vlastností LuAG:Ce tkví v přítomnosti mělkých elektronových pastí, spojených s existencí tzv. Lu_{Al} antisite defektů, tj. iontů Lu^{3+} v místě jinak vyhrazeném pro Al^{3+} ionty [23] [28] [29] [30] [31]. Elektrony v pasti setrvávají relativně dlouhou dobu. Po jejich uvolnění sice může dojít k rekombinaci v luminiscenčním Ce^{3+} centru, avšak s příliš velkým zpožděním. Foton nepřispívá k měřenému signálu, díky čemuž je světelný výtěžek nižší, namísto toho se objevují nežádoucí pomalé složky scintilační odezvy.

V principu se nabízí dvojí řešení problému. Za prvé, vyrobit materiál s výrazně nižší koncentrací antisite defektů. Jelikož antisite defekty mají svou příčinu v růstu za vysoké teploty,

[1] V uvedeném odkazu [27] obr. 5 uvádí teoretický limit světelného výtěžku a jeho skutečnou hodnotu pro LuAG:Pr. Hodnoty pro LuAG:Ce se však liší minimálně (resp. teoretický limit je dán šíří zakázaného pásu E_g, a ta je dána matricí, tedy prakticky stejná). Odkaz [26]pak udává hodnotu světelného výtěžku LuAG:Ce.

je třeba využít metod přípravy materiálu za nižších teplot, např. epitaxe z kapalné fáze (LPE – Liquid Phase Epitaxy) [28] [32] [33] nebo připravit keramické materiály [34]. Vliv na tvorbu LuAl antisite defektů má ovšem i složení materiálu, např. při přebytku Lu_2O_3 vznikají i v keramikách [31].

Za druhé, potlačit nežádoucí projevy antisite defektů s tím, že jejich množství se výrazně nezmění. Zde byly s úspěchem použity dva přístupy: „band-gap engineering“ [35] [36] [37] [38] [39] [40] [41] [42] [43] a „defect engineering“ [44] [45] [46] [47] [48] [49] [50] [51] [52] [53] [54] [55] [56] [57] [58] [59][133] [60][123] [61] [62] [63] [64] [65] [66] (horní index u reference značí, že článek je součástí přílohy 2, a to na straně odpovídající číslu). Band-gap engineering využívá změny polohy vodivostního pásu, které způsobuje změna složení matrice [36] [38]. Výsledkem jsou materiály $(Lu,Gd)_3(Al,Ga)_5O_{12}$:Ce, které vykazují výrazně vyšší světelný výtěžek i zásadní potlačení pomalých složek odezvy [35] [39] [67][253] [68][231] [69].

„Defect engineering“ využívá introdukce malého množství defektů, obvykle ve formě kodopantů (připadá však v úvahu i nestechiometrické složení [44] [45] atd.). Nejúspěšnějším se zatím jeví použití iontu Mg^{2+} [54] [55] [56] [57]. Přidání Mg^{2+} v optimální koncentraci způsobí potlačení pomalých složek odezvy a zvýšení světelného výtěžku, ovšem ne takové, jakého se dosáhlo aplikací band-gap engineeringu.

Kombinace obou přístupů byla též testována, ovšem výrazného zlepšení světelného výtěžku se současným potlačením pomalých složek odezvy již dosaženo nebylo [58] [59][133] [66] [70]. V případě materiálů $(Lu,Gd)_3(Al,Ga)_5O_{12}$:Ce optimálního složení již světelný výtěžek prakticky dosahuje teoretického limitu.

Náplní práce autora habilitační práce byl výzkum vlastností scintilačních materiálů. Jmenovitě byly studovány:

1) Monokrystaly $(Lu,Gd)_3(Al,Ga)_5O_{12}$:Ce

3) LPE epitaxní filmy $(Lu,Gd)_3(Al,Ga)_5O_{12}$:Ce

4) LPE epitaxní filmy $(Lu,Gd)_3(Al,Ga)_5O_{12}$:Ce,Mg

5) LPE epitaxní filmy $Lu_3Al_5O_{12}$:Ce,Mg

Autor prováděl následující měření, včetně vyhodnocení dat:

- Amplitudová spektrometrie pro určení světelného výtěžku, jeho závislosti na nastavení elektroniky a určení energetické rozlišovací schopnosti (skupina vzorků 1-4)

- Měření scintilačních dosvitových křivek (skupiny 2-4)
- Měření termolumiscenčních charakteristik (skupiny 3 a 4)
- Měření tzv. bright burn charakteristiky (skupiny 3 a 4)

Mimo vlastních měření však k diskusi a interpretaci svých dat používá i výsledků získaných kolegy z týmu Fyzikálního ústavu AV ČR, řady spolupracujících pracovišť a samozřejmě publikací autorů z celého světa.

Habilitační práce je členěna do 8 kapitol. Úvodní kapitolu čtenář právě čte. Kapitola druhá popisuje princip aktivovaných anorganických scintilátorů se zvláštním zřetelem k Ce dopovaným granátům. Třetí kapitola se zabývá základními charakteristikami scintilačních materiálů a jejich vzájemnými vztahy. Tato kapitola rovněž uvádí konkrétní charakteristiky nekodopovaného monokrystalického LuAG:Ce jako základního referenčního materiálu a srovnává je s vybranými dalšími materiály. Čtvrtá kapitola obecně popisuje metody přípravy v práci prezentovaných materiálů – hodnotí jejich výhody a nevýhody. Kapitola pátá pojednává o metodách užitých v této práci k charakterizaci scintilátorů a rozebírá, jaké informace mohou tyto metody poskytnout.

Kapitola šestá podrobněji hovoří o mechanismu zlepšení odezvy: 1) s využitím „band-gap engineeringu“; 2) „defect engineeringu“ se zvláštním důrazem na kodopování hořčíkem. Sedmá kapitola prezentuje data získaná měřením zkoumaných vzorků a interpretuje je, a to s použitím informací z předchozích kapitol. Dále představuje především popis scintilačního mechanismu, tak jak je dnes chápán, zatímco sedmá kapitola je podrobnější interpretací s užitím tohoto modelu.

Model popsaný v šesté kapitole samozřejmě vznikal postupně, přičemž byl v důsledku nových experimentálních zjištění upravován, aby mohl být konfrontován s dalšími experimentálními daty. Autor se rozhodl v práci nerekonstruovat historický proces vzniku současného chápání scintilačního procesu ve zkoumaných materiálech. Vedou ho k tomu dva důvody. Za prvé zvolený přístup práci do určité míry zkrátí. Za druhé čtenáři předloží ucelený obraz současného konsenzu a otevřených problémů. „Historický“ pohled může čtenáři poskytnout chronologické čtení publikovaných prací v přílohách.

Kapitola osmá shrnuje dosažené výsledky a ukazuje, jakými směry se pravděpodobně bude ubírat budoucí výzkum. V přílohách se nachází stručný popis aparatur, na nichž bylo získáno největší množství experimentálních výsledků prezentovaných v práci, a články z impaktovaných časopisů, jejichž je autor habilitační práce autorem či spoluautorem.

Pro zhodnocení, je-li autor kvalifikován obdržet titul docent, je nezbytné znát autorův přínos. Osobně se autor zabývá především měřením tzv. amplitudových spekter, přičemž odezva je buzena jednotlivými částicemi ionizujícího záření. Na základě těchto měření lze stanovit veličiny jako světelný výtěžek a energetickou rozlišovací schopnost. Samo o sobě toto měření dává vcelku jasnou představu o kvalitě scintilátoru. Např. vysoký světelný výtěžek nutně znamená vysokou účinnost přenosu energie k luminiscenčnímu centru i vysokou účinnost luminiscenčního centra samého. O mechanismu scintilačního procesu se z hodnot světelného výtěžku nedá zjistit prakticky nic dalšího.

Určitým zlepšením je měření závislosti světelného výtěžku na časové konstantě zesilovače, jenž zpracovává impulzy z předzesilovače, k němuž je připojen fotonásobič registrující scintilační fotony. Do tohoto na Oddělení optických materiálů již dříve provozovaného měření autor přinesl užitečné inovace. Během vypracování disertační práce zavedl praxi měření s jedním umístěním vzorku a změřením při všech časových konstantách zesilovače. To vedlo ke značnému zvýšení přesnosti měření [71].

Měření závislosti světelného výtěžku na časové konstantě zesilovače poskytuje informace o kinetice scintilačního dosvitu – to je obecně známý fakt. Řada vědců však, neznaje přesně práci aparatury pro amplitudovou spektrometrii, výsledky interpretuje značně zjednodušeně a v konečném důsledku i nesprávně. Očekávají, že pokud je poměr světelného výtěžku při časové konstantě 0,5 μs a 1 μs např. 1,15, muselo být v čase 0,0-1,0 μs vyzářeno o 15 % více fotonů než v čase 0,0-0,5 μs.

Autor vypracoval metodu umožňující převést změřený scintilační dosvit na závislost světelného výtěžku a metodu komplementární, umožňující převod opačným směrem, nicméně vzhledem k malému množství experimentálních bodů s podstatně nižší přesností. S využitím těchto metod ukázal přesný, netriviální vztah mezi oběma charakteristikami [72][142].

Autor dále umožnil výpočet světelného výtěžku epitaxních filmů buzených zářením alfa. Do té doby byly světelné výtěžky udávány buď relativně k referenčnímu vzorku, nebo se udávaly pouze tzv. fotoelektronové výtěžky. V důsledku toho byly hodnoty výtěžků obtížně srovnatelné s hodnotami z literatury, zvláště v případě nebyla-li známa absolutní hodnota světelného výtěžku pro referenční vzorek. I když je světelný výtěžek určen s nižší přesností, než v případě monokrystalických materiálů buzených zářením gama, představuje jeho určení užitečný nástroj pro srovnání vzorků různých výzkumných týmů mezi sebou [73][214].

Ve své disertační práci vysvětlil autor tvar spektra vzorků epitaxních filmů s tloušťkou nižší, než je dosah α částic. Pravdou je, že tyto vzorky se díky optimalizaci technologie přípravy filmů již vyskytují pouze ojediněle. Autor popis tvaru spektra naposledy použil při recenzním řízení článku, v němž byly takto tenké vzorky charakterizovány. V této práci se daný model uplatnil pouze u studie o epitaxních filmech z roku 2013 [74][248].

Autor prohloubil pohled na výsledky měření kinetiky scintilační odezvy, jež se provádí pomocí jednoduché aparatury sestávající z fotonásobiče a osciloskopu. Výhodou této metody je vysoká rychlost měření proti typické konkurenční metodě TCSPC (Time correlated single photon counting). Bohužel však výsledky získané touto rychlejší metodou vykazují za určitých okolností artefakty a nepřesnosti. Autor vysvětlil původ těchto artefaktů a přibližně stanovil, na jakých parametrech jejich výskyt závisí, a jaké jsou meze použitelnosti měření.

Konečně se autor důsledně snaží interpretovat výsledky měření světelného výtěžku pomocí využití dat z jiných charakterizačních metod, především radioluminiscence, fotoluminiscenčních a scintilačních dosvitů, ale i dalších. Díky tomu je schopen získat dodatečné informace, např. o účinnosti transportu energie S k luminiscenčnímu centru. Ty pak lze využít k interpretaci dalších dat, např. zhodnocení pravděpodobnosti zachycení v pasti η_{tr} [75].

Poznámka: Pokud není uvedena nejistota měření, je výsledek měření zaokrouhlen tak, že nejistota se týká posledního platného místa (např. světelný výtěžek uvedený jako 22 500 foton/MeV má nejistotu menší než 500 foton/MeV). Jedná se o běžnou praxi v oboru (nikoli však všeobecnou), což lze ověřit letmým nahlédnutím do literatury o scintilačních materiálech. Pravděpodobně je dána tím, že rozdíly mezi individuálními vzorky jsou často větší než nejistota měření. Jelikož není časově a finančně únosné připravit množství vzorků, které by umožnilo i tento zdroj nejistoty zahrnout, není tato udávána vůbec.

Poznámka k referencím: Odkazuje-li autor na články, které jsou jeho prací, činí tak ve formátu $[X]^{Y}$, kde X je číslo reference podle pořadí výskytu a Y číslo strany v příloze 2 této práce, kde se nachází kompletní citovaný článek.

Kapitola 2

Princip aktivovaných anorganických scintilátorů

2.1. Průběh scintilačního procesu

Scintilátor je materiál, jenž převádí energii ionizujícího záření na energii fotonů z oblasti UV záření a viditelného světla. Zdůrazněme, že emise scintilačních fotonů je formou luminiscence, v tomto případě stimulovaná ionizujícím zářením, tj. např. čerenkovovy fotony nejsou fotony scintilačními.

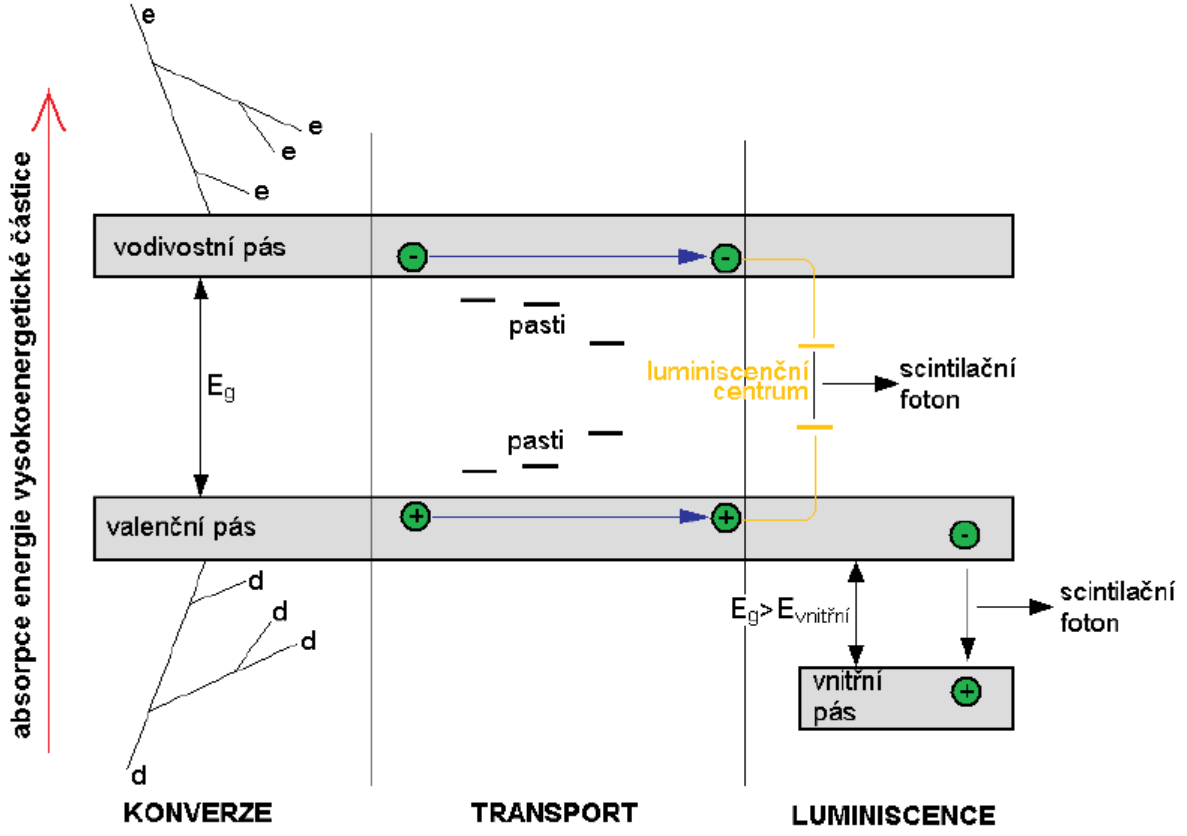

Obr. 2.1 - Schéma scintilačního procesu v anorganických scintilátorech. E_g – šířka zakázaného pásu, $E_{vnitřní}$ – šířka pásu mezi vnitřním a valenčním pásem, e – elektron, d – díra [76].

Scintilační proces se skládá z několika kroků, které ukazuje schéma na obr. 2.1 [76]. Nejdříve probíhá fáze konverze, na jejímž počátku částice ionizujícího záření předává energii elektronům ve scintilátoru. Povětšinou se jedná o elektrony z hlubších, vnitřních pásů. Vznikají tak vysokoenergetické elektrony a hluboce ležící díry. Interakci lze považovat za prakticky okamžitou [77].

Po interakci následuje relaxace. Elektrony předávají svoji energii elektronům s energií nižší, elektrony se postupně přesouvají do vodivostního pásu. Díry ve vnitřních pásech jsou zaplňovány elektrony z vyšších pásů. Uvolněná energie se předává elektronům ve valenčním pásu, zároveň tak ve valenčním pásu vznikají další díry. Na konci elektron-elektronové relaxace, tj. asi za 10^{-15}-10^{-13} s se nachází elektrony ve vodivostním pásu a díry v pásu valenčním, přičemž mají nižší energii, než je dvojnásobek šíře zakázaného pásu E_g, viz obr. 2.2 [78]. Následující ztráty energie nevedou ke vzniku nových vodivostních elektronů a děr.

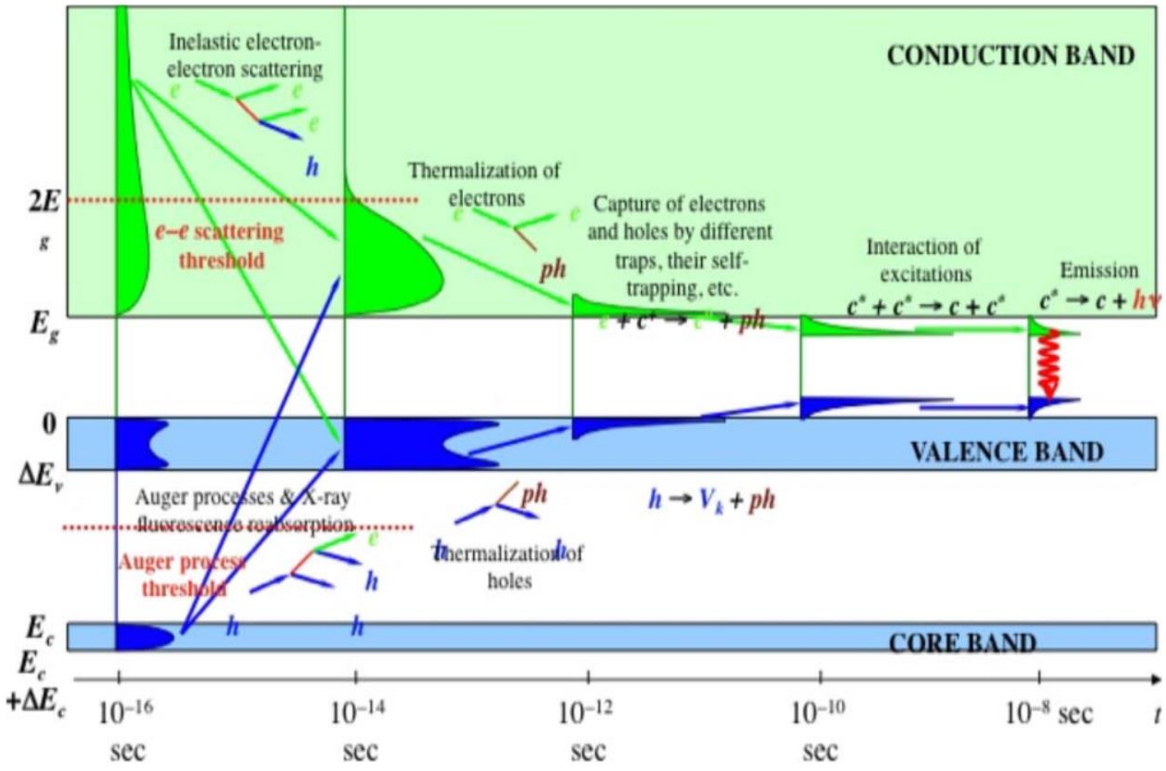

Obr. 2.2 - Schéma relaxačního mechanismu ve scintilátoru, ukazující, jak elektrony a díry v čase ztrácejí energii [78]**.**

Elektrony ve vodivostním pásu a díry ve valenčním nicméně mají přebytek energie, která se uvolňuje během tzv. termalizace. Elektrony se přesouvají na dno vodivostního pásu, díry na vrchol valenčního pásu. Přebytečná energie se mění převážně v teplo, uvolňují se fonony – odtud název termalizace [77] [78].

Již během termalizace nicméně může docházet k emisi luminiscenčních fotonů. Jedná se o jeden z nejrychlejších luminiscenčních procesů, tzv. HIBL (Hot-Intraband Luminescence) [79] [80] [81]. Emisi fotonů lze z hlediska „klasické“ luminiscence prostřednictvím luminiscenčního centra, jakým je např. iont Ce^{3+}, považovat za prakticky okamžitou. HIBL považuje řada vědců za nadějnou možnost, jak výrazně zlepšit tzv. CTR (Coincidence timing resolution), tj.

koincidenční časové rozlišení [82]. K naplnění takových nadějí je ovšem nezbytné řádově zvýšit účinnost [83], neboť HIBL je sice procesem nesmírně rychlým, ale zároveň značně neefektivním. Publikované hodnoty světelného výtěžku HIBL se pohybují přibližně kolem 5-35 fotonů/MeV [80]. Pro srovnání, nejnižší světelný výtěžek v praxi užívaných scintilátorů vykazuje $PbWO_4$, a to několik málo set fotonů/MeV.

Vlastní interakce, elektron-elektronová relaxace a termalizace, na rozdíl od následujících fází scintilačního procesu, nejsou přímým předmětem zájmu habilitační práce. Po skončení termalizace, se během tzv. fáze migrace (někdy též transportu) mohou nosiče náboje (tj. elektrony a díry) materiálem volně pohybovat [76] [77].

Z hlediska habilitační práce je obzvláště důležitou možnost zachycení nosičů náboje v pastech. Pasti jsou energetické stavy, v nichž může být zachycen elektron (typicky např. kyslíková vakance) nebo díra. Pasti jsou charakterizovány především tzv. frekvenčním faktorem s a hloubkou pasti (více v části o termoluminiscenci). Čím nižší frekvenční faktor a čím větší hloubka pasti, tím je delší setrvání nosiče v ní.

Délka setrvání nosiče náboje v pasti je vysoce variabilní, pohybuje se od hodnot tak nízkých, že lze vliv pastí na odezvu scintilátoru prakticky zanedbat, až po doby v řádu let i delší. Vliv pastí na odezvu je poměrně komplexní téma, v tuto chvíli si povšimneme dvou možností. Při krátkém setrvání nosiče náboje v pasti dochází k prodloužení doby dosvitu, scintilační foton však lze stále přiřadit k interakci částice, jejž foton vyvolala. Negativním efektem je především snížení maximální měřitelné četnosti impulzů či zhoršení CTR.

Dlouhé setrvání lze efektivně považovat za ztrátu excitační energie. Foton sice nakonec může být vyzářen, impulz však již dávno odezněl. Snížením počtu využitelných fotonů dochází ke zhoršení energetické rozlišovací schopnosti i CTR. Pozdní emise fotonu dokonce může falešně přispět k jinému impulzu a tím zhoršit energetickou rozlišovací schopnost ještě více. Tento tzv. „detrapping noise“ se může významně uplatňovat v některých polovodičových detektorech a polovodičových součástkách [84], u scintilátorů se uvažuje podstatně méně.

Žádoucím zakončením fáze migrace je rekombinace nosičů náboje v luminiscenčním centru, která vede k jeho excitaci. Právě během deexcitace dochází k emisi luminiscenčních fotonů. Po skončení fáze luminiscence se scintilátor navrací do původního stavu. Fázi luminiscence pojednáme podrobněji v následující podkapitole.

Je třeba říci, že hranice mezi jednotlivými fázemi není ostrá. Např. elektrony se během termalizace již pohybují, tedy migrují. Naopak elektrony zachycené v pastech a posléze z nich se značným zpožděným uvolněné se stále nacházejí ve fázi migrace, ačkoliv většina fáze luminiscence již proběhla. HIBL je luminiscenčním procesem, který probíhá během termalizace. Tzv. „cross-luminescence“, velmi rychlá luminiscence uplatňující se v materiálech s $E_{vnitřní} < E_g$ [85], viz obr. 2.1, probíhá, když ještě nejsou všechny díry ve vodivostním pásu. Nicméně i přes tyto drobnosti je výše uvedené rozdělení scintilačního procesu užitečným nástrojem pro jeho popis.

2.1.1. Luminiscence

Obecně je luminiscence jakákoliv stimulovaná emise fotonů UV, IR záření i viditelného světla. Energii nezbytnou ke stimulaci luminiscence lze dodat různými způsoby: teplotou (termoluminiscence), světlem (fotoluminiscence), tlakem (triboluminiscence), energií chemických reakcí (chemiluminiscence), zářením X (radioluminiscence), urychlenými elektrony (katodoluminiscence), atd. O scintilaci hovoříme tehdy, když excitační energii dodá částice ionizujícího záření.

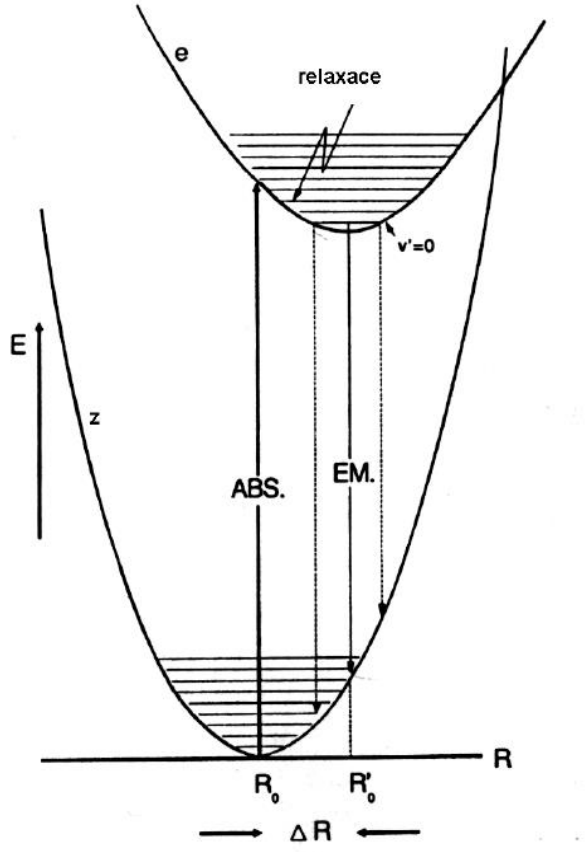

Obr. 2.3 – Konfiguračně koordinační diagram systému o základním stavu z a vzbuzeném stavu e [86]**.**

K základnímu výkladu fyziky luminiscence použijeme tzv. konfiguračně koordinační diagram, viz obr. 2.3 [86]. Obrázek reprezentuje luminiscenční centrum se dvěma energetickými elektronovými stavy: základním a vzbuzeným. Předpokládejme pro zjednodušení, že luminiscenční centrum se nachází mezi ligandy, které kolem iontu kmitají ve fázi, viz obr. 2.4 [86].

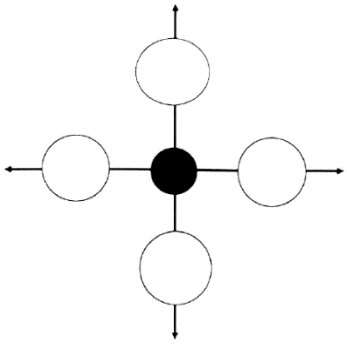

Obr. 2.4 – - Kmity ligandů (bílé kruhy) kolem kovového iontu (černý kruh) [86]**.**

Síla působící na ligandy má velikost $F = -k (R - R_0)$, kde R_0 je rovnovážná poloha, tedy potenciální energie $E = ½ k (R – R_0)^2$. Řešení pro takový potenciál je v kvantové mechanice dobře známé. $E_v = (v + ½)\cdot h\nu$, kde $v = 0, 1, 2...$ a ν je frekvence oscilátoru. Pokud $v = 0$, je nejpravděpodobnější nalezení systému v poloze blízké R_0, při vyšších v, pak v polohách symetricky kolem R_0 rozložených [86].

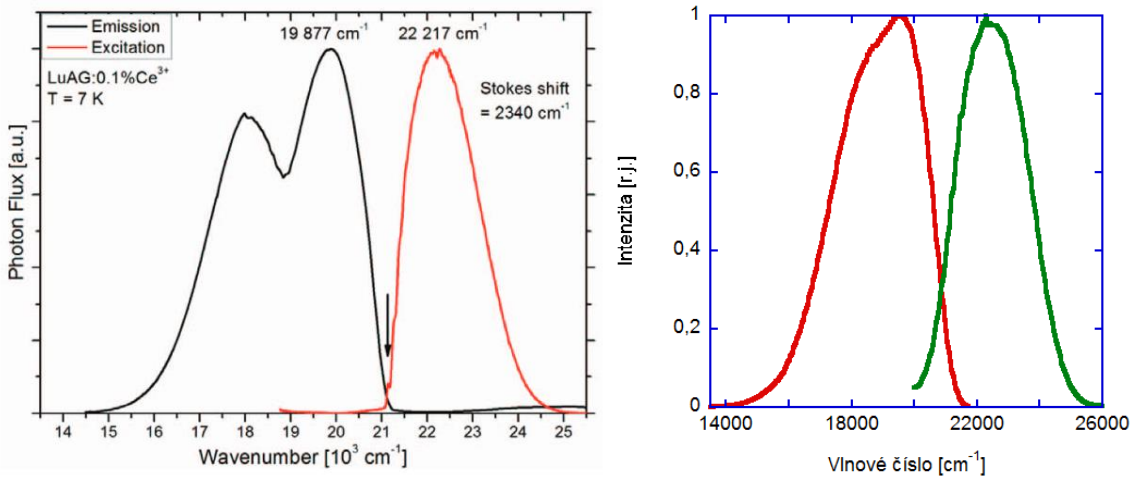

Obr. 2.5 – - Vlevo: Emisní a excitační spektrum LuAG:Ce při teplotě 7 K. Šipka označuje přechod mezi tzv. „zero-phonon lines“. Je uveden Stokesův posun [87]**. Vpravo: Emisní a excitační spektrum LuAG:Ce epitaxního filmu (vzorek 1LM1) při pokojové teplotě.**

Když si vyneseme pro základní stav a každou vibrační hladinu body s nejpravděpodobnějším R, budou se tyto body nacházet na dolní parabole. Když totéž učiníme pro vzbuzený stav,

získáme horní parabolu. V případě obr. 2.3 $\Delta R = R_0' - R_0 \neq 0$. Některá luminiscenční centra vykazují vzbuzené stavy s nulovým ΔR (typicky 4f-4f přechody), pro scintilátory je však nenulovost ΔR zásadní.

Konfiguračně koordinační diagram umožňuje vysvětlení celé řady jevů a charakteristik scintilačních materiálů. Naprostým základem je podoba a teplotní závislost absorpčních, emisních a excitačních spekter.

Obrázek 2.5 [87] ukazuje rozdíl mezi excitačními a emisními spektry LuAG:Ce měřenými při teplotě 7 K a pokojové teplotě (300 K). Při teplotě 7 K se prakticky všechny luminiscenční centra Ce^{3+} nachází v základním, tj. v nejnižším možném stavu. Vzbuzený stav může být excitován fotony různých vlnových délek, ovšem s největší účinností se tak děje podél šipky označené ABS v obr. 2.3 [86]. Je však možný i přechod mezi oběma nejnižšími vibračními substavy. Ten je označen šipkou v obr. 2.5 [87].

Při pokojové teplotě se již řada center nachází i na vyšších vibračních hladinách a k absorpci dochází i z nich. Pásy v absorpčních a excitačních spektrech se tedy proti situaci při teplotě 7 K rozšiřují, jak ukazuje obr. 2.5 [87]. Zcela analogická je situace u emisních spekter. Při teplotě 7 K se prakticky všechny emise uskutečňují ze stavu „zero-phonon line“, při pokojové teplotě tomu tak není a opět dochází k rozšíření.

Obr. 2.3 [86] vysvětluje i tzv. teplotní zhášení. Při vyšších teplotách se elektrony ve vzbuzeném stavu mohou s nezanedbatelnou pravděpodobností dostávat na vibrační hladiny v okolí průsečíku parabol e a z v obr. 2.3 [86]. Z tohoto bodu může elektron nezářivě deexcitovat (zrelaxovat) postupnou emisí většího množství fononů, v důsledku čehož se veškerá excitační energie přemění v teplo. Luminiscenční účinnost Q začíná velmi rychle klesat s rostoucí teplotou. Teplota, od které se výrazně uplatní toto, tzv. teplotní zhášení, velmi silně závisí na matrici i luminiscenčním centru.

Existuje i jiná možnost přeměny excitační energie na teplo, tzv. multifononová emise. Jde o nezářivý přechod, při němž nejsou fonony emitovány postupně, ale najednou – tolik kolik odpovídá délce šipky EM v obr. 2.3 [86] děleno energie jednoho fononu. V případě obr. 2.3 by to odpovídalo asi 40 fononům, což je extrémně nepravděpodobné. Některým materiálům postačí emitovat jednotky fononů, což již nevede k zanedbatelné pravděpodobnosti.

Před dalším výkladem ještě definujme tzv. Stokesův posun. Jedná se o rozdíl mezi emisním a absorpčním maximem (rozdíl mezi EM a ABS v obr. 2.3 nebo viz obr. 2.5). Materiály s větším

Stokesovým posunem vykazují nižší reabsorpci scintilačních fotonů, což je výhodné. Na druhou stranu luminiscenční centra s velkým Stokesovým posunem trpí obecně teplotním zhášením již při nižších teplotách.

2.2. Scintilační mechanismus LuAG:Ce

LuAG:Ce krystalizuje v kubické soustavě a je opticky izotropní. Čistý LuAG bez příměsí je bezbarvý a čirý. Kation Lu^{3+} , obklopen osmi kyslíkovými ionty, se nachází v dodekahedrální poloze. Kation Al^{3+} se nachází v poloze oktahedrální (40 % Al atomů) obklopen šesti kyslíkovými ionty nebo v poloze tetrahedrální (60 % Al atomů) obklopen čtyřmi kyslíkovými ionty [88]. Mřížková konstanta a_{LuAG} = 11,9164 Å [89].

Šíře zakázaného pásu LuAG:Ce se pohybuje kolem 7 eV, pravděpodobně je mírně vyšší [90], viz obr. 2.6 [91] a inset 2.7 [36].

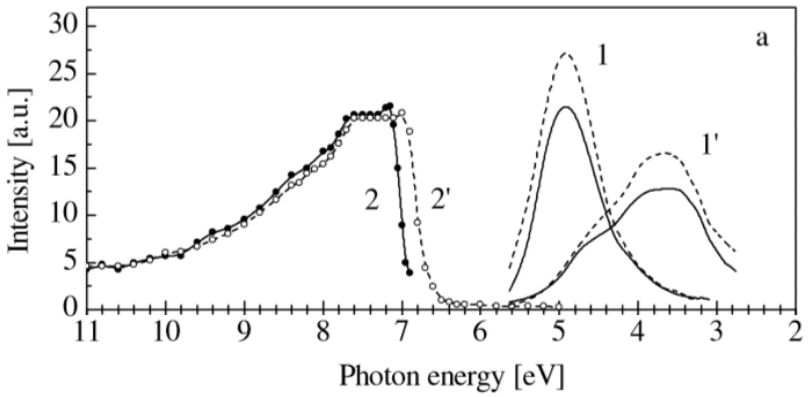

Obr. 2.6 – Emisní (E_{exc} = 7,7 eV) a normalizovaná excitační spektra LuAG měřená při 85 K (1 a 2) a 295 K (1´ a 2´) [91].

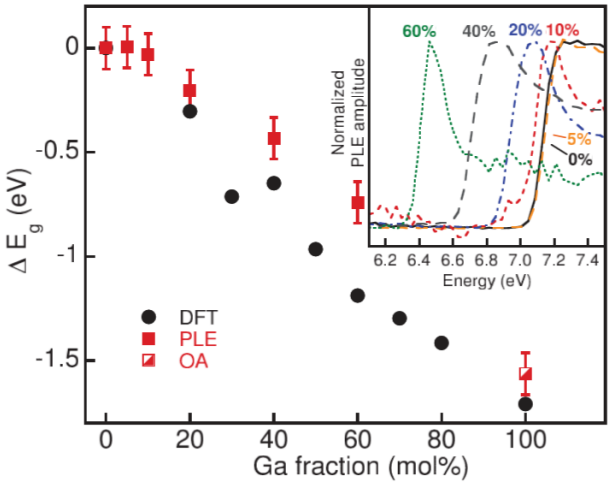

Obr. 2.7 – Změna šířky zakázaného pásu $Lu_3(Al,Ga)_5O_{12}$:Ce v závislosti na obsahu Ga stanovená výpočetně (DFT – Density Functional Theory) a experimentálně (PLE – PhotoLuminescence Excitation; OA – Optical Absorption). Inset: Excitační spektra pro různé koncentrace Ga [36].

2.2.1. Luminiscenční centrum Ce^{3+}

Naprostá většina Ce^{3+} je substituentem Lu^{3+} iontů, zaujímá tedy dodekahedrální pozici. Malá část iontů zaujímá oktahedrální polohu namísto Al^{3+} [92], obdobně jako v YAG:Ce [93]. Díky tomu, že Ce^{3+} má pouze jeden elektron ve valenční slupce, jsou jeho absorpční, emisní a excitační spektra relativně jednoduchá [94].

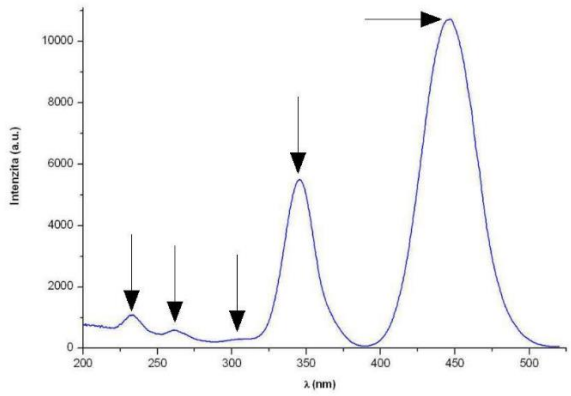

Obr. 2.8 – Excitační spektrum LuAG:Ce epitaxního filmu s pěti maximy. Emisní (E_{exc} = 7,7 eV) a normalizovaná excitační spektra LuAG měřená při 85 K (1 a 2) a 295 K (1´ a 2´) [95]**.**

Excitační spektra ukazují 5 absorpčních maxim, viz obr. 2.8 [95]. Jedná se o přechody ze základního stavu $4f^1(^2F_{5/2})$ do několika vzbuzených stavů. V řadě publikací tyto stavy bývají označovány $5d_1$ (nejdelší vlnová délka v obr. 2.8) až $5d_5$ (nejkratší vlnová délka v obr. 2.8), přesnější označení je $4f^05d^1(^2E_g)$ a $4f^05d^1(^2T_{2g})$. Nižší stav $4f^05d^1(^2E_g)$ je dvakrát rozštěpen a vyšší stav $4f^05d^1(^2T_{2g})$ je rozštěpen třikrát, viz obr. 2.9 [96] a 2.10 [97]. Nejdůležitější absorpční maxima mají vlnové délky přibližně 345 a 445 nm, viz obr. 2.8.

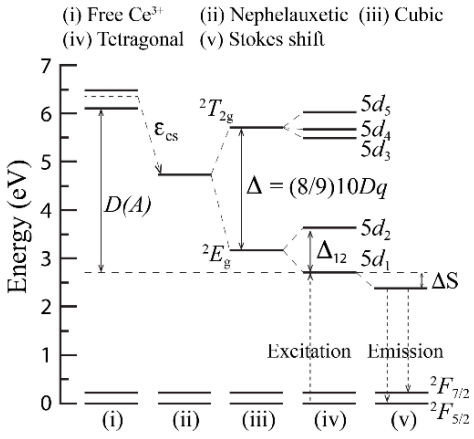

Obr. 2.9 – Energetické stavy (i) izolovaného Ce^{3+}, (ii) po započítání nefelauxetického efektu v YAG:Ce, (iii) s uvážením krystalické mříže a (iv) symetrie luminiscenčního centra. (v) již jen zohledňuje Stokesův posun. YAG:Ce je stejné struktury jako LuAG:Ce, kvalitativně se jedná o stejný systém, polohy jednotlivých stavů budou pouze mírně odlišné [96]**.**

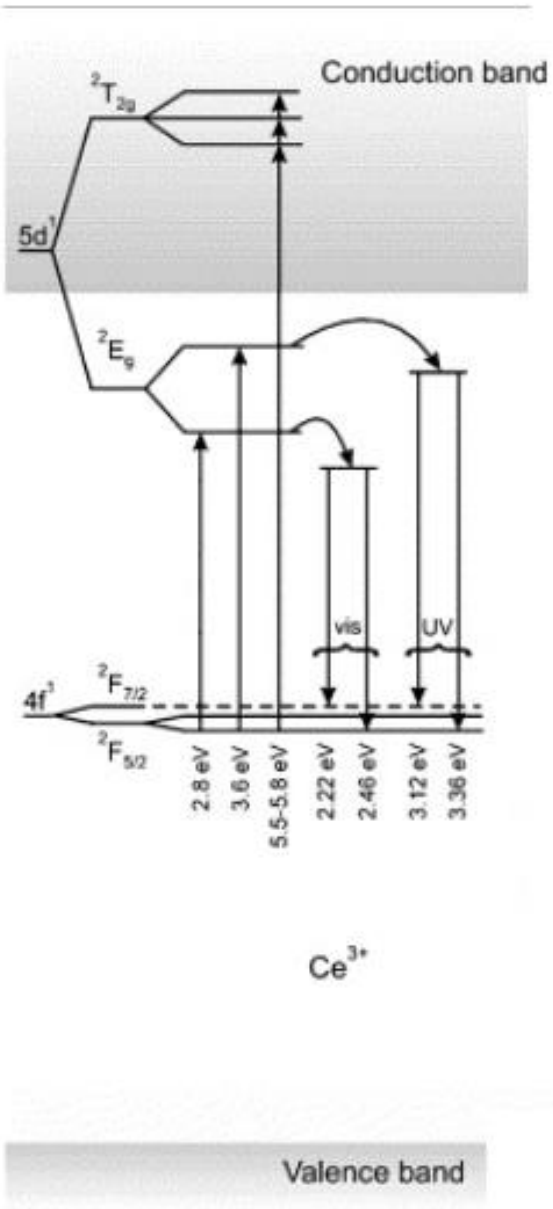

Obr. 2.10 – Energetické stavy a přechody Ce^{3+} v LuAG:Ce [97].

Emisi pozorujeme ze stavu $5d^1$ do stavů $4f^1(^2F_{5/2})$ a $4f^1(^2F_{7/2})$. V důsledku toho je v emisních spektrech Ce-dopovaných scintilátorů běžně pozorován charakteristický dublet, viz obr. 2.11. V LuAG:Ce se maximum nachází přibližně na vlnové délce 530-535 nm [21] [32], viz obr. 2.11 [95].

Na základě měření emisních a excitačních spekter při různých teplotách lze sestavit konfiguračně koordinační diagram. Situaci pro stavy $5d_1$, $4f^1(^2F_{5/2})$ a $4f^1(^2F_{7/2})$ ukazuje obr. 2.12 [87]. Právě tyto stavy jsou pro nás nejdůležitější, neboť přechody mezi nimi dominují emisi při vzbuzení Ce^{3+} excitovaného stavu v LuAG:Ce.

2.2.2. Luminiscence matrice

Radioluminiscenční spektra monokrystalického LuAG:Ce vykazují též emisi jiného původu než z Ce^{3+} centra. V případě buzení přímo Ce^{3+} excitovaných stavů uvnitř zakázaného pásu se tato luminiscence neobjevuje, viz obr. 2.11. Na druhou stranu je přítomná v radioluminiscenčním spektru nedopovaného LuAG [98], i v izostrukturním YAG [99]. Má tedy původ v samotné matrici.

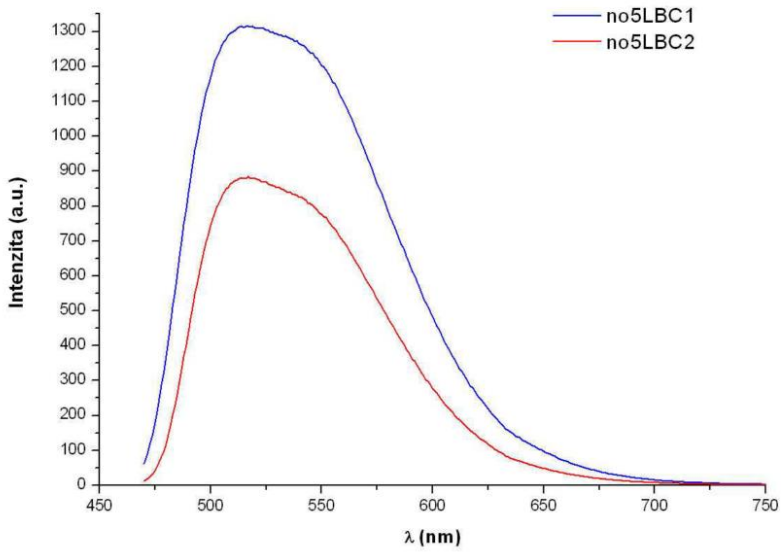

Obr. 2.11 – Emisní spektrum dvou epitaxních vrstev LuAG:Ce dvěma zřetelnými maximy. Excitační vlnová délka λ_{exc} = 445 nm [95]**.**

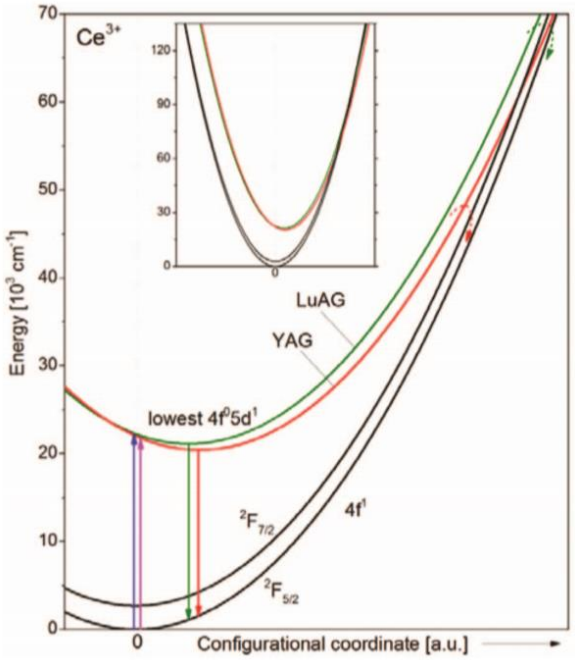

Obr. 2.12 – Konfiguračně koordinační diagram pro 4f stavy a nejnižší 5d stav v LuAG:Ce a YAG:Ce [87]**.**

Maximum emise se nachází v oblasti vlnových délek zhruba 300-350 nm, viz obr. 2.13 [100]. Emise se přisuzuje defektu spojenému s Lu_{Al} antisite defektem [101]. Za nepřímý důkaz této hypotézy lze považovat např. vymizení této emise u epitaxních granátových filmů [102] [103] a keramik [104], které jsou připravovány při podstatně nižších teplotách.

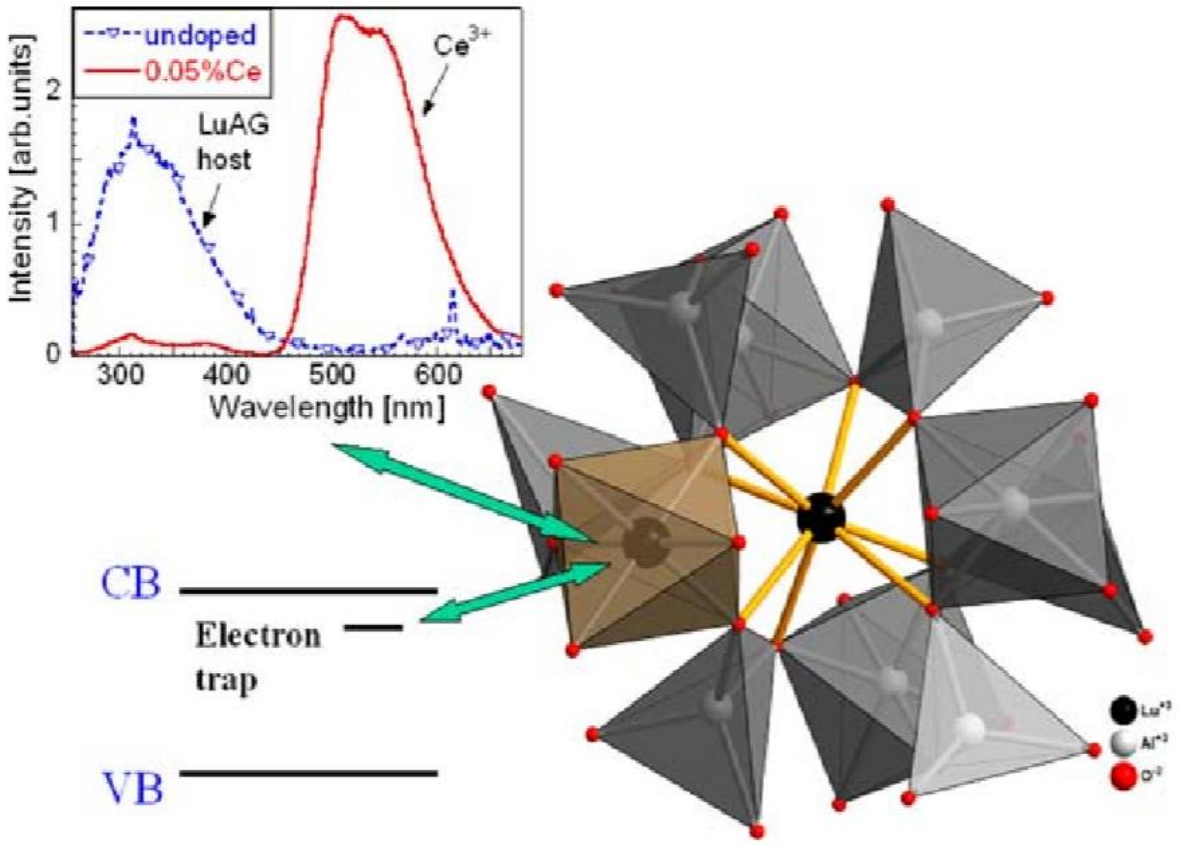

Obr. 2.13 – Lu_{Al} antisite defekt. Vlevo nahoře radioluminiscenční spektra LuAG a LuAG:Ce, obě vykazující emisi v rozmezí asi 250-450 nm připisovanou tomuto defektu. S defektem je též spojena mělká elektronová past, viz vlevo dole [100].

Kapitola 3

Základní charakteristiky scintilačních materiálů, hodnoty pro LuAG:Ce

Tato kapitola se bude zabývat pouze vlastnostmi s přímým vztahem ke zkoumané problematice, případně uvažovaným aplikacím.

3.1. Interakční parametry

Detekční účinnost pro fotony je určena rozměry, hustotou ρ a efektivním atomovým (protonovým) číslem Z_{eff}. Detekční účinnost pro jiné druhy částic diskutovat nebudeme, neboť je buď prakticky rovna 100 % (alfa částice) nebo se LuAG:Ce neuvažuje k jejich detekci (např. β záření, u nějž je výhodou spíše nízké Z_{eff}).

Hustota ρ = 6,73 $g \cdot cm^{-3}$ [103] [105] je mezi scintilátory poměrně vysoká. Z_{eff} počítáme podle vztahu [106]:

$$Z_{eff} = \sqrt[4]{\frac{xM_A Z_A^4 + yM_B Z_B^4 + zM_C Z_C^4}{xM_A + yM_B + zM_C}} \qquad \text{R- 3.1}$$

v němž Z_A, Z_B, Z_C jsou protonová čísla, M_A, M_B, M_C atomové hmotnosti atomů A, B, C ze sloučeniny $A_xB_yC_z$. Existují i jiné aproximativní vztahy, výsledky získané na základě nich se však zásadně neodlišují. R-3.1 poskytuje Z_{eff} = 63, opět relativně vysoké číslo. Scintilátor LuAG:Ce má spíše vyšší detekční účinnost, viz obr. 3.1.

Vzhledem k tomu, že k měření světelného výtěžku epitaxních filmů se užívá záření α, uvedeme si hodnoty dosahu α částic z různých radionuklidů v LuAG:Ce. ^{239}Pu (5,157 MeV) 10,15 μm, ^{241}Am (5,486 MeV) 11,25 μm a ^{244}Cm (5,805 MeV) 12,31 μm. Hodnoty byly vypočteny dle [107].

3.2. Radioluminiscenční spektrum

Radioluminiscenční spektrum již bylo uvedeno na obr. 2.13. Dosud jsme však nehodnotili praktické dopady tvaru radioluminiscenčního spektra. Požadujeme především, aby se radioluminiscenční spektrum nepřekrývalo se spektrem absorpčním, k čemuž obvykle postačí dostatečný Stokesův posun. Dále je žádoucí, aby co největší procento scintilačních fotonů bylo

emitováno v oblasti největší citlivosti fotodetektoru, kterým může být fotonásobič, fotodioda, SiPM (Silicon PhotoMultiplier) atd.

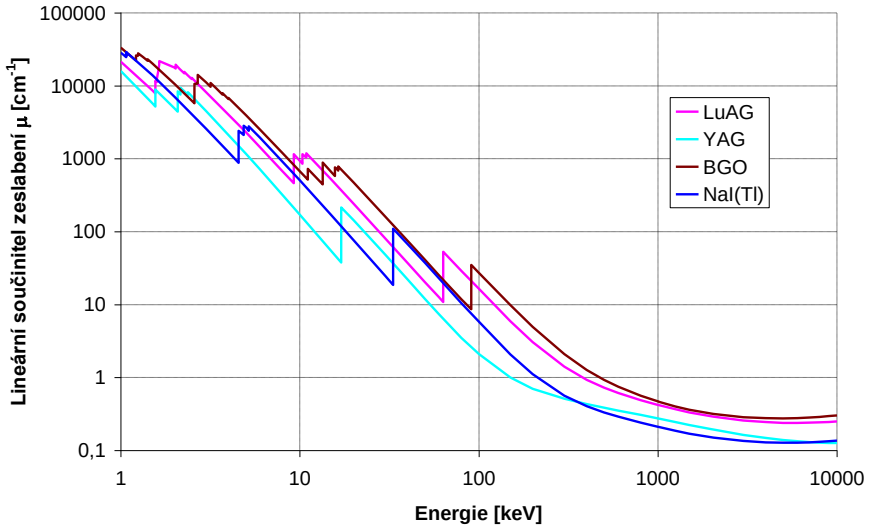

Obr. 3.1 – Lineární součinitele zeslabení YAG, LuAG, BGO a NaI(Tl) vypočtené pomocí programu X-COM [108]**.**

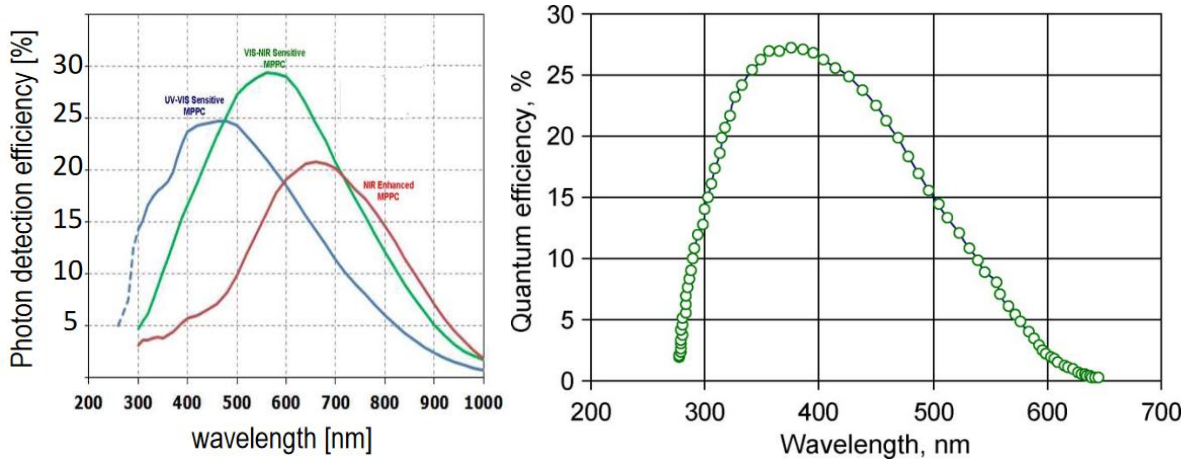

Obr. 3.2 – Kvantová účinnost MPPCs firmy Hamamatsu (vlevo) [109]**, kvantová účinnost fotokatody fotonásobiče R1306 užívaného ve scintilační technice (vpravo)** [110]**.**

Obr. 3.2 vlevo [109] ukazuje kvantové účinnosti některých MPPC (Multi-Pixel Photon Counter, v podstatě SiPM) fotodetektorů, obr. 3.2 vpravo fotonásobičů [110]. Porovnáním s obr. 2.13 (radioluminiscenční spektrum LuAG:Ce) je zřejmé, že LuAG:Ce i další Ce-dopované granáty, na rozdíl od většiny „tradičních“ scintilátorů, emitují v oblasti delších vlnových délek, tedy v oblasti vyšší účinnosti polovodičových fotodetektorů. Vzhledem k značnému rozvoji jejich využití, především ve formě SiPM, to může do budoucna představovat výhodu [111]

[112] [113]. S maximem citlivosti klasických fotonásobičů se maximum emise LuAG:Ce nekryje.

3.3. Světelný výtěžek, integrální scintilační účinnost

Nechť v důsledku interakce jedné částice o energii E vznikne N_f scintilačních fotonů, a to v čase od okamžiku interakce do nekonečna. Pak platí [114] [77]:

$$N_f = \frac{E}{\beta E_g} SQ \qquad \text{R-3.2}$$

Kde E_g je šířka zakázaného pásu, S kvantová účinnost transportu, Q kvantová účinnost luminiscenčního centra a β fenomenologický parametr, jeho hodnota se pro většinu materiálů a pro fotonové záření pohybuje mezi 2-3. Hodnota β v podstatě představuje podíl energie využité k tvorbě jednoho páru ku šířce zakázaného pásu, hodnota zlomku pak počet vzniklých elektron děrových párů.

Podělením N_f energií E získáme veličinu η_{sc}, tj. integrální scintilační účinnost:

$$\eta_{sc} = \frac{N_f}{E} = \frac{SQ}{\beta E_g} \qquad \text{R-3.3}$$

která vyjadřuje, jak velký počet scintilačních fotonů bude emitován na jednotku energie. Hodnota η_{sc} pro záření α bývá v naprosté většině případů několikrát, byť ne řádově, nižší než pro záření γ. Rozdíly až v řádu desítek procent se mohou vyskytnout i v závislosti na energii interagující částice.

Světelný výtěžek je s η_{sc} velmi úzce související veličinou. Měříme-li odezvu vyvolanou jednou částicí, je nejen nepraktické, ale i nemožné čekat do nekonečna na sebrání všech scintilačních fotonů. Světelný výtěžek (LY – light yield) je tak definován jako velikost odezvy vyjádřená v počtu fotonů, která je naměřena určitým způsobem nastavenou aparaturou. Pokud má mít hodnota světelného výtěžku nějaký smysl, je nezbytné způsob jeho měření udat. V případě aparatury použité v této práci jsou podstatné především použité přístroje, časová konstanta zesilovače a způsob tvarování impulzu. Rozdílné nastavení při měření světelného výtěžku je jednou z příčin značného rozptylu publikovaných hodnot LY.

V případě okamžitého vyzáření všech fotonů by platilo η_{sc} = LY. I při zanedbatelném množství pomalejších složek odezvy můžeme tuto rovnost považovat za platnou. Pokud však jsou fotony

emitovány ve větším množství s výraznějším zpožděním, platí: LY < η_{sc}. Rozdíl může být poměrně malý, ale při převaze pomalých fotonů i několikanásobný.

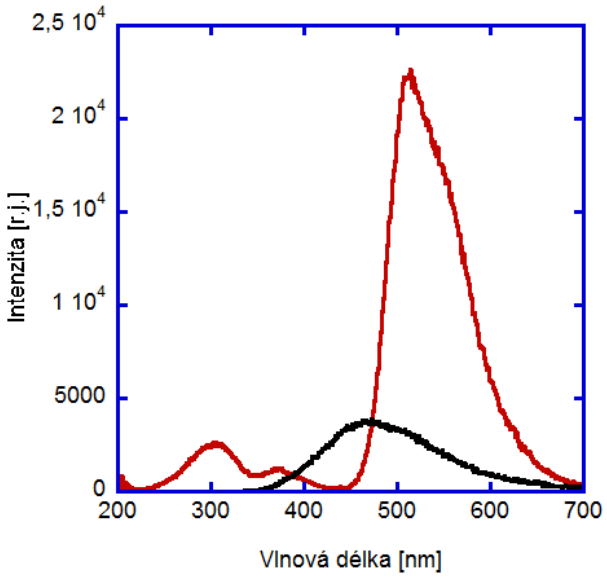

Obr. 3.3 – RL spektra LuAG:Ce epitaxního filmu (červeně) a BGO krystalu (černě).

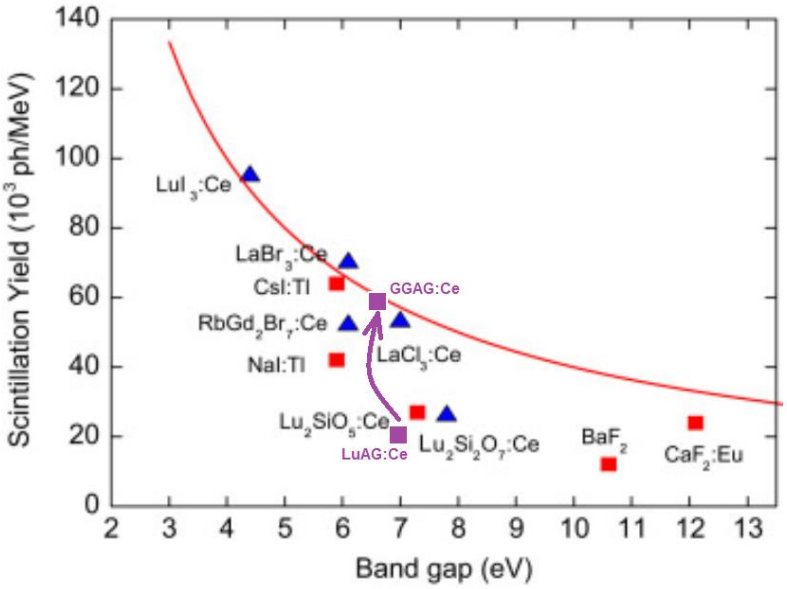

Obr. 3.4 – Přibližný teoretický limit světelného výtěžku v závislosti na šířce zakázaného pásu [13]**. Autor habilitační práce doplnil body pro LuAG:Ce a GGAG:Ce ($Gd_3Al_5O_{12}$:Ce). Šipka ukazuje, jakého zlepšení bylo dosaženo aplikací „band-gap engineeringu“.**

Velmi dobře to lze demonstrovat při srovnání světelného výtěžku a intenzity radioluminiscenčního spektra BGO a právě LuAG:Ce. BGO totiž patří k materiálům, jež mají pomalou složku odezvy zanedbatelnou a můžeme proto předpokládat η_{sc} = LY. Obr. 3.3 ukazuje RL (radioluminiscenční) spektrum epitaxního filmu LuAG:Ce a BGO. Vidíme téměř

čtyřnásobný rozdíl v intenzitě RL spekter, přitom rozdíl ve světelných výtěžcích je velmi přibližně dvojnásobný [115]. To jasně indikuje přítomnost pomalých složek odezvy LuAG:Ce, jež nepřispívají k hodnotě světelného výtěžku.

Obr. 3.4 zobrazuje přibližný teoretický limit světelného výtěžku v závislosti na šířce zakázaného pásu [13]. LuAG:Ce se nachází poměrně hluboko pod tímto teoretickým limitem. Optimalizací LuAG:Ce by tedy mělo být možné dosáhnout značného zlepšení vlastností tohoto materiálu.

Pro světelný výtěžek lze v principu zavést obdobný vztah vztahu R-3.3:

$$LY = \frac{S_{LY} Q_{LY}}{\beta E_g} \qquad \text{R-3.4}$$

S_{LY} , resp. Q_{LY} bychom pak chápali jako účinnost transportu, resp. účinnost luminiscenčního centra z hlediska světelného výtěžku, tj. procento excitační energie, jež „stihne včas dorazit" k luminiscenčnímu centru, resp. procento excitovaných luminiscenčních center, jež „stihne včas" zářivě deexcitovat. V praxi se však s veličinami S_{LY}, resp. Q_{LY} nesetkáme.

Světelný výtěžek není přímo měřenou veličinou, tou je tzv. výtěžek fotoelektronový (PhY – Photoelectron Yield). Vztah mezi nimi je triviální:

$$PhY = LY \times Q_{PD} \qquad \text{R-3.5}$$

Kde Q_{PD} je kvantová účinnost fotodetektoru, jež závisí na emisním spektru a liší se pro každý materiál. Fotoelektronový výtěžek je tak vlastností nejen materiálu, ale systému materiál-fotodetektor.

Světelný výtěžek pro LuAG:Ce při časové konstantě zesilovače 1 μs (semigausovské tvarování) činí velmi přibližně 12,5-26 fotonů/keV [116] [25]. Vysoký rozptyl je způsoben rozdíly ve zpracování signálu, ale i reálně existujícími rozdíly mezi různými krystaly LuAG:Ce.

3.4. Energetická rozlišovací schopnost a neproporcionalita

Energetická rozlišovací schopnost se nejčastěji kvantifikuje jako tzv. FWHM (Full Width on Half Maximum), tj. plnou šířku píku úplné absorpce v polovině jeho maxima. Vzhledem k tomu, že proces vzniku signálu, včetně samotného scintilačního procesu, je komplexní, různé stochastické procesy přispívají k zvýšení rozptylu FWHM proti ideální situaci. Následující výklad je založen především na referenci [117].

Energetickou rozlišovací schopnost ΔE/E lze rozepsat jako:

$$(\Delta E/E)^2 = (\delta_{sc})^2 + \left(\delta_p\right)^2 + (\delta_{st})^2 + (\delta_n)^2 \qquad \text{R-3.6}$$

kde δ_{sc} je intrinsická rozlišovací schopnost krystalu, δ_p zohledňuje vliv transportu fotonů k fotodetektoru, δ_{st} je statistický rozptyl počtu nosičů informace z fotodetektoru a δ_n zastupuje příspěvek temného proudu/pulzů.

Intrinsická rozlišovací schopnost δ_{sc} velmi úzce souvisí s tzv. neproporcionalitou scintilátoru, což je v podstatě míra (ne)závislosti světelného výtěžku na energii částice [118]. Čím lepší je proporcionalita, tím nižší je δ_{sc}. Učebnicovým příkladem vlivu neproporcionality je dvojice scintilátorů LSO:Ce a BGO. Oba mají prakticky totožnou energetickou rozlišovací schopnost i přes to, že BGO má asi 4× nižší LY(PhY) [119].

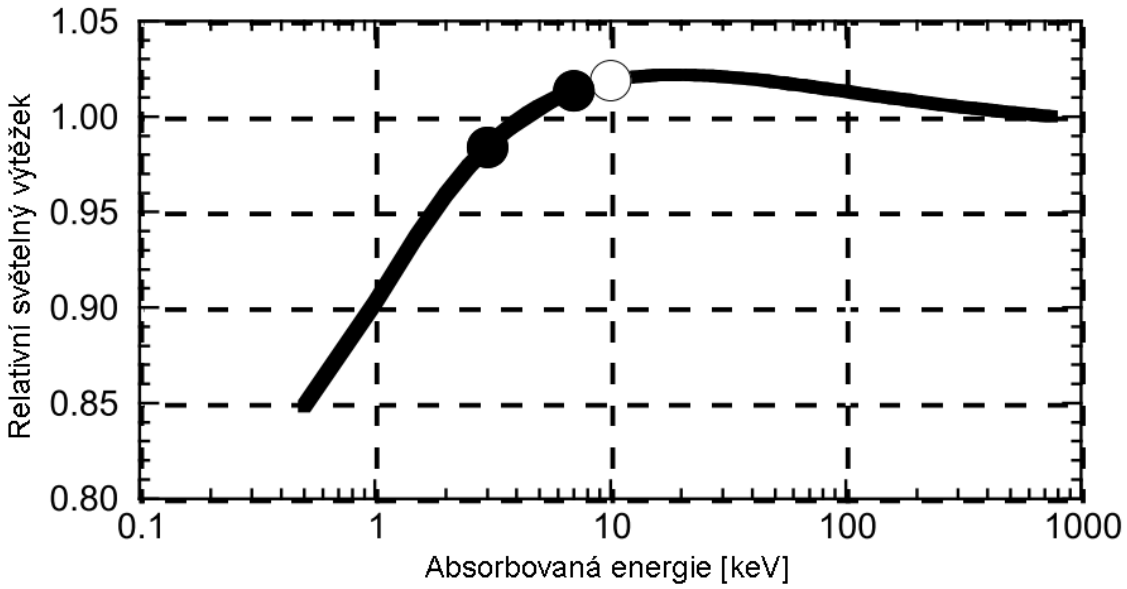

Obr. 3.5 – Relativní světelný výtěžek hypotetického scintilátoru v závislosti na energii a vliv této závislosti na rozlišovací schopnost scintilátoru [120]**.**

Obr. 3.5 ukazuje možnou závislost relativního světelného výtěžku na energii a zároveň dvě možnosti uložení energie 10 keV ve scintilátoru. 1) jedním 10 keV elektronem (bílý kruh), 2) jedním 3 keV a druhým 7 keV elektronem (černé kruhy). Třebaže je energie totožná, v druhém případě je odezva nižší. Jelikož může být stejná energie uložena nekonečně mnoha způsoby, vede popsaný jev ke zhoršení rozlišovací schopnosti.

Nyní víme, že rozlišovací schopnost závisí na neproporcionalitě. Kde má ovšem příčiny samotná neproporcionalita? V práci není prostor na důsledný rozbor současných teorií s tímto tématem, namísto toho si pouze naznačíme jejich východiska. Rozdíl v odezvách závisí především na hustotě ionizace přímo ionizujících částic (ať už primárních či sekundárních). V případě velmi husté ionizace dochází k vzájemné interakci vytvořených nosičů náboje a excitovaných stavů, která velmi často vede k energetickým ztrátám (nezářivým přechodům). Světelný výtěžek se s rostoucím lineárním přenosem energie (LPE_Δ) snižuje. To je typické pro většinu scintilátorů.

V případě některých dalších scintilátorů, mimo jiné NaI:Tl, pozorujeme s růstem LPE_Δ nejdříve růst odezvy, teprve pro vysoká LPE_Δ odpovídající elektronům s energiemi pod 20 keV (u NaI:Tl) se opět dostaví pokles odezvy. Nízká hustota ionizace a vysoká počáteční mobilita elektronů vede k tomu, že se elektrony a díry v prostoru navzájem značně vzdálí a nemohou spolu rekombinovat. Při vyšších LPE_Δ se pravděpodobnost zářivé rekombinace zvyšuje, zatímco pravděpodobnost interakcí nosičů náboje a excitovaných stavů vedoucích ke ztrátám energie zůstává relativně nízká. Až při vyšších LPE_Δ tyto ztráty převládnou.

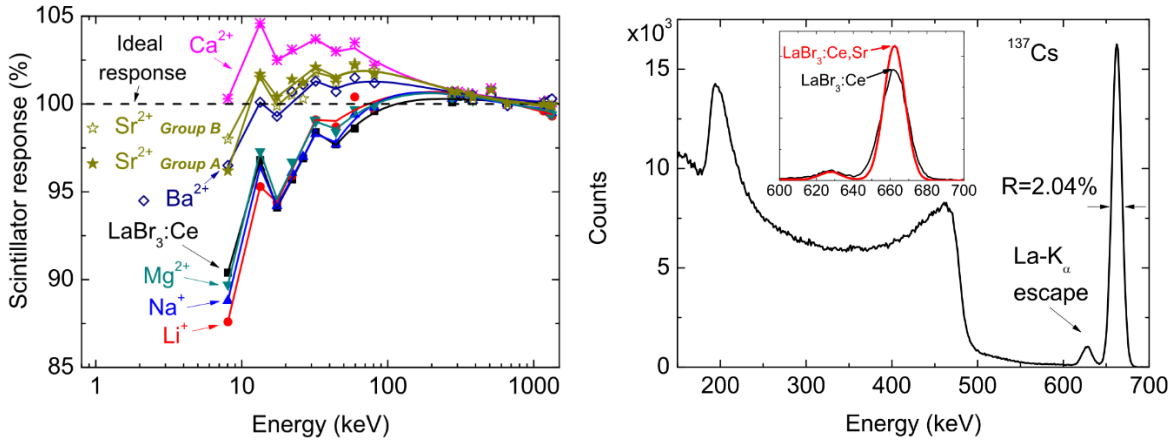

Obr. 3.6 – Vlevo: Závislost relativního světelného výtěžku na energii pro různě kodopovaný $LaBr_3$:Ce. Vpravo: Spektrum ^{137}Cs (662 keV) měřené $LaBr_3$:Ce,Sr. Inset: Srovnání FWHM Sr kodopovaného a nekodopovaného $LaBr_3$:Ce [121].

Souvislost neproprocionality, intrinsické rozlišovací schopnosti a mobility nosičů náboje je stále otevřený problém. V posledních letech bylo nicméně dosaženo značného pokroku ve snaze vypracovat teorie co nejpřesněji popisující a vysvětlující pozorované skutečnosti, např. viz [122] [123] [124] [125].

Je to i problém velmi praktický, protože úpravou technologie výroby scintilátoru lze závislost světelného výtěžku na energii „narovnat“, přičemž se dostaví zlepšení energetické rozlišovací

schopnosti, viz obr. 3.6, jenž ukazuje zmírnění neproporcionality scintilátoru $LaBr_3$:Ce a současné zlepšení FWHM pomocí kodopace ionty Sr^{2+} [121]. Téhož lze do určité míry dosáhnout i vhodným tvarováním signálu [126] nebo aplikací tvarové analýzy signálu [127].

Vliv neproporcionality na energetickou rozlišovací schopnost bohužel nebylo možno v práci zkoumat, neboť α částice z radionuklidových zdrojů se odlišují svojí energií minimálně. Rovněž není znám přesný příspěvek dalších členů ze vztahu R-3.6.

M. Moszyński [117] připomíná, že do δ_{sc} je nezbytné zahrnout i lokální variace světelného výtěžku a neuniformitu odrazivosti reflektoru. Tyto faktory pravděpodobně hrají významnou roli při měření energetické rozlišovací schopnosti některých epitaxních filmů.

Statistický příspěvek δ_{st} závisí především na počtu fotoelektronů (u fotonásobiče) N, resp. počtu elektron-děrových párů fotodiody:

$$\delta_{st} = 2\sqrt{ln4} \times \sqrt{N} \times \sqrt{1+\varepsilon} \qquad \text{R-3.7}$$

kde ε vyjadřuje rozptyl celkového zesílení fotonásobiče, jež u dnešních běžných fotonásobičů činí 0,1-0,2 [128]. U námi používaného HPMT (Hybrid PhotoMultiplier Tube – hybridní fotonásobič) je ε nižší. Jelikož $N = LY \times Q_{PD} \times E$, tj. světelný výtěžek násobený kvantovou účinností fotodetektoru a energií částice ionizujícího záření, představuje zvýšení LY rovněž cestu ke zlepšení energetické rozlišovací schopnosti.

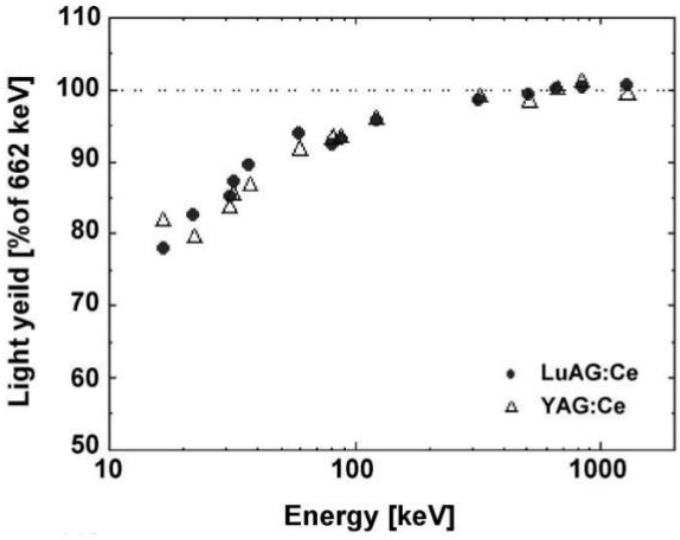

Obr. 3.7 – Závislost relativního světelného výtěžku na energii záření γ [22]**.**

Nyní se podívejme na scintilátor LuAG:Ce ve světle výše popsaných informací. Světelný výtěžek patří spíše k průměrným, rovněž neproporcionalita odezvy nepatří k výjimečným – ani

v pozitivním, ani v negativním slova smyslu, viz obr. 3.7 [22]. Proto nepřekvapí, že výjimečná není ani energetická rozlišovací schopnost, jež pro ^{137}Cs (662 keV) činí 6,7 % [22].

3.5. Fotoluminiscenční a scintilační kinetika, afterglow

V případě excitace stavu $5d_1$ Ce^{3+} v libovolném Ce dopovaném scintilátoru následuje za běžných okolností jednoexponenciální dosvit s časovou konstantou τ. Lze-li zanedbat teplotní zhášení luminiscence, přenos energie z luminiscenčního centra a ionizaci excitovaného stavu, platí [77]:

$$\tau = \frac{cm_e}{8\pi e^2}\frac{\lambda^2}{fn}\left(\frac{3}{n^2+2}\right)^2 \qquad \text{R-3.8}$$

kde c je rychlost světla, m_e hmotnost elektronu, e elementární náboj, n index lomu materiálu, λ vlnová délka a f síla oscilátoru. Doba dosvitu roste s rostoucí vlnovou délkou emise, viz příklad: $LaBr_3$:Ce (τ = 16 ns, λ = 380 nm, n = 1,9) [129], LuAG:Ce (τ = 70 ns, λ = 535 nm, n = 1,84) [130], LuAG:Pr (τ = 20 ns, λ = 310 nm, n = 2,03) [131].

V případě, že dochází k ionizaci excitovaného stavu, elektron se dostává do vodivostního pásu. Posléze může být zachycen v pasti. Pokud je doba setrvání v pasti delší než doba dosvitu centra τ, objevují se ve změřené dosvitové křivce delší komponenty. Za určitých okolností, se mohou objevit i neexponenciálních složky dosvitu.

Naopak neradiační přenos energie mimo luminiscenční centrum se projeví zrychlením dosvitu, doprovázeným snížením intenzity emitovaného světla. Pokud se neradiační přenos energie mimo centrum týká jenom určité, byť významné části luminiscenčních center, objevují se v dosvitu další, rychlejší složky, ale původní složka je též přítomna.

Dochází tak ke snížení kvantové účinnosti luminiscenčního Q. Relativní změnu Q lze spočítat jako podíl ploch pod dosvitovými křivkami (rychlejší/pomalejší). Znalost Q se může uplatnit při interpretaci experimentálních dat světelných výtěžků, resp. intenzity radioluminiscence.

Teplotní zhášení luminiscence se rovněž projeví jako zrychlení dosvitu při současném poklesu počtu scintilačních fotonů. Dosvit zůstane exponenciální. Platí [86]:

$$\tau(T) = \tau_0 q(T) \qquad \text{R-3.9}$$

kde T je termodynamická teplota, τ_0 doba dosvitu při T = 0 K a q(T) je relativní kvantová účinnost při teplotě T (q=1 pro T=0 K) [86]:

$$q(T) = \frac{1}{1+Cexp\left(-\frac{E_q}{k_B T}\right)} \qquad \text{R-3.10}$$

kde C je zhášecí konstanta, E_q zhášecí energie (viz obr. 2.3, rozdíl mezi dnem paraboly e a výškou průsečíku obou parabol) a k_B Boltzmanova konstanta. Průběh zrychlení τ s teplotou za současného poklesu intenzity luminiscence ukazuje obr. 3.8 [132]. Vztah R-3.10 tvrdí, že pokles bude v obou případech relativně stejný, což obr. 3.8 nepotvrzuje zcela beze zbytku, a to v důsledku uplatnění dosud neuvažovaného jevu, ionizace excitovaného stavu.

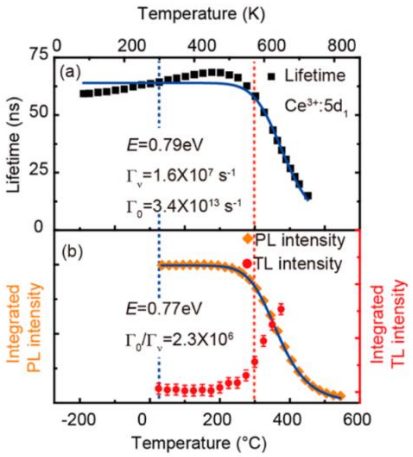

Obr. 3.8 – Závislost doby života Ce^{3+} na teplotě (nahoře) a intenzity fotoluminiscence na teplotě. YAG:Ce. Obě závislosti vykazují velmi podobný průběh, přibližně v souladu se vztahem R-3.10. Odchylky jsou způsobeny ionizací excitovaného stavu [132]**.**

Scintilační dosvit je podstatně komplikovanější než dosvit fotoluminiscenční, neboť vznikají elektrony ve vodivostním pásu a díry ve valenčním pásu. Ty jsou během fáze migrace zachytávány v pastech, objevují se tedy dlouhé složky dosvitu. V granátech existuje několik typů pastí různých hloubek.

Navíc se uplatňuje zmíněné tunelování elektronů z pastí k luminiscenčnímu centru, což se ve výsledku projevuje dosvitem ve tvaru mocninné funkce. Jedná se o důsledek vzájemné distribuce pastí a luminiscenčních center. Pokud by past od centra byla vždy stejně daleko, dosvit by byl exponenciální, ale v reálném krystalu tomu tak není. Obecný předpis pro tuto situaci zní [133] [23]:

$$I(t) = A(t + t_0)^{-p} \qquad \text{R-3.11}$$

kde I(t) je intenzita fosforescence (druh perzistentní luminiscence), A a t_0 konstanty. Parametr p je obecně z intervalu 1-2.

Daný typ dosvitu byl u LuAG:Ce skutečně pozorován, poprvé v roce 2007 (obr. 3.9 vlevo) [23], na jiné časové škále pak v roce 2009 (obr. 3.9 vpravo) [22].

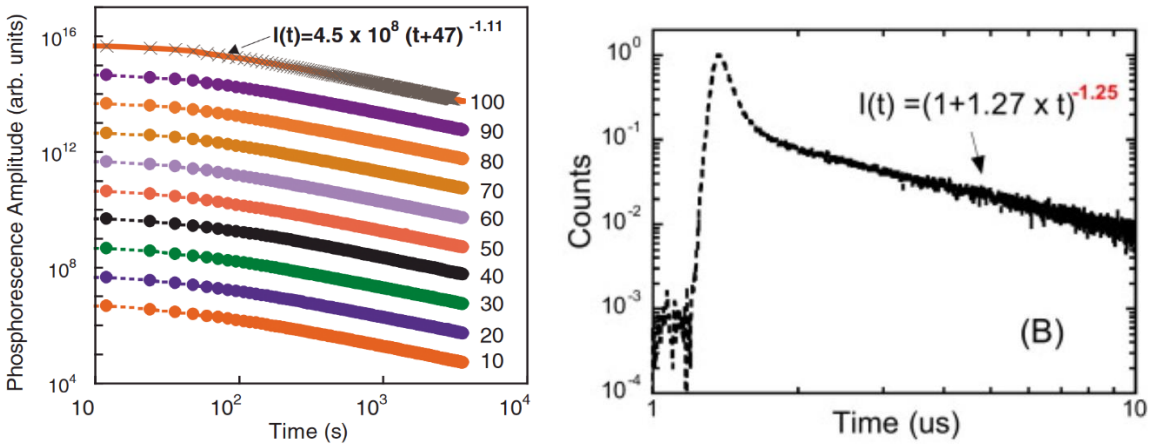

Obr. 3.9 – Vlevo: Fosforescenční dosvity LuAG:Ce po ozáření 12 Gy při různých teplotách (v K) [23]**. Vpravo: Scintilační dosvit LuAG:Ce s vysokým dynamickým rozlišením** [22]**.**

Jsou to právě tyto složky dosvitu (viditelné zvláště dobře na obr. 3.9 vpravo), které jsou zodpovědné za výrazné zhoršení užitných vlastností LuAG:Ce.

Ještě pomalejší složky luminiscence se označují jako afterglow. Pojem afterglow není používán naprosto jednotně. Může být definován jako podíl počtu scintilačních fotonů vyzářených 3 ms a později po skončení krátkého excitačního pulzu záření X, k počtu všech scintilačních fotonů.

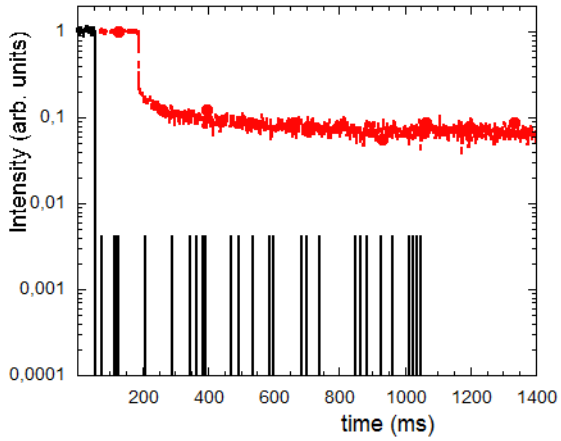

Obr. 3.10 – Afterglow BGO (černá) a LuAG:Ce (červená) (změřil V. Babin, poskytl M. Nikl).

Dnes obvyklá definice hovoří o afterglow jako podílu úrovně signálu 3 ms po skončení kontinuální excitace scintilátoru zářením X k úrovni signálu během kontinuální excitace zářením X. Podmínkou je, aby úroveň signálu během ozařování byla ustálená. Typický průběh pro monokrystal LuAG:Ce připravený metodou μ-PD a monokrystal BGO připravený

Czochralského metodou ukazuje obr. 3.10. μ-PD krystaly obvykle vykazují větší množství defektů a tedy i pastí, nicméně i v případě LuAG:Ce krystalu připraveného Czochralského metodou by byla úroveň afterglow výrazně vyšší než u BGO. Afterglow BGO patří naopak k těm nejnižším [134] [135].

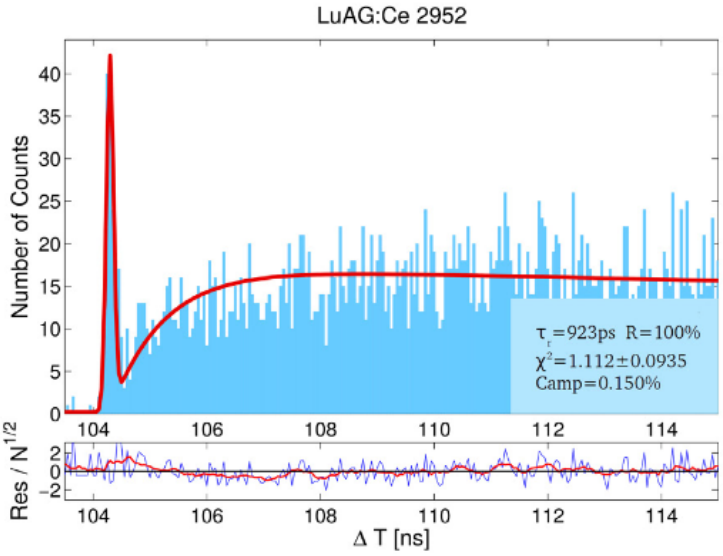

Obr. 3.11 – Scintilační kinetika LuAG:Ce v prvních 10 ns. Kromě nenulové náběžné doby je zřetelně přítomen i pík od okamžitých fotonů čerenkovova záření [136]**.**

Některé scintilátory vykazují scintilační kinetiku s nezanedbatelně pomalým náběhem [137] [138], což je způsobeno relativně pomalým přenosem excitační energie k luminiscenčnímu centru. V případě Ce^{3+} dopovaných scintilátorů se obvykle náběžná doba zanedbává. Pokud se ovšem uvažuje o scintilátoru jako materiálu pro dosažení co nejnižší CTR, ani velmi krátká (typicky subnanosekundová) náběžná doba LuAG:Ce se zanedbat nedá. U LuAG:Ce je způsobena především relativně pomalou migrací děr, které musí k Ce^{3+} centru dorazit před elektrony. Teprve potom, co díra přemění Ce^{3+} na dočasné Ce^{4+}, může atom Ce zachytit elektron z vodivostního pásu a excitovat se. Ukázka měření scintilační kinetiky na velmi krátké časové škále, dobře zobrazující nenulovou náběžnou dobu, je na obr. 3.11 [136].

3.6. CTR – Koincidenční rozlišovací schopnost

Měření koincidenční rozlišovací schopnosti scintilačního detektoru či přesněji celé scintilační detekční jednotky není zcela běžnou charakterizační metodou. CTR je však klíčovým parametrem pro některé aplikace, např. přesná časová měření ve fyzice vysokých energií či v TOF PET (Time-Of-Flight PET). Určuje ji jak časové rozlišení fotodetektoru a vyhodnocovací elektroniky, tak rozlišení dané produkcí scintilačních fotonů v čase po interakci.

Pomocí rychle spínaného zdroje světla lze změřit CTR tzv. akviziční části aparatury [139], pomocí zdroje ^{22}Na a dvou scintilačních detekčních jednotek pak CTR celku. Odečtením kvadrátu obou CTR tak lze získat CTR samotného scintilačního detektoru.

Pokud lze zanedbat náběžnou dobu v kinetice scintilační odezvy τ_r, CTR je přibližně rovno:

$$CTR \approx \sqrt{\frac{\tau_d}{NQ_{PD}}} = \sqrt{\frac{\tau_d}{LY \times E \times Q_{PD}}} \qquad \text{R-3.12}$$

kde N je počet emitovaných scintilačních fotonů, τ_d doba dosvitu scintilátoru, LY světelný výtěžek, E absorbovaná energie částice ionizujícího záření, Q_{PD} kvantová účinnost fotodetektoru.

Obecně však náběžnou dobu τ_r zanedbat nelze a je nutno použít podstatně komplikovanější vztah než R-3.12. Podrobnosti může čtenář nalézt v [139]. V uvedeném článku se předpokládá nutnost překročení určité diskriminační hladiny. Časový okamžik interakce se ztotožňuje právě s touto událostí. V publikaci [140] se čtenář může dozvědět o možnosti využití změřené časové distribuce detekce jednotlivých scintilačních fotonů, což by CTR dále podstatně zlepšilo. Habilitační práce se však tímto dále zabývat nebude.

Z [139] i [140] je zřejmé, že pro dosažení co nejlepšího CTR potřebujeme krátké τ_d i τ_r, vysoký světelný výtěžek i emisní spektrum v blízkosti maxima kvantové účinnosti fotodetektoru Q_{PD}.

CTR dosažené s použitím LuAG:Ce za nejrychlejšími materiály nezanedbatelně zaostává, publikace [65] udává hodnotu 530 ps. Pro srovnání, nejlepší hodnota v téže publikaci byla naměřena pro 2 × 2 × 3 mm^3 krystal LSO:Ce,C, a to 73 ps.

3.7. Další charakteristiky

Kromě výše uvedených vlastností se u scintilátorů sledují i další parametry. Např. LuAG:Ce pozitivně vyniká v následujícím: chemická stabilita, mechanické a termomechanické vlastnosti, je nehygroskopický a vykazuje značnou radiační odolnost. Bohužel přirozeně obsahuje radionuklid ^{176}Lu (2,6 % v přírodní izotopové směsi) s poločasem 3,78 × 10^{10} let, což vede k hmotnostní aktivitě 32 Bq/g [59][133]. Při jedné přeměně je emitována částice β- s maximální energií 596 keV a fotony o energiích 88 (13,3 %), 202 (86 %), 307 (94 %) a 401 keV (0,33 %). Podrobněji se těmito dalšími vlastnostmi zabývat nebudeme, jejich vztah k tématu práce je marginální, byť mohou být (ne)výhodné pro řadu aplikací.

Kapitola 4

Metody přípravy zkoumaných vzorků

V této kapitole poskytneme pouze základní informace o metodách přípravy měřených vzorků, s hlavním důrazem na vliv použití té které metody na výsledné vlastnosti (zvláště vlastnosti scintilační) vyrobeného scintilátoru.

4.1. Czochralského metoda

Czochralského metoda patří k nejrozšířenějším metodám růstu monokrystalů. Umožňuje připravit monokrystaly relativně velkých rozměrů a s malým množstvím dislokací.

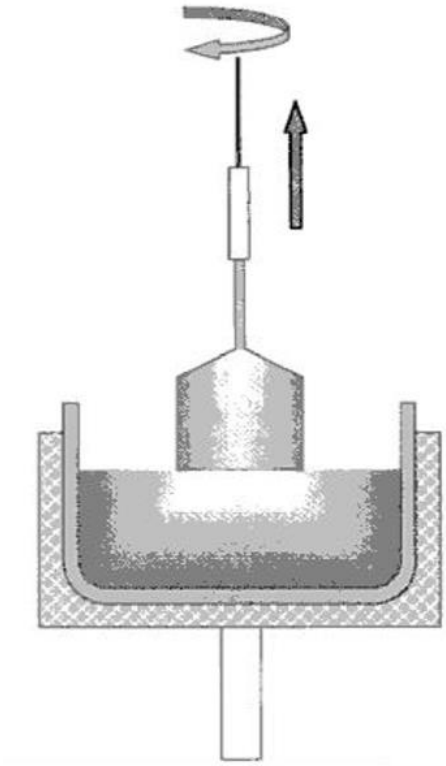

Obr. 4.1 – Schéma Czochralského metody [141]**.**

Růst krystalu probíhá z taveniny výchozích látek, jež se nachází v kelímku z vhodně zvoleného materiálu. Rotující zárodečný krystal se ponoří těsně pod hladinu a pak již táhnutím vzhůru za stálé rotace roste krystal, viz obr. 4.1.

Materiál kelímku nejenže musí udržet svoji pevnost při obrovských teplotách, jež v růstových pecích panují, ale nesmí chemicky reagovat s taveninou, ani s přítomnou atmosférou. Typickými materiály pro výrobu kelímků jsou iridium, molybden, grafit či platina [142].

Kelímky z některých materiálů jsou velmi drahé, částečně pro jejich vzácnost, částečně pro jejich obtížnou opracovatelnost, např. iridium. Levnější materiály, např. Mo, zřejmě nejčastěji užívaný při růstu granátů Czochralského metodou, mohou pro změnu při vysokých teplotách intenzivně oxidovat, nepoužije-li se růst v redukční atmosféře.

Růst v redukční atmosféře ovšem nevyhnutelně v granátech vede ke vzniku kyslíkových vakancí, jež se se projevují jako hluboké elektronové pasti. Naštěstí lze jejich koncentraci zredukovat žíháním při vysoké teplotě za přítomnosti kyslíku, např. ve vzduchu [143].

Teplota tání LuAG:Ce kolem 2000°C , která je k růstu krystalu nezbytná, vede též ke vzniku již zmíněných Lu_{Al} antisite defektů [144]. Ty bohužel z krystalu již nijak odstranit nelze a LuAG:Ce tak trpí jejich přítomností v podobě snížení světelného výtěžku a zvýšení intenzity pomalých složek dosvitu.

Růst Czochralského metodou je relativně pomalý a metoda není příliš flexibilní, pokud chceme obměnit složení krystalu. Pokud např. zkoumáme závislost vlastností scintilátoru na složení a potřebujeme mít k dispozici větší množství různě složených vzorků, použijeme spíše metody μ-PD nebo LPE.

Naopak pro přípravu krystalů nejvyšší kvality již optimalizovaného složení v průmyslovém měřítku je Czochralského metoda velmi vhodná.

4.2. Micro-pulling down

K provádění tzv. „material screeningu“, tedy průzkumu závislosti různých vlastností materiálu (scintilátoru) na složení, je metoda μ-PD lepším nástrojem než Czochralského metoda. Umožňuje podstatně rychlejší růst krystalu, zhruba 0,05-20 mm/min [145], vyšší rychlost je však pro kvalitu krystalu spíše nepříznivá.

Růst probíhá z taveniny nacházející se v kelímku z vhodného materiálu (mohou být stejné jako u Czochralského metody), v jehož dně je otvor přecházející směrem dolů v kapiláru, viz obr. 4.2 [146]. Při přiložení zárodečného krystalu se, díky povrchovému napětí, tažením dá tavenina „vytahovat“ ven skrze kapiláru, kde při nižší teplotě tuhne a krystalizuje.

Je zřejmé, že při tažení jednou kapilárou sice mohou vzniknout krystaly značné délky, ale poměrně malých průměrů, viz obr. 4.2. Existují nicméně i přístroje s více kapilárami, které růst krystalů větších průměrů umožňují, viz Obr. 4.2 [146]. Pro „material screening“ však větších objemů není obvykle třeba, tj. ani pro potřeby této práce.

Bohužel, μ-PD krystaly mají obvykle nižší kvalitu, vyskytuje se v nich množství dislokací, mohou vykazovat nehomogenní složení podél osy tažení i kolmo na ni, atd. [38]. Výzkum obvykle těmito nevýhodami netrpí zásadně, pokud nějaký parametr (např. LY) závisí v sadě μ-PD vzorků s různým složením určitým způsobem na složení, zůstává tato závislost běžně zachována i v obdobných vzorcích připravených jinou metodou. Konkrétní hodnoty sledovaného parametru mohou být nicméně jiné.

Pokud jde o výskyt antisite defektů a kyslíkových vakancí, μ-PD krystaly je obsahují podobně jako Czochralského metodou připravené krystaly. Růst probíhá za stejné teploty a v redukční atmosféře. Příklad μ-PD krystalu je na obr. 4.3 [143].

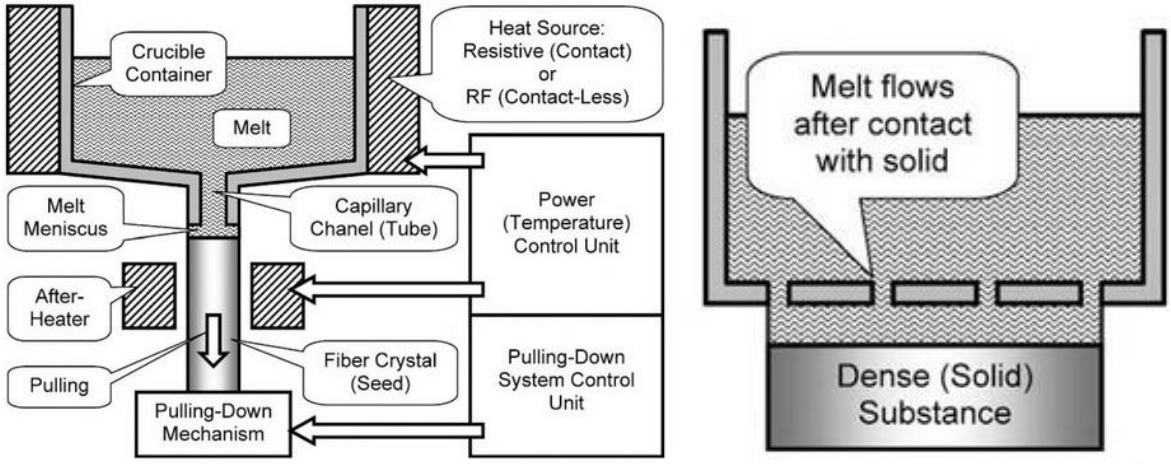

Obr. 4.2 – Princip metody růstu krystalů micro-pulling down. Vlevo: monokapilární růst, vpravo polykapilární růst pro přípravu krystalů většího průměru [146]**.**

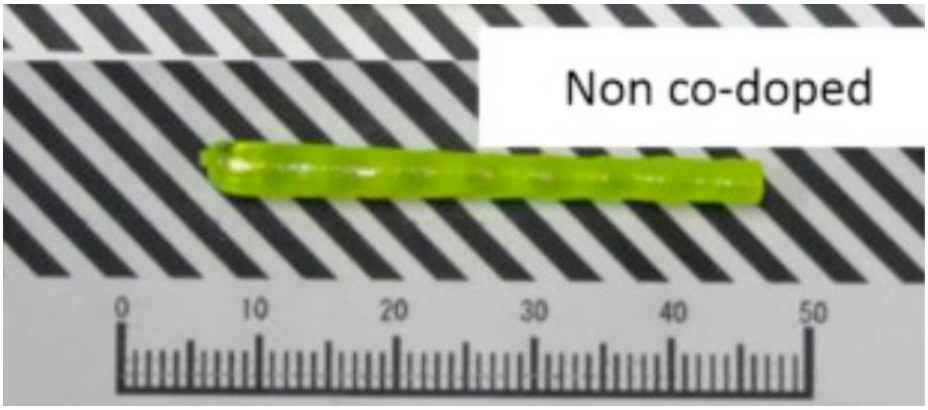

Obr. 4.3 – Krystal LuAG:Ce připravený metodou μ-PD [147]**.**

4.3. Epitaxe z kapalné fáze

Princip epitaxe z kapalné fáze spočívá ve vysrážení rozpuštěných látek v krystalické formě na zárodečném krystalu – substrátu. Nejprve se připraví roztok výchozích, krystalotvorných látek

v tzv. tavidle. Krystalizace začíná po snížení teploty nasyceného roztoku krystalotvorných látek, v případě LuAG:Ce se jedná o směs velmi čistých oxidů Lu_2O_3, Al_2O_3 a CeO_2. Ty pak začínají na substrátu krystalizovat a vytvářejí tenký epitaxní film.

Jako substrát se v ideálním případě používá monokrystalu materiálu stejného složení, jaké má mít výsledný epitaxní film, ovšem nedopovaného. Jedná se o tzv. homoepitaxní růst. V případě LuAG:Ce tedy homoepitaxní růst probíhá na LuAG.

Tzv. heteroepitaxní růst probíhá na substrátu odlišného složení. Nevýhodou této varianty je obvykle nezanedbatelný rozdíl mřížkových konstant mezi filmem a substrátem, který působí napětí zvláště v okolí rozhraní substrát-film a může vést k horší kvalitě filmů, v případě ještě výraznějších rozdílů se růst stává prakticky nemožným [148]. Heteroepitaxní růst se tak používá především v případě nedostupnosti vhodných substrátů pro homoepitaxní růst. Jak uvidíme dále, v případě „band-gap engineeringu“ to znamená „poměrně často“.

Z krystalu zvoleného pro přípravu substrátu se uřízne destička (tvaru nízkého válce) o průměru několika málo cm a tloušťce asi 0,5-1 mm. Rovina řezu se volí ve směru některé významné krystalografické roviny, např. <111>. Destička se vyleští a očistí, čímž je příprava substrátu ukončena.

Tavenina se nachází v platinovém kelímku, viz obr. 4.4. Tavenina se ohřeje na teplotu asi o 100°C vyšší než je teplota nasycení a zhruba hodinu se při této teplotě homogenizuje. Po homogenizaci taveniny se její teplota sníží pod nasycenou teplotu (maximálně o 50°C níže), k hladině se přiblíží substrát, který se po asi třech minutách ohřeje na stejnou teplotu. Růst začíná okamžitě po rychlém ponoření substrátu pod hladinu [149].

Během růstu se substrát neustále otáčí, přibližně rychlostí 100 otáček za minutu. Po každých asi 5 otáčkách se směr otáčení mění. Po skončení růstu se otáčení zastaví, vzorek se vynoří a zbytky taveniny se odstříkne rychlým roztočením (asi 500 otáček za minutu) a pak odstraní lázní v horké kyselině dusičné [149].

V případě potřeby tenkých vrstev scintilátorů, např. těch užívaných v mikroradiografii, představuje metoda LPE podstatně levnější variantu oproti běžně užívané, tj. růstu monokrystalu Czochralského metodou a jeho následného opracování do podoby tenké destičky. Metodou LPE jsou dosažitelné i tloušťky, které pro mechanické opracování monokrystalu nepřipadají v úvahu, tj. i jednotky μm. Rovněž z hlediska „material screeningu“ je metoda LPE finančně výhodná.

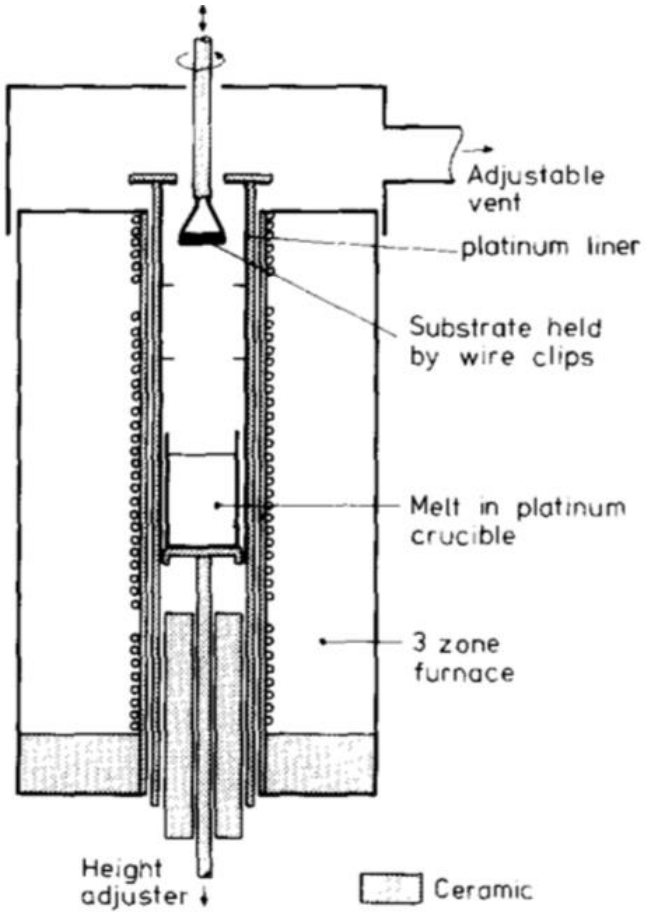

Obr. 4.4 – Schéma zařízení určeného k růstu granátových epitaxních vrstev pomocí metody epitaxe z kapalné fáze [149]**.**

Růst granátových epitaxních filmů probíhá zhruba při teplotě 1000°C, tj. asi o 1000°C níže, než růst metodou Czochralského, Bridgmanovou či μ-PD. Výsledkem je podstatně nižší koncentrace antisite defektů, tedy další výhoda metody LPE [28] [32]. Rovněž do již zmíněného snížení ceny se nižší teplota růstu promítne.

Podobně jako v případě metody μ-PD lze díky poměrně vysokému segregačnímu koeficientu dosáhnout vyšší koncentrace dopantu, zde Ce, než umožňuje Czochralského metoda [148].

Metoda LPE má samozřejmě i několik podstatných nevýhod. Tloušťka epitaxních filmů nepřesahuje několik desítek μm. To může být dostatečné pro účinnou detekci těžkých nabitých částic nebo nízkoenergetického záření X, ovšem pro záření β či γ vyšších energií je detekční účinnost zcela nedostatečná. Znamená to významné zúžení množiny aplikací, k nimž by bylo možno materiálu s příslušným složením použít. V úvahu připadá např. mikroradiografie [150][272] [151] [152], monitoring svazků z urychlovačů [153] [154] a samozřejmě námi užívaný „material screening“.

Kvalita povrchu obvykle nedosahuje kvality povrchu vyleštěného monokrystalu. Z hlediska aplikace v zobrazovacích metodách je to podstatná nevýhoda [150][272]. Z hlediska sběru světla na fotodetektor se paradoxně může jednat o výhodu, neboť pravděpodobně dochází ke snížení počtu fotonů odražených na rozhraní scintilátor-okénko fotodetektoru, viz [155]. Na rozdíl od odkazované publikace se u filmů nejedná o záměrně vytvořenou strukturu, jejíž podoba je pod kontrolou, přesto nelze určité zvýšení počtu registrovaných scintilačních fotonů vyloučit.

Dále existuje riziko zanesení kontaminantu z tavidla do epitaxního filmu, viz níže. Konečně je spektrum složení připravitelných materiálů do značné míry omezeno dostupností substrátů. V případě granátů je z tohoto hlediska situace dobrá, ovšem s omezeními, jejichž povaha bude z dalšího textu zřejmá.

Při dalším hodnocení metody LPE již musíme přihlédnout ke složení tavidla. Autorovi jsou známa čtyři tavidla, jež byla v minulosti alespoň jednou použita k výzkumu scintilujících epitaxních granátových filmů: PbO-B_2O_3 (T-Pb), BaO-B_2O_3-BaF_2 (T-Ba), Bi_2O_3-B_2O_3 a MoO_3-Li_2MoO_4 [156][262] [148] [72][142]. Poslední dvě tavidla nebyla v této práci použita, pročež se jimi nebudeme dále zabývat.

4.3.1. Tavidlo PbO-B_2O_3

T-Pb tavidlo je nejdéle a nejčastěji, „tradičně“ používaným tavidlem pro výroby epitaxních granátových filmů. Poskytuje filmy hladkých povrchů relativně vysoké optické kvality. Podstatnou nevýhodou však je nevyhnutelná kontaminace epitaxního filmu ionty Pb^{2+}, jež se projevují jako tzv. zhášecí centra. Jedná se o luminiscenční centra, u nichž dochází k teplotnímu zhášení již při značně nízkých teplotách [97].

Emisní spektra LuAG s obsahem Pb^{2+} iontů vykazují při teplotě 80 K emisní pás s vrcholem na 3,61 eV (343 nm) [97]. Excitační spektrum pro emisi 343 nm fotonů má vrchol v blízkosti 4,75 eV (261 nm). Při zvyšování teploty nad 100 K, tato emise v důsledku teplotního zhášení rychle slábne, při 130 K již dosahuje pouze 50 % maxima, viz obr. 4.5, křivka 1. V souladu s teoretickým vysvětlením teplotního zhášení rovněž rychle klesá doba dosvitu [97].

Excitační pás Ce^{3+} do stavu $5d_2$ se naštěstí kryje s emisním pásem Pb^{2+} s vlnovou délkou 343 nm. Díky tomu dochází při přítomnosti Ce^{3+} k účinnému přenosu energie z Pb^{2+} iontu na toto luminiscenční centrum. Přesto je v důsledku teplotního zhášení nezanedbatelná část energie ztracena, což se v obr. 4.5 projevuje rychlejším poklesem křivky 2 (buzení excitovaného stavu Pb^{2+}, sledování intenzity emise Ce^{3+}) oproti křivce 3 (buzení excitovaného

stavu Ce^{3+}, sledování intenzity emise Ce^{3+}). O energetickém uspořádání poskytuje informace obr. 4.6 [97].

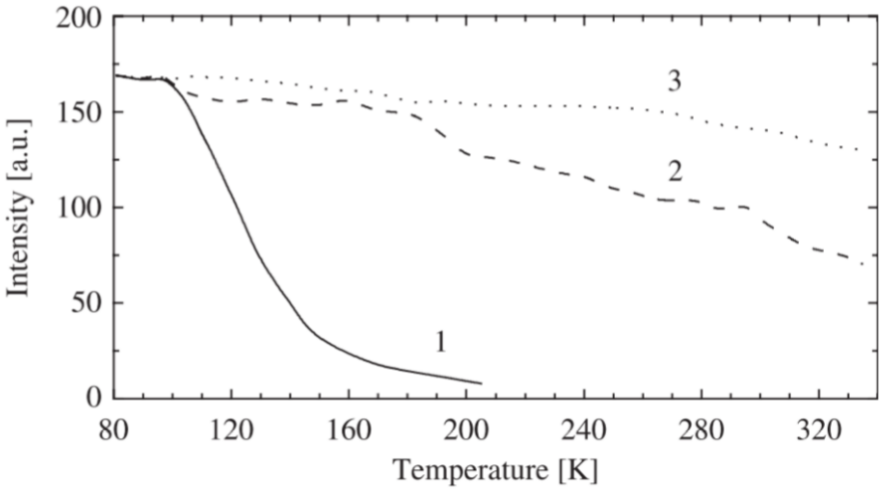

Obr. 4.5 – Teplotní závislost intenzity luminiscence: 1) emise 3,61 eV, excitace 4,75 eV v LPE LuAG; 2) emise 2,46 eV, excitace 4,75 eV v LPE LuAG:Ce; 3) emise 2,46 eV, excitace 2,8 eV v LPE LuAG:Ce [97].

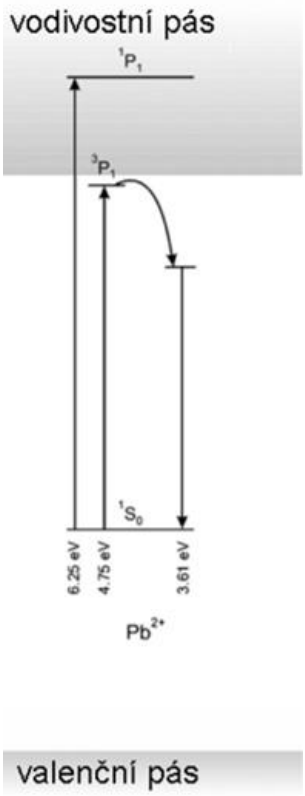

Obr. 4.6 – Energetické stavy iontů Ce^{3+} a Pb^{2+} v LuAG:Ce a přechody mezi nimi [97].

V některých případech lze vliv kontaminace na kvalitu LPE filmů připravených z T-Pb tavidla snížit na přijatelnou úroveň, tj. pokles světelného výtěžku v důsledku této kontaminace není příliš významný. V jiných případech je použití T-Pb tavidla naprosto vyloučené.

Pokud čtenáře zajímají podrobnosti o tom, jaké defekty se v důsledku přítomnosti Pb^{2+} v LuAG tvoří a jaké jsou jejich projevy, nalezne je v [97] [157] [158].

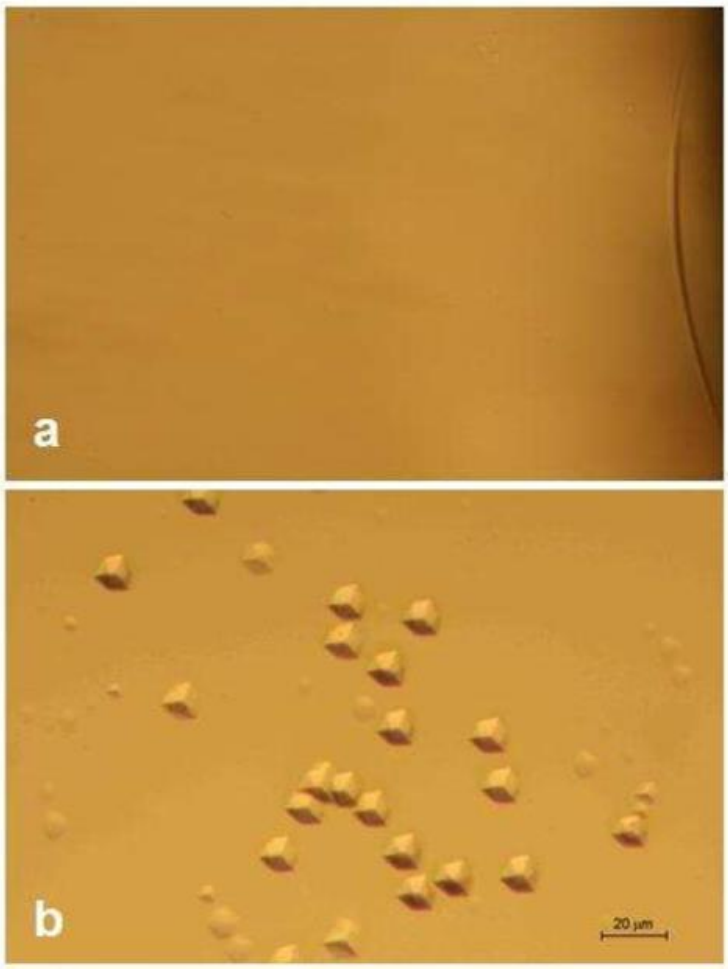

Obr. 4.7 – Povrch epitaxních vrstev YAG:Ce připravených s použitím tavidla a) T-Pb, b) T-Ba [156][262]**.**

4.3.2. Tavidlo BaO-B_2O_3-BaF_2

T-Ba tavidlo není zdrojem žádné kontaminace ovlivňující luminiscenci a scintilační vlastnosti LPE filmů z něj připravených. Kromě toho umožňuje dosažení vyšších segregačních koeficientů pro Ce^{3+} a tím i vyšší koncentrace Ce ve filmech.

Tavidlo T-Ba vykazuje nicméně podstatně vyšší viskozitu a povrchové napětí. Ulpívá na povrchu substrátu a jeho odstranění je problematické [159]. Důsledkem je vznik povrchových defektů daných dislokacemi, především tzv. pitů, viz obr. 4.7 [156][262]. Pity jsou jednou z příčin horších optických vlastností filmů připravených s použitím T-Ba tavidla.

Kapitola 5
Metody charakterizace scintilátorů

Tato kapitola se zaměřuje pouze na ty metody charakterizace scintilátorů, s kterými pracoval autor habilitační práce přímo, tj. přímo prováděl měření i zpracování dat. Portfolio metod používaných k charakterizaci scintilátorů je obecně mnohem širší a autor je částečně využívá též. Měření a vyhodnocení nicméně prováděli jeho kolegové / spoluautoři. Zájemce bližší popis těchto dalších metod nalezne v odkazovaných článcích a disertační práci autora [71]. Kapitola si klade za cíl poskytnutí pouhého základního přehledu. Pokud v některých případech zabíhá do podrobností, tak proto, že je popisována metodika zavedená/použitá autorem, která umožňuje buď přesnější změření žádané informace, získaní informace nové, případně se jedná o prokázání spolehlivosti metody (alespoň v rámci určitých mezí).

Popis aparatur amplitudové spektrometrie a měření scintilačního dosvitu se nachází uveden v příloze 1 na konci práce.

5.1. Amplitudová spektrometrie

Amplitudová spektrometrie impulzů buzených ionizujícím zářením se v principu neliší od spektrometrie záření γ nebo α. Scintilátor je, pokud to lze, obalen reflektorem, a připojen k fotonásobiči, jenž detekuje scintilační fotony a produkuje elektrické pulzy. Ty jsou dále zesíleny a tvarovány předzesilovačem a zesilovačem, načež vstupují do mnohokanálového analyzátoru, který je rozděluje dle amplitudy do jednotlivých kanálů. Tím vzniká amplitudové spektrum.

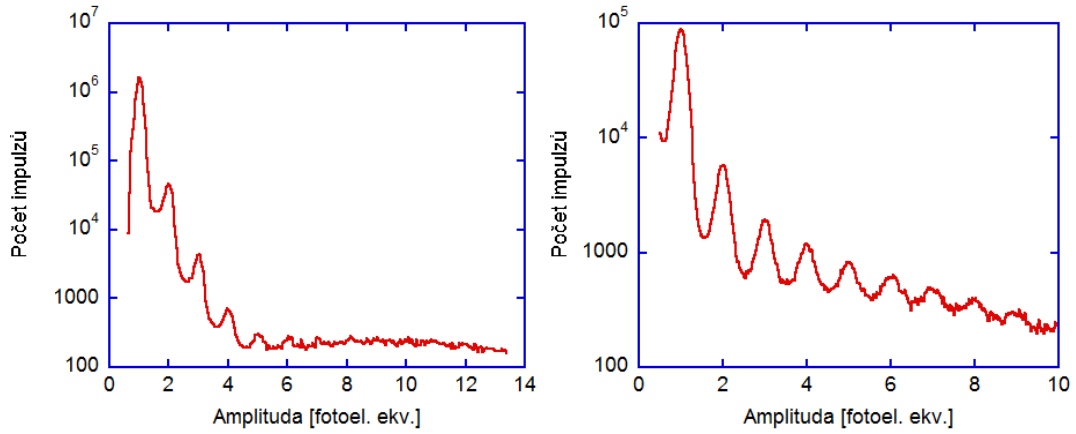

Obr. 5.1 – Kalibrační spektra. Vlevo: HPMT DEP PP0475B citlivější v červené oblasti, temné impulzy. Vpravo: HPMT Photonis méně citlivý v červené oblasti, scintilační záblesky z PWO buzeného ^{137}Cs.

Oproti spektrometrii ionizujícího záření však existují některé podstatné rozdíly. Amplitudové spektrum není kalibrováno v jednotkách energie, ale v počtu fotonů či, přesněji řečeno, fotoelektronů. Účelem není stanovit energii částice ionizujícího záření – ta je vždy známá. Účelem je stanovit počet emitovaných fotoelektronů.

Z toho důvodu se podstatně liší kalibrační spektra. Namísto měření spektra s píky se známou energií je nezbytné mít k dispozici spektra s píky se známým počtem fotoelektronů. Ty se získají změřením tzv. spektra temných impulzů fotonásobiče, případně změřením spekter velmi krátkých (maximálně několik málo desítek ns) a velmi slabých záblesků světla (maximálně jednotky fotonů). Podle použitého HPMT používal autor obou možností, u HPMT s vyšší citlivostí v delších vlnových délkách postačilo spektrum temných impulzů, viz obr. 5.1 vlevo, HPMT s nižší citlivostí k fotonům s delšími vlnovými délkami používal slabý zdroj světla, viz obr. 5.1 vpravo [71]. Ten autor realizoval jako na fotonásobič volně položený krystal $PbWO_4$ (PWO) ozařovaný ^{137}Cs. PWO je scintilátor s velice malým světelným výtěžkem a zároveň velmi rychlým dosvitem bez pomalých komponent [160] [161] [162].

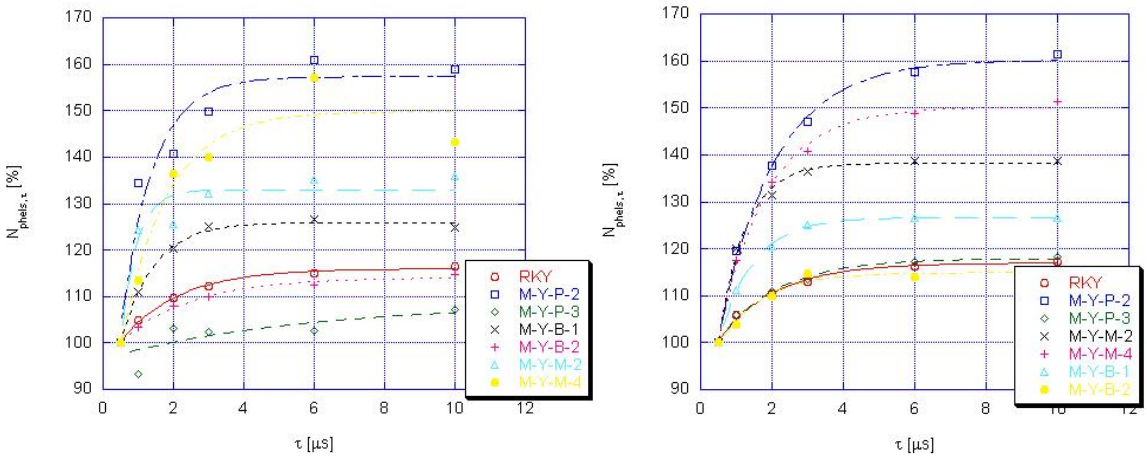

Obr. 5.2 – Závislost relativního světelného výtěžku na časové konstantě zesilovače τ. Vlevo: Velký rozptyl bodů způsoben nedokonalou reprodukovatelností umístění vzorků. Vpravo: Rozptyl výrazně redukován jedním umístěním vzorku a následným změřením výtěžku pro všechna τ. N_{phels} je totožný s RLY [71]**.**

Již během disertační práce [71] autor ověřil linearitu odezvy aparatury, stanovil dlouhodobou stabilitu aparatury a teoreticky zdůvodnil tvar spekter získaných při měření vzorků s tloušťkou menší, než je dosah budících α částic – tento výsledek publikoval v anglickém jazyce nicméně až po získání titulu Ph.D. [72][142]. Dále triviálním způsobem zpřesnil stanovení světelného výtěžku a energetické rozlišovací schopnosti. Postačilo přestat při vyhodnocení spoléhat na program MAESTRO, který zřejmě není optimalizován pro scintilační spektra s nevýraznými píky úplné absorpce, ale s výraznými píky únikovými, a provádět proklady spekter samostatně.

Konečně autor zpřesnil měření závislosti světelného výtěžku na časové konstantě zesilovače – triviálním krokem. Namísto sekvence měření vzorků „všechny při jedné časové konstantě“, „všechny při další časové konstantě…“ používá sekvenci „jeden vzorek při všech časových konstantách“, „druhý vzorek při všech časových konstantách,“ atd. Tím byla vyloučena chyba daná obtížnou reprodukovatelností umístění vzorků na fotonásobič. Výsledky zlepšení ukazuje obr. 5.2 [71].

Toto zpřesnění bylo tak výrazné, že umožnilo nejen úvahy o stanovení přesného vztahu mezi scintilačním dosvitem a závislostí světelného výtěžku na časové konstantě zesilovače, ale pokusit se teoretické odvození této vzájemné souvislosti experimentálně ověřit.

5.1.1. Souvislost závislosti světelného výtěžku na časové konstantě zesilovače a scintilačního dosvitu

Na obr. 5.2 vpravo se nachází typická, zpřesněná závislost relativního světelného výtěžku RLY (relative light yield), který je zaveden jako poměr LY měřený při použití časové konstanty zesilovače. V disertační práci autor zavedl její prokládání vztahem [71]:

$$RLY = m_1 - m_2 e^{-m_3 t} \qquad \text{R-5.1}$$

Odvození tohoto vztahu vychází z předpokladu okamžitého vyzáření určitého procenta fotonů, následované jednoexponenciálním dosvitem. Rychlou složku scintilační odezvy (doba dosvitu τ_d maximálně desítky ns) lze chápat jako okamžitou (a bude tak dále označována) ve vztahu k nejkratší časové konstantě zesilovače, jež je k dispozici, tj. 0,5 μs.

Předpoklad jednoexponenciálního dosvitu s promptní složkou na dané časové škále není vždy platný. Vzhledem k existenci pouhých 6 experimentálních bodů nelze ovšem složitější proklady považovat za oprávněné. Proklad dle vztahu R-5.1 nelze zcela interpretovat jednoduchým způsobem. Přisouzení jednoznačného fyzikálního významu získaným parametrům, případně veličinám, jež se na jejich základě dají vypočítat, je komplikované, jak dále uvidíme.

Vztah R-5.1 má nicméně svůj smysl jako nástroj pro srovnávání rychlosti scintilačních odezev na škále blízké jednotkám μs. Extrapolací vztahu k nekonečnu a k nule lze odvodit podíl okamžitých fotonů na signálu (neztotožňovat s podílem počtu okamžitých fotonů) $K_{f/e}$:

$$K_{f/e} = 100 \times \frac{RLY\ (0)}{RLY(\infty)} = 100 \times \frac{m_1 - m_2}{m_1} \qquad \text{R-5.2}$$

$K_{f/e}$ a vztah R-5.1 je na Oddělení optických materiálů běžně používán k porovnání vzorků mezi sebou.

Pokud je podíl pomalejších složek méně výrazný, parametry vztahu R-5.1 ztrácejí na přesnosti a $K_{f/e}$ taktéž. V takovém případě vyjadřuje autor vliv pomalých složek odezvy prostě podílem světelných výtěžků pro dvě různé časové konstanty zesilovače, typicky 0,5 μs a 10 μs. Použití pouhého podílu dvou světelných výtěžků se stávalo stále nezbytnějším s tím, jak byl naplňován jeden z cílů výzkumu, potlačení podílu pomalých složek v granátech.

Pokud dochází k výraznějšímu nárůstu RLY s τ, je možno použít sofistikovanějšího způsobu vyhodnocení této závislosti. Nejprve je však třeba mít k dispozici metodu výpočtu závislosti RLY na τ na základě znalosti scintilačního dosvitu. Tu si nyní popíšeme.

Scintilační záblesk se skládá z jednotlivých fotonů. Pokud známe tvar výstupu zesilovače, jenž vyvolal jeden fotoelektron v HPMT (tj. registrovaný foton), můžeme popsat odezvu na N fotonů ve scintilačním záblesku jako sumu N jednotlivých odezev, jež se liší pouze v okamžiku svého počátku. Schematicky to pro 8 fotonů ukazuje obr. 5.3. Tím je možno získat amplitudu výsledného pulzu. Odezva vůči jednotlivým fotonům závisí na nastavení časové konstanty zesilovače.

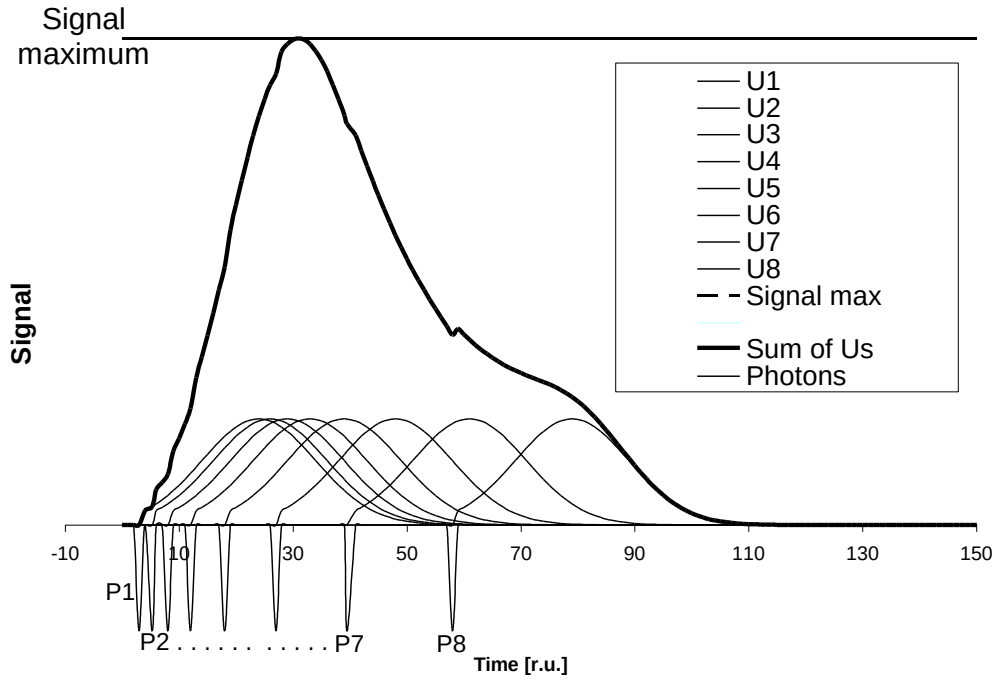

Obr. 5.3 – Idea výpočtu odezvy na scintilační záblesk. Každý z osmi fotonů vytváří totožnou odezvu. Celková odezva je součtem všech jednotlivých odezev. Nakonec je vyhodnocena amplituda [72][142]**.**

Odezva od jednotlivých fotonů se samozřejmě ve skutečnosti liší jak v amplitudě, tak tvaru, a to vlivem fluktuace zesílení HPMT či šumu, rozdíly však neovlivní průměrnou amplitudu, pouze budou mít vliv na rozdělení všech amplitud. Rozšíření rozdělení amplitud způsobí i individuální odlišnosti mezi scintilačními záblesky.

Matematicky daný problém odpovídá konvoluci scintilačního dosvitu a odezvy vyvolané jedním fotonem. Jelikož dosvit obvykle máme reprezentovaný dosvitovou křivkou, která vyjadřuje úroveň signálu v časovém intervalu o délce Δt, problém diskretizujeme. Platí [72][142]:

$$R_k = \sum_{i=0}^{k} N_i RU_{k-i} \qquad \text{R-5.3}$$

kde R_k je odezva v čase kΔt až (k+1)Δt, N_i je počet fotonů emitovaných v čase iΔt až (i+1)Δt a RU_{k-i} je odezva v k-tém intervalu na jeden fotoelektron, jenž interagoval v i-tém intervalu.

Doposud jsme neuvažovali vliv předzesilovače. V aparatuře s HPMT DEP PP0475B je předzesilovač s časovou konstantou 500 μs, což by mohlo vést k chybě maximálně několik jednotek procent. Autor přesto raději vliv předzesilovače do finálního tvaru výpočtu zahrnul.

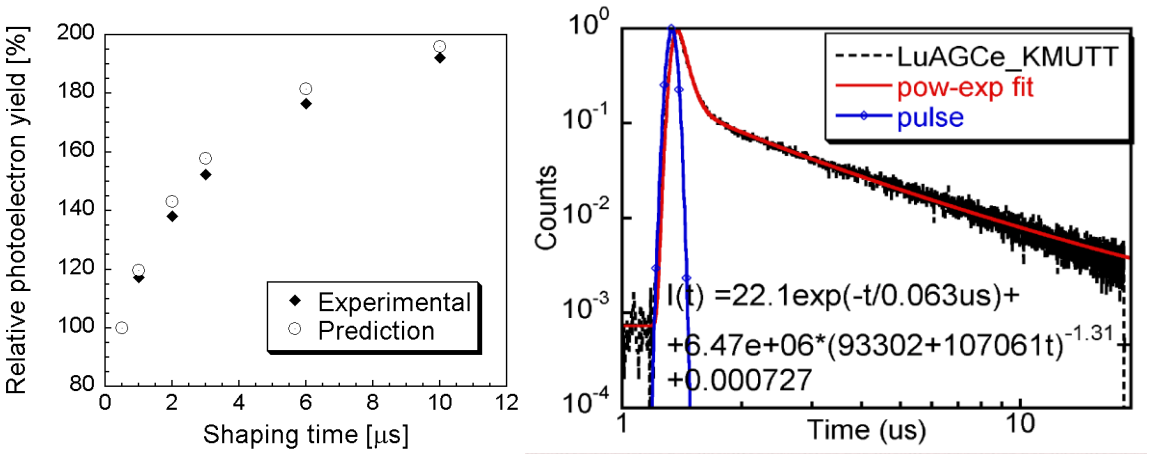

Obr. 5.4 – Vlevo: Srovnání experimentální závislosti RLY na časové konstantě zesilovače se závislostí vypočtenou na základě modelu a scintilačního dosvitu [72][142]**. Vpravo: Příslušný scintilační dosvit** [163]**.**

Úprava je relativně jednoduchá. Vztah R-5.3 zůstane beze změny, pouze N_i nahradíme Δi, kde $\Delta_i = S_{preamp,i} - S_{preamp,i-1}$ bude znamenat změnu úrovně signálu z předzesilovače mezi časy iΔt až (i+1)Δt. Ta již není jednoduše přímo úměrná N_i:

$$S_{preamp,i} = S_{preamp,i-1} e^{-\Delta t/\tau_{PA}} + kN_i \qquad \text{R-5.4}$$

kde τ_{PA} je časová konstanta předzesilovače (500 μs) a k je konstanta, která sice ovlivní celkovou amplitudu pulzu, ale nikoliv relativní světelný výtěžek. Při výpočtu předpokládáme, že

$S_{preamp,0} = 0$. To obecně nemusí být pravda. Pro splnění této podmínky je vhodné měření světelného výtěžku při nízké četnosti impulzů, což se autor snažil zajistit. Dále je nezbytné vyřadit z provozu tzv. Pole Zero Cancellation zesilovače, jehož vliv by bylo obtížné kvantifikovat. V případě velmi nízké četnosti impulzů by nemělo vyřazení Pole Zero Cancellation přinášet problémy.

Jakmile je známo R_k, lze RLY (τ) pro časovou konstantu τ spočítat:

$$RLY(\tau) = \frac{\max R_k(\tau)}{\max R_k(\tau_r)} \qquad \text{R-5.5}$$

Kde max $R_k(\tau)$, resp. max $R_k(\tau_r)$, je amplituda pulzu pro časovou konstantu τ, resp. τ_r, tj. referenční časovou konstantu, v našem případě 0,5 μs.

Ověření přístupu bylo provedeno na monokrystalu LuAG:Ce připraveného Czochralského metodou. Srovnání RLY naměřeného a předpovězeného ukazuje obr. 5.4 vlevo. Dosvit je na obr. 5.4 vpravo.

Cesta opačným směrem, tj. od závislosti RLY na časové konstantě zesilovače τ ke scintilačnímu dosvitu je též realizovatelná. Postačí zvolit vhodný model scintilačního dosvitu popsaný vhodnou funkcí s několika parametry a postupně parametry iterativně měnit tak, aby se předpověď závislosti RLY na τ shodovala s experimentálními daty.

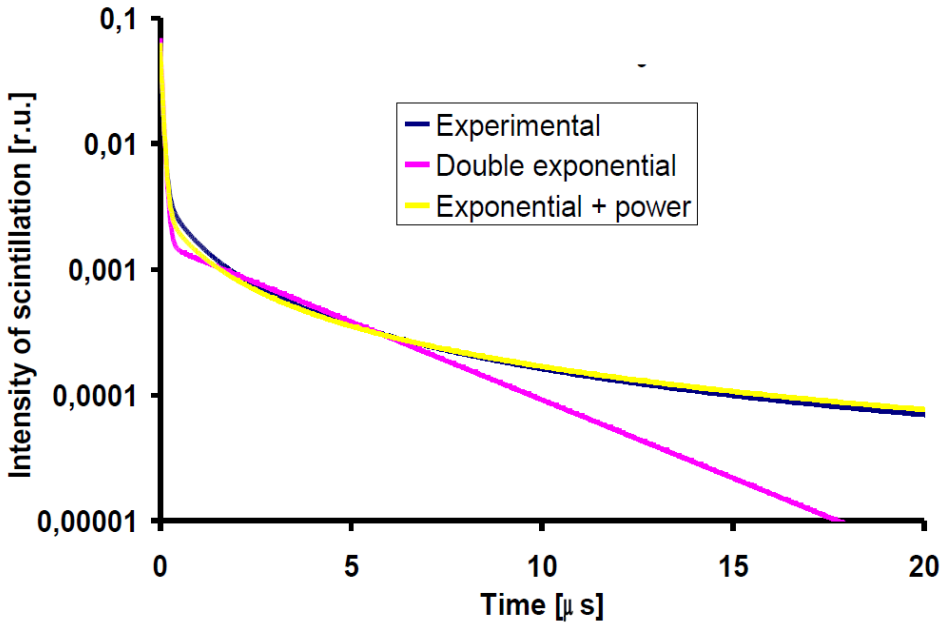

Obr. 5.5 – Srovnání dosvitu získaného experimentálně (modře) a na základě výpočtu s užitím modelu dvouexponenciálního dosvitu (fialově) a mocninného + exponenciálního dosvitu (žlutě) [164]**.**

Obr. 5.5 ukazuje srovnání scintilačního dosvitu získaného na základě výpočtu z experimentální závislosti RLY na τ pro model dvouexponenciálního dosvitu a mocninného dosvitu. Zatímco u dvouexponenciálního dosvitu vidíme velmi přibližnou shodu přibližně v intervalu 1-8 μs, v případě mocninné funkce je shoda dobrá téměř v celém zobrazeném rozsahu.

Srovnání počtu scintilačních fotonů vyzářených od 0 do času t, tj. v podstatě integrálu dosvitové křivky od 0 do t, na obr. 5.6 ukazuje ještě lepší shodu. Poměrně dobrá shoda je pozorována i u dvouexponenciálního dosvitu, navíc v širším intervalu.

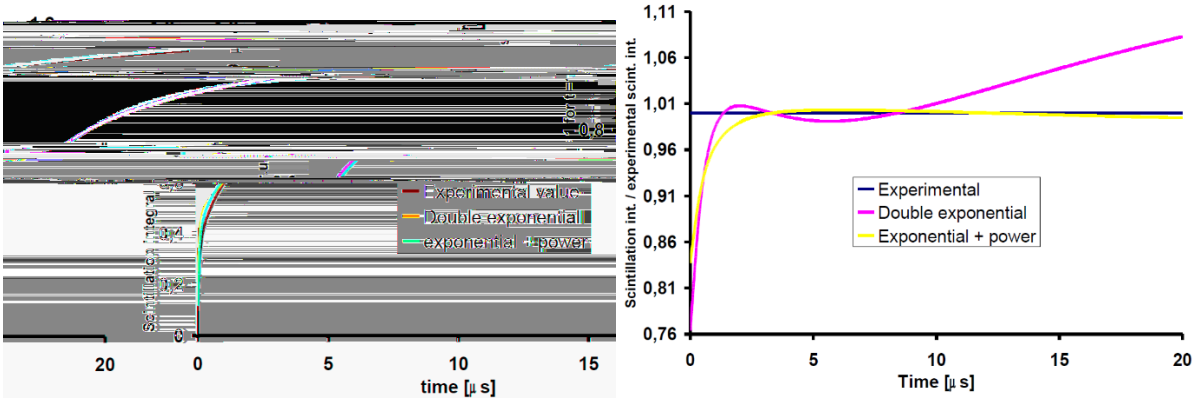

Obr. 5.6 – Vlevo: Srovnání scintilačního integrálu získaného experimentálně (modře) a na základě výpočtu s užitím modelu dvouexponenciálního dosvitu (fialově) a mocninného + exponenciálního dosvitu (žlutě). Vpravo: Podíl k experimentálním datům, tj. relativní odchylka od experimentálních dat [164].

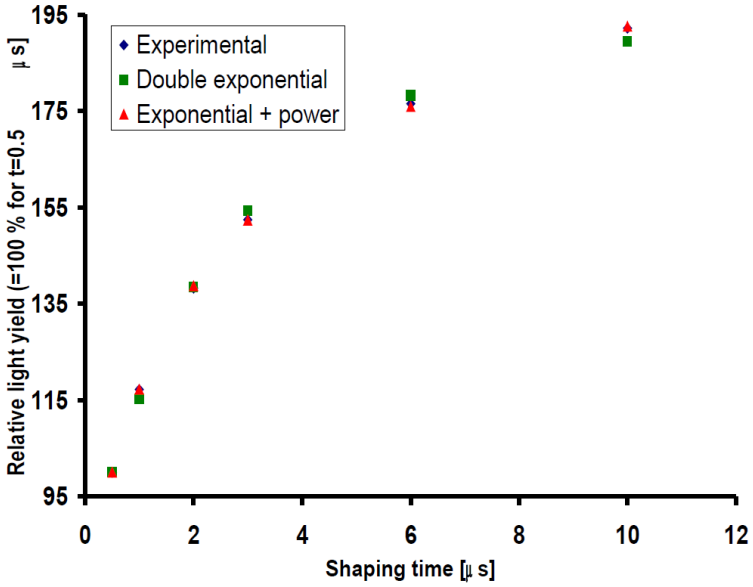

Obr. 5.7 – Srovnání závislosti RLY na τ: experimentální, vypočtený na základě nejlepšího odhadu dosvitu s užitím modelu dvouexponenciálního dosvitu a mocninného+exponenciálního dosvitu [164].

Jak ale rozhodnout, který model je lepší, když nemáme dosvitovou křivku k dispozici? Pokud určitý model vede k predikci závislosti RLY na τ zcela nesouhlasící s experimentálními daty,

je jeho vyřazení na místě. To ovšem není případ prezentovaného vzorku, jak ukazuje obr. 5.7. Menší odchylka modelu exponenciálního + mocninného může souviset s tím, že obsahuje jeden parametr fitu navíc. Lepší výsledek modelu s mocninnou funkcí tak lze např. považovat za indicii významného uplatnění tunelování elektronů z pastí do luminiscenčních center, ne však za jeho důkaz nade všechnu pochybnost.

Výše popsaná metoda nicméně dává velmi dobrý odhad tzv. scintilačního integrálu, což umožňuje např. relativně přesně vypočítat, jak by se scintilátor choval při zcela jiném způsobu tvarování, pokud by relevantní časy byly z intervalu asi 1-20 μs.

Na okraj poznamenáváme, že neshoda v časech asi 0-1 μs je dána dalším apriorním parametrem modelu, kterým je doba dosvitu rychlé složky. Pro hodnocení kvality modelu to není relevantní, experimentální nepřístupnosti časů 0-1 μs při měření světelného výtěžku si byl autor vědom předem.

Daným přístupem lze získat pouze jedinou relevantní informaci o fotonech rychlé složky, totiž jejich procentuální zastoupení. Na rozdíl od poměru hodnoty $K_{f/e}$ se jedná opravdu o podíl počtu fotonů, nikoli jejich podíl na signálu.

V případě jednoexponenciálních, pomalých dosvitů lze daným přístupem stanovit dobu dosvitu. Autor ověřil tuto možnost na vzorku $LiCaAlF_6$:Eu, pro nějž stanovil výpočtem ze závislosti RLY hodnotu 1,61 μs, přičemž experimentální hodnota stanovená z dosvitové křivky činí 1,68 μs [72][142].

5.1.2. Odezva epitaxních filmů s tloušťkou nižší než dosah budících α částic

V roce 2008 měřil autor sérii vzorků epitaxních filmů YAG:Ce, z nichž některé vykazovaly anomální tvar spektra, totiž spektra obsahovala dva píky, viz obr. 5.8, vlevo běžné spektrum, vpravo anomální spektrum. Všechny vzorky s anomálními spektry měly tloušťku podstatně nižší než je dosah α částic v YAG:Ce. V roce 2009 autor publikoval model, který vysvětloval velikost poměru ploch mezi oběma píky [156][262].

Odvození předpokládá přímou dráhu všech α částic, stejný dosah všech částic, nulovou tloušťku zdroje, izotropní emisi a kontakt zdroje přímo s epitaxním filmem. Dle obr. 5.9 [156][262] všechny částice emitované pod úhlem větším než je kritický úhel $\theta_{critical}$, odevzdají veškerou svoji energii v epitaxním filmu, zatímco ostatní částice předají pouze část své energie.

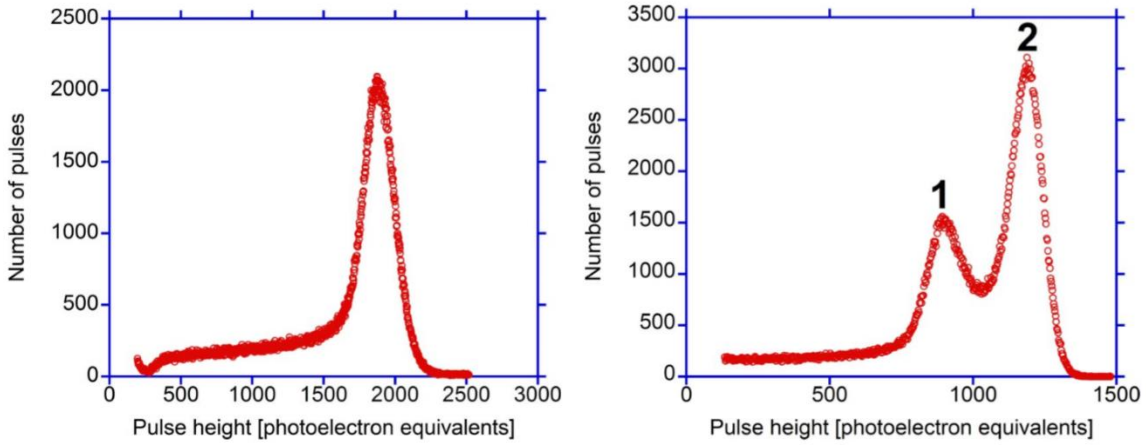

Obr. 5.8 – Vlevo: Amplitudové spektrum epitaxního filmu YAG:Ce s tloušťkou větší než dosah α částic. Vpravo: Totéž, ale vzorek s tloušťkou menší, než je dosah α částic. Pík 1 je od částic deponujících pouze část energie, pík 2 od částic deponujících veškerou energii [156][262]**.**

Uvažujme nyní plochu spojující všechny body, kde končí dráhy alfa částic emitovaných z jednoho bodu do epitaxního filmu. Jedná se o povrch polokoule se středem v bodě emise a poloměrem rovným dosahu α částic R_α. Koncové body drah částic, které pronikly až do substrátu, tvoří povrch kulového vrchlíku s poloměrem R_α a výškou $R_\alpha - d$, kde d je tloušťka filmu. Zřejmě platí, že podíl plochy kulového vrchlíku k ploše polokoule je i podílem počtu částic, jež předaly pouze část své energie ve filmu k počtu všech částic. Pro $d < R_\alpha$ tento podíl činí $1 - d/R_\alpha$. Naopak podíl částic, které předaly veškerou energii, činí d/R_α, více viz [156][262].

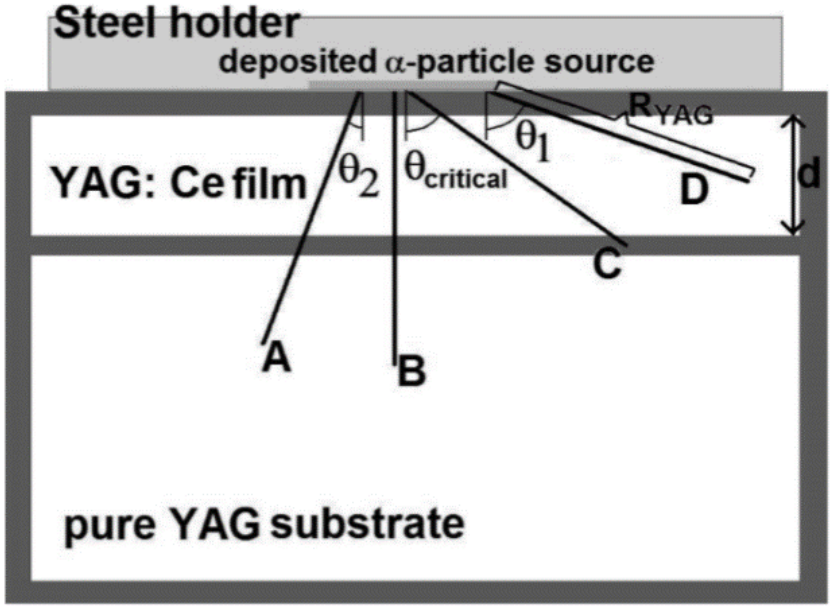

Obr. 5.9 – Geometrické uspořádání experimentu. Částice pouze prolétávající filmem (A,B) deponují jen část energie a přispívají k píku 1 v Obr. 5.8. Částice C a D deponují veškerou energii ve filmu a přispívají k píku 2 v Obr. 5.8 [156][262]**.**

Díky tomuto vysvětlení bylo prokázáno, že lze měřit světelný/fotoelektronový výtěžek a energetickou rozlišovací schopnost i při tloušťkách nižších než je dosah α částic. Kritická hranice se pohybuje asi u tloušťky d rovné třetině dosahu R_α. Pak je již pík úplné absorpce relativně nízký a vyhodnocení trpí značnou, s klesající tloušťkou zhoršující se nepřesností.

Článek [156][262] nicméně nijak neřeší, proč by částice vrstvou prolétající skrz měly vytvořit asymetrický pík. Vysvětlení této skutečnosti autor nabídl až v disertační práci a dále publikoval v [72][142]. Odvození je podstatně komplikovanější, zájemci jej naleznou v [71] a [72][142], zde je uveden pouze výsledek a jeho aplikace na jednu vrstvu YAG:Ce, viz obr. 5.10 a rovnice R-5.6:

$$\frac{dN}{dO} = \frac{1}{2} d \frac{E_\alpha}{R} \frac{\left(PhY_f - PhY_s\right)}{\left(O - PhY_s E_\alpha\right)^2} At \qquad \text{R-5.6}$$

kde E_α je energie α částice, R její dosah, PhY_f je fotoelektronový výtěžek filmu, PhY_s fotoelektronový výtěžek substrátu, O je odezva (ve fotoelektronových ekvivalentech), A aktivita zářiče, t doba měření a d tloušťka filmu [71] [72][142].

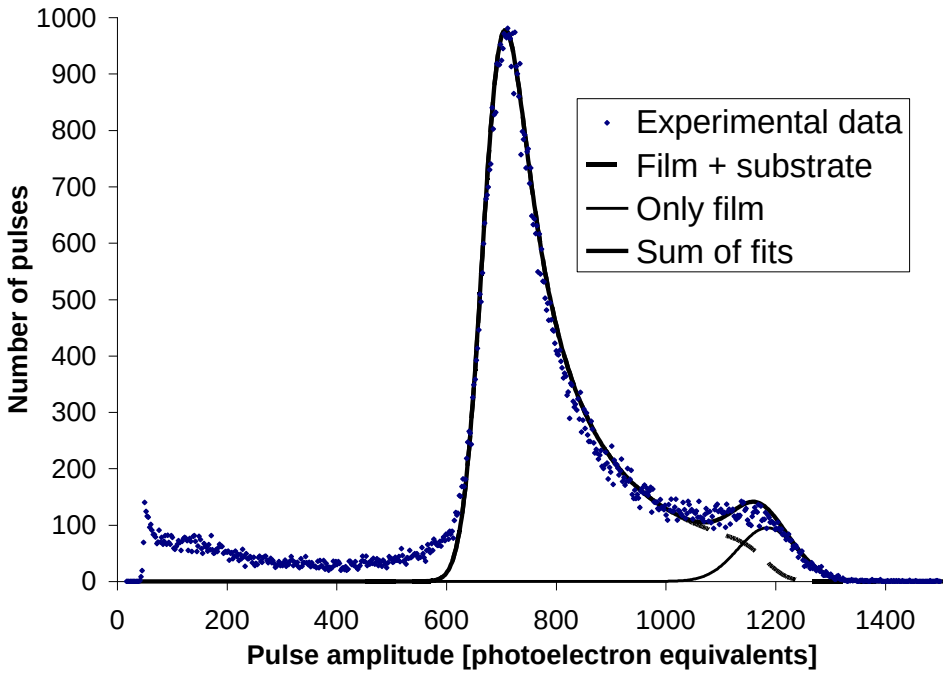

Obr. 5.10 – Spektrum epitaxního filmu YAG:Ce s tloušťkou menší než 2 µm fitované konvolucí gaussovy funkce a vztahu R-5.6 [72][142]**.**

V obr. 5.10 je výsledek dle rovnice R-5.6 navíc konvoluován s Gaussovou funkcí, aby byla zohledněna energetická rozlišovací schopnost, přičemž je uvažována i závislost energetické rozlišovací schopnosti na energii [72][142].

Možnost odkázat se na podrobné vysvětlení tvaru spektra rozptyluje případnou nedůvěru recenzentů, která může vzniknout, vidí-li nestandardní tvary spekter. V případě této práce se to týká vzorků z publikace [74][248], jež částečně vykazovaly tloušťku nižší než je dosah α částic.

5.2. Scintilační dosvity

Na rozdíl od měření fotoluminiscenčních dosvitů dochází při ozařováním částicemi ionizujícího záření nikoliv k přímému buzení jednoho konkrétního excitovaného stavu, ale ke vzniku množství elektron-děrových párů, jež mohou excitovat různé stavy řady luminiscenčních center, formovat excitony, být zachytávány v pastech apod. Z pastí se mohou nosiče náboje dostat díky tepelné energii, ale mohou z nich i tunelovat. Oblíbený příměr hovoří o fotoluminiscenci jako o stisknutí jedné klávesy klavíru a o scintilaci jako o shození klavíru ze schodiště. Scintilace je tedy podstatně složitější proces než fotoluminiscence.

Z tohoto důvodu není měření scintilačních dosvitů z hlediska získávání informací o scintilačním mechanismu ani zdaleka tak přesně zacílené, jako měření fotoluminiscenčních dosvitů. Jedná se však o zásadní užitný parametr, rozhodující o možnosti použití scintilátoru v řadě aplikací. Určité aplikace vyžadují velmi nízký podíl pomalých složek a velmi rychlý dosvit – např. zobrazovací metody s vysokou frekvencí snímání obrazu, spektrometrie při velmi vysokých četnostech. Jiné nevyžadují extrémně rychlý dosvit, nezbytný je však velmi nízký afterglow – typicky CT. K tzv. tvarové diskriminaci se využívá existence rozdílného průběhu impulzů v závislosti na druhu částice.

Z hlediska informací o scintilačním mechanismu, má měření scintilačních dosvitů spíše indikační charakter. V případě výskytu (i velmi) pomalých složek ukazuje na existenci pastí, případně dlouho žijících excitovaných stavů. Naměří-li se složky dosvitu rychlejší, než je dosvit aktivátoru, musí se ve scintilátoru nacházet jiné, velmi rychlé luminiscenční centrum.

Přínos autora k metodice měření scintilačních dosvitů dosud spočívá spíše v rovině identifikace problémů, určení podmínek, za nichž se tyto problémy (ne)vyskytují a návrhů jejich řešení. Jmenovitě se jedná o satelitní pulzy, „falešné pulzy“, amplitude walk a rozptyl v detekci prvního fotoelektronu.

Problém se satelitními pulzy byl triviální – spočíval v nevhodném výběru fotonásobiče, který produkoval relativně intenzivní satelitní pulzy se zpožděním asi 700 ns, viz obr. 5.11. Literatura o tomto druhu pulzů výslovně hovoří a dává je do souvislosti s nedokonalým vakuem ve fotonásobiči [165]. Zbytkové plyny jsou ionizovány procházejícím oblakem elektronů, přičemž

vzniklé kladné ionty asi za 700 ns (v našem případě) dopadnou na fk (fotokatodu) a vyrazí z ní určité množství elektronů. K řešení postačilo vyměnit PMT.

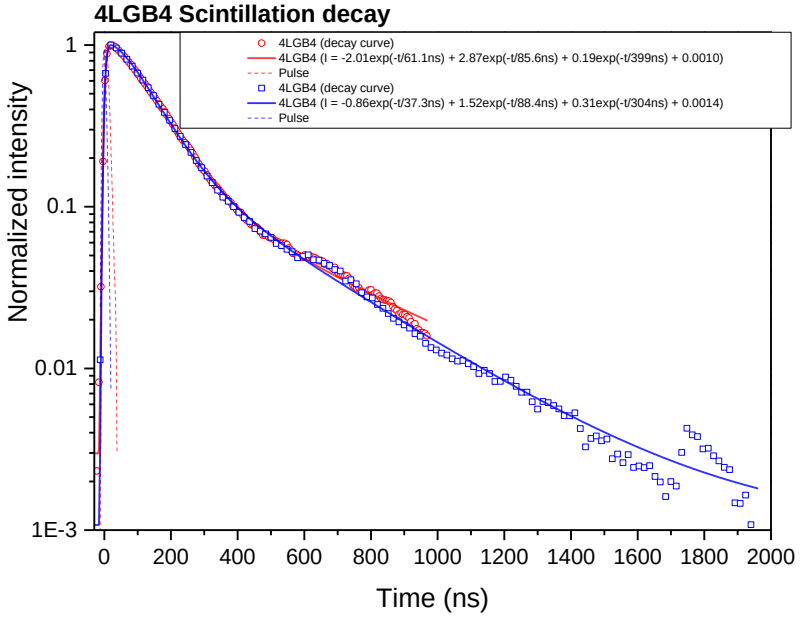

Obr. 5.11 – Scintilační dosvit multikomponentního granátového epitaxního filmu se zřetelnými satelitními pulzy (zhruba 700 a 1800 ns po excitaci) (Měřila Z. Lučeničová, poskytl M. Kučera).

Druhý problém spočíval v metodice měření. Aparatura k měření scintilačních dosvitů sestává pouze z PMT a osciloskopu, jenž zaznamenává scintilační pulzy. Jedinou použitelnou trigrovací metodou je u daného osciloskopu LET (leading edge triggering), tj. zobrazení průběhu od okamžiku překročení diskriminační hladiny. Při prvních měřeních osciloskop průměroval 512 měření. Pokud se mezi průměrované průběhy dostal impulz, který neodpovídal scintilační odezvě, změřená křivku se zdeformovala. Diskriminační hladinu nebylo možno položit příliš vysoko, neboť by se tím mohl zvýraznit tzv. amplitude walk. V případě měření vzorků s nízkým světelným výtěžkem to platí zvláště. V takovém případě existovalo vysoké riziko, že se do průměru „přimíchají“ velmi krátké temné impulzy (jedno-fotoelektronové události, čerenkovovo záření v okénku PMT). V současné době se již průběhy nabírají jednotlivě a ručně se vyřazují – automatický algoritmus je teprve v plánu. Tím byl i tento problém vyřešen. Zároveň tím odpadl problém amplitude walku – trigger osciloskopu slouží nyní pouze k rozhodnutí, zda pulz zaznamenat. Referenční časový okamžik je stanoven na základě LET až při zpracování dat. Po vyřazení „falešných“ pulzů lze v případě, že byly nabrány jen pulzy s relativně vysokou amplitudou, bez nebezpečí položit diskriminační hladinu velmi nízko a tím amplitude walk téměř eliminovat.

Dosud nevyřešeným problémem je rozptyl doby mezi interakcí částice a detekcí prvního scintilačního fotonu. Referenční okamžik, tj. „domnělý“ okamžik interakce, určujeme na základě samotného zaznamenaného signálu, žádné nezávislé určení referenčního času t = 0 nemáme k dispozici. Na scintilační odezvu lze nahlížet jako na sled v čase emitovaných scintilačních fotonů. Změřená odezva je pak součet odezev od jednotlivých zaznamenaných fotonů emitovaných v různých dobách po interakci. V tomto případě však první foton vždy zaznamenáme v čase t = 0, což působí níže popsané potíže.

Autor byl schopen prokázat, že se daný problém nezanedbatelně projevuje jenom u vzorků s malým světelným výtěžkem, resp. vzorků s malým výtěžkem v rychlé komponentě. Problém se komplikuje u vzorků s nezanedbatelnou náběžnou dobou. To si nyní ukážeme. Výklad zahájíme prezentací a interpretací dat získaných jednoduchými simulacemi. Prezentované simulace nebyly publikovány, prokazují nicméně, že výsledky měření scintilačních dosvitů jsou na časových škálách od zhruba 10 ns dále spolehlivé, i přes výskyt určitých „artefaktů“, které by mohly bez znalosti důvodů jejich vzniku vést k zpochybnění měření dosvitových křivek.

5.2.1. Vliv triggerovací metody na tvar změřené dosvitové křivky

Budeme uvažovat následující:

- Náběžné doby τ_r = 0, 1, 2 a 5 ns – první tři případy odpovídají reálným granátům, poslední je zařazen pro srovnání
- Různé počty fotoelektronů
- Doba dosvitu τ_d = 50 ns – pomalé složky nejsou uvažovány, jejich měření je ovlivněno minimálně.

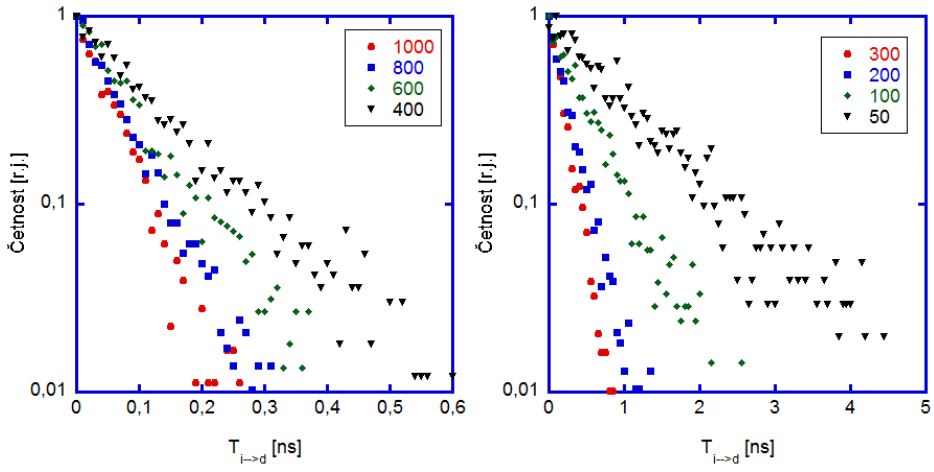

Obr. 5.12 – Frekvence scintilačních záblesků, u nichž první fotoelektron byl registrován v čase $T_{i\to d}$ po interakci. τ_r = 0. Střední počet fotoelektronů v záblesku je uveden v grafu.

V první sadě simulací budeme sledovat, jak je zpožděná registrace prvního fotoelektronu za interakcí. Simulace pracuje nejméně s tisíci scintilačními záblesky. Simulace jednoho záblesku nejprve generuje počet fotoelektronů v záblesku. Pro jednoduchost se předpokládá Poissonovo rozdělení se středním počtem N fotoelektronů.

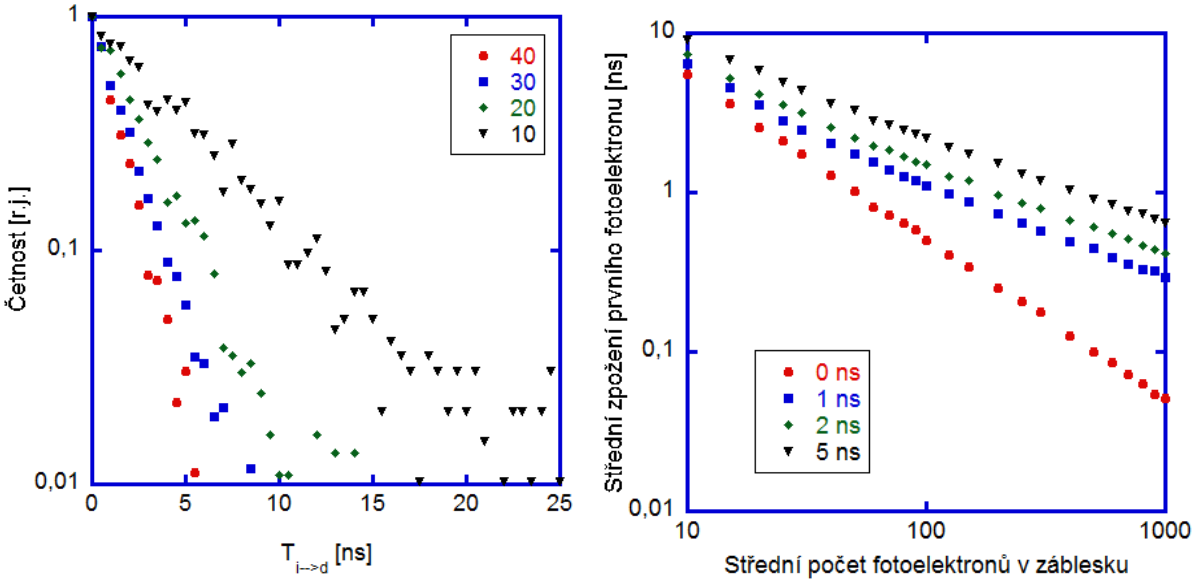

Obr. 5.13 – Vlevo: Frekvence scintilačních záblesků, u nichž první fotoelektron byl registrován v čase $T_{i\to d}$ po interakci. τ_r = 0. Střední počet fotoelektronů v záblesku je uveden v grafu. Vpravo: Závislost průměrného zpoždění prvního fotoelektronu na středním počtu fotoelektronů pro různé náběžné doby τ_r.

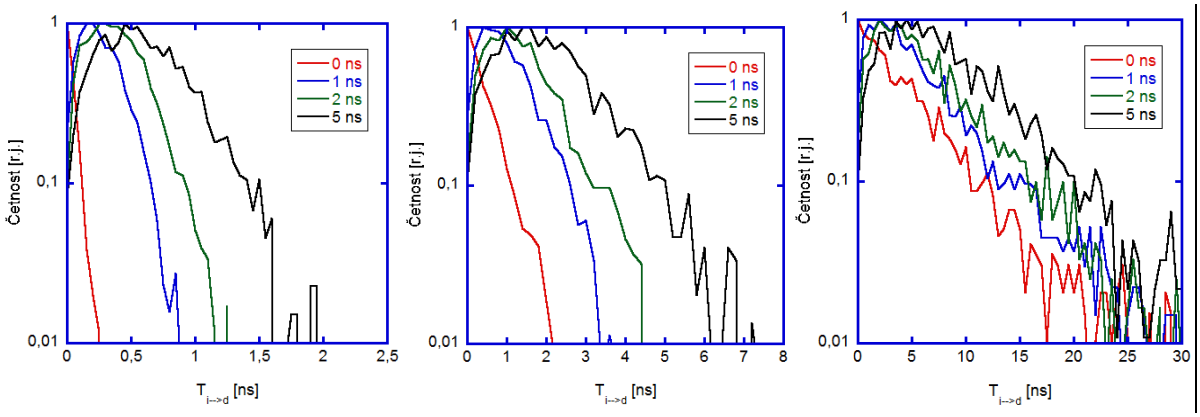

Obr. 5.14 – Frekvence scintilačních záblesků, u nichž první fotoelektron byl registrován v čase $T_{i\to d}$ po interakci pro různá τ_r. Střední počet fotoelektronů v záblesku je zleva doprava 1000, 100 a 10. Čáry namísto experimentálních bodů jsou použity kvůli větší přehlednosti.

Pro každý fotoelektron je pak generován čas zaznamenání od interakce. Minimální z těchto časů pro každý záblesk ztotožňujeme se zpožděním pulzu za interakcí. Obr. 5.12-5.14 ukazují, jak se liší distribuce tohoto zpoždění v závislosti na N a τ_r. Při τ_r = 0 vždy pozorujeme exponenciální distribuci, přičemž s nižším počtem fotonů se detekce prvního fotoelektronu

stále více opožďuje. V případě malého počtu fotonů může být zpoždění již poměrně značné. Obr. 5.13 vpravo ukazuje závislost průměrného zpoždění na středním počtu fotoelektronů, která je pro τ_r nepřímo úměrná počtu fotoelektronů. V případě velmi malého počtu fotoelektronů lze očekávat určitý vliv na změřený scintilační dosvit.

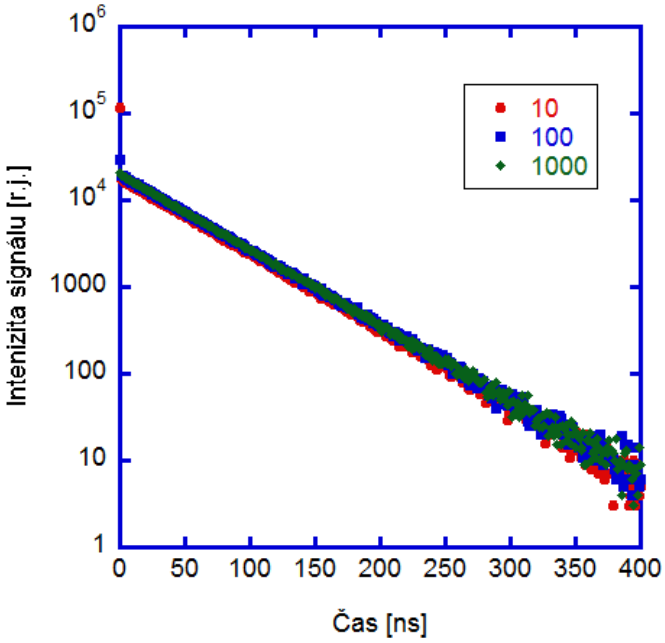

Obr. 5.15 – Tvar simulované odezvy v případě τ_r = 0 ns pro střední počet fotoelektronů 10, 100 a 1 000.

V souladu s očekáváním se distribuce mění v případě nenulové náběžné doby, viz obr. 5.13 vpravo a 5.14. Průměrné zpoždění za interakcí se zvětšuje, nejpravděpodobnější zpoždění se stává nenulovým a s rostoucím τ_r se prodlužuje. Nyní zjistíme, jak se tato zpoždění projeví v měřené odezvě.

Na rozbor nejjednodušší je opět případ s nulovou náběžnou dobou, viz obr. 5.15. Dosvit zůstal jednoexponenciální s dosvitovou konstantou τ_d = 50 ns, ovšem s jedním důležitým rozdílem. Všechny první fotony se shromáždily v čase 0 a jeví se jako okamžitá, promptní složka. Pokud vypustíme první bod pro t = 0 z grafu na obr. 5.15, proložíme závislosti exponenciálou a extrapolujeme do nuly, pak rozdíl mezi nasimulovanou a extrapolovanou hodnotou odpovídá počtu prvních fotonů. Podíl počtu prvních fotonů (roven počtu simulovaných scintilačních záblesků) k počtu všech fotonů logicky odpovídá 10 % při středním počtu 10 fotonů na záblesk, 1 % při 100 fotonech a zhruba (kvůli horší statistice) i 0,1 % při 1000 fotonech. Pokud se v prezentovaných grafech jeví promptní složka intenzivnější, je tomu kvůli volbě šířce časového intervalu (binu) Δt, širší interval by hodnotu opticky snížil, užší naopak ještě zvýšil. Promptní fotoelektrony padnou do intervalu 0-Δt vždy, zatímco množství fotoelektronů

v následujících intervalech je zhruba úměrné Δt. Provedení konvoluce s odezvovou funkcí aparatury tento „optický klam“ odstraní.

Falešná promptní složka signálu se objeví i v případě nenulových náběžných dob τ_r. Situaci ukazují obr. 5.16-5.18. Její podíl je prakticky totožný jako v případě nulové τ_r. Po skončení náběhu následuje exponenciální dosvit totožný s dosvitem reálným, od času zhruba 10 ns dále lze všechny křivky proložit exponenciálou s časovou konstantou τ_r = 50 ns. Ovšem na časové škále několika málo jednotek ns situace již tak jednoduchá není.

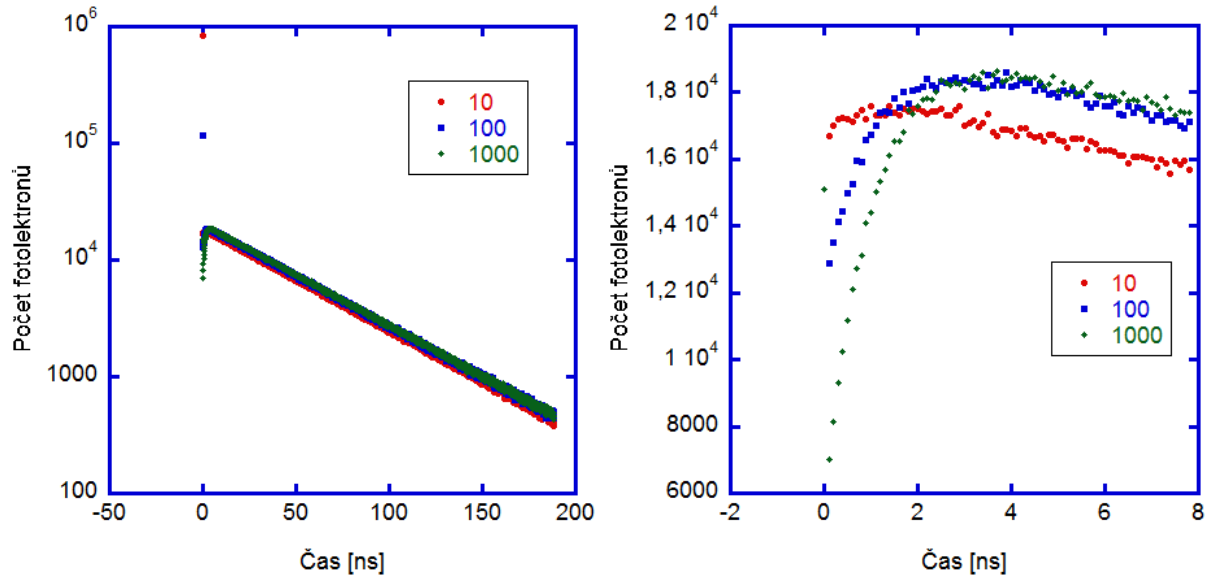

Obr. 5.16 – Tvar simulované odezvy v případě τ_r = 1 ns pro střední počet fotoelektronů 10, 100 a 1 000.

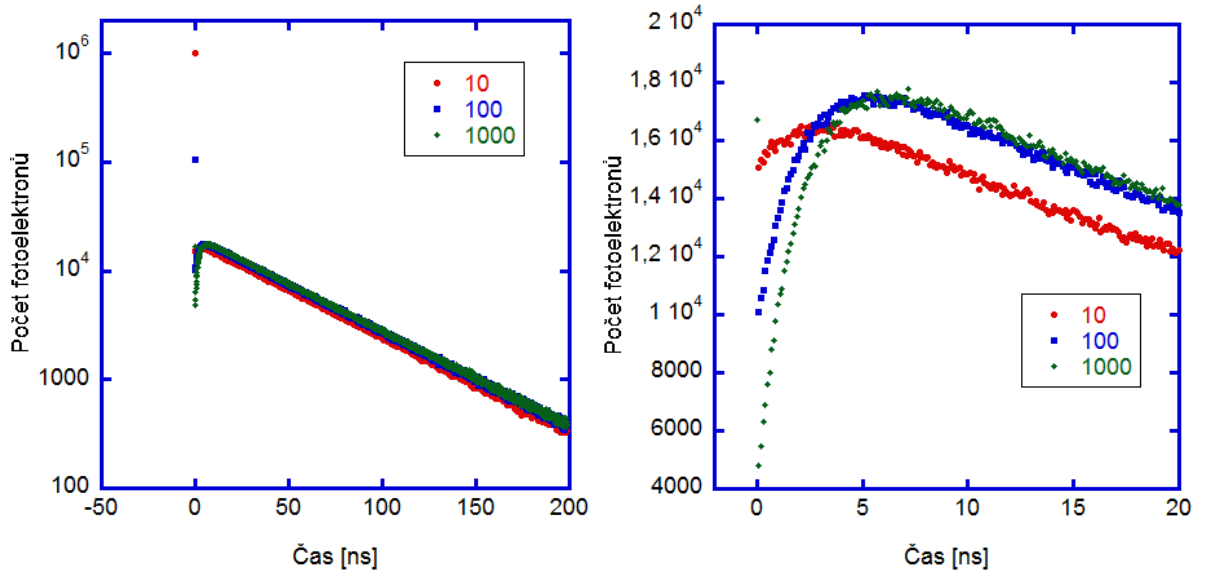

Obr. 5.17 – Tvar simulované odezvy v případě τ_r = 2 ns pro střední počet fotoelektronů 10, 100 a 1 000.

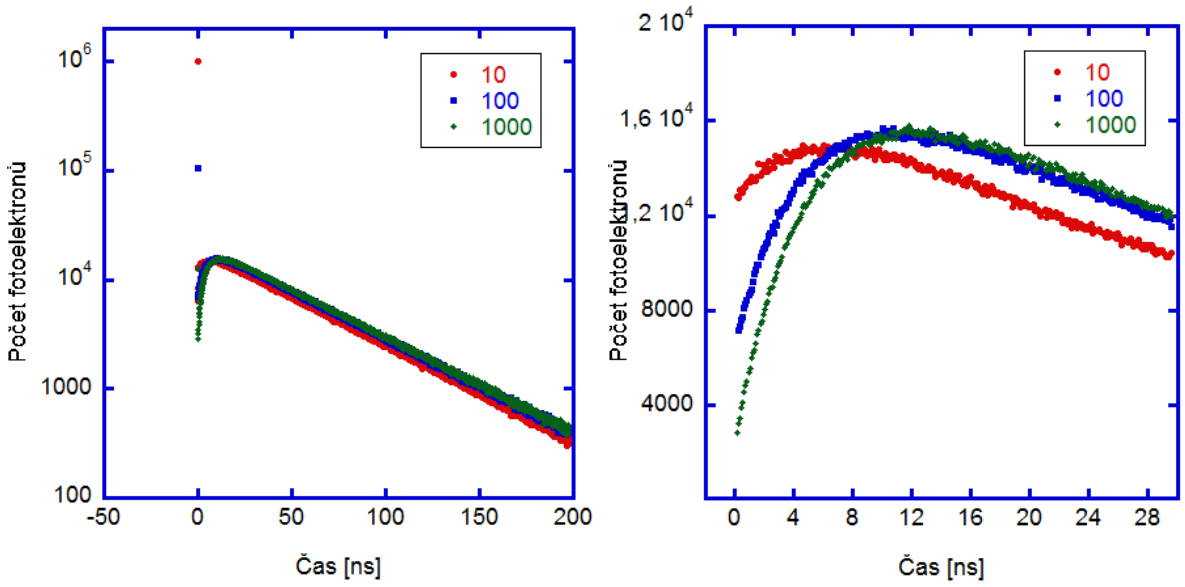

Obr. 5.18 – Tvar simulované odezvy v případě τ_r = 5 ns pro střední počet fotoelektronů 10, 100 a 1 000.

Odezva velmi silně závisí na počtu fotoelektronů. V případě 1000 fotoelektronů se situace blíží skutečnému průběhu scintilační odezvy, v případě 10 naopak pozorujeme relativně ploché maximum. Maximum se posouvá ke kratším časům s klesajícím počtem fotoelektronů. Je tomu tak proto, že v případě nižšího počtu fotoelektronů, první z nich dorazí relativně později, tj. v mnoha případech v době, v níž už náběh proběhl zcela nebo z velké části.

Z praktického hlediska jde o důležitý výsledek. Toto chování může působit potíže programu SpectraSolve při dekonvoluci odezvy, protože předpokládá pouze exponenciální odpad a náběh počínající ve stejném čase. Výsledky na časové na škále několik málo jednotek ns tak nelze považovat za zcela spolehlivé. Na druhou stranu jsou výsledky uklidňující v tom smyslu, že i při malém počtu fotoelektronů se chyby nejpozději v časech 10 ns beze zbytku „zahladí“. V době před vysvětlením tohoto jevu, se řada experimentálních dat „zahazovala“ s tím, že se jedná o „nesmysly“. Právě v prvních několika ns se v některých případech objevovaly „artefakty“, které neodpovídaly fyzikálními úvahami podloženému očekávání. Nyní víme nejen, čím jsou způsobeny, ale i to, že prakticky jakékoliv měření je vyhodnotitelné a pravděpodobně poskytne věrohodné výsledky, pokud se vzdáme informace z prvních několika málo ns.

Zbývá kardinální otázka, mají-li vypočtené simulace vztah k realitě. Existuje možnost, že budou měřeny vzorky s tak nízkým fotoelektronovým výtěžkem, že se simulované efekty projeví? Byly simulované jevy pozorovány? Odpovědi jsou po řadě: určitě ano, s vysokou pravděpodobností ano.

Světelný výtěžek LuAG:Ce dosahuje asi 20 000 fotonů/MeV. K vybuzení odezvy se používá běžně ^{137}Cs, s energií 662 keV. V případě menších vzorků (tj. skoro vždy) nemůžeme očekávat pravděpodobnou totální absorpci a musíme uvažovat pouze Comptonovo kontinuum. Z praktického hlediska (doba měření) můžeme volit nejenergetičtější třetinu kontinua, se střední energií zhruba 400 keV. 8 000 fotonů na scintilační záblesk při běžné kvantové účinnosti PMT pro LuAG:Ce asi 12,5 % a 100 % se dostáváme k číslu 1 000 fotoelektronů. Ovšem v případě některých vzorků jen asi 20 % z toho připadá na rychlou složku odezvy. Tj. hodnota 200 fotoelektronů nemusí být vzácnou ani u kvalitního vzorku.

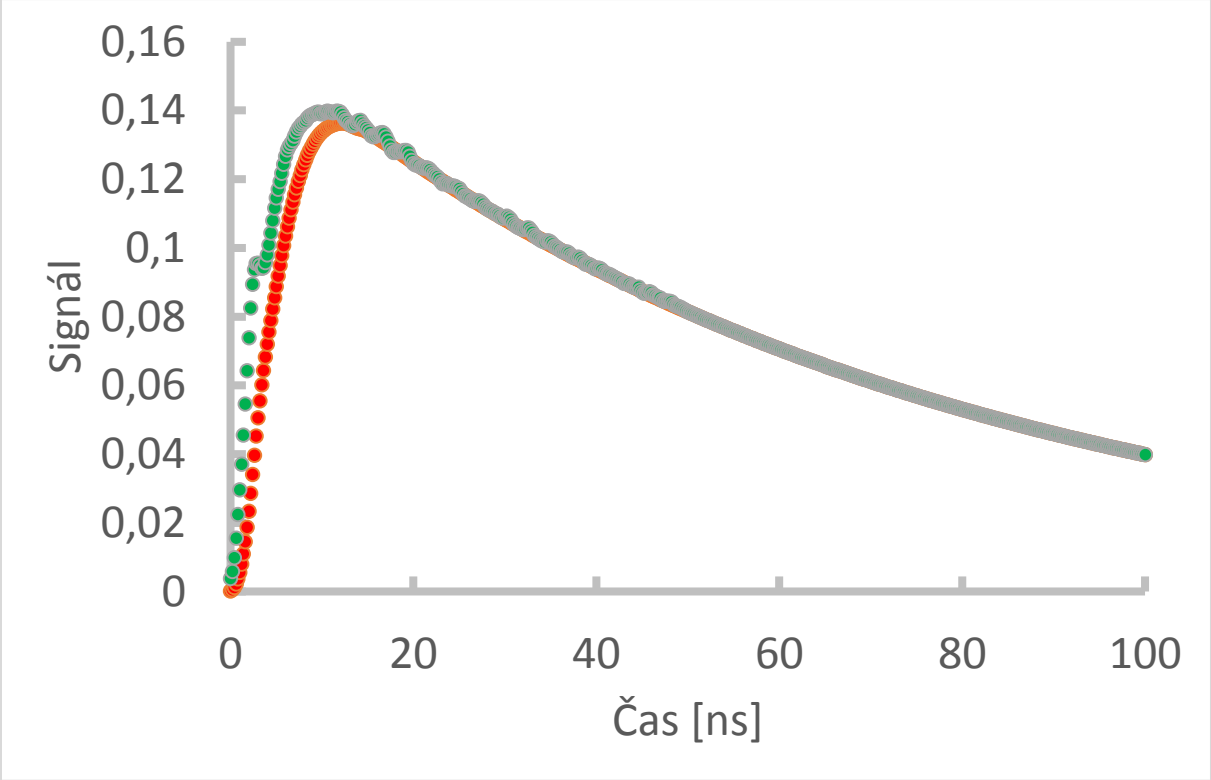

Obr. 5.19 – Konvoluce simulované odezvy s instrumentální odezvovou funkcí bez promptní složky (červeně) a s promptní složkou (červeně).

U ještě menších vzorků se někdy používá ^{241}Am s energií přibližně 60 keV, což vede k počtu pouhých 30 fotoelektronů. Při vědomí, že ne každý krystal má dobrou kvalitu, pak snadno přijmeme za možné, že průměrný scintilační záblesk skutečně může vyvolat odezvu sestávající z pouhých 10 fotoelektronů, tj. nejzazší hranice, pro niž jsme výpočty prováděli. V žádném případě nemá smysl uvažovat menší počet, takové pulzy by nebyly zaznamenány jako scintilační.

Projev falešně promptní složky by měl být jednoduchý. Pokud provedeme konvoluci odezvové funkce s nepromptní složkou odezvy, získáme hladkou křivku, viz obr. 5.19 vlevo (červeně).

Promptní složku přidáme jednoduše tak, že přičteme k-násobek odezvové funkce (obr. 5.20 - zelená křivka). Volba k říká, jaký je podíl promptní složky na celkovém počtu fotonů. Výsledkem je zelená křivka na obr. 5.19. Všechny nedokonalosti (vrcholy) odezvové funkce se nám nyní objevují v naměřené křivce, spojitá (nepromptní) složka nic takového nevykazuje. Hovorově řečeno, zelená křivka je hrbolatá. Že se i v reálném měření jedná o vliv promptní složky, vidíme na obr. 5.20. Zvýrazněná trojice vrcholů je za počátkem pulzu opožděna stejně v křivce instrumentální odezvy[2] i ve změřené dosvitové křivce. Naštěstí program SpectraSolve dokáže falešně promptní složku proložit s využitím tzv. funkce spike.

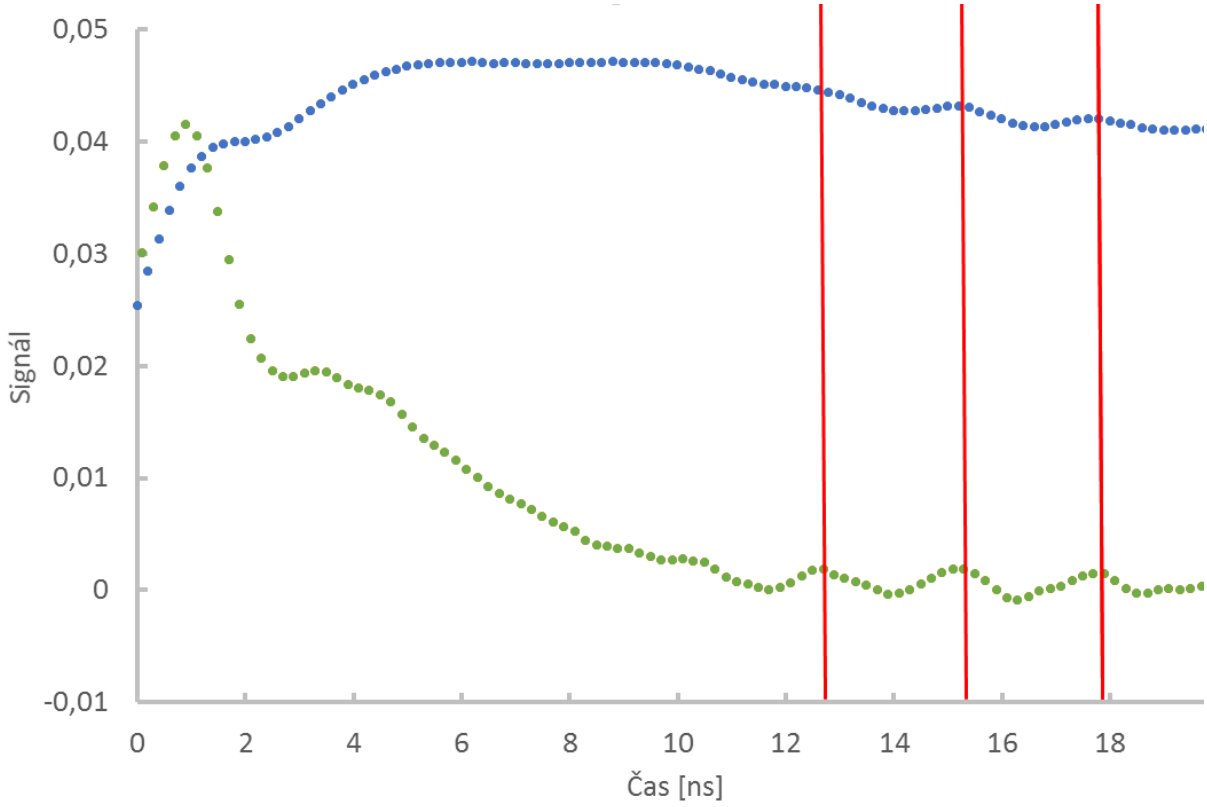

Obr. 5.20 – Srovnání naměřené instrumentální odezvové funkce (zeleně) a naměřené dosvitové křivky vzorku 1LGM2 (viz níže). Vidíme, že vrcholy instrumentální odezvové funkce se díky promptní složce fotoelektronů objevují i v naměřené dosvitové křivce.

Vliv počtu fotonů a náběžné doby na nepromptní složku signálu je podstatně subtilnější. Projevuje se jako krátký flat-top na vrcholu dosvitové křivky, který na pohled nemusí být významný, ovšem program SpectraSolve jej obvykle nedokáže zcela uspokojivě proložit.

[2] V tomto případě je instrumentální odezvová funkce obzvláště nedokonalá. Je to v důsledku snahy řešit problém míchání odezvové funkce do průměru odezev pomocí sofistikovanější triggrovací metody. To se sice podařilo, ale za cenu zhoršení odezvové funkce vlivem odrazů signálu. Amplitude walk se též touto metodou nepodařilo zcela eliminovat. Dnes oba problémy řešíme vyhodnocením všech průběhů signálu zvlášť, viz výše. Tato dosvitová křivka nicméně dobře demonstruje přítomnost promptní složky signálu.

Podobná odezva ale může vznikat i díky promptní složce. Vzhledem k tomu, že změny nepromptní složky jsou výraznější při nižším počtu fotoelektronů a podíl promptní složky téže roste s klesajícím počtem fotoelektronů, nelze jejich vliv jednoznačně oddělit.

Zajímavostí je, že pracovníci zodpovědní za měření a zpracování dat raději měří s pomalejším PMT (k dispozici jsou dva). Důvodem zřejmě je, že se podstatně méně setkávají s „artefakty" za něž je zodpovědná promptní složka signálu. Ta se v případě PMT s pomalejší odezvou rozloží do delšího času a tím se její vliv relativně sníží, protože nepromptní složka je rozložena v čase již ze své přirozenosti. Rozdíl mezi rychlým a pomalým PMT může vést až k pocitu, že, cituji: „něco je špatně." Podle všeho „nic špatně není", při použití pomalejšího PMT pouze efekt není pozorovatelný, případně je méně výrazný. Přítomen je však stále.

Poznatky části 5.2.1 jsou velmi čerstvé a nebyly dosud využity k úpravě experimentu.

Shrnutí a návrhy: Podařilo se vysvětlit původ některých „artefaktů" v dosvitových křivkách a prokázat, že jejich vliv poklesne s množstvím detekovaných fotoelektronů. Je tedy nanejvýš vhodné, aby byly voleny zářiče, jež účinně ukládají v detektoru větší množství energie a zajistil se účinný sběr fotonů (reflektor, optický gel).

V tuto chvíli nemá smysl měřit s rozlišením lepším než 1-2 ns. Na kratší časové škále jsou již „artefakty" dané odezvovou funkcí výrazné. Pokud nebude existovat nezávislý trigger, je promptní složka v principu neodstranitelná. Ten nicméně realizovat lze, např. pomocí velmi rychlého detektoru (i scintilačního) a zářiče ^{22}Na (2 současné fotony z anihilace pozitronu). Nevýhodou je snížení účinnosti měření a tím jeho prodloužení.

5.3. Termoluminiscenční měření

Ozářením pevné, krystalické látky ionizujícím zářením dochází k tvorbě elektron-děrových párů, viz obr. 2.1 [166]. Během fáze migrace mohou být tyto nosiče náboje zachyceny v pastech a tam dlouhou dobu setrvávat. Pokud později zahřejeme krystal na dostatečně vysokou teplotu, nosiče náboje začnou past opouštět a opět mohou volně migrovat krystalem. Pokud dorazí k luminiscenčnímu centru, rekombinují v něm a tím jej excitují. Při deexcitaci může být vyzářen luminiscenční foton. Jelikož byla tato emise stimulována zahřátím krystalu, nazýváme jev termoluminiscencí.

Termoluminiscenční měření se rutině používají k měření absorbované dávky, a to pomocí tzv. termoluminiscenčních dozimetrů. Pro tuto práci je nicméně významné, že dává možnost získat informace o pastech v krystalu a jejich základních charakteristikách.

V případě využití termoluminiscence ke studiu scintilátorů existují určitá specifika. U scintilátorů hrají významnou roli i pasti, v nichž nosiče náboje setrvávají pouhé μs či ms, neboť mohou podstatně prodloužit dobu dosvitu. Jak však změřit příslušný termoluminiscenční signál, když je za pokojové teploty de facto součástí scintilačního signálu? Řešením je ozařování krystalu při velmi nízkých teplotách, při nichž již je doba života nosiče náboje i v mělké pasti dostatečně dlouhá. Typicky se užívají teploty kolem 10 K. Postupným ohříváním pak lze uvolnit z těchto mělkých pastí nosiče náboje a pozorovat termoluminiscenci.

Hluboké pasti vykazující termoluminiscenci při teplotách nad pokojovou teplotou jsou předmětem zájmu též, neboť jsou zodpovědné za ztráty nosičů náboje během fáze migrace.

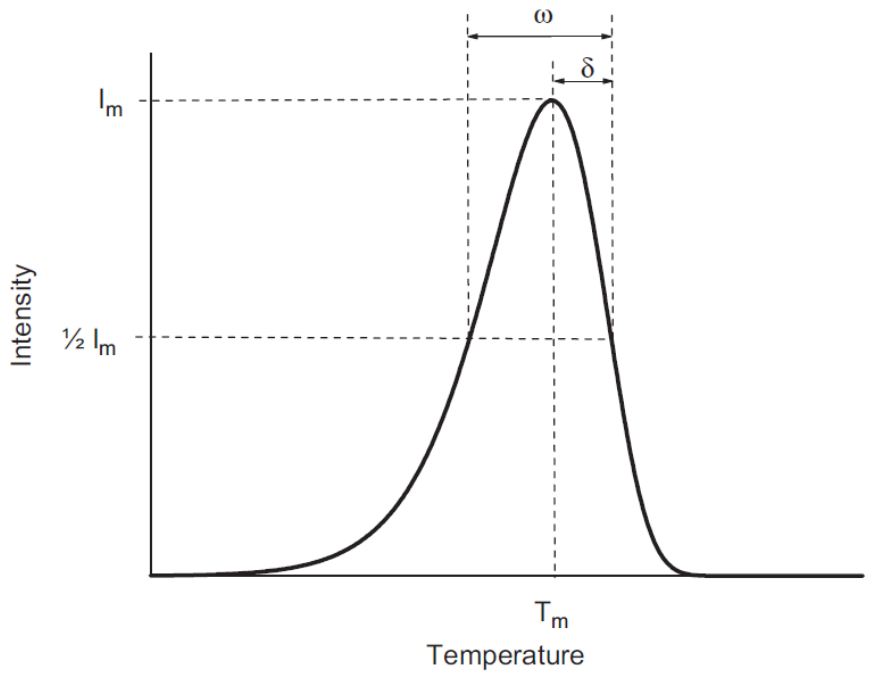

Obr. 5.21 – Termoluminisceční pík podle Randallova-Wilkinsova vztahu R-5.7 [166]**.**

Měření probíhá nejčastěji za lineárního nárůstu teploty rychlostí β (K/s) a současného měření intenzity luminiscenčního signálu, nejčastěji fotonásobičem. Každá past je charakterizována tzv. frekvenčním faktorem s a aktivační energií E (hloubkou pasti). Frekvenční faktor s lze intuitivně chápat jako počet pokusů opustit past, které nosič náboje vykoná za jednotku času. V článku [166] či knize [167] se nachází podrobnější výklad teorie termoluminiscence, zde se omezíme jen na základy.

V případě existence jediného typu pasti, kinetiky prvního řádu a lineárního ohřevu lze intenzitu signálu v závislosti na teplotě T popsat [166]:

$$I(T) = -\frac{1}{\beta}\frac{\mathrm{d}n}{\mathrm{d}t} = n_0 \frac{s}{\beta} \exp\left\{-\frac{E}{kT}\right\} \times \exp\left\{-\frac{s}{\beta}\int_{T_0}^{T} \exp\left\{-\frac{E}{kT'}\right\} \mathrm{d}T'\right\} \qquad \text{R-5.7}$$

kde β je rychlost růstu teploty, s frekvenční faktor, E aktivační energie, T_0 počáteční teplota a n_0 počáteční počet nosičů náboje v pasti. Průběh dle vztahu R-5.7 je obr. 5.21. Pík je nesymetrický, poměr δ/ω = 0,42 [166].

Pro případy kinetiky vyšší řádu byly odvozeny jiné vztahy, praxe nicméně ukazuje, že kinetika prvního řádu je zdaleka nejčastější. V materiálech je téměř vždy více typů pastí než pouze jedna, celková odezva se obvykle dá spočíst jako součet odezev od jednotlivých typů pastí, tj. lze využít principu superpozice.

V případě kinetiky prvního řádu závisí poloha pasti na vyhřívací křivce na frekvenčním faktoru s (s růstem s se pík posouvá směrem k nižším teplotám) a na aktivační energii E (s růstem E se pík posouvá směrem do vyšších teplot), n_0 ovlivňuje pouze plochu píku. Pokud by n_0 mělo vliv i na polohu, je to známka toho, že model kinetiky prvního řádu není pro danou past platný.

Tato práce se nicméně nezaměřuje na stanovení aktivační energie E a frekvenčního faktoru s, ani na stanovení fyzikální podstaty jednotlivých pastí. Snahou je ověření modelu zrychlení a zefektivnění scintilační odezvy kodopací Ce aktivovaných granátů kodopací hořčíkem. Dle zde použité interpretace přítomnost Mg^{2+} iontů výrazně snižuje pravděpodobnost zachycení elektronů v pasti η_{tr}. Platí [166]:

$$\eta_i = \frac{h\nu}{\beta' E_g} \eta_{tr} p S Q \eta_{esc} \qquad \text{R-5.8}$$

kde η_i je intrinstická luminiscenční účinnost, hν energie částice ionizujícího záření, β´ fenomenologický parametr (tentýž jako ve vztazích R-3.2 až R-3.4), E_g šířka zakázaného pásu, η_{tr} pravděpodobnost zachycení elektronu v pasti, p pravděpodobnost uvolnění elektronu z pasti, S pravděpodobnost, že uvolněný elektron rekombinuje v luminiscenčním centru, Q pravděpodobnost zářivé deexcitace luminiscenčního centra (účinnost luminiscenčního centra) a η_{ESC} pravděpodobnost detekce fotonu.

V práci nestanovujeme přímo hodnotu η_{tr}, zajímáme si nicméně o to, kolikrát se v případě Mg^{2+} kodopovaných vzorků změní oproti vzorkům nekodopovaným (více v následující kapitole). Je-li TL_A a TL_{Ref} intenzita termoluminiscenčního signálu získaného měřením vzorku A a referenčního vzorku (nekodopovaného), pak platí:

$$\frac{TL_A}{TL_{Ref}} = \frac{\eta_{i,A}}{\eta_{i,Ref}} = \frac{\eta_{tr,A} S_A Q_A}{\eta_{tr,Ref} S_{Ref} Q_{Ref}} \qquad \text{R-5.9}$$

S a Q na rozdíl od vykrácených veličin taktéž závisí na koncentraci Mg^{2+}. Díky měření světelného výtěžku a fotoluminiscenčního výtěžku však lze stanovit, když ne přímo S a Q, tak alespoň jejich poměry a tedy můžeme psát:

$$\frac{\eta_{tr,Ref}}{\eta_{tr,A}} = \frac{TL_{Ref} S_A Q_A}{TL_A S_{Ref} Q_{Ref}} \qquad \text{R-5.10}$$

Ve vztahu R-5.10 již vystupují pouze známé hodnoty.

Pro práci je důležitá možnost měření spektrálně rozlišeného termoluminiscenčního signálu. Díky tomu lze identifikovat, v jakém centru dochází k luminiscenční rekombinaci. Tento nástroj pak lze použít např. ke zjištění, zda se jedná o elektronovou nebo děrovou past. V této práci spektrální měření posloužilo zjištění, zda měřený signál pochází z Ce^{3+} (filmu) nebo jiného centra (substrátu).

Kapitola 6

Zvýšení kvality granátových scintilátorů – metoda a fyzikální model

Dle obr. 3.4 má materiál LuAG:Ce značný deficit světelného výtěžku oproti teoretickým možnostem. Přitom jeho radioluminiscence je podstatně intenzivnější. To naznačuje, že velká část (dokonce většina) scintilačních fotonů je vyzářena v době, kdy již nemají šanci přispět k užitečnému signálu (mimo jiné i při měření světelného výtěžku). Intenzivní složky s dlouhým dosvitem pak byly ve scintilačních dosvitových křivkách pozorovány přímo [163].

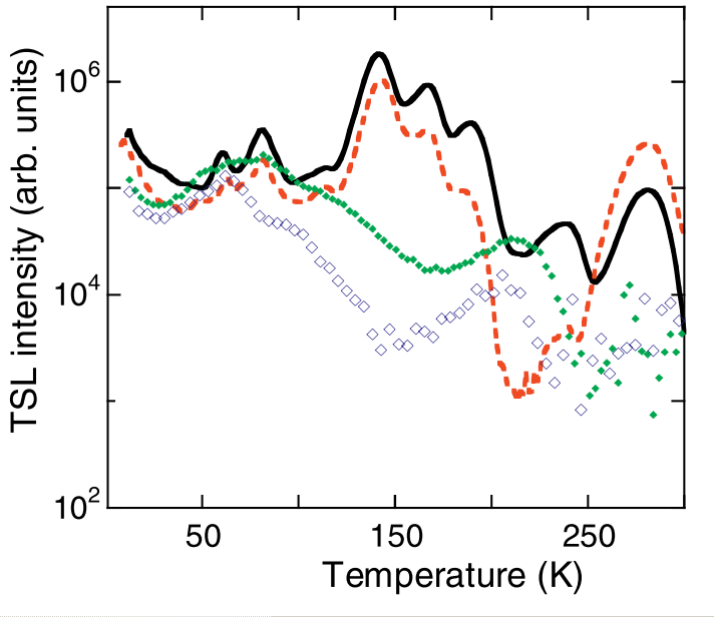

Obr. 6.1 – Vyhřívací křivky LuAG:Ce krystalů (černá, červená) a epitaxních filmů (modrá, zelená) [28].

Za výrazné zpomalení scintilační odezvy mohou pasti, což prokazují termoluminiscenční měření. Současný konsenzus říká, že za ně jsou zodpovědné tzv. Lu_{Al} antisite defekty, vznikající v důsledku růstu při vysoké teplotě. Metody růstu při nízké teplotě, např. LPE jejich vznik potlačují, což se projeví redukcí řady píků v termoluminiscenčních odezvách, viz obr. 6.1 [28]. Tolik stručné shrnutí stavu poznání zhruba v roce 2010.

Tato kapitola pojedná o dvou přístupech uplatněných ve snaze zlepšit vlastnosti granátových scintilátorů o vyšším Z: „band-gap engineering“ a „defect engineeringu“ v podobě kodopování ionty Mg^{2+}. Obě tyto metody mají v jádru podobnou „filozofii“. Snahou není zabránit vzniku antisite defektů a s nimi spojených pastí, ale zajistit, že tyto pasti nebudou mít negativní vliv na vlastnosti scintilátoru.

6.1. Band-gap engineering

Pro granátové scintilátory byla idea band-gap engineeringu [168] prvně prezentována v práci [36]. Vodivostní pás je tvořen stavy iontů Al^{3+}, které tedy určují jeho polohu. Substituce Al za Ga (Ga je v periodické tabulce hned pod Al) vede k posunu dna vodivostního pásu tak, že při určité koncentraci Ga již pasti nejsou uvnitř zakázaného pásu, ale v pásu vodivostním, viz obr. 6.2 [36].

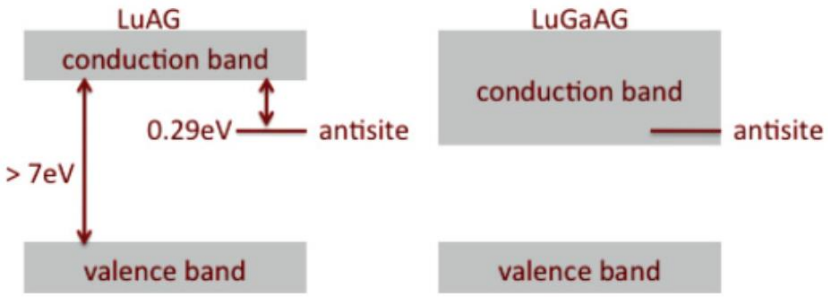

Obr. 6.2 – Schéma pásové struktury LuAG a LuGAG ($Lu_3(Ga,Al)_5O_{12}$). V LuAG se past spojená s AD nachází v zakázaném pásu, v LuGAG v pásu vodivostním [36]**.**

Experimentální důkaz tohoto modelu lze demonstrovat např. termoluminiscenčními měřeními, viz obr. 6.3 [169]. S růstem koncentrace Ga klesá plocha dominantního píku i některých dalších. Také dochází k posunu píku směrem k nižším teplotám, což indikuje pokles aktivační energie pasti (hloubky pasti).

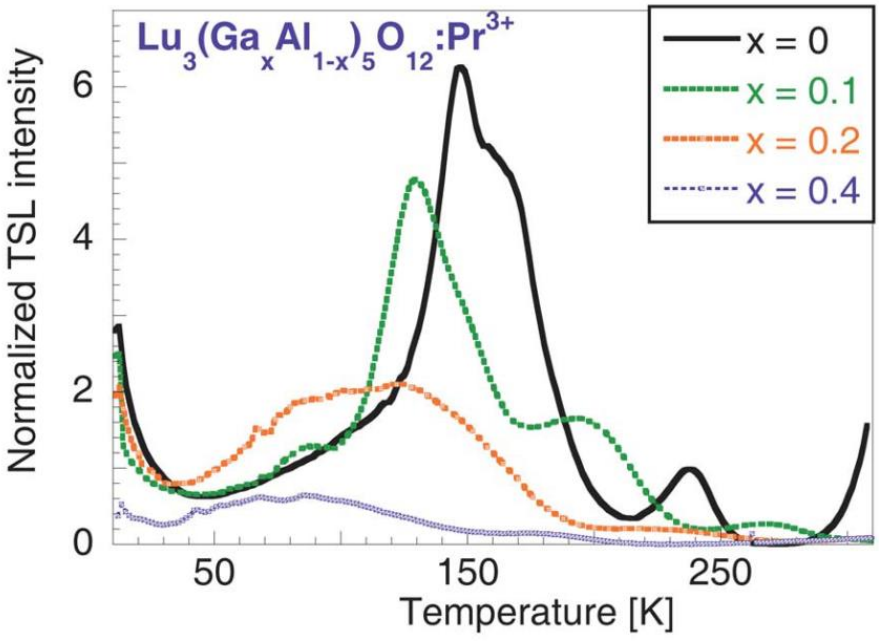

Obr. 6.3 – Vyhřívací křivky LuGAG:Pr a LuAG:Pr keramik s různou koncentrací Ga [169]**.**

Snížení dna vodivostního pásu má však i negativní efekt. Dno vodivostního pásu se přiblížilo $5d_1$ excitovanému stavu Ce^{3+}, čímž se stala nezanedbatelně pravděpodobnou jeho ionizace [38]. I při pokojové teplotě je pozorován únik elektronu z tohoto stavu do vodivostního pásu [170].

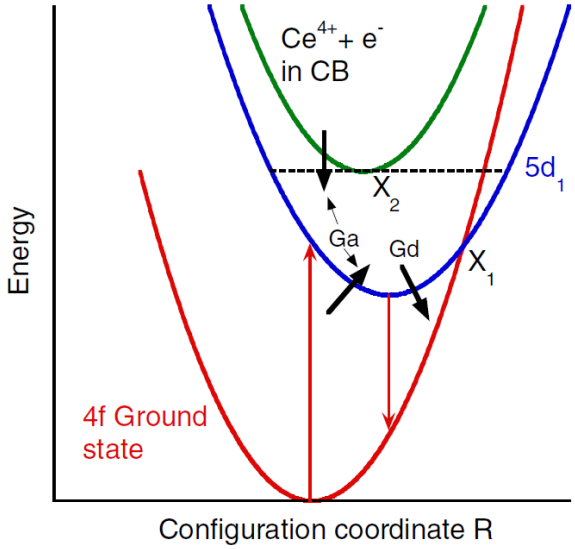

Obr. 6.4 – Zjednodušený konfiguračně koordinační diagram LGGAG:Ce čili $(Lu,Gd)_3(Al,Ga)_5O_{12}$:Ce [38].

Substituce, tentokrát Lu^{3+} za Gd^{3+},umožňuje ovšem i posun polohy tohoto excitovaného stavu, viz obr. 6.4 [38]. Experimentální optimalizace vzájemného poměru Lu/Gd a Al/Ga vedla k velmi dobrým výsledků, přičemž nejlepší výsledky vykazoval materiál přibližného složení $Gd_3Ga_xAl_{5-x}O_{12}$:Ce (GGAG:Ce), kde x je z intervalu 2-3. Světelný výtěžek se značně přiblížil teoretickému limitu, zlepšila se energetická rozlišovací schopnost a byly výrazně potlačeny pomalé složky odezvy, včetně afterglow. V současné době nejlepší monokrystaly dosahují hodnot (LY = 60 000 fotonů/MeV [171], FWHM = 3,7 % [172]), keramiky (LY = 70 000 fotonů/MeV [39], FWHM = 8,3 % (pravděpodobně PMT) [173] a epitaxní filmy LY = 8 750 fotonů/MeV, FWHM = 7,4 % [73][214]. Výsledky uvedené pro epitaxní filmy jsou získány při buzení α částicemi z ^{239}Pu, ostatní fotony γ z ^{137}Cs.

Tolik stručné vysvětlení a popis výsledků. Zájemce o podrobnosti a další prameny autor odkazuje na své články [74][248] [73][214] [59][133].

6.2. Mg^{2+} kodopování

Již delší dobu bylo známo, že kodopování ortosilikátů LYSO:Ce a LSO:Ce ionty Ca^{2+} a Mg^{2+} vede ke zlepšení jejich scintilačních vlastností, zrychlení odezvy a zvýšení světelného výtěžku [174] [175] [176] [177]. Vysvětlení mechanismu tohoto zlepšení přišlo s publikací [176].

Ionty Ca^{2+} a Mg^{2+} jsou v materiálu LYSO a LSO aliovalentní, tj. v materiálu musí dojít ke kompenzaci elektrického náboje. Částečně se tak děje přeměnou Ce^{3+} iontů v Ce^{4+}. Je kuriózní, že iont Ce^{4+}, jenž přímo zodpovídá za zlepšení scintilačních vlastností, byl v minulosti velkou částí vědecké komunity považován za nežádoucí [178].

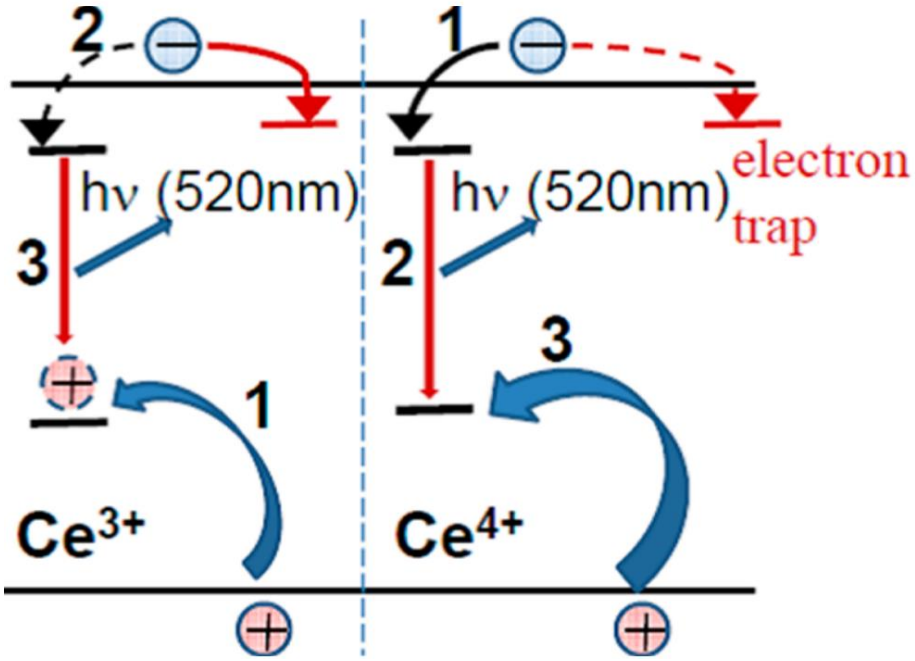

Obr. 6.5 – Schéma scintilačního mechanismu zprostředkovaného ionty Ce^{3+} (vlevo) a Ce^{4+} (vpravo) v LuAG:Ce [54].

Pochopení mechanismu zlepšení poskytuje obr. 6.5 [54], z nějž je zřetelný rozdíl mezi luminiscencí (scintilací) zprostředkovanou Ce^{3+} a Ce^{4+} centrem:

- Ce^{3+} nejdříve zachytí díru, čímž se dočasně změní v Ce^{4+} iont. Ce^{4+} potom zachytí elektron, vzniká excitovaný stav Ce^{3+}. Při deexcitaci je vyzářen scintilační foton.
- Ce^{4+} nejdříve zachytí elektron, což vede ke vzniku excitovaného stavu Ce^{3+}. Pak je vyzářen foton. Zachycení díry dočasným Ce^{3+} centrem jen vrací systém do původního stavu.

Právě v čekání na zachycení díry spočívá kritický rozdíl mezi Ce^{3+} a Ce^{4+} iontem. Než Ce^{3+} ionty zachytí díry, podstatná část elektronů se zachytí v pastech. Rozhodují první nanosekundy, což lze demonstrovat např. náběžnou dobou nekodopovaného LuAG:Ce [136]. Ce^{4+} ionty jsou připraveny k zachycení elektronů již v okamžiku interakce, soutěží tedy s pastmi o elektrony s mnohem vyšší účinností.

Aplikace metody poprvé použité v ortosilikátech na granáty vedla k úspěchu, s tím drobným rozdílem, že namísto Ca^{2+} se jako vhodnější kodopant ukázal být Mg^{2+}. Došlo, jak k potlačení pomalých složek odezvy, tak k nárůstu světelného výtěžku u LuAG:Ce [56] i YAG:Ce [52], a to v monokrystalech, keramikách i epitaxních filmech. Teoretického limitu z obr. 3.4 nicméně dosaženo nebylo, nejlepší hodnoty jsou 25 000 fotonů/MeV [56]. Při vyšších koncentracích Mg^{2+} dochází sice k dalšímu zrychlování odezvy, světelný výtěžek však klesá [54]. Obojí je konzistentní s existencí tzv. rekombinačních center. Ty dávají elektron-děrovým párům další možnost rekombinace, která je však nezářivá. Nejdůležitějším rekombinačním centrem v granátech je pravděpodobně O^- [179] [180].

Kodopování Mg^{2+} není beze zbytku přínosné pro všechny Ce dopované granáty. V GGAG:Ce dochází sice ke zrychlení odezvy, ale významnější zlepšení světelného výtěžku pozorováno nebylo [58] [181]. Předpokládá se, že v GGAG:Ce již naprostá většina scintilačních fotonů pochází z rychlé složky odezvy a v pastech jsou elektrony zachytávány jen málo. Ce^{4+} sice částečně zabrání zachycení těchto elektronů v pastech, efekt je však nevýrazný z hlediska světelného výtěžku. Naopak konkurence O^- vede ke zhášení luminiscence – a též k jejímu dalšímu zrychlování. Mg kodopovaný GGAG:Ce lze tedy doporučit jen tehdy, jsou-li pomalé složky scintilační odezvy více nežádoucí, než světelný výtěžek žádoucí.

Pokud čtenáře zajímají další podrobnosti, nalezne je v úvodu autorovy publikace [59][133] [60][123], která mu zároveň poslouží jako seznam recentní literatury o tomto tématu.

Kapitola 7

Zvýšení kvality granátových scintilátorů – experimentální výsledky a jejich interpretace

V kapitole 7 se nachází výtah z publikací autora věnujících se zlepšení vlastností granátových scintilátorů. Jelikož se veškeré autorovy publikace s danou tematikou nacházejí v přílohách této práce, kapitola se soustředí pouze na autorův přínos, případně doplňuje některé informace neznámé v době publikace či z jiného důvodu v publikacích nezmíněné.

7.1. Monokrystaly $(Lu,Gd)_3(Al,Ga)_5O_{12}$:Ce

V roce 2008 byly připraveny první scintilační keramické materiály se složením $Gd_3(Al,Ga)_5O_{12}$:Ce, vykazující mezi granáty nízký afterglow [182]. Zvýšení světelného výtěžku a dalších scintilačních vlastností v granátech složení $(Lu,Y,Gd)_3(Al,Ga)_5O_{12}$:Ce bylo publikováno v roce 2009 [37]. Následovaly práce věnující se hledání optimálního složení, z nichž pro účely této práce je zvláště důležitý článek [35]. Pro danou studii bylo metodou μ-PD připraveno velké množství vzorků s různými poměry Lu/Gd a Al/Ga. Nejvyšší světelný výtěžek vykázaly vzorky se složením $Gd_3Al_2Ga_3O_{12}$:Ce (42 200 foton/MeV) a $Gd_3Al_3Ga_2O_{12}$:Ce (45 900 foton/MeV), což znamenalo dvojnásobný LY proti nejlepším LuAG:Ce monokrystalům té doby [183]. Pozorováno bylo dále zrychlení scintilační odezvy i snížení intenzity termoluminiscenčního signálu. Následovaly první vzorky připravené Czochralského metodou [69].

Díky spolupráci s Tohoku University dostal autor v roce 2012 příležitost změřit scintilační vlastnosti obdobných vzorků, připravených metodou Czochralského [67][253] [184]. Složení vzorků bylo $Lu_xY_yGd_{3-x-y}Al_2Ga_3O_{12}$:Ce. Téměř všechny vzorky obsahovaly 1 % Ce, jeden pak 2 a ještě jeden 3 %. Složení i s výsledky měření jsou v Tabulce 7.1, index u písmene G odpovídá stechiometrickému koeficientu Gd (3-x-y), u písmene L odpovídá Lu (x), u písmene Y odpovídá Y (y) a u písmene C obsahu Ce. Vzorky byly velikosti 5 × 5 × h mm, kde h = 1 mm, pokud není pomocí indexu uvedeno jinak. Počáteční číslice značí sérii vzorků.

Nejvyššího světelného výtěžku bylo dosaženo v případě první série u vzorku $1G_3C_{1\%}$, který rovněž v rámci série vykazoval nejlepší rozlišovací schopnost. Jeho neproporcionalita sice nebyla nejnižší, viz též obr. 7.1, ale rozdíl ve velikosti světelných výtěžků převážil.

Vyšší obsah Ce obecně vede k vyšší účinnosti přenosu energie k luminiscenčnímu centru Ce^{3+}. Přesto však pozorujeme pokles světelného výtěžku, jenž je zřejmě dán tzv. koncentračním zhášením vlivem toho, že Ce se agreguje a vytváří tak centra s odlišnými vlastnostmi od izolovaného Ce^{3+} centra. Alternativní vysvětlení v podobě vzniku defektů díky vyšší koncentraci Ce^{3+} je méně pravděpodobné, neboť nebyly pozorovány projevy těchto hypotetických defektů v termoluminiscenčních měřeních [185].

Sample	LY [ph/MeV]	FWHM [%]	LY_{22}/LY_{662} [%]	$K_{f/e}$ [%]
$1G_3C_{1\%}$	48 300	7.3	84	86
$1G_3C_{2\%}$	22 700	13.2	90	94
$1G_3C_{3\%}$	29 500	9.4	88	95
$1Y_2G_1C_{1\%}$	28 900	11.3	66	84
$1L_2G_1C_{1\%}$	25 800	12.9	81	58
$1L_2Y_1C_{1\%}$	21 300	17.0	67	85
$1L_1G_2C_{1\%}$	12 100	16.3	90	41
$2G_3C_{1\%,1mm}$	50 600	5.5	85	91
$2G_3C_{1\%,2mm}$	50 300	6.2	84	94
$2G_3C_{1\%,4.5mm}$	43 100	7.3	82	94
$2G_3C_{1\%,10mm}$	41 100	7.3	85	92

Tabulka 7.1 – Složení vzorků $Lu_xY_yGd_{3-x-y}Al_2Ga_3O_{12}$:Ce, jejich světelný výtěžek LY (τ = 1 μs), poměr světelného výtěžku měřeného při energii 22 a 662 keV vyjadřující neproporcionalitu odezvy a podíl rychlých fotonů na odezvě $K_{f/e}$ [67][253].

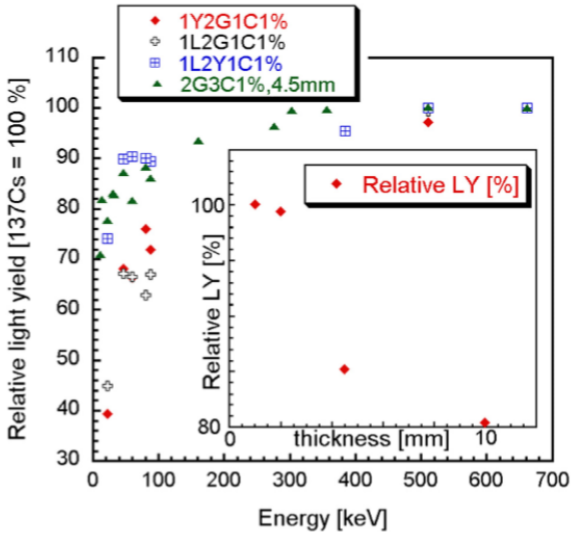

Obr. 7.1 – Závislost světelného výtěžku vzorků první série na energii budícího záření, 100 % odpovídá 622 keV (^{137}Cs). Inset: Závislost světelného výtěžku vzorků druhé série na tloušťce vzorku, 100 % odpovídá 1 mm [67][253].

Vyšší světelný výtěžek vzorku 1 $G_3C_{1\%}$ v rámci první série rovněž souvisí s vyšší hodnotou $K_{f/e}$ a menším podílem pomalých složek dosvitu na odezvě, viz obr. 7.2. Při nižším obsahu Gd pravděpodobně dochází k ionizaci $5d_1$ stavu Ce^{3+} a následnému zachycení elektronu v pasti. V případě vzorku 1 $G_3C_{1\%}$ již od času 2 μs prakticky vůbec nedochází ke zvýšení odezvy, snížení polohy excitovaného stavu je tedy dostatečné.

Inset obr. 7.1 ukazuje závislost změřeného světelného výtěžku na velikosti vzorku. Pokles je poměrně běžným jevem a je způsoben zhoršeným sběrem fotonů v důsledku reabsorpce a nedokonalého odrazu na stěnách opatřených reflektorem [186] (zde teflonová páska).

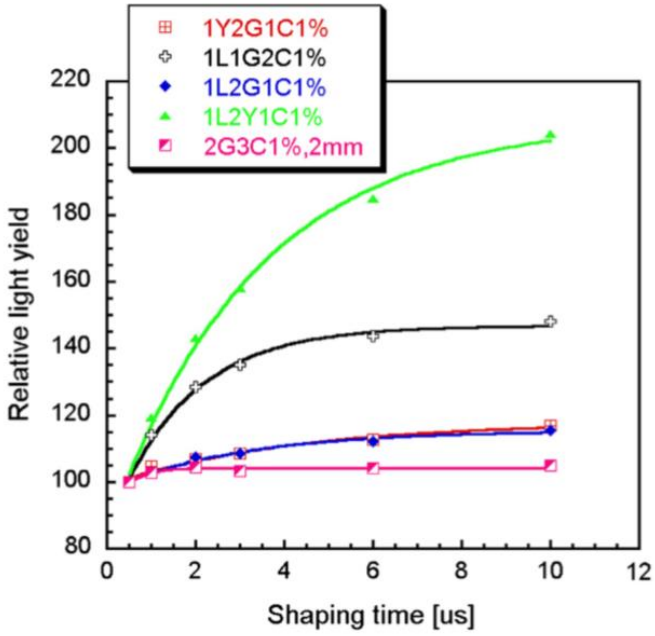

Obr. 7.2 – Závislost relativního světelného výtěžku vzorků první série na časové konstantně zesilovače τ, 100 % odpovídá τ = 0,5 μs [67][253]**.**

Vzorky druhé série měly vyšší kvalitu než vzorky série první díky tomu, že podmínky růstu byly též optimalizovány. Světelný výtěžek přesáhl 50 000 foton/MeV a energetická rozlišovací schopnost byla 5,5-7,3 % při měření s HPMT. Scintilátor GAGG:Ce má emisní spektrum položené v oblasti, kde může být výhodnější použití polovodičových fotodetektorů. Proto hodnoty FWHM získané při měření např. s APD (Avalanche PhotoDiode, lavinová fotodioda) mohou být lepší než zde uvedené, např. v práci [68][231] činí FWHM 4,2 %.

Další optimalizace mimo jiné směřovala k přesnějšímu určení ideálního poměru Ga/Al, např. práce [68][231], v níž byl autor zodpovědný za proměření proporcionality odezvy vzorků $Gd_3Al_{2,6}Ga_{2,4}O_{12}$:Ce a $Gd_3Al_2Ga_3O_{12}$:Ce, viz obr. 7.3. První vzorek měl světelný výtěžek méně závislý na energii, což se pozitivně projevilo na jeho energetické rozlišovací schopnosti. Pro

srovnání: vzorek $Ga_{2,4}$ FWHM = 4,2 % (měřeno APD), LY = 46 000 foton/MeV, vzorek Ga_3 FWHM = 5,2 %, LY = 55 000 foton/MeV. Jedná se o téměř učebnicový případ negativního vlivu neproporcionality na energetickou rozlišovací schopnost. Energetická rozlišovací schopnost je horší i přesto, že světelný výtěžek je vyšší.

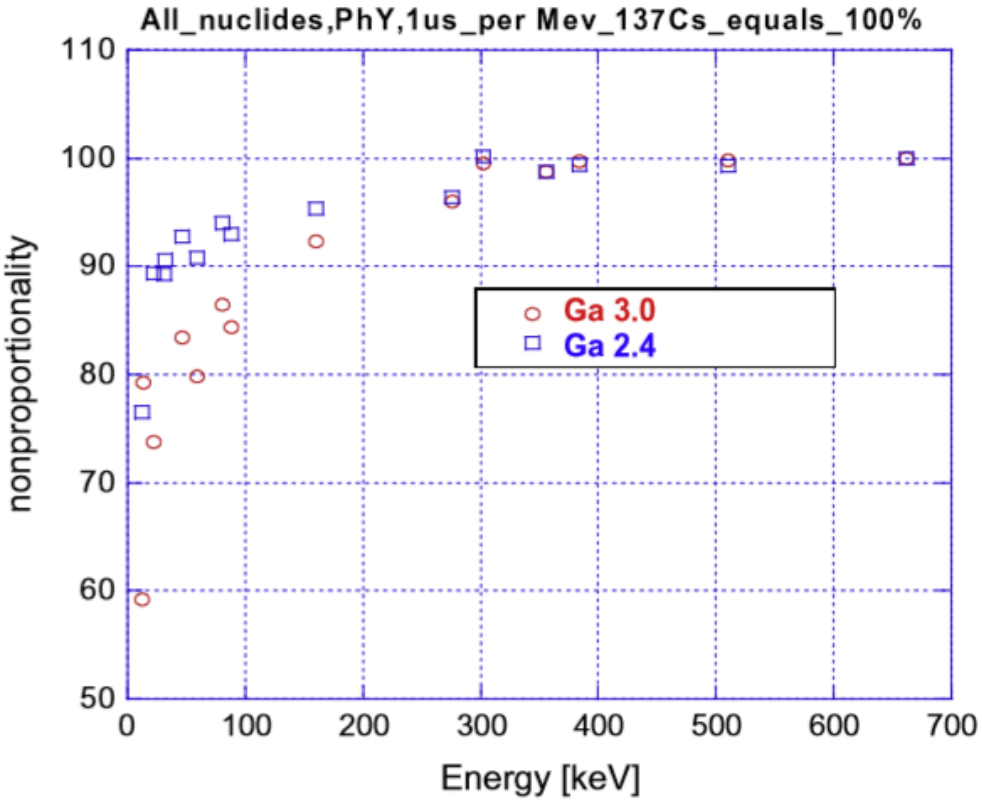

Obr. 7.3 – Závislost světelného výtěžku vzorků $Gd_3Al_{2,6}Ga_{2,4}O_{12}$:Ce a $Gd_3Al_2Ga_3O_{12}$:Ce připravených Czochralského metodou na energii budícího záření, 100 % odpovídá 622 keV (^{137}Cs) [68][231].

Další podrobnosti nalezne čtenář v článcích [67][253] [68][231] [184] [187][227] [188][223] [189][235]. Pokud autor habilitační práce není uveden jako corresponding author, tak byl zodpovědný za měření a vyhodnocení neproporcionality a závislosti světelného výtěžku na časové konstantě zesilovače.

7.2. Epitaxní filmy $(Lu,Gd)_3(Al,Ga)_5O_{12}$:Ce

Materiály na bázi $(Lu,Gd)_3(Al,Ga)_5O_{12}$:Ce v podobě monokrystalů i keramik vykázaly kromě výrazného nárůstu světelného výtěžku i snížení intenzity pomalých složek scintilační odezvy. Za tyto pomalé složky scintilační odezvy jsou zodpovědné AD defekty, které se v epitaxních filmech vyskytují v podstatně nižších koncentracích než v krystalech. Přesto i epitaxní filmy vykazují pomalé složky odezvy, zřejmě v důsledku existence jiných pastí. Předpokládalo se, že

i v tomto případě může substituce Al/Ga a Lu/Gd vést k výraznému zlepšení scintilačních vlastností.

7.2.1. První série vzorků multikomponentních granátových filmů – rok 2013

Měření z první série vzorků tohoto směru výzkumu bylo publikováno v roce 2013 [74][248]. Vzhledem k obtížné dostupnosti substrátů se větší část vzorků připravovala na podložkách YAG a LuAG, což neumožňovalo pěstovat vzorky se složením, jež by bylo blízké optimálnímu. Pouze jeden vzorek na substrátu GGG ($Gd_3Ga_5O_{12}$) označený jako GG1 se optimálnímu složení přibližoval. Byl připraven z tavidla T-Pb, s kterým je zajištění růstu filmu jednodušší, nicméně hrozí riziko kontaminace filmu ionty Pb^{2+}. Základní informace o vzorcích shrnuje Tabulka 7.2.

Dva vzorky měly tloušťku podstatně menší než je dosah α částic použitých k buzení odezvy, další 2 jen o málo menší. V té době už díky autorovi práce nebyl problém s interpretací těchto měření a vyhodnocením světelného výtěžku a dalších veličin [156][262].

Sample	Substrate	Crystal orientation	Flux	Thickness (μm)	Composition
LY1	LuAG	111	BaO	12.3	$Lu_3Al_5O_{12}$:Ce
LY2	LuAG	111	BaO	19.7	$Lu_{2.43}Y_{0.57}Al_5O_{12}$:Ce
LGY1	LuAG	111	BaO	10.4	$Lu_{2.35}Y_{0.44}Gd_{0.12}Al_{5.06}O_{12}$:Ce
LGYG2	YAG	111	BaO	15.9	$Lu_{2.02}Y_{0.38}Gd_{0.55}Al_{3.74}Ga_{1.31}O_{12}$:Ce
LGYG3	YAG	111	BaO	17.0	$Lu_{1.98}Y_{0.37}Gd_{0.61}Al_{3.73}Ga_{1.31}O_{12}$:Ce
LGYG4	YAG	111	BaO	9.3	$Lu_{1.66}Y_{0.38}Gd_{0.96}Al_{3.48}Ga_{1.51}O_{12}$:Ce
LGYG5	YAG	111	BaO	7.0	$Lu_{1.45}Y_{0.42}Gd_{0.96}Al_{3.68}Ga_{1.48}O_{12}$:Ce
GG1	GGG	100	PbO	10.5	$Gd_{2.97}Ga_{1.19}Al_{3.83}O_{12}$:Ce
GY1	YAG	111	PbO	43.9	$Gd_{1.50}Y_{1.44}Al_{5.05}O_{12}$:Ce

Tabulka 7.2 – Složení epitaxních filmů, použitý substrát včetně jeho krystalografické orientace, použité tavidlo (BaO = T-Ba, PbO = T-Pb), tloušťka a složení [74][248]**.**

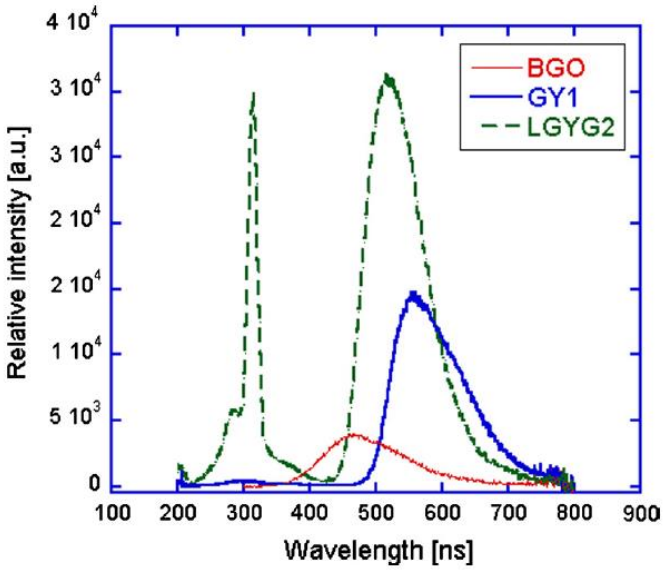

Obr. 7.4 – Radioluminiscenční spektra vzorků GY1, LGYG2 (viz Tabulka 7.2) a referenčního krystalu BGO [74][248]**.**

Vzorky z T-Ba tavidla, s malým množstvím Gd (LGYG2, LGYG3) vykazovaly sice intenzivní radioluminiscenci Ce^{3+} centra (maximum asi 530 nm), rovněž však i intenzivní emisi ostrého maxima Gd^{3+} 4f-4f přechodu (maximum asi 315 nm) a o něco méně intenzivní emisi defektu ze substrátu, viz obr. 7.4. Obě tyto emise jsou problematické dosvitem, který je mnohem delší, viz obr. 7.5.

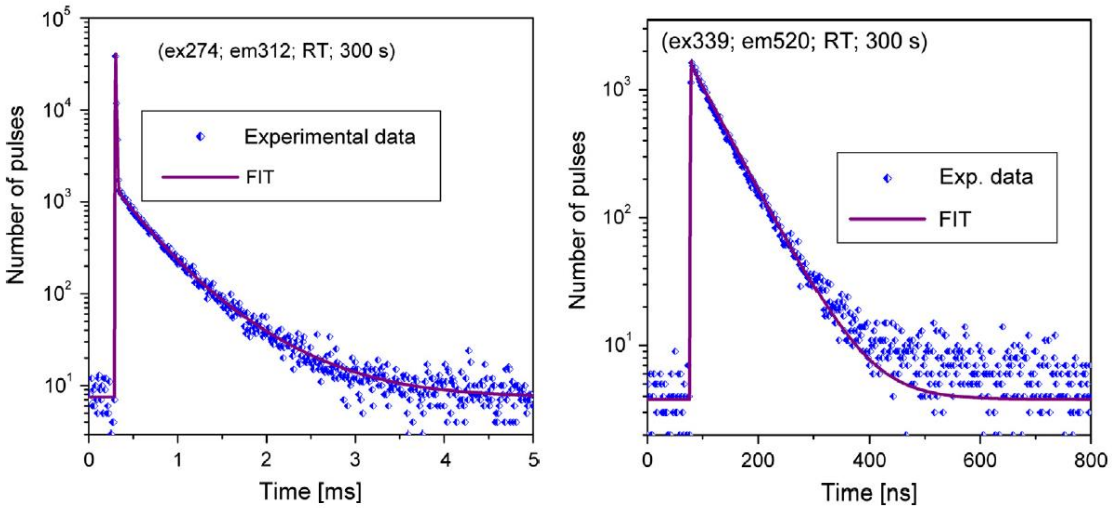

Obr. 7.5 – Fotoluminiscenční dosvitové křivky. Vlevo: λ_{exc} = 274 nm, λ_{em} = 312 nm (Gd^{3+}). Vpravo: λ_{exc} = 339 nm, λ_{em} = 520 nm (Ce^{3+}) [74][248].

V Tabulce 7.3 vidíme, že intenzita emise Gd^{3+} v RL spektru je nejvyšší, relativně i absolutně, u vzorku s nejnižším obsahem Gd. Tento zdánlivě paradoxní fakt lze vysvětlit jako projev tzv. koncentračního zhášení. Jaký je však jeho mechanismus?

Nárůst intenzity emise Ce^{3+} s rostoucím obsahem Gd ukazuje na nárůst účinnosti přenosu energie z Gd^{3+} na Ce^{3+} s rostoucí koncentrací Gd. Proces probíhá předáváním excitační energie mezi jednotlivými Gd^{3+} ionty (přesněji migrací energie v rámci Gd^{3+} „sublattice“), které jsou si při vyšší koncentraci bližší, dokud se nepřenese na Ce^{3+} iont. Energie excitovaných stavů Ce^{3+} je už příliš nízká na to, aby došlo k přenosu zpět na Gd^{3+}. Pro podrobnější rozbor tohoto jevu viz [190][240]. Tato publikace mimo jiné uvádí i emisní spektra při λ_{exc} = 273 nm (tj. Gd^{3+}), které obsahují emisi Ce^{3+} s intenzitou závislou na koncentraci Ce, viz obr. 7.6.

Daný mechanismus se pak odráží i v hodnotách světelného výtěžku, RL spektrech a v závislosti (relativního) světelného/fotoelektronového výtěžku na časové konstantě zesilovače, viz Tabulka 7.3, obr. 7.4 a 7.7. Při nulové koncentraci Gd pochází RL emise v UV oblasti především od substrátu, který ovšem není α částicemi buzen. Při zvýšení koncentrace se podstatná část energie vyzařuje skrze Gd^{3+} emisi, která je velmi pomalá, zvláště pak při nízké

koncentraci Gd. Dochází k tomu, že fotony nepřispívají k hodnotě LY (PhY) a klesá i hodnota $K_{f/e}$. S dalším růstem koncentrace Gd již světelný výtěžek roste, stejně tak i hodnota $K_{f/e}$. Z hlediska užitných vlastností nutno konstatovat, že při nižším obsahu Gd nedošlo k výraznějšímu zlepšení scintilačních vlastností.

Sample	PhY/MeV (1 µs)	FWHM (%) (1 µs)	$K_{f/e}$ (%)	$1/m_3$ (ns)	RL (Ce/ BGO)	RL (UV/ BGO)
LY1	310	9.4	52.2	2261	160.9	82.5
LY2	376	11.0	60.8	2180	188.4	82.0
LGY1	150	19.3	36.4	3541	143.3	475.8
LGYG2	381	10.5	44.4	2348	591.4	153.0
LGYG3	335	10.7	41.5	3567	580.3	149.4
LGYG4	344	15.0	44.8	–	404.5	182.4
LGYG5	307	19.1	48.8	2370	343.0	138.2
GG1	69	47.0	96.7	3938	308.2	0.8
GY1	415	8.3	55.6	1273	289.4	5.6

Tabulka 7.3 – Fotoelektronový výtěžek (PhY), energetická rozlišovací schopnost FWHM, podíl rychlé složky dosvitu na odezvě, parametr $1/m_3$ (viz rovnice R-5.1), intenzita radioluminiscenčního signálu v určitém intervalu vlnových délek k celkové intenzitě radioluminiscenčního signálu BGO (Ce – 400-700 nm; UV – 200-400 nm) [74][248].

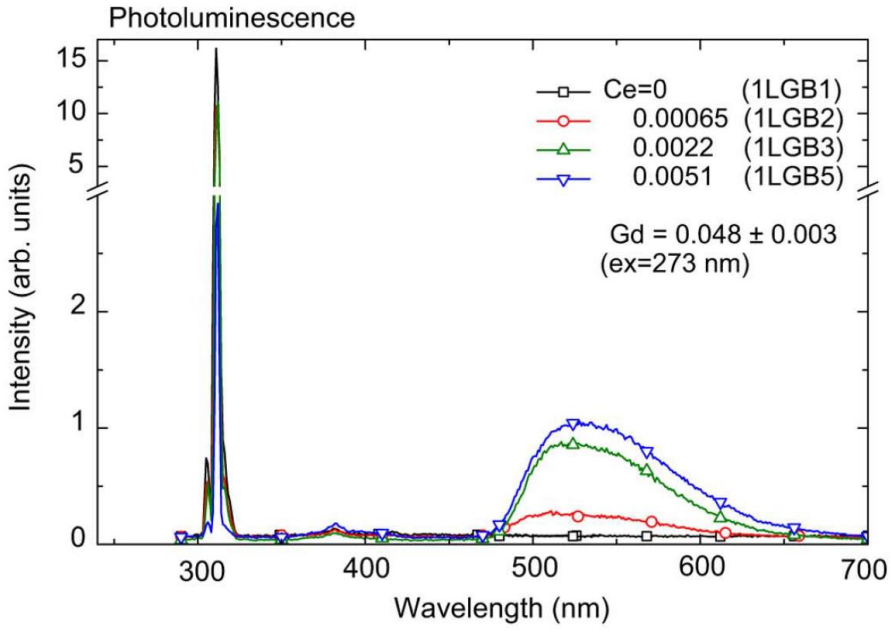

Obr. 7.6 – Emisní spektrum vzorků epitaxních filmů $(Lu,Gd)_3Al_5O_{12}$:Ce s různou koncentrací Ce při λ_{exc} = 273 nm, tj. buzení Gd^{3+}. Nárůst intenzity Ce^{3+} emise s rostoucí Ce koncentrací svědčí o přenosu energie Gd^{3+} → Ce^{3+} [190][240].

Vzorky z tavidla T-Pb, obsahovaly menší množství Ga. Vzorek GG1 vykazuje vysokou intenzitu radioluminiscence, ale nízký světelný výtěžek. To ukazuje na vyšší intenzitu komponent s delší dobou dosvitu. Jelikož hodnota je vysoká, viz Tabulka 7.3, musí být scintilační fotony vyzařovány s mnohem výraznějším zpožděním než v řádu μs. Zpoždění pravděpodobně působí množství defektů, vzniklých v důsledku vysokého (nejvyššího v rámci série vzorků) rozdílu mezi mřížkovou konstantou filmu a substrátu.

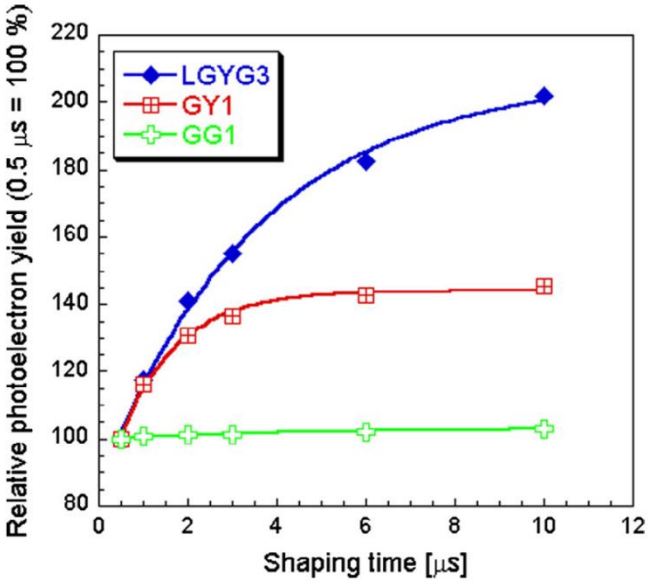

Obr. 7.7 – Závislost relativního světelného výtěžku vzorků epitaxních filmů multikomponentních granátů z roku 2013 na časové konstantně zesilovače τ, 100 % odpovídá τ = 0,5 μs [74][248]**.**

Alternativně lze nízký světelný výtěžek a vysokou intenzitu radioluminiscence vzorku GG1 vysvětlit tím, že RL spektra tvoří fotony emitované ze strany, v nichž se budí odezva. Fotony přispívající k signálu při měření světelného výtěžku musí proletět prakticky celým filmem a substrátem. Vzorek GG1 má nejnižší transparentnost a nejvyšší tloušťku, což je v souladu s touto možností.

Emise Gd^{3+} se u vzorku GG1 nepozorovala, byť prakticky všechny dodekahedrální pozice obsadily právě tyto ionty. V tomto případě již je přenos energie k luminiscenčním centrům skrze „sublattice“ Gd^{3+} vysoce účinný. Dokonce ani u vzorku GY1 se tato emise téměř nepozoruje, tedy i poměr Gd/Y = 0,5 je dostatečný.

Vzorek GY1 vykazuje nejvyšší fotoelektronový výtěžek, nejlepší energetickou rozlišovací schopnost a i přes hodnotu $K_{f/e}$ 55,6 % poměrně malý nárůst fotoelektronového výtěžku s časovou konstantou zesilovače τ, pro τ > 3 μs, viz obr. 7.7. Rozdíl ve světelném výtěžku proti většině ostatních vzorků by byl ještě větší než v případě fotoelektronového výtěžku, neboť UV

emise je u vzorku GY1 jen málo zastoupena, viz tabulka 7.3. Přitom právě v UV je použitý HPMT podstatně (zhruba 2 ×) citlivější, viz příloha 1.

7.2.2. Další zlepšení vlastností – rok 2015 [73][214]

sample	substrate	x	y	thickness [μm]	Δa [Å]
1LGB3	LuAG	0.14	0.00	17.9	0.006
1LGB4	LuAG	0.14	0.00	12.0	
2LGB2	LuAG	0.45	0.00	17.3	
2LGB4	LuAG	0.84	0.00	9.4	0.054
2LGB5	YAG	0.95	0.00	15.3	−0.031
3LGB1	YAG	1.15	0.81	22.0	
3LGB2	YAG	1.12	1.41	17.2	0.070
3LGB3	YAG	1.17	1.94	22.4	
4LGB1	YAG	1.62	2.02	34.5	0.117
4LGB2	YAG	2.08	2.10	23.3	
4LGB3	YAG	2.19	2.62	32.2	0.184
4LGB4	GGG	2.20	2.70	24.0	−0.183
4LGB5	YGG	2.19	2.69	11.9	−0.095
5LGB5	GGG	3.02	2.70	25.5	
5LGB6	YGG	3.02	2.69	21.9	
5LGB9	YGG	3.05	3.54	28.1	
L2G3	crystal	1.00	3.00		
L1G3	crystal	2.00	3.00		
L0G3	crystal	3.00	3.00		
L0G2.6	crystal	3.00	2.60		

Tabulka 7.4 – Složení epitaxních filmů $Lu_{3-x}Gd_xAl_{5-y}Ga_yO_{12}$:Ce, použitý substrát, tloušťka, složení a rozdíl mřížkové konstanty substrátu a filmu [73][214]**.**

Další série vzorků pokrývala široké rozmezí složení $(Lu,Gd)_3(Al,Ga)_5O_{12}$:Ce. Všechny vzorky byly připraveny z tavidla T-Ba při teplotách 1040-1060°C na vhodně zvolených granátových substrátech, viz tabulka 7.4. Všechny vzorky vykazovaly vynikající krystalografickou kvalitu. Díky vysoké viskozitě T-Ba tavidla vznikaly makroskopické defekty, především tzv. pity, viz obr. 7.8. Tyto defekty však nemají negativní vliv na luminiscenční vlastnosti, s výjimkou rozptylu světla na nich.

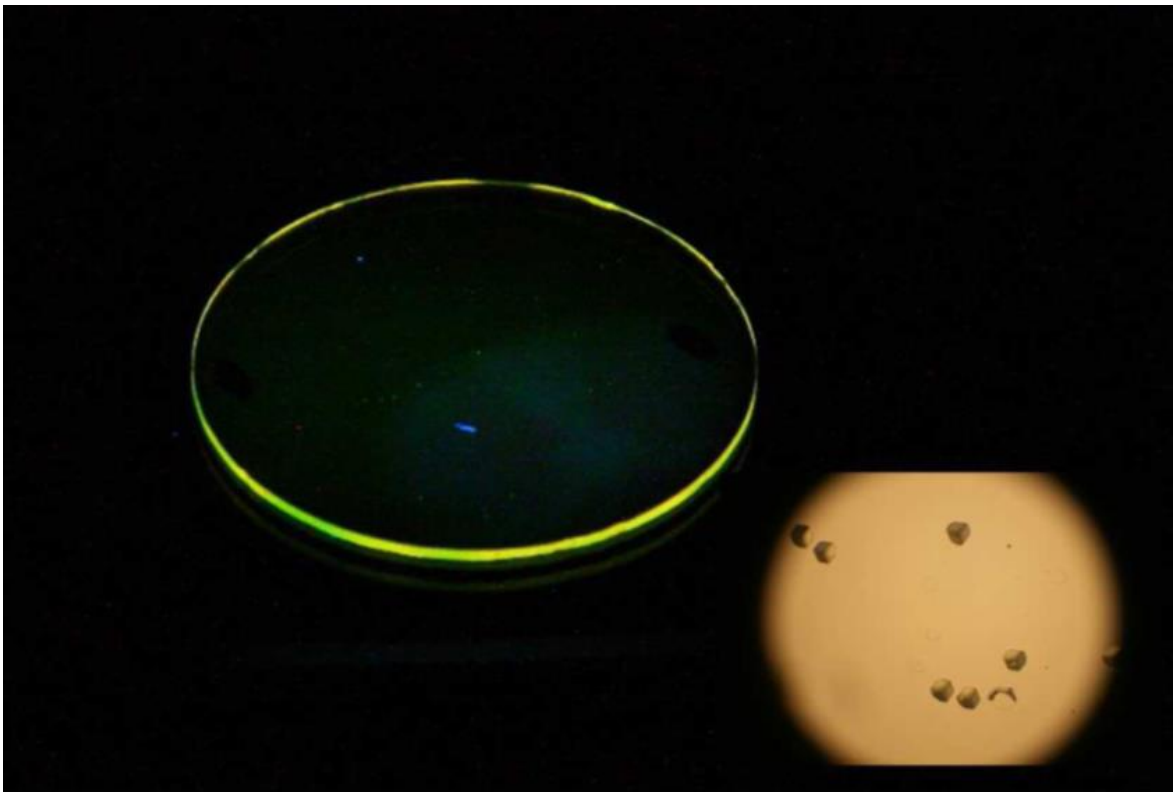

Obr. 7.8 – Fotografie epitaxního filmu na substrátu $(Lu,Gd)_3(Al,Ga)_5O_{12}$:Ce ozářená fotony o vlnové délce 355 nm. Na okrajích filmu je zřetelná zeleno-žlutá emise. Inset: 200 × zvětšený obraz z mikroskopu se zřetelnými pity [73][214]**.**

Excitační, emisní a radioluminiscenční spektra na obr. 7.9 a 7.10 ukazují již v předchozí sérii pozorovaný efekt zvyšující se účinnosti přenosu energie z Gd^{3+} excitovaných stavů na luminiscenční centrum Ce^{3+}. V případě malého obsahu Gd^{3+}, tj. relativně izolovaných Gd atomů, zůstává excitační energie lokalizována. V excitačním spektru (λ_{em} = 520 nm, tj. Ce^{3+} emise) vzorku 1LGB3 se nevyskytují píky odpovídající přechodům 4f-4f v Gd^{3+} $^8S \rightarrow {}^6I_J$ a $^8S \rightarrow {}^6P_J$. Naopak u vzorku 4LGB2 se vyskytují, což znamená, že přenos energie z Gd^{3+} na Ce^{3+} se uskutečňuje. Radioluminiscenční spektrum ukazuje, že se uskutečňuje velmi účinně, neboť emise Gd^{3+}, která je vzorku 1LGB3 velmi intenzivní, u vzorku 4LGB2 zcela mizí. Namísto toho vzrůstá intenzita emise Ce^{3+}.

V souladu s obr. 6.4 ovlivňují poměry Lu/Gd a Al/Ga polohu maxim v excitačních i emisních spektrech. V excitačních i emisních spektrech se zvýšení obsahu Ga projeví posunem maxim ke kratším vlnovým délkám, zvýšení obsahu Gd k delším vlnovým délkám.

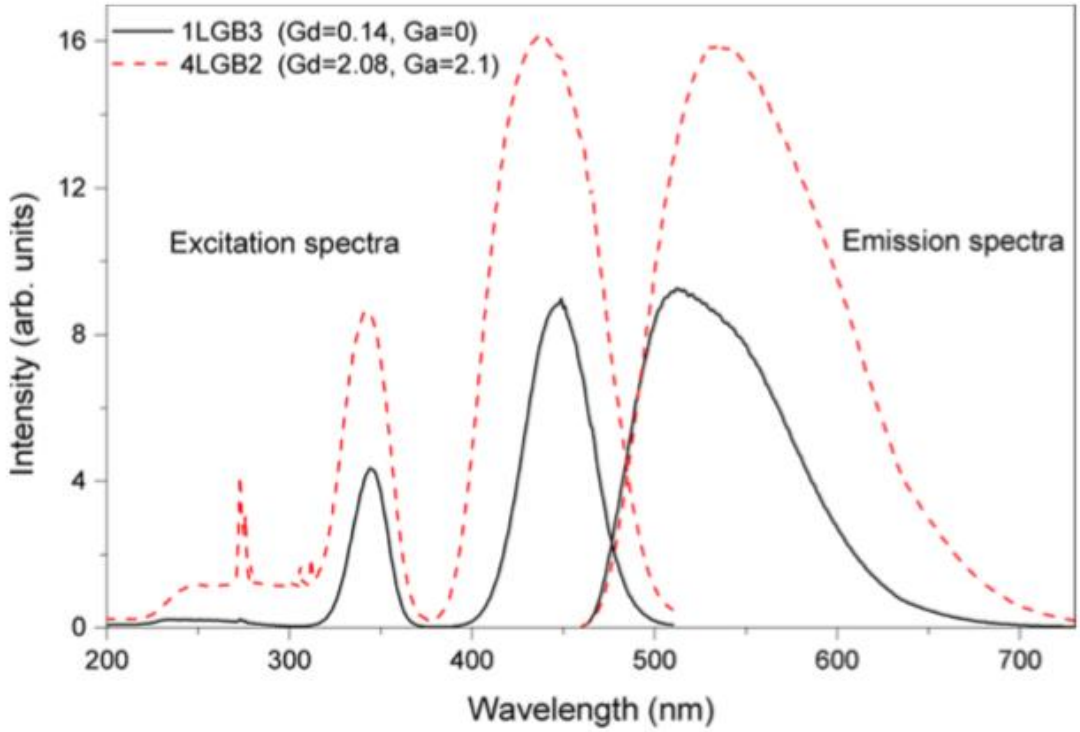

Obr. 7.9 – Excitační (λ_{em} = 520 nm) a emisní (λ_{exc} = 440 nm) spektra vzorků 1LGB3 a 4LGB2 [73][214].

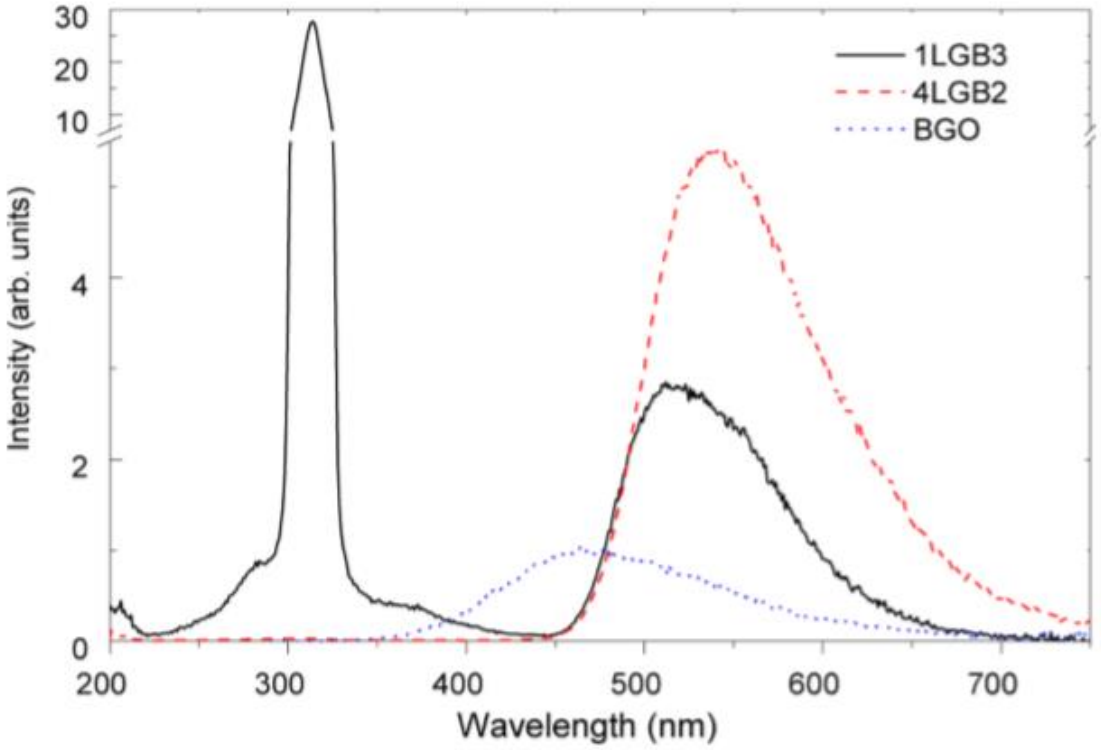

Obr. 7.10 – Radioluminiscenční spektra vzorků 1LGB3 a 4LGB2 [73][214].

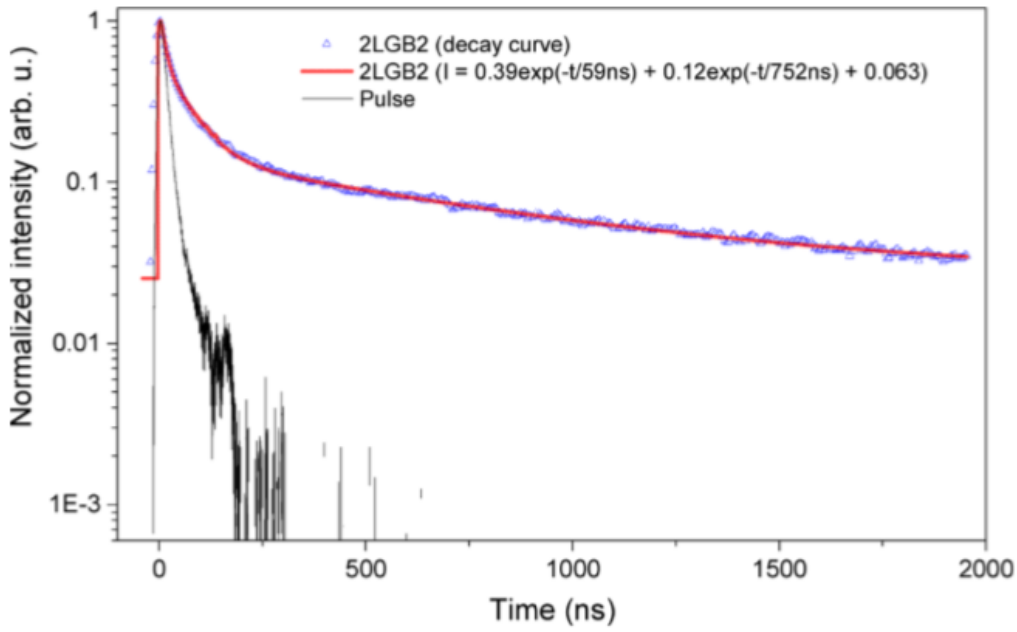

Obr. 7.11 – Scintilační dosvitová křivka vzorku 2LGB2 buzeného α částicemi [73][214]**.**

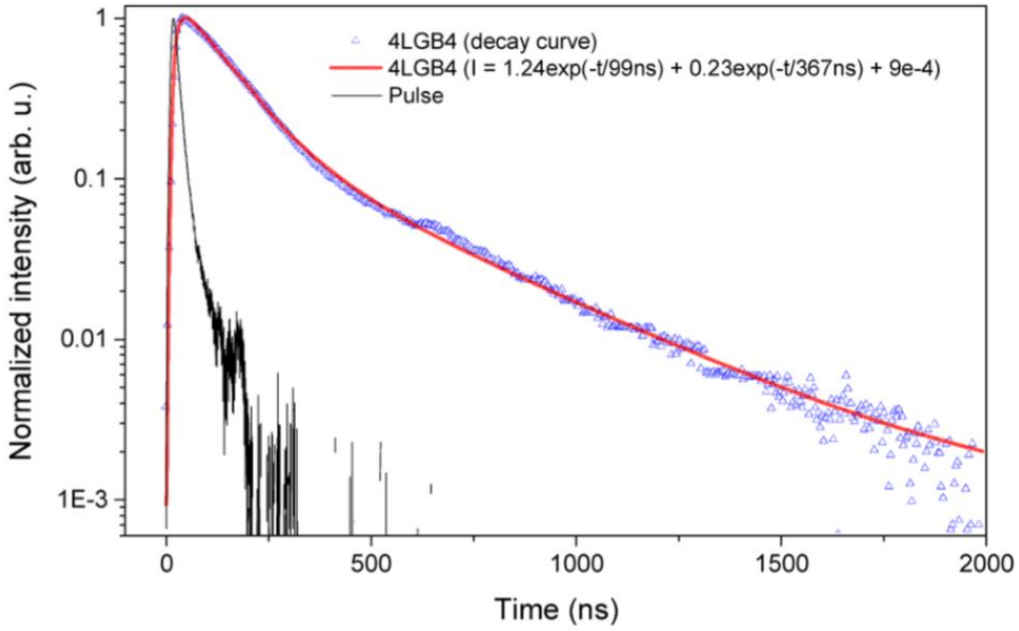

Obr. 7.12 – Scintilační dosvitová křivka vzorku 4LGB4 buzeného α částicemi [73][214]**.**

Všechny filmy vykazují při buzení α částicemi rychlou složku dosvitu s časovou konstantou 58-78 ns (s výjimkou 4LGB4 – 99 ns), což přibližně odpovídá časové konstantě při buzení 440 nm. V případě buzení α částicemi se vyskytují i pomalejší složky dovitu: 622-714 ns (vzorky 1LGBX), 742-752 ns (2LGBX), 643-744 (3LGBX), 349-373 ns (4LGBX) a méně něž 250 ns (5LGBX), viz též obr. 7.11 a 7.12. Doby dosvitu se do určité míry liší od dosvitů monokrystalů obdobného složení, např. dvojice 5LGB6 (60-70 ns a ≈ 200 ns) a monokrystal

$Gd_3Al_2Ga_3O_{12}$:Ce (145 a 764 ns). To je pravděpodobně důsledkem jiné povahy a koncentrace pastí u monokrystalů a filmů [73][214].

Výsledky měření fotoelektronového výtěžku při časové konstantě zesilovače τ = 1 μs jsou shrnuty v tabulce 7.5. Hodnoty řady vzorků přesáhly 700 fotoel./MeV, dvou dokonce 800 fotoel./MeV. Před třemi lety se jednalo o nejvyšší hodnoty mezi epitaxními filmy vůbec a dodnes nebyla tato hodnota výrazně překonána (srovnání ztěžuje fakt, že řada publikací neuvádí absolutní hodnoty fotoelektronového výtěžku). Proti nejlepším LuAG:Ce filmům se jedná o více než dvojnásobné zlepšení [191][282].

sample	PhY_{Am} [a,f]	$PhY_{Cs,r}$ [a,f] ($PhY_{Cs,nr}$)	γ/α [b,f]	$fwhm_{\alpha(\gamma)}$ [c,f]	aftergl [%]	$A_{10/0.5}$ [%]	LY_{γ} [d,f]	LY_{α} [e,f]
1LGB3	139			15.1		208		1331
1LGB4	185			14.5		197		1779
2LGB2	163			12.8		302		1682
2LGB4	170			13.1		226		1827
2LGB5	180			12.4		283		1935
3LGB1	173			17.5		255		1849
3LGB2	432			10.6		192		4393
3LGB3	753			8.2	0.20	179		7351
4LGB1	826			9.2	0.09	133		8691
4LGB2	801			10.4	0.22	109		8749
4LGB3	733			12.7	0.25	108		7833
4LGB4	774			9.3	0.72	103		8276
4LGB5	797			7.4	0.96	104		8562
5LGB5	710			8.3	0.44	100		5922
5LGB6	771			12.2	1.00	100		6481
5LGB9	99			16.0		100		808
L2G3	383	3371(2642)	6.9	15.6 (17.0)		115	21300	3088
L1G3	387	3562(2632)	6.8	17.4 (12.9)		148	25800	3793
L0G3	883	7013(5099)	5.7	8.0 (5.8)		109	53800	9427
L0G2.6	884	5295(3663)	4.1	6.7 (5.4)		131	41100	9918

Tabulka 7.5 – PhY_{Am} – Fotoelektronový výtěžek měřený při buzení α částicemi z ^{241}Am. $PhY_{Cs,r}$, resp. $PhY_{Cs,nr}$ – Fotoelektronový výtěžek měřený při buzení γ zářením z ^{137}Cs s reflektorem, resp. bez reflektoru. γ/α – poměr $PhY_{Cs,nr}$/ PhY_{Am}. $fwhm_{\alpha}$ a $fwhm_{\gamma}$ – energetické rozlišovací schopnosti změřené při buzení α částicemi z ^{241}Am a fotony γ z ^{137}Cs. Afterglow. $A_{10/0,5}$ – poměr PhY_{Am} při časové konstantě zesilovače τ = 10 μs a 0,5 μs. LYγ – světelný výtěžek změřený při buzení fotony γ z ^{137}Cs. LY_{α} – světelný výtěžek změřený při buzení α částicemi z ^{241}Am [73][214]**.**

Světelný výtěžek výrazně roste se zvyšujícím se obsahem Ga v intervalu 0,81 < y < 1,8, pak je v intervalu 1,8 < y < 2,7 přibližně konstantní, při dosažení hodnoty y = 2,98 velmi výrazně klesne (99 fotoel./MeV), viz tabulka 7.5 a obr. 7.13. Vliv Gd je obtížně sledovatelný, neboť z technických důvodů a z důvodu snahy kompenzovat přibližování dna vodivostního pásu excitovanému stavu Ce^{3+} koncentrace Gd a Ga do určité míry koreluje. Další podrobnosti k vlivu složení epitaxních filmů multikomponentních granátů jsou v [74][248] [73][214] [190][240] [72][142] [192] [193].

Již zmíněnou nevýhodou udávání fotoelektronového výtěžku je fakt, že jeho hodnota je ovlivněna nejen vlastností samotného scintilátoru, ale též účinností sběru fotonů η_{col} a kvantovou účinností fk HPMT Q_{PD}: $PhY = LY \times \eta_{col} \times Q_{PD}$. Stanovení Q_{PD} se provede díky znalosti radioluminiscenčního spektra, stanovení η_{col} je problematičtější. V práci [73][214] jsme se jej pokusili stanovit pomocí poměru $PhY_{Cs,nr}/PhY_{Cs,nr}$ u monokrystalů, viz tabulka 7.5. Měření bez reflektoru probíhalo tak, že byl monokrystal překryt neaktivním „dummy" α-zdrojem, což vede k dosažení podobné η_{col}. Pokud $\eta_{col} \approx 1$ je-li použit reflektor, pak $\eta_{col} \approx PhY_{Cs,nr}/PhY_{Cs,nr}$ pokud reflektor použit není. Tloušťka vzorků byla srovnatelná s tloušťkou substrátů s filmy. Pro jednotlivé vzorky vycházejí hodnoty η_{col}: 0,78; 0,74; 0,73; 0,69, tj. $\eta_{col} = 73{,}5 \pm 3{,}7$ %, což odpovídá 5 % (100 × (3,7 / 73,5)) relativní nejistotě světelného výtěžku LY. Tuto hodnotu nyní používáme v případě všech vzorků s obdobným RL spektrem. Na odlišná radioluminiscenční spektra není přenositelná, neboť odrazivost (nejen) α zdroje je spektrálně závislá. Naše měření bohužel nepodchycuje rozdíly v buzení α (při povrchu) a γ (v objemu) a ani skutečnost, že v krystalu není přítomno nic podobného rozhraní film/substrát. Přesto je užitečné, mít možnost alespoň přibližného srovnání hodnot světelného výtěžku, neboť ten již je charakteristikou pouze a jenom samotného scintilátoru.

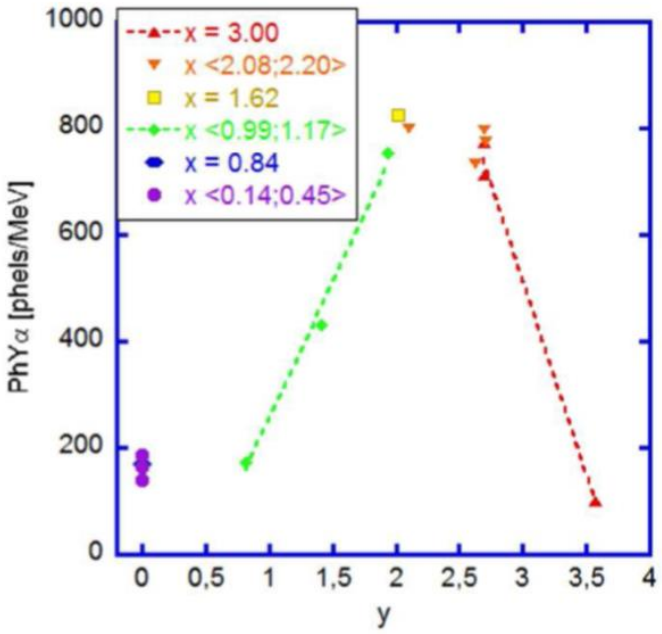

Obr. 7.13 – Závislost fotoelektronového výtěžku na složení filmu $Lu_{3-x}Gd_xGa_yAl_{5-y}O12:Ce$ [73][214]**.**

Zkoumané filmy vykazují vysokou kvalitu i při srovnání s monokrystalickým vzorkem GGAG:Ce [73][214] s výtěžkem 53 800 fotonů/MeV, což v té době byla jedna z nejvyšších hodnot. Vzorek 4LGB1 zaostal o pouhých 7 %. Rovněž rozlišovací schopnost nejlepších filmů

se blížila rozlišovací schopnosti monokrystalů, viz Tabulka 7.5. Bohužel není dosud z technických důvodů možné určit vliv nehomogenity vzorku, nehomogenity sběru fotonů a neproporcionality na FWHM. Měření s monokrystaly potvrzuje značný význam neproporcionality, neboť vzorek L0G2.6 vykazuje nižší výtěžek a lepší FWHM než L0G3 (dva nejlepší monokrystaly). Na větší neproporcionalitu vzorku L0G3 zřetelně ukazuje podstatně vyšší poměr γ/α. Ten zatím zůstává u filmů neměřitelný.

V souladu s modelem scintilačního mechanismu multikomponentních granátů je i závislost parametru $A_{10/0,5}$, viz tabulka 7.5. V případě nízkých koncentrací Ga dosahuje velmi vysokých hodnot, které začnou výrazně klesat při $y > 1,4$. Při $x,y > 2$ klesne $A_{10/0,5}$ pod 110 % a s rostoucím y (a x) dále klesá. K vzrůstu nedojde ani v případě vzorku 5LGB9, u nějž došlo k výraznému poklesu světelného výtěžku.

Na základě dat PhY a $A_{10/0,5}$ lze formulovat následující hypotézu. Přidání malého množství Gd nemá přílišný vliv na PhY, ani $A_{10/0,5}$. Od určité hodnoty x však již začíná alespoň částečně přenos energie pomocí Gd^{3+} sub-lattice k Ce^{3+} centrům. To se projevuje jako nárůst světelného výtěžku, především u delších časových konstant zesilovače τ a zároveň nárůstem $A_{10/0,5}$. Extrémně dlouhý dosvit izolovaných iontů Gd^{3+} se v hodnotě $A_{10/0,5}$ neprojeví, ta je ovlivněna pouze stavy s dobou života v řádu μs, nikoliv ms. Při vysokých koncentracích Gd^{3+} je již přenos energie z Gd^{3+} na Ce^{3+} vysoce účinný. Pokud však není přítomno Ga, na scintilační mechanismus mají výrazný vliv pasti, které snižují světelný výtěžek především při kratších τ a rovněž jsou odpovědné za vyšší hodnoty $A_{10/0,5}$. S růstem koncentrace Ga výtěžek roste a $A_{10/0,5}$ klesá.

Při vysokých koncentracích Ga dochází k účinné ionizaci excitovaných stavů Ce^{3+}. Ionizované elektrony pak mohou být opět zachyceny v pastech. Pokud je doba života excitovaného stavu vůči ionizaci podstatně kratší než vůči deexcitaci, pak nutně dojde k poklesu světelného výtěžku, přičemž nemusí dojít k nárůstu $A_{10/0,5}$, neboť namísto relativně mělkých pastí, které byly díky vyšší koncentraci efektivně eliminovány, se mohou významněji uplatnit pasti hlubší. U vzorku 5LGB9 se nicméně s vysokou pravděpodobností významněji uplatňuje teplotní zhášení, které se částečně projevuje i u GGAG:Ce optimálního složení [194], a jež se projeví jak poklesem PhY, tak zachováním $A_{10/0,5} = 100\%$.

Celý problém není v současnosti uzavřen, struktura vodivostního pásu multikomponentních granátů je komplikovaná. Ga i Al obsazují jak oktahedrální, tak tetrahedrální pozice, byť Ga

preferuje tetrahedrální pozice [195]. Vyšší koncentrace Ga může mít i negativní následky v podobě elektronových pastí vzniklých v okolí perturbovaného Ga^{3+} iontu [196].

V rámci studie [73][214] byl zkoumán i afterglow. Výsledky nejsou zcela jednoznačné, a to díky vlivu substrátu, jehož buzení se nepodařilo zcela vyhnout. Byla pozorována negativní korelace mezi tloušťkou vzorku a hodnotou afterglow. Nicméně i tak byly změřeny hodnoty, byť je lze považovat spíše za horní odhady skutečného afterglow, dobře odpovídající hodnotám naměřeným s monokrystaly.

7.2.3. Vzorky LGGAG:Ce, Mg – vliv kodopace Mg– rok 2017 [59][133]

V další studii byl zkoumán vliv kodopace Mg^{2+} o různých koncentracích na scintilační vlastnosti multikomponentních granátů se složením $Mg_x(Ce_{0,01}Lu_{0,27}Gd_{0,74})_{3-x}(Ga_{2,48}Al_{2,46})O_{12}$. Ve studiích provedených na monokrystalech a keramických materiálech byl pozorován pozitivní vliv na světelný výtěžek a potlačení pomalých složek scintilační odezvy u YAG:Ce a LuAG:Ce. Při vysokých koncentracích (typicky1000 ppm a výše) se odezva dále zrychlovala, ale světelný výtěžek klesal. U GGAG:Ce bylo pozorováno potlačení pomalých složek odezvy a pokles světelného výtěžku, viz kapitola 6.2 a odkazy v ní uvedené.

Článek autora [59][133] se nicméně zabýval materiálem blízkým GGAG:Ce, s určitým obsahem Lu. Navíc se jednalo o první studii Mg kodopovaných multikomponentních granátů na epitaxních filmech. Vzhledem k velmi nízké koncentraci AD ve filmech byly očekávány ještě o něco nižší intenzity pomalých složek odezvy, než vykazují monokrystaly, včetně afterglow. Pokud jde o změnu světelného výtěžku, byl očekáván pokles u vyšších koncentrací Mg, ovšem chování při nižších koncentrací nebylo možno s jistotou anticipovat.

Sample[a)]	Mg conc. x [10^{-5}] / [at. ppm][a)]	Thickness [μm]	LY [ph MeV^{-1}]	FWHM [%]	$A_{10/0.5}$ [%]
1LGM2	0/0	15.0	6780	9.3	104.1
1LGM3	2/7	16.3	7390	9.3	105.0
1LGM4	4/15	17.7	7140	8.2	104.7
1LGM5	10/30	17.2	6770	7.8	104.7
1LGM6	30/100	17.7	6680	9.2	104.9
1LGM7	80/300	16.8	5390	10.7	103.4
1LGM8	200/700	16.7	2940	11.5	101.3

Tabulka 7.6 – Koncentrace Mg ve filmech složení $Mg_x(Ce_{0,01}Lu_{0,27}Gd_{0,74})_{3-x}(Ga_{2,48}Al_{2,46})O_{12}$, tloušťka filmů, světelný výtěžek, energetická rozlišovací schopnost. $A_{10/0,5}$ – poměr PhY_{Am} při časové konstantě zesilovače τ = 10 μs a 0,5 μs [59][133].

Vzorky byly připraveny z T-Ba tavidla. Tloušťka vždy přesahovala dosah α částic použitých k buzení scintilační odezvy, viz Tabulka 7.6. Přítomnost Mg^{2+} ve filmech byla zřejmá

z výrazného nárůstu absorpce v oblasti vlnových délek pod 325 nm, viz obr. 7.14, která byla způsobena přenosem náboje k Ce^{4+} centrům stabilizovaným právě přítomností Mg^{2+}. Málo zřetelný je pokles absorpčního maxima na 435 nm v důsledku poklesu koncentrace Ce^{3+}, což znamená, že naprostá většina Ce iontů ve vzorcích jsou ionty právě Ce^{3+}.

Emisní a excitační spektra byla zcela typická pro Ce-dopované multikomponentní granáty. Při vyšších koncentracích Mg^{2+} silně klesá intenzita emise v obou spektrech. Rovněž se zrychluje fotoluminiscenční dosvit, přičemž vykazuje dvě složky, první se „standardní“ časovou konstantou dosvitu τ_d 57-60 ns (výjimka: 1LGM8 – 50,3 ns) a rychlou 22-31 ns (výjimka: 1LGM8 – 14 ns). Vzhledem k obdobné absorpci všech vzorků tyto výsledky silně indikují neradiační přenos energie z excitovaného stavu Ce^{3+} nebo tunelování elektronu do blízké pasti či „zhášecího“ centra, např. O^-.

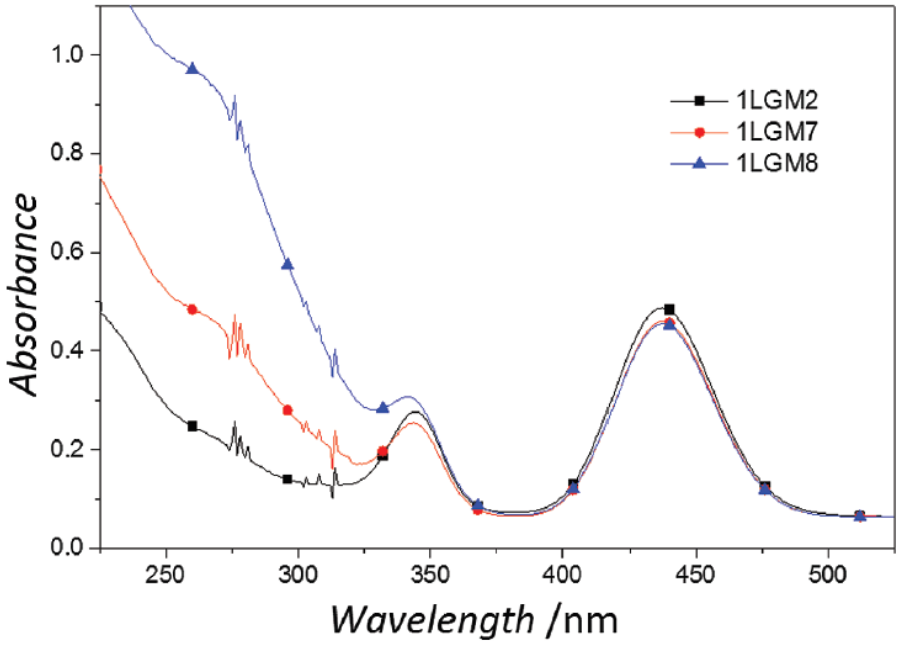

Obr. 7.14 – Absorpční spektra LGGAG:Ce epitaxních filmů s různými koncentracemi kodopantu Mg^{2+}. 1LGM2 0 ppm, 1LGM7 300 ppm, 1LGM8 700 ppm [59][133].

Očekávaný pokles intenzity pomalých složek scintilační odezvy byl pozorován, jak při měření scintilačních dosvitových křivek (buzení α částicemi i velmi měkkým zářením X – stovky eV), tak v poklesu parametru $A_{10/0,5}$ (statisticky významně však jen u vzorků 1LGM7 a 1LGM8) a konečně i v poklesu hodnoty afterglow. Ten dosáhl nejnižší, dosud nepřekonané hodnoty mezi granátovými scintilátory, i přes to, že mezi 5-10 % fotonů záření X budících odezvu, proniklo do substrátu, který vykazuje vyšší hodnoty afterglow. Intenzita scintilačního signálu poklesne

za 3 ms o více než 3 řády, viz obr. 7.15. Tyto hodnoty umožňují aplikaci při 2D radiografickém snímkování s vysokou frekvencí.

Zvýšení světelného výtěžku při velmi nízkých koncentracích Mg^{2+} je překvapivé, jeho další pokles s rostoucí koncentrací Mg^{2+} již je zcela v souladu s předchozími výsledky na multikomponentních granátech, viz Tabulka 7.6. Hodnoty jsou blízké světelnému výtěžku z předchozí publikace [73][214]. Zajímavé je zlepšení energetické rozlišovací schopnosti, která dosahuje optima při 30 ppm Mg^{2+}, což indikuje pozitivní vliv nižších koncentrací Mg^{2+} na proporcionalitu odezvy (případně homogenitu filmu), viz Tabulka 7.6.

Pokud skutečně došlo k potlačení neproporcionality odezvy, lze nabídnout alternativní vysvětlení, proč nebylo pozorováno zvýšení světelného výtěžku u krystalů a keramik GGAG:Ce,Mg s rostoucí koncentrací Mg, ale v našem měření pozorováno bylo. Existuje zřetelná korelace mezi neproporcionalitou a poměrem γ/α (v literatuře též často jako α/γ, alternativně α/β) [197]. Pokud se snížila neproporcionalita, pak zřejmě klesl poměr γ/α. To znamená, že nelze zcela vyloučit nárůst světelného výtěžku při buzení zářením α ani u monokrystalů a keramik GGAG:Ce. Záření α se však u nich používá zřídka, neboť to není (na rozdíl od filmů) nezbytné. Analogicky platí, že nárůst světelného výtěžku u filmů by nemusel být pozorován při buzení odezvy zářením γ, jež je bohužel při energii ^{137}Cs (662 keV) nemožné. Autor v současné době hledá reprezentativní sérii vzorků monokrystalů GGAG:Ce,Mg, kterou by s využitím záření α proměřil.

Vzhledem ke zrychlení fotoluminiscenčního dosvitu s rostoucí koncentrací Mg^{2+} bylo zřejmé, že za pokles světelného výtěžku s dále rostoucí koncentrací Mg^{2+} je částečně zodpovědný pokles účinnosti luminiscenčního centra Q. Připadá však v úvahu i možnost poklesu účinnosti přenosu energie S k luminiscenčnímu centru, který se taktéž podařilo prokázat, byť s jistotou pouze pro vzorky 1LGM7 a 1LGM8, neboť pouze u nich je pokles světelného výtěžku významný.

Na těchto vzorcích byla též provedena v časopise dosud nepublikovaná série termoluminiscenčních měření (předběžné výsledky prezentovány na konferenci Dny radiační ochrany 2016), která prokazuje významné snížení termoluminiscenčního signálu všech ve filmu přítomných pastí, snížení několikanásobně větší než je pokles světelného výtěžku. Elektrony jsou tedy prokazatelně v pastech zachytávány s nižší pravděpodobností. Může tomu tak být díky nižší koncentraci pastí, se současným stavem poznání je však více v souladu interpretace tvrdící, že o elektrony s pastmi soutěží Ce^{4+}, Ce^{3+} a O^- centra, přičemž Ce^{4+} a O^-, jež jsou

zároveň stabilizovány ionty Mg^{2+}, tak činí účinněji. Měření je bohužel v této sérii zatíženo značnou nepřesností kvůli velmi nízkému TL signálu LGGAG:Ce filmů i v případě nulové koncentrace Mg a světlocitlivosti vzorků.

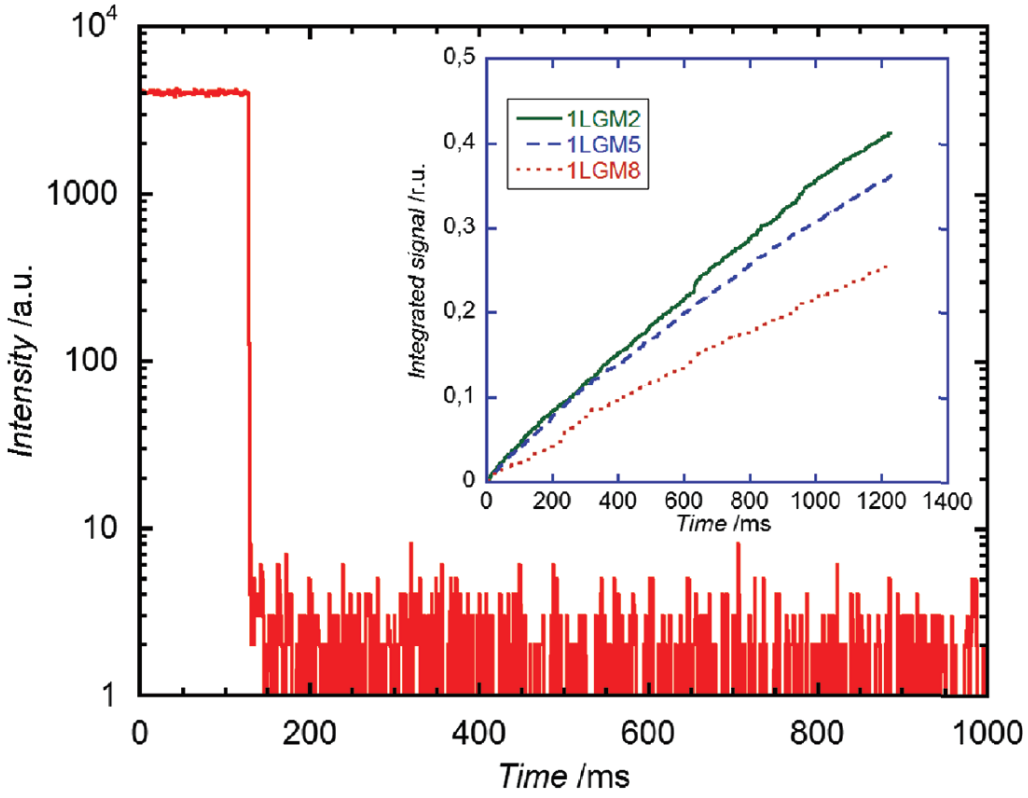

Obr. 7.15 – Pokles intenzity signálu vzorku 1LGM5 po vypnutí zdroje záření X. Inset: Integrál signálu (relativně k ustálenému signálu během ozařování) v čase 3 ms po vypnutí zdroje a dále [59][133]**.**

7.2.4. Vzorky LuAG:Ce, Mg – vliv kodopace Mg– rok 2018 [60][123]

sample	Mg [ppm]	thickness [μm]	Ly$_\alpha$ [ph/MeV]	fwhm [%]	afterglow [%] 4–50 ms	afterglow [%] 4 ms	$A_{10/0.5}$ [%]
1LM1	0	30.0	3340 ± 100	12.6 ± 0.6	1.9 ± 0.06	4.1 ± 0.1	178 ± 4
1LM2	100	24.7	3480 ± 110	11.6 ± 0.6	1.2 ± 0.05	3.0 ± 0.1	173 ± 4
1LM3	300	22.0	3910 ± 120	12.1 ± 0.6	0.35 ± 0.03	1.3 ± 0.2	164 ± 4
1LM4	700	21.9	3950 ± 120	10.8 ± 0.5	0.11 ± 0.02	0.8 ± 0.2	134 ± 3
1LM5	1500	21.9	2940 ± 90	12.6 ± 0.6	0.03 ± 0.01	0.6 ± 0.2	110 ± 2
1LM7	3000	17.7	1520 ± 50	8.3 ± 0.6	Afterglow not measured		103 ± 2
ref. SC	0	Bulk	3450 ± 110	9.8 ± 0.5	Afterglow not measured		173 ± 4
SC-0$_a$	0	Bulk	4850$_\gamma$		16 ± 0.3	19 ± 0.5	
SC-500$_a$	500	Bulk	18800$_\gamma$		0.7 ± 0.04	2.5 ± 0.3	
SC-3000$_a$	3000	Bulk	14100$_\gamma$		0.03 ± 0.01	0.2 ± 0.4	
Ceramics$_b$	3000	Bulk	25070$_\gamma$	4.9$_\gamma$	0.39 ± 0.01	0.8 ± 0.1	115
BGO	0	Bulk			0.01 ± 0.01	0.2 ± 0.2	

Tabulka 7.7 – Koncentrace Mg ve filmech LuAG:Ce,Mg, tloušťka filmů, LY$_\alpha$ světelný výtěžek měřený s použitím záření α, energetická rozlišovací schopnost, afterglow, $A_{10/0,5}$ – poměr PhY_{Am} při časové konstantě zesilovače τ = 10 μs a 0,5 μs [60][123]**.**

Vzorky LuAG:Ce,Mg byly připraveny z tavidla T-Ba. Oproti vzorkům LGGAG:Ce byl pokryt širší interval koncentrací Mg^{2+} (do 3000 ppm), a to na základě zkušeností s monokrystaly a keramikami, viz Tabulka 7.7. V autorově studii byl posouzen vliv koncentrace Mg^{2+} na scintilační a luminiscenční vlastnosti materiálu, včetně důsledného porovnání s monokrystaly i keramikami stejného/podobného složení.

Podobně jako u vzorků LGGAG:Ce,Mg dochází s nárůstem koncentrace Mg^{2+} k nárůstu koncentrace Ce^{4+}, což se projevuje nárůstem absorpce v oblasti vlnových délek pod asi 325 nm, vlivem přenosu náboje (elektronu) od kyslíkových ligandů k Ce^{4+}. Rovněž dochází k poklesu koncentrace Ce^{3+}, v tomto případě podstatně zřetelnějšímu, viz obr. 7.16. Bylo prokázáno, že kodopací Mg^{2+} lze na Ce^{4+} přeměnit veškerý Ce a absorpční pásy s maximy na 450 nm a 345 nm zcela zaniknou. RL spektra přesto vykazují tvar typický pro Ce^{3+} dopovaný granát [54] [58].

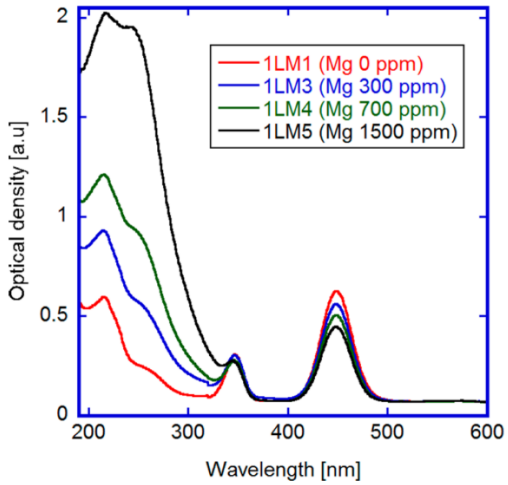

Obr. 7.16 – Absorpční spektrum vybraných epitaxních filmů LuAG:Ce,Mg [60][123].

Tvar excitačních a emisních spekter nijak nezávisí na koncentraci Mg^{2+}, ovšem intenzita s rostoucí koncentrací Mg^{2+} rychle klesá, viz obr. 7.17 vlevo. Rovněž klesá doba života excitovaného stavu Ce^{3+} $5d^1$, obr. 7.17 vpravo. Oba tyto výsledky indikují snížení luminiscenční účinnosti Ce^{3+} centra Q, což se jistě týká trvalých Ce^{3+} center a s vysokou pravděpodobností i dočasných Ce^{3+} center (Ce^{4+} po záchytu elektronu).

Např. dvojice vzorků 1LM1 a 1LM5 vykazuje poměr intenzit excitačních i emisních spekter 2,5. Vzorek 1LM1 je tlustší a s vyšší koncentrací Ce^{3+}, je v něm vzbuzeno asi 1,6 × více stavů $5d^1$ Ce^{3+}, což je podstatně méně než 2,5 ×. Významná část energie se tedy musí ve vzorku 1LM5 neradiačně přenášet z Ce^{3+} centra jinam. Předpokládaná ztráta dobře koreluje se zrychlením PL dosvitu. Poměr ploch 1LM1/1LM5 PL dosvitových křivek v obr. 7.17 činí 1,5.

1,5 × 1,6 = 2,4 ≈ 2,5, tj. účinnost Q je u vzorku 1LM5 snížena o asi 30 %. Příčina není zcela zřejmá, v článku [60][123] jsou uvedeny nejpravděpodobnější možnosti.

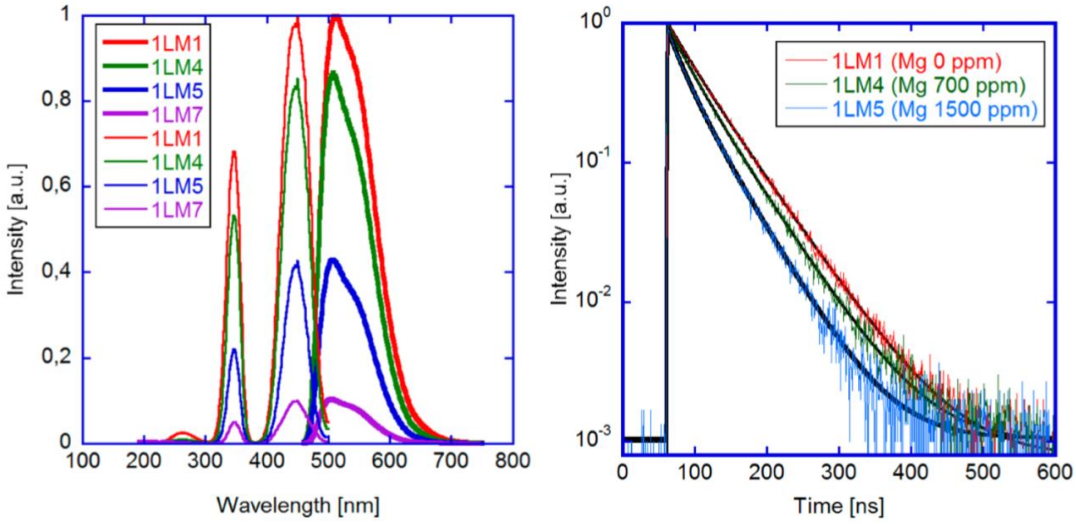

Obr. 7.17 – Vlevo: Emisní a excitační spektra epitaxních filmů LuAG:Ce,Mg. Vpravo: Fotoluminiscenční dosvitové křivky vybraných epitaxních filmů (λ_{ex} = 445 nm, λ_{em} = 510 nm) [60][123].

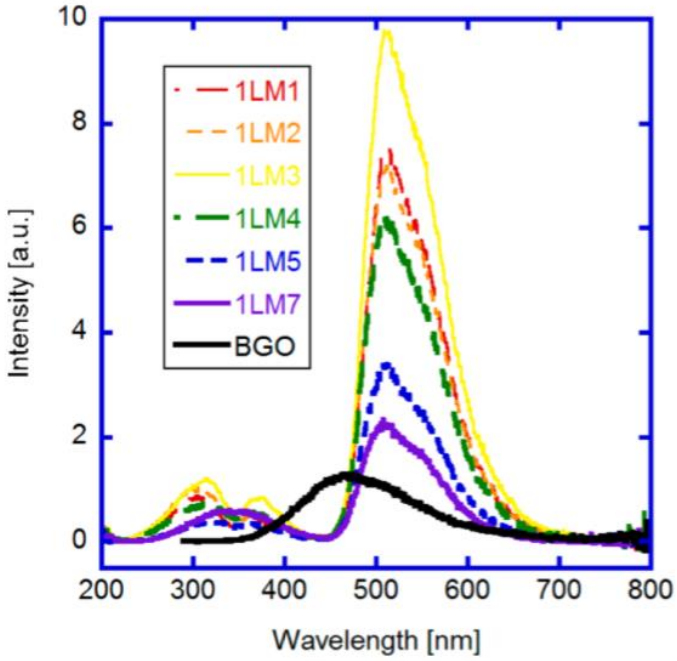

Obr. 7.18 – Radioluminiscenční spektra epitaxních filmů LuAG:Ce,Mg [60][123].

V RL spektru naprosto převládá emise Ce center, přičemž intenzita na Mg^{2+} koncentraci závisí jiným způsobem než v excitačních/emisních spektrech, neboť krom snížení účinnosti luminiscenčního centra Q se zároveň do určité míry (a do určité koncentrace Mg) zvyšuje účinnost přenosu excitační energie na luminiscenční centra S, viz obr. 7.18. Nejintenzivnější RL emisi tak vykazuje vzorek 1LM3 (300 ppm). V RL spektru se v oblasti asi 240-420 nm

nachází emise defektu v LuAG substrátu, který tedy nutně přispíval i k signálu při měření afterglow.

S rostoucí koncentrací Mg^{2+} pozorujeme zrychlení dosvitu na všech časových škálách. Zrychluje se dosvit při excitaci α částicemi, měkkým zářením X (stovky eV), snižuje se parametr $A_{10/0,5}$ a snižuje se i afterglow. Průběh dosvitu při buzení α částicemi a zářením X se zpočátku liší, ovšem od času nejdéle 700 ns dále, se již shodují. Od této chvíle je dosvit nejspíše určen totožným typem pasti, v dřívějších časech se uplatňuje rozdíl v lineární brzdné schopnosti. Bohužel není možné diskutovat průběh signálu v časech 0-10 ns, viz kapitola 5.2.1.

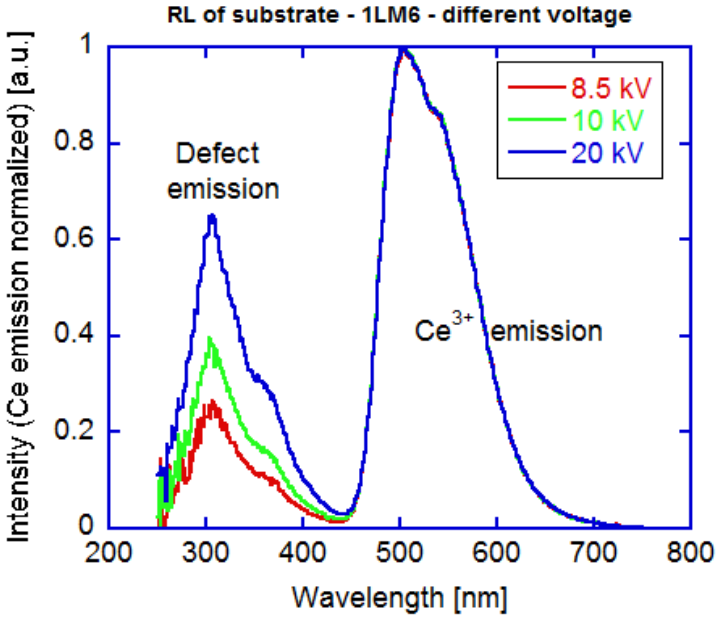

Obr. 7.19 – RL spektra vzorku 1LM6 (stejné složení jako 1LM5) při různém napětí na rentgence, normované k emisi Ce^{3+} [75].

Světelný výtěžek vykazuje zprvu s rostoucí koncentrací Mg^{2+} nárůst, mezi 300-700 ppm se nachází maximum (3910 a 3950 fotonů/MeV), nakonec následuje pokles, viz tabulka 7.7. Energetická rozlišovací schopnost se světelným výtěžkem významně nekoreluje, není zřetelný žádný trend. Nejlepší rozlišovací schopnost vykazuje vzorek 1LM7 s nejnižším světelným výtěžkem, pro což v tuto chvíli není jisté vysvětlení, byť nejpravděpodobnější příčinou je lepší homogenita vzorku nebo nižší neproporcionalita.

Příčinou zvýšení světelného výtěžku a zrychlení scintilačního dosvitu s rostoucí koncentrací Mg^{2+} je zvýšená koncentrace Ce^{4+} iontů, které účinně soutěží s pastmi o elektrony, viz kapitola 6.2. Koncentrace > 700 ppm vedou sice k dalšímu zrychlení odezvy, ale také poklesu světelného výtěžku. Odezvu stále více ovlivňují neradiační deexcitační cesty, zvláště pak O^- centra.

Většina dat výrazně koreluje s daty získanými studiem monokrystalů LuAG:Ce,Mg, s několika drobnými odchylkami. Zvýšení světelného výtěžku ve srovnání s nekodopovanými vzorky není u epitaxních filmů pro optimální složení tak výrazné, viz tabulka 7.7, pravděpodobně kvůli nižší koncentraci defektů ve filmech. Ze stejného důvodu vykazují filmy při stejné koncentraci Mg^{2+} nižší afterglow, s výjimkou vysokých koncentrací (≥ 1500 ppm), u nichž jsou kombinace výtěžku a afterglow srovnatelné. Hodnota afterglow u epitaxních filmů může být nicméně ovlivněna, tj. zvýšena, odezvou substrátu.

Tato série vzorků byla též studována termoluminiscenčními metodami. Na základě těchto výsledků dosud nevznikla publikace v impaktovaném časopise, proběhla však jejich prezentace na mezinárodní konferenci LUMDETR 2018 v Praze.

Vzorky byly ozařovány a vyhodnocovány autorem na Univerzitě Milano-Bicocca rentgenovým zářením z rentgenky, bohužel nebyl k dispozici ozařovač s radionuklidovým α zdrojem. Z těchto důvodů se přibližně 5-10 % z celkové dávky deponovalo v substrátu, konkrétní hodnota závisela na tloušťce filmu. Nižší hodnoty nepřipadaly v úvahu, použité napětí 10 kV představuje minimální prakticky použitelné. Důkaz klesajícího ozáření substrátu s klesajícím napětím na rentgence poskytují RL spektra, viz obr. 7.19. Emise defektu, jenž se nachází pouze v substrátu, se relativně k emisi Ce^{3+} snižuje s klesajícím napětím.

V průběhu měření se naštěstí ukázalo, že termoluminiscenční odezva substrátu je minimální, což lze prokázat jednak pomocí výsledků ze spektrálně rozlišených měření a též z měření odezvy substrátu, z něhož byl epitaxní film odstraněn.

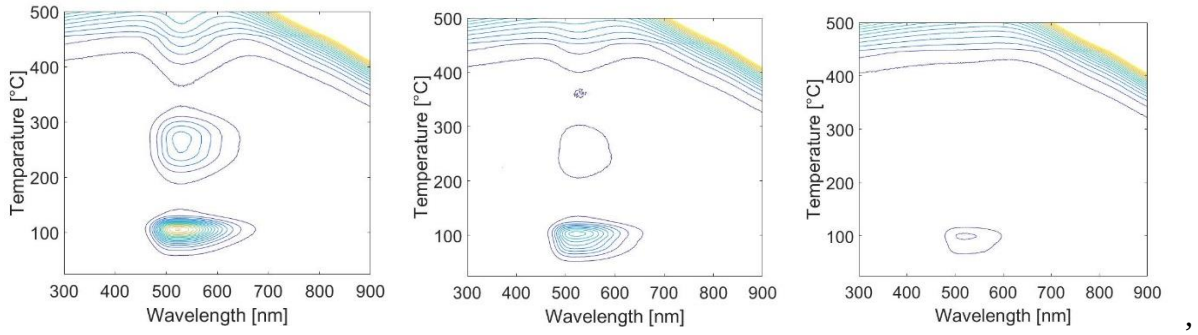

Obr. 7.20 – Spektrálně rozlišená termoluminiscenční odezva vzorků 1LM1 (vlevo), 1LM2 (uprostřed) a 1LM3 (vpravo) [75]**.**

Spektrálně rozlišená měření nad pokojovou teplotou vykazují pouze emise Ce^{3+}, který se v substrátu vůbec nenachází. Vzorky byly ozařovány 5 minut, ve vzdálenosti 7 cm od ohniska rentgenky, při napětí 10 kV a proudu 20 mA. Dávka není udána záměrně, neboť se výrazně

mění s hloubkou ve filmu a její průměrná hodnota nemá žádnou vypovídací hodnotu (při nárůstu tloušťky je ceteris paribus deponováno ve filmu více energie, ale dávka klesne). Intenzita emise výrazně klesá s rostoucí koncentrací Mg^{2+}, viz Obr. 7.20. Na obr. 7.20 neprezentovaný vzorek 1LM5 vykazuje signál těsně nad detekčním limitem, 1LM7 již měřitelný signál nevykazuje.

Integrace signálu přes emisi Ce^{3+} (450-650 nm) vede k tvarově velmi podobným vyhřívacím křivkám. Z obr. 7.21 vlevo je opět patrný výrazný pokles intenzity signálu s růstem Mg koncentrace. V Mg^{2+} kodopovaných vzorcích se objevují dva píky, které ve vzorku 1LM1 nepozorujeme. První má vrchol mezi 70-80°C, druhý okolo 360°C. Je tedy možné, že přítomnost Mg^{2+} modifikuje část stávajících defektů nebo introdukuje do vzorku defekt nového typu. Nicméně i intenzita těchto nových píků se s rostoucí koncentrací Mg^{2+} snižuje.

Obdobný jev vidíme i v případě citlivějšího měření spektrálně nerozlišeného. Obr. 7.21 vpravo ukazuje jak píky existující pouze u Mg^{2+}kodopovaných vzorků, tak výrazný pokles TL signálu s rostoucí koncentrací Mg^{2+}. V signálu se projevuje i vliv substrátu, především u silněji dopovaných a zároveň tenčích filmů, nejvýrazněji v podobě píku s vrcholem mezi 80-90°C. Obr. 7.21 vpravo též demonstruje, že u vzorku 1LM7 je zhruba 10 % energie záření absorbováno v substrátu. Odezva substrátu dělená 10 se velmi blíží odezvě vzorku 1LM7.

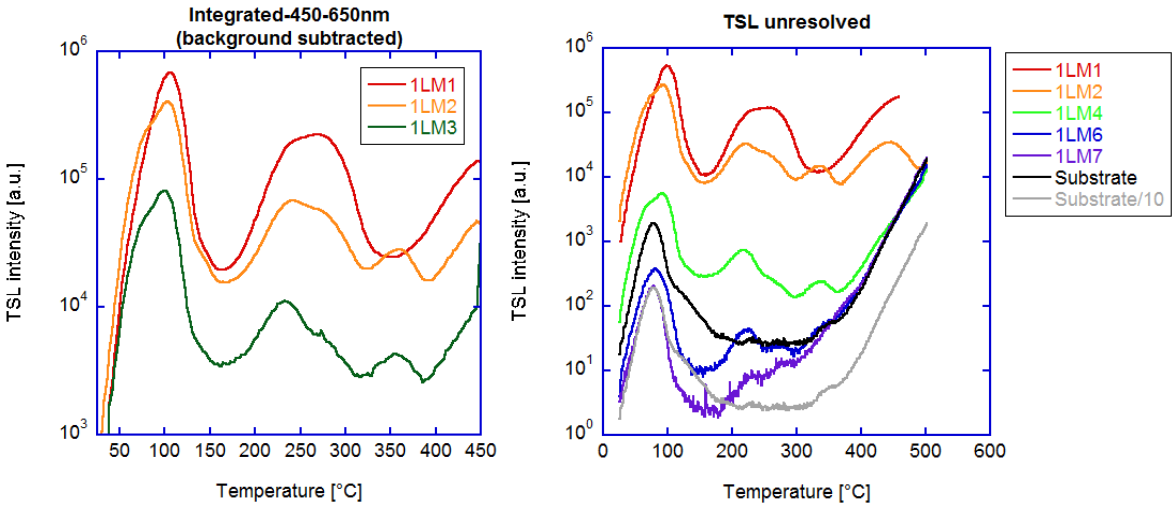

Obr. 7.21 – Vlevo: Vyhřívací křivky vybraných epitaxních filmů LuAG:Ce,Mg, vzniklé integrováním TL signálu v intervalu vlnových délek 450-650 nm. Vpravo: Spektrálně nerozlišená termoluminiscenční odezva filmů LuAG:Ce,Mg a substrátu [75].

Integrál spektrálně nerozlišených vyhřívacích křivek vykazuje velmi rychlý pokles s rostoucí koncentrací Mg^{2+}, od 0 do 3000 ppm o více než 5 řádů, viz obr. 7.22. Vztah R-5.10 říká, že za tento pokles může být zodpovědný buď pokles luminiscenční účinnosti Q, účinnosti transportu

energie ve fázi migrace S nebo pravděpodobnosti zachycení elektronu v pasti η_{tr}. Poměr nejvyššího a nejnižšího světelného výtěžku v rámci série činí 3,6, poměr integrálu RL spekter je nižší než 4,5. Přibližně tedy platí, že pokles $S \times Q \leq 4{,}5$. Za pokles integrálu TL signálu tedy musí být zodpovědný především snížení η_{tr}.

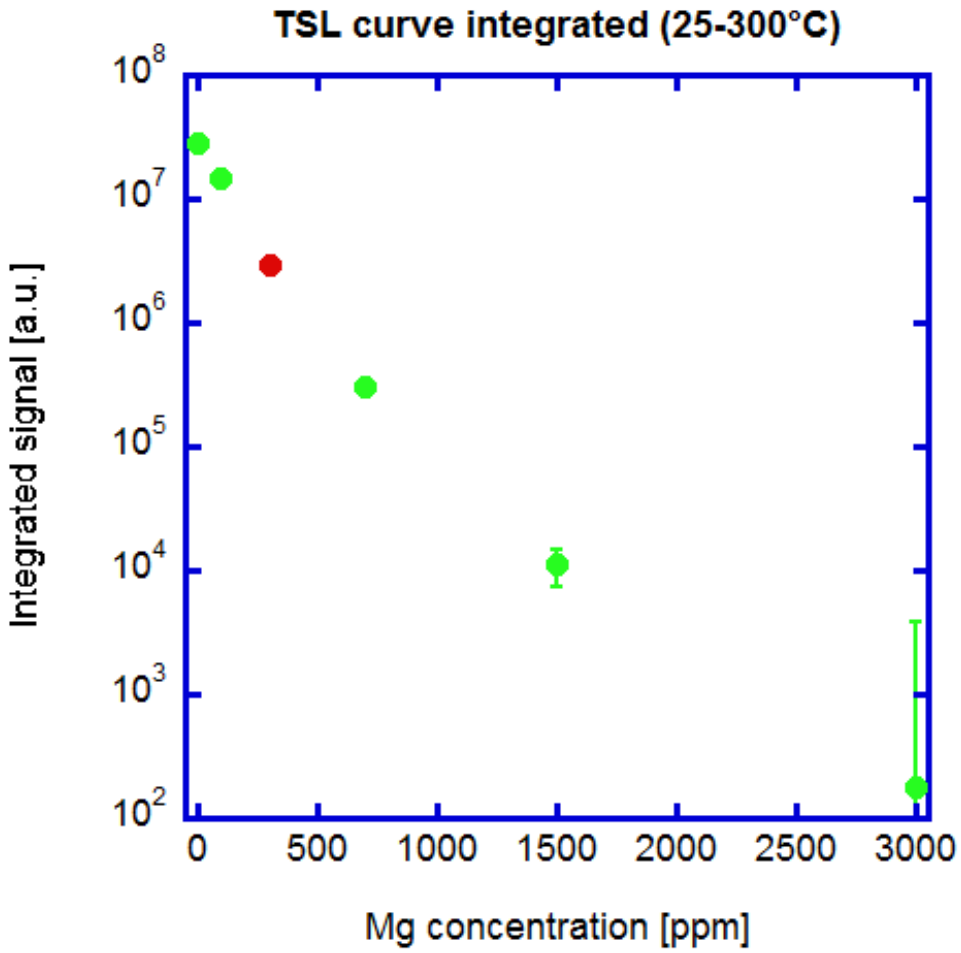

Obr. 7.22 – Vlevo: Integrál spektrálně nerozlišeného TL signálu v rozmezí 25-300°C LuAG:Ce,Mg epitaxních filmů v závislosti na koncentraci Mg^{2+}. Výjimka: Červený bod je dopočítán na základě poměrů spektrálně rozlišeného TL signálu vzorku 1LM3 k ostatním vzorkům [75].

Rozhodující jsou zřejmě stovky ps až jednotky ns po interakci, jak ukazují měření náběžné doby scintilačního signálu LuAG:Ce a LuAG:Ce,Mg [136]. Ta je v případě LuAG:Ce podstatně delší, neboť Ce^{3+} se dostávají do excitovaného stavu teprve po sekvenci „záchyt díry, záchyt elektronu“, což trvá déle než záchyt elektronu Ce^{4+}. Než dosáhne počet excitovaných stavů Ce^{3+} maxima, je již podstatná část elektronů zachycena v pastech.

V případě spektrálně rozlišených měření v rozsahu teplot 10-310 K je rovněž pozorován výrazný pokles intenzity TL signálu, viz obr. 7.23. Vzhledem k vytíženosti aparatury a značné časové náročnosti měření (asi 1 vzorek/den) je sada měření bohužel neúplná. Kromě poklesu

intenzity signálu ve spektrální oblasti emise Ce^{3+} se ve všech odezvách projevuje emise defektu ze substrátu, viz obr. 7.23.

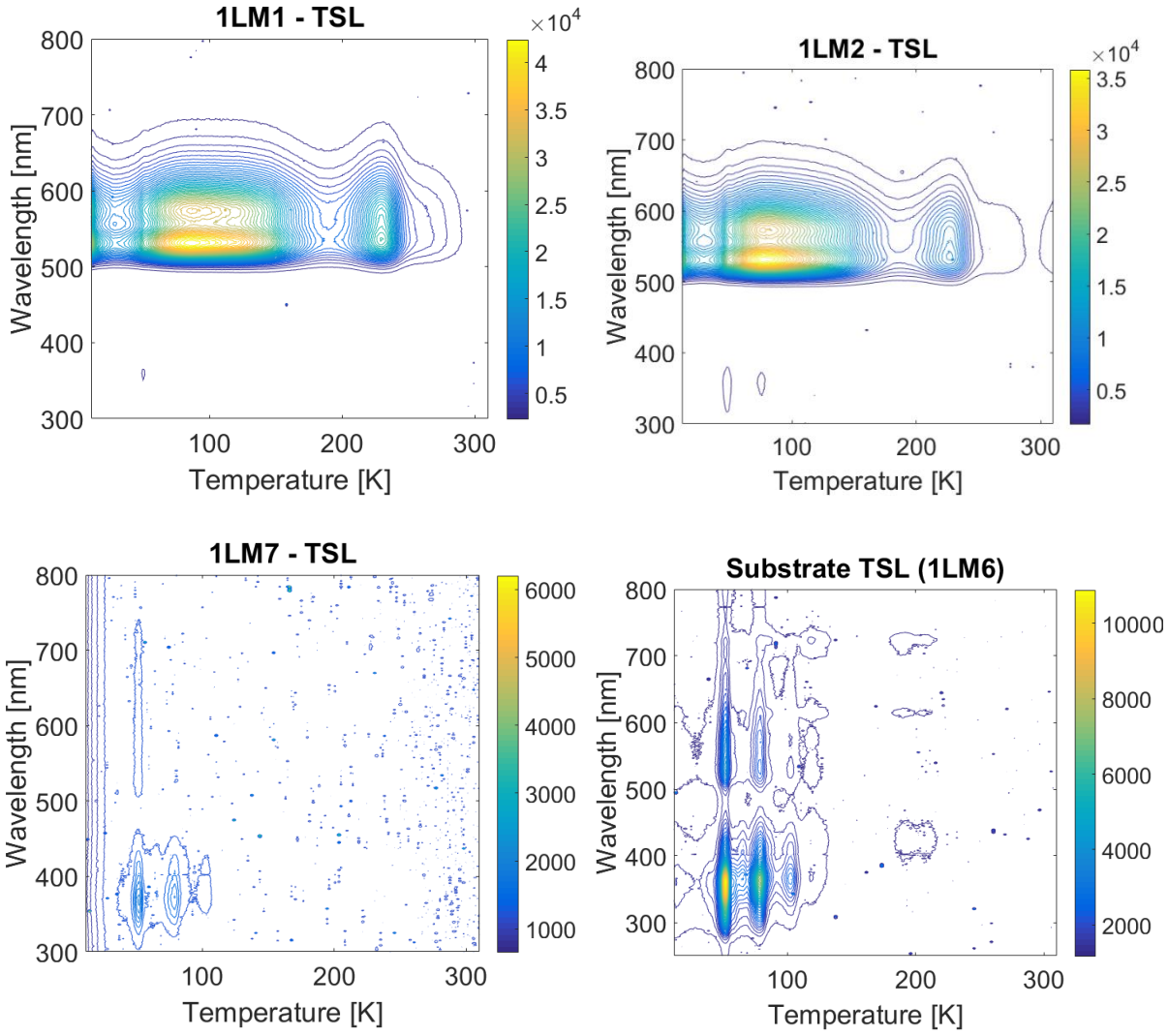

Obr. 7.23 – Spektrálně rozlišená termoluminiscenční odezva vybraných epitaxních filmů LuAG:Ce,Mg a substrátu [75]**.**

Na první pohled překvapivá je emise Ce^{3+} indukovaná ozářením substrátu, viz obr 7.24 vlevo. Měření ovšem probíhalo na vzorku 1LM6, z jehož jedné strany byla odstraněna vrstva epitaxního LuAG:Ce,Mg. Druhá strana byla filmem pokryta i nadále. Buď tedy emise Ce^{3+} pochází z ozáření hran vzorku nebo UV emise ze substrátu vybudila emisi Ce^{3+}. Emisní spektrum defektu a excitační spektrum Ce^{3+} se totiž překrývají. Vybuzení emise Ce^{3+} UV emisí ze substrátu se jeví mnohem pravděpodobnějším, neboť intenzita obou typů emisí závisí na teplotě prakticky stejně, viz obr. 23 vpravo dole.

Emise substrátu, viz obr. 7.24 vpravo, vykazuje tři poměrně úzké píky, což naznačuje možnost relativně vysokého frekvenčního faktoru [166]. Tato emise však nebyla dále studována, neboť

není předmětem zájmu výzkumu. Znát ji musíme pouze proto, abychom ji omylem nepřisoudili filmu.

Sada měření tzv. bright burn, tj. nárůst intenzity RL emise s rostoucí dávkou ve filmu, rovněž ukazuje vliv pastí na odezvu, viz obr. 7.25. U vzorku 1LM1 dochází s rostoucí dávkou k výraznému nárůstu. Pasti, které již zachytily elektron, nemohou zachytit elektron další, dokud se nevyprázdní. S rostoucí dávkou je stále více pastí zaplněno a tak elektrony s větší pravděpodobností rekombinují v luminiscenčních centrech. Zároveň může v průběhu měření docházet k uvolňování elektronů z pastí, které rovněž mohou zářivě rekombinovat. Při určité dávce nutně dojde k nasycení, množství elektronů v pastech se ustálí.

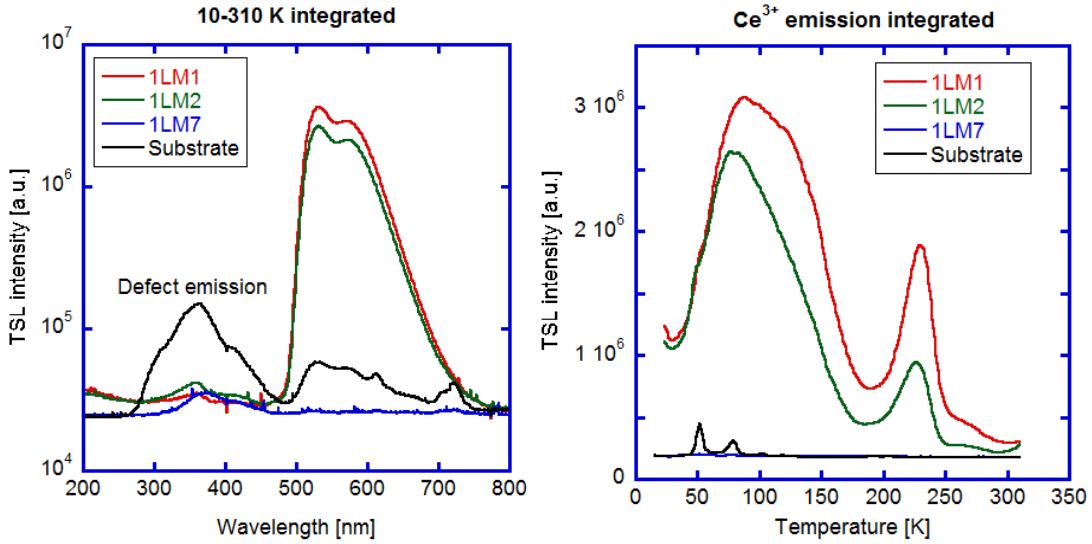

Obr. 7.24 – Vlevo: Spektrum TL emise vybraných epitaxních filmů a substrátu, integrované v teplotním intervalu 10-310 K. Vpravo: Vyhřívací křivky vybraných epitaxních filmů LuAG:Ce,Mg, vzniklé integrováním TL signálu v intervalu vlnových délek 450-650 nm [75].

Prezentovaná sada měření nejde až k dávkám, které by nasycení zajistily. Je nicméně zřetelné, že při stejné dávce je bright burn vyšší u vzorků s nižším obsahem Mg, tj. jedná se o další, nezávislé potvrzení snížené pravděpodobnosti záchytu elektronu v pastech. Rozdíl je tak podstatný, že již u vzorku 1LM4 není nárůst prakticky pozorovatelný při dávce, která ve vzorku 1LM1 vede k nárůstu o téměř 25 %, viz obr. 7.25.

Data získaná TL měřeními i data z měření bright burn jsou přibližně v souladu s daty publikovanými v [198] a rovněž s teorií, jež vysvětluje vliv Mg^{2+} na vlastnosti LuAG:Ce,Mg granátů, epitaxní filmy nevyjímaje.

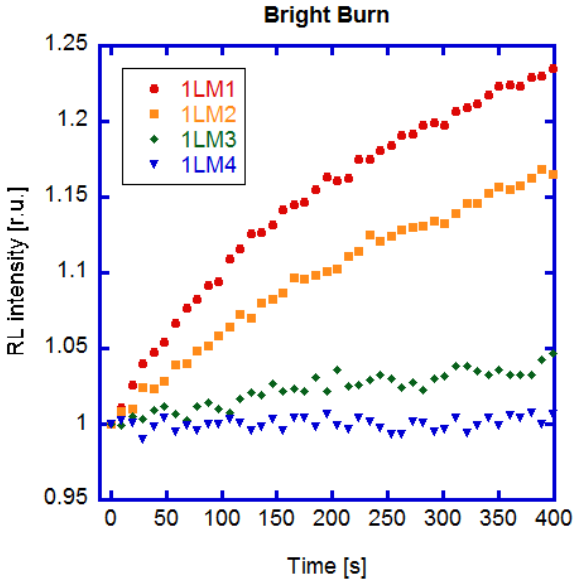

Obr. 7.26 – Bright burn vzorků 1LM1, 1LM2, 1LM3 a 1LM4. Napětí 10 kV, proud 10 mA [75]**. Bližší popis měřící aparatury v** [198]**.**

Kapitola 8
Závěr

V uplynulém desetiletí jsme byli svědky značného pokroku ve výzkumu scintilačního mechanismu jako takového, ve vývoji řady konkrétních materiálů, jejichž užitné parametry byly významně zlepšeny, či zdokonalení charakterizačních metod. Tyto směry výzkumu se běžně navzájem prolínají a ovlivňují. Typickým příkladem může být Sr kodopace $LaBr_3$:Ce, která vede ke snížení neproporcionality odezvy, a tím (jak říká teorie) ke zlepšení energetické rozlišovací schopnosti i přes to, že nedošlo ke zvýšení světelného výtěžku.

Jiným případem, který již má vztah k této práci, je vysvětlení mechanismu zlepšení scintilačních vlastností LSO:Ce/LYSO:Ce pomocí kodopace Mg/Ca. Zjištění, že zlepšení scintilačních vlastností souvisí s nárůstem koncentrace Ce^{4+} iontů v materiálu, vedlo k přesvědčení, že obdobné zlepšení může být pozorováno i v dalších Ce aktivovaných krystalech, což se u granátů beze zbytku potvrdilo. Rozpoznání role Ce^{4+} iontů v odezvě bylo zase do značné míry podmíněno přístupností některých charakterizačních metod, např. měřením kinetiky scintilační odezvy s velmi krátkým časovým rozlišením.

Tato práce se věnuje především vývoji granátových scintilátorů s vyšším Z_{eff}, s důrazem na jejich důslednou charakterizaci. Během posledních deseti let došlo ke zlepšení vlastností jak s využitím metody „band-gap engineering," jež vyústila v Ce-dopované multikomponentní granáty, tak „defect engineering", jejímž výsledkem je materiál LuAG:Ce,Mg.

Práce autora je součástí širšího výzkumu prováděného celosvětově řadou týmů špičkové úrovně. Autor musí skromně přiznat, že jeho výsledky v rámci tohoto výzkumu nejsou převratné, ale věří, že nepatří ani k těm zcela zanedbatelným, např. již proto, že přinesl některé podstatné inovace do charakterizačních metod užívaných týmem Oddělení optických materiálů FzÚ AV ČR, který patří k významným pracovištím v oboru výzkumu scintilátorů. Tyto inovace si nyní shrneme.

Triviální je změna sekvence měření „šest časových konstant zesilovače – šest umístění vzorku" na „šest časových konstant zesilovače – jedno umístění vzorku" při měření závislosti světelného výtěžku na časové konstantě zesilovače. Díky této změně, provedené v roce 2008 nebo 2009, došlo ke značnému zpřesnění měření relativního světelného/fotoelektronového výtěžku, resp. jeho závislosti na časové konstantě. Ukázalo se totiž, že právě umístění je zdaleka

nejvyšším zdrojem nejistoty při měření fotoelektronového výtěžku. Pro úplnost je nezbytné zdůraznit, že zpřesnění se skutečně týká jen poměrů světelných/fotoelektronových výtěžků změřených při různých časových konstantách zesilovače, nikoliv světelného/fotoelektronového výtěžku jako takového.

Bez výše popsaného zpřesnění by nepřipadalo v úvahu vypracování popisu vztahu mezi scintilačními dosvity a závislostí světelného/fotoelektronového výtěžku na časové konstantě zesilovače. V první fázi se podařilo na základě znalosti světelného výtěžku a odezvy aparatury na záblesk světla nulové délky (jednotkový skok na výstupu předzesilovače) s přesností do zhruba 5 % predikovat závislost světelného výtěžku na časové konstantě zesilovače. Autor ukázal i možnost postupu opačným směrem, od závislosti výtěžku na časové konstantě k dosvitu. Výsledky mají omezenou platnost pouze pro časový interval jednotek až několika málo desítek μs a rovněž omezenou přesnost. Přesto umožňují důslednější a hlubší interpretaci naměřených závislostí.

Vysvětlení tvaru spekter při měření s epitaxními filmy tloušťky menší, než je dosah α částic ve filmech má význam na první pohled banální, který by se dal shrnout do poučky: „Jsou-li přítomny dva píky, světelný výtěžek vyhodnocujeme z píku v oblasti vyšších energií, druhý pík ignorujeme.“ Ale bez podrobného vysvětlení tvaru spektra by tento postup byl diskutabilní, až nepodložený. Že výsledek nelze označit za zcela triviální lze demonstrovat následující autorovou zkušeností jakožto recenzenta článku jinak kvalitního autorského kolektivu.

V tomto článku autoři hodnotili kvalitu filmu (v podstatě skrze světelný výtěžek či veličinu na něm závislou) dle průměrné amplitudy impulzu, přičemž některé vzorky měly nestejnou tloušťku menší tloušťky kritické. Tenčí vzorky se tím pádem neoprávněně jevily jako horší. Díky publikovanému podrobnému vysvětlení se snadno podařilo autory i editora přesvědčit o nutnosti reinterpretovat výsledky.

Dále autor dokázal stanovit světelný výtěžek epitaxních filmů – před tím byly publikovány pouze hodnoty fotoelektronového výtěžku (byť jsou v publikacích často označovány jako světelný výtěžek). I přes mírně nižší přesnost stanovení se tím zlepšila možnost srovnávat výsledky dosažené s epitaxními filmy a dalšími typy materiálů mezi sebou.

V případě měření scintilačních dosvitů se autorovi podařilo především vysvětlit vznik určitých artefaktů a stanovit, pro které časy je dosavadní způsob vyhodnocení relevantní a pro které nikoliv. Víme, v případě jakých vzorků nastávají výraznější problémy a naopak, u kterých vzorků se téměř neprojevují a proč. Kritickou veličinou je především množství fotonů

emitovaných během několika málo ns po interakci částice ionizujícího záření ve scintilátoru. Roli také hraje náběžná doba scintilačního pulzu, která v případě malého množství fotonů dále komplikuje vyhodnocení.

Autor využívá určité podobnosti ve vztazích R-3.3 a R-5.8, která mu umožňuje kombinací výsledků získaných pomocí termoluminiscenčních metod a hodnoty světelného výtěžku (případně jinak získaných odhadů S × Q) přibližně stanovit pravděpodobnosti zachycení elektronu v pasti η_{tr}.

Rozvoj charakterizačních metod však není jediným přínosem autora – tím je i jejich využití k charakterizaci zkoumaných materiálů. Jeho výsledky na granátech v tomto směru shrnuje kapitola 7. Téměř beze zbytku se jedná o výsledky publikované v impaktovaných časopisech. Podkapitola 7.1 se zabývá sérií měření monokrystalů se složením $(Lu,Gd)_3(Al,Ga)_5O_{12}$:Ce, které v případě optimálního složení přinesly výrazné zvýšení světelného výtěžku (až 50 000 fotonů/MeV), zlepšení energetické rozlišovací schopnosti (téměř 5 % s HPMT, téměř 4 % s APD) i potlačení pomalých složek odezvy.

Podkapitola 7.2 se věnuje epitaxním granátovým filmům. Nejdříve byl uplatněn přístup „band-gap engineering“. V části 7.2.1 bylo výrazné zlepšení spíše naznačeno jedním vzorkem, než jednoznačně pozorováno. Důvodem byla příprava vzorků suboptimálního složení, která byla dána špatnou dostupností vhodných substrátů. V případě vzorku teoreticky nejbližšího optimálnímu složení (GG1) byl rozdíl mezi mřížkovými konstantami filmu a substrátu již příliš vysoký, navíc se film pěstoval v tavidle T-Pb, které kontaminuje film ionty Pb^{2+}, které silně zhášejí luminiscenci.

V části 7.2.2 se tyto obtíže podařilo překonat. Světelný výtěžek dosáhl hodnot u epitaxních granátových filmů předtím nepozorovaných (až 8750 fotonů/MeV při buzení α částicemi), výrazně též pokleslo zastoupení pomalých složek dosvitu v odezvě. Pro úplnost je třeba dodat, že světelný výtěžek buzený α částicemi byl u multikomponentních granátů nižší asi 4-7 ×, než světelný výtěžek buzený fotony γ. Za předpokladu, že α/γ poměr je podobný i v epitaxních filmech, by při buzení zářením γ bylo možné očekávat hodnotu 35 000-61 250 fotonů/MeV, což koresponduje s hodnotami změřenými na monokrystalech i keramikách. Značný rozptyl α/γ poměru nicméně neumožňuje přesnější srovnání. Optimální složení pro filmy nebylo zcela totožné s tím pro monokrystaly, což může souviset s vhodností substrátu z hlediska mřížkové konstanty.

V části 7.2.3 se uplatňuje „defect engineering," jmenovitě kodopování Mg^{2+}, které přeměňuje část iontů Ce^{3+} na ionty Ce^{4+}. Ty účinněji konkurují pastem v zachytávání elektronů, čímž se přeměňují v dočasná centra Ce^{3+} v excitovaném stavu. V důsledku toho, se v podstatě část „pomalých" scintilačních fotonů přemění v „rychlé." V případě LGGAG:Ce,Mg jsme s nárůstem koncentrace Mg pozorovali pokles intenzity pomalých složek odezvy, mimo jiné též afterglow. Afterglow byl vůbec nejnižší mezi granátovými scintilátory. Při malých koncentracích Mg^{2+} bylo pozorováno mírné zlepšení světelného výtěžku (do určité míry diskutabilní) a energetické rozlišovací schopnosti (podstatně průkaznější). Výrazné zlepšení světelného výtěžku ani nebylo možno očekávat. Pokud zjednodušeně popisujeme vliv Mg^{2+} jako „přeměnu pomalého světla v rychlé", pak v případě LGGAG:Ce, který příliš „pomalého světla" nevykazuje, není co „přeměňovat." Naopak, při vyšších koncentracích Mg^{2+} se dostavuje snížení světelného výtěžku, neboť Mg^{2+} v materiálu vytváří též nezářivá rekombinační centra, jmenovitě O^- centra. Dosvit samozřejmě dále zrychluje.

Část 7.2.4 popisuje výsledky kodopování Mg^{2+} v LuAG:Ce. Mechanismus zlepšení scintilačních vlastností je stejný. LuAG:Ce nicméně vykazuje intenzivní pomalé složky scintilačního dosvitu. Dostavilo se tak nejen zlepšení časových vlastností, ale i světelného výtěžku. Světelný výtěžek při 300 ppm Mg^{2+} je asi o 15 % vyšší než u nekodopovaného vzorku, což souhlasí s daty získanými na monokrystalech. Pomalé složky odezvy, včetně afterglow, též byly výrazně potlačeny.

Výsledky týmu, jehož je autor součástí tedy prokázaly, že zlepšení scintilačních vlastností při substitucích Al/Ga a Gd/Lu i při kodopování Mg^{2+} se dostavuje i v epitaxních filmech a je tedy do značné míry nezávislé na technologii výroby. Flexibilita epitaxní technologie rovněž umožnila proměřit závislosti scintilačních vlastností na složení s větší přesností a podrobněji. Speciálně u kodopace Mg^{2+} ionty jsou výsledky výmluvné. Oproti Czochralského metodě je snazší připravit značné množství vzorků s rozdílnými koncentracemi Mg^{2+}. Mg je napříč filmem rozprostřeno podstatně rovnoměrněji a reprodukovatelněji než v monokrystalech připravených metodou μ-PD, u nichž koncentrace závisí na hloubce, i v keramikách, u nichž se Mg koncentruje na rozhraní zrn.

Výzkum granátových scintilátorů již nyní má praktické důsledky, na trhu se objevily spektrometry záření gama osazené scintilátory GGAG:Ce (Furukawa) a GGAG:Ce,Mg (Georadis).

Habilitační práce se důsledně zabývá jen těmi publikovanými články v impaktovaných časopisech, které přímo souvisí s tématem práce. Autor pro představu přikládá v příloze 3 i další publikace věnující se výzkumu scintilátorů, u nichž je uveden jako (spolu)autor.

Ve výzkumu scintilátorů, granátových i jiných, zůstává řada nezodpovězených otázek a nevyřešených problémů a otevírají se další možnosti výzkumu. V případě scintilátoru GGAG:Ce je např. logické usilovat o „narovnání“ neproporcionality, které by mohlo vést k výraznému zlepšení světelného výtěžku. Autor v tuto chvíli nehodlá spekulovat, jaká kombinace složení matrice, kodopantu a koncentrace aktivátoru k němu povede. Dovoluje si nicméně připomenout, že pozoroval dílčí zlepšení rozlišovací schopnosti GGAG:Ce,Mg u nízkých koncentrací Mg. Pro řadu uživatelů je právě energetická rozlišovací schopnost tím nejdůležitějším parametrem detektoru.

V případě scintilátoru LuAG:Ce má autor již dnes k dispozici vzorky s dalšími kodopanty: Ca a Li, které by měly vykazovat podobný efekt na odezvu jako Mg. Předběžné výsledky na Ca kodopovaných granátech, které tento předpoklad potvrzují, již prochází recenzním řízením v časopise Optical Materials.

Týmy věnující se scintilátorům připraveným epitaxí z kapalné fáze se zabývají nejen růstem filmů granátových, ale i perovskitových, jejichž růst je komplikovanější. Autor práce má nyní k dispozici nové série perovskitových filmů a záhy započne s jejich charakterizací. Výsledky zatím k dispozici nejsou.

V důsledku útoků z 11. září 2001 významně posílil obor zvaný „homeland security,“ v jehož rámci přirozeně nacházejí uplatnění i detektory ionizujícího záření. Zvláštní důraz se klade na detekci neutronů, jež se uplatní při odhalování přítomnosti štěpitelných materiálů a při užití zobrazovacích metod založených na prozařování neutrony, jež jsou vhodnější k zobrazení objektů s nižším Z_{eff}, než záření X. Ideální je kombinace obou druhů záření. Autor rozšíří aparaturu k měření světelného výtěžku o využití neutronového zdroje k buzení odezvy.

Zvýšení rychlosti odezvy scintilátorů je též široce vznášeným požadavkem na scintilátory. Aby bylo možno provádět výzkum v tomto směru, je v plánu vybudovat na FJFI aparaturu k měření kinetiky scintilační odezvy s vysokým rozlišením, založenou na MCP-PMT a ps-laserem buzené rentgenové lampě. Zakoupen bude rovněž velmi rychlý life-time spectrometer (buzení ps diodou). Díky tomu, že Katedra jaderné chemie FJFI ČVUT se věnuje přípravě a výzkumu rychlých scintilujících nanoprášků, budou mít vybudované a zakoupené aparatury nezanedbatelný synergický efekt.

Použité zkratky

μ-PD	Micro-pulling down
APD	Avalanche PhotoDiode (lavinová fotodioda)
BGO	$Bi_4Ge_3O_{12}$
CT	Computed tomography (výpočetní tomografie)
CTR	Coincidence timing resolution (koincidenční rozlišovací doba)
DFT	Density functional theory
fk	photocathode (fotokatoda)
FWHM	Full width on half maximum (plná šířka v polovině maxima)
GGAG	$Gd_3(Ga,Al)_5O_{12}$
GGG	$Gd_3Ga_5O_{12}$
GOS	Gd_2O_2S
HIBL	Hot intraband luminescence
HPMT	Hybrid photomultiplier (hybridní fotonásobič)
IR	Infrared (infračervené)
LET	Leading edge triggering (doslova „spouštění z náběžné hrany“)
LGGAG	$(Lu,Gd)_3(Ga,Al)_5O_{12}$
LPE	Liquid phase epitaxy (epitaxe z kapalné fáze)
LPE_Δ	Lineární přenos energie
LSO	Lu_2SiO_5
LuAG	$Lu_3Al_5O_{12}$
LuGAG	$Lu_3(Ga,Al)_5O_{12}$
LY	Light yield (světelný výtěžek)
LYSO	$Lu_{2(1-x)}Y_{2x}SiO_5$
OA	Optical absorption (optická absorpce)
PET	Positron emission tomography (pozitronová emisní tomografie)
PhY	Photoelectron yield (fotoelektronový výtěžek)
PLE	Photo-luminescence excitation (fotoluminiscenční excitace)
PMT	Photomultiplier (fotonásobič)
ppm	parts per million (miliontina)
PWO	$PbWO_4$
RL	Radioluminescence (radioluminiscence)
SiPM	Silicon Photomultiplier (křemíkový fotonásobič)
SPECT	Single-photon emission tomography (doslova „jednofotonová emisní tomografie“)
T-Ba	Tavidlo $BaO-B_2O_3-BaF_2$
T-Pb	Tavidlo $PbO-B_2O_3$
UV	Ultraviolet (ultrafialové)
YAG	$Y_3Al_5O_{12}$

Označení fyzikálních veličin a konstant

β	Fenomenologický parametr (zohledňuje ztráty energie při tvorbě nosičů náboje)
β (pouze v části 5.3)	Rychlost růstu teploty
η_{col}	Účinnost sběru fotonů na fk
η_{tr}	Pravděpodobnost, že vodivostní elektron (díra) bude zachycen v pasti
λ	Vlnová délka
λ_{em}	Vlnová délka emitovaného fotonu
λ_{exc}	Excitační vlnová délka
ν	Frekvence oscilátoru
ρ	Hustota
τ	Časová konstanta zesilovače
τ_d	Doba dosvitu
τ_r	Náběžná doba scintilačního pulzu
$A_{10/0.5}$	Poměr světelných výtěžků při τ= 10 μs a τ= 0,5 μs
c	Rychlost světla
C	Zhášecí konstanta
CTR	Koincidenční rozlišovací schopnost
d	Tloušťka (epitaxního filmu)
E	Energie
E	Hloubka pasti, její aktivační energie
E_{em}	Energie emise
E_{exc}	Excitační energie
E_g	Šíře zakázaného pásu
E_q	Zhášecí energie
FWHM	Plná šířka v polovině maxima; kvantifikuje energetickou rozlišovací schopnost
h	Planckova konstanta
k_B	Boltzmanova konstanta
$K_{f/e}$	Podíl rychlé složky vysvícení na odezvě
LPE_Δ	Lineární přenos energie
LY	Světelný výtěžek
M_A	Atomová hmotnost atomu A
n	Index lomu
N_f	Počet scintilačních fotonů
N_{phels}	Počet fotoelektronů
Q	Účinnost luminiscenčního centra
Q(T)	Relativní kvantová účinnost luminiscenčního centra při teplotě T
Q_{PD}	Kvantová účinnost fotodetektoru
PhY	Fotoelektronový výtěžek
R_α	Dosah částice α
s	Frekvenční faktor
S	Účinnost transportu energie k luminiscenčnímu centru
t	Čas
T	Termodynamická teplota
Z_A	Protonové číslo atomu A
Z_{eff}	Efektivní protonové číslo

Reference

[1] W. RÖNTGEN, “On a new kind of rays,” *Science,* vol. 3, no. 59, pp. 227-231, 1896.

[2] H. BECQUEREL, “Sur les radiations invisibles emises par les corps phosphorescents,” *Comptes Rendus,* vol. 122, pp. 501-503, 1896.

[3] R. W. WOOD, “The scintillations produced by radium,” *Philosophical magazine series 6,* vol. 10, p. 513, 1905.

[4] H. GEIGER and E. MARSDEN, “The laws of deflexion of α particles through large angles,” *Philosophical magazine series 6,* vol. 25, no. 148, pp. 604-623, 1913.

[5] H. GEIGER and J. NUTTAL, “The ranges of α particles from various radioactive substances and a relation between range and period of transformation,” *Philosophical magazine series 6,* vol. 22, no. 130, pp. 613-621, 1911.

[6] J. D. COCKCROFT and E. WALTON, “Experiments with high velocity positive ions. II. – The disintegration of elements by high velocity protons,” *Proceedings of the royal society of London, series A,* vol. 137, pp. 229-242, 1932.

[7] W. LEO, Techniques for Nuclear and Particle Physics Experiments, Springer, 1994, p. 157.

[8] R. HOFSTADTER, “The detection of gamma-rays with thallium-activated sodium iodide crystals,” *Physical review,* vol. 75, p. 796–810, 1949.

[9] W. VAN SCIVER and R. HOFSTADTER, “Scintillations in thallium-activated CaI2 and CsI,” *Physical review,* vol. 84, pp. 1062-1063, 1951.

[10] P. R. BELL, “The use of anthracene as a scintillation counter,” *Physical Review,* vol. 73, no. 11, pp. 1405-1406, 1948.

[11] M. WEBER and R. MONCHAMP, “Luminescence of Bi4Ge3O12: spectral and decay properties,” *Journal of apllied physics,* vol. 44, pp. 5495-5499, 1973.

[12] R. DEYCH and E. DOLAZZA, “New Trends in X-ray CT Imaging,” *Proceedings of the NATO Advanced Research Workshop on Radiation Detectors for Medical Applications,* pp. 15-35, 2005.

[13] P. LECOQ, “Development of new scintillators for medical applications,” *Nuclear Instruments and Methods in Physics Research Section A: Accelerators, Spectrometers, Detectors and Associated Equipment,* vol. 809, pp. 130-139, 2016.

[14] C. MICHAIL, I. VALAIS, I. SEFERIS, N. KALYVAS, S. DAVID, G. FOUNTOS and I. KANDARAKIS, “Measurement of the luminescence properties of Gd2O2S:Pr,Ce,F powder scintillators under X-ray radiation,” vol. 70, pp. 59-64, 2014.

[15] M. SPAHN, “X-ray detectors in medical imaging,” *Nuclear Instruments and Methods in Physics Research Section A: Accelerators, Spectrometers, Detectors and Associated Equipment,* vol. 731, pp. 57-63, 2013.

[16] W. W. MOSES, V. GAYSHAN and A. GEKTIN, “The Evolution of SPECT - From Anger To Today And Beyond,” *Proceedings of the NATO Advanced Research Workshop on Radiation Detectors for Medical Applications,* pp. 37-80, 2005.

[17] G. BLASSE and A. BRILL, “A New Phosphor for Flying-Spot Cathode-ray Tubes for Color Television: Yellow-emitting Y3Al5O12−Ce3+,” *Applied Physics Letters,* vol. 11, p. 53, 1967.

[18] R. AUTRATA, P. SCHAUER, J. KVAPIL and J. KVAPIL, “A single crystal of YAG-new fast scintillator in SEM,” *Journal of Physics E: Scientific Instruments,* vol. 11, p. 707−708, 1978.

[19] P. SCHAUER and J. BOK, “Study of spatial resolution of YAG:Ce cathodoluminescent imaging screens,” *Nuclear Instruments and Methods in Physics Research Section B: Beam Interactions with Materials and Atoms,* vol. 308, pp. 68-73, 2013.

[20] „CRYTUR - Electron Microscopy,“ 2018. [Online]. Available: http://www.crytur.cz/solutions/electron-microscopy/. [Přístup získán 19 11 2018].

[21] C. W. E. VAN EIJK, J. ANDRIESSEN, P. DORENBOS and R. VISSER, “Ce3+ doped inorganic scintillators,” *Nuclear Instruments and Methods in Physics Research, Section A: Accelerators, Spectrometers, Detectors and Associated Equipment,* vol. 348, p. 546−550, 1994.

[22] W. CHEWPRADITKUL, L. SWIDERSKI, M. MOSZYŃSKI, T. SZCZSESNIAK, A. SYNTFELD-KAZUCH, C. WANARAK and P. LIMSUWAN, “Comparative studies of Lu3Al5O12:Ce and Y3Al5O12:Ce scintillators for gamma-ray detection,” *Physica Status Solidi A,* vol. 206, p. 2599−2605., 2009.

[23] M. NIKL, A. VEDDA, M. FASOLI, .. FONTANA, V. V. LAGUTA, E. MIHÓKOVÁ, J. PEJCHAL, J. ROSA and K. NEJEZCHLEB, “Shallow traps and radiative recombination processes in single crystal scintillator,” *Physical Review B: Condensed Matter and Materials Physics,* vol. 76, p. 195121, 2007.

[24] M. NIKL, V. V. LAGUTA and A. VEDDA, “Energy transfer and charge carrier capture processes in wide-band-gap scintillators,” *Physica Status Solidi A,* vol. 204, pp. 683-689, 2007.

[25] C. DUJARDIN, C. MANCINI, D. AMANS, G. LEDOUX, D. ABLER, E. AUFFRAY, P. LECOQ, D. PERRODIN, A. PETROSYAN and K. L. OVANESYAN, “LuAG: Ce fibers for high energy calorimetry,” *Journal of Applied Physics,* vol. 108, p. 013510, 2010.

[26] A. G. PETROSYAN, K. L. OVANESYAN, R. V. SARGSYAN, G. O. SHIRINYAN, D. ABLER, E. AUFFRAY, P. LECOQ, C. DUJARDIN and C. PEDRINI, “Bridgman growth and site occupation in LuAG: Ce scintillator crystals,” *Journal of Crystal Growth,* vol. 312, p. 3136−3142, 2010.

[27] P. DORENBOS, “Fundamental Limitations in the Performance of Ce3+-, Pr3+-, and Eu2+-Activated Scintillators,” *IEEE Transactions on Nuclear Sciences,* vol. 57, pp. 1162-1167, 2010.

[28] M. NIKL, E. MIHÓKOVÁ, J. PEJCHAL, A. VEDDA, Y. ZORENKO and K. NEJEZCHLEB, "The antisite LuAl defect-related trap in Lu3Al5O12:Ce single crystal," *Physica Status Solidi B,* vol. 242, p. R119−R121, 2005.

[29] C. R. STANEK, K. J. MCCLELLAN, M. R. LEVY and R. W. GRIMES, "Extrinsic defect structure of RE3Al5O12 garnets," *Physica Status Solidi B,* vol. 243, p. R75−R77, 2006.

[30] H. PRZYBYLIŃSKA, A. WITTLIN, C.-G. MA, M. G. BRIK, A. KAMIŃSKA, P. SYBILSKI, Y. ZORENKO, M. NIKL, V. GORBENKO, A. FEDOROV, M. KUČERA and A. SUCHOCKI, "Rare-earth antisites in lutetium aluminum garnets: Influence on lattice parameter and Ce3+ multicenter structure," *Optical Materials,* vol. 36, pp. 1515-1519, 2014.

[31] C. HU, S. LIU, Y. SHI, H. KOU, J. LI, Y. PAN, X. FENG and Q. LIU, "Antisite defects in nonstoichiometric Lu3Al5O12:Ce ceramic scintillators," *Physica Status Solidi B,* vol. 252, pp. 1993-1999, 2015.

[32] Y. ZORENKO, V. GORBENKO, I. KONSTANKEVYCH, G. STRYGANYUK, V. MIKHAILIN, V. KOLOBANOV and D. SPASSKY, "Single-crystalline films of Ce-doped YAG and LuAG phosphors: Advantages over bulk crystals analogues," *Journal of Luminescence,* vol. 114, pp. 85-94, 2005.

[33] Y. ZORENKO, V. GORBENKO, G. STRYGANYUK, V. KOLOBANOV, D. SPASSKY, K. BLAŽEK and M. NIKL, "Luminescence of excitons and antisite defects in Lu3Al 5O12:Ce single crystals and single-crystal films," *Optika i Spektroskopiya,* vol. 99, pp. 923-931, 2005.

[34] M. NIKL, J. A. MAREŠ, N. SOLOVIEVA, H.-L. LI, X.-J. LIU, L.-P. HUANG, I. FONTANA, M. FASOLI, A. VEDDA and C. D'AMBROSIO, "Scintillation characteristics of Lu3Al5O12: Ce optical ceramics," *Journal of Applied Physics,* vol. 101, p. 033515, 2007.

[35] K. KAMADA, R. ENDO, K. TSUTSUMI, T. YANAGIDA, Y. FUJIMOTO, A. FUKABORI, A. YOSHIKAWA, J. PEJCHAL and M. NIKL, "Composition engineering in cerium-doped (Lu,Gd)3(Ga,Al) 5O12 single-crystal scintillators," *Crystal Growth and Design,* vol. 11, pp. 4484-4490, 2011.

[36] M. FASOLI, A. VEDDA, M. NIKL, C. JIANG, B. P. UBERUAGA, D. A. ANDERSSON, K. J. MCCLELLAN a C. R. STANEK, „Band-gap engineering for removing shallow traps in rare-earth Lu3 Al5 O12 garnet scintillators using Ga3+doping," *Physical Review B: Condensed Matter and Materials Physics,* sv. 84, p. 081102, 2011.

[37] H. OGINO, A. YOSHIKAWA, M. NIKL, J. MAREŠ, J.-I. SHIMOYAMA and K. KISHIO, "Growth and optical properties of Lu3(Ga,Al)5O12 single crystals for scintillator application," *Journal of Crystal Growth,* vol. 311, 2009.

[38] K. KAMADA, T. YANAGIDA, J. PEJCHAL, M. NIKL, T. ENDO, K. TSUTSUMI, Y. FUJIMOTO, A. FUKABORI and A. YOSHIKAWA, "Scintillator-oriented combinatorial search in Ce-doped (Y,Gd) 3(Ga,Al) 5O 12 multicomponent garnet compounds," *Journal of Physics D: Applied Physics,* vol. 44, p. 505104, 2011.

[39] T. YANAGIDA, K. KAMADA, Y. FUJIMOTO, H. YAGI and T. YANAGITANI, "Comparative study of ceramic and single crystal Ce:GAGG scintillator," *Optical Materials,* vol. 35, pp. 2480-2485, 2013.

[40] J. M. OGIEGLO, A. KATELNIKOVAS, A. ZYCH, T. JÜSTEL, A. MEIJERINK and C. R. RONDA, "Luminescence and luminescence quenching in Gd3(Ga,Al) 5O12 scintillators doped with Ce3+," *Journal of Physical Chemistry A,* vol. 117, pp. 2479-2484, 2013.

[41] P. DORENBOS, "Electronic structure and optical properties of the lanthanide activated RE3(Al1-xGax)5O12 (RE=Gd, Y, Lu) garnet compounds," *Journal of Luminescence,* vol. 134, pp. 310-318, 2013.

[42] Z. M. SEELEY, N. J. CHEREPY a S. A. PAYNE, „Expanded phase stability of Gd-based garnet transparent ceramic scintillators," *Journal of Materials Research,* sv. 29.

[43] N. J. CHEREPY, J. D. KUNTZ, Z. M. SEELEY, S. E. FISHER, O. B. DRURY, B. W. STURM, T. A. HURST, R. D. SANNER, J. J. ROBERTS and S. A. PAYNE, "Transparent ceramic scintillators for gamma spectroscopy and radiography," *Proceedings of SPIE - The International Society for Optical Engineering,* vol. 7805, p. 78050I, 2010.

[44] S. LIU, J. A. MAREŠ, V. BABIN, C. HU, H. KOU, C. D'AMBROSIO, Y. PAN and M. NIKL, "Effect of reducing Lu3+ content on the fabrication and scintillation properties of non-stoichiometric Lu3−xAl5O12:Ce ceramics," *Optical Materials,* pp. 179-184, 2017.

[45] S. LIU, J. A. MAREŠ, V. BABIN, C. HU, H. KOU, C. D'AMBROSIO, J. LI, Y. PAN and M. NIKL, "Composition and properties tailoring in Mg2+ codoped non-stoichiometric LuAG:Ce,Mg scintillation ceramics," *Journal of the European Ceramic Society,* vol. 37, pp. 1689-1694, 2017.

[46] M. TYAGI, F. MENG, M. KOSCHAN, A. K. SINGH, C. L. MELCHER and S. GADKARI, "Effect of Co-doping On the Radiation Hardness of Gd3Ga3Al2O12: Ce Scintillators," *IEEE Transactions on Nuclear Science,* vol. 62, pp. 336-339, 2015.

[47] M. TYAGI, F. MENG, M. KOSCHAN, S. B. DONNALD, H. ROTHFUSS and C. L. MELCHER, "Effect of codoping on scintillation and optical properties of a Ce-doped Gd3Ga3Al2O12 scintillator," *Journal of Physics D: Applied Physics,* vol. 46, p. 475302, 2013.

[48] K. KAMADA, Y. SHOJI, V. V. KOCHURIKIN, M. YOSHINO, S. OKUMURA, S. YAMAMOTO, J. Y. YEOM, S. KUROSAWA, Y. YOKOTA, Y. OHASHI, M. NIKL, M. YOSHINO and A. YOSHIKAWA, "2 in. size Czochralski growth and scintillation properties of Li+ co-doped Ce: Gd3Ga3Al2O12," *Optical Materials,* vol. 65, pp. 52-55, 2017.

[49] S. LIU, X. FENG, C. HU, H. KOU, J. LI, J. A. MAREŠ, V. BABIN, M. NIKL, C. D'AMBROSIO and Y. PAN, "Effect of Li+ ions co-doping on luminescence, scintillation properties and defects characteristics of LuAG:Ce ceramics," *Optical Materials,* vol. 64, pp. 245-249, 2017.

[50] K. KAMADA, M. NIKL, S. KUROSAWA, A. BEITLEROVÁ, A. NAGURA, Y. SHOJI, J. PEJCHAL, Y. OHASHI, Y. YOKOTA a A. YOSHIKAWA, „Growth and scintillation properties of Li and Ce co-doped Lu3Al5O12 scintillator," *Journal of Crystal Growth,* sv. 452, p. 85−88, 2016.

[51] P. T. DICKENS, D. T. HAVEN, S. FRIEDRICH, M. SALEH and K. G. LYNN, "Increased luminescence and improved decay kinetics in lithium and cerium co-doped yttrium aluminum garnet scintillators grown by the Czochralski method," *Journal of Applied Physics,* vol. 121, p. 123104, 2017.

[52] A. NAGURA, K. KAMADA, M. NIKL, S. KUROSAWA, J. PEJCHAL, Y. YOKOTA, A. OHASHI and A. YOSHIKAWA, “Improvement of scintillation properties on Ce doped Y3Al5O12 scintillator by divalent cations codoping,” *Japanese Journal of Applied Physics,* vol. 54, p. 04DH17, 2015.

[53] M. T. LUCCHINI, S. GUNDACKER, P. LECOQ, A. BENAGLIA, M. NIKL, K. KAMADA, A. YOSHIKAWA and E. AUFFRAY, “Timing capabilities of garnet crystals for detection of high energy charged particles,” *Nuclear Instruments and Methods in Physics Research, Section A: Accelerators, Spectrometers, Detectors and Associated Equipment,* vol. 852, pp. 1-9, 2017.

[54] M. NIKL, K. KAMADA, V. BABIN, J. PEJCHAL, K. PILAŘOVÁ, E. MIHÓKOVÁ, A. BEITLEROVÁ, K. BARTOSIEWICZ, S. KUROSAWA and A. YOSHIKAWA, “Defect engineering in Ce-doped aluminum garnet single crystal scintillators,” *Crystal Growth and Design,* vol. 14, pp. 4827-4833, 2014.

[55] S. LIU, F. X., Z. ZHOU, M. NIKL, Y. SHI and Y. PAN, “Effect of Mg2+ co-doping on the scintillation performance of LuAG: Ce ceramics,” *Physica Status Solidi Rapid Research Letters,* vol. 8, pp. 105-109, 2014.

[56] S. LIU, J. A. MAREŠ, X. FENG, A. VEDDA, M. FASOLI, Y. SHI, H. KOU, A. BEITLEROVÁ, L. WU, C. D'AMBROSIO, Y. PAN and M. NIKL, “Towards Bright and Fast Lu3Al5O12:Ce,Mg Optical Ceramics Scintillators,” *Advanced Optical Materials,* pp. 731-736, 2016.

[57] M. NIKL, V. BABIN, J. PEJCHAL, V. V. LAGUTA, M. BURYI, J. A. MAREŠ, K. KAMADA, S. KUROSAWA, A. YOSHIKAWA, D. PÁNEK, T. PARKMAN, P. BRŮŽA, K. MANN and M. MÜLLER, “The Stable Ce4+ Center: A New Tool to Optimize Ce-Doped Oxide Scintillators,” *IEEE Transactions on Nuclear Sciences,* vol. 63, pp. 433-438, 2016.

[58] K. KAMADA, M. NIKL, S. KUROSAWA, A. BEITLEROVÁ, A. NAGURA, Y. SHOJI, J. PEJCHAL, Y. OHASHI, Y. YOKOTA and A. YOSHIKAWA, “Alkali earth co-doping effects on luminescence and scintillation properties of Ce doped Gd3Al2Ga3O12 scintillator,” *Optical Materials,* vol. 41, pp. 63-66, 2015.

[59] P. PRŮŠA, M. KUČERA, V. BABIN, P. BRŮŽA, D. PÁNEK, A. BEITLEROVÁ, J. A. MAREŠ, M. HANUŠ, Z. LUČENIČOVÁ, M. NIKL a T. PARKMAN, „Garnet Scintillators of Superior Timing Characteristics: Material, Engineering by Liquid Phase Epitaxy,“ *Advanced optical materials,* sv. 5, p. 1600875, 2017. (strana 133 v příloze 2)

[60] P. PRŮŠA, M. KUČERA, V. BABIN, P. BRŮŽA, T. PARKMAN, D. PÁNEK, A. BEITLEROVÁ, J. A. MAREŠ, M. HANUŠ, Z. LUČENIČOVÁ, M. POKORNÝ and M. NIKL, “Tailoring and Optimization of LuAG:Ce Epitaxial Film Scintillation Properties by Mg Co-Doping,” *Crystal Growth and Design,* vol. 18, pp. 4998-5007, 2018. (strana 123 v příloze 2)

[61] Y. WU, F. MENG, Q. LI, M. KOSCHAN and C. MELCHER, “Role of Ce4+ in the scintillation mechanism of co-doped Gd3Ga3Al2O12:Ce,” *Physical Review Applied,* vol. 2, p. 044009.

[62] M. YOSHINO, K. KAMADA, Y. SHOJI, A. YAMAJI, S. KUROSAWA, Y. YOKOTA, Y. OHASHI, A. YOSHIKAWA and V. I. CHANI, “Effect of Mg codoping on scintillation properties of Ce: Gd3(Ga,Al)5O12 single crystals with various Ga/Al ratios,” *Journal of Crystal Growth,* vol. 468, pp. 420-423, 2017.

[63] H. YAMAGUCHI, K. KAMADA, J. PEJCHAL, S. KUROSAWA, Y. SHOJI, Y. YOKOTA, Y. OHASHI and A. YOSHIKAWA, “Effects of Mg-codoping on luminescence and scintillation properties of Ce doped Lu3(Ga,Al)5O12 single crystals,” *Optical Materials,* vol. 65, pp. 60-65, 2017.

[64] K. KAMADA, A. YAMAJI, S. KUROSAWA, Y. YOKOTA, Y. OHASHI and A. YOSHIKAWA, “Mg co-doping effects on Ce doped Y3(Ga,Al)5O12 scintillator,” *IOP Conference Series: Materials Science and Engineering,* vol. 169, p. 012013, 2017.

[65] S. GUNDACKER, F. ACERBI, E. AUFFRAY, A. FERRI, A. GOLA, M. V. NEMALLAPUDI, G. PATERNOSTER, C. PIEMONTE and P. LECOQ, “State of the art timing in TOF-PET detectors with LuAG, GAGG and L(Y)SO scintillators of various sizes coupled to FBK-SiPMs,” *Journal of Instrumentation,* vol. 11, p. P08008, 2016.

[66] Y. WANG, C. BALDONI, Y. BRECHER, W. H. RHODES, U. SHIRWADKAR, J. GLODO, I. SHAH and C. JI, “Properties of transparent (Gd,Lu)3(Al,Ga)5O12:Ce ceramic with Mg, Ca and Ce co-dopants,” *Proceedings of SPIE,* vol. 9594, p. 95940C, 2015.

[67] P. PRŮŠA, K. KAMADA, M. NIKL, A. YOSHIKAWA and J. A. MAREŠ, “Light yield of (Lu, Y, Gd)3Al2Ga3O12:Ce garnets,” *Radiation Measurements,* vol. 56, pp. 62-65, 2013. (strana 253 v příloze 2)

[68] K. KAMADA, S. KUROSAWA, P. PRŮŠA, M. NIKL, V. V. KOCHURIKIN, T. ENDO, K. TSUTSUMI, H. SATO, Y. YOKOTA, K. SUGIYAMA and A. YOSHIKAWA, “Cz grown 2-in. size Ce:Gd3(Al,Ga)5O12 single crystal; Relationship between Al, Ga site occupancy and scintillation properties,” *Optical Materials,* vol. 36, pp. 1942-1945, 2014. (strana 231 v příloze 2)

[69] K. KAMADA, T. YANAGIDA, T. ENDO, K. TSUTSUMI, Y. USUKI, M. NIKL, Y. FUJIMOTO, A. FUKABORI a A. YOSHIKAWA, „2 inch diameter single crystal growth and scintillation properties of Ce:Gd3Al2Ga3O,“ *Journal of Crystal Growth,* sv. 352, pp. 88-90, 2012.

[70] K. KAMADA, Y. SHOJI, V. V. KOCHURIKIN, A. NAGURA, S. OKUMURA, S. YAMAMOTO, J. Y. YEOM, S. KUROSAWA, J. PEJCHAL, Y. YOKOTA, T. OHASHI, M. NIKL, M. YOSHINO and A. YOSHIKAWA, “Single crystal growth of Ce: Gd3(Ga,Al)5O12 with various Mg concentration and their scintillation properties,” *Journal of Crystal Growth,* vol. 468, pp. 407-410, 2017.

[71] P. PRŮŠA, Scintilační charakteristiky komplexních oxidových materiálů - Disertační práce, C. Školitel: Doc. Ing. Martin Nikl, Editor, Praha: FJFI ČVUT, 2010.

[72] M. KUČERA and P. PRŮŠA, “LPE-Grown Thin-Film Scintillators,” in *Nanocomposite, Ceramic, and Thin Film Scintillators*, M. NIKL, Ed., Pan Stanford Publishing, 2016, pp. 155-226. (strana 142 v příloze 2)

[73] P. PRŮŠA, M. KUČERA, J. A. MAREŠ, Z. ONDERIŠINOVÁ, M. HANUŠ, V. BABIN, A. BEITLEROVÁ and M. NIKL, “Composition Tailoring in Ce-Doped Multicomponent Garnet Epitaxial Film Scintillators,” *Crystal Growth and Design,* vol. 15, pp. 3715-3723, 2015. (strana 214 v příloze 2)

[74] P. PRŮŠA, M. KUČERA, J. A. MAREŠ, M. HANUŠ, A. BEITLEROVÁ, Z. ONDERIŠINOVÁ and M. NIKL, “Scintillation properties of the Ce-doped multicomponent garnet epitaxial films,” *Optical Materials,* vol. 35, pp. 2444-2448, 2013. (strana 248 v příloze 2)

[75] P. PRŮŠA, M. KUČERA, F. MORETTI, M. FASOLI, A. VEDDA, M. HANUŠ, Z. LUČENIČOVÁ and M. NIKL, “Thermoluminescence of LuAG:Ce,Mg epitaxial films,” LUMDETR 2018, Praha, 2018.

[76] M. NIKL, “Scintillation detectors for x-rays,” *Measurement Science and Technology,* vol. 17, pp. R37-R54, 2006.

[77] P. A. RODNYI, Physical Processes in Inorganic Scintillators, 1st edition editor, New York, Baco Raton: CRC Press, 1997.

[78] A. VASILIEV, “Relaxation of hot electronic excitations in scintillators: Account for scattering, track effects, complicated electronic structure,” *Proceedings of Fifth International Conference on Inorganic Scintillators and Their Applications SCINT'99,* pp. 43-52, 2000.

[79] V. NAGIRNYI, E. FELDBACH, L. JÖNSSON, M. KIRM, A. LUSHCHIK, C. LUSHCHIK, L. L. NAGORNAYA, V. D. RYZHIKOV, F. SAVIKHIN, G. SVENSSON and I. A. TUPITSINA, “Excitonic and recombination processes in CaWO4 and CdWO4 scintillators under synchrotron irradiation,” *Radiation Measurements,* vol. 29, pp. 247-250, 1998.

[80] S. OMELKOV, V. NAGIRNYI, S. GUNDACKER, D. A. SPASSKY, E. AUFFRAY, P. LECOQ a M. KIRM, „Scintillation yield of hot intraband luminescence,“ *Journal of Luminescence,* sv. 198, pp. 260-271, 2018.

[81] S. I. OMELKOV, V. NAGIRNYI, A. N. VASILEV and M. KIRM, “New features of hot intraband luminescence for fast timing,” *Journal of Luminescence,* vol. 176, pp. 309-317, 2016.

[82] P. LECOQ, M. KORZHIK and A. VASILIEV, “Can transient phenomena help improving time resolution in scintillators?,” *IEEE Transactions on Nuclear Science,* vol. 61, pp. 229-234, 2014.

[83] C. DUJARDIN, E. AUFFRAY, E. BOURRET-COURCHESNE, P. DORENBOS, P. LECOQ, M. NIKL, A. VASILIEV, A. YOSHIKAWA and R.-Y. ZHU, “Needs, trends, and advances in inorganic scintillators,” *IEEE Transactions on Nuclear Science,* vol. 65, pp. 1977-1997, 2018.

[84] R. Y. DESHPANDE, “Statistics of carrier recombination and trapping and energy resolution in silicon junction detectors,” *Nuclear Instruments and Methods,* vol. 75, pp. 245-253, 1969.

[85] C. VAN EIJK, “Cross-luminescence,” *Journal of Luminescence,* Vols. 60-61, pp. 930-935, 1994.

[86] G. BLASSE and B. GRABMAIER, Luminescent materials, 1st edition, Berlin: Springer Verlag, 1994, p. 232.

[87] K. V. IVANOVSKIKH, J. M. OGIEGLO, A. ZYCH, C. R. RONDA and A. MEIJERINK, “Luminescence temperature quenching for Ce3+ and Pr3+ d-f emission in YAG and LuAG,” *ECS Journal of Solid State Science and Technology,* vol. 2, pp. R3148-R3152, 2013.

[88] D. MATEIKA, E. VÖLKEL a J. HAISMA, „Lattice-constant-adaptable crystallographics. II. Czochralski growth from multicomponent melts of homogeneous mixed-garnet crystals,“ *Journal of crystal growth,* sv. 102, pp. 994-1013, 1990.

[89] Y. KUWANO, K. SUDA, N. ISHIZAWA and T. YAMADA, “Crystal growth and properties of (Lu,Y)3Al5O12,” *Journal of crystal growth,* vol. 260, pp. 159-165, 2004.

[90] Y. ZORENKO, I. KONSTANKEVYCH, V. MIKHAILIN, V. KOLOBANOV and D. SPASKII, "Luminescence of excitons in single crystal garnets," *Optics and spectroscopy,* vol. 96, pp. 436-443, 2004.

[91] V. BABIN, K. BLAŽEK, A. KRASNIKOV, K. NEJEZCHLEB, M. NIKL, T. SAVIKHINA and S. ZAZUBOVICH, "Luminescence of undoped LuAG and YAG crystals," *Physica Status Solidi C,* vol. 2, pp. 97-100, 2005.

[92] V. V. LAGUTA, A. M. SLIPENYUK, M. D. GLINCHUK, I. P. BYKOV, Y. ZORENKO, M. NIKL, J. ROSA and K. NEJEZCHLEB, "Paramagnetic impurity defects in LuAG:Ce thick film scintillators," *Radiation Measurements,* vol. 42, pp. 835-838, 2007.

[93] A. LUPEI, V. LUPEI, C. GHEOGHE, S. HAU and A. IKESUE, "Multicenters in Ce3+ visible emission of YAG ceramics," *Optical Materials,* vol. 37, pp. 727-733, 2014.

[94] G. BLASSE and A. BRILL, "Investigation of Some Ce3+ phosphors," *The Journal of Chemical Physics,* vol. 47, pp. 5139-5145, 1967.

[95] M. HANUŠ, Tenké scintilační vrstvy pro 2D zobrazení: diplomová práce, Praha: Karlova Univerzita, Matematicko-fyzikální fakulta,, 2009.

[96] Y.-C. LIN, Dynamic local structural symmetries and luminescence properties of the yellow emitting phosphor Ce3+-doped Y3Al5O12, Göteborg, Švédsko: Department of Physics, Chalmers University of Technology, 2016, p. 9.

[97] V. BABIN, A. GORBENKO, A. MAKHOV, J. A. MAREŠ, M. NIKL, S. ZAZUBOVICH and Y. ZORENKO, "Luminescence characteristics of Pb2+ centres in undoped and Ce3+-doped Lu3Al5O12 single-crystalline films and Pb2+→Ce3+ energy transfer processes," *Journal of Luminescence,* vol. 127, pp. 384-390, 2007.

[98] K. BLAŽEK, A. KRASNIKOV, K. NEJEZCHLEB, M. NIKL, T. SAVIKHINA and S. ZAZUBOVICH, "Luminescence and defects creation in Ce3+-doped Lu3Al5O12 crystals," *Physica Status Solidi B,* vol. 241, p. 1134–1140, 2004.

[99] E. ZYCH, C. BRECHER and H. LINGERTAT, "Host-associated luminescence from YAG optical ceramics under gamma and optical excitation," *Journal of Luminescence,* vol. 78, pp. 121-134, 1998.

[100] M. NIKL, V. V. LAGUTA and A. VEDDA, "Complex oxide scintillators: Material defects and scintillation performance," *Physica Status Solidi B,* vol. 245, pp. 1701-1722, 2008.

[101] Y. ZORENKO, V. GORBENKO, I. KONSTANKEVYCH, V. MIKHAILIN, V. KOLOBANOV, D. SPASSKY and G. ZIMMERER, "The nature of intrinsic luminescence of garnet structure oxides," *Functional materials,* vol. 9, p. 291, 2002.

[102] Y. ZORENKO, T. ZORENKO, V. V. GORBENKO, T. VOZNYAK, V. SAVCHYN, P. BILSKI and A. TWARDAK, "Peculiarities of luminescent and scintillation properties of YAG:Ce phosphor prepared in different crystalline forms," *Optical Materials,* vol. 34, pp. 1314-1319, 2012.

[103] Y. ZORENKO, V. GORBENKO, I. KONSTANKEVYCH, B. GRINEV and M. GLOBUS, "Scintillation properties of Lu3Al5O12:Ce single-crystalline films," *Nuclear Instruments and Methods in*

Physics Research Section A: Accelerators, Spectrometers, Detectors and Associated Equipment, vol. 486, pp. 309-314, 2002.

[104] E. ZYCH, C. BRECHER and H. LINGERTAT, "Depletion of high-energy carriers in YAG optical ceramic materials," *Spectrochimica Acta Part A: Molecular and Biomolecular Spectroscopy,* vol. 54, pp. 1771-1777, 1998.

[105] M. J. WEBER, S. E. DERENZO, C. DUJARDIN and W. W. MOSES, "Dense Ce3+-Activated Scintillator Materials," *Proceedings of 1995 SCINT Conference,* pp. LBL-37789, 1995.

[106] M. ISHII and M. KOBAYASHI, "Single crystals for radiation detectors," *Progress in Crystal Growth and Characterization of Materials,* vol. 23, pp. 245-311, 1992.

[107] H. CEMBER, Introduction to Health Physics (3rd edition), New York: McGraw-Hill, 1996, p. 733.

[108] M. J. BERGER, J. H. HUBBELL, S. M. SELTZER, J. CHANG, J. S. COURSEY, R. SUKUMAR, D. .. ZUCKER and K. OLSEN, "NIST – XCOM: Photon Cross Section Database," 2009. [Online]. Available: https://www.nist.gov/pml/xcom-photon-cross-sections-database. [Accessed 20 11 2018].

[109] S. PIATEK, "Silicon Photomultiplier - Operation, Performance & Possible Applications," [Online]. Available: http://www.hamamatsu.com/sp/hc/osh/sipm_webinar_1.10.pdf. [Accessed 20 11 2018].

[110] B. V. GRINYOV, V. D. RYZHIKOV, O. SIDLETSKIY, G. M. ONYSHCHENKO, S. N. GALKIN, A. I. IVANOV, V. A. TARASOV, O. V. ZELENSKAYA, D. A. KURTSEV, L. A. PIVEN and I. M. ZENYA, "Absolute Light Yield Determination for LGSO:Ce, CWO, ZnSe:Al, and GSO:Ce Crystals," *IEEE Transactions on Nuclear Science,* vol. 57, pp. 1236-1240, 2010.

[111] S. R. BORENSTEIN, R. B. PALMER and R. C. STRAND, "Optical Fibers and Avalanche Photodiodes for Scintillator Counters," *Physica Scripta,* vol. 23, pp. 550-555, 1981.

[112] K. SHIMAZOE, M. YOSHINO, Y. OHSHIMA, M. UENOMACHI, K. OOGANE, T. ORITA, H. TAKAHASHI, K. KAMADA and A. YOSHIKAWA, "Development of simultaneous PET and Compton imaging using GAGG-SiPM based pixel detectors," *Nuclear Instruments and Methods in Physics Research Section A: Accelerators, Spectrometers, Detectors and Associated Equipment,* vol. IN PRESS, 2018.

[113] E. L. SWANBERG, Z. M. SEELEY, P. R. BECK, B. WIHL, N. J. CHEREPY, S. A. PAYNE, S. L. HUNTER, S. E. FISHER, P. A. THELIN, T. STEFANIK a J. KINDEM, „Recent advances in garnet scintillator gamma spectrometers," *Proceedings of SPIE,* sv. 10392, 2017.

[114] D. J. ROBBINS, „On Predicting the Maximum Efficiency of Phosphor Systems Excited by Ionizing Radiation," *Journal of Electrochemical Society,* sv. 127, pp. 2694-2702, 1980.

[115] I. HOLL, E. LORENZ and G. MAGERAS, "A measurement of the light yield of common inorganic scintillators," *IEEE Transactions on Nuclear Science,* vol. 35, pp. 105-109, 1988.

[116] J. A. MAREŠ, A. BEITLEROVÁ, M. NIKL, N. SOLOVIEVA, C. D'AMBROSIO, K. BLAŽEK, P. MALÝ, K. NEJEZCHLEB and F. DE NOTARISTEFANI, "Scintillation response of Ce-doped or intrinsic

scintillating crystals in the range up to 1 MeV," *Radiation Measurements,* vol. 38, pp. 4-6, 2004.

[117] M. MOSZYŃSKI, A. SYNTFELD-KAZUCH, L. SWIDERSKI, M. GRODZICKA, J. IWANOWSKA, P. SIBCZYŃSKI and T. SZCZEŚNIAK, "Energy resolution of scintillation detectors," *Nuclear Instruments and Methods in Physics Research, Section A: Accelerators, Spectrometers, Detectors and Associated Equipment,* vol. 805, pp. 25-35, 2016.

[118] J. D. VALENTINE, B. D. ROONEY and J. LI, "The light yield nonproportionality component of scintillator energy resolution," *IEEE Transactions on Nuclear Science,* vol. 45, pp. 512-517, 1998.

[119] V. V. AVDEICHIKOV, L. BERGHOLT, M. GUTTORMSEN, J. E. TAYLOR, L. WESTERBERG, B. JAKOBSSON, W. KLAMRA and Y. A. MURIN, "Light output and energy resolution of Csi, YAG, GSO, BGO and LSO scintillators for light ions," *Nuclear Instruments and Methods in Physics Research Section A: Accelerators, Spectrometers, Detectors and Associated Equipment,* vol. 349, pp. 216-224, 1994.

[120] W. MOSES, S. PAYNE, W.-S. CHOONG, G. HULL and B. REUTER, "Scintillator non-proportionality: present understanding and future challenges," *IEEE Transactions on nuclear science,* vol. 55, pp. 1049-1053, 2008.

[121] M. S. ALEKHIN, D. A. BINER, K. V. KRÄMER and P. DORENBOS, "Improvement of LaBr3:5%Ce scintillation properties by Li +, Na+, Mg2+, Ca2+, Sr2+, and Ba2+ co-doping," *Journal of Applied Physics,* vol. 113, no. 22, p. 224904, 2013.

[122] G. BIZARRI, W. W. MOSES, J. SINGH, A. N. VASILEV and R. .. WILLIAMS, "An analytical model of nonproportional scintillator light yield in terms of recombination rates," *Journal of Applied Physics,* vol. 105, p. 044507, 2009.

[123] Q. LI, J. Q. GRIM, R. T. WILLIAMS, G. A. BIZARRI and W. W. MOSES, "A transport-based model of material trends in nonproportionality of scintillators," *Journal of Applied Physics,* vol. 109, p. 123716, 2011.

[124] R. T. WILLIAMS, J. Q. GRIM, Q. LI, K. B. UCER a W. W. MOSES, „Excitation density, diffusion-drift, and proportionality in scintillators," *Physica Status Solidi B,* sv. 248, pp. 426-438, 2011.

[125] A. V. GEKTIN and A. N. VASILEV, "Fluctuations of ionizing particle track structure and energy resolution of scintillators," *Functional Materials,* vol. 24, pp. 621-627, 2017.

[126] M. BERETTA, S. CAPELLI, L. GIRONI, E. PREVITALI and M. SISTI, "Non proportionality dependence on shaping time," *Journal of Instrumentation,* vol. 12, p. P04007, 2017.

[127] S. GRIDIN, D. R. ONKEN, R. T. WILLIAMS, L. SWIDERSKI, Z. MIANOWSKA, A. SYNTFELD-KAZUCH, M. MOSZYŃSKI, V. GAYSHAN, S. VASIUKOV and A. GEKTIN, "Pulse shape analysis of individual gamma events—Correlation to energy resolution and the possibility of its improvement," *Journal of Applied Physics,* vol. 124, p. 154504, 2018.

[128] G. F. KNOLL, Radiation detection and measurement (4th edition), New York: Wiley & Sons, 2010.

[129] SAINT-GOBAIN CRYSTALS, „Lanthanum Bromide and Enhanced Lanthanum Bromide,“ 2017. [Online]. Available: https://www.crystals.saint-gobain.com/sites/imdf.crystals.com/files/documents/lanthanum-material-data-sheet.pdf. [Přístup získán 20 11 2018].

[130] CRYTUR S.R.O., „LuAG:Ce,“ 2018. [Online]. Available: https://www.crytur.cz/materials/luagce/. [Přístup získán 20 11 2018].

[131] FURUKAWA, [Online]. Available: http://www.furukawa-denshi.co.jp/cgi-bin/pdfdata/20140428162950.pdf. [Přístup získán 20 11 2018].

[132] J. UEDA, P. DORENBOS, A. J. J. BOS, A. MEIJERINK and S. TANABE, “Insight into the Thermal Quenching Mechanism for Y3Al5O12:Ce3+ through Thermoluminescence Excitation Spectroscopy,” *Journal of Physical Chemistry C,* vol. 119, pp. 25003-25008, 2015.

[133] P. AVOURIS and T. N. MORGAN, “A tunneling model for the decay of luminescence in inorganic phosphors: The case of Zn2SiO4:Mn,” *The journal of chemical physics,* vol. 74, p. 4347, 1981.

[134] M. MOSZYŃSKI, C. GRESSET, J. VACHER and R. ODRU, “Timing properties of BGO scintillator,” *Nuclear Instruments and Methods in Physics Research,* vol. 188, pp. 403-409, 1981.

[135] T. YANAGIDA, Y. FUJIMOTO, T. ITO, K. UCHIYAMA a K. MORI, „Development of X-ray-induced afterglow characterization system,“ *Applied Physics Express,* sv. 7, p. 062401, 2014.

[136] S. GUNDACKER, R. M. TURTOS, E. AUFFRAY and P. LECOQ, “Precise rise and decay time measurements of inorganic scintillators by means of X-ray and 511 keV excitation,” *Nuclear Instruments and Methods in Physics Research, Section A: Accelerators, Spectrometers, Detectors and Associated Equipment,* vol. 891, pp. 42-52, 2018.

[137] F. S. EBY and W. K. JENTSCHKE, “Fluorescent Response of NaI (Tl) to Nuclear Radiations,” *Physical review,* vol. 96, p. 911, 1954.

[138] S. E. DERENZO, M. J. WEBER, W. W. MOSES a C. DUJARDIN, „Measurements of the Intrinsic Rise Times of Common Inorganic Scintillators,“ *IEEE Transactions on Nuclear Science,* sv. 47, pp. 860-864, 2000.

[139] S. GUNDACKER, E. AUFFRAY, B. FRISCH, P. JARRON, A. KNAPITSCH, T. MEYER, M. PIZZICHEMI and P. LECOQ, “Time of flight positron emission tomography towards 100ps resolution with L(Y)SO: An experimental and theoretical analysis,” *Journal of Instrumentation,* vol. 8, p. P07014, 2013.

[140] S. SEIFERT, H. T. VAN DAM and D. R. SCHAART, “The lower bound on the timing resolution of scintillation detectors,” *Physics in Medicine and Biology,* vol. 57, pp. 1797-1814, 2012.

[141] S. e. B. K. OISHI a T. B. S. V. 2. 5. s. I. 3.-5.-0.-3. OHACHI, „Crystal Growth of Gemstones,“ v *Crystal Growth Technology*, K. BYRAPPA a T. OHACHI, Editoři, Berlin, Německo: Springer Verlag, 2003, p. 590.

[142] H. J. SCHEEL a T. FUKUDA, Crystal Growth Technology, Chichester: Wiley & Sons, 2003.

[143] H.-L. LI, X.-J. LIU and L.-P. HUANG, “Fabrication of Transparent Cerium-Doped Lutetium Aluminum Garnet (LuAG:Ce) Ceramics by a Solid-State Reaction Method,” *Journal of the American Ceramic Society,* vol. 88, pp. 3226-3228, 2005.

[144] C. R. STANEK, K. J. MCCLELLAN, M. R. LEVY, C. MILANESE and R. W. GRIMES, “The effect of intrinsic defects on,” *Nuclear Instruments and Methods in Physics Research Section A: Accelerators, Spectrometers, Detectors and Associated Equipment,* vol. 579, pp. 27-30, 2007.

[145] A. YOSHIKAWA, B. M. EPELBAUM, K. HASEGAWA, S. D. DURBIN and T. FUKUDA, “Microstructures in oxide eutectic fibers grown by a modified micro-pulling-down method,” *Journal of Crystal Growth,* vol. 205, pp. 305-316, 1999.

[146] V. I. CHANI, „Micro-Pulling-Down (m-PD) and Related Growth Methods,“ v *Shaped Crystals: Growth by Micro-Pulling-Down Technique*, Berlin, Springer, 2007, p. 340.

[147] K. KAMADA, M. NIKL, S. KUROSAWA, A. BEITLEROVÁ, A. NAGURA, Y. SHOJI, J. PEJCHAL, Y. OHASHI, Y. YOKOTA and Y. YOSHIKAWA, “Co-doping effects on luminescence and scintillation properties of Ce doped Lu3Al5O12 scintillator,” *Nuclear Instruments and Methods in Physics Research, Section A: Accelerators, Spectrometers, Detectors and Associated Equipment,* vol. 782, pp. 9-12, 2015.

[148] M. KUČERA, K. NITSCH, M. NIKL, M. HANUŠ and S. DANIŠ, “Growth and characterization of YAG and LuAG epitaxial films for scintillation applications,” *Journal of Crystal Growth,* vol. 312, pp. 1538-1545, 2010.

[149] J. ROBERTSON and M. VAN TOL, “Cathodoluminescent garnet layers,” *Thin solid films,* vol. 114, pp. 221-240, 1984.

[150] M. NIKL, J. TOUŠ, J. A. MAREŠ, P. PRŮŠA, E. MIHÓKOVÁ, K. BLAŽEK, A. VEDDA, Y. ZORENKO, V. GORBENKO and V. BABIN, “Lu3Al5O12-based materials for high 2D-resolution scintillation detectors,” *Proceedings of SPIE,* vol. 7310, p. 731008, 2009. (strana 271 v příloze 2)

[151] J. TOUŠ, K. BLAŽEK, M. KUČERA, M. NIKL and J. A. MAREŠ, “Scintillation efficiency and X-ray imaging with the RE-Doped LuAG thin films grown by liquid phase epitaxy,” *Radiation Measurements,* vol. 47, pp. 311-314, 2012.

[152] G. LI, S. LUO, Y. YAN a N. GU, „A method of extending the depth of focus of the high-resolution X-ray imaging system employing optical lens and scintillator: a phantom study,“ *Biomedical Engineering Online,* sv. 14, p. 120, 2015.

[153] R. ISCHEBECK, B. BEUTNER, G. ORLANDI, M. PEDROZZI, T. SCHIETINGER, V. SCHLOTT and V. THOMINET, “Profile Monitors for the SwissFEL Injector Test Facility,” *Proceedings of Linear Accelerator Conference LINAC2010,* vol. TUP103, pp. 656-658, 2010.

[154] S. GERMER, F. PIETAK, J. POLAK and T. ARNOLD, “Quanttative low-energy ion beam characterization by beam profiling and imaging via scintillation screens,” *Review of Scientific Instruments,* vol. 87, p. 113301, 2016.

[155] M. SOLOMONI, R. POTS, P. LECOQ, E. AUFFRAY, S. GUNDACKER, M. PAGANONI, B. SINGH, M. MARSHALL and V. V. NAGARKAR, "Photonic Crystal Slabs Applied to Inorganic Scintillators," *IEEE Transactions on Nuclear Science,* vol. 65, pp. 2191-2195, 2018.

[156] P. PRŮŠA, M. NIKL, J. MAREŠ, M. KUČERA, K. NITSCH and A. BEITLEROVÁ, "The α-particle excited scintillation response of YAG:Ce thin films grown by liquid phase epitaxy," *Physica status solidi A,* vol. 206, pp. 1494-1500, 2009. (strana 262 v příloze 2)

[157] V. BABIN, V. BICHEVIN, V. GORBENKO, A. NAKHOV, E. MIHÓKOVÁ, M. NIKL, A. VEDDA, S. ZAZUBOVICH and Y. ZORENKO, "Luminescence of dimer lead centers in aluminium perovskites and garnets," *Physica status solidi B,* vol. 246, pp. 1318-1326, 2009.

[158] BABIN.V., V. GORBENKO, A. KRASNIKOV, A. MAKHOV, M. NIKL, S. ZAZUBOVICH and Y. ZORENKO, "Influence of lead related centers on luminescence of Ce3+ and Pr3+ centers in single crystalline films of aluminium perovskites and garnets," *Radiation measurements,* vol. 45, pp. 415-418, 2010.

[159] M. KUČERA, K. NITSCH, M. KUBOVÁ, N. SOLOVIEVA, M. NIKL and J. A. MAREŠ, "Ce-doped YAG and LuAG Epitaxial Films for Scintillation Detectors," *IEEE Transactions on Nuclear Science,* vol. 55, pp. 1201-1205, 2008.

[160] M. NIKL, "Energy transfer phenomena in the luminescence of wide band-gap scintillators," *Physica Status Solidi A,* vol. 202, pp. 201-206, 2005.

[161] G. TAMULAITIS, S. BURAČAS, V. P. MARTINOV, V. D. RYZHIKOV, H. H. GUTBROD, V. I. MANKO and M. TEREKHIN, "Luminescence Kinetics of PbWO4 Crystals," *Physica Status Solidi A,* vol. 161, pp. 533-541, 1997.

[162] P. LECOQ, I. DAFINEI, E. AUFFRAY, M. SCHNEEGANS, M. V. KORZHIK, O. V. MISSEVITCH, V. B. PAVLENKO, A. A. FEDOROV, A. N. ANNENKOV, V. L. KOSTYLEV and V. D. LIGUN, "Lead tungstate (PbWO4) scintillators for LHC EM calorimetry," *Nuclear Instruments and Methods in Physics Research Section A: Accelerators, Spectrometers, Detectors and Associated Equipment,* vol. 365, pp. 291-298, 1995.

[163] W. CHEWPRADITKUL, L. SWIDERSKI, M. MOSZYŃSKI, T. SZCZESNIAK, A. SYNTFELD-KAZUCH, C. WANARAK and L. P, "Scintillation properties of LuAG:Ce, YAG:Ce and LYSO:Ce crystals for gamma-ray detection," *IEEE Transactions on Nuclear Science,* pp. 3800-3805, 2009.

[164] P. PRŮŠA, J. A. MAREŠ, W. CHEWPRADITKUL and M. NIKL, *Light yield as a function of amplifier shaping time and its relation to scintillation decay curves (POSTER),* Šanghaj: 2011 SCINT Conference, 2011.

[165] Hamamatsu Photonics K.K., "Photomultiplier Tubes: Basics and Applications (3rd edition)," 2007. [Online]. Available: https://www.hamamatsu.com/resources/pdf/etd/PMT_handbook_v3aE.pdf. [Accessed 30 11 2018].

[166] A. J. J. BOS, "Theoryofthermoluminescence," *Radiation Measurements,* vol. 41, pp. S45-S56, 2007.

[167] S. W. S. MCKEEVER, Thermoluminescence of Solids, Cambridge University Press, 1985.

[168] S. K. YADAV, B. P. UBERUAGA, M. NIKL, C. JIANG and C. R. STANEK, "Band-Gap and Band-Edge Engineering of Multicomponent Garnet Scintillators from First Principles," *Physical Review Applied,* vol. 4, p. 054012, 2015.

[169] M. NIKL, J. PEJCHAL, E. MIHÓKOVÁ, J. A. MAREŠ, H. OGINO, A. YOSHIKAWA, T. FUKUDA, A. VEDDA and C. D'AMBROSIO, "Antisite defectfree Lu3(GaxAl1-x)5O12:Pr scintillator," *Applied physics letters,* vol. 88, p. 141916, 2006.

[170] X. CHEN, Z. HU, J. DAI, H. CHEN, Y. SHI, H. KOU, R. KUČERKOVÁ, A. BEITLEROVÁ, M. NIKL a J. LI, „Fabrication and optical properties of cerium doped Lu3Ga3Al2O12 scintillation ceramics," *Optical Materials,* sv. 85, pp. 121-126, 2018.

[171] M. TYAGI, A. K. SINGH, S. G. SINGH, D. G. DESAI, G. D. PATRA, S. SEN and S. C. GADKARI, "Improvement of the scintillation properties of Gd3Ga3Al2O12: CE,B single crystals having tailored defect structure," *Physica Status Solidi - Rapid Research Letters,* vol. 9, pp. 530-534, 2015.

[172] P. SIBCZYNSKI, J. IWANOWSKA-HANKE, M. MOSZYŃSKI, L. SWIDERSKI, M. SZAWLOWSKI, M. GRODZICKA, T. SZCZESNIAK, K. KAMADA and A. YOSHIKAWA, "Characterization of GAGG:Ce scintillators with various Al-to-Ga ratio," *Nuclear Instruments and Methods in Physics Research, Section A: Accelerators, Spectrometers, Detectors and Associated Equipment,* vol. 772, pp. 112-117, 2015.

[173] Z. LUO, H. JIANG, J. JIANG and R. MAO, "Microstructure and optical characteristics of Ce:Gd3(Ga,Al)5O12 ceramic for scintillator application," *Ceramics International,* vol. 41, pp. 873-876, 2015.

[174] M. SPURRIER, P. SZUPRYCZYNSKI, K. YANG, A. CAREY and C. MELECHER, "Effects of Ca2+ Co-Doping on the Scintillation Properties of LSO:Ce," *IEEE Transactions on Nuclear Science,* vol. 55, p. 1178−1182, 2008.

[175] K. YANG, C. MELCHER, P. RACK and L. ERIKSSON, "Effects of calcium codoping on charge traps in LSO: Ce crystals," *IEEE Transactions on Nuclear Science,* vol. 56, p. 2960−2965, 2009.

[176] S. BLAHUTA, A. BESSIERE, B. VIANA, P. DORENBOS and V. OUSPENSKI, "Evidence and Consequences of Ce4+ in LYSO: Ce,Ca and LYSO:Ce,Mg Single Crystals for Medical Imaging Applications," *IEEE Transactions on Nuclear Science,* vol. 60, p. 3134−3141, 2013.

[177] W. CHEWPRADITKUL, C. WANARAK, T. SZCZESNIAK, M. MOSZYŃSKI, V. JARÝ, A. BEITLEROVÁ and M. NIKL, "Comparison of absorption, luminescence and scintillation characteristics in Lu1.95Y0.05SiO5: Ce,Ca and Y2SiO5: Ce scintillators," *Optical Materials,* vol. 35, p. 1679−1684, 2013.

[178] C. L. MELCHER, S. FRIEDRICH, S. P. CRAMER, M. SPURRIER, P. SZUPRYCZYNSKI and R. NUTT, "Cerium oxidation state in LSO:Ce scintillators," *IEEE Transactions on Nuclear Science,* vol. 52, pp. 1809 - 1812, 2005.

[179] C. HU, S. LIU, M. FASOLI, A. VEDDA, M. NIKL, X. FENG and Y. PAN, “ESR and TSL study of hole and electron traps in LuAG: Ce, Mg ceramic scintillator,” *Optical Materials,* vol. 45, p. 252−257, 2015.

[180] C. HU, S. LIU, M. FASOLI, A. VEDDA, M. NIKL, X. FENG and Y. PAN, “O− centers in LuAG: Ce,Mg ceramics,” *Physica Status Solidi RRL,* vol. 9, p. 245−249, 2015.

[181] M. T. LUCCHINI, V. BABIN, P. BOHÁČEK, S. GUNDACKER, K. KAMADA, M. NIKL, A. PETROSYAN, A. YOSHIKAWA a E. AUFFRAY, „Effect of Mg2+ ions co-doping on timing performance and radiation tolerance of Cerium doped Gd3Al2Ga3O12 crystals,“ *Nuclear Instruments and Methods in Physics Research Section A: Accelerators, Spectrometers, Detectors and Associated Equipment,* sv. 816, p. 176−183, 216.

[182] T. KANAI, M. SATOH and I. MIURA, “Characteristics of a Nonstoichiometric Gd3+δ(Al,Ga)5−δO12:Ce Garnet Scintillator,” *Journal of the American Ceramic Society,* vol. 91, pp. 456-462, 2008.

[183] C. DUJARDIN, C. MANCINI, D. AMANS, G. LEDOUX, D. ABLER, E. AUFFRAY, P. LECOQ, D. PERRODIN, A. PETROSYAN and K. L. OVANESYAN, “LuAG:Ce fibers for high energy calorimetry,” *Journal of Applied Physics,* vol. 108, p. 013510, 2010.

[184] K. KAMADA, P. PRŮŠA, M. NIKL, C. PIEMONTE, A. TAROLLI, T. YANAGIDA, T. ENDO, K. TSUTSUMI and A. YOSHIKAWA, “2-inch size crystal growth of Ce:Gd3A12Ga3012 with various Ce concentration and their scintillation properties,” *2012 IEEE Nuclear Science Symposiwn and Medical Imaging Conference Record (NSS/MIC),* pp. 1698-1701.

[185] E. MIHÓKOVÁ, K. VÁVRŮ, K. KAMADA, V. BABIN, A. YOSHIKAWA and M. NIKL, “Deep trapping states in cerium doped (Lu, Y, Gd)3(Ga, Al)5O12single crystal scintillators,” *Radiation Measurements,* vol. 56, pp. 98-101, 2013.

[186] W. DROZDOWSKI, P. DORENBOS, A. J. J. BOS, J. T. M. DE HAAS, S. KRAFT, E. MADDOX, A. OWENS, F. G. A. QUARATI, C. DATH and V. OUSPENSKI, “Effect of Proton Dose, Crystal Size, and Cerium Concentration on Scintillation Yield and Energy Resolution of LaBr,” *IEEE Transactions on Nuclear Science,* vol. 54, pp. 736-740, 2007.

[187] K. KAMADA, P. PRŮŠA, M. NIKL, K. BLAŽEK, T. ENDO, K. TSUTSUMI, S. KUROSAWA, Y. YOKOTA and A. YOSHIKAWA, “Czochralski Growth and Scintillation Properties of Ce: (Gd,Y,Lu)3(Al,Ga)5O12 Single Crystals,” *IEEE Transactions on Nuclear Science,* vol. 61, pp. 293-296, 2014. (strana 227 v příloze 2)

[188] K. KAMADA, A. YOSHIKAWA, T. ENDO, K. TSUTSUMI, Y. SHOJI, S. KUROSAWA, Y. YOKOTA, P. PRŮŠA and M. NIKL, “Growth of 2-inch size Ce:doped Lu2Gd1Al2Ga3O12 single crystal by the Czochralski method and their scintillation properties,” *Journal of Crystal Growth,* vol. 410, pp. 14-17, 2015. (strana 223 v příloze 2)

[189] O. SAKHTONG, W. CHEWPRADITKUL, C. WANARAK, K. KAMADA, A. YOSHIKAWA, P. PRŮŠA and M. NIKL, “Scintillation propertiesofGd3Al2Ga3O12:Ce3+ single crystal scintillator,” *Nuclear Instruments and Methods in Physics Research Section A: Accelerators, Spectrometers, Detectors and Associated Equipment,* vol. 751, pp. 1-5, 2014. (strana 235 v příloze 2)

[190] M. KUČERA, M. HANUŠ, Z. ONDERIŠINOVÁ, P. PRŮŠA, A. BEITLEROVÁ and M. NIKL, "Energy transfer and scintillation properties of Ce3+ doped (LuYGd)3(AlGa)5O12 multicomponent garnets," *IEEE Transactions on Nuclear Science,* vol. 61, pp. 282-289, 2014. (strana 240 v příloze 2)

[191] P. PRŮŠA, T. ČECHÁK, J. A. MAREŠ, M. NIKL, A. BEITLEROVÁ, N. SOLOVIEVA, Y. V. ZORENKO, V. I. GORBENKO, J. TOUŠ and K. BLAŽEK, "The alpha-particle excited scintillation response of the liquid phase epitaxy grown LuAG:Ce thin films," *Applied Physics Letters,* vol. 92, p. 041903, 2008. (strana 282 v příloze 2)

[192] V. BABIN, M. HANUŠ, A. KRASNIKOV, M. KUČERA, M. NIKL and S. ZAZUBOVICH, "Determination of the position of the 5d excited levels of Ce3+ ions with respect to the conduction band in the epitaxial films of the multicomponent (Lu,Gd)3(Ga,Al)5O12:Ce garnets," *Optical Materials,* vol. 62, pp. 465-474, 2016.

[193] V. BABIN, K. CHERNENKO, M. KUČERA, M. NIKL and S. ZAZUBOVICH, "Photostimulated luminescence and defects creation processes in Ce3+-doped epitaxial films of multicomponent Lu3−xGdxGayAl5−yO12 garnets," *Journal of Luminescence,* vol. 179, pp. 487-495, 2016.

[194] M. KORJIK, V. ALENKOV, A. BORISEVICH, O. BUZANOV, V. DORMENEV, G. DOSOVITSKIY, A. FEDOROV, D. KOZLOV, V. MECHINSKY, R. W. NOVOTNY, G. TAMULAITIS, V. VASILIEV, H.-G. ZAUNICK and A. A. VAITKEVIČIUS, "Significant improvement of GAGG:Ce based scintillation detector performance with temperature decrease," *Nuclear Instruments and Methods in Physics Research, Section A: Accelerators, Spectrometers, Detectors and Associated Equipment,* vol. 871, pp. 42-46, 2017.

[195] Y. O. ZAGORODNIY, V. CHLAN, H. ŠTĚPÁNKOVÁ, Y. FOMICHOV, J. PEJCHAL, V. V. LAGUTA a M. NIKL, „Gallium preference for the occupation of tetrahedral sites in Lu3(Al5-xGax)O12 multicomponent garnet scintillators according to solid-state nuclear magnetic resonance and density functional theory calculations," *Elsevier,* sv. 126, pp. 93-104, 2019.

[196] V. BABIN, M. BURYI, V. CHLAN, Y. FOMICHOV, K. KAMADA, V. V. LAGUTA, M. NIKL, J. PEJCHAL, H. ŠTĚPÁNKOVÁ, A. YOSHIKAWA, Y. ZAGORODNIY and S. ZAZUBOVICH, "Influence of gallium content on Ga3+ position and photo- and thermally stimulated luminescence in Ce3+ -doped multicomponent (Y,Lu)3GaxAl5-xO12 garnets," *Journal of Luminescence,* vol. 200, pp. 141-150, 2018.

[197] W. WOLSZCZAK a P. DORENBOS, „Nonproportional Response of Scintillators to Alpha Particle Excitation," *IEEE Transactions on Nuclear Science,* sv. 64, pp. 1580-1591, 2017.

[198] E. DELL'ORTO, M. FASOLI, G. REN and A. VEDDA, "Defect-Driven Radioluminescence Sensitization in Scintillators: The," *The Journal of Physical Chemistry C,* vol. 117, pp. 20201-20208, 2013.

Příloha 1 – Amplitudové spektrometrie; Měření scintilačních dosvitů – popis aparatur

A. Amplitudová spektrometrie

Uvnitř temného boxu se nachází hybridní fotonásobič (HPMT). V případě všech zde uvedených výsledků jde o model DEP PPO 475B (v polovině roku 2018 byl nahrazen novějším typem). Spektrální kvantová účinnost je obr. P1.1. Použité napětí se podle potřeby pohybuje od 6 kV do 12 kV. Nižší hodnoty jsou používány při měření vzorků s nižším světelným výtěžkem, tak aby nedocházelo k nasycení odezvy. Použité napětí na PIN diodě uvnitř HPMT je 65 V.

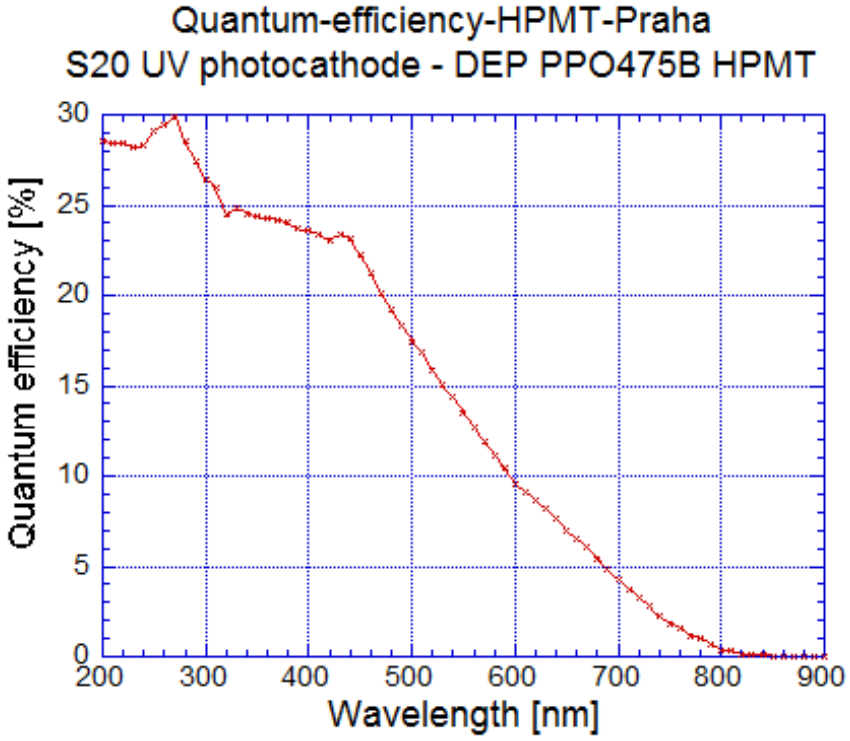

Obr. P1.1 – Spektrální kvantová účinnost fotokatody HPMT DEP PPO 475B (fk S20 UV) (poskytl J.A.Mareš).

Signál z PIN diody je zpracován předzesilovačem s odporovou zpětnou vazbou s časovou konstantou 500 μs, který je rovněž zabudován uvnitř HPMT. Signál z předzesilovače je zpracován zesilovačem ORTEC 672, volba zesílení závisí na velikosti signálu (tj. světelném výtěžku a energii budící částice). Vždy je použito semigaussovské tvarování. Zesílený a natvarovaný signál zpracovává mnohokanálový analyzátor ORTEC ASPEC 927, komunikující USB kabelem s počítačem. Akvizice dat je prováděna pomocí programu MAESTRO dodávaného k mnohokanálovému analyzátoru.

Před měřením je zkoumaný vzorek umístěn na vstupní okénko fotokatody HPMT. Optický kontakt zajišťuje transparentní silikonový gel. V případě buzení odezvy zářením gama se používá reflektor. Pro Ce dopované granáty je nejvhodnější teflonová páska, která má v oblasti emise těchto granátů vysokou odrazivost, je levná a dobře se s ní manipuluje. Pro materiály emitující v UV oblasti používáme $BaSO_4$ (netýká se této habilitační práce). Při buzení odezvy zářením alfa se reflektor nepoužívá, zářič je téměř v kontaktu s měřeným vzorkem.

B. Scintilační dosvity.

Scintilační dosvity jsou měřeny fotonásobičem R7207-01, signál zaznamenává digitální osciloskop Tektronix TDS3052C. Kritériem pro zaznamenání signálu je překročení dolní diskriminační hladiny (tzv. leading edge triggering), kterou nastavujeme tak, aby ji překračovaly jen pulzy s nejvyšší amplitudou. Každý individuální pulz/průběh signálu je přenesen do počítače. V počítači jsou z dalšího zpracování vyloučeny signály s výrazně odlišnou amplitudou a defektní signály. Zbylé průběhy jsou synchronizovány podle nízké diskriminační hladiny. Teprve nyní jsou signály zprůměrovány. Program pro synchronizaci a průměrování vypracoval Martin Pokorný.

Kromě vzorků je měřena i odezvová funkce aparatury, vyvolaná čerenkovovým zářením, jež vzniká působením kosmického záření v okénku fotokatody PMT. Iterativní matematickým postupem se tak lze od naměřené odezvy dobrat reálného scintilačního dosvitu – to je úkol programu SpectraSolve 3.01 Pro.

Příloha 2 – Publikační činnost autora přímo související s tématem habilitační práce

PRŮŠA, P.; KUČERA, M.; BABIN, V.; BRŮŽA, P.; PÁNEK, D.; PARKMAN, T.; BEITLEROVÁ, A.; MAREŠ, J.A.; HANUŠ, M.; LUČENIČOVÁ, Z.; POKORNÝ, M.; NIKL, M., Martin: Tailoring and Optimization of LuAG:Ce Epitaxial Film Scintillation Properties by Mg Co-Doping, *Crystal Growth and Design,* 2018, vol. 18, p. 4998-5007

PRŮŠA, P.; KUČERA, M.; BABIN, V.; BRŮŽA, P.; PÁNEK, D.; PARKMAN, T.; BEITLEROVÁ, A.; MAREŠ, J.A.; HANUŠ, M.; LUČENIČOVÁ, Z.; NIKL, M.; Garnet Scintillators of Superior Timing Characteristics: Material, Engineering by Liquid Phase Epitaxy, *Advanced Optical Materials,* 2017, vol. 5, 1600875

M. KUČERA and P. PRŮŠA, "LPE-Grown Thin-Film Scintillators," in *Nanocomposite, Ceramic, and Thin Film Scintillators*, M. NIKL, Ed., Pan Stanford Publishing, 2016, pp. 155-226

PRŮŠA, P.; KUČERA, M.; MAREŠ, J.A.; ONDERIŠINOVÁ, Z.; HANUŠ, M.; BABIN, V.; BEITLEROVÁ, A.; NIKL, M.; Composition Tailoring in Ce-Doped Multicomponent Garnet Epitaxial Film Scintillators, *Crystal Growth and Design*, 2015, vol. 15, Iss. 8, p. 3715-3723

KAMADA, K.; YOSHIKAWA, A.; ENDO, T.; TSUTSUMI, K.; SHOJI, Y.; KUROSAWA, S.; YOKOTA, Y.; PRUSA, P.; NIKL, M.; Growth of 2-inch size Ce:doped $Lu_2Gd_1Al_2Ga_3O_{12}$ single crystal by the Czochralski method and their scintillation properties, *Journal of Crystal Growth,* 2015, vol. 410, p. 14-17

KAMADA, K.; PRUSA, NIKL, M.; P.; BLAŽEK, K.; ENDO, T.; TSUTSUMI, K.; KUROSAWA, S.; YOKOTA, Y.; YOSHIKAWA, A.; Czochralski growth and scintillation properties of Ce: (Gd, Y,Lu) $_3$ $(Al,Ga)_5O_{12}$ single crystals, *IEEE Transaction on Nuclear Science*, 2014, vol. 61, iss. 1, p. 293-296

KAMADA, S. KUROSAWA, P. PRŮŠA, M. NIKL, V. V. KOCHURIKIN, T. ENDO, K. TSUTSUMI, H. SATO, Y. YOKOTA, K. SUGIYAMA and A. YOSHIKAWA, "Cz grown 2-in. size Ce:Gd3(Al,Ga)5O12 single crystal; Relationship between Al, Ga site occupancy and scintillation properties," *Optical Materials,* vol. 36, pp. 1942-1945, 2014

SAKHTONG, O.; CHEWPRADITKUL, W.; WANARAK, C.; KAMADA, K.; YOSHIKAWA, A.; PRUSA, P.; NIKL, M.: Scintillation properties of $Gd_3Al_2Ga_3O_{12}:Ce^{3+}$ single crystal scintillators, *Nuclear Instruments and Methods in Physics Research, Section A: Accelerators, Spectrometers, Detectors and Associated Equipment*, 2014, vol. 751, p. 1-5

KUČERA, M.; HANUŠ, M.; ONDERIŠINOVÁ, Z.; PRŮŠA, P.; BEITLEROVÁ, A.; NIKL, M.: Energy Transfer and Scintillation Properties of Ce^{3+} Doped $(LuYGd)_3(AlGa)_5O_{12}$ Multicomponent Garnets, *IEEE Transaction on Nuclear Science*, 2014, vol. 61, iss. 1, p. 282-289

PRŮŠA, P.; KUČERA, M.; MAREŠ, J.A.; HANUŠ, M.; BEITLEROVÁ, A.; ONDERIŠINOVÁ, Z.; NIKL, M.; Scintillation properties of the Ce-doped multicomponent garnet epitaxial films, *Optical Materials*, 2013, vol. 35, iss. 12, p. 2444-2448, **DOI:** 10.1016/j.optmat.2013.06.051

PRŮŠA, P.; KAMADA, K.; NIKL, M.; YOSHIKAWA, A.; MAREŠ, J.A.; Light yield of $(Lu, Y, Gd)_3Al_2Ga_3O_{12}$:Ce garnets, *Radiation Measurements*, 2013, vol. 56, p. 62-65, **DOI:** 10.1016/j.radmeas.2013.01.055

PRŮŠA, P.; MAREŠ, J.A.; NIKL, M.; KUČERA, M.; NITSCH, K.; HANUŠ, M.; P. Průša, Scintillation properties of LuAG:Ce single crystalline films grown by LPE method, *Optical materials*, 2010, vol. 32, p. 1360-1363

PRŮŠA, P.; NIKL, M.; MAREŠ, J.A.; KUČERA, M.; NITSCH, K.; BEITLEROVÁ, The α-particle excited scintillation response of YAG:Ce thin films grown by liquid phase epitaxy, *Physica status solidi A*, 2009, vol. 206, p. 1494-1500

MAREŠ, J.A.; PRŮŠA, P.; NIKL, M.; NITSCH, K.; BEITLEROVÁ, A.; KUČERA, M.; HANUŠ, M.; ZORENKO, Y.; Ce^{3+}-doped crystalline garnet films – scintillation characterization using α-particle exctitation, *Radiation measurements*, 2010, vol. 45, p. 369-371

NIKL, M.; TOUŠ, J.; MAREŠ, J.A.; PRŮŠA, P.; MIHÓKOVÁ, E.; BLAŽEK, K.; VEDDA, A.; ZORENKO, Y.; GORBENKO, V.; BABIN, V.; $Lu_3Al_5O_{12}$-based materials for high 2D-resolution scintillation detectors, *Proceedings of SPIE*, 2009, vol. 7310, p. 731008-731017

PRŮŠA, P.; ČECHÁK, T.; MAREŠ, J.A.; NIKL, M.; BEITLEROVÁ, A.; SOLOVIEVA, N.; ZORENKO, Y.V.; GORBENKO, V.I.; TOUŠ, J.; BLAŽEK, K.; The α-particle excited scintillation response of the liquid phase epitaxy grown LuAG:Ce thin films, *Applied physics letters*, 2008, vol. 92, 041903

CRYSTAL GROWTH & DESIGN

Article

Cite This: *Cryst. Growth Des.* 2018, 18, 4998−5007

pubs.acs.org/crystal

Tailoring and Optimization of LuAG:Ce Epitaxial Film Scintillation Properties by Mg Co-Doping

Petr Prusa,*[,†,‡] Miroslav Kučera,[§] Vladimir Babin,[†] Petr Bruza,[∥] Tomas Parkman,[∥] Dalibor Panek,[∥] Alena Beitlerova,[†] Jiri A. Mares,[†] Martin Hanus,[§] Zuzana Lucenicova,[§] Martin Pokorny,[†] and Martin Nikl[†]

[†]Institute of Physics of the Czech Academy of Sciences, Cukrovarnicka 10, 16253 Prague, Czech Republic

[‡]Faculty of Nuclear Sciences and Physical Engineering, Czech Technical University in Prague, Brehova 7, 11519 Prague 1, Czech Republic

[§]Faculty of Mathematics and Physics, Charles University, Ke Karlovu 5, 12116 Prague 2, Czech Republic

[∥]Faculty of Biomedical Engineering, Czech Technical University in Prague, Nám. Sítná 3105, 27201 Kladno, Czech Republic

ABSTRACT: Six Mg co-doped $Lu_3Al_5O_{12}$:Ce scintillating films were prepared by a liquid phase epitaxy method, having Mg concentration of 0−3000 ppm. The following luminescence and scintillation characteristics and their dependence on Mg concentration were studied: photoluminescence emission and excitation spectra, radioluminescence spectra, photoluminescence and scintillation decay curves, light yield, energy resolution, and afterglow. Light yield increases with Mg concentration until 700 ppm and becomes 15−20% higher than in the Mg-free sample. Further increase of Mg concentration leads to light yield decrease. Scintillation decay is getting faster with an increasing Mg concentration and the afterglow is significantly reduced. The results are compared to ceramics and crystals of very similar compositions.

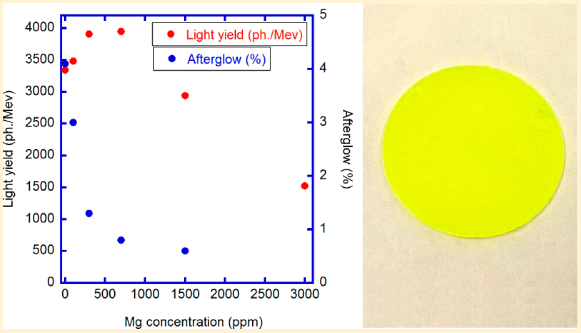

1. INTRODUCTION

Ce- and Pr-doped garnets ($RE_3X_5O_{12}$, RE = Gd, Lu, Y, and X = Al, Ga) crystallizing in cubic lattice constitute a high-performance family of scintillators. They are chemically stable, nonhygroscopic, and radiation resistant and show excellent mechanical properties. The maximum emission of Ce-doped garnets is above 500 nm, which allows efficient coupling with semiconductor photon detectors. Therefore, they can be applied in fields, where photomultiplier tubes are not usable.[1]

A standard garnet scintillator, YAG:Ce,[2,3] exhibits a very good light yield (up to 28−30 ph/keV), decent energy resolution (5−6%), and fast scintillation decay dominated by 60−80 ns decay time.[4−8] YAG:Ce is suitable for charged particle detection. However, low density ρ = 4.56 g cm^{-3} and low effective atomic (proton) number Z_{eff} = 31.9 is responsible for low γ photon detection efficiency.

From the detection efficiency point of view, LuAG:Ce ($Lu_3Al_5O_{12}$:Ce) is the best choice among garnet scintillators due to high density ρ = 6.67 g cm^{-3} and Z_{eff} = 62.9.[7−9] Light yield over 20 ph/keV[9] and energy resolution below 7%[10] are decent as well. Unfortunately, fast decay component of scintillation response ($\tau \sim 60$ ns) is accompanied by an intense, much slower nonexponential components,[10−13] and the integral intensity of them prevails in the melt-grown crystals. This main LuAG:Ce disadvantage is caused by shallow electron traps, attributed to Lu_{Al} antisite defects (AD).[11,14−17]

ADs are formed during high-temperature growth, and thus are always present in melt-grown single crystals. However, the strategies for reduction of the negative influence of ADs have been found. At first, so-called "band-gap engineering" is discussed. The substitution of Al by Ga leads to a downward shift of conduction band bottom.[18] Electron traps become buried in the conduction band and the trapping is no longer possible. The light yield increases and slow scintillation component is reduced significantly. Al/Ga substitution must be combined with Gd/Lu substitution in order to reduce Ce^{3+} excited state ionization probability, which would otherwise result in energy losses.[19,20]

Band-gap engineering resulted in a discovery of a new subset of garnet scintillators, the so-called multicomponent garnets $(Gd/Lu/Y)_3(Al/Ga)_5O_{12}$:Ce of enhanced scintillation properties.[19−28] The optimized single crystal material exhibits the light yield slightly below 60 ph/keV,[29,30] energy resolution 4.2%,[29] and reduced slow scintillation component.[29] The optimized ceramics connected to an avalanche photodiode (APD) exhibits an even higher light yield value of 70 ph/keV[31] and energy resolution 3.7%.[24] Furthermore, better performance is possible below room temperature.[32]

Received: March 18, 2018
Revised: July 18, 2018
Published: July 18, 2018

DOI: 10.1021/acs.cgd.8b00411
Cryst. Growth Des. 2018, 18, 4998−5007

"Defect engineering strategy" applies nonstoichiometrically,[33,34] which affects the AD concentration, and co-doping. In this paper, only co-doping is discussed further. Different co-dopants have been tested and studied for garnet scintillator improvement and optimization in YAG:Ce, LuAG:Ce, and in Ce-doped multicomponent garnets, e.g., B, Ba for improvement of radiation hardness,[35] and overall scintillation performance.[36] Some of the latest publications report about the influence of Li^+ co-doping on scintillation properties.[37−40] Nonetheless, most publications deal with Mg^{2+}, and to a lesser extent with Ca^{2+} as well.

At first, scintillation property improvement, namely, afterglow reduction by Mg/Ca co-doping, was discovered in orthosilicates,[41−44] and the mechanism of improvement was proposed[43] based on the positive role of stable Ce^{4+} center in scintillation mechanism. The essential point is that the stable Ce^{4+} competes much more effectively for electron capture from a conduction band with traps than the Ce^{3+} does.[43] The primary purpose of Mg/Ca co-doping is thus the stabilization of Ce^{4+} center.

Ca/Mg co-doping cannot be successfully implemented in all Ce-doped scintillators. For example, in YAP:Ce ($YAlO_3$:Ce), the Ce^{3+} emission strongly overlaps with Ce^{4+} charge transfer (CT) absorption.[45,46] However, positive effects of Mg co-doping have been observed in all tested garnets, YAG:Ce,[47,48] LuAG:Ce,[34,49−52] and multicomponent garnets;[53−60] and in single crystals,[47−49,52,53,55−59] ceramics,[50,51,60] and epitaxial films[54] as well. The results in the Ca-co-doped garnets are generally less promising.[36,55]

In co-doped YAG:Ce and LuAG:Ce, the light yield increases significantly[47,49−51] (~25 ph/keV values are reported for LuAG:Ce), scintillation decay is generally faster and slow scintillation components are reduced[47,49,50,52] for the optimized Mg concentration. In multicomponent garnets, much faster rise time,[59,61−63] faster decay,[53,54,57,60,61,64] and reduction of slow scintillation component relative intensity[54] are observed, but light yield decreases with increasing Mg concentration.[53,54,60,64] Tentative explanations of light yield decrease in multicomponent garnets are based on stabilization of quenching recombination centers (e.g., O^-) by Mg^{2+},[65,66] overlap between Gd^{3+} 4f-4f (^6P_J−$^8S_{7/2}$) transition in Gd-containing multicomponent garnets and CT absorption toward Ce^{4+} center,[67] and/or lower gap between conduction band minimum and $5d^1$ (^2E_g) state of temporary Ce^{3+} arising from stable Ce^{4+}.[55]

The increase of Mg concentration beyond the optimum value leads to even faster decay but is accompanied by an undesired decrease of light yield in both YAG:Ce and LuAG:Ce. The O^- center stabilization by Mg^{2+} is considered to be a reason for this behavior again. The presence of the O^- center has been proven by electron spin resonance measurement (ESR) in LuAG:Ce,Mg ceramics[66] and single crystal as well.[52] Influence is not entirely negative, since it can be the hole source which enables the return of the stable Ce^{4+} center to starting state in the scintillation cycle.[55,65] Furthermore, oxygen vacancies, representing deep electron traps, may be formed at higher Mg concentration.[34,51]

The most straightforward method of the reduction of the AD negative influence on scintillation properties in garnets is the growth at a lower temperature. It results in a lower AD concentration, proved experimentally, e.g., by thermoluminescence measurement.[14,68−70] Although single crystals could not be prepared at a lower temperature, bulk material can be obtained—in the form of ceramics. Epitaxial films are grown at a much lower temperature as well. Indeed, a reduction of slow scintillation component has been observed in both the LuAG:Ce ceramics[71] and epitaxial films.[72−75]

Epitaxial garnet scintillator films of various compositions have been produced mainly by the liquid phase epitaxy (LPE) method so far.[1,54,67,69,70,72−80] The growth temperature is approximately 1000 °C, much lower than the melt temperature for single crystal growth. The production cost of thin film 2D imaging screens is lower and the LPE method is very flexible, allowing preparation of films with various compositions in a short time. Therefore, the LPE method is very suitable for material screening as well.

Two types of fluxes are used for the garnet epitaxial film preparation. The first one is "traditional", more commonly used PbO-B_2O_3 (PbO-flux). Produced films exhibit very low concentration of macrostructural defects and the surface is mirror-like. However, Pb^{2+} ions are incorporated partially into the crystal lattice and act as luminescence quenching centers.[81,82] Novel BaO-B_2O_3-BaF_2 flux (BaO-flux) is not a source of any contamination which results in a generally higher light yield of films in comparison to those produced in PbO-flux. However, a higher concentration of macrostructural defects is observed due to higher flux viscosity.[83−85]

The thickness of epitaxial films is usually a few tens of micrometers. Therefore, LPE grown film scintillators could be used only for applications exploiting soft X-rays, lower energy electron beams, and/or heavy charged particles. Among these applications, beam diagnostic,[1,86−88] microradiography,[1,89,90] or electron microscopy[91] can be mentioned. There are materials with very slow decays, so-called storage phosphors, applicable in X-ray imaging.[92] On the other hand, we pursue the shorest possible image acquisition time and fastest decay time in this article.

LuAG:Ce films offer the best photon detection efficiency among garnets at given thickness, as mentioned above. However, the light yield is significantly lower and the slow scintillation component more intense than in YAG:Ce or optimized multicomponent garnet films. Light yield improvement would be useful for any application, reduction of slow scintillation component intensity, especially for high frame-rate imaging.

Recently, the Mg-co-doping has been applied in multicomponent garnet epitaxial film[54] for the first time. The results were consistent with observations made on single crystal and ceramics multicomponent garnets. However, the slow scintillation component and afterglow was even less intense, since the AD concentration is intrinsically low in epitaxial films.

In this paper, we present a study of scintillator characteristics of the set of the Mg-co-doped LuAG:Ce epitaxial films with various Mg concentration. In principle, Mg^{2+} co-doping should be useful in diminishing the negative influence of any electronic traps, regardless of their origin. Therefore, an increase of the light yield, and a decrease of slow scintillation component, including the afterglow, is expected. Scintillation and luminescence properties of the Mg-co-doped LuAG:Ce epitaxial films are presented for the first time.

2. EXPERIMENTS AND METHODS

The $Lu_3Al_5O_{12}$:Ce,Mg epitaxial garnet films with Ce doping of 0.7 at. % and different Mg content from 0 to 3000 ppm were grown in the Technology laboratory of the Charles University, Prague, by the

DOI: 10.1021/acs.cgd.8b00411
Cryst. Growth Des. 2018, 18, 4998−5007

Table 1. Properties of LuAG:Ce(0.7%),Mg Epitaxial Garnet Films[a]

sample	Mg [ppm]	thickness [μm]	Ly_α [ph/MeV]	fwhm [%]	afterglow [%] 4−50 ms	afterglow [%] 4 ms	$A_{10/0.5}$ [%]
1LM1	0	30.0	3340 ± 100	12.6 ± 0.6	1.9 ± 0.06	4.1 ± 0.1	178 ± 4
1LM2	100	24.7	3480 ± 110	11.6 ± 0.6	1.2 ± 0.05	3.0 ± 0.1	173 ± 4
1LM3	300	22.0	3910 ± 120	12.1 ± 0.6	0.35 ± 0.03	1.3 ± 0.2	164 ± 4
1LM4	700	21.9	3950 ± 120	10.8 ± 0.5	0.11 ± 0.02	0.8 ± 0.2	134 ± 3
1LM5	1500	21.9	2940 ± 90	12.6 ± 0.6	0.03 ± 0.01	0.6 ± 0.2	110 ± 2
1LM7	3000	17.7	1520 ± 50	8.3 ± 0.6	Afterglow not measured		103 ± 2
ref. SC	0	Bulk	3450 ± 110	9.8 ± 0.5	Afterglow not measured		173 ± 4
$SC\text{-}0_a$	0	Bulk	4850_γ		16 ± 0.3	19 ± 0.5	
$SC\text{-}500_a$	500	Bulk	18800_γ		0.7 ± 0.04	2.5 ± 0.3	
$SC\text{-}3000_a$	3000	Bulk	14100_γ		0.03 ± 0.01	0.2 ± 0.4	
$Ceramics_b$	3000	Bulk	25070_γ	4.9_γ	0.39 ± 0.01	0.8 ± 0.1	115
BGO	0	Bulk			0.01 ± 0.01	0.2 ± 0.2	

[a]Mg concentration in ppm relative to Lu, film thickness, light yield, LY_α, measured under α-particle excitation at 1 μs amplifier shaping time, energy resolution (fwhm), afterglow averaged over 4−50 ms region, afterglow value at 4 ms after excitation cutoff, $A_{10/0.5}$ = LY ratio at 10 and 0.5 μs shaping times. SC-0, SC-500, and SC-3000 = reference LuAG:Ce, Mg single crystals. Index a = from ref 49; b = from ref 51. γ = ^{137}Cs used for excitation.

isothermal dipping liquid phase epitaxy from $BaO\text{-}B_2O_3\text{-}BaF_2$ flux onto the Czochralski grown LuAG garnet substrates of 20 mm in diameter, 0.5 mm thickness, and (111) crystallographic orientation. The film thicknesses determined by weighing were in the range from 17.7 to 30 μm (see Table 1).

The Mg^{2+} concentrations are given as stoichiometric coefficient x in formula $(Ce_{0.007}Lu_{0.993})_{3-x}Mg_xAl_5O_{12}$, x = 0 to 0.009 (0−3000 ppm) (see Table 1). Sample composition was determined by Electron Probe Micro-Analysis (EPMA) and by GDMS (Glow Discharge Mass Spectrometry). All samples were grown under the same conditions, at the growth temperature of 1030 °C and from the same melt but Mg doping. Therefore, the Ce content and also the concentration of potential accidental impurities coming from the flux, such as Ba and B ions, are the same in all the samples. The content of divalent Ba^{2+} ions in samples is <10 ppm according to the GDMS, and their influence can be neglected.

Absorption and photoluminescence spectra were measured using commercial spectrometers Specord 250 and Horiba JY Fluoromax 3. Radioluminescence spectra and photoluminescence decays were measured at the custom-made spectrofluorometer 5000M, Horiba Jobin Yvon using an X-ray tube (10 kV, 50 mA) and nanoLED pulse excitation sources, respectively. The X-ray tube is the DX-W 10 × 1-S 2400 W (tungsten) short anode type powered by high voltage supply ISO-DEBYEFLEX 3003 − 60 kV (Seifert Gmbh).

Photoluminescence decay is fitted by 2 exponential terms:

$$I = \sum_{i=1}^{n} A_i \times \exp(-t/\tau_i) \quad (1)$$

where A_i are the relative amplitudes of the exponential component with decay time τ_i, and n is the number of components. Parameters A_i and τ_i are obtained iteratively by convolution of eq 1 and instrument response function.

Pulse-height spectrometry was used for photoelectron yield (PhY), energy resolution (full width on half maximum − fwhm), and PhY-amplifier shaping time dependence determination. The scintillation response was excited by the α-particles from ^{239}Pu (5.157 MeV) radionuclide source; the α-particles application is necessary due to the small sample thickness. Thickness > 17 μm is larger than the α-particle penetration range; i.e., the α-particle energy is fully absorbed in the film. Radioactive source was placed in direct contact with an epitaxial film to minimize energy losses in the air.[93] Pulse-height spectra were recorded by an experimental setup consisting of hybrid photomultiplier (HPMT) model DEP PPO 475B,[94] spectroscopy amplifier ORTEC model 672 and multichannel buffer ORTEC 927TM. HMPT and films were optically coupled by a silicon grease.

Small penetration range of the α-particles (10 μm approximately) prohibits a reflector application, resulting in a poorer and badly defined photon collection efficiency. The photon collection efficiency (CE) is roughly estimated, CE = 0.735. CE determination method is described in ref 77. The light yield (LY) is calculated using CE estimate, HPMT photocathode quantum efficiency (QE), and photoelectron yield (PhY): LY = PhY/(QE × CE).

If slow components (decay constant at least several μs) are present in scintillation response, the photoelectron/light yield (PhY/LY) rises with amplifier shaping time. In this article, we used parameter $A_{10/0.5}$ = PhY (10 μs)/PhY (0.5 μs) to quantify its increase, where PhY (t) means photoelectron yield measured using amplifier shaping time t. Higher $A_{10/0.5}$ reflects more intense slower component.

As for the afterglow measurement, film response was excited by X-ray tube (the same as for RL spectra measurement) operated at 10 kV. Low voltage was used for films in order to avoid the substrate excitation as much as possible. During the afterglow measurement, the sample was irradiated for tens of seconds until the radioluminescence intensity is stabilized. The signal (number of detected photons per ms) recording starts a few milliseconds before X-ray excitation cutoff.

Scintillation decay under the α-particle (5.157 MeV, ^{239}Pu) excitation was measured in the range 0−2 μs. Decay curves were measured using photomultiplier type Hamamatsu R7207-01 and Tektronix TDS3052C digital Phosphor Oscilloscope. Decay curves were approximated by the sum of 3−4 exponential terms, using eq 1. The convolution of such multiexponential function with instrumental response was fitted to experimental data using software SpectraSolve 3.01 PRO (1997 Ames Photonics, Inc.).

A certain percentage of emitted photons corresponds to each ith exponential term. The percentage is called relative intensity (RI_i) and can be calculated in the following way:

$$RI_i = \frac{A_i\tau_i}{\sum_{j=1}^{3-4} A_j\tau_j} \quad (2)$$

The scintillation decay was also measured under the excitation by nanosecond-pulsed SXR (soft X-rays) photons from the infrared laser-produced plasma in gaseous argon target.[25,95] The incoherent SXR photon burst had fwhm of 4.7 ns and photon energy was within 350−450 eV,[95] for which the attenuation length is a few hundreds of nanometers. In the detection part, a quartz collection lens and a Hamamatsu R7056 fast PMT operated in the direct current mode were used to detect scintillation light. The instrument response function (IRF) was obtained by the measurement of spectrally unresolved scintillation decay of superfast Ga-doped ZnO powder (scintillation response well below 1 ns)[96] under the same

DOI: 10.1021/acs.cgd.8b00411
Cryst. Growth Des. 2018, 18, 4998−5007

experimental conditions. The same mathematical approach as for the alpha-excited decay was used.

Presented data are compared to the data obtained by μ-PD grown single crystals[49] and ceramics[51] whenever possible. It must be noted that MgO in ceramics is used as a sintering agent; most of MgO is thus present at grain boundaries and does not directly affect the scintillation process. Therefore, the direct quantitative comparison of ceramics and film with the same Mg-concentration is not possible.

3. RESULTS AND DISCUSSION

In the absorption spectra, all the samples exhibit two characteristic absorption maxima (centered around 345 and 450 nm) caused by the well-known $4f^1(^2F_{5/2})-5d(^2E_g)$ Ce^{3+} transitions (see Figure 1). Below 250 nm, the $4f^1(^2F_{5/2})-5d(^2T_{2g})$ absorption bands are observed as well.

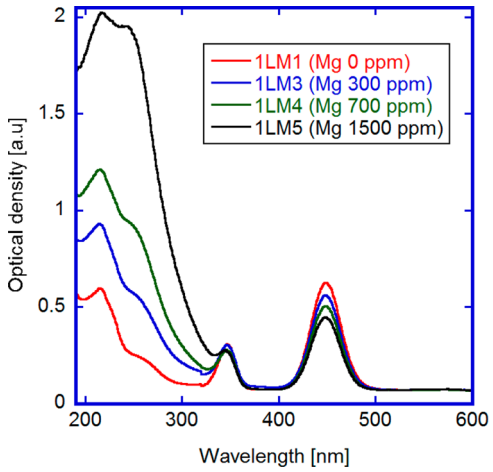

Figure 1. Absorption spectra of LuAG:Ce(0.7%),Mg epitaxial films with various Mg concentrations.

The Ce^{4+} presence, important for this article, is reflected in a significant increase of a broad absorbance in the UV region (approximately below 350 nm) with the increasing Mg^{2+} ions concentration. This broad absorption band is caused by the charge transfer transition from oxygen ligands (energy levels within the valence band) toward Ce^{4+} ions. The presence of Ce^{4+} is a product of an inevitable charge compensation of aliovalent Mg^{2+} ions embedded at trivalent lattice sites.

A slight decrease of absorption maxima of $4f^1(^2F_{5/2})-5d(^2E_g)$ Ce^{3+} transitions is observed with the increasing Mg^{2+} concentration (see Figure 1). Since the Ce concentration is approximately the same in all samples, the increase of Ce^{4+} concentration must be accompanied by the Ce^{3+} concentration decrease. Such behavior has already been observed—even a total elimination of $4f^1(^2F_{5/2})-5d(^2E_g)$ Ce^{3+} absorption bands was reported.[49,53] The correlation of the Ce^{4+} and Mg^{2+} concentration in garnets has been proved as well, by using the XANES (X-ray absorption near edge spectroscopy) method.[51,55] Since the Mg concentration in films is much smaller than the Ce one, slight decrease of absorption maxima of $4f^1(^2F_{5/2})-5d(^2E_g)$ Ce^{3+} transitions in films is observable (Figure 1), and correlates with the Mg^{2+} concentration increase.

The shapes of excitation and emission spectra, typical for LuAG:Ce, are practically the same for all samples, but the intensity is significantly lower for the samples containing a greater amount of Mg^{2+} ions (above 1500 ppm) (see Figure 2). At a higher Mg concentration (>700 ppm), photoluminescence decay is significantly faster as well (see Figure 3 and Table 2).

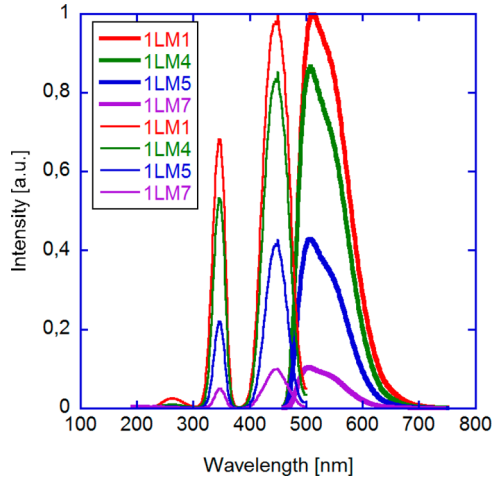

Figure 2. Excitation (510 nm emission) and emission (445 nm excitation) spectra of LuAG:Ce,Mg epitaxial garnet films.

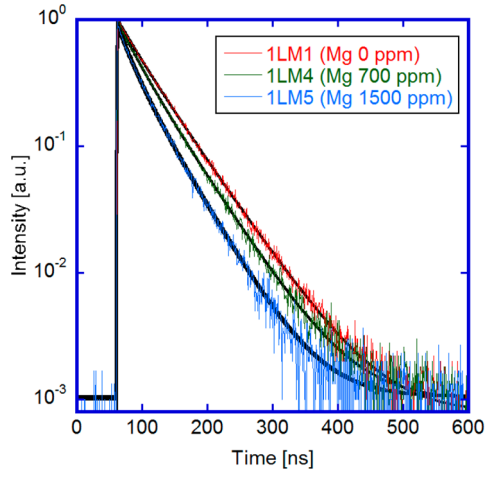

Figure 3. Photoluminescence decays of LuAG:Ce,Mg samples with Mg content 0−1500 ppm, excitation at 445 nm, emission at 510 nm. The solid lines represents the fits, calculated by convolution of the instrument response function and eq 1. Fit parameters are recorded in Table 2.

Ce^{3+} emission (region between 460 and 640 nm) is the most intense component of radioluminescence (RL) spectra (see Figure 4). At a lower Mg^{2+} concentration, the dependence of RL intensity on the Mg^{2+} concentration is unclear. For samples 1LM3−7, the decrease of RL intensity with the Mg^{2+} concentration is evident. A similar observation has been made in different systems.[50,65,66] An antisite defect-related emission in RL spectra in the wavelength range 240−420 nm is observable in Figure 4 as well. It is due to substrate excitation, because of the small film thickness.

Both sets of scintillation decay curves (alpha/SXR excited) show similar results, i.e., the acceleration of scintillation decay with an increasing Mg^{2+} concentration (see Figures 5a and 6). The α-particle and SXR excited decays are practically the same in the time interval between 700 and 2000 ns after excitation (see Figure 5b). At this time interval, the luminescent centers are probably excited by charge carriers released from the same

DOI: 10.1021/acs.cgd.8b00411
Cryst. Growth Des. 2018, 18, 4998−5007

Table 2. Scintillation Decay Times τ_i with Relative Intensities (RI_i – defined by eq 2) of the *i*th Component Measured under soft X-ray (SXR) or α-Particle Excitations[a]

		scintillation decay				PL decay	
sample	ex	τ_1/RI_1 [ns/%]	τ_2/RI_2 [ns/%]	τ_3/RI_3 [ns/%]	τ_4/RI_4 [ns/%]	τ_1/A_1 [ns/-]	τ_2/A_2 [ns/-]
1LM1	α	11.0/11.2	48.9/32.1	514/56.7		32/0.24	59/0.77
1LM2	α	12.2/11.4	50.8/31.5	486/57.1			
1LM3	α	15.3/12.9	59.9/32.9	549/54.2			
1LM4	α	15.3/16.1	65.9/38.3	545/45.7		27/0.31	55/0.67
1LM5	α	14.7/19.2	52.1/51.3	385/29.6		20/0.37	49/0.54
1LM7	α	15.7/34.2	38.4/25.1	63.5/23.2	868/17.5		
1LM1	SXR	19.3/6.4	68.1/27.4	628/20.3	4067/45.9		
1LM5	SXR	11.1/8.7	50.6/64.9	273/16.0	1096/10.3		

[a]The scintillation decay τ_i and RI_i parameters do not have a direct physical meaning and are meant to be used only for the reconstruction of the measured decay curves. Photoluminescence decay times (excitation at 445 nm, emission at 510 nm), PL decay parameter precision is approximately 1%.

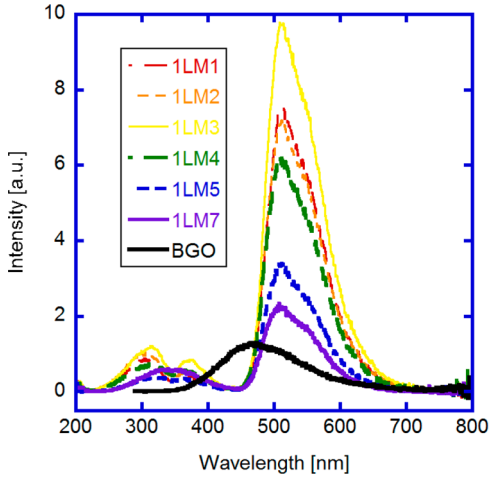

Figure 4. Radioluminescence spectra of LuAG:Ce,Mg epitaxial films, X-ray tube at 10 kV.

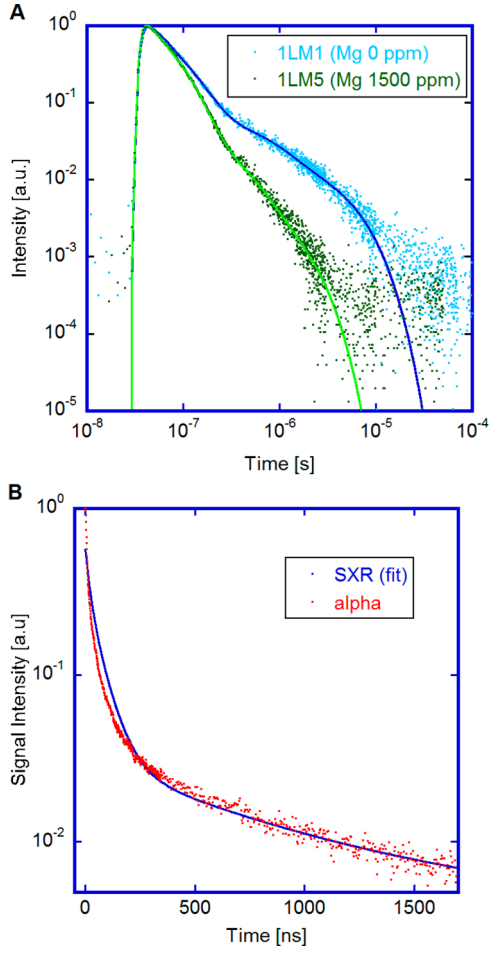

Figure 5. (a) Scintillation decay curves (dots) measured under soft X-ray (SXR) excitation of samples 1LM1 and 1LM5, Mg = 0 and 1500 ppm. Fits (solid lines) are convolutions of instrumental response function and eq 1 (see Table 2 for fit parameters). (b) Comparison of SXR-excited scintillation decay and α-particle excited scintillation decays, normalized at the tail, sample 1LM1, Mg = 0. For SXR-excited one, the fit from Figure 5a is shown instead of the measured data in order to make the graph clearer.

type of trap. Due to the experimental artifact arising from the triggering method used for measurement under α-particle excitation, the decay curve is slightly deformed at the time interval approximately 0–10 ns after excitation. Therefore, a more thorough comparison of the α-particle and SXR excited decay curves is not presented.

RI_i and τ_i obtained using eqs 1 and 2 are presented in Table 2. Unfortunately, a straightforward comparison with single crystals from ref 49 is not possible, since only the first and the second exponential terms are presented in the reference. Also, ref 51 presents only 2 exponential terms for ceramics. Still, the comparison is possible, since the first and the second term represent the decay of ceramic sample sufficiently. Decays of all films are faster than the decay of the fastest ceramics which may be caused by a lower defect concentration (see Figure 6).

The parameter $A_{10/0.5}$ – Mg^{2+} concentration dependence is consistent with both scintillation decay measurements (see Table 1). It monotonically decreases with an increasing Mg^{2+} concentration from 178% to 103%. According to ref 51, $A_{10/0.5}$ ≈ 115% for the Mg concentrations 0.1, 0.3, and 0.6 at. % in ceramics. More detailed dependence of PhY on amplifier shaping time is displayed in Figure 7.

The afterglow measurement is presented in Figure 8 and Table 1. The afterglow values in Table 1 are calculated as an average number of detected scintillation photons per 1 ms in the time interval 4–50 ms after X-ray excitation cut-off divided by a number of detected scintillation photons per 1 ms during X-ray excitation on. Less precise afterglow values 4 ms after excitation cut-off are given as well. The afterglow measurement data of ceramics (ref 51) and single crystals (ref 49) are used for reference purposes (see Figure 8b and Table 1). From

DOI: 10.1021/acs.cgd.8b00411
Cryst. Growth Des. 2018, 18, 4998–5007

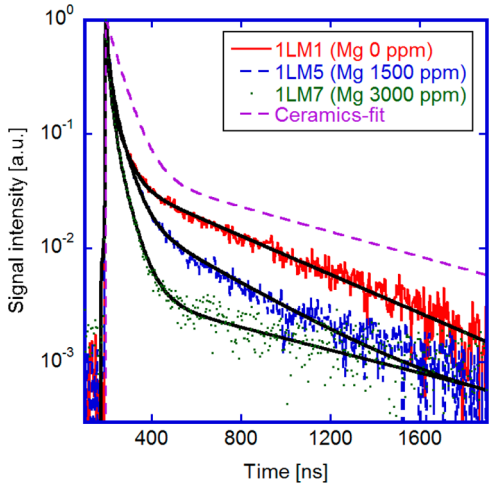

Figure 6. Scintillation decay curves measured under α-particle excitation for selected samples with Mg = 0–3000 ppm. The decays of samples with a low Mg content < 700 ppm (1LM2–4) are very similar to that of Mg-free 1LM1 sample and are not shown here. The solid lines are represents the fits, calculated as convolution of instrumental response function and eq 1. Fit parameters are recorded in Table 2. The scintillation decay fit of the fastest ceramics (0.6% Mg, annealed) measured under the gamma ray excitation was added for comparison.[51]

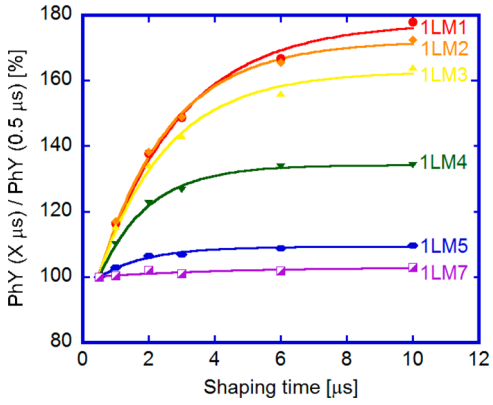

Figure 7. Relative light yield dependence on amplifier shaping time t; 100% = PhY for 0.5 7 μs amplifier shaping time. Curves differ by Mg concentration: from 1LM1 to 1LM7 (0, 100, 300, 700, 1500, and 3000 ppm). The solid lines represents the fits in the form $m_1 - m_2 \times \exp(-t/m_3)$, where m_i are the parameters of the fit.

Figure 8a and b, it is evident that films exhibit significantly lower afterglow than LuAG:Ce,Mg ceramics[51] and single crystals[49] of the same/similar Mg concentration. This is caused by higher defect concentration in μ-PD crystals and ceramics, especially evident when the SC-0 and 1LM1 afterglows are compared. The afterglow of heavily Mg-doped (3000 ppm) μ-PD grown crystal,[49] film 1LM5 (Mg-1500) and BGO reference sample drops below detection limit within a few milliseconds. Therefore, the results are not included in Figure 8b.

The improvement of the afterglow with increasing Mg concentration is evident in Table 1 as well. The value reached for the sample 1LM5 (Mg-1500) is almost on par with that of single crystal from ref 49 (Mg-3000) of lower light yield.

During the afterglow measurement, the LuAG substrate was excited inevitably. According to the calculation using the X-ray tube spectrum and linear attenuation coefficients found in NIST X-COM database,[97] approximately 5% of X-ray photons

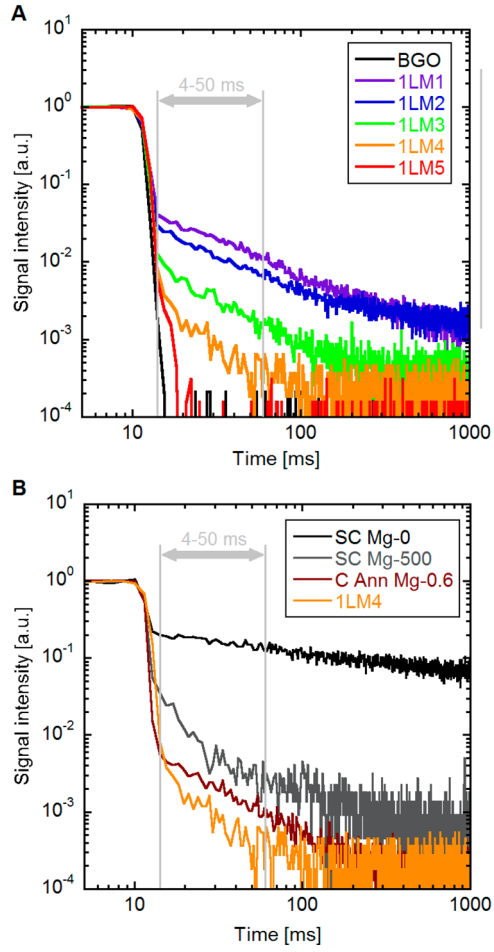

Figure 8. (a) Spectrally unresolved afterglow measurement of films at Mg = 0–1500 ppm. (b) Comparison of spectrally unresolved afterglow of film 1LM4 (700 ppm Mg), reference single crystal (from ref 49), and reference ceramic sample.[51] SC = single crystal (0 ppm and 500 ppm Mg), C Ann 0.6 = annealed ceramics (0.6 at% Mg). Excitation cutoff at time t = 10 ms.

reach the substrate even if the voltage of 10 kV is used, as evidenced in Figure 4, wavelength range 240–420 nm. Therefore, the afterglow measurement of the film–substrate system gives the upper limit of the real afterglow value of the film.

The LY is increasing with an increasing Mg concentration up to 1LM3 (Mg-300) and 1LM4 (Mg-700) samples, and then decreases (see Table 1). Such behavior is consistent with the previous findings.[49,51] In comparison to the Mg-free sample, the best Mg co-doped sample exhibits light yield higher by 15% or 1 μs shaping time. It is much smaller improvement compared to ceramics (higher by 70%)[51] and μ-PD crystals (470%),[49] but only 30% in comparison to Czochralski grown crystal. It probably reflects the poorer quality of Mg-free crystals and ceramics reported in the literature.

The measured energy resolution does not exhibit any trend. The fwhm values are between 10.8% and 13.2% for 1 μs shaping time (see Table 1). Only the sample 1LM7 (Mg-3000) exhibits fwhm = 8.3%. The best fwhm value and the worst light yield observed while measuring the same sample are surprising and need further research. Similar behavior was observed in Mg co-doped multicomponent GAGG:Ce epitaxial films (see authors' previous study[54]).

DOI: 10.1021/acs.cgd.8b00411
Cryst. Growth Des. 2018, 18, 4998–5007

Thus, the overall increase of the luminescence/scintillation decay speed with increasing Mg concentration was observed at the time scale 10 ns − 2 μs (PL decay, alpha and SXR excited scintillation decay), 0.5−10 μs time scale (PhY × shaping time dependence), and 1−1000 ms time scale (afterglow). It is consistent with the hypothesis that Mg^{2+} presence leads to the production of additional, fast radiative and nonradiative de-excitation pathways, which effectively compete for electron capture from the conduction band. Therefore, the percentage of trapped electrons elsewhere is decreasing with the increasing Mg concentration.

The most desirable is the radiative Ce^{4+} de-excitation-based pathway.[49,50] Higher LY at higher Mg^{2+} (Ce^{4+}) concentration would be expected, since photons emitted later than a few microseconds after excitation due to retrapping do not contribute to LY signal. Indeed, we do observe the LY increase with increasing Mg^{2+} concentration up to some limit. At higher Mg^{2+} concentration, additional nonradiative channels appear and we tentatively associate them with the O^- centers using analogy with reported results on crystals or ceramics.[52,65] No measurement providing direct evidence of the presence of O^- centers in films was done in this study. However, the presence of O^- centers has been proven in other LuAG:Ce,Mg systems by electron paramagnetic resonance,[52,65,66] and their presence in the films is very probable as well.

Nonradiative recombination channels are responsible for the further increase of the decay speed with an increasing Mg^{2+} concentration (Mg > 700 ppm), yet at the expense of the decreasing LY and RL intensity. The possibility of nonradiative decay of an excited Ce^{3+} center induced by increasing the Mg^{2+} concentration should be considered as well. There are two indications of this effect among the presented data. The first indication is a rapid decrease of the excitation/emission spectra intensity with Mg^{2+} concentration. For example, the intensity ratio of samples 1LM1 and 1LM5 equals 2.5 for both spectra. According to the absorption spectra, approximately 1.6× more photons are absorbed in 1LM1 in comparison to 1LM5, due to the higher Ce^{3+} concentration and greater thickness. Therefore, a nonradiative energy transfer from 5d(^2E_g) Ce^{3+} excited state away is highly probable. The second indication is a faster PL decay of the Ce^{3+} center at a higher Mg^{2+} concentration. The ratio of the areas under the decay curves 1LM1/1LM5 is 1.5. That is, the efficiency of Ce^{3+} luminescence center Q is 1.5× lower for sample 1LM1 than for 1LM5. Interestingly, combined lower absorption and lower Q lead to the value 1.5 × 1.6 = 2.4, which is practically the same as the excitation/emission spectra intensity ratio 1LM1/1LM5 2.5.

A similar effect was observed in multicomponent garnet films.[54] The energy is probably transferred toward an electron trap or the recombination center stabilized by Mg^{2+} ion (O^-, oxygen vacancy, etc.). Since no absorption has been observed at the wavelength of Ce^{3+} emission so far, one could also consider the intervalence charge transfer states of mixed valence Ce^{3+}−Ce^{4+} pairs, as analogously done for Yb^{2+}−Yb^{3+} and Ce^{3+}−Yb^{3+} pairs in YAG.[98] This aspect requires further experimentation and study. Lower Q at a higher Mg^{2+} concentration leads to an even faster decrease of the LY and RL intensity with an increasing Mg^{2+} concentration.

4. CONCLUSIONS

Reported results prove that the Mg^{2+} co-doping significantly improves scintillation characteristics of $Lu_3Al_5O_{12}$:Ce,Mg LPE-grown films. At the optimal Mg concentration (~300−700 ppm), the light yield increases by 15−20% in comparison with Mg-free film. At a higher Mg concentration the light yield decreases. The intensity of a slow scintillation component and afterglow is continuously reduced with an increasing Mg co-doping. The results of the study correlate with the previous findings on single crystals and ceramics. For ceramics, direct comparison of samples with the same starting Mg concentration is improper, since Mg could be present at the grain boundaries mainly.

We assume that the light yield increase and faster response are caused by an increase of the stable Ce^{4+} centers concentration, which are stabilized by Mg^{2+} co-dopant. At the same time, Mg^{2+} in higher concentration gives a rise to an unknown nonradiative recombination pathway which we tentatively associate with the stabilization of the O^- centers arising in the charge compensation process.

Mg-free sample 1LM1 exhibits the light yield value of 3340 ph/MeV (α-particle excited) and relatively high afterglow (at 4 ms after X-ray cutoff) of 4.1%. The brightest sample 1LM4 (Mg-700) exhibits the light yield value of 3950 ph/MeV and afterglow 0.8%. One of the fastest samples 1LM5 (Mg-1500) exhibits the light yield value of 2940 ph/MeV and afterglow reaches 0.6% at 4 ms.

Epitaxial films retain better light yield at a given afterglow value compared to both crystals and ceramics of analogous composition.[49,51] Presumably, it is due to the lower intrinsic concentration of defects in epitaxial films. Fast LuAG:Ce,Mg epitaxial films might serve in X-ray imaging devices with a high frame rate and for beam diagnostics at accelerators. The high effective atomic number of LuAG:Ce will bring further benefits in such applications as well. We also emphasize the suitability of the liquid phase epitaxy method for material screening, which is evidenced in this study by very smooth dependencies of the most measured parameters on the Mg concentration.

AUTHOR INFORMATION

Corresponding Author

*E-mail: petr.prusa@fjfi.cvut.cz.

ORCID

Petr Prusa: 0000-0002-2766-2907

Notes

The authors declare no competing financial interest.

ACKNOWLEDGMENTS

Financial support of Czech Science foundation 16-15569S project and MEYS RVO 68407700 project is gratefully acknowledged.

REFERENCES

(1) Martin, T.; Koch, A.; Nikl, M. Scintillator materials for x-ray detectors and beam monitors. *MRS Bull.* **2017**, *42*, 451−457.

(2) Blasse, G.; Bril, A. A New Phosphor for Flying-Spot Cathode-ray Tubes for Color Television: Yellow-emitting $Y_3Al_5O_{12}$−Ce^{3+}. *Appl. Phys. Lett.* **1967**, *11*, 53.

(3) Autrata, R.; Schauer, P.; Kuapil, J.; Kuapil, J. A single crystal of YAG-new fast scintillator in SEM. *J. Phys. E: Sci. Instrum.* **1978**, *11*, 707−708.

(4) Moszyński, M.; Ludziejewski, T.; Wolski, D.; Klamra, W.; Norlin, L. O. Properties of the YAG: Ce scintillator. *Nucl. Instrum. Methods Phys. Res., Sect. A* **1994**, *345*, 461−467.

(5) Yanagida, T.; Takahashi, H.; Ito, T.; Kasama, D.; Enoto, T.; Sato, M.; Hirakuri, S.; Kokubun, M.; Makishima, K.; Yanagitani, T.;

DOI: 10.1021/acs.cgd.8b00411
Cryst. Growth Des. 2018, 18, 4998−5007

Yagi, H.; Shigeta, T.; Ito, T. Evaluation of properties of YAG (Ce) ceramic scintillators. *IEEE Trans. Nucl. Sci.* **2005**, *52*, 1836−1841.
(6) Mares, J. A.; Nikl, M.; Beitlerova, A.; Horodysky, P.; Blazek, K.; Bartos, K.; D'Ambrosio, C. Scintillation Properties of Ce^{3+}- and Pr^{3+}-Doped LuAG, YAG and Mixed $Lu_xY_{1-x}AG$ Garnet Crystals. *IEEE Trans. Nucl. Sci.* **2012**, *59*, 2120−2125.
(7) van Eijk, C. W. E.; Andriessen, J.; Dorenbos, P.; Visser, R. Ce^{3+} doped inorganic scintillators. *Nucl. Instrum. Methods Phys. Res., Sect. A* **1994**, *348*, 546−550.
(8) Nikl, M.; Yoshikawa, A.; Kamada, K.; Nejezchleb, K.; Stanek, C. R.; Mares, J. A.; Blazek, K. Development of LuAG-based scintillator crystals−a review, Progr. Cryst. Growth Charact. *Prog. Cryst. Growth Charact. Mater.* **2013**, *59*, 47−72.
(9) Petrosyan, A. G.; Ovanesyan, K. L.; Sargsyan, R. V.; Shirinyan, G. O.; Abler, D.; Auffray, E.; Lecoq, P.; Dujardin, C.; Pedrini, C. Bridgman growth and site occupation in LuAG: Ce scintillator crystals. *J. Cryst. Growth* **2010**, *312*, 3136−3142.
(10) Chewpraditkul, W.; Swiderski, L.; Moszynski, M.; Szczesniak, T.; Syntfeld-Kazuch, A.; Wanarak, C.; Limsuwan, P. Comparative studies of $Lu_3Al_5O_{12}$:Ce and $Y_3Al_5O_{12}$:Ce scintillators for gamma-ray detection. *Phys. Status Solidi A* **2009**, *206*, 2599−2605.
(11) Nikl, M.; Vedda, A.; Fasoli, M.; Fontana, I.; Laguta, V. V.; Mihokova, E.; Pejchal, J.; Rosa, J.; Nejezchleb, K. Shallow traps and radiative recombination processes in single crystal scintillator. *Phys. Rev. B: Condens. Matter Mater. Phys.* **2007**, *76*, 195121.
(12) Nikl, M.; Laguta, V. V.; Vedda, A. Energy transfer and charge carrier capture processes in wide-band-gap scintillators. *Phys. Status Solidi A* **2007**, *204*, 683−689.
(13) Dujardin, C.; Mancini, C.; Amans, D.; Ledoux, G.; Abler, D.; Auffray, E.; Lecoq, P.; Perrodin, D.; Petrosyan, A.; Ovanesyan, K. L. LuAG: Ce fibers for high energy calorimetry. *J. Appl. Phys.* **2010**, *108*, 013510.
(14) Nikl, M.; Mihokova, E.; Pejchal, J.; Vedda, A.; Zorenko, Yu.; Nejezchleb, K. The antisite Lu_{Al} defect-related trap in $Lu_3Al_5O_{12}$:Ce single crystal. *Phys. Status Solidi B* **2005**, *242*, R119−R121.
(15) Stanek, C. R.; McClellan, K. J.; Levy, M. R.; Grimes, R. W. Extrinsic defect structure of $RE_3Al_5O_{12}$ garnets. *Phys. Status Solidi B* **2006**, *243*, R75−R77.
(16) Przybylińska, H.; Wittlin, A.; Ma, C.-G.; Brik, M. G.; Kamińska, A.; Sybilski, P.; Zorenko, Yu.; Nikl, M.; Gorbenko, V.; Fedorov, A.; Kučera, M.; Suchocki, A. Rare-earth antisites in lutetium aluminum garnets: Influence on lattice parameter and Ce^{3+} multicenter structure. *Opt. Mater.* **2014**, *36*, 1515−1519.
(17) Hu, C.; Liu, S.; Shi, Y.; Kou, H.; Li, J.; Pan, Y.; Feng, X.; Liu, Q. Antisite defects in nonstoichiometric $Lu_3Al_5O_{12}$:Ce ceramic scintillators. *Phys. Status Solidi B* **2015**, *252*, 1993−1999.
(18) Fasoli, M.; Vedda, A.; Nikl, M.; Jiang, C.; Uberuaga, B. P.; Andersson, D. A.; McClellan, K. J.; Stanek, C. R. Band-gap engineering for removing shallow traps in rare-earth $Lu_3Al_5O_{12}$ garnet scintillators using Ga^{3+} doping. *Phys. Rev. B: Condens. Matter Mater. Phys.* **2011**, *84*, No. 081102(R), DOI: 10.1103/PhysRevB.84.081102.
(19) Kamada, K.; Endo, T.; Tsutumi, K.; Yanagida, T.; Fujimoto, Y.; Fukabori, A.; Yoshikawa, A.; Pejchal, J.; Nikl, M. Composition Engineering in Cerium-Doped $(Lu,Gd)_3(Ga,Al)_5O_{12}$ Single-Crystal Scintillators. *Cryst. Growth Des.* **2011**, *11*, 4484−4490.
(20) Kamada, K.; Yanagida, T.; Pejchal, J.; Nikl, M.; Endo, T.; Tsutumi, K.; Fujimoto, Y.; Fukabori, A.; Yoshikawa, A. Scintillator-oriented combinatorial search in Ce-doped $(Y,Gd)_3(Ga,Al)_5O_{12}$ multicomponent garnet compounds. *J. Phys. D: Appl. Phys.* **2011**, *44*, 505104.
(21) Nikl, M.; Yoshikawa, A. Recent R&D trends in inorganic single-crystal scintillator materials for radiation detection. *Adv. Opt. Mater.* **2015**, *3*, 463−481.
(22) Wang, C.; Wu, Y.; Ding, D.; Li, H.; Chen, X.; Shi, J.; Ren, G. Optical and scintillation properties of Ce-doped $(Gd_2Y_1)Ga_{2.7}Al_{2.3}O_{12}$ single crystal grown by Czochralski method. *Nucl. Instrum. Methods Phys. Res., Sect. A* **2016**, *820*, 8−13.
(23) Wu, Y.; Luo, Z.; Jiang, H.; Meng, F.; Koschan, M.; Melcher, C. L. Single crystal and optical ceramic multicomponent garnet scintillators: A comparative study. *Nucl. Instrum. Methods Phys. Res., Sect. A* **2015**, *780*, 45−50.
(24) Sibczynski, P.; Iwanowska-Hanke, J.; Moszyński, M.; Swiderski, L.; Szawlowski, M.; Grodzicka, M.; Szczesniak, T.; Kamada, K.; Yoshikawa, A. Characterization of GAGG: Ce scintillators with various Al-to-Ga ratio. *Nucl. Instrum. Methods Phys. Res., Sect. A* **2015**, *772*, 112−117.
(25) Yoshikawa, A.; Kamada, K.; Kurosawa, S.; Shoji, Y.; Yokota, Y.; Chani, V. I.; Nikl, M. Crystal growth and scintillation properties of multi-component oxide single crystals: Ce: GGAG and Ce: La-GPS. *J. Lumin.* **2016**, *169*, 387−393.
(26) Yadav, S.; Uberuaga, B.; Nikl, M.; Jiang, C.; Stanek, C. R. Band-gap and band-edge engineering of multicomponent garnet scintillators from first principles. *Phys. Rev. Appl.* **2015**, *4*, 054012.
(27) Luo, J.; Wu, Y.; Zhang, G.; Zhang, H.; Ren, G. Composition−property relationships in $(Gd_{3-x}Lu_x)(Ga_yAl_{5-y})O_{12}$: Ce (x= 0, 1, 2, 3 and y= 0, 1, 2, 3, 4) multicomponent garnet scintillators. *Opt. Mater.* **2013**, *36*, 476−481.
(28) Cherepy, N. J.; Payne, S. A.; Sturm, B. W. Comparative gamma spectroscopy with SrI_2(Eu), GYGAG(Ce) and Bi-loaded plastic scintillators. *IEEE Nuclear Science Symposium & Medical Imaging Conference Record* **2010**, 1288−1291.
(29) Kamada, K.; Kurosawa, S.; Prusa, P.; Nikl, M.; Kochurikhin, V. V.; Endo, T.; Tsutumi, K.; Sato, H.; Yokota, Y.; Sugiyama, K.; Yoshikawa, A. Cz grown 2-in. size Ce: $Gd_3(Al, Ga)_5O_{12}$ single crystal; relationship between Al, Ga site occupancy and scintillation properties. *Opt. Mater.* **2014**, *36*, 1942−1945.
(30) Yokota, Y.; Kudo, T.; Ohashi, Y.; Kurosawa, S.; Kamada, K.; Zeng, Z.; Kawazoe, Y.; Yoshikawa, A. Effects of dopant distribution improvement on optical and scintillation properties for Ce-doped garnet-type single crystals. *J. Mater. Sci.: Mater. Electron.* **2017**, *28*, 7151−7156.
(31) Yanagida, T.; Kamada, K.; Fujimoto, Y.; Yagi, H.; Yanagitani, T. Comparative study of ceramic and single crystal Ce: GAGG scintillator. *Opt. Mater.* **2013**, *35*, 2480−2485.
(32) Korjik, M.; Alenkov, V.; Borisevich, A.; Buzanov, O.; Dormenev, V.; Dosovitskiy, G.; Dosovitskiy, A.; Fedorov, A.; Kozlov, D.; Mechinsky, V.; Novotny, R. W.; Tamulaitis, G.; Vasiliev, V.; Zaunick, H.-G.; Vaitkevičius, A. A. Significant improvement of GAGG: Ce based scintillation detector performance with temperature decrease. *Nucl. Instrum. Methods Phys. Res., Sect. A* **2017**, *871*, 42−46.
(33) Liu, S.; Mareš, J. A.; Babin, V.; Hu, C.; Kou, H.; D'Ambrosio, C.; Pan, Y.; Nikl, M. Effect of reducing Lu^{3+} content on the fabrication and scintillation properties of non-stoichiometric $Lu_{3-x}Al_5O_{12}$:Ce ceramics. *Opt. Mater.* **2017**, *63*, 179−184.
(34) Liu, S.; Mareš, J. A.; Babin, V.; Hu, C.; Kou, H.; D'Ambrosio, C.; Li, J.; Pan, Y.; Nikl, M. Composition and properties tailoring in Mg^{2+} codoped non-stoichiometric LuAG: Ce,Mg scintillation ceramics. *J. Eur. Ceram. Soc.* **2017**, *37*, 1689−1694.
(35) Tyagi, M.; Meng, F.; Koschan, M.; Singh, A. K.; Melcher, C. L.; Gadkari, S. Effect of Co-doping On the Radiation Hardness of $Gd_3Ga_3Al_2O_{12}$: Ce Scintillators. *IEEE Trans. Nucl. Sci.* **2015**, *62*, 336−339.
(36) Tyagi, M.; Meng, F.; Koschan, M.; Donnald, S. B.; Rothfuss, H.; Melcher, C. L. Effect of codoping on scintillation and optical properties of a Ce-doped $Gd_3Ga_3Al_2O_{12}$ scintillator. *J. Phys. D: Appl. Phys.* **2013**, *46*, 475302.
(37) Kamada, K.; Shoji, Y.; Kochurikhin, V. V.; Yoshino, M.; Okumura, S.; Yamamoto, S.; Yeom, J. Y.; Kurosawa, S.; Yokota, Y.; Ohashi, Y.; Nikl, M.; Yoshino, M.; Yoshikawa, A. 2 in. size Czochralski growth and scintillation properties of Li^+ co-doped Ce: $Gd_3Ga_3Al_2O_{12}$. *Opt. Mater.* **2017**, *65*, 52−55.
(38) Liu, S.; Feng, X.; Mareš, J. A.; Babin, V.; Hu, C.; Kou, H.; D'Ambrosio, C.; Li, J.; Pan, Y.; Nikl, M. *Opt. Mater.* **2017**, *64*, 245−249.
(39) Kamada, K.; Nikl, M.; Kurosawa, S.; Beitlerova, A.; Nagura, A.; Shoji, Y.; Pejchal, J.; Ohashi, Y.; Yokota, Y.; Yoshikawa, A. Growth

DOI: 10.1021/acs.cgd.8b00411
Cryst. Growth Des. 2018, 18, 4998−5007

and scintillation properties of Li and Ce co-doped $Lu_3Al_5O_{12}$ scintillator. *J. Cryst. Growth* **2016**, *452*, 85−88.
(40) Dickens, P. T.; Haven, D. T.; Friedrich, S.; Saleh, M.; Lynn, K. G. Increased luminescence and improved decay kinetics in lithium and cerium co-doped yttrium aluminum garnet scintillators grown by the Czochralski method. *J. Appl. Phys.* **2017**, *121*, 123104.
(41) Spurrier, M.; Szupryczynski, P.; Yang, K.; Carey, A.; Melcher, C. Effects of Ca^{2+} Co-Doping on the Scintillation Properties of LSO: Ce. *IEEE Trans. Nucl. Sci.* **2008**, *55*, 1178−1182.
(42) Yang, K.; Melcher, C.; Rack, P.; Eriksson, L. Effects of calcium codoping on charge traps in LSO: Ce crystals. *IEEE Trans. Nucl. Sci.* **2009**, *56*, 2960−2965.
(43) Blahuta, S.; Bessiere, A.; Viana, B.; Dorenbos, P.; Ouspenski, V. Evidence and Consequences of Ce^{4+} in LYSO: Ce,Ca and LYSO: Ce,Mg Single Crystals for Medical Imaging Applications. *IEEE Trans. Nucl. Sci.* **2013**, *60*, 3134−3141.
(44) Chewpraditkul, W.; Wanarak, C.; Szczesniak, T.; Moszyński, M.; Jary, V.; Beitlerova, A.; Nikl, M. Comparison of absorption, luminescence and scintillation characteristics in $Lu_{1.95}Y_{0.05}SiO_5$: Ce, Ca and Y_2SiO_5: Ce scintillators. *Opt. Mater.* **2013**, *35*, 1679−1684.
(45) Baryshevsky, V. G.; Korzhik, M. V.; Minkov, B. I.; Smirnova, S. A.; Fyodorov, A. A.; Dorenbos, P.; van Eijk, C. W. E. Spectroscopy and scintillation properties of cerium doped $YAlO_3$ single crystals. *J. Phys.: Condens. Matter* **1993**, *5*, 7893−7902.
(46) Gumanskaya, E. G.; Yegorycheva, O. A.; Korzhik, M. V.; Smirnova, S. A.; Pavlenko, V. B.; Fedorov, A. A. Spectroscopic characteristics and scintillation efficiency of $YAlO_3$ monocrystals activated by cerium. *Opt. Spektrosk* **1992**, *72*, 395−399.
(47) Nagura, A.; Kamada, K.; Nikl, M.; Kurosawa, S.; Pejchal, J.; Yokota, Y.; Ohashi, A.; Yoshikawa, A. Improvement of scintillation properties on Ce doped $Y_3Al_5O_{12}$ scintillator by divalent cations co-doping, Jap. *J. Appl. Phys.* **2015**, *54*, 04DH17.
(48) Lucchini, M. T.; Gundacker, S.; Lecoq, P.; Benaglia, A.; Nikl, M.; Kamada, K.; Yoshikawa, A.; Auffray, E. Timing capabilities of garnet crystals for detection of high energy charged particles. *Nucl. Instrum. Methods Phys. Res., Sect. A* **2017**, *852*, 1−9.
(49) Nikl, M.; Kamada, K.; Babin, V.; Pejchal, J.; Pilarova, K.; Mihokova, E.; Beitlerova, A.; Bartosiewicz, K.; Kurosawa, S.; Yoshikawa, A. Defect engineering in Ce-doped aluminum garnet single crystal scintillators. *Cryst. Growth Des.* **2014**, *14*, 4827−4833.
(50) Liu, S.; Feng, X.; Zhou, Z.; Nikl, M.; Shi, Y.; Pan, Y. Effect of Mg^{2+} co-doping on the scintillation performance of LuAG: Ce ceramics. *Phys. Status Solidi RRL* **2014**, *8*, 105−109.
(51) Liu, S.; Mareš, J. A.; Feng, X.; Vedda, A.; Fasoli, M.; Shi, Y.; Kou, H.; Beitlerová, A.; Wu, L.; D'Ambrosio, C.; Pan, Y.; Nikl, M. Towards Bright and Fast $Lu_3Al_5O_{12}$:Ce,Mg Optical Ceramics Scintillators. *Adv. Opt. Mater.* **2016**, *4*, 731−736.
(52) Nikl, M.; Babin, V.; Pejchal, J.; Laguta, V. V.; Buryi, M.; Mareš, J. A.; Kamada, K.; Kurosawa, S.; Yoshikawa, A.; Pánek, D.; Parkman, T.; Brůža, P.; Mann, K.; Müller, M. The Stable Ce^{4+} Center: A New Tool to Optimize Ce-Doped Oxide Scintillators. *IEEE Trans. Nucl. Sci.* **2016**, *63*, 433−438.
(53) Kamada, K.; Nikl, M.; Kurosawa, S.; Beitlerova, A.; Nagura, A.; Shoji, Y.; Pejchal, J.; Ohashi, Y.; Yokota, Y.; Yoshikawa, A. Alkali earth co-doping effects on luminescence and scintillation properties of Ce doped $Gd_3Al_2Ga_3O_{12}$ scintillator. *Opt. Mater.* **2015**, *41*, 63−66.
(54) Průša, P.; Kučera, M.; Babin, V.; Brůža, P.; Pánek, D.; Beitlerová, A.; Mareš, J. A.; Hanuš, M.; Lučeničová, Z.; Nikl, M. Garnet scintillators of superior timing characteristics: material, engineering by liquid phase epitaxy. *Adv. Opt. Mater.* **2017**, *5*, 1600875.
(55) Wu, Y.; Meng, F.; Li, Q.; Koschan, M.; Melcher, C. Role of Ce^{4+} in the scintillation mechanism of co-doped $Gd_3Ga_3Al_2O_{12}$:Ce. *Phys. Rev. Appl.* **2014**, *2*, 044009.
(56) Yoshino, M.; Kamada, K.; Shoji, Y.; Yamaji, A.; Kurosawa, S.; Yokota, Y.; Ohashi, Y.; Yoshikawa, A.; Chani, V. I. Effect of Mg co-doping on scintillation properties of Ce: $Gd_3(Ga,Al)_5O_{12}$ single crystals with various Ga/Al ratios. *J. Cryst. Growth* **2017**, *468*, 420−423.
(57) Yamaguchi, H.; Kamada, K.; Pejchal, J.; Kurosawa, S.; Shoji, Y.; Yokota, Y.; Ohashi, Y.; Yoshikawa, A. Effects of Mg-codoping on luminescence and scintillation properties of Ce doped $Lu_3(Ga,Al)_5O_{12}$ single crystals. *Opt. Mater.* **2017**, *65*, 60−65.
(58) Kamada, K.; Yamaji, A.; Kurosawa, S.; Yokota, Y.; Ohashi, Y.; Yoshikawa, A. Mg co-doping effects on Ce doped $Y_3(Ga,Al)_5O_{12}$ scintillator. *IOP Conf. Ser.: Mater. Sci. Eng.* **2017**, *169*, 012013.
(59) Gundacker, S.; Acerbi, F.; Auffray, E.; Ferri, A.; Gola, A.; Nemallapudi, M. V.; Paternoster, G.; Piemonte, C.; Lecoq, P. State of the art timing in TOF-PET detectors with LuAG, GAGG and L(Y)SO scintillators of various sizes coupled to FBK-SiPMs. *J. Instrum.* **2016**, *11*, P08008.
(60) Wang, Y.; Baldoni, C.; Brecher, Y.; Rhodes, W.H.; Shirwadkar, U.; Glodo, J.; Shah, I.; Ji, C. Properties of transparent $(Gd,Lu)_3(Al,Ga)_5O_{12}$:Ce ceramic with Mg, Ca and Ce co-dopants. *Proc. SPIE* **2015**, 95940C.
(61) Lucchini, M. T.; Babin, V.; Boháček, P.; Gundacker, S.; Kamada, K.; Nikl, M.; Petrosyan, A.; Yoshikawa, A.; Auffray, E. Effect of Mg2+ ions co-doping on timing performance and radiation tolerance of Cerium doped $Gd_3Al_2Ga_3O_{12}$ crystals. *Nucl. Instrum. Methods Phys. Res., Sect. A* **2016**, *816*, 176−183.
(62) Tamulaitis, G.; Vaitkevičius, A.; Nargelas, S.; Augulis, S.; Gulbinas, V.; Boháček, P.; Nikl, M.; Borisevich, V.; Fedorov, A.; Korjik, M.; Auffray, E. Subpicosecond luminescence rise time in magnesium codoped GAGG: Ce scintillator. *Nucl. Instrum. Methods Phys. Res., Sect. A* **2017**, *870*, 25−29.
(63) Lucchini, M. T.; Buganov, O.; Auffray, E.; Boháček, P.; Korjik, M.; Kozlov, D.; Nargelas, S.; Nikl, M.; Tikhomirov, S.; Tamulaitis, G.; Vaitkevičius, A.; Kamada, K.; Yoshikawa, A. Measurement of non-equilibrium carriers dynamics in Ce-doped YAG, LuAG and GAGG crystals with and without Mg-codoping. *J. Lumin.* **2018**, *194*, 1−7.
(64) Kamada, K.; Shoji, Y.; Kochurikhin, V. V.; Nagura, A.; Okumura, S.; Yamamoto, S.; Yeom, J. Y.; Kurosawa, S.; Pejchal, J.; Yokota, Y.; Ohashi, T.; Nikl, M.; Yoshino, M.; Yoshikawa, A. Single crystal growth of Ce: $Gd_3(Ga,Al)_5O_{12}$ with various Mg concentration and their scintillation properties. *J. Cryst. Growth* **2017**, *468*, 407−410.
(65) Hu, C.; Liu, S.; Fasoli, M.; Vedda, A.; Nikl, M.; Feng, X.; Pan, Y. O^- centers in LuAG: Ce,Mg ceramics. *Phys. Status Solidi RRL* **2015**, *9*, 245−249.
(66) Hu, C.; Liu, S.; Fasoli, M.; Vedda, A.; Nikl, M.; Feng, X.; Pan, Y. ESR and TSL study of hole and electron traps in LuAG: Ce, Mg ceramic scintillator. *Opt. Mater.* **2015**, *45*, 252−257.
(67) Kučera, M.; Hanuš, M.; Onderišinová, Z.; Průša, P.; Beitlerová, A.; Nikl, M. Energy Transfer and Scintillation Properties of Formula Not Shown Doped Formula Not Shown Formula Not Shown Multicomponent Garnets. *IEEE Trans. Nucl. Sci.* **2014**, *61*, 282−289.
(68) Zych, E.; Brecher, C.; Lingertat, H. Depletion of high-energy carriers in YAG optical ceramic materials. *Spectrochim. Acta, Part A* **1998**, *54*, 1771−1777.
(69) Zorenko, Y.; Zorenko, T.; Gorbenko, V. V.; Voznyak, T.; Savchyn, V.; Bilski, P.; Twardak, A. Peculiarities of luminescent and scintillation properties of YAG: Ce phosphor prepared in different crystalline forms. *Opt. Mater.* **2012**, *34*, 1314−1319.
(70) Schauer, P.; Lalinský, O.; Kučera, M.; Lučeničová, Z.; Hanuš, M. Effect of Mg co-doping on cathodoluminescence properties of LuGAGG: Ce single crystalline garnet films. *Opt. Mater.* **2017**, *72*, 359−366.
(71) Cherepy, N. J.; Kuntz, J. D.; Tillotson, T. M.; Speaks, D. T.; Payne, S. A.; Chai, B. H. T.; Porter-Chapman, Y.; Derenzo, S. E. Cerium-doped single crystal and transparent ceramic lutetium aluminum garnet scintillators. *Nucl. Instrum. Methods Phys. Res., Sect. A* **2007**, *579*, 38−41.
(72) Zorenko, Y.; Gorbenko, V.; Konstankevych, I.; Voloshinovskii, A.; Stryganyuk, G.; Mikhailin, V.; Kolobanov, V.; Spassky, D. Single-crystalline films of Ce-doped YAG and LuAG phosphors: advantages over bulk crystals analogues. *J. Lumin.* **2005**, *114*, 85−94.
(73) Průša, P.; Čechák, T.; Mareš, J. A.; Nikl, M.; Beitlerová, A.; Solovieva, N.; Zorenko, Yu.V.; Gorbenko, V.; Touš, J.; Blažek, K. The

DOI: 10.1021/acs.cgd.8b00411
Cryst. Growth Des. 2018, 18, 4998−5007

α-particle excited scintillation response of the liquid phase epitaxy grown LuAG: Ce thin films. *Appl. Phys. Lett.* **2008**, *92*, 041903.
(74) Průša, P.; Kučera, M.; Mareš, J. A.; Nikl, M.; Nitsch, K.; Hanuš, M.; Onderišinová, Z.; Čechák, T. Scintillation properties of Sc-, Pr-, and Ce-doped LuAG epitaxial garnet films. *J. Cryst. Growth* **2011**, *318*, 545−548.
(75) Zorenko, Yu.; Gorbenko, V.; Voloshinovskii, A.; Stryganyuk, G.; Mikhailin, V.; Kolobanov, V.; Spassky, D.; Nikl, M.; Blažek, K. Exciton-related luminescence in LuAG: Ce single crystals and single crystalline films. *Phys. Status Solidi A* **2005**, *202*, 1113−1119.
(76) Douissard, P. A.; Martin, T.; Riva, F.; Zorenko, Y.; Zorenko, T.; Paprocki, K.; Fedorov, A.; Bilski, P.; Twardak, A. Epitaxial Growth of LuAG: Ce and LuAG: Ce,Pr Films and Their Scintillation Properties. *IEEE Trans. Nucl. Sci.* **2016**, *63*, 1726−1732.
(77) Průša, P.; Kučera, M.; Mareš, J. A.; Onderišinová, Z.; Hanuš, M.; Babin, V.; Beitlerová, A.; Nikl, M. Composition tailoring in Ce-doped multicomponent garnet epitaxial film scintillators. *Cryst. Growth Des.* **2015**, *15*, 3715−3723.
(78) Zorenko, Yu.; Gorbenko, V.; Konstankevych, I.; Grinev, B.; Globus, M. Scintillation properties of $Lu_3Al_5O_{12}$:Ce single-crystalline films. *Nucl. Instrum. Methods Phys. Res., Sect. A* **2002**, *486*, 309−314.
(79) Zorenko, Yu.; Voznyak, T.; Vistovsky, V.; Zorenko, T.; Nedilko, S.; Batentschuk, M.; Osvet, A.; Winnacker, A.; Zimmerer, G.; Kolobanov, V.; Spassky, D. Energy transfer to Ce3+ ions in $Tb_3Al_5O_{12}$: Ce single crystalline films. *Radiat. Meas.* **2007**, *42*, 648−651.
(80) Zorenko, Yu.; Zych, E.; Voloshinovskii, A. Intrinsic and Ce^{3+}-related luminescence of YAG and YAG: Ce single crystals, single crystalline films and nanopowders. *Opt. Mater.* **2009**, *31*, 1845−1848.
(81) Babin, V.; Gorbenko, V.; Makhov, A.; Nikl, M.; Zazubovich, S.; Zorenko, Y. The role of Pb^{2+} ions in the luminescence of LuAG: Ce single crystalline films. *Phys. Status Solidi C* **2007**, *4*, 797−800.
(82) Babin, V.; Gorbenko, V.; Makhov, A.; Mareš, J. A.; Nikl, M.; Zazubovich, S.; Zorenko, Yu Luminescence characteristics of Pb^{2+} centres in undoped and Ce^{3+}-doped $Lu_3Al_5O_{12}$ single-crystalline films and $Pb^{2+} \rightarrow Ce^{3+}$ energy transfer processes. *J. Lumin.* **2007**, *127*, 384−390.
(83) Kučera, M.; Nitsch, K.; Kubová, M.; Solovieva, N.; Nikl, M.; Mareš, J. A. Ce-doped YAG and LuAG epitaxial films for scintillation detectors. *IEEE Trans. Nucl. Sci.* **2008**, *55*, 1201−1205.
(84) Kučera, M.; Nitsch, K.; Nikl, M.; Hanuš, M.; Daniš, S. Growth and characterization of YAG and LuAG epitaxial films for scintillation applications. *J. Cryst. Growth* **2010**, *312*, 1538−1545.
(85) Kucera, M.; Nitsch, K.; Nikl, M.; Hanus, M. Defects in Ce-doped LuAG and YAG scintillation layers grown by liquid phase epitaxy. *Radiat. Meas.* **2010**, *45*, 449−452.
(86) Ischebeck, R.; Beutner, B.; Orlandi, G.; Pedrozzi, M.; Schietinger, T.; Schlott, V.; Thominet, V. Profile Monitors for the SwissFEL Injector Test Facility. In *Proceedings of Linear Accelerator Conference LINAC2010*, Tsukuba, Japan, 2010, TUP103; pp 656−658.
(87) Lumpkin, A. H.; Yang, B. X.; Berg, W. J.; White, M.; Lewellen, J. W.; Milton, S. V. Optical techniques for electron-beam characterizations on the APS SASE FEL project. *Nucl. Instrum. Methods Phys. Res., Sect. A* **1999**, *429*, 336−340.
(88) Germer, S.; Pietag, F.; Polak, J.; Arnold, T. Quantitative low-energy ion beam characterization by beam profiling and imaging via scintillation screens. *Rev. Sci. Instrum.* **2016**, *87*, 113301.
(89) Tous, J.; Horodysky, P.; Blazek, K.; Nikl, M.; Mares, J. A. High resolution low energy X-ray microradiography using a CCD camera. *J. Instrum.* **2011**, *6*, C01048.
(90) Li, G.; Luo, S.; Yan, Y.; Gu, N. A method of extending the depth of focus of the high-resolution X-ray imaging system employing optical lens and scintillator: a phantom study,. *Biomedical Engineering Online* **2015**, *14*, 120.
(91) Bok, J.; Lalinsky, O.; Hanus, M.; Onderisinova, Z.; Kelar, J.; Kucera, M. GAGG: Ce single crystalline films: New perspective scintillators for electron detection in SEM. *Ultramicroscopy* **2016**, *163*, 1−5.
(92) Li, S.; Liu, Y.; Liu, C.; Yan, D.; Zhu, H.; Yang, J.; Zhang, M.; Xu, C.; Ma, L.; Wang, X. Design, fabrication and characterization of nanocaged $12CaO{\cdot}7Al_2O_3$:Tb^{3+} photostimulable phosphor for high-quality X-ray imaging. *Mater. Des.* **2017**, *134*, 1−9.
(93) Prusa, P.; Nikl, M.; Mares, J. A.; Kucera, M.; Nitsch, K.; Beitlerova, A. The α-particle excited scintillation response of YAG: Ce thin films grown by liquid phase epitaxy. *Phys. Status Solidi A* **2009**, *206*, 1494−1500.
(94) D'Ambrosio, C.; Leutz, H. Hybrid photon detectors. *Nucl. Instrum. Methods Phys. Res., Sect. A* **2003**, *501*, 463−498.
(95) Chewpraditkul, W.; Bruza, P.; Panek, D.; Pattanaboonmee, N.; Wantong, K.; Chewpraditkul, W.; Babin, V.; Bartosiewicz, K.; Kamada, K.; Yoshikawa, A.; Nikl, M. Optical and scintillation properties of Ce^{3+}-doped $YGd_2Al_{5-x}Ga_xO_{12}$ (x= 2, 3, 4) single crystal scintillators. *J. Lumin.* **2016**, *169*, 43−50.
(96) Burešová, H.; Procházková, L.; Turtos, R. M.; Jarý, V.; Mihóková, E.; Beitlerová, A.; Pjatkan, R.; Gundacker, S.; Auffray, E.; Lecoq, P.; Nikl, M.; Čuba, V. Preparation and luminescence properties of ZnO: Ga − polystyrene composite scintillator. *Opt. Express* **2016**, *24*, 15289.
(97) Berger, M. J.; Hubbell, J. H.; Seltzer, S. M.; Chang, J.; Coursey, J. S.; Sukumar, R.; Zucker, D. S.; Olsen, K. *XCOM: Photon Cross Section Database*, 1998; NIST, NBSIR 87-3597
(98) Barandiarán, Z.; Meijerink, A.; Seijo, L. Configuration coordinate energy level diagrams of intervalence and metal-to-metal charge transfer states of dopant pairs in solids. *Phys. Chem. Chem. Phys.* **2015**, *17*, 19874−19884.

DOI: 10.1021/acs.cgd.8b00411
Cryst. Growth Des. 2018, 18, 4998−5007

Garnet Scintillators of Superior Timing Characteristics: Material, Engineering by Liquid Phase Epitaxy

Petr Průša, Miroslav Kučera, Vladimir Babin, Petr Brůža, Dalibor Pánek, Alena Beitlerová, Jiri A. Mareš, Martin Hanuš, Zuzana Lučeničová, and Martin Nikl*

Using liquid phase epitaxy, the Mg co-doped multicomponent garnet film scintillators of composition $(Ce_{0.01}Lu_{0.27}Gd_{0.74})_{3-x}Mg_x(Ga_{2.48}Al_{2.46})O_{12}$, $x = 0$–0.002 (0–700 at. ppm) are prepared. Following luminescence and scintillation characteristics and their dependence on Mg concentration are studied: photoluminescence emission and excitation spectra, radioluminescence spectra, photoluminescence and scintillation decay curves, light yield, energy resolution, and afterglow. At lower Mg concentration, the timing characteristics are slightly improved, while light yield and energy resolution are not negatively influenced. At higher Mg concentration, scintillation decay is significantly accelerated, although light yield is somewhat reduced. Afterglow values become extraordinarily low for a garnet scintillator, at least two times better than the best values published so far, which paves the way for their application in fast frame imaging applications. A mechanism of the improvement is shortly discussed.

1. Introduction

Single crystal garnets, i.e., materials of general $RE_3X_5O_{12}$ composition crystallizing in the cubic system, are used for many purposes, e.g., as gemstones, solid state lasers,[1] ferrimagnetic materials, thermometers,[2] in lighting,[3] and as scintillators. For scintillators, RE = Gd, Lu, and Y, and X = Al and Ga. First bulk single crystal garnet scintillator, namely YAG:Ce ($Y_3Al_5O_{12}$:Ce), was introduced in 1967,[4] and further investigated in 1970s.[5] YAG:Ce exhibits good light yield (≈21 photons keV^{-1}), decent energy resolution (5%–6%),[6–8] fast scintillation decay dominated by 60–80 ns decay time,[6–9] high thermal and chemical stability, high thermal conductivity,[10] and good mechanical properties.[11]

However, YAG:Ce detection efficiency for high-energy photons is low due to low effective atomic (proton) number $Z_{eff} = 31.9$ and density $\rho = 4.56$ g cm^{-3}. Isostructural, novel heavy garnet scintillator, LuAG:Ce ($Lu_3Al_5O_{12}$:Ce) shows $Z_{eff} = 62.9$ and density $\rho = 6.67$ g cm^{-3}.[12–14] Therefore, it has much better detection efficiency. Unfortunately, it exhibits noticeably higher intensity of slow scintillation decay components compared to YAG:Ce.[15–18] The Lu_{Al} antisite defects and related electron traps have been identified as the main reason of deteriorated timing performance.[16,19–22] Another LuAG:Ce drawback is an inevitable presence of a radioactive contaminant, ^{176}Lu isotope. Natural abundance of ^{176}Lu is ≈2.6% and half-life is 3.78×10^{10} years. This isotope emits photons of energy 88 keV (13.3%), 202 keV (86%), 307 keV (94%), and 401 keV (0.33%) and the β spectrum with a maximum energy of 596 keV. The half-life and natural abundance allow us to calculate the mass activity 32 Bq g^{-1} (of LuAG).

Most recent members of the garnet scintillators family are $(Lu,Y,Gd)_3(Ga,Al)_5O_{12}$:Ce multicomponent garnets.[23–31] Negative influence of electron traps is diminished in them by adopting the so-called "band-gap engineering strategy," which allows the downward shift of conduction band bottom and Ce^{3+} $5d_1$ excited state by optimizing the matrix composition. Consequently, influence of electron traps and Ce^{3+} excited state ionization were minimized.[28,32]

An effort to find optimal Lu/Y/ Gd and Ga/Al concentration ratios was undertaken.[29,31] The "band-gap engineering" approach led to an unparalleled improvement. The very slow component of scintillation response of $Gd_3Al_xGa_{5-x}O_{12}$:Ce (GGAG:Ce) ($x \approx 2$–3) was significantly reduced, while light yield of bulk crystals reached 58 ph keV^{-1} and energy resolution 4.2%@662 keV values.[33] Ceramic GGAG:Ce exhibits even higher light yield, 70 ph keV^{-1}.[34] An energy resolution of 3.7%@662 keV was reached using an avalanche photodiode as a photodetector.[26] Improvement in light yield and energy resolution was also reported in similar systems, e.g., GYGAG:Ce ceramics (light yield: 50 ph keV^{-1}, energy resolution: 4.8%@662 keV).[35] Moreover, there is negligible amount of radioactive contaminants in GGAG:Ce, since Lu is not used.

Dr. P. Průša, Dr. V. Babin, A. Beitlerová,
Dr. J. A. Mareš, Prof. M. Nikl
Institute of Physics AS CR
Cukrovarnicka 10, 16253 Prague, Czech Republic
E-mail: petr.prusa@fzu.cz
Dr. P. Průša
Department of Dosimetry and Application of Ionizing Radiation
Faculty of Nuclear Sciences and Physical Engineering
Czech Technical University in Prague
Brehova 7, 11519 Prague 1, Czech Republic
M. Kučera, M. Hanuš, Dr. Z. Lučeničová
Division of Magentooptics
Faculty of Mathematics and Physics
Charles University
Ke Karlovu 5, 12116 Prague 2, Czech Republic
Dr. P. Brůža, Dr. D. Pánek
Department of Natural Sciences
Faculty of Biomedical Engineering
Czech Technical University in Prague
Nám. Sítná 3105, 27201 Kladno, Czech Republic

DOI: 10.1002/adom.201600875

Table 1. Comparison of Mg co-doped Ce-doped garnet scintillators by various authors.

Matrix[a)]	Mg conc. [at. ppm]	LY [ph keV^{-1}]	τ_1 [ns]/RI$_1$ [%][b)]	τ_2 [ns]/RI$_2$ [%][b)]
LuAG[c)]	0	13.9	NA[d)]	NA
LuAG$_C$[c)]	1000	21.9	NA	NA
LuAG$_{CZ}$[e)]	0	17.2	58/42	958/58
LuAG$_\mu$[e)]	0	4.9	58/48	300/52
LuAG$_\mu$[e)]	100	23.1	48/58	380/42
LuAG$_\mu$[e)]	500	18.8	48/57	275/43
LuAG$_\mu$[e)]	3000	14.1	15/11	51/89
GGAG$_\mu$[f)]	0	100%[g)]	62/52	225/48
GGAG$_\mu$[f)]	100	94%[g)]	40/53	132/47
GGAG$_\mu$[f)]	200	86%[g)]	40/50	140/50
GGAG$_\mu$[f)]	500	87%[g)]	40/49	144/51
GGAG$_\mu$[f)]	1000	76%[g)]	40/55	131/45
YAG$_\mu$[h)]	0	16.2	99/77	464/23
YAG$_\mu$[h)]	100	21.0	91/82	292/18
YAG$_\mu$[h)]	200	19.5	90/90	544/10
YAG$_\mu$[h)]	500	16.8	84/82	257/18
YAG$_\mu$[h)]	3000	11.9	24/10	64/88

[a)]CZ: Czochralski grown, μ: Micro-pulling down, and C: Ceramics; [b)]Scintillation decay time and relative intensity of ith component; [c)]Ref. [40]; [d)]Not available; [e)]Ref. [39]; [f)]Ref. [44]; [g)]Relative LY; [h)]Ref. [43].

The so-called defect engineering strategy may be seen as an additional optimization tool to band-gap engineering and a tool of further optimization. Various co-dopants have been adopted for different purposes in garnets.[36] Divalent Mg^{2+} and Ca^{2+} have already been adopted for the purpose of improving scintillation properties in various garnets; in GGAG:Ce, boron was used as well.[37,38] Improvement of light yield was reported for LuAG:Ce[39–42] and YAG:Ce.[43] However, light yield of Mg^{2+} and Ca^{2+} co-doped GGAG:Ce decreases in comparison with Mg/Ca-free counterparts.[44–46] Nonetheless, improvement of timing characteristics was reported for all the material systems.[39–47] Previous results achieved by Mg co-doping of the Ce-doped garnet scintillators are presented in **Table 1**.[39,40,43,44] Please note that concentration given at at. ppm denotes relative content of Mg in dodecahedral site in the whole paper.

Widely accepted explanation of the above-mentioned improvements states that Mg^{2+} ions stabilize Ce^{4+} ions in the material. The stable Ce^{3+} center at first captures a hole (turns temporarily to Ce^{4+}), then it is excited by a captured electron originating from the conduction band, and photon emission is the final step. The stable Ce^{4+} turns to excited Ce^{3+} by electron capture at first, then a photon is emitted, finally, the original state is restored by a hole capture. Therefore, the stable Ce^{4+} centers compete more efficiently with electron traps for migrating electrons in conduction band than Ce^{3+} centers can do.[39,40,42,47] Interestingly, in 1990s, the Ce^{4+} center was considered undesired in scintillators by scientific community.[48,49] In case of perovskites, the reason is an inevitable overlap of Ce^{3+} emission and Ce^{4+} charge transfer (CT) absorption.[49,50] The "Ce^{3+}-like" cathodoluminescence of the stable Ce^{4+} center has been reported in the Ca co-doped YAG:Ce already in 1992,[51] but the information remained unnoticed. Absorption caused by the Ce^{4+} presence,[52,53] faster decay time,[52] and decrease of thermoluminescence signal was observed in Mg^{2+} co-doped YAG:Ce samples later as well.[53] However, the reported changes were not ascribed to the presence of Ce^{4+} ions. The consensus changed after the reported improvement of LSO:Ce (Lu_2SiO_5), LYSO:Ce ($(Lu,Y)_2SiO_5$) single crystal scintillators by Ca^{2+} and Mg^{2+} co-doping, especially their afterglow decrease.[54–57] The above-mentioned role of stable Ce^{4+} center in scintillation mechanism of orthosilicates was proposed.[56]

In orthosilicates, Ca^{2+} co-doping produces favorable results.[54,56,58] In garnets, however, improvements in the scintillation properties achieved by Mg^{2+} co-doping are much better than the results obtained by Ca^{2+} co-doping.[39–41] Explanation of the difference is still a matter of discussion. As mentioned above, timing characteristics are improved by Mg^{2+} co-doping in garnets generally, while light yield increases in LuAG:Ce and YAG:Ce, but decreases in GGAG:Ce.[44,45]

The consensus about the mechanism of light yield decrease in Mg co-doped GGAG:Ce has not been reached yet in the scientific community, but there are some tentative explanations. Mg^{2+} as well as Ca^{2+} co-doping does not necessarily stabilize only Ce^{4+} ions; the charge equilibrium is also reached by other means, e.g., O^- center stabilization or oxygen vacancy formation. In fact, the presence of O^- centers in Mg^{2+} co-doped garnets has already been proven. O^- centers might serve as non-radiative recombination centers.[59–61] Furthermore, there exists an overlap between Gd^{3+} 4f–4f (^6P_J–$^8S_{7/2}$) transition in GGAG and CT absorption toward the Ce^{4+} center. Such an overlap may create an energy loss pathway in scintillation mechanism of GGAG-based materials taking into account that some energy is collected in the Gd-sublattice[62] in scintillation mechanism of GGAG:Ce and that the CT absorption of Ce^{4+} does not have any luminescence output.

The liquid phase epitaxy (LPE) method has extensively been used for preparation of single crystalline garnet films and offers several advantages over single crystal growth from high-temperature melt.[63–66] Much lower growth temperature, around 1000 °C, leads to lower production costs. Also, antisite defects do not practically form in LPE-grown film due to low growth temperature.[67,68] Absence of shallow electron traps formed by the antisite defect has been proven, e.g., by thermoluminescence.[19] As only films of thickness up to a few tens of micrometers can be prepared by LPE usually, they can be used only in applications exploiting soft X-rays, lower energy electron beams, and/or heavy charged particles.[69–71] However, even small increase in thickness could allow efficient detection allowing application in radiography using photons of higher energy.[72]

Recently, liquid phase epitaxy technology has been adopted for production of multicomponent $(Lu,Y,Gd)_3(Al,Ga)_5O_{12}$:Ce films.[62,73–76] Successful result, light yield of 8700 ph MeV^{-1} under α-particle excitation, i.e., 93% of reference bulk crystal light yield (reference crystal light yield: 53 800 ph MeV^{-1} under γ-ray excitation) and suppressed slow scintillation component, was made possible only by the application of a novel

Table 2. Sample parameters: Mg concentration (stoichiometric/in at. ppm), film thickness, light yield (LY) measured under α-particle excitation, and 1 µs shaping time, FWHM (same conditions), parameter $A_{10/0.5}$—relative change of the LY between 0.5 and 10 µs shaping times.

Sample[a)]	Mg conc. x [10^{-5}] / [at. ppm][a)]	Thickness [µm]	LY [ph MeV^{-1}]	FWHM [%]	$A_{10/0.5}$ [%]
1LGM2	0/0	15.0	6780	9.3	104.1
1LGM3	2/7	16.3	7390	9.3	105.0
1LGM4	4/15	17.7	7140	8.2	104.7
1LGM5	10/30	17.2	6770	7.8	104.7
1LGM6	30/100	17.7	6680	9.2	104.9
1LGM7	80/300	16.8	5390	10.7	103.4
1LGM8	200/700	16.7	2940	11.5	101.3

[a)]Mg concentration, x is the stoichiometric coefficient in $Mg_x(Ce_{0.01}Lu_{0.27}Gd_{0.74})_{3-x}(Ga_{2.48}Al_{2.46})O_{12}$. Concentration given at at. ppm denotes relative content of Mg in dodecahedral site.

$BaO–B_2O_3–BaF_2$ flux (BaO flux).[74] Bright luminescence response was already successfully exploited in scanning electron microscopy.[77]

More commonly used $PbO–B_2O_3$ is a source of film contamination by Pb^{2+} ions that act as luminescence quenching centers.[65,75,76,78–81] The band-gap engineering strategy thus appeared useful also for the LPE-grown garnet films despite the origin of different traps in comparison with bulk crystals. Tentatively, these traps may originate from unspecified macrostructural defects due to high viscosity of BaO flux.[82]

In principle, Mg^{2+} co-doping should be useful against negative influence of any electronic traps, regardless of their origin. Improvement of light yield and energy resolution is not very probable in GGAG-based scintillators, but rather timing characteristics should be improved.[44,45] Namely, lower afterglow, faster decay, and shorter rise time are expected.

GGAG:Ce was recently studied as a potential scintillator for fast timing application.[83,84] The rise time of several nanoseconds was considered to be the main drawback of GGAG:Ce for fast timing measurement. The 8 ns rise time was measured under 254 nm excitation,[83] while 2 ns was under γ-ray excitation.[84] Mg co-doping in GGAG:Ce reduced the rise time down to 50 ps, and timing coincidence resolution values become close to those reported in commercial LYSO:Ce,Ca scintillators used in TOF-PET (time-of-flight positron emission tomography).

High fps (frames per second) rate imaging techniques could also benefit from high light yield and fast decay of a scintillator. However, absolute necessity for them is as low as possible afterglow. Minimal afterglow prevents mixing of signals of consecutive frames. Such detectors could find applications in industry, in science, or in military fields.[85,86]

Finally, low afterglow, fast scintillation decay, and high light yield are advantageous in applications based on pulse counting and analysis, e.g., high counts per second (cps) γ-ray spectrometry. High light yield improves signal/noise ratio, as well as low afterglow does. Short decay time decreases the probability of pulse pileup. Rise time is usually not considered.

The LPE method has never been used before for production of the Mg co-doped multicomponent films.

In this paper, we present the correlated study of scintillator characteristics of a set of the Mg co-doped $(Lu,Gd)_3(Al,Ga)_5O_{12}$:Ce epitaxial films with various Mg contents (see **Table 2**). The chosen host composition and content of Gd and Ga ions are similar to Mg-free samples with best scintillator properties reported in the authors' previous study.[74] In this work, we focused on the impact of co-doping with divalent Mg^{2+} ions on scintillation properties of multicomponent garnet films.

2. Results and Discussion

All samples exhibit two absorption maxima centered around 440 and 345 nm corresponding to the well-known 4f–$5d_{1,2}$ Ce^{3+} transitions; see **Figure 1**. Positions of the absorption maxima are the same for all the samples and their amplitudes change only slightly. In the UV spectrum region (≈225–325 nm), there is a significant increase of absorbance with the increase in Mg^{2+} ion concentration. This broad absorption band originates from the electron transfer (CT) from oxygen ligands toward Ce^{4+} ions, which arises due to the necessity of charge compensation of aliovalent Mg^{2+} ions embedded in trivalent sites. The weak sharp lines observed around 275 and 310 nm correspond to spin and parity forbidden 4f–4f transitions, $^8S \rightarrow {}^6I_J$ and $^8S \rightarrow {}^6P_J$, respectively, in the Gd^{3+} ions.[87]

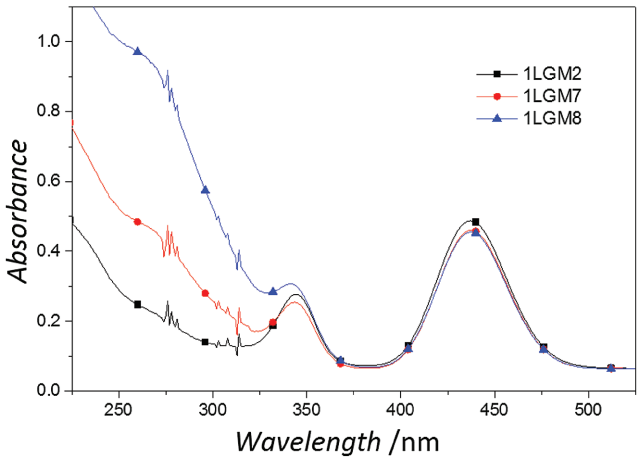

Figure 1. Wavelength dependence of the absorption coefficient: samples 1LGM2 (Mg-free), 1LGM7 (Mg = 300 at. ppm), and 1LGM8 (Mg = 700 at. ppm).

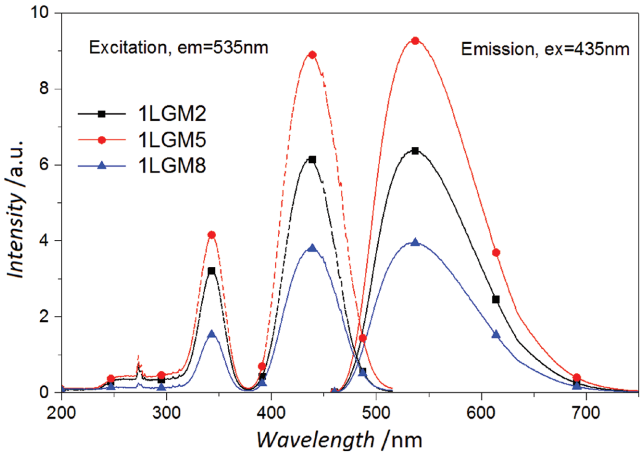

Figure 2. Emission and excitation spectra of selected Mg co-doped LGGAG:Ce epitaxial films: samples 1LGM2 (Mg-free), 1LGM5 (Mg = 30 at. ppm), and 1LGM8 (Mg = 700 at. ppm).

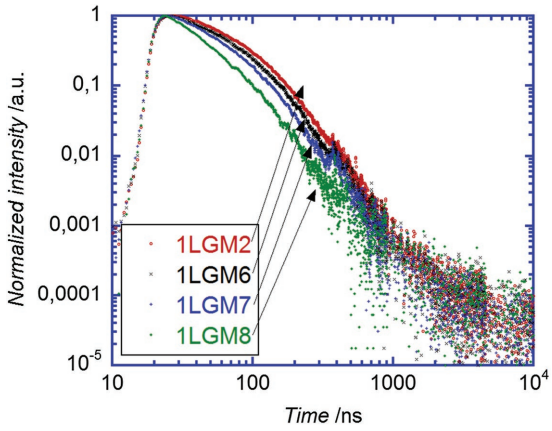

Figure 3. X-ray excited scintillation decay of selected samples with Mg = 0, 100, 300, and 700 at. ppm (decays of remaining samples are between 1LGM2 and 1LGM6).

It must be noted that only a small part of Ce atoms is stabilized in 4+ charge state by Mg^{2+}, despite the significant amplitude of CT Ce^{4+} absorption. Otherwise, significant decrease of Ce^{3+} absorption band intensity would be observable. Such a result is expectable, since even sample 1LGM8 with highest Mg^{2+} concentration exhibits a Ce/Mg stoichiometric ratio equal to 15. Previously, a significant decrease in Ce^{3+} absorption was reported in Mg^{2+} highly concentrated garnets.[39,44] We also note that independent evidence of the presence of both the stable Ce^{3+} and Ce^{4+} centers can be obtained by X-ray absorption near edge spectroscopy, and their concentration ratio can be established with modest precision.[56] This experiment, however, was not available for the present study.

In emission spectra excited at 435 nm, see **Figure 2**, typical doublet of Ce^{3+} luminescent center originating in $5d_1$–4f transition can be seen. No other emissions were observed. Excitation spectra, Figure 2, exhibit the same maxima as the absorption spectra do, i.e., 4f–$5d_{1,2}$ Ce^{3+} transitions around 435 and 345 nm. 4f–4f transitions in the Gd^{3+} ions are present due to the overlap of Gd^{3+} 312 nm emission and Ce^{3+} 4f–$5d_2$ absorption, and indicate energy transfer from Gd^{3+} to Ce^{3+}.[62,87] Any transitions to higher 5d excited states of Ce^{3+} are not observed in the excitation spectra.

Photoluminescence (PL) decays of Ce^{3+} (emission: 540 nm; excitation: 455 nm) were deconvoluted into two exponential terms. Faster exponential term decay time varies in the interval 22–31 ns; only for sample 1LGM8 with the highest Mg content, the decay decreases to 14 ns. Slower exponential term decay time is in the interval of 57–60 ns for all samples, except for sample 1LGM8 (50.3 ns).

Sample 1LGM8 (Mg = 700 at. ppm) exhibits the fastest excited Ce^{3+} decay and the lowest intensity of Ce^{3+} emission, **Figures** 2 and **3**, even though the Ce^{3+} absorption bands in 1LGM8 are of similar intensity in comparison with the other samples. It indicates a nonradiative energy transfer from the Ce^{3+} excited $5d_1$ state away. Since no absorption is observed at the wavelength of Ce^{3+} emission, such a transition is either forbidden or the electron tunnels from $5d_1$ level into an electron trap stabilized by Mg^{2+} ions (oxygen vacancy, O^- centers, etc.).[40,59,60] We note that amplitudes in photo- and radioluminescence spectra, Figure 2 and Figure S1 in the Supporting Information, can be partly influenced by unequal thicknesses of films (Table 2); however, the decrease of intensities in samples with higher Mg content, ≥300 at. ppm, is plausible and is supported by LY and decay kinetics measurements.

Radioluminescence (RL) spectra are practically the same as the photoluminescence ones in Figure 2, i.e., the Ce^{3+} emission completely dominates. The intensity of all samples is significantly higher (≈4–5×) than that of BGO ($Bi_4Ge_3O_{12}$) reference single crystal, except for sample 1LGM8 which shows only ≈2× higher intensity (see Figure S1 in the Supporting Information). The dependence of RL intensity on Mg^{2+} concentration at lower concentrations does not follow a simple pattern. Decrease of intensity at highest Mg concentration cannot be explained by Ce^{3+} decreasing concentration, since Ce^{4+} contributes to the response as well, unlike in PL spectra. Somewhat similar behavior was reported by many authors in various systems;[39,41,44] we note that the O^- centers and/or the above-mentioned energy transfer, $Gd^{3+} \rightarrow Ce^{4+}$ CT, may be responsible for decrease in RL intensity as well.

We have performed four different types of measurement that reflect the scintillation decay kinetics: the measurement of scintillation decay using the soft X-rays (SXR), pulsed source, or α-particle excitation using an oscilloscope and a fast photomultiplier (PMT) in current regime in the detection part. The latter excitation was also used for the afterglow measurement and $A_{10/0.5}$ parameter determination.

SXR-excited scintillation decay, see Figure 3, and α-particle excited scintillation decay, see Figure S2 in the Supporting Information, show similar results, i.e., significantly accelerated decay with increasing Mg^{2+} concentration.

Scintillation decay of the same sample is clearly faster under X-ray excitation than under α-particle one; see Figure S3 in the Supporting Information. At higher ionization density, i.e., under α-particle excitation, the density of charge carriers is probably too high for immediate recombination at Ce luminescent centers. Therefore, they are more often trapped, which leads to slower scintillation decay. Such an effect has been reported before and is studied for the purpose of pulse-shape particle discrimination.[88,89]

Table 3. Decay times with relative intensities (RI—in brackets) of the components measured under X-ray excitation, obtained by deconvolution in order, from shortest (T_1) to longest (T_4).

Sample	T_1 [ns] (RI_1 [%])	T_2 [ns] (RI_2 [%])	T_3 [ns] (RI_3 [%])	T_4 [ns] (RI_4 [%])
1LGM2	10.4 (3.5)	55.0 (72.7)	166 (22.2)	1360 (1.6)
1LGM3	12.5 (3.6)	64.6 (73.3)	221 (20.3)	971 (2.9)
1LGM4	8.9 (2.8)	53.9 (72.1)	168 (23.5)	1237 (1.7)
1LGM5	11.3 (3.4)	61.6 (70.4)	187 (22.7)	747 (3.5)
1LGM6	6.2 (4.4)	47.3 (71.0)	148 (22.9)	979 (1.6)
1LGM7	7.8 (8.5)	42.8 (70.9)	146 (18.9)	740 (1.7)
1LGM8	1.9 (6.2)	13.4 (26.7)	45.4 (59.4)	216 (7.8)

Table 3 shows the decay times obtained by deconvolution of scintillation decays measured under X-ray excitation and Table S1 (Supporting Information) the same under α-particle excitation. Decays were approximated by four exponential terms under SXR excitation and two to four terms under α-particle excitation

$$I = \sum_{i=1}^{n} A_i \times \exp(-t/\tau_i) \quad (1)$$

where A_i is the relative intensity of the exponential component with decay time τ_i, and n is number of components. In both cases, the dominant decay exponential component is getting shorter with increasing Mg^{2+} concentration. The behavior is most apparent for higher Mg^{2+} concentration.

Comparison with Mg^{2+} co-doped single crystals from ref. [44] could be made for X-ray scintillation decay measurement, especially not only for sample 1LGM6 (the same concentration of Mg as in ref. [44]) but also for other samples. The dominant component of decay is slightly slower in films than in crystals (47 and 40 ns, respectively, for 100 at. ppm). On the other hand, it is also significantly more intense (71% and 53%, respectively). The second most intense component decay time is very similar as well (148 and 132 ns, respectively); see Tables 1, 2, 3 for more thorough comparison. It must be noted that in this paper, the quadruple exponential term was used for decay curve fit, while in ref. [44] it is the double exponential one. Such a difference in the approximation function may cause small variations in the obtained decay times.

The relative intensity of fast (≈40 ns) and slow (≈140 ns) components is ≈50:50 in micro-pulling-down grown crystals,[39,41,44] while 70:30 in our films and Czochralski grown crystals.[45] Most probably, such a difference arises due to higher concentrations of traps responsible for the longer component in micro-pulling-down crystals. Small variations in matrix composition (different amount of Lu) and different linear energy transfer of particles used for excitation may be responsible as well. At much higher concentration of Ca/Mg co-dopants, the relative intensity of fast components increases in GGAG:Ce[44] and/or LuAG:Ce[39] micro-pulling-down grown crystals. High concentration of the co-dopant, however, has severe negative impact on the LY.[39,44]

The parameter $A_{10/0.5}$ = PhY (0.5 µs)/PhY(10 µs) of Mg^{2+} concentration dependence is consistent with both scintillation decay measurements; see Table 2. It stays in the interval 104.1%–105% for samples 1LGM2–6 with lower Mg content,

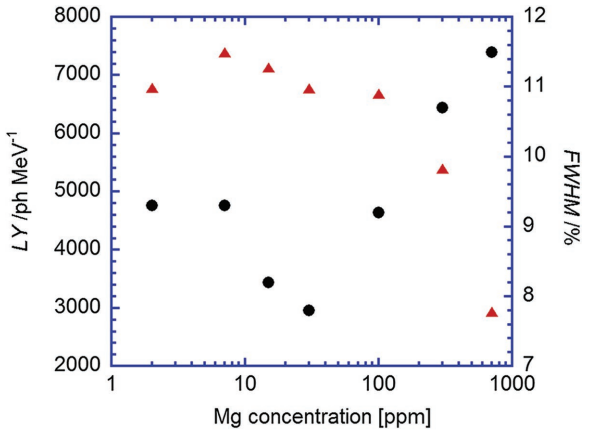

Figure 4. FWHM (circles) and LY estimate (triangles) dependence on Mg^{2+} concentration. Please note that sample 1LGM2 Mg^{2+} concentration is 0 at. ppm, which is set to 2 at. ppm in the graph, because of the logarithmic scale.

decreases to 103.4% for sample 1LGM7 (Mg = 300 at. ppm), and is lowest for sample 1LGM8 (Mg = 700 at. ppm), i.e., 101.3%. It must be noted that this type of measurement is sensitive only to slower scintillation response components within several hundreds of nanoseconds up to (very) few tens of microseconds.

Regarding LY, see **Figure 4**, for samples 1LGM2–6, its value is in the interval 6770–7390 ph MeV^{-1}. Relatively sharp decrease follows at higher concentration; 1LGM7 (Mg = 300 at. ppm) exhibits 5390 ph MeV^{-1} and 1LGM8 (Mg = 700 at. ppm) exhibits 2940 ph MeV^{-1}. It is relatively consistent with the previous findings,[44,84,87] though low Mg concentration was not studied thoroughly in the past.

Let E_g be the band gap, β the phenomenological parameter, S the energy transport efficiency, Q the luminescence center efficiency, and η_{sc} the integral scintillation efficiency

$$\eta_{sc} = \frac{SQ}{E_g \beta} \quad (2)$$

In case of negligible slow scintillation component intensity, i.e., exactly as our case, η_{sc} = LY. We assume $\beta \times E_g$ to be almost the same for all studied samples, since host composition does not change. Let relative light yield of sample 1LGMX be defined as

$$\mathrm{RLY}_X = \frac{\mathrm{LY}_X}{\mathrm{LY}_2} = \frac{S_X Q_X}{S_2 Q_2} \quad (3)$$

where LY_X is the light yield, S_X is the energy transport efficiency, and Q_X is the luminescence center efficiency, all for sample 1LGMX, and LY_2, S_2, and Q_2 are the same for sample 1LGM2. According to experimental data, RLY_X decreases at highest Mg concentrations. Is it because of lower S, Q, or both?

Parameter Q is reflected in photoluminescence decay curves. Let $I_{X,p}$ be defined as an area below normalized photoluminescence decay curve (excitation: 455 nm; emission: 540 nm) for sample 1LGMX

$$I_{X,p} = \int_0^\infty I_n(t)\,dt \quad (4)$$

where $I_n(t)$ is defined as the same as in Equation (1), but for photoluminescence decay. Also, $I_n(0) = 1$, i.e., the decay curve is normalized. Let us define $RI_{X,p} = I_{X,p}/I_{2,p}$—faster decay of the 1LGMX sample will cause $RI_{X,p}$ decrease. If the decrease of the decay time is caused only by energy transfer from Ce^{3+} center, $RI_{X,p} = Q_X/Q_2$. Otherwise, and more generally

$$RI_{X,p} \le \frac{Q_X}{Q_2} \quad (5)$$

By combining Equations (3) and (5), we obtain

$$RLY_X \frac{S_2}{S_X} = \frac{Q}{Q_2} \ge RI_{X,p} \quad (6)$$

$$RLY_X \ge RI_{X,p} \frac{S_X}{S_2} \quad (7)$$

Since $RLY_X < RI_{X,p}$, according to experimental data for 1LGM7 and 1LGM8 samples, see **Figure 5**, $S_X/S_2 < 1$. It means that energy transport efficiency S is by all means lower for 1LGM7 and 1LGM8 samples than for others.

The reason must be the existence of some competing non-radiative recombination centers, traps, or the afore-mentioned energy transfer from Gd^{3+} toward CT transition of Ce^{4+}.

Energy resolution decreases with increasing Mg concentration at first, reaches a best value of 7.8% for sample 1LGM5, and then increases with increasing Mg concentration; see Figure 4. Interestingly, full width at half maximum (FWHM) is getting better with slightly decreasing LY at lower Mg^{2+} concentration, which points to possible decrease of scintillator nonproportionality. Unfortunately, nonproportionality measurement of few micrometer thick samples cannot be realized by available setup. Tentatively, the alternative explanation may be related to homogeneity of light collection efficiency or light yield homogeneity.

Afterglow measurement results are consistent with $A_{10/0.5}$ parameter measurement; see **Figure 6**. For samples 1LGM2–4 (Mg < 30 at. ppm), no trend is observable; afterglow values

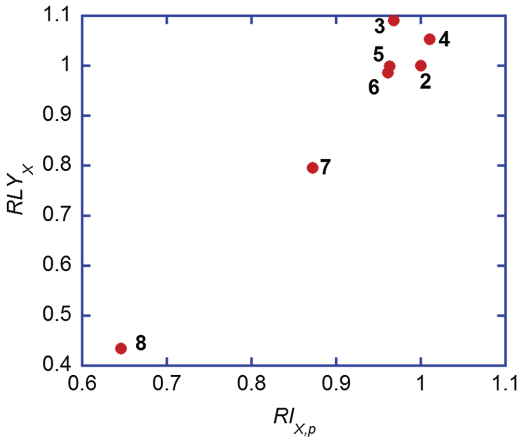

Figure 5. Relative light yield (RLY_X) dependence on relative photoluminescence decay integral ($RI_{X,p}$). Values normalized to Mg-free sample 1LGM2. Number X in the figure denotes sample 1LGMX.

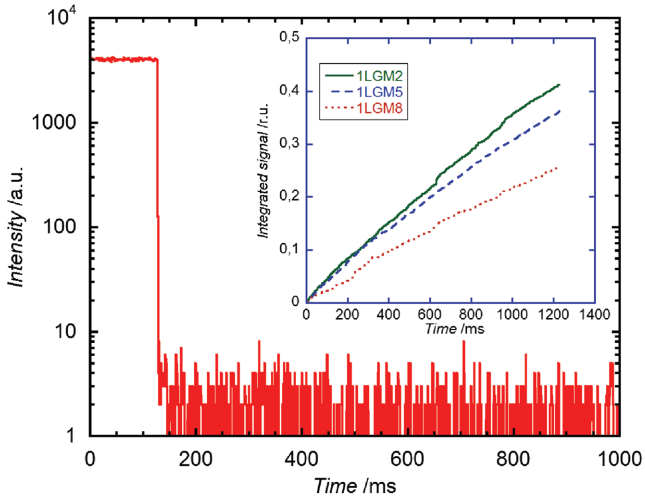

Figure 6. Time dependence of signal intensity of sample 1LGM5, Mg = 30 at. ppm. The sample is irradiated by X-ray for a few seconds until constant radioluminescence intensity is reached (flat top in the left). Drop corresponds to the end of irradiation. Inset: Dependence of signal integrated in time t from 3 to X ms, where t = 0 ms corresponds to irradiation cutoff. Integrated signal is divided by average signal during irradiation.

measured at 3 ms after excitation cutoff are in the interval of 0.073%–0.088%. Higher Mg^{2+} concentration leads to afterglow decrease—1LGM5 (Mg = 30 at. ppm): 0.065%; 1LGM6 (Mg = 100 at. ppm): 0.058%, 1LGM7 (Mg = 300 at. ppm) 0.048%, and 1LGM8 (Mg = 700 at. ppm): 0.045%. The decrease of afterglow with Mg concentration is also demonstrated in the inset of Figure 6. According to our calculation based on X-ray tube spectra and attenuation coefficient obtained from NIST X-COM,[90] roughly 5%–10% of energy from the 10 keV X-ray tube spectrum is absorbed in the GGAG substrate. Fortunately, the film thicknesses are very similar, and substrate radioluminescence is very weak. Therefore, the trend of these results seems to be unaffected by the signal from the substrate.

Afterglow reduction by a factor of 2 seems to be only a small success in comparison with Mg co-doped single crystals at first sight. The reduction of afterglow by a factor of 25 in GGAG:Ce was reported by Mg co-doping,[84] and by 1–2 orders of magnitude in Mg-codoped LuAG:Ce.[43] The explanation of the difference is extremely simple; afterglow of films is very small even in the Mg-free samples.[74] In fact, afterglow of the Mg-free 1LGM2 sample is smaller than afterglow of any (Mg co-doped or Mg-free) bulk single crystals reported so far.[39,84] The afterglow values of LuGGAG:CeMg set of film samples reported in this study are the lowest ever observed in the fast Ce or Pr-doped garnet scintillators.

As mentioned in the "Introduction" section, the high fps rate imaging techniques and high cps γ-ray spectrometry can benefit such advanced thin film scintillators reported in this paper. At the same time, film morphology must be of very high quality over a relative large area of such a detector (up to a few inches of diameter) and it is so far compromised by high viscosity of the BaO flux.[91] Further technical work is necessary to improve this aspect.

3. Conclusion

Presented results prove that the Mg^{2+} co-doping can significantly improve the timing characteristics of $(Lu,Gd)_3(Al,Ga)_5O_{12}$:Ce,Mg LPE-grown films. Namely, relative intensity of slow scintillation component decreases; the decay constants are getting shorter; and afterglow is reduced. We assume that faster response is caused by an increase concentration of stable Ce^{4+} centers, which are stabilized by Mg^{2+} co-dopant. At the same time, Mg^{2+} might give rise to an unknown (nonradiative) recombination pathway, which accelerates scintillation decay as well, however, at the cost of light yield reduction.

The Mg-free sample, 1LGM2, shows dominant decay time in scintillation response of 55 ns with 73% intensity; afterglow is 0.074%. Better timing results are obtained with sample 1LGM6 (≈100 at. ppm Mg), dominant scintillation component decay time is 47 ns with 71% intensity; afterglow is 0.058%. Even faster response in terms of decay time and afterglow could be achieved by higher Mg^{2+} concentration, but at the cost of lower light yield, reduced to 79% of Mg-free sample value (≈300 at. ppm, 1LGM7, afterglow: 0.048%) or even to 43% (≈700 at. ppm, 1LGM8, afterglow: 0.045%). At the highest concentrations, the Mg co-dopant apparently introduces undesired negative effects, and new nonradiative recombination centers might arise due to some unknown complex defects. Tentatively, energy transfer from the Gd^{3+} sublattice toward CT absorption band of Ce^{4+} may also play a role in energy loss and light yield reduction.

Timing characteristics are improved also in comparison with our previous study of Mg-free multicomponent garnet films, where the decay times of dominant component were in the 50–70 ns range,[74] while for the fastest samples of this study are well below 50 ns, and the intensity and decay time of slower components are reduced as well. Furthermore, the lowest afterglow value reported for Mg-free LPE-grown garnets was 0.09% and the very same sample exhibited intense slower scintillation decay components in few microsecond time range.[74] All other Mg-free samples exhibited afterglow at least four times higher than the best, here studied Mg co-doped samples.[74] On the other hand, comparing the best samples from both studies, the Mg co-doped one shows the LY value by 15% lower.

In terms of timing characteristics, $(Lu,Gd)_3(Al,Ga)_5O_{12}$:Ce,Mg epitaxial films represent probably the best garnet scintillator samples ever reported. The most striking feature of these films is very low afterglow, at least two times better than reported for any garnet so far. Moreover, it follows from the decays under SXR excitation that the signal level reaches 0.1% after just 1 µs in all the samples which makes them competitive candidates for superhigh fps rate imaging techniques. This result was made possible by combination of band-gap engineering, defect engineering (by Mg co-doping), and liquid phase epitaxy technology, which all reduce the negative influence of electron traps.

4. Experimental Section

The Ce,Mg co-doped epitaxial garnet films $(Lu,Gd)_3(Al,Ga)_5O_{12}$:Ce, Mg with Ce doping of 1 at% and different Mg contents were grown in the Technology laboratory of the Charles University, Prague, by the isothermal dipping liquid phase epitaxy from the $BaO–B_2O_3–BaF_2$ flux onto the Czochralski-grown undoped GGAG garnet substrates of 13 mm diameter, 1 mm thickness, and (100) crystallographic orientation. The garnet forming oxides comprise about 20 mol% of the melt; the details on the LPE technique and the film growth from the BaO flux were reported elsewhere.[65,91] Resulting film thicknesses determined by weighing were in the range from 15 to 17.7 µm; see Table 2. The crystallographic properties and lattice parameters of 1LGM8 film were checked using XRD (X-ray diffraction) on a PANalytical X-ray high-resolution diffractometer and found similar to our previous study.[74]

The Mg^{2+} concentrations are given as stoichiometric coefficient x in formula $(Ce_{0.01}Lu_{0.27}Gd_{0.74})_{3-x}Mg_x(Ga_{2.48}Al_{2.46})O_{12}$, x = 0–0.002 (0–700 at. ppm); see Table 2. Sample composition was determined by electron probe micro-analysis; Mg content was measured by glow discharge mass spectrometry (GDMS). All samples were grown under the same conditions, at a growth temperature of 1030 °C, and from the same melt, but Mg doping. Therefore, the Ce content and also the content of potential accidental impurities coming from the flux, such as Ba and B ions, were the same in all samples. Content of divalent Ba^{2+} ions in samples is <10 at. ppm according to GDMS, and their influence can be neglected. Content of trivalent boron B^{3+} ions in films is 100–200 at. ppm; they have $[He]1s^2$ electronic structure, and their electronic states do not take part in optical or emission processes.

Absorption and photoluminescence spectra were measured using the commercial spectrometers Specord 250 and Horiba JY Fluoromax 3. Radioluminescence spectra and photoluminescence decays were measured at a custom-made spectrofluorometer 5000M, Horiba Jobin Yvon, using an X-ray tube (10 kV, 50 mA) and nanoLED pulse excitation sources, respectively. The X-ray tube is type DX-W 10×1-S 2400 W (tungsten) short anode powered by high-voltage supply ISO-DEBYEFLEX 3003—60 kV (Seifert Gmbh).

Pulse-height spectrometry of pulses induced by α-particles was used for photoelectron yield (PhY), energy resolution (FWHM) and PhY-amplifier shaping time-dependence determination. Pulse-height spectra were recorded by an experimental setup consisting of hybrid photomultiplier (HPMT) model DEP PPO 475B, spectroscopy amplifier ORTEC model 672, and multichannel buffer ORTEC 927TM. Silicon grease was used for the optical coupling of HPMT and samples. Given the film thickness, only the α-particles from ^{239}Pu (5.157 MeV) could be used for the excitation of film scintillation response. A radioactive source was placed in direct contact with epitaxial film to minimize energy losses in air.[92,93]

Due to slow components in scintillation response, the PhY rises with amplifier shaping time. In this article, parameter $A_{10/0.5}$ = PhY (10 µs)/PhY (0.5 µs) was used to quantify its increase, where PhY (t) means photoelectron yield measured using amplifier shaping time t. Higher $A_{10/0.5}$ reflects more intense slower component with decay constants several micrometers long.

A small penetration range of α-particles (≈10 µm) prohibits a reflector application, resulting in poorer and badly defined photon collection efficiency. Due to their small penetration range, all energy is deposited in films and the substrate is not excited. Previously,[74] a method used for rough estimation of photon collection efficiency (CE) was published. In this study, the same value, i.e., CE = 0.735, is used. CE and HPMT photocathode quantum efficiency (QE) enable the recalculation of PhY to LY: PhY = LY × QE × CE.

As for afterglow measurement, substrate response was excited by the X-ray tube (the same as for RL spectral measurement) operated at 40 kV, film response was excited by the same tube operated at 10 kV. Lower voltage was used for films in order to avoid the substrate excitation as much as possible. It was calculated that even at high voltage, 10 kV, a few percent of X-ray photons penetrates into the substrate. Afterglow was determined as a ratio of luminescence intensity during long X-ray excitation and average luminescence intensity in an interval starting 3 ms after the excitation cutoff, and ending 50 ms after the excitation cutoff. The excitation cutoff was executed after the photomultiplier current stabilization.

Scintillation decay under the α-particle (5.5 MeV, ^{241}Am) was measured. Decay curves were measured using a photomultiplier type

Hamamatsu R7207-01 and Tektronix TDS3052C digital Phosphor Oscilloscope. Decay curves were decomposed into 2–4 exponential terms. The convolution of multiexponential function with instrumental response was fitted to experimental data using software SpectraSolve 3.01 PRO (1997 Ames Photonics, Inc.).

The scintillation decay was also measured under the excitation by nanosecond-pulsed SXR photons from the infrared laser-produced plasma in a gaseous argon target.[27,94] The incoherent SXR photon burst had an FWHM of 4.7 ns and photon energy was within 350–450 eV,[94] for which the attenuation length was of a few hundreds of nanometers. In the detection part a quartz collection lens, Thorlabs FB550–40 (550 nm/40 nm FWHM) dielectric bandpass filter, and a Hamamatsu R7056 fast PMT operated in the direct current mode were used to detect scintillation light. The instrumental response function was obtained by measurement of spectrally unresolved scintillation decay of superfast Ga-doped ZnO powder (scintillation response below 1 ns)[95] under the same experimental conditions.

Supporting Information

Supporting Information is available from the Wiley Online Library or from the author.

Acknowledgements

Financial support of Czech Science Foundation No. 16-15569S and RVO 68407700 projects is gratefully acknowledged.

Received: October 21, 2016
Revised: December 21, 2016
Published online:

[1] U. Wittrock, *Adv. Mater.* **1992**, *4*, 295.
[2] A. Benayas, B. del Rosal, A. Pérez-Delgado, K. Santacruz-Gómez, D. Jaque, G. A. Hirata, F. Vetrone, *Adv. Opt. Mater.* **2015**, *3*, 687.
[3] X. Wang, X. Yan, W. Li, K. Sun, *Adv. Mater.* **2012**, *24*, 2742.
[4] G. Blasse, A. Bril, *Appl. Phys. Lett.* **1967**, *11*, 53.
[5] R. Autrata, P. Schauer, J. Kvapil, J. Kvapil, *J. Phys. E: Sci. Instrum.* **1978**, *11*, 707.
[6] M. Moszyński, T. Ludziejewski, D. Wolski, W. Klamra, L. O. Norlin, *Nucl. Instrum. Methods Phys. Res., Sect. A* **1994**, *345*, 461.
[7] T. Yanagida, H. Takahashi, T. Ito, D. Kasama, T. Enoto, M. Sato, S. Hirakuri, M. Kokubun, K. Makishima, T. Yanagitani, H. Yagi, T. Shigeta, T. Ito, *IEEE Trans. Nucl. Sci.* **2005**, *52*, 1836.
[8] J. A. Mares, M. Nikl, A. Beitlerova, P. Horodysky, K. Blazek, K. Bartos, C. D'Ambrosio, *IEEE Trans. Nucl. Sci.* **2012**, *59*, 2120.
[9] T. Ludziejewski, M. Moszyński, M. Kapusta, D. Wolski, W. Klamra, K. Moszyńska, *Nucl. Instrum. Methods Phys. Res., Sect. A* **1997**, *398*, 287.
[10] P. H. Klein, W. J. Croft, *J. Appl. Phys.* **1967**, *38*, 1603.
[11] D. B. Sirdesmukh, L. Sirdesmukh, K. G. Subhadra, K. Kishan Rao, S. Bal Laxman, *Bull. Mater. Sci.* **2001**, *24*, 469.
[12] C. W. E. van Eijk, J. Andriessen, P. Dorenbos, R. Visser, *Nucl. Instrum. Methods Phys. Res., Sect. A* **1994**, *348*, 546.
[13] M. Nikl, A. Yoshikawa, K. Kamada, K. Nejezchleb, C. R. Stanek, J. A. Mares, K. Blazek, *Prog. Cryst. Growth Charact. Mater.* **2013**, *59*, 47.
[14] A. G. Petrosyan, K. L. Ovanesyan, R. V. Sargsyan, G. O. Shirinyan, D. Abler, E. Auffray, P. Lecoq, C. Dujardin, C. Pedrini, *J. Cryst. Growth* **2010**, *312*, 3136.
[15] W. Chewpraditkul, L. Swiderski, M. Moszynski, T. Szczesniak, A. Syntfeld-Kazuch, C. Wanarak, P. Limsuwan, *IEEE Trans. Nucl. Sci.* **2009**, *56*, 3800.
[16] M. Nikl, A. Vedda, M. Fasoli, I. Fontana, V. V. Laguta, E. Mihokova, J. Pejchal, J. Rosa, K. Nejezchleb, *Phys. Rev. B* **2007**, *76*, 195121.
[17] W. Chewpraditkul, L. Swiderski, M. Moszynski, T. Szczesniak, A. Syntfeld-Kazuch, C. Wanarak, P. Limsuwan, *Phys. Status Solidi A* **2009**, *206*, 2599.
[18] C. Dujardin, C. Mancini, D. Amans, G. Ledoux, D. Abler, E. Auffray, P. Lecoq, D. Perrodin, A. Petrosyan, K. L. Ovanesyan, *J. Appl. Phys.* **2010**, *108*, 013510.
[19] M. Nikl, E. Mihokova, J. Pejchal, A. Vedda, Yu. Zorenko, K. Nejezchleb, *Phys. Status Solidi* **2005**, *242*, R119.
[20] C. R. Stanek, K. J. McClellan, M. R. Levy, R. W. Grimes, *Phys. Status Solidi* **2006**, *243*, R75.
[21] H. Przybylińska, A. Wittlin, C.-G. Ma, M. G. Brik, A. Kamińska, P. Sybilski, Yu. Zorenko, M. Nikl, V. Gorbenko, A. Fedorov, M. Kučera, A. Suchocki, *Opt. Mater.* **2014**, *36*, 1515.
[22] C. Hu, S. Liu, Y. Shi, H. Kou, J. Li, Y. Pan, X. Feng, Q. Liu, *Phys. Status Solidi* **2015**, *252*, 1993.
[23] M. Nikl, A. Yoshikawa, *Adv. Opt. Mater.* **2015**, *3*, 463.
[24] C. Wang, Y. Wu, D. Ding, H. Li, X. Chen, J. Shi, G. Ren, *Nucl. Instrum. Methods Phys. Res., Sect. A* **2016**, *820*, 8.
[25] Y. Wu, Z. Luo, H. Jiang, F. Meng, M. Koschan, C. L. Melcher, *Nucl. Instrum. Methods Phys. Res., Sect. A* **2015**, *780*, 45.
[26] P. Sibczynski, J. Iwanowska-Hanke, M. Moszyński, L. Swiderski, M. Szawlowski, M. Grodzicka, T. Szczesniak, K. Kamada, A. Yoshikawa, *Nucl. Instrum. Methods Phys. Res., Sect. A* **2015**, *772*, 112.
[27] A. Yoshikawa, K. Kamada, S. Kurosawa, Y. Shoji, Y. Yokota, V. I. Chani, M. Nikl, *J. Lumin.* **2016**, *169*, 387.
[28] S. Yadav, B. Uberuaga, M. Nikl, C. Jiang, C. R. Stanek, *Phys. Rev. Appl.* **2015**, *4*, 054012.
[29] K. Kamada, T. Endo, K. Tsutsumi, T. Yanagida, Y. Fujimoto, A. Fukabori, A. Yoshikawa, J. Pejchal, M. Nikl, *Cryst. Growth Des.* **2011**, *11*, 4484.
[30] K. Kamada, T. Yanagida, J. Pejchal, M. Nikl, T. Endo, K. Tsutsumi, Y. Fujimoto, A. Fukabori, A. Yoshikawa, *J. Phys. D: Appl. Phys.* **2011**, *44*, 505104.
[31] J. Luo, Y. Wu, G. Zhang, H. Zhang, G. Ren, *Opt. Mater.* **2013**, *36*, 476.
[32] M. Fasoli, A. Vedda, M. Nikl, C. Jiang, B. P. Uberuaga, D. A. Andersson, K. J. McClellan, C. R. Stanek, *Phys. Rev. B* **2011**, *84*, 081102(R).
[33] K. Kamada, S. Kurosawa, P. Prusa, M. Nikl, V. V. Kochurikhin, T. Endo, K. Tsutsumi, H. Sato, Y. Yokota, K. Sugiyama, A. Yoshikawa, *Opt. Mater.* **2014**, *36*, 1942.
[34] T. Yanagida, K. Kamada, Y. Fujimoto, H. Yagi, T. Yanagitani, *Opt. Mater.* **2013**, *35*, 2480.
[35] N. J. Cherepy, S. A. Payne, B. W. Sturm, *IEEE Nucl. Sci. Symp. Med. Imaging Conf. Rec.* **2010**, 1288.
[36] M. Tyagi, F. Meng, M. Koschan, A. K. Singh, C. L. Melcher, S. Gadkari, *IEEE Trans. Nucl. Sci.* **2015**, *62*, 336.
[37] M. Tyagi, F. Meng, M. Koschan, S. B. Donald, H. Rothfuss, C. L. Melcher, *J. Phys. D* **2013**, *46*, 475302.
[38] M. Tyagi, V. V. Desai, A. K. Singh, S. G. Singh, S. Sen, B. K. Nayak, S. C. Gadkari, *Phys. Status Solidi A* **2015**, *212*, 2213.
[39] M. Nikl, K. Kamada, V. Babin, J. Pejchal, K. Pilarova, E. Mihokova, A. Beitlerova, K. Bartosiewicz, S. Kurosawa, A. Yoshikawa, *Cryst. Growth Des.* **2014**, *14*, 4827.
[40] S. Liu, X. Feng, Z. Zhou, M. Nikl, Y. Shi, Y. Pan, *Phys. Status Solidi RRL* **2014**, *8*, 105.
[41] K. Kamada, M. Nikl, S. Kurosawa, A. Beitlerova, A. Nagura, Y. Shoji, J. Pejchal, Y. Ohashi, Y. Yokota, A. Yoshikawa, *Nucl. Instrum. Methods Phys. Res., Sect. A* **2015**, *782*, 9.
[42] S. Liu, J. A. Mares, X. Feng, A. Vedda, M. Fasoli, Y. Shi, H. Kou, A. Beitlerova, L. Wu, C. D'Ambrosio, Y. Pan, M. Nikl, *Adv. Opt. Mater.* **2016**, *4*, 731.

[43] A. Nagura, K. Kamada, M. Nikl, S. Kurosawa, J. Pejchal, Y. Yokota, A. Ohashi, A. Yoshikawa, *Jpn. J. Appl. Phys.* **2015**, *54*, 04DH17.
[44] K. Kamada, M. Nikl, S. Kurosawa, A. Beitlerova, A. Nagura, Y. Shoji, J. Pejchal, Y. Ohashi, Y. Yokota, A. Yoshikawa, *Opt. Mater.* **2015**, *41*, 63.
[45] Y. Wu, F. Meng, Q. Li, M. Koschan, C. Melcher, *Phys. Rev. Appl.* **2014**, *2*, 044009.
[46] F. Meng, M. Koschan, Y. Wu, C. L. Melcher, *Nucl. Instrum. Methods Phys. Res., Sect. A* **2015**, *797*, 138.
[47] M. Nikl, A. Yoshikawa, *Adv. Opt. Mater.* **2015**, *3*, 463.
[48] C. Melcher, S. Friedrich, S. P. Cramer, M. Spurrier, P. Szupryczynski, R. Nutt, *IEEE Trans. Nucl. Sci.* **2005**, *52*, 1809.
[49] V. G. Baryshevsky, M. V. Korzhik, B. I. Minkov, S. A. Smirnova, A. A. Fyodorov, P. Dorenbos, C. W. E. van Eijk, *J. Phys.: Condens. Matter* **1993**, *5*, 7893.
[50] E. G. Gumanskaya, O. A. Yegorycheva, M. V. Korzhik, S. A. Smirnova, V. B. Pavlenko, A. A. Fedorov, *Opt. Spektrosk.* **1992**, *72*, 395.
[51] S. R. Rotman, H. R. Tuller, C. Warde, *J. Appl. Phys.* **1992**, *71*, 1209.
[52] J. Barzowska, A. Kubicki, M. Grinberg, S. Kaczmarek, Z. Luczynski, A. J. Wojtowicz, Cz. Koepke, *Acta Phys. Pol., A* **1999**, *95*, 395.
[53] K. Wisniewski, C. Z. Koepke, A. J. Wojtowicz, W. Drozdowski, M. Grinberg, S. M. Kaczmarek, J. Kisielewski, *Acta Phys. Pol., A* **1999**, *95*, 403.
[54] M. Spurrier, P. Szupryczynski, K. Yang, A. Carey, C. Melcher, *IEEE Trans. Nucl. Sci.* **2008**, *55*, 1178.
[55] K. Yang, C. Melcher, P. Rack, L. Eriksson, *IEEE Trans. Nucl. Sci.* **2009**, *56*, 2960.
[56] S. Blahuta, A. Bessiere, B. Viana, P. Dorenbos, V. Ouspenski, *IEEE Trans. Nucl. Sci.* **2013**, *60*, 3134.
[57] W. Chewpraditkul, C. Wanarak, T. Szczesniak, M. Moszyński, V. Jary, A. Beitlerova, M. Nikl, *Opt. Mater.* **2013**, *35*, 1679.
[58] K. Yang, C. Melcher, M. Koschan, M. Zhuravleva, *IEEE Trans. Nucl. Sci.* **2011**, *58*, 1394.
[59] C. Hu, S. Liu, M. Fasoli, A. Vedda, M. Nikl, X. Feng, Y. Pan, *Phys. Status Solidi RRL* **2015**, *9*, 245.
[60] C. Hu, S. Liu, M. Fasoli, A. Vedda, X. Feng, Y. Pan, *Opt. Mater.* **2015**, *45*, 252.
[61] S. Liu, X. Feng, J. A. Mares, V. Babin, M. Nikl, A. Beitlerova, Y. Shi, Y. Zeng, Y. Pan, C. D'Ambrosio, Y. Huang, *J. Lumin.* **2016**, *169*, 72.
[62] M. Kucera, M. Hanus, Z. Onderisinova, P. Prusa, A. Beitlerova, M. Nikl, *IEEE Trans. Nucl. Sci.* **2014**, *61*, 282.
[63] Y. Zorenko, M. Batenchuk, M. Pashovsky, I. V. Konstankevych, V. Gorbenko, P. Yurchyshyn, V. Martynova, T. Duzyj, *Proc. SPIE* **1998**, *3359*, 261.
[64] Y. Zorenko, V. Gorbenko, I. Konstankevych, B. Grinev, M. Globus, *Nucl. Instrum. Methods Phys. Res., Sect. A* **2002**, *486*, 309.
[65] M. Kucera, K. Nitsch, M. Kubova, N. Solovieva, M. Nikl, J. A. Mares, *IEEE Trans. Nucl. Sci.* **2008**, *55*, 1201.
[66] Y. Zorenko, V. Gorbenko, I. Konstankevych, A. Voloshinonovskii, G. Stryganyuk, V. Mikhailin, V. Kolobanov, D. Spassky, *J. Lumin.* **2005**, *114*, 85.
[67] Y. Zorenko, A. Voloshinonovskii, V. Savchyn, T. Voznyak, M. Nikl, K. Nejezchleb, V. Mikhailin, V. Kolobanov, D. Spassky, *Phys. Status Solidi A* **2007**, *244*, 2180.
[68] J. A. Mares, A. Beitlerova, M. Nikl, N. Solovieva, K. Nitsch, M. Kucera, M. Kubova, V. Gorbenko, Yu. Zorenko, *Radiat. Meas.* **2007**, *42*, 533.
[69] J. Tous, P. Horodysky, K. Blazek, M. Nikl, J. A. Mares, *J. Instrum.* **2011**, *6*, C01048.
[70] R. Ischebeck, B. Beutner, G. Orlandi, M. Pedrozzi, T. Schietinger, V. Schlott, V. Thominet, in *Proc. Linear Accelerator Conf. LINAC2010* (Eds: M. Ikegami, V. R. W. Schaa, H. Sako), TUP103, Tsukuba, Japan **2010**, p. 656.
[71] L. Drummy, J. Yang, D. Martin, *Ultramicrosopy* **2004**, *99*, 247.
[72] D. Sengupta, S. Miller, Z. Marton, F. Chin, V. Nagarkar, G. Pratx, *Adv. Healthcare Mater.* **2015**, *4*, 2064.
[73] P. Prusa, M. Kucera, J. A. Mares, M. Hanus, A. Beitlerova, Z. Onderisinova, M. Nikl, *Opt. Mater.* **2013**, *35*, 2444.
[74] P. Prusa, M. Kucera, J. A. Mares, Z. Onderisinova, M. Hanus, V. Babin, A. Beitlerova, M. Nikl, *Cryst. Growth Des.* **2015**, *15*, 3715.
[75] Y. Zorenko, V. Gorbenko, T. Zorenko, O. Sidletskiy, A. Fedorov, P. Bilski, A. Twardak, *Phys. Status Solidi RRL* **2015**, *9*, 489.
[76] Y. Zorenko, V. Gorbenko, V. Savchyn, T. Zorenko, A. Fedorov, O. Sidletskiy, *J. Cryst. Growth* **2014**, *401*, 532.
[77] J. Bok, O. Lalinsky, M. Hanus, Z. Onderisinova, J. Kelar, M. Kucera, *Ultramicroscopy* **2016**, *163*, 1.
[78] Yu. Zorenko, V. Gorbenko, T. Zorenko, T. Voznyak, F. Riva, P. A. Doussiard, T. Martin, A. Fedorov, A. Suchocki, Ya. Zhydachevskii, *J. Cryst. Growth* **2017**, *457*, 220.
[79] F. Riva, P.-A. Doussiard, T. Martin, F. Carla, Y. Zorenko, C. Dujardin, *CrystEngComm* **2016**, *18*, 608.
[80] Y. Zorenko, V. Gorbenko, T. Voznyak, T. Zorenko, *Phys. Status Solidi B* **2008**, *245*, 1618.
[81] V. Babin, V. Gorbenko, A. Makhov, M. Nikl, S. Zazubovich, Y. Zorenko, *Phys. Status Solidi C* **2007**, *4*, 797.
[82] M. Kucera, K. Nitsch, M. Nikl, M. Hanus, *Radiat. Meas.* **2010**, *45*, 449.
[83] E. Auffray, R Augulis, A. Borisevich, V. Gulbinas, A. Fedorov, M. Korjik, M. T. Lucchini, V. Mechinsky, S. Nargelas, E. Songaila, G. Tamulaitis, A. Vaitkevičius, S. Zazubovich, *J. Lumin.* **2016**, *178*, 54.
[84] M. Lucchini, V. Babin, P. Bohacek, S. Gundacker, K. Kamada, M. Nikl, A. Petrosyan, A. Yoshikawa, E. Auffray, *Nucl. Instrum. Methods Phys. Res., Sect. A* **2016**, *816*, 176.
[85] V. Nagarkar, S. Tipnis, T. Gupta, S. Miller, V. Gaysinskiy, Y. Klugerman, M. Squillante, G. Entine, W. Moses, *IEEE Trans. Nucl. Sci.* **1999**, *46*, 232.
[86] L. D'Aries, S. Miller, R. Robertson, B. Singh, V. Nagarkar, *Proc. SPIE* **2016**, *9847*, 98470G–1.
[87] M. Kučera, M. Hanuš, M. Nikl, Z. Onderišinová, *Phys. Status Solidi RRL* **2013**, *7*, 571.
[88] Y. Tamagawa, Y. Inukai, I. Ogawa, M. Kobayashi, *Nucl. Instrum. Methods Phys. Res., Sect. A* **2015**, *795*, 192.
[89] M. Kobayashi, Y. Tamagawa, S. Tomita, A. Yamamoto, I. Ogawa, Y. Usuki, *Nucl. Instrum. Methods Phys. Res., Sect. A* **2012**, *694*, 91.
[90] M. J. Berger, J. H. Hubbell, S. M. Seltzer, J. Chang, J. S. Coursey, R. Sukumar, D. S. Zucker, K. Olsen, *XCOM: Photon Cross Section Database*, NBSIR 87-3597, NIST, Gaithersburg, MD, USA, **1998**.
[91] M. Kucera, K. Nitsch, M. Nikl, M. Hanus, S. Danis, *J. Cryst. Growth* **2010**, *312*, 1538.
[92] P. Prusa, M. Nikl, J. A. Mares, M. Kucera, K. Nitsch, A. Beitlerova, *Phys. Status Solidi A* **2009**, *206*, 1494.
[93] C. D'Ambrosio, H. Leutz, *Nucl. Instrum. Methods Phys. Res., Sect. A* **2003**, *501*, 463.
[94] W. Chewpraditkul, P. Bruza, D. Panek, N. Pattanaboonmee, K. Wantong, W. Chewpraditkul, V. Babin, K. Bartosiewicz, K. Kamada, A. Yoshikawa, M. Nikl, *J. Lumin.* **2016**, *169*, 43.
[95] H. Burešová, L. Procházková, R. M. Turtos, V. Jarý, E. Mihóková, A. Beitlerová, R. Pjatkan, S. Gundacker, E. Auffray, P. Lecoq, M. Nikl, V. Čuba, *Opt. Express* **2016**, *24*, 15289.

Chapter 5

LPE-Grown Thin-Film Scintillators

Miroslav Kucera[a] and Petr Prusa[b,c]
[a]*Faculty of Mathematics and Physics, Charles University, Ke Karlovu 5, 12116 Prague, Czech Republic*
[b]*Faculty of Nuclear Sciences and Physical Engineering, Czech Technical University, Brehova 7, 11819 Prague, Czech Republic*
[c]*Institute of Physics, Czech Academy of Sciences, Cukrovarnicka 10, 16253 Prague, Czech Republic*
miroslav.kucera @mff.cuni.cz

In scintillators, the high-energy particles (electrons, protons, neutrons, alpha particles) or photons (X-rays or gamma rays) can excite electrons in atoms, which then return to the ground state and this return is accompanied by emission of visible photons, which can be easily detected (measured) by standard detectors such as photomultipliers, CCD, etc. The de-excitation can be prompt (in nanosecond time scale) or delayed (miliseconds up to hours)—both types are used in practice.

The single crystalline films with thickness of several micrometers can be used for high resolution electron, cathodoluminescent, or X-ray screens, in various applications for imaging of microscopic objects with submicron resolution. Such films can be grown by the

Nanocomposite, Ceramic, and Thin Film Scintillators
Edited by Martin Nikl

ISBN 978-981-4745-22-2 (Hardcover), 978-981-4745-23-9 (eBook)
www.panstanford.com

liquid phase epitaxy (LPE) from the flux. In this chapter the present status of epitaxial oxide films, particularly garnets, perovskites, and oxyorthosilicates, will be reviewed. We focus especially on the growth procedure, and their luminescent and scintillation properties in comparison with the properties of bulk single crystal.

5.1 Introduction

X-ray or electron microimaging with high spatial submicrometer resolution using a single crystalline thin-film scintillator have found number of applications [14, 15]. It is operating in many synchrotron hard X-ray light sources [19] and X-ray screens where luminescence image of a scintillation screen is coupled to a CCD digital camera [2, 24–26]. Transparent single crystalline films provide better spatial resolution compared to powder phosphor screens due to eliminating light scattered by phosphor particles [29]. On the other hand, their efficiency is somewhat reduced due to waveguide effects in high optical quality films. The films of high crystalline perfection are needed where number of impurity ions and defects, which would otherwise induce electron/hole traps in the energy gap, have to be radically reduced. Due to low thickness, the scintillating films cannot be used for gamma detection (large penetration depth). Their main application is thus in detection of energetic particles (e.g., electrons, cathodoluminescent screens) or soft X-rays. On the other hand, in imaging applications, the energy resolution of scintillators is often of minor importance.

Liquid phase epitaxy (LPE) is a versatile method suitable for the growth of single-crystal films on single crystal substrates from high-temperature solution. The method can be also used in material research for development of new scintillators and it is more flexible compared to growth of bulk single crystals by Czochralski or Bridgman methods.

In the next sections we focus on the LPE growth of single crystalline oxide scintillator films, especially aluminum garnets, perovskites, and orthosilicates doped with rare earth ions such as Ce^{3+}, Pr^{3+}, Tb^{3+}, etc. The growth process and factors influencing the scintillation efficiency such as melt composition, growth conditions (i.e., growth temperature, supercooling, growth rate, used

substrates) are described. Analysis of various fluxes with respect of their influence on the LY, material performance, and defects in films is discussed. The characterization methods with special emphasis to examination of scintillation properties of thin films are described, as well. Finally, the optical and scintillation properties of selected garnet, perovskite, and orthosilicate epitaxial films are reviewed.

5.2 Liquid Phase Epitaxy

5.2.1 Principles of LPE of Oxide Scintillators

In the liquid phase epitaxy (LPE) technique a single-crystalline oxide film is grown from high-temperature solution, widely known as flux growth, on an oriented single crystalline substrate. Commonly used oxide fluxes are PbO, PbF_2, BaO, B_2O_3, Bi_2O_3, MoO_3, etc. and combination of them. The films are grown from supersaturated (supercooled) melt at temperatures much lower than the melting point of crystals. The supersaturation is usually obtained by cooling the melt below the liquidus (saturation) temperature. In the undercooled metastable region of the melt, the growth of crystalline films begins on the atomic flat surface of the substrate whereby the crystalline structure and orientation of the film is continuation of that of the substrate. The method is suitable also for crystals that melt incongruently, i.e., that decompose or have a phase transition below the melting point.

In the flux LPE technique a slow transport of the crystal species to the liquid–solid interface and low growth rate guarantee the growth conditions close to thermodynamic equilibrium. Lower growth temperature supports improved structural perfection and excellent stoichiometry and enables to use lower growth rates for improved thickness control and better surface morphology.

The LPE method was developed to high reproducibility in 1970s and applied for the growth of iron garnets [31–33] for magnetic bubble memories, or integrated optical devices—planar waveguide solid state lasers, e.g., YAG:Nd, Er, Yb, Ho, Tm [34–40], saturable absorbers [34], high-temperature superconductors [43], or compound semiconductors laser diodes, for review, e.g., Refs. [44, 45]. In other thin-film growth methods based on physical vapor

depositions (MBE, MOCVD, etc.), the films are deposited at extremely high supersaturation far from equilibrium and they usually suffer from much lower crystallographic quality what brings problems in scintillation applications.

In this report we call attention to important aspects, which have to be considered in material research based on LPE. The oxides epitaxial layers are grown from the flux. Therefore, the flux ions are always present as impurities in the lattice as discussed below. This requires very careful examination of the physical properties of films, and scintillation properties combined with optical absorption and luminescence spectroscopies, PL decay kinetics, and composition analysis (EPMA, GDMS) are particularly useful.

It is worth noting that epitaxial films grown on a substrate are single phase, other phases are, in principal, suppressed and are not constituted during the epitaxial growth on the oriented crystalline substrate. This is essential advantage of the LPE process.

5.2.2 Isothermal LPE

In the epitaxial growth the melt is supercooled below saturation temperature. In this metastable temperature region, the nucleation of a crystalline material begins on a seed, i.e., on a substrate immersed into the melt. Since the deposition of 1 μm thick oxide film takes from tens of seconds up to a few minutes, the LPE growth can be conducted isothermally, which is easy to control. The isothermal LPE method provides high-quality films with uniform thickness, composition, and concentration of dopants.

The complex oxides (garnets, perovskites, etc.) are grown from the flux at temperatures ~1000 °C, i.e., considerably lower compared to single-crystal melting point (~2000°C), which is significant advantage. For typical practical supercoolings ~2–20 K, the melt is stable with respect to garnet nucleation and remain supercooled for periods as long as 48 hours [33].

The isothermal dipping technique is schematically shown in Fig. 5.1. The melt is first heated to temperatures 40–80 K above saturation and homogenized by stirring for several hours. Temperature is then decreased toward growth temperature and a polished substrate, mounted horizontally on a Pt holder, is dipped into the supersaturated melt. In order to prevent the depletion of

garnet compounds at the growth boundary, the substrate is rotated in the melt and the direction of rotation is periodically reversed. In this way the melt is also homogenized during the LPE process especially with respect to temperature and concentration homogeneity, which results in uniform composition and thickness (~1–2%). Typical rotations are 50–200 rpm with reversion every 2–20 revolutions.

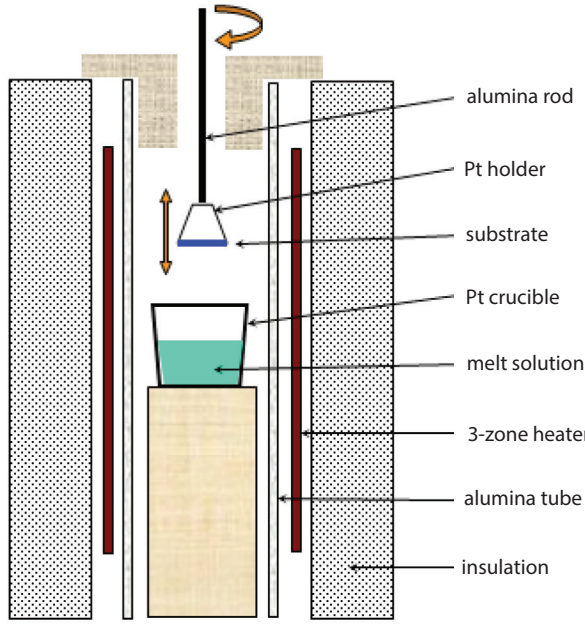

Figure 5.1 Schematic showing apparatus for isothermal LPE.

The saturation temperature, T_S, is determined from zero growth rate—below T_S the film growths on a substrate, while above T_S the substrate is dissolved in the melt. The growth rate depends on several factors: along with the flux type and melt composition, the most important factors are supersaturation, growth temperature, and substrate orientation. The growth rate is typically 1 μm/min but rates between 0.1 and 3 μm/min are ordinarily used. This enables to grow reproducibly films with thickness from submicrometers up to tens (or even hundreds) of micrometers. The best quality and uniform films are obtained at low growth rates, i.e., at low supersaturation.

There are several basic technological aspects which influence the emission efficiency and the LY of LPE film scintillators. Together with the flux composition it is primarily the supercooling, ΔT, and the growth temperature, T_G. Other important factors are growth rate (which is closely related to ΔT and T_G), crystal orientation and the lattice match with the substrate. These factors influence, e.g., the segregation coefficients of dopants and thus the concentration of both activators and impurities. They are discussed in the next sections.

Provided that oriented and perfectly polished substrates without structural defects (dislocation, inclusions, etc.) are available, perfectly uniform single-crystalline garnet films are fabricated using this technique from the PbO-B_2O_3 flux with low defect density and excellent surface morphology with nanometer surface roughness. Since the growth is near equilibrium, the film properties, such as concentration of dopants and impurities or surface morphology, principally depend on the growth conditions (melt composition, growth temperature, supercooling) and the growth process and temperature should be well controlled.

Advantages and properties of the LPE:

- The LPE technique provides single-crystalline films with structure quality comparable to that of used substrate; the films grown at low supersaturation have excellent stoichiometry with minimum defects.
- The quasi-equilibrium growth process of the LPE is favorable for very uniform distribution of activator ions. It ensures minimum concentration of intrinsic defects and high structural perfection (low dislocation density, low concentration of point defects) and high quality surface morphology.
- LPE is highly versatile method for material research—it is easy to change composition (or doping) of films by gradual modification of the melt, i.e., from a single melt a set of samples with different composition (doping) can be produced.
- Epitaxial growth of samples ensures that no second phases are present in the single-crystalline films.

Limitations and drawbacks of the growth from the flux:

- Impurity and contaminant ions from the flux (such as Pb^{2+}, B^{3+}, etc.) are inevitably present in the crystal and the growth

of chemically pure samples is impossible. This is fundamental drawback of the flux growth especially in case when the flux impurities may have detrimental effect on physical properties of samples (e.g., quench emission of scintillation films).

- Most frequently used PbO flux partly attacks the Pt crucible, which results in contamination of the films also with Pt^{4+} impurity.
- LPE is unsuitable for growing very thin layers (<100 nm) with sharp interfaces, where accurate layer thickness uniformity and reproducibility are required.
- Availability of high-quality substrates with good surface quality and good lattice match to the film is essential.
- Film morphology is very sensitive to substrate properties (lattice misfit, misorientation), substrate surface quality and surface defects (dislocations, surface point defects, dust particles) and such defects are invariably replicated in the films.

5.2.3 Fluxes

The crystal-forming oxides are melted in the flux. Various fluxes are used for the growth of garnet, perovskite, or orhosilicate LPE films. Standard and commonly used flux is $PbO\text{-}Ba_2O_3$, alternate lead-free fluxes are $BaO\text{-}B_2O_3\text{-}BaF_2$, rarely $MoO_3\text{-}LiO_2$ or Bi_2O_3 fluxes (for growth of Bi-doped films) were also used. Aluminum garnets, perovskites, and orthosilicates melt congruently. However, when complex oxides are grown from the flux, the solute has usually different composition than the solution. One of the reasons is the necessity to stabilize a particular phase—e.g., while growing aluminum garnets it is necessary to select that region of the phase diagram in which garnet is the only stable phase. Therefore high excess of Al compared to Y is necessary in order to stabilize the garnet phase and to suppress the perovskite one. The second reason is different tendency of specific ions for incorporation into the crystal lattice. This tendency is described by the *segregation coefficient*, k, i.e., concentration ratio of a specific element in the melt and in the crystal, $k = c_{crystal}/c_{melt}$. Some large ions, e.g., Ce or Pr, have very low segregation in garnets or perovskites, $k \ll 1$. Basic properties of common fluxes are described in the following paragraphs.

5.2.3.1 PbO-B_2O_3 flux (here referred as PbO flux)

The PbO flux is the most common flux, considered as standard, for preparation of oxide films. Examples of garnet epitaxial films are shown in Fig. 5.2. Growth occurs under isothermal conditions. The advantages of this flux is reproducible growth, high structural quality films with uniform dopant distribution, smooth atomic-like surface can be achieved, reasonable growth temperatures 900–1050°C, low viscosity, and it is suitable for large-scale production. Addition of small amount of B_2O_3 into PbO largely improves the flux properties and especially formation of defects in films is considerably reduced [33, 46, 47]. The molar ratio PbO:B_2O_3 is usually between 10:1 and 20:1. The supercooled melt is stable with respect to garnet nucleation and highly diluted PbO-B_2O_3-garnet oxides melt can be supercooled up to 150 K without spontaneous nucleation of the garnet phase. In practice, however, films with the best properties (structure morphology, surface properties, low impurity concentration) are grown at low supercooloing (1–10 K) and at low or moderate growth rates < 1 μm/min. The growth rate is approximately proportional to the undercooling and rates from < 0.1 up to several μm/min can be achieved.

There are some severe disadvantages of the PbO flux, which have to be carefully considered in growing of scintillation films. The flux impurities, such as Pb^{2+} and Pt^{4+} ions from the flux (PbO flux attacks the Pt crucible), inevitably enter the crystal lattice. In scintillator oxides (garnets, orthosilicates, perovskites) especially Pb^{2+} ions quench the Ce^{3+} emission. Finally, the PbO flux suffers from higher evaporation and volatility above 1000°C. To overcome limitations of the PbO flux, especially to avoid Pb^{2+} impurity, alternative lead-free fluxes have also been employed.

Important parameter which determines the quality of films and concentration of dopants (and also impurities) is supersaturation, $\Delta T = T_S - T_G$, where T_G is the growth temperature. The best quality films grown from the PbO flux are obtained at low undercooling with well-controlled growth conditions. Under these conditions the concentration of impurities, including Pb^{2+} ions, in the garnet lattice is significantly reduced. Likewise higher T_G contributes to reduction of impurities; however, at temperatures above 1000°C, increased evaporation of the melt appears. Concentration of the doping ions,

such as Ce or Pr, depends similarly on the undercooling due to their very low segregation coefficients. In optimized growth process at low supercoolings the Pb^{2+} impurity can be kept below 50 wt ppm in YAG or LuAG and the effect of Pb quenching on Ce emission can be reduced.

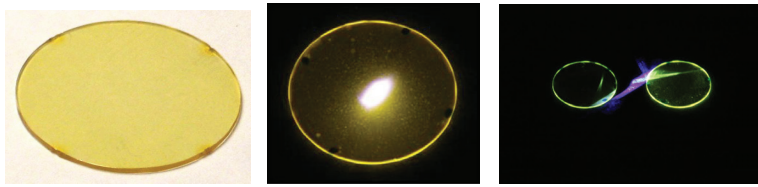

(a) (b) (c)

Figure 5.2 Garnet epitaxial films: (a) YAG:Ce film grown on YAG substrate; (b) emission from GdYAG:Ce film excited by a blue laser beam at λ = 450 nm; the white bright spot is due to yellow Ce^{3+} luminescence and scattered blue excitation light from rough surface; (c) green luminescence from LuAG:Ce films excited at 450 nm. The emission is observed from edges due to the waveguide effect. The thickness of films is 8–15 μm, diameter 20 mm.

5.2.3.2 $BaO\text{-}B_2O_3\text{-}BaF_2$ flux (here referred as BaO flux)

The BaO flux was developed for iron garnet film growth [48–50], and adapted for the growth of high-purity aluminum garnets [4, 5]. This flux is primarily suitable for the growth of high-purity samples with lowest-possible contamination, which depends only on purity of input raw materials. Large Ba^{2+} ions do not enter the garnet lattice (according to the GDMS analysis Ba content in garnet films is <5 ppm [12]). Although boron ions were detected in films 100–300 ppm, they have not any noticeable effect on the scintillation properties of garnet films [12]. The scintillation and emission properties of LPE films grown from the BaO flux are markedly better compared to PbO-grown films and comparable with high quality single crystal counterparts [51–54].

Evaporation of the BaO flux is low, the flux does not attack the Pt crucible, and high supercoolings up to 80 K were also demonstrated [4]. However, the basic disadvantage of the BaO flux is much higher viscosity compared to the PbO flux. The melt cannot be completely

removed from the sample surface after the growth process and aftergrowth may occur. Likewise increased content of crystal forming oxides (which are close to the crystal stoichiometric ratio and form ~15– 25% of the melt) leads to higher viscosity. This all results in higher number of surface defects [21, 49] (especially surface pits, where some of them may come from imperfectly dissolved oxides) and worse surface quality compared to PbO-grown films, see Section 5.2.5.

5.2.3.3 Other fluxes

MoO_3-$LiMoO_4$ flux (gradient deposition technique)

This flux was rarely used for garnet growth [5, 55, 56]. This melt does not attack the Pt crucible and its low viscosity and low evaporation is an advantage. Garnet films with promising emission properties were reported [5]. However, the solubility of garnet oxides in this flux is very low, <2 %, and the growth in the temperature gradient is inevitable. Rather problematic growth reproducibility is fundamental disadvantage of this flux since the growth process is essentially dependent on the temperature profile and also on temperature history of the melt.

Bi_2O_3-B_2O_3 flux

This flux can be favorably used for the growth of Bi-doped (garnet) oxides [57–59]. Large Bi ions partly enter the garnet lattice, their maximum concentration is, however, limited and depends on the lattice constant of the host. This flux eliminates occurrence of Pb^{2+} ions in films; however, the films grown from Bi_2O_3 do not reach the quality of PbO grown films.

5.2.3.4 Ion segregation coefficients

In the growth of substituted or multicomponent oxide systems (e.g., garnets, silicates), the knowledge of segregation of ion species between the melt and the crystal is important. The effect of cation size of RE ions on the segregation coefficients in iron and gallium garnets was frequently studied, e.g., Refs. [60–62], and general conclusions are valid also for aluminum garnets. We report here results concerning doping of Ce, Pr, Gd, Tb, Ga, and Sc atoms into aluminum garnets, YAG, and LuAG.

The segregation depends on the radius of a doped ion, but also on growth conditions, such as the growth rate, supersaturation, growth temperature, used flux, and on lattice constant of grown crystal (i.e., on crystal composition). Segregation coefficients of several ions used in scintillation garnet systems grown by the LPE from PbO and BaO fluxes are surveyed in Table 5.1, data are from Refs. [4, 5, 12, 20, 48, 63]. The ionic radii of light RE ions in garnet crystal sites with CN = 8, Ce^{3+} (1.143 Å) and Pr^{3+} (1.126 Å) are much higher compared to those of the host ions Y^{3+} (1.019 Å) or Lu^{3+} (0.977 Å) and their segregation coefficients are very low. Therefore high excess of Ce or Pr oxides in the melt is inevitable. Furthermore, amount of CeO_2 or Pr_6O_{11} oxides in the melt is limited by their solubility in the flux: e.g., as for CeO_2 its maximum is about 0.2 g and 0.5 g in 100g of PbO [15] and BaO flux [4], respectively. Above these limits the oxides are not completely dissolved and form second phases on the melt surface with negative impact on the morphology of the epitaxial film. Second, the segregation depends significantly also on the growth rate especially for ions with low segregation such as Ce and Pr. In Fig. 5.3 concentration of cerium in Ce:LuAG films grown from PbO fluxes with various content of garnet forming oxides in the melt is shown as a function of the growth temperature. It is evident, that segregation coefficient of Ce can differ by a factor of 3 for a specific flux composition in dependence on the supersaturation (growth temperature). Similar development is observed also for films grown the BaO flux [4]. Since the growth rate is roughly proportional to supersaturation, we can infer general trends and common properties of both melts: the higher the growth rate (i.e., supersaturation), the weaker is segregation of ion species between liquid and solid, and vice versa. This indicates, that at high growth rates (high supersaturation) concentrations of Ce or Pr ions in the crystal are significantly increased. However, this tendency is observed also for other large ions including Pb^{2+}(1.29 Å) impurity, which quench the Ce^{3+}(5d–4f) emission.

While segregation of the RE ions does not differ much for both PbO and BaO fluxes, interestingly, it is very different for Ga ions, which substitutes for Al in octahedral and tetrahedral sites (see Table 5.1).

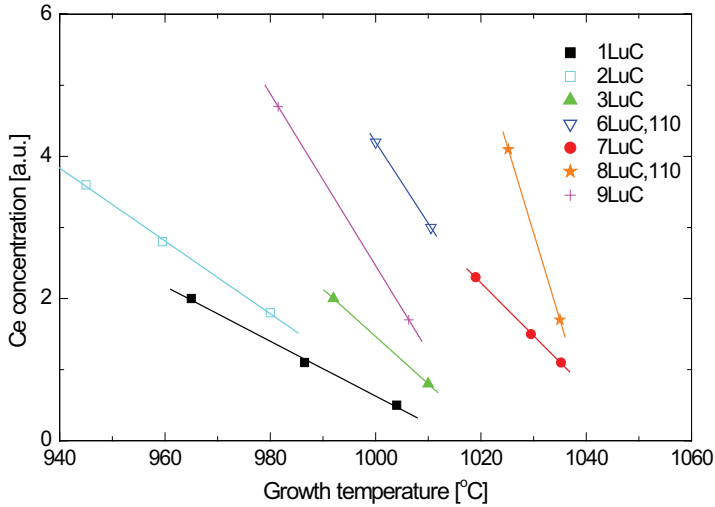

Figure 5.3 Concentration of cerium in LuAG:Ce films grown from various PbO-Ba_2O_3 fluxes as a function of the growth temperature. The films were grown on (111) oriented LuAG substrates except for series 6LuC and 8LuC which were grown on (110) oriented substrates. The content of garnet forming oxides in particular fluxes varied in the range from 4.1 to 5.6 mol. %, cerium content was in the range from 2.7 mol. % (1LuC) to 5.6 mol. % (9LuC) of garnet oxides. Reprinted from Ref. 4, Copyright 2010, with permission from Elsevier.

Table 5.1 Segregation coefficients for selected trivalent ions in LuAG and multicomponent GAGG garnet epitaxial films grown from PbO-B_2O_3 and BaO-B_2O_3-BaF_2 fluxes

	PbO flux		BaO flux	
	LuAG*	LGAGG**	LuAG	LGAGG
Y	0.9		1.1	
Ce	0.01–0.05	0.05–0.08	0.05–0.2	0.1–0.2
Pr	0.03		0.03–0.06	
Gd	0.65–0.75	0.8–0.9	0.5–0.7	0.8–0.95
Tb	0.5–0.7		0.7–0.9	
La	0.005			
Ga	0.35–0.5	0.55–0.65	1.3	1.3–1.5
Sc	1.2–1.8	2–4	1–1.6	

* LuAG = $Lu_3Al_5O_{12}$

** LGAGG = $(LuGd)_3(GaAl)_5O_{12}$

Furthermore, the lattice parameter plays also substantial role for ion segregation. LuAG and GAGG have different lattice constant, a = 11.91 and 12.3 Å, respectively. Higher k values for large RE ions (Ce, Pr and also Pb, Ga, Sc) in multicomponent GAGG films is mostly related to their larger lattice parameter and consequently more space available for large RE or Ga substitution.

5.2.4 Epitaxial Growth on Substrates

Growth of high quality single crystalline films by the LPE is limited by availability of suitable substrates. Since the LPE is a near-equilibrium process, it is very sensitive to growth parameters. Basic requirements on substrates are low lattice misfit at growth temperature, similar thermal expansion coefficients of the substrate and the film, low misorientation, and good chemical/thermal stability. In homoepitaxial growth, the substrate should have the same crystallographic structure and match the lattice constant with the film. The formation energy of dislocations in garnets is so high that mechanical stress induced by a difference in the lattice constants of film and substrate cannot be released through misfit dislocations. Instead, the film on the substrate is elastically strained. The lattice misfit (mismatch), i.e., difference between substrate and film lattice constants, $\Delta a = a_s - a_f^{\perp}$, can easily be determined by X-ray diffraction. At low misfit, $\Delta a/a_s < 0.2\%$, the film is grown under the tension or stress and in-plane lattice constant $a_f^{\parallel}$ of the film is the same as that of substrate, while out of plane constant $a_f^{\perp}$ differs. High quality garnet films with nanometer rms surface roughness (see Fig. 5.4) can only be grown on substrates at low lattice mismatch, <0.1 %. In heteroepitaxial growth, the growth of single crystal garnet (or silicates) films on garnet (silicate) substrate at mismatch as high as ~2 % was demonstrated [4, 63, 64]; however, at the expense of surface morphology and flatness. At high mismatch the rms surface roughness is as high as hundreds of nm and the film surface is matte.

The lattice misfit has a substantial effect on nucleation and epitaxial growth and consequently on structural perfection of an epitaxial layer. During the layer growth the misfit is first accommodated by a homogeneous strain, and after reaching a critical layer thickness, which depends on the degree of misfit and thickness of the film, the strain is released by cracking of the film-substrate

structure. In garnets the misfit dislocations, which accommodate the strain are prevented—they are energetically unfavorable due to the high energy necessary for their formation. As a consequence, if the mismatch between film and substrate exceeds critical value (about ~2% in garnets or orthosilicates), nucleation does not occur even in strongly supersaturated melt. Critical mismatch depends to some extend on material to be grown, flux used, substrate parameters (orientation, composition).

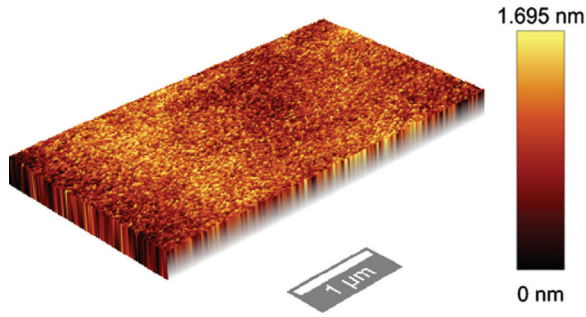

Figure 5.4 AFM topography of the surface morphology of $Yb_3(AlGa)_5O_{12}$:Er garnet epitaxial film grown homoepitaxially onto (111) oriented YAG substrate from the PbO flux. Reprinted from Ref. 16, Copyright 2015, with permission from Elsevier.

One of possible mechanisms of growth of films with large misfit is formation of a transient layer at the film–substrate interface [31]. It is formed both in homo- and heteroepitaxial growth. Its thickness is from tens of nanometers up to micrometers. The composition of the transient layer gradually varies, it contains usually surplus of flux or doping ions, e.g., Pb, Ga. At small misfit it balances the lattice constants of the epilayer and the substrate.

Homoepitaxially and heteroepitaxially grown films observed in optical microscope are shown in Fig. 5.5. The homoepitaxial films with lattice mismatch $\Delta a < 0.2$ % have smooth glossy surface, those grown heteroepitaxially with $\Delta a > 0.5$ % are matte with rough surface. The rms surface roughness measured by the Zygo interferometric profiler is ~1 nm and ~300 nm in homo- and heteroepitaxial films, respectively.

An important issue is the morphology of the film surface and film/substrate interface. Large lattice mismatch between the Ce:LuAG film and the YAG substrate at heteroepitaxial growth, Δa

= –0.09 Å, is the main problem in obtaining films of high surface perfection. The formation of a transient layer at the film-substrate interface is of real importance, especially for very thin films. In the transient layer the chemical composition changes and a crucial issue is its contamination by impurity ions from the flux and presence of other defects. For small film-substrate lattice mismatch, $\Delta a < 0.02$ Å, this transient layer is usually narrow from several to dozens of nanometers. For higher lattice mismatch the morphology of the transient layer is more complicated. The edges of samples cleaved normal to the film-substrate interface are shown in Fig. 5.6. Sharp film-substrate interface is observed at homoepitaxial growth of the Ce:LuAG/LuAG system (Fig. 5.6a), where the lattice constants of the film and substrate virtually merge. Because of nearly the same chemical composition, the optical contrast between film and substrate is very weak and the film-substrate interface is difficult to observe. On the other hand, at heteroepitaxial growth of Ce:LuAG/YAG system, where the lattice mismatch is high and the film-substrate interface is apparent, Fig. 5.6b. An oriented columnar-like structure of the film is observed in optical microscope. The morphology of the transient layer may be critical especially in micrometer thick films and a detailed study of its structure is called for.

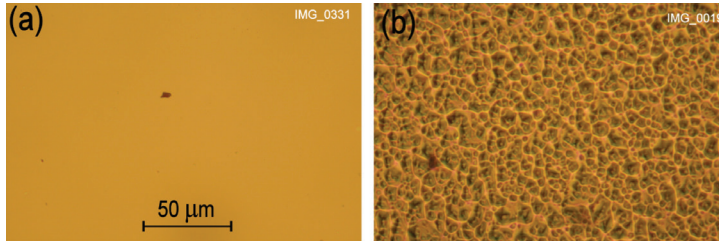

Figure 5.5 Optical microscopy of (111) oriented LuAG:Ce epitaxial films grown from PbO-flux: (a) high quality film grown on LuAG substrate, lattice misfit $\Delta a < 0.01$ Å (homoepitaxial growth), (b) LuAG:Ce film grown on YAG substrate (heteroepitaxial growth), lattice misfit $\Delta a = 0.09$ Å. Reprinted from Ref. 21, Copyright 2010, with permission from Elsevier.

The LPE growth process depends also on substrate crystallographic orientation. The misorientation of a substrate from optimal direction may lead to step-like surface of films. Only LPE at low supersaturation can yield atomically flat surfaces.

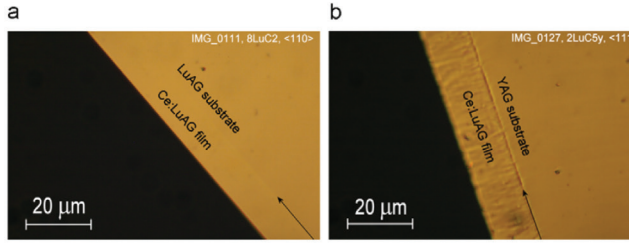

Figure 5.6 Cross section of cleaved samples observed in optical microscope; the arrows point to the film/substrate interface. (a) Homoepitaxially grown Ce:LuAG film on LuAG substrate, lattice constants of the film and substrate are almost the same, $\Delta a < 0.01$ A, and sharp film-substrate interface is observed. (b) Heteroepitaxially grown Ce:LuAG film on YAG substrate, the lattice mismatch is rather high, $\Delta a = 0.9$ A. Transient layer and columnar-like film growth is easily observed. Both films were grown from the PbO flux. Reprinted from Ref. 4, Copyright 2010, with permission from Elsevier.

Aluminum garnets are routinely grown on YAG substrates cut from Czochralski grown single crystals, which are available in diameters up to 100 mm. Other garnet substrates with different lattice parameters such as LuAG, GGG, rarely NdGG, YGG, etc., were also used, their structural parameters are shown in Table 5.2. Substrates with perovskite and orthosilicate crystal structure are of limited availability, the epitaxial films are usually grown on YAP or YSO, respectively.

The substrates reported in Table 5.2 suffer from one disadvantage: under high-energy excitation the host emission is induced in the UV spectral range. This may cause problems in some thin-film applications, since gamma or hard X-rays penetrates through the film into the substrate and the substrate emission is excited simultaneously with the emission from epitaxial film. Because of different timing characteristics of film and substrate emissions, it is be desirable to suppress the substrate emission. This can be carried out by intentional substitution of the host crystal by appropriate rare earth ions, e.g., Yb, Tm. At high RE concentrations, the RE emission also disappears due to concentration quenching [65]. As an example, crystals such as YbAG, YGG, GGG, YbSO have negligible emission. This approach was used for LSO:Tb scintillation films for microimaging using hard synchrotron radiation in ESRF [2].

Table 5.2 Parameters of typical garnet, perovskite, and orthosilicate substrates. CN, coordination number; Z_{eff}, effective atomic number; ρ [g/cm^3], density

Substrate	Crystal structure, space group	Lattice constant [Å]	Cation CN, (Y^{3+} symmetry)	Z_{eff}/ρ	References
Garnet					
YAG	cubic, Ia3d	a = 12.008	Y-8 (D_2), Al-6, 4	32/4.56	[31]
LuAG	"	a = 11.913	"	62/6.70	
GGG	"	a = 12.383	"	70/7.08	
Perovskite					
YAP	orthorhombic Pnma	a = 5.332 b = 7.356 c = 5.176	Y-12 (C_{1h}), Al-6	33/5.35	[66]
LuAP	"	a = 5.330 b = 7.294 c = 5.100	"	65/8.34	[66]
Orthosilicate					
YSO	monoclinic B2/b	a = 14.371 b = 10.388 c = 6.710 γ =122.17°	Y1-7, Y2-6 (C_1), Si-4	39/4.54	[67]
GSO	$P2_1/c$	a = 9.131 b =7.045 c = 6.749 γ =107.52°	Y1-9, Y2-7 (C_1)		[68]
LSO	B2/b	a = 14.277 b = 10.246 c = 6.640 γ =122.22°	Y1-7, Y2-6 (C_1)	66/7.4	[69]

5.2.5 Defects in LPE Films

Compared to Czochralski grown single crystals, the layers prepared by the liquid phase epitaxy (LPE) are grown from the flux at much lower temperatures and hence with lower structural disorder and lower number of intrinsic defects, e.g., antisite defects. On the other

hand, various impurities can enter into the crystal lattice from the flux and some new defects specific to the LPE technology are induced during the growth. Furthermore, other factors inherent for epitaxial layers such as flux properties (composition, viscosity), growth conditions (growth temperature, supercooling, growth rate), substrate properties (film–substrate lattice match, defects in substrates) influence the quality of epitaxial films and subsequently their scintillation properties.

The crystallographic quality of substrates is of primary importance for growth of high-quality epitaxial films. All defects which intersect the substrate surface, e.g., dislocations, inclusions near the surface, scratches due to imperfect polishing, dust particles on the surface, etc., are replicated into the film and result in macroscopic defects. Although such defects usually do not affect notably the scintillation properties, however, they have to be eliminated in imaging screen application, where also high-quality surface morphology is of crucial importance.

The second type of defect are intrinsic ones on the microscopic (atomic) scale, such as impurity ions, various structural defects, vacancies, antisite defects, which may have, on the other hand, a dramatic impact on the scintillation properties since they may induce trap states in the forbidden gap.

Lattice (structural) defects

- Antisite defects (AD) Y_{Al}, Lu_{Al}, observed in oxides with two or more cation crystal sites (YAG, YAP), where Y or Lu ion is situated in octahedral (preferable Al) site instead of its preferred dodecahedral site. They form shallow trap states and induce slow component in the scintillation decay and seriously reduce the LY. AD defects are produced due to high crystal growth temperature in Czochralski or Bridgman techniques. In epitaxial films the AD are significantly reduced compared to SC due to lower growth temperature [70]; however, recent studies indicate non-negligible AD content even in films grown from the flux [71].
- Deep traps formed by oxygen vacancies, such as F+ or F color centers, drastically decrease the scintillation LY. These

vacancies form very effective electron traps. The vacancies are induced during the growth of single crystals in the reducing protective atmosphere [72] and they are eliminated by post growth heat treatment in oxidizing atmosphere. The color centers are effectively suppressed in epitaxial films due to the growth in oxidizing atmosphere and at significantly lower growth temperatures ~1000°C compared to single crystals.

Impurities

In the LPE techniques the films are grown from the flux and elimination of impurities is of significant importance.

- Isoelectronic trivalent impurity with closed electron shell, such as $B^{3+}(1s^2)$ $Sc^{3+}(3p^6)$ $La^{3+}(5p^6)$ do not show any radiative transitions in the visible and UV spectral regions. At low concentrations they do not influence notably the LY. However, as a point defect in the lattice they change the ion–ion distance and cause deformation of the crystalline field due to different ionic radii. Generally, the efficiency of scintillator materials is decreased by processes associated with electrons or holes trapped at point defects. When Sc- or La-doped YAG/LuAG is excited at the bandedge or by high-energy photons/particles, an intense broad emission band is induced near 275 nm in photoluminescence or radioluminescence spectra [73]. This emission, which has decay time of ~0.6–1 μs, originates from recombination of an exciton located near the Sc defect.
- Divalent or tetravalent impurities with closed electron shell np^6 (e.g., Mg^{2+}, Ca^{2+}, Zr^{4+}, Hf^{4+}): their effect on scintillation properties is divers depending on their concentration and type of the host lattice. At higher concentrations the non-isovalent ions always quench the 5d–4f luminescence of Ce^{3+} or Pr^{3+} ions since they are electron/hole capture centers. However, at low concentrations as trace impurities, they can sometimes even improve scintillation properties, e.g., co-doping with Ca^{2+} in LSO/YSO:Ce increases LY and shorten decays [74] and reduce afterglow. It has been proposed that doping YAP:Ce with Zr^{4+} can change the concentration of point defects [75], e.g., decrease concentration of oxygen vacancies [76].

Divalent ions Mg^{2+} or Ca^{2+} change valency of cerium to Ce^{4+}. Stabilization of a part of the cerium in the tetravalent charge state provides an additional fast radiative recombination pathway in the scintillation mechanism [77]. Discussion of intrinsic or extrinsic defects ("defect engineering") can be found in number of publications [70, 78–86].

- Transition metals (TM) usually quench RE emission, e.g., Fe^{3+} heavily quenches the PL, its emission is at 780 nm at RT.
- Pb, Pt are typical impurities in LPE films grown from the PbO flux. Pb^{2+} ion has large radius and its concentration is typically tens of ppm in YAG/LuAG [4, 63]. Nevertheless, presence of Pb^{2+} appeared problematic since they induce absorption in the deep UV range and quench effectively the Ce^{3+} emission [87, 88]. Furthermore, in garnets with larger lattice constant (GAGG) and especially in perovskites and othosilicates, where larger lattice space is available, concentration of Pb ions significantly increases.
- Energy levels of most of defects are situated in the energy gap. These trap states can capture electrons or holes, and represent thus a parallel channel for recombination (either radiative or nonradiative) with negative impact on scintillation efficiency (decreased LY, delayed decay or afterglow).

Macroscopic defects in epitaxial films

Good lattice match between the layer and the substrate is required in order to obtain good-quality single-crystalline layers. If the lattice mismatch exceeds about ± 0.02 Å, faceting or cracking appears in layers grown under pressure or under strain, respectively.

The epitaxial garnet films can be grown on substrates of various orientation, the best results are usually obtained for (111) oriented substrates. While a slight misorientation of (111) planes, even of several degrees, has a negligible effect on the surface quality, a misorientation of (110) plane of 0.5 deg resulted in faceted surface.

Many of surface defects of the LPE films are closely connected to the growth process and to the flux properties. The surface pits are frequent defects observed in LPE layers. Typical triangular and hexagonal pits observed in (111) surfaces are shown in Fig. 5.7a.

The orientation of pits is closely related to the crystal axis, the edges of triangles are in 110 directions. The origin of the pits is diverse—they may come from the point defects in the substrate (dislocation pits), from microscopic dust particles firmly attached on the surface during immersing the substrate into the flux, or directly from the flux (solvent particles).

In addition, the defects in the substrate that intersect the surface (such as dislocations, cation inclusions or mechanical defects) are often replicated into the film in the form of pits. Mechanical defects (scratches) in the substrate induced during the polishing are amplified in films and pit lines may appear (Fig. 5.7b).

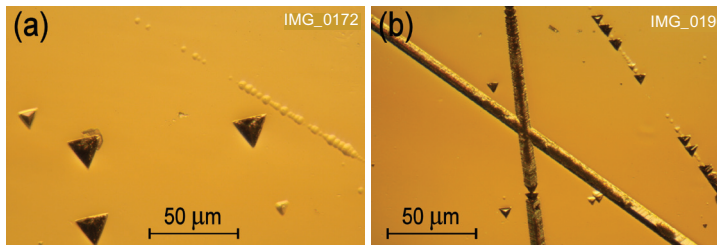

Figure 5.7 Triangular and hexagonal surface pits observed by optical microscopy in YAG:Ce films grown on (111) oriented YAG substrates (a), the pit lines in epitaxial film grown onto insufficiently polished YAG substrate (b); the films were grown from the MoO_3 flux. Reprinted from Ref. 21, Copyright 2010, with permission from Elsevier.

The pit defects are usually created at the very beginning of the growth process in the film/substrate interface due to the starting instability of the growth. However, a detailed inspection of Fig. 5.7 reveals also pits of smaller dimensions, which do not originate from the interface but were generated later during the layer growth. This is supported also by the fact that thick layers (dozens of micrometers) contain higher number of pits than the thin ones. Such pits come from "solvent particles," namely from some oxide components insufficiently dissolved in the flux. Particularly the layers grown from the BaO flux are susceptible to the pit creation. This flux suffers from high viscosity and high surface tension compared to the PbO or MoO_3 ones. This brings about a reduced flowing of the BaO flux and slows down dissolving of individual melt components. The surface

pits cause scattering of emitted light and they should be eliminated in high resolution scintillation imaging screens.

Dislocation defects, shown in Fig. 5.8 (left), result in individual dislocation pits as those in Fig. 5.7a. Very rough surface in Fig. 5.8 (right), with large number of pits was grown from nonhomogenous flux with undissolved solvent particles.

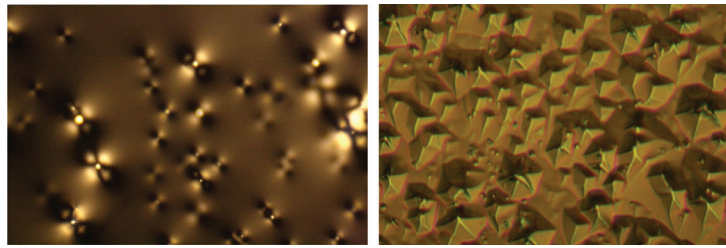

Figure 5.8 Left: Dislocations in LuAG single-crystal substrate observed in polarizing microscope. Right: Large number surface pits in Ce:LuAG epitaxial film grown on (111) oriented substrate; the pits were induced during the growth due to undissolved solvent particles.

5.3 Characterization Methods: Experimental Techniques

Characterization methods for thin-film scintillator differ in many details from those commonly used for characterization of bulk materials. As an example, the LY or scintillation decays cannot be measured by standard γ-excitation, since the penetration depth of γ rays is much larger than the films thickness (mm x μm) and thus the effective signal comes mostly from the substrate. The films are usually excited either by soft X-rays (e.g., steady state RL measurements) or by alpha particles at 5.166 MeV (which have penetration depth about 10–15 μm in YAG/LuAG [41]) or by energetic electrons, penetration depth < 1 μm for 10 keV electrons [89].

5.3.1 XRD and Structural Properties of Films

The films grown by the LPE are single crystalline and single phase and their structural properties are comparable to those of substrate.

Combination of XRD, EPMA, and lattice constant calculations [90] provide valuable information not only on composition but also on occupation of individual crystallographic sites by particular ions.

XRD properties of several films are demonstrated in Fig. 5.9. The diffraction profile of the symmetric 444 diffraction of a Ce:YAG film grown on YAG substrate (homoepitaxy) from the PbO flux is shown in Fig. 5.9a. Lower intensity of substrate diffraction is due to radiation absorption in 11 μm thick film. Observed half-width of 444 diffraction peak in the epitaxial film, 12 ang. seconds, is comparable to that of the substrate (10 ang. seconds) giving evidence of high crystallographic quality of the film. From the position of the 444 diffraction peak in this sample, the lattice constant in the direction normal to the film surface was determined as $a_{\perp}$ = 12.0114(1) Å. The measured lattice constant of the YAG substrate was a_S = 12.0093(1) Å. The higher lattice constant of the films compared to the substrate is in accord with the doping of large Ce^{3+} ions, ionic radius r^{VIII} = 1.143 Å, into the dodecahedral sites of YAG. On the contrary, the XRD study shows that the lattice constant of Ce-doped LuAG films is even lower than that of pure LuAG substrates. This discrepancy can be explained due to the antisite Lu_{Al} defects which occur in the Cz grown LuAG crystals, i.e., a part of small Lu^{3+} ions, r^{VIII} = 0.977 Å, is situated in the octahedral sites instead of regular Al^{3+} ions. These defects increase the lattice constant of a substrate compared to the stoichiometric crystal. In epitaxial LuAG films the concentration of these Lu_{Al} defects is presumed to be much smaller than in the substrates [7, 30] due to much lower growth temperature of films compared to that of the Czochralski or Bridgman grown crystals. As concerned the YAG substrates, the ionic radius of the Y^{3+} ions is much higher (r^{VIII} = 1.016 Å) compared to Lu^{3+} ions. Therefore the concentration of antisite Y_{Al} defects in YAG crystals is accordingly lower than that in LuAG crystals and the deviation from the stoichiometry of YAG is also significantly lower.

The asymmetrical reciprocal space map (RSM) around the asymmetric diffraction 664 (Fig. 5.9b) suggests that homoepitaxially grown samples, i.e. Ce:YAG/YAG and Ce:LuAG/LuAG, showed pseudomorphic film on substrate (the intensities of scattered X-rays in the reciprocal space exhibit the same Q_x coordinate in the RSM), i.e. the film lattice parameter in the plane is the same as that of substrate, $a_{\parallel} = a_S$. Since $a_{\perp}$ differs only slightly, $<2 \times 10^{-4}$, any misfit

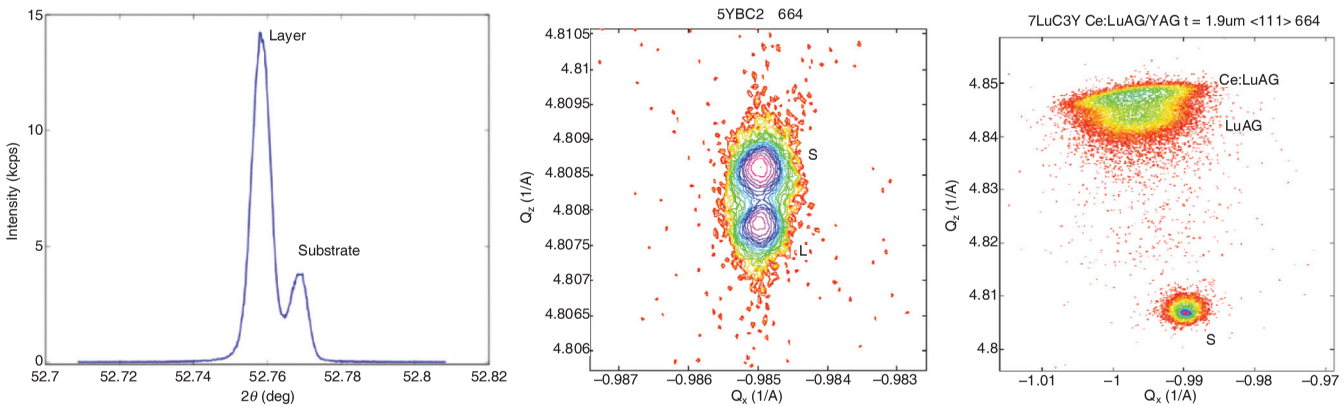

Figure 5.9 (a) 444 diffraction of 10.7 μm thick Ce:YAG film grown on (111) oriented YAG substrate from the PbO flux. (b) Asymmetrical reciprocal map of 664 diffraction of the same sample, z is direction normal to the film plane. A pseudomorphic film was grown on substrate, i.e. the in-plane lattice parameters of the film and substrate are the same; $a_{\perp}$ = 12.0114(1) Å, $a_{\parallel} = a_{subs}$ = 12.0093(1) Å. (c) Map of 664 diffraction of Ce:LuAG 13.4 μm thick film grown on (111) oriented YAG substrate from the PbO flux—a relaxed layer was grown: the lattice parameter of the film corresponds to that of the LuAG single crystal, $a_{\perp} = a_{\parallel}$ = 11.918(1) Å, a_{subs} = 12.009(1) Å. Reprinted from Ref. 4, Copyright 2010, with permission from Elsevier.

dislocations are not expected in the film/substrate interface and a macroscopic elastic strain is present in the film.

In the hetereoepitaxy, i.e., Ce:LuAG films grown on the YAG substrates or vice versa, due to their different compositions, an emergence of the film-substrate mismatch is expected. The prepared films were admittedly crack-free but they were relaxed and exhibited different growth morphology than the homoepitaxial films. The lattice mismatch between the substrate and the film was as high as $\Delta a = a_s - a_f = -0.09$ Å ($\Delta a/a = 0.8$ %). This value is too large for the pseudomorphic growth. It is worth noting that for iron garnets the condition for the mismatch is rather severe and the mismatch should not exceed ±0.02 Å to avoid cracking or faceting of films. At excessive mismatch the films do not even nucleate [31]. In contrast, the crack-free LuAG epitaxial films on YAG substrates were successfully grown in spite of large mismatch. In this case the films were completely relaxed and both the normal and in plane lattice parameters of a film and a substrate strictly differ. The RSM around the asymmetric diffraction 664 for Ce:LuAG film grown on (111) oriented YAG substrate from the PbO flux is shown in Fig. 5.9c. The lattice parameter of the Ce:LuAG film corresponds to that of LuAG crystal, $a = 11.916$ Å, while the measured parameter of YAG substrate is $a_s = 12.009$ Å. Therefore the misfit dislocations that release the misfit strain are in the film/substrate interface. This fact enables to grow rather thick heteroepitaxial garnet films. The RSM of the film diffraction is broad compared to that of the substrate, Fig. 5.9c, which shows that macroscopic defects are present in films. Nevertheless, the XRD proved that the films are of single garnet phase and the films exhibit a distinct (111) orientation. The other parameters of heteroepitaxial films, e.g. growth rates, concentration of cerium or impurity ions, optical and emission properties, decay kinetics, are quite comparable with those for the homoepitaxial films. The major difference between these two types of films is surface roughness, film/substrate interface and different growth morphology.

5.3.2 Optical Methods: Absorption, Photoluminescence, PL Decay Kinetics

The optical methods—absorption, PL, and PL decay method—are in principle the same as those for bulk sample measurement.

We mention here only some problems specific to thin-film measurements.

Photoluminescence (PL) spectroscopy. Mutual comparison of the emission spectra in an absolute way (i.e., comparison of PL intensities) of thin-film samples is problematic due to various geometric factors influencing the PL intensity, which are difficult to take into consideration, as waveguide effect, quality of the edge profile, surface quality. Especially scattering centers on the surface—ideal optical waveguide with emission from the edge in high-quality films with perfect surface morphology vs. intense emission from the rough surface of heteroepitaxially grown films. Nevertheless, the PL spectra can be reliably compared in a relative way (normalized spectra). When the PL spectra are to be compared in an absolute way, great care should be devoted to the elimination of the geometric and surface factors (such as surface quality and scattering centers on the surface, edge profile, thickness of films, etc.). In the PL experiments the substrate can be also excited, since the films are semitransparent in the visible and UV spectral ranges up to 200 nm. If the substrate contains intentional RE or TM impurities or color centers it can contribute to the measured signal.

Thermo stimulated luminescence (TSL) is important technique providing information on shallow defects (e.g., AD). However, only limited number of experiments were published in thin films [13] due to very weak signal from the film (several micrometers thick). Attention should be paid to filter out the signal from the substrate, which can be orders of magnitude higher, the best way is to polish the substrate out.

Scintillation decay kinetics of emission centers—very important and reliable method providing information on physical processes in the scintillator (on emission centers, traps, energy transfer, possible quenching centers, etc.). In epitaxial films decays excited by alpha particles or by electrons (CL decay) are the only possible ways.

5.3.3 Scintillation Properties

Radioluminescence spectroscopy (RL) excited by X-rays or by alpha particles, cathodoluminescence (CL) is excited by an electron beam.

Both RL and CL originate from host-to-activator energy transfer mechanism and characterize the steady state scintillation properties. The RL is measured under X-ray excitation usually at lower excitation voltage of 10 kV (just to decrease the penetration depth) which would ensure that the film is primarily excited and contribution of the substrate to the RL emission is suppressed as much as possible. However, low excitation voltage is at the expense of decreased signal-to-noise ratio. Absorption efficiency as a function of X-ray energy, in % of absorbed radiation, for several garnets and oxide scintillators is displayed in Fig. 5.10. It is evident that thin films are not suitable for detection of high-energy X-rays.

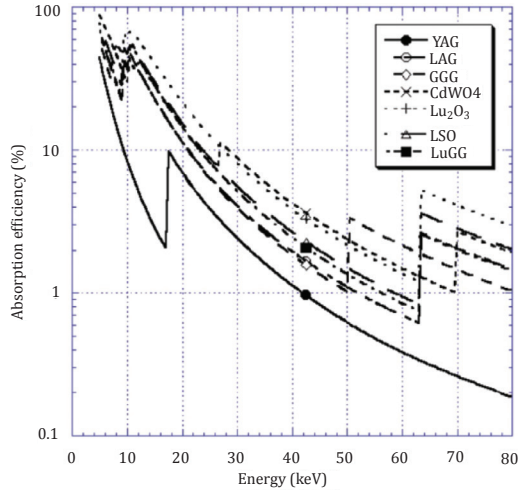

Figure 5.10 Absorption efficiency of oxide scintillators used for high-resolution X-ray imaging for 5 μm thick films. Reproduced from Ref. 19, with permission of the International Union of Crystallography.

The penetration depth of electrons [89] is significantly lower compared to α particles or X-rays and submicrons films can be reliably measured. Apparatus for cathodoluminescence characterization of materials is described in ref. [91].

5.3.4 LY Measurements of Scintillating Epitaxial Films

In this section we present analysis of light yield (LY) measurements of thin films using alpha particle excitation. The LY measurement of

epitaxial films must face a problem of very low thickness of the films, from ~1 μm up to a few tens of micrometers [4, 5, 92, 93]. Probability of photon interaction in the film is very low, probability of interaction in the substrate is much higher. Unfortunately, substrate generates scintillation response also. In case of thin films, penetration range of secondary electrons must be considered. The range is at least several tens of μm in LuAG or YAG for photons over 100 keV, greater than film thickness.

Low-energy photon radiation is not of practical use either. It is absorbed in the film almost entirely, but low energy leads to low response, few tens of photoelectrons at best for relatively high light yield. Problems are caused by low quantum efficiency, low photon collection efficiency and low number of scintillation photons. It is very hard to measure such low response precisely. Beta radiation sources face the same problem and they are not even monoenergetic.

On the other hand, penetration range of alpha particles R_α emitted by common radionuclides is from 10 to 14 μm in LuAG/YAG [41, 51]. Energy over 5 MeV ensures sufficiently high response, R_α is usually lower than film thickness. Alpha particles may be considered monoenergetic. Measurement chamber must be either evacuated or source must be in direct contact with the film [41, 51]. Vacuum offers better reproducibility and safety, "contact" is simpler, cheaper and allows measurement of response of films with thickness $d < R_\alpha$, see below.

Unfortunately, low R_α excludes usage of reflector. Scintillation photon collection efficiency diminishes and is hard to quantify. Usage of reference bulk crystals with known light yield is recommended. Otherwise, photoelectron yield for given geometry would be known only.

Experimental setup for light yield (photoelectron yield) measurement is almost the same as for bulk crystals, the application of alpha particle sources is the only one significant difference. In the detection unit a hybrid photomultiplier (HPMT) [94, 95] coupled with preamplifier, amplifier, multichannel analyzer and PC is used. Calibration of setup is done by dark pulses spectrum measurement [96].

Measured spectra usually contain one broad peak with very long tail on low energetic side. The peak can be fitted by Gaussian. Thus, photoelectron yield and energy resolution are obtained [41].

If R_α is longer than film thickness, two peaks arise in the spectrum, see Fig. 5.11 [41]. Higher energy peak (HEP) is created by alpha particles depositing entire energy in the film, see particles C and D in Fig. 5.12. Lower energy peak (LEP) is created by particles only passing through the film, as A and B in Fig. 5.12. If number of detected particles is N_{DET}, number of pulses in HEP N_{HEP}, then relative peak area $N_{HEP}/N_{DET} = d/R_\alpha$ [41].

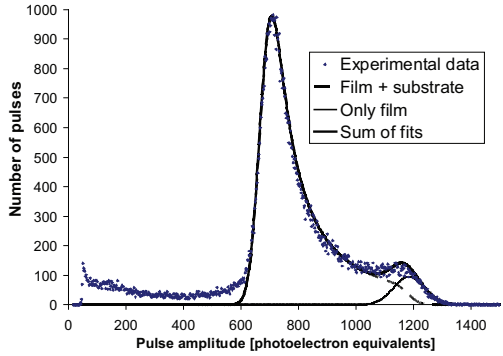

Figure 5.11 Spectrum of film with thickness below 2 μm fitted using equations (5.3) and $N_{HEP}/N_{DET} = d/R_\alpha$.

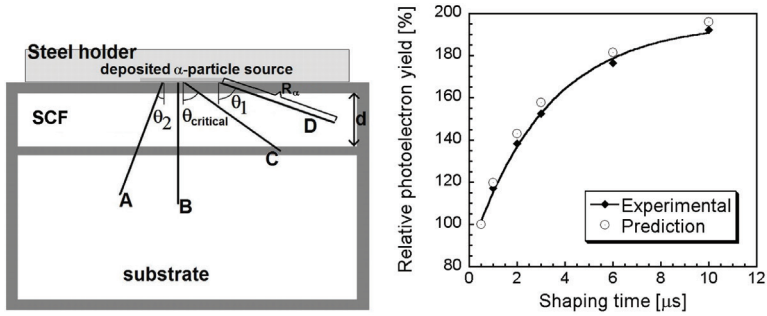

Figure 5.12 Left: Geometry of measurement. Particles C and D are depositing entire energy in the film, particles A and B are depositing part of the energy in the substrate. Right: Dependence of $PhY(t_s)/PhY(t_r = 0.5\ \mu s)$ on shaping time and the fit, see text for details. Results for LuAG:Ce bulk crystal.

Energy deposition of particles contributing in HEP is monoenergetic, response should be Gaussian. For LEP shape calculation, straight track of alpha particles, constant R_α and constant linear energy transfer (LET) were assumed, i.e., Bragg peak

was omitted. Last assumption is acceptable, because response per track length is not strongly dependent on LET for high LET.

Let S_r be the scintillation response, film photoelectron yield is PhY_f, substrate photoelectron yield is PhY_s, E_s is energy deposited in the substrate, E_f is energy deposited in the film, E_α is energy of alpha particle, and θ is the angle in Fig. 5.12. $S_r = PhY_f E_f + PhY_s E_s$.

For $\theta < \theta_{critical}$:

$$S_r = PhY_f \frac{d}{R\cos\theta} E_\alpha + PhY_s \left(E_\alpha - \frac{d}{R\cos\theta} E_\alpha \right) \tag{5.1}$$

The goal is to find dN/dS_r, i.e., distribution of number of pulses in dependence on response (channel number). If dN is a number of particles emitted in the angle from θ to $\theta + d\theta$, $dN = A \cdot t(2\pi/4\pi) \sin(\theta) d\theta$, where A is the source activity and t is time of measurement.

Now $dN/d\theta = (dN/dS_r)\cdot(dS_r/d\theta)$; $dN/dS_r = (dN/d\theta)/(dS_r/d\theta)$. Let us calculate $dS_r/d\theta$ from Eq. 5.1. Now dN/dS_r is obtained:

$$\frac{dN}{dS_r} = \frac{1}{2(PhY_f - PhY_s)} \frac{R_\alpha}{d} \frac{\cos^2\theta}{E_\alpha} At \tag{5.2}$$

$\cos\theta$ can be expressed from Eq. 5.1 and substituted in Eq. 5.2. Finally,

$$\frac{dN}{dS_r} = \frac{d}{2R_\alpha} E_\alpha \frac{(PhY_f - PhY_s)}{(S_r - PhY_s E_\alpha)^2} At \tag{5.3}$$

Equation 5.3 is valid for S_r from $(PhY_f E_\alpha d/R_\alpha + PhY_s E_\alpha(1 - d/R_\alpha))$, i.e., perpendicular penetration, to $PhY_f E_\alpha$, i.e., entire energy deposition. Equation 5.3 does not take into account imperfect energy resolution, but using a simple convolution, real spectrum could be calculated, see Fig. 5.11. Small discrepancies of experiment and calculation should be contributed to initial assumptions.

Decay kinetics is important source for information about processes in the scintillator. If one is not able to measure decay curves conventionally, photoelectron yield measurement is able to give rough estimation of decay kinetics in the time interval of few μs [41, 51]. At first, dependence of photoelectron yield on amplifier shaping time is measured (see Fig. 5.12, right). This dependence can be fitted by equation $PhY(t_s)/PhY(t_r = 0.5\ \mu s) = m_1 - m_2 \cdot \exp(-m_3 t_s)$, t_r is reference shaping time, usually 0.5 μs. Percentage of "fast" photons (with decay times below hundreds of nanoseconds) $K_{f/e}$ can be calculated as $K_{f/e} = 100\ (1 - m_2/m_1)$ [41].

There is one more complex and precise method: the convolution of one photoelectron response with decay kinetics. If channels in

decay curves measurement are short enough, i.e., one photoelectron response does not change significantly between channels i and i+1, pulse shape can be calculated as

$$R_k = \sum_{i=0}^{k} N_i \cdot RU_{k-i} \tag{5.4}$$

Where R_k is the response in time bin k, N_i is the number of photons emitted during time bin i, and RU_{k-i} is one photoelectron response in *k*-th bin, which started in *i*-th bin. It means that entire response is a sum of all one-photoelectron responses. Relative photoelectron yield $PhY(t_s)/PhY(t_r) = \max(R_k(t_s))/\max(R_k(t_r))$, t_r is reference shaping time, usually 0.5 μs.

Calculation of decay curve from $PhY(t_s)/PhY(t_r)$ uses following method. At first, $N_i = f(t,p_i)$ is assumed. Parameters p_i are then changed iteratively, until the best agreement of experimental and calculated $PhY(t_s)/PhY(t_r)$ is found. Type of $f(t,p_i)$ must be chosen a priori. Single or double exponential, or exponential + power are used mostly.

The number of parameters p_i must be lower than number of available shaping times and the information about decay kinetics is reliable only in the time interval between 0.5 and 20 μs approximately.

Deconvolution and convolution have been tested on several samples, one example is in Fig. 5.12 (right) and Fig. 5.13. Also, $LiCaAlF_6$:Eu sample with single exponential decay was measured. Decay time measured by decay curve experiment was 1.68 μs and decay time calculated by deconvolution was 1.61 μs.

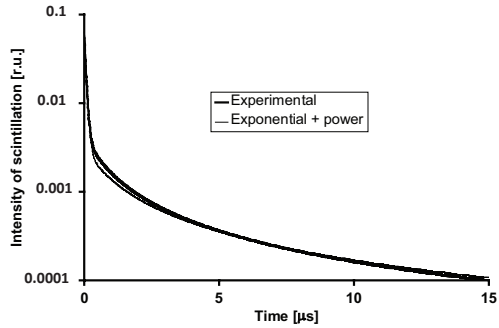

Figure 5.13 Comparison of measured decay curve with decay curve calculated using $PhY(t_s)/PhY(t_r = 0.5\ \mu s)$ measured dependence. Exponential + power decay function was assumed. Decay time of fast (exponential) component was assumed to be 60 ns.

5.4 Materials

Within the last two decades, a great number of oxide scintillators were prepared by the LPE; for review see [34, 97]. Main attention was paid to aluminum garnets [4, 5, 11, 30, 34, 52, 92], perovskites [3, 34, 98], and orthosilicates [2, 22, 34, 99–102]. Rare attempts were to grow other scintillators as ZnO [93, 103] or CdWO4 [104] were prepared by the LPE. The LPE was applied for production of waveguide solid state RE:YAG garnet lasers [34, 38, 39, 105]. A lot of oxide materials which are routinely prepared by other methods (Czochralski or Bridgman single crystals, polycrystals, solid state reaction or sol gel) were also grown by the LPE, for review until 1999 see ref. [34]. We shall not make here any exhausting survey but rather discuss some interesting material systems prepared by LPE. In Table 5.2 basic crystallographic properties of typical hosts are shown.

We shall focus here on scintillation properties of the most promising oxides especially Ce^{3+} and Pr^{3+} doped garnets, perovskites, and orthosilicates and compare their optical and scintillation properties with single crystal counterparts. These materials are non-hygroscopic, chemically stable, and have excellent optical and mechanical properties with large application potential. They have good light yield, fast scintillation response and adequate energy resolution—the properties of which have been incessantly improved. Luminescence and scintillation properties of above-mentioned SC materials have been recently described in several review papers [82, 106, 107] and references therein.

Ce^{3+} doped garnets, perovskites, and orthosilicates are considered as excellent and fast scintillator materials [82, 108, 109]. In the last decade Pr^{3+} doping has also been studied for even faster scintillators with comparable LY [110–113]. Doping with other RE ions, Tb, Eu, etc., provides very efficient PL and may be used for various phosphors in steady state applications, e.g., cathodoluminescent or X-ray screens [15, 29] where slow f–f emission in the millisecond time range is acceptable.

5.4.1 Garnets

Garnets have high-symmetry cubic structure with O_h^{10} space group, Table 5.2. The garnet structure is very flexible for cation substitution

due to the three cation sites of tetra-, octa-, and dodecahedral symmetry.

Application of YAG:Ce in SEM detection was proposed in 1970s [114], its scintillation properties were reported 20 years ago [8]. It is excellent detector of electrons in SEM and for soft X-rays. Isostructural LuAG:Ce have higher density and higher effective atomic number, Z_{eff}, and associated higher stopping power of the lattice and is more efficient for hard X-ray and gamma-ray detection.

YAG:Ce films and Ga and RE (Gd, Tb, Eu, Tm) substituted films were first grown by Robertson in Philips Laboratories in the beginning of 1980s from the PbO flux [15, 29, 115, 116] for the cathodoluminescence application. LuAG:Ce film grown on YAG substrate from the PbO flux was reported in 2002 [92]. During last 15 years great number of substituted aluminum garnets has been grown and tested for scintillation applications. However, the scintillation efficiency, such as the LY, of epitaxial films grown from the PbO flux was lower as compared to single crystals grown from the melt (Czochralski or Bridgman). It was soon recognized that the impurity ions coming from the flux, especially Pb^{2+}, represent the main problem since they form trap states and parallel channels of nonradiative recombination [88, 117, 118]. Furthermore, effective nonradiative energy transfer from Pb^{2+} ions to Ce^{3+} ions results in appearance of slower components in the luminescence decay kinetics of Ce^{3+} centers [119]. Therefore, alternative lead-free fluxes have been tested and developed. Practical application of the BaO and MoO_3 fluxes for growth of aluminum garnet films was first reported in 2008 [4, 5]. Especially the BaO flux appeared very promising for growth of Ce and Pr doped epitaxial films with significantly improved scintillation properties [4, 11, 12, 51, 52, 120, 121]. Recently, it has been demonstrated that the scintillation properties (LY, suppressed slow components) of the epitaxial films of multicomponent GAGG:Ce garnets grown from the BaO flux are comparable to those of the best single crystals counterparts with the LY of ~50 phot/keV [11, 121], see below.

In YAG:Ce and especially in LuAG:Ce single crystals a substantial slow component in emission is observed which negatively affect their scintillation performance. This "slow light" is related to various types of shallow traps, which contribute to electron/hole trapping processes. The most important intrinsic defects, degrading the scintillation performance, are antisite defects (AD), which result

in formation of shallow electron traps in the energy gap, and color centers related to oxygen vacancies [7, 13, 80]. Both AD and color centers are effectively suppressed during the LPE growth process due to the growth in oxidizing atmosphere and at significantly lower temperatures ~1000 °C.

TSL glow curves of single crystals and LPE films are compared in Fig. 5.14. In the LPE films the dominating TSL peaks at 120–170 K completely vanish. Furthermore, LPE samples show an absence of even deeper traps related to TSL peaks at 240 K and mainly at 280 K. Traps related to the latter peak may have detrimental influence to the overall stability of scintillator characteristics since the peak position is close to room temperature.

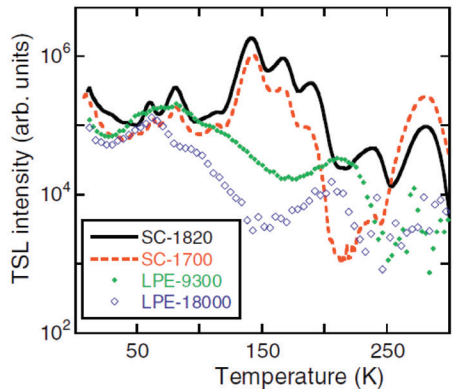

Figure 5.14 TSL glow curves of the LuAG:Ce single crystals, SC, and epitaxial films, LPE, grown from the PbO flux after X-ray irradiation with similar doses at 10 K. Reprinted from Ref. 13, Copyright 2005, with permission from John Wiley and Sons.

In Ce^{3+} and Pr^{3+} doped YAG and LuAG intense and fast luminescence originating from parity allowed 5d–4f transitions is observed in the transparency region of aluminum garnets. This shows on very good coupling of these ions to the lattice. Owing to high crystal field at c-sites in garnets the maximum of 5d broad band emission is located in the green-yellow range with maximum at 510–530 nm and at 308–320 nm in Ce^{3+} and Pr^{3+} ions, respectively. The scintillation decay is fast with decay times of ~60 ns and ~20 ns for Ce and Pr doping, respectively. The thermal quenching is well above the RT, for YAG/LuAG:Ce >700 K [122], for Pr:LuAG > 400 K and in Pr:YAG > 250 K [113].

However, because of their large ionic radii (Ce – 1.143 Å and Pr – 1.126 Å) only low content of Ce and Pr, rarely exceeding 1% in single crystals, is reached. Somewhat higher Ce concentration is obtained LPE films, especially those grown from the BaO flux [4, 5]. However, Ce and Pr concentration is constrained due to their very low segregation coefficients (Table 5.1), which would require high excess of Ce and Pr in the melt. The Ce content can be increased by growth at high supercooling or at lower growth temperatures (Fig. 5.3). However, this is not a very effective way—in films grown from PbO owing to the simultaneous increase of quenching Pb^{2+} ions (Fig. 5.15), and in films grown from BaO, the increase in the flux viscosity at temperatures below 1000°C and consequent worsened surface morphology is the main constraint.

The position of the 5d–4f emission band depends to some extent on the host composition—generally for large RE ions substituted in c-sites (Gd, Tb) the emission maximum of Ce^{3+} ions is red shifted towards 560 nm, for small RE ions (Lu) the blue shift is observed with maximum at 510 nm. The substitution of Ga ions causes blue shift of the emission and decrease of crystal field 5d splitting, presumably due to increased symmetry in c-sites of YGG compared to YAG; for details see Refs. [116, 123–126].

5.4.1.1 Ce^{3+}-doped YAG and LuAG

Comparison of scintillation properties of bulk Czochralski grown single crystals and epitaxial films of Ce-doped YAG and LuAG is shown in Table 5.3. The most obvious is the presence of strong slow component in scintillation and lower photoelectron yield in bulk crystals—e.g., in Ce:LuAG almost 70% of light of the Ce^{3+} emission center itself is related to the delayed radiation recombination [6]. This suggests a considerable influence of several traps of different origin and different energy depths, which participate in charge carrier trapping processes, cf. also Fig. 5.14. The antisite defects, i.e., Y or Lu situated at the octahedral Al site, $Lu(Y)_{Al}$, are often considered as an origin of the shallow traps in YAG or LuAG crystals [7]. These defects are strongly reduced in epitaxial films [13, 30]; however, they are not suppressed completely [71, 127]. The wide spectral band with slower decay situated near 300 nm in the bulk Cz-grown crystals was ascribed to the exciton localized near the $Lu(Y)_{Al}$ antisite defect [27].

Table 5.3 Comparison of scintillation properties of Czochralski single crystals and epitaxial Ce-doped YAG and LuAG films. τ_{PL} (530), photoluminescence decay time of Ce^{3+} emission; τ_{SC} (530), scintillation decay times of fast and slow components of Ce^{3+} emission for various excitation sources, CL – cathodoluminescence. T_G – growth temperature, N_{phe} –photoelectron yield excited by α particles at shaping time of 0.5 μs (increase of N_{phe} at 10 μs shaping time)

	YAG:Ce		LuAG:Ce		Refs.
	Single crystal	**Epitaxial film**	**Single crystal**	**Epitaxial film**	
τ_{PL} (530 nm) [ns]	62	60	54	54–56	[5, 6]
τ_{SC} (530 nm) [ns]:					
α excitation, 5.49MeV	68(35%) + 247		58(40%) + 1000		[7, 8]
γ excitation, 662 keV	96 + 230 + 1400	*	61 + 510 + 2400	*	[23]
X-ray excitation, 25 kV			58(30%) + 150 + 1600		[27]
synchrotron, 150 eV		81		10 + 70	[30]
CL, 10 keV	75			52	[10]
N_{phe} [phe/MeV] (N_{phe} increase)	320–360 (20%)	330–400 (15–30%)	380 (70%)	260–315 (50–70%)	[41] [42]
T_G [°C]	1970	950–1070	2020	950–1070	

* γ excitation cannot be used for thin epitaxial films because of low absorption.

The optical absorption spectra of Ce:LuAG films grown on LuAG and YAG substrates from the same PbO flux at various supercooling are displayed in Fig. 5.15. The first two low energy 4f–5d (Ce^{3+}) absorption bands are clearly resolved at 445 and 345 nm, but remaining three spectral bands situated below 280 nm are overlapped by Pb^{2+} absorption. The absorption peak near 262 nm and strongly increased absorption below 250 nm originate from allowed transitions in Pb^{2+} impurity ions [119, 128]. The peak at 262 nm is missing in films grown from BaO and MoO_3 fluxes [5]. It is worth noting that the content of both the Ce and impurity ions strongly depends on the growth conditions. It is obvious that concentrations of both Ce^{3+} and Pb^{2+} ions increase with supercooling, cf. peaks at 445 nm and 262 nm in Fig. 5.15. Undesirable consequence of Pb admixture is strongly increased absorption in the deep UV range which has negative impact on the emission efficiency of scintillator, especially those with luminescence in the UV (e.g., LuAG:Pr or perovskite and orthosilicate scintillators described below).

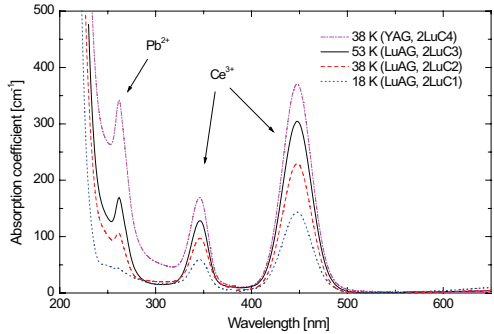

Figure 5.15 Optical absorption coefficient of epitaxial Ce:LuAG films grown from the same PbO flux under various undercoolings (substrates and undercooling are in the legend), saturation temperature T_S = 998 °C. Both Ce and Pb concentrations increase with increasing undercooling. Reprinted from Ref. 4, Copyright 2010, with permission from Elsevier.

The PL excitation and emission spectra of YAG:Ce and LuAG:Ce epitaxial films grown from both PbO and BaO fluxes along with YAG:Ce single crystal for comparison are displayed in Fig. 5.16. The spectra can be compared in an absolute way. The structure in the excitation spectra comes from the Ce^{3+} ions and it shows a close correspondence with the absorption curves. The broad emission

band in the PL emission spectra has maximum around 520 nm. The maxima of the Ce peaks are mutually slightly shifted due to the different crystal fields of the host crystals. Generally, films grown from the BaO flux exhibit substantially higher intensity of PL emission compared to the PbO grown films. This can be partly explained by higher Ce content in the BaO grown films. Furthermore, the Pb^{2+} ions compete for the charge carrier capture with the Ce^{3+} ions and form additional nonradiative de-excitation channel which leads to quenching of the luminescence [88, 117, 119].

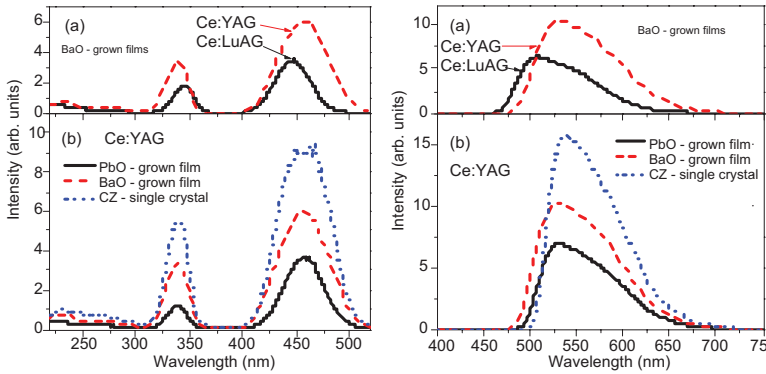

Figure 5.16 Left: excitation spectra (λ_{em} = 520 nm), right: emission spectra (λ_{ex} = 340 nm) of epitaxial YAG:Ce and LuAG:Ce films grown from PbO and BaO fluxes, also YAG:Ce single crystal is shown for comparison, [5].

The photoluminescence and scintillation decay curves of a LuAG:Ce film grown from the BaO flux are shown in Fig. 5.17. The PL Ce^{3+} related decays of films grown from the lead-free BaO flux exhibit one-exponential dependence over three orders of magnitude with the decay times t = 52–56 ns. These values are in close relation with those reported for high purity Cz single crystals. The inspection of Ce decay curves of films grown from the PbO flux shows some distortion [4, 5, 21] and additional fast component in the PL kinetics indicates nonradiative transfer of energy from the Ce^{3+} relaxed excited $5d_1$ state towards an impurity ion or nearby defect state [5, 6].

Spectrally unresolved cathodoluminescence decay is shown in Fig. 5.17. The decay is evidently multicomponent. The fundamental fast exponential component of 52 ns correlates with the PL decay

of 5d–4f(Ce^{3+}) emission. At longer times, >300 ns, the decay can be approximated by power law function $\propto t^{-p}$, where p is a constant [121] and can be correlated with tunneling of a trapped electron to a nearby recombination center [129, 130]. De-excitation of an electron captured on a virtual trap can include also thermal ionization of shallow traps, which may occur simultaneously with tunneling. The possible pathways are discussed in more detail in [120, 121].

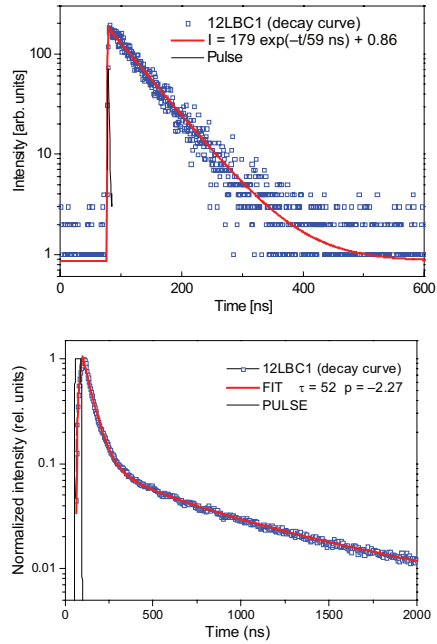

Figure 5.17 Decay kinetics of LuAG:Ce epitaxial film grown from the BaO flux; left: the PL decay, λ_{ex} = 340 nm, λ_{em} = 510 nm; right: spectrally unresolved e-beam excited scintillation decay. The solid lines are convolutions of excitation pulses with 1-exp decay (PL decay) and 1-exp decay with power law function (scintillation decay), for details see the text.

5.4.1.2 Ce^{3+}-doped multicomponent garnets

Recently, the "band-gap engineering" strategy was adopted to reduce the negative effects of shallow traps in bulk garnet crystals grown from the melt [123, 124, 131, 132]. Using the substitution of Ga and Gd ions into LuAG:Ce, the bottom of the conduction band is lowered, due to admixture of 4s(Ga^{3+}) states, and simultaneously the crystal

field splitting of the excited 5d states is enlarged, due to Gd-induced decreased CF symmetry in c-states. This approach leads to strong suppression of the trapping effects, which degrade the scintillation response [133]. The scintillation properties of multicomponent $(Lu,Y,Gd)_3(Al,Ga)_5O_{12}$:Ce single crystals or ceramics are much better in comparison with LuAG:Ce or YAG:Ce. Very high light yield approaching 50 photons/keV, excellent energy resolution, and low afterglow were observed in bulk crystals [134–136]

The LPE technology was adopted also for production of multicomponent garnet films [63, 137, 138]. The first results in samples grown from the PbO flux were rather ambivalent. Some improvement of light yield and energy resolution was observed but any positive role of Ga admixture, observed in bulk crystals, was not found in films due to different origin of traps in epitaxial films which are connected likely to the Pb^{2+} impurities [63, 137].

Excellent scintillation properties were, however, very recently demonstrated in epitaxial garnet films $(Lu,Gd)_3(Al,Ga)_5O_{12}$:Ce grown from the BaO flux [11]. Compared to high quality bulk crystals with analogous composition, the films with optimized composition exhibit similar values of α-excited photoelectron yield and similar energy resolution. The obtained values of the LY were the highest in garnet epitaxial films exceeding at least two times the values previously reported for LuAG/YAG:Ce [41, 51, 53].

In Fig. 5.18 the Ce^{3+} -related emission and excitation PL spectra and X-ray excited RL spectra are shown demonstrating significant increase of the emission intensity in multicomponent GdGaLuAG:Ce films.

Photoluminescence 5d–4f(Ce^{3+}) decays and spectrally unresolved α-particle excited scintillation decays are shown in Fig. 5.19. The PL decay times of 5d(Ce) emission in GdYAG/GdLuAG:Ce are not affected by Gd substitution into these hosts. The PL decays are strictly one exponential with decay times 61 and 56 ns in Ce:GdLuAG and Ce:GdYAG, respectively, for Gd content up to 50% [63]. Due to Ga co-doping the decay time partially decreases and weak faster component ~20–30 ns appears in the PL decays indicating energy transfer from the 5d states due to beginning of the thermal ionization. Two-exponential decay was observed in all heavily Ga substituted samples. The main fast component of the scintillation decays under α-particle excitation was within 60–100 ns [11] corresponding to Ce^{3+} centers.

Another important progress of multicomponent garnets being considerable reduction of slow decay components in microsecond

– millisecond time ranges. Likewise the measured afterglow of the films is very low, reaching the value around 0.1% [11].

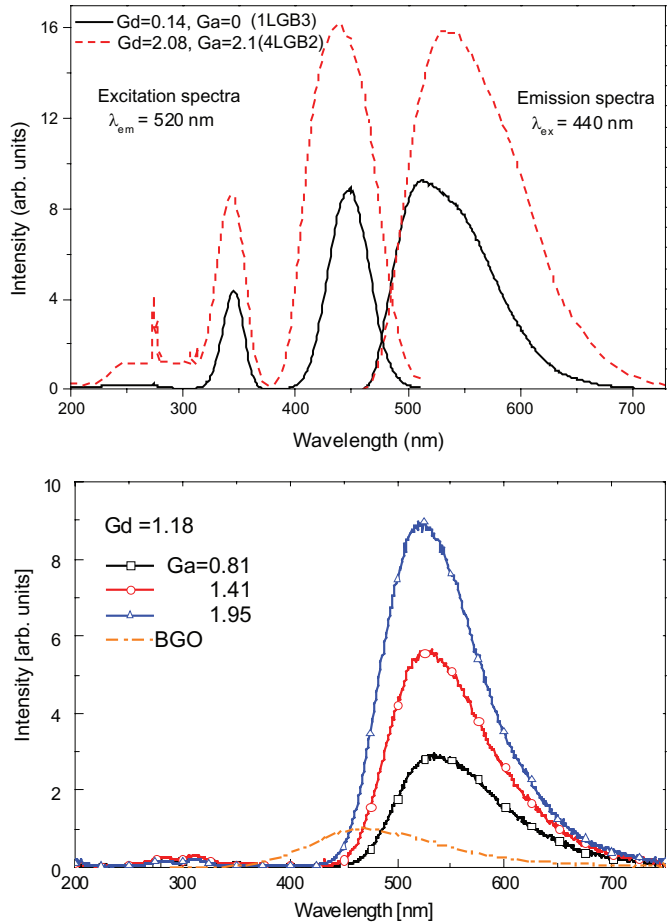

Figure 5.18 Emission and excitation spectra of epitaxial films (above) and X-ray excited RL spectra (below) for $Lu_xGd_{3-x}Ga_yAl_{5-y}O_{12}$:Ce samples with various content of Gd and Ga. Reprinted from Ref. 11, Copyright 2015, with permission from American Chemical Society.

The photoelectron yield measured under α-particle excitation of several epitaxial films exceeded 800 phels/MeV at 1 μs shaping times, the value quite comparable with multicomponent single crystals with gamma excited LY of 50 photons/keV, Fig. 5.20. These are the

highest values ever reached in garnet epitaxial films, exceeding 2–3 times those measured in LuAG:Ce, YAG:Ce epitaxial films. The best scintillation performance was observed in films at higher Ga ($1.8 < y_{Ga} < 3$) and Gd ($x_{Gd} > 1.8$) concentrations, Fig. 5.20. Thermal quenching starts at Ga concentrations $y > 3$, and luminescence is completely quenched above $y > 4$ at RT. The optimal Gd content is $1.8 < x < 3$ when slow f–f(Gd) emission at 312 nm is completely suppressed due to concentration quenching.

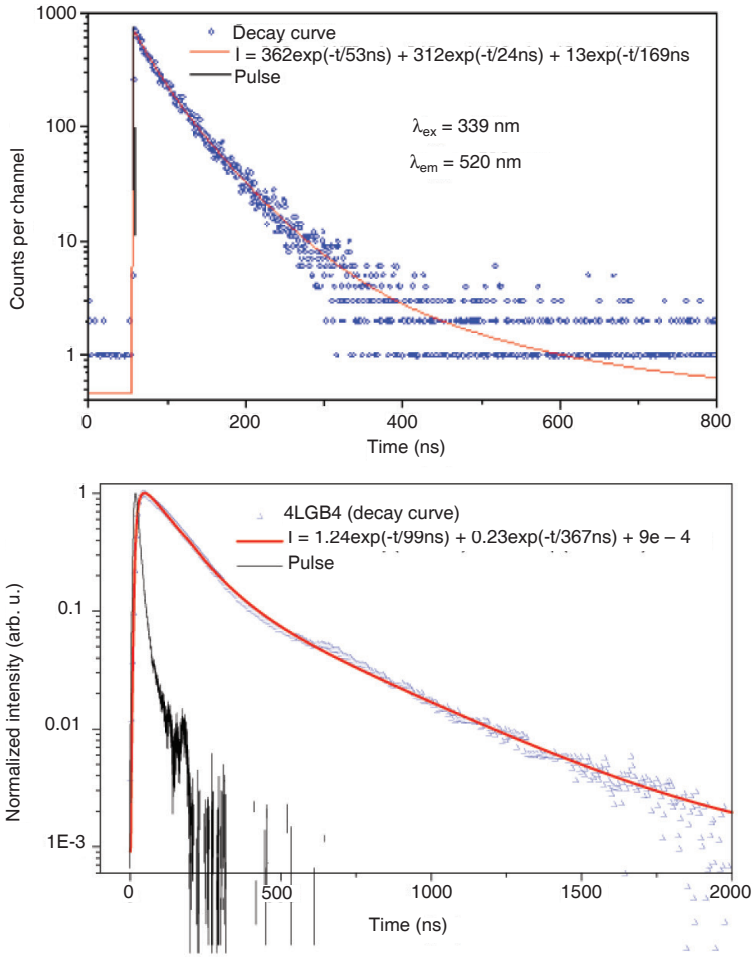

Figure 5.19 PL decay (above) and spectrally unresolved α-excited scintillation decay curves (below) of for $Lu_xGd_{3-x}Ga_yAl_{5-y}O_{12}$:Ce sample. Reprinted from Ref. 11, Copyright 2015, with permission from American Chemical Society.

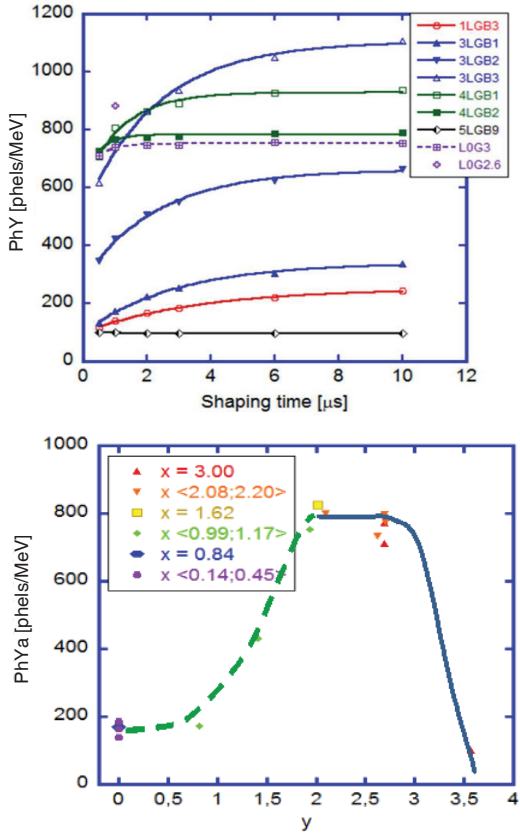

Figure 5.20 Dependence of the α-particle excited photoelectron yield on shaping time (above) and dependence of α-excited photoelectron yield on Ga content for some $Lu_xGd_{3-x}Ga_yAl_{5-y}O_{12}$:Ce films (below). Sample LOG3 in the left panel is reference GAGG:Ce single crystal wit LY of 50 phot/keV. Lines are only to guide the eye. Reprinted from Ref. 11, Copyright 2015, with permission from American Chemical Society.

In multicomponent garnets the role of Ga substitution is essential in suppression the shallow traps [133]. Most of excitation energy is, however, captured by heavy Gd ions. The nonradiative energy transfer from the Gd^{3+} sensitizer to Ce^{3+} activator ions was proved in (Ce, Gd) co-doped YAG and LuAG [139]. Such energy transfer is beneficial just for significant increase of scintillation efficiency in heavily Gd doped GAGG:Ce scintillators when the excitation energy

migrating over the Gd sublattice is effectively transferred to Ce^{3+} activators [63, 120, 139]. The excitation energy migrates over the Gd^{3+} sublattice and (provided it is not lost at trap states originating, e.g., from structural defects or impurities) it is finally captured by Ce^{3+} ions and subsequently released by their characteristic green–yellow emission. The side effect of the fast migration is concentration quenching of slow f–f(Gd) emission at Gd content $x_{Gd} > 1.8$ at RT.

5.4.1.3 Pr^{3+}-doped garnets

Pr^{3+} doped LuAG and YAG with the dominant 5d–4f emission in the UV range between 300 and 400 nm belong to the family of fast (< 20 ns decay time), high performance (LY > 20 phot/MeV) complex oxide scintillators [110, 113, 140–145]. However, the epitaxial garnet YAG/LuAG:Pr films grown from the PbO flux [146, 147] suffer from serious negative influence of Pb^{2+}impurities, cf. previous section, and their scintillation performance was low. It was soon recognized that lead-free flux is necessary for the growth of epitaxial films. Here we review the scintillation properties and achievements of LuAG:Pr and LuAG:PrSc epitaxial films which were grown exclusively from the BaO flux [12, 52]. The reason for Sc,Pr codoping follows from expected LY increase due to energy transfer from Sc to Pr, and from the effort to suppress also the slow scintillation component in the decay kinetics.

The excitation and emission spectra of LuAG:Pr film are shown in Fig. 5.21a left. The broad emission double peak which dominates in the UV range with the main maximum at 308 nm originates from parity allowed interconfigurational 5d–4f transitions. Narrow 4f–4f transition observed near 480 and 615 nm are very weak. Almost all the emission in LuAG:Pr is located in the UV spectral range between 300 and 400 nm; integral intensity of the slow f–f emission is only 4%. The broad 5d(Pr^{3+}) bands in the excitation spectra at 240 and 282 nm are closely related to the absorption ones, Fig. 5.22 left. All these PL features of LuAG:Pr are virtually identical to those observed in single crystals.

Slow scintillation component in LuAG exists due to retrapping migrating electrons at shallow electron traps [143, 148]. The Pr^{3+}–Sc^{3+} codoping may speed up the scintillation response, because Sc^{3+} ions could simplify the energy migration towards Pr^{3+} centers due to good overlap of the Sc-related emission (Sc-trapped exciton) at around 275 nm with the 4f–$5d_1$ absorption band of Pr^{3+} center at 280 nm, Fig. 5.22.

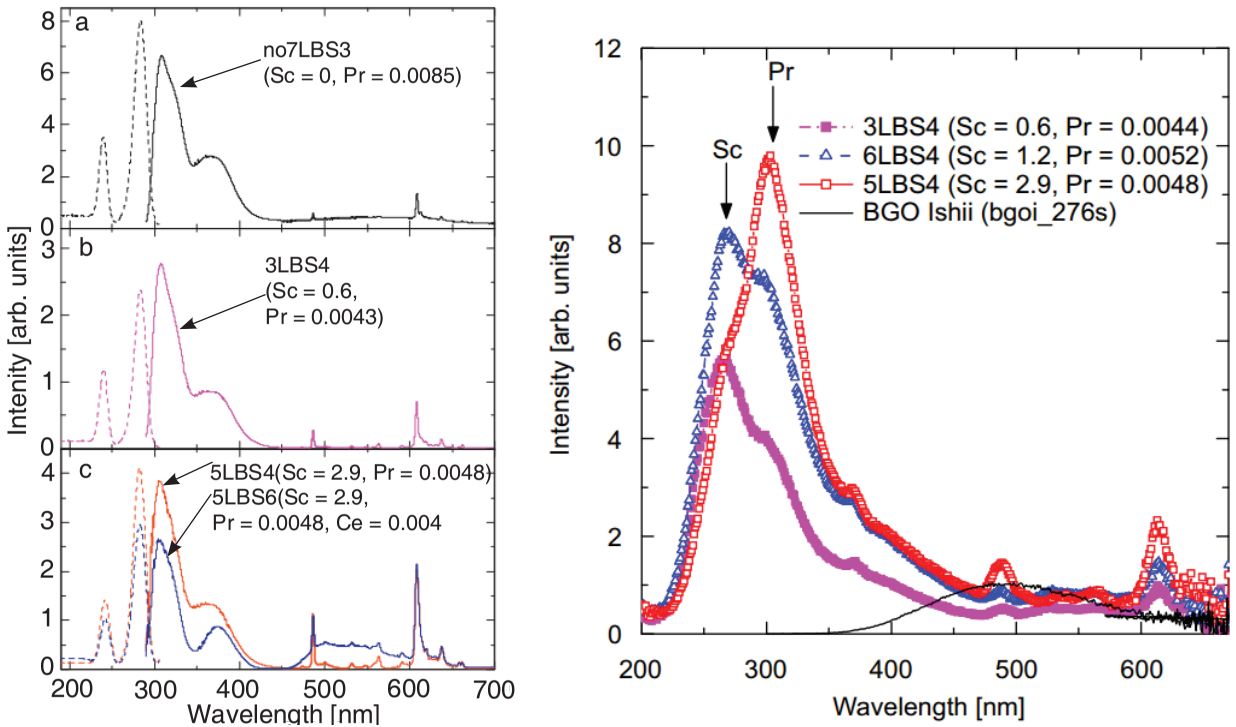

Figure 5.21 Left: PL excitation (λ_{em} = 308 nm) and emission (λ_{ex} = 282 nm) spectra of epitaxial LuAG:Pr (a) and co-doped LuAG:PrSc, LuAG:PrScCe (b, c) epitaxial films grown from BaO flux, Right: X-ray excited RL spectra of LuAG:PrSc films with various content of Sc. Reprinted from Ref. 12, Copyright 2011, with permission from Elsevier.

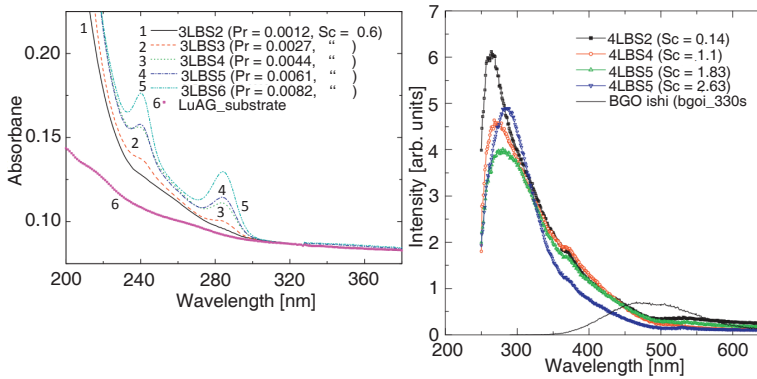

Figure 5.22 Left: Absorbance of ScPr co-doped LuAG epitaxial layers with 0.6 at% of Sc and Pr content specified in the legend grown on LuAG substrates; Right: X-ray excited radioluminescence spectra of LuAG:Sc epitaxial films. The RL of reference BGO crystal is also shown. Concentrations of Sc are shown in the legend. Reprinted from Ref. 12, Copyright 2011, with permission from Elsevier.

The PL spectra of ScPr co-doped LuAG films are shown in Fig. 5.21b left. Any Sc related emission is not observed. Additional Ce^{3+} co-doping, sample LuAG:ScPrCe in Fig. 5.21c left, however, partly quenches the UV emission of Pr^{3+} ions and Ce-Pr co-doping is useless for scintillation applications.

The X-ray excited RL spectra of co-doped LuAG:ScPr films are displayed in Fig. 5.21 right. The major Sc^{3+} and Pr^{3+}-related peaks are situated at 280 and 308 nm, respectively. The most remarkable feature of Sc co-doping is significant increase in intensity of the Pr^{3+} peak at 308 nm with increase in Sc content while the Pr content almost does not change, cf. Fig. 5.21 right. This notable dependency was explained by energy transfer from sensitizer Sc^{3+} to activator Pr^{3+} ions.

The Sc co-doping does not influence 5d–4f(Pr^{3+}) decay kinetics, Fig. 5.23 left. The dominating decay time, 18–20 ns, is in close relation with that reported for single crystals [113].

The photoelectron yield (PhY), of LuAG:PrSc films measured under alpha particle excitation for different shaping times is shown in Fig. 5.23 right. In films with optimized Sc content, $0.05 < x_{Sc} < 0.2$, the PhY exceeds the reference single crystal LuAG:Pr. Furthermore, the film is much better at shortest shaping times and its time dependence is also significantly improved.

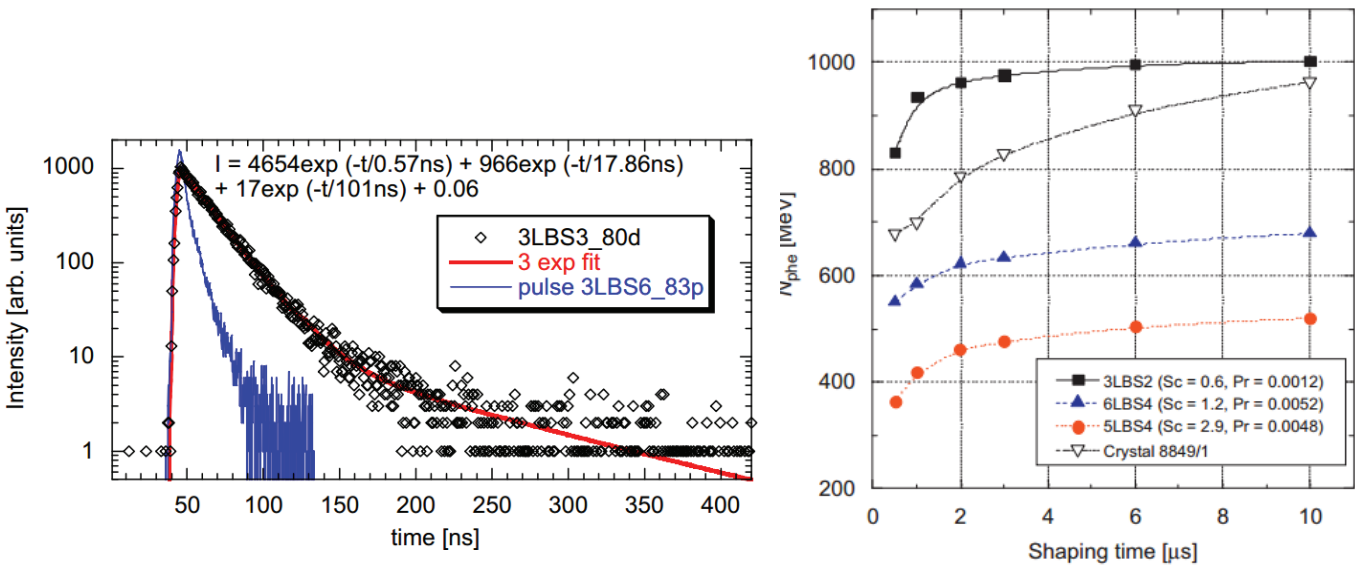

Figure 5.23 Left: Photoluminescence decay of PrSc-doped LuAG epitaxial film measured at Pr^{3+}(5d–4f) emission, λ_{em} = 320 nm and λ_{ex} = 282 nm; Right: Photoelectron yield *N*phe per 1 MeV at different shaping times under alpha particles (^{239}Pu) excitation of ScPr:LuAG epitaxial films, reference single crystal LuAG:Pr, sample 8849/1 is shown also. Reprinted from Ref. 12, Copyright 2011, with permission from Elsevier.

Co-doping of Sc^{3+} and Pr^{3+} thus appears as a suitable way of preparing high figure-of-merit scintillating films, even though optimum concentrations are rather critical.

Similar approach was also used for development of efficient Tb-Sc co-doped LuAG phosphors [20, 26]. Tb-doped garnets display intense f–f emission lines between 480 and 600 nm (at higher doping, 2–15 %) with dominant green emission at 543 nm, Fig. 5.24. Co-doped LuAG:TbSc shows improved PL and RL properties compared to LuAG:Tb. Furthermore, the Tb^{3+} doping quenches the host and Sc-related emissions situated in the UV range. Enhanced material performance can be understood as energy transfer from Sc sensitizer to Tb activator ions, due to the overlap of Sc-related emission and Tb(5d) absorption spectral bands.

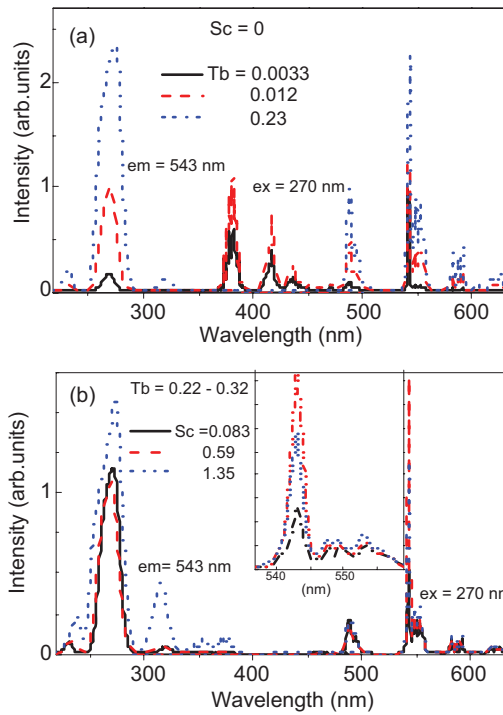

Figure 5.24 Photoluminescence excitation spectra at λ_{em} = 543 nm ($^5D_4$) and emission spectra excited at 5d(Tb^{3+}) band, λ_{ex} = 270 nm. (a) Tb:LuAG epitaxial films for several concentrations of Tb, (b) TbSc:LuAG films for various concentrations of Sc, see also Ref. [20].

5.4.2 Perovskites

Ce^{3+}- and Pr^{3+}-doped perovskites YAP/LuAP represent very fast scintillators with 5d–4f decay times of 18 ns [149] and 8 ns [1, 150, 151], respectively. YAP:Ce is excellent scintillator in SEM detector [152]. The LY of YAP:Ce about 20 000 ph/MeV was reported [96, 151, 153, 154], however, it is decreased in LuAP:Ce to half of that value due to shallow traps [155]. The LY of the best YAP:Pr is about 80% of that of YAP:Ce [1]. This suggests the presence of delayed radiative recombination processes. Most of the scintillation losses in these samples are due to shallow short-lived traps [156] and various charge carrier trapping centers, color centers, and yttrium antisite defects Y_{Al} directly proved by NMR [157], which play a major role in decreased LY.

Basic parameters of YAP/LuAP host systems are summarized in Table 5.2.

LuAP single crystal is difficult to grow from the melt due to instability of its perovskite phase (often twin formation and garnet phase appearance). The scintillation properties of more stable mixed (LuY)AP:Ce system is, however, significantly worsen compared to the end compounds due to increased content of slow components [155, 158].

On the other hand, both rare earth doped YAP, LuAP or TbAP epitaxial films were successfully grown onto YAP substrate from the PbO flux [34, 159]. The perovskite films are grown under similar conditions as garnets—the PbO/B_2O_3 ratio is chosen ~12 : 1, Y(Lu)/Al is close to stoichiometric ratio 1 : 1 in order to stabilize the perovskite phase and CeO_2 is in excess due to low Ce segregation coefficient, $k_{Ce} \sim 0.01$. At growth temperatures around 1000°C the growth rate is 0.5–1 μm/min [98].

Fundamental problem of perovskite films grown from the PbO flux is their contamination by Pb^{2+} ions due spacious crystal sites of 12 fold coordination, which is more favorable for positioning of large lead ions as compared to garnets. The Pb^{2+} ions quench the 5d–4f emission of Ce^{3+} and Pr^{3+} ions and significantly decrease the LY. Reported LY of the YAP:Ce epitaxial films grown from the PbO flux is < 10 % of the SC counterparts [3, 99, 147].

YAP and (YLu)AP epitaxial films grown from the lead-free BaO-B_2O_3-BaF_2 flux [3, 18] provide better emission and scintillation characteristics in spite of their worse structural and surface quality

compared to PbO-grown films [3]. Although the LY of BaO-grown films is higher compared to those grown from the PbO flux, it is still far from the SC counterparts (4–15× lower) and growth from the BaO flux has potential for further development.

In the following paragraphs scintillation properties of most promising perovskites YAP and LuAP doped by Ce^{3+} and Pr^{3+} ions grown from the both fluxes are described.

5.4.2.1 Ce^{3+}-doped YAP/LuAP

The absorption spectra of the YAP:Ce and LuYAP:Ce films grown from the PbO and BaO are displayed in Fig. 5.25. In the UV range below 260 nm, the samples grown from BaO flux (curves 1 and 3) show much lower parasitic absorption than those grown from PbO flux. The strong absorption below 260 nm is connected primarily with Pb^{2+} impurity ions and originates from $^1S_0 \rightarrow {}^3P_1(Pb^{2+})$ transitions ions [128]. The split band centered around 290 nm is due to the $4f^1(^2F_{5/2}) \rightarrow 5d_1$ transitions of the Ce^{3+} ions [160].

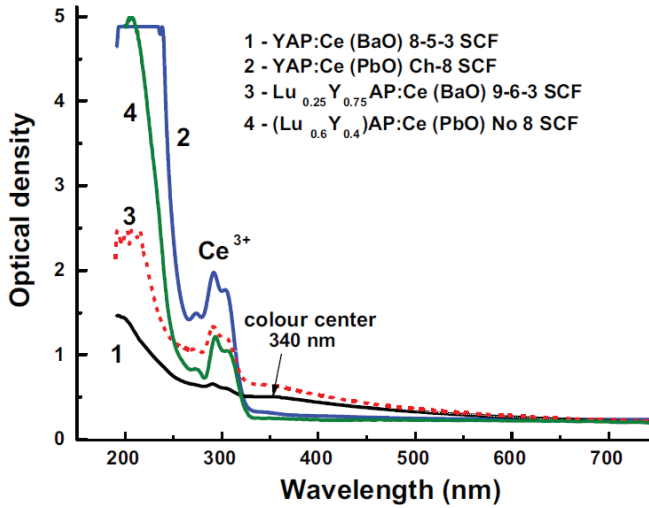

Figure 5.25 Absorption spectra of Ce^{3+}doped YAP:Ce and LuYAP:Ce films grown from BaO and PbO fluxes. The concentration of CeO_2 in the melt was 2 mol% (1,3) and 13–15 mol% (2,4). Reprinted from Ref. 18, Copyright 2013, with permission from Elsevier.

The CL spectra of YAP:Ce films grown from PbO and BaO fluxes are compared in Fig. 5.26. The emission bands centered at around

~375 nm originate from $5d_1$–$4f^1(^2F_{5/2,7/2})$ radiative transitions in the Ce^{3+} ions. However, in films grown from PbO this Ce^{3+}- related emission is overlapped with the emission of single and dimer Pb^{2+} centers [88]. This resulted in observed wider emission band of films grown from PbO, curve 1 and the inset in Fig. 5.26.

The effect of Pb^{2+} ions in the emission spectra is demonstrated in Fig. 5.27, where undoped YAP (BaO) and YAP:Pb (PbO) doped by intentional Pb impurities are compared. The low intensive luminescence in the UV and visible ranges of YAP (BaO), Fig. 5.27a, are most probably connected with the Ce^{3+} trace impurity and host defect emission centers, respectively [3]. The emission of YAP:Pb films is orders of magnitude higher, Fig. 5.27b, and is related to the Pb impurity and to various contributions in UV and vis ranges; for details see, e.g., Refs. [88, 117, 118, 157, 161].

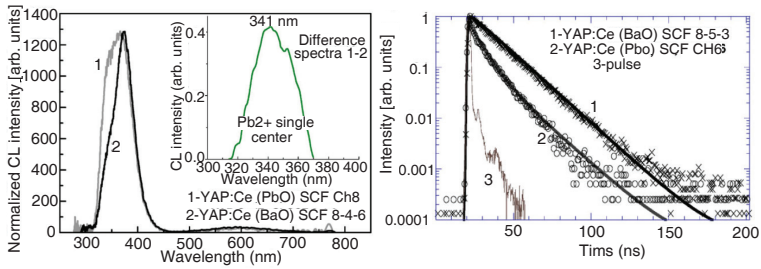

Figure 5.26 Left: Normalized CL spectra of YAP:Ce epitaxial films at 300 K grown from the PbO (1) and BaO (2) fluxes; inset: difference between the spectra; Right: the PL decay kinetics of Ce^{3+} luminescence in YAP:Ce grown from the BaO (1) and PbO (2) fluxes under excitation in the Ce^{3+} absorption band at 300 nm. The decay times from the exponential fits: τ = 15.7 ns and (6.5 + 16.1) ns for respective BaO and PbO grown samples. Reprinted from Ref. 3, Copyright 2009, with permission from John Wiley and Sons.

Typical PL decay kinetics of YAP:Ce films grown from BaO and PbO are shown in Fig. 5.26 right. The single-exponential decay up to four orders of magnitude is obtained for BaO-grown YAP:Ce films and the average decay time for several samples is 16±1 ns. Such values are close to typical decay time (17–18 ns) SC cozunterparts [107].

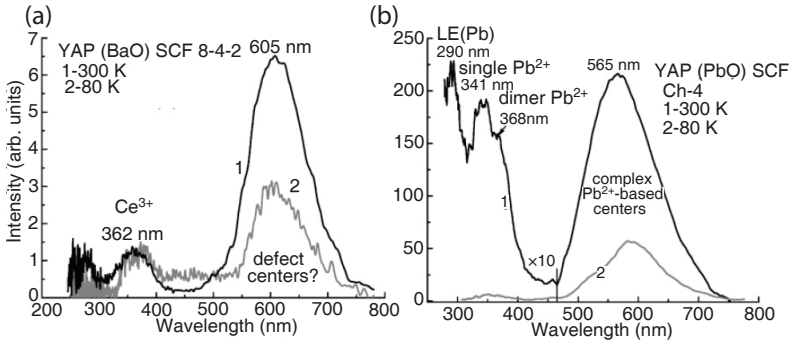

Figure 5.27 The CL spectra of undoped YAP grown from BaO (a) and PbO (b) fluxes at 80 and 300 K. Spectra in both panels can be mutually compared in an absolute way. Reprinted from Ref. 3, Copyright 2009, with permission from John Wiley and Sons.

Visible acceleration of the PL decay kinetics is observed in YAP:Ce films grown from PbO, curve 2 in Fig. 5.26 right. The decay curve can be quantitatively approximated by the superposition of two components with decay times of 6.5 and 16.1 ns. This can be explained by energy transfer from Ce^{3+} ions to the Pb^{2+}-based centers (Pb^{2+} dimer or more complex Pb^{2+} centers) [119]. The excitation of these Pb centers is possible due to the overlap of their excitation bands with the 350–370 nm Ce^{3+} emission band in YAP:Ce. Integration of decays shows that in films grown from PbO the losses due to energy transfer away from Ce^{3+} $5d_1$ relaxed excited state are more than 50% [3]. Such huge losses partly explain low scintillation efficiency of PbO-grown YAP:Ce films.

Photoelectron yield (LY) of YAP:Ce films measured under excitation by alpha-particles ^{241}Am (5.48 MeV) is definitely significantly reduced compared to SC. The reported LY of YAP:Ce grown from PbO is only 2–10 % of the value of SC counterpart [3]. The LY of films grown from BaO is notably higher but still only about 12–24 % [3, 18]. It shows the large potential of the BaO-based flux for improving scintillation properties of aluminum perovskites.

5.4.2.2 Pr^{3+}, Tb^{3+}-doped perovskites

The Pr^{3+} ions in YAP/LuAP show intensive and fast emission in the UV spectral range, Fig. 5.28 left. The wide double band with maxima at about 242 nm and 280 nm is due to allowed Pr radiative transition

from its $5d_1$ level to $4f_2$ (^3H_J,^3F_J) levels. Corresponding PL decay is very fast, ~8ns, the shortest in the family of complex oxides. The structure between 480 and 650 nm comes from f–f(Pr^{3+}) transitions. A striking difference between spectra of SC and films is evident—the UV emission dominates in the SC, Fig. 5.28 left, while it is drastically suppressed in films grown from the PbO flux, Fig. 5.28 right, at the expense of slow f–f emission in the visible range. Therefore the LY of YAP/LuAP:Pr films is enormously low and reaches only about ~5 % of reference YAP:Ce SC [146]. The main reason for very low LY of Pr^{3+}-doped films is the strong quenching influence of Pb^{2+} impurity dopant. Namely, strong Pb^{2+}-related absorption below 260 nm is overlapped with 5d–4f(Pr^{3+}) emission. This leads to energy transfer from Pr^{3+} ions to Pb^{2+} centers, which is the main reason for the reduced LY in perovskites grown from the PbO flux [117]. Another reason for reduced LY of Pr^{3+}-doped epitaxial films of perovskites is the presence of the f–f luminescence of Pr^{3+} ions in the visible range, Fig. 5.28, which plays a role of competing channel for dissipation of the excitation energy [146].

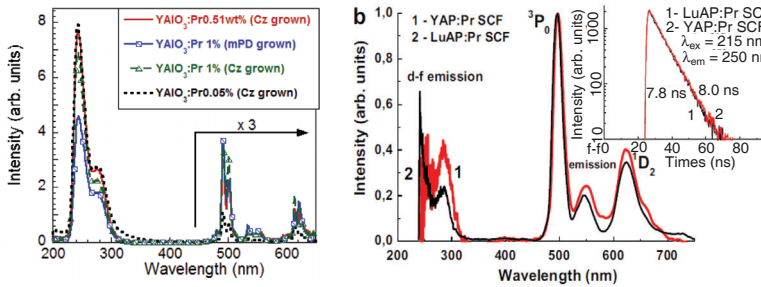

Figure 5.28 Left: X-ray excited RL spectra of Pr-doped YAP single crystals at RT, see also Ref. 1. Right: The CL spectra and decay kinetics of Pr^{3+} luminescence in YAP:Pr (1) and LuAP:Pr (2) epitaxial films grown from the PbO flux. Reprinted from Ref. 146, Copyright 2010, with permission from Elsevier.

On the other hand, the sharp f–f emission in trivalent rare earth ions is not markedly influenced by Pb^{2+} impurity. The problem of low LY of YAP:Ce or YAP:Pr films can be partly eliminated by co-doping with Tb^{3+} ions. Tb has large segregation coefficient (about 0.7–1.0) as compared to Ce^{3+} ions (~0.006–0.01) [98]. In Fig. 5.29 the RL spectra of LuAG:Ce and LuAG:Ce,Tb films co-doped with different

content of Tb are displayed. The intensity of the Ce^{3+}-related luminescence in Ce,Tb co-doped films is strongly decreased. This observation confirms effective energy transfer $Ce^{3+} \rightarrow Tb^{3+}$ which is due to the overlap of the Ce(5d–4f) emission with transitions in Tb^{3+} between 380 and 420 nm [17]. However, due to this energy transfer, the light output of X-ray excited luminescence of from Tb^{3+} ions is about 2 times larger in LuAP:Ce,Tb as compared to LuAP:Tb counterpart and 30–40% larger than that of a bulk YAG:Ce standard sample [162]. The as-grown LuAP:Tb and LuAP:Tb,Ce films were tested for high-resolution X-ray imaging using a spatial resolution target at the ESRF, and displayed promising result [162].

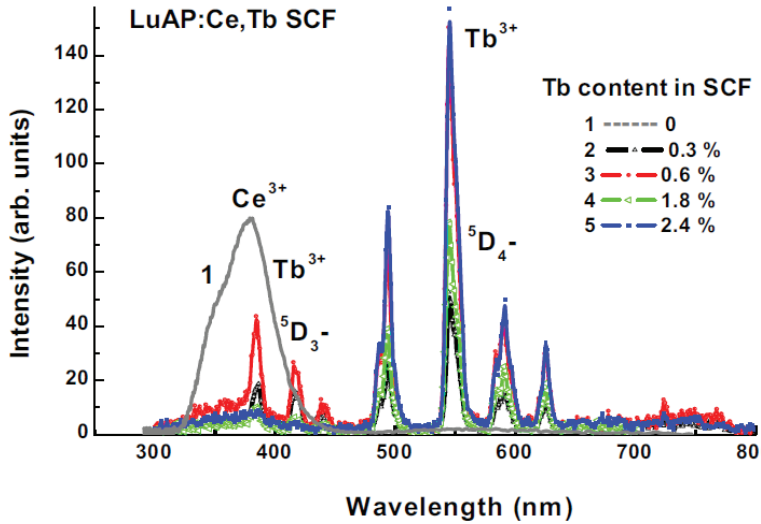

Figure 5.29 The X-ray excited spectra of LuAP:Ce and LuAP:CeTb epitaxial films at 300 K grown from PbO flux. Reprinted from Ref. 17, Copyright 2013, with permission from Elsevier.

5.4.2.3 Concluding remarks

The results reported above demonstrate detrimental influence of Pb^{2+} contamination and lead-induced centers on the scintillation characteristics of Ce^{3+} and Pr^{3+} doped aluminum perovskites. Adoption of a lead-free BaO flux is essential for production fast, high performance Ce, Pr doped YAP/LuAP thin-film scintillators.

5.4.3 Orthosilicates

Ce^{3+}-doped oxyorthosilicates RE_2SiO_5, where RE = Y, Lu, Gd, or combination of these ions, are promising scintillating oxide materials for gamma ray and high energy particle applications. Orthosilicates crystalize in monoclinic structure [163]. Crystals with small rare earth ions, e.g., Y_2SiO_5–YSO, Lu_2SiO_5–LSO, have space group C2/c (structure X1) and those with large RE ions, e.g., Gd_2SiO_5 – GSO, have space group $P2_1/c$ (structure X2). In both these structures, there are two crystallographically unequal rare earth sites, RE1 and RE2, with coordination numbers 7 and 6 (X1 structure) and 9 and 7 (X2 structure), respectively, for more details see also [69, 163–166]. The dopants and impurities with large ionic radii (Ce, Pr, Pb, etc.) prefer to occupy larger RE1 sites with higher coordination numbers of 7 and 9, respectively. Not all oxygen ions are bound to both yttrium and silicon and possible defects, especially the oxygen vacancies and related color centers F^+ or F, are more easily created in oxygen sites bound only to the yttrium ions.

The epitaxial films have been grown so far in several laboratories exclusively from the PbO-Ba_2O_3 flux [2, 34, 102, 167]. The reported quality of the YSO/LSO:RE films can be very good under optimal growth conditions (at low undercooling and suitable appropriately (010) oriented substrate). The melt used for the epitaxial growth has composition PbO-Ba_2O_3 with molar ratio 1:10 – 1:20 and solute Y_2O_3 + SiO_2 with SiO_2 in excess for stabilization of the orthosilicate phase [34]. Due to very low segregation coefficient of Ce, k_{Ce} ~0.01, large excess of CeO_2 in the melt is necessary, however, samples with higher Ce content is difficult to obtain due to limited solubility of CeO_2 in the melt. The growth temperatures are around 1000 °C.

5.4.3.1 Ce^{3+}-doped YSO, LSO

YSO:Ce has good LY and fast scintillation decay of 30–40 ns and is used for electron detection in SEM. Practical application of YSO/LSO:Ce crystals is limited owing to fairly high afterglow [168], likely due to electron trapping centers related to oxygen vacancies [169, 170]. This disadvantage was eliminated in mixed LYSO:Ce system and further improved by aliovalent co-doping by divalent ions LYSO:Ce,Ca,Mg [74, 171]. This optimized material found application

in medical positron emission tomography PET due to its excellent LY, fast response, high stopping power and low afterglow. On the other hand, in epitaxial films the oxygen vacancies and related deep traps are substantially reduced due to much lower growth temperature and afterglow is suppressed in films.

Large Ce^{3+} ions are located predominantly in bigger coordination 7, site Ce1, in LSO/YSO (X2 structure), however, a part of Ce ions is in site Ce2 with coordination number 6. Ce1 and Ce2 have different absorption and emission spectral properties and kinetics of luminescence.

The principal disadvantage of YSO/LSO films grown from the PbO flux is quite high Pb^{2+} content due to spacious crystal sites more favorable for positioning of large lead ions into the orthosilicate lattice. According to the EPMA analysis, content of Ce and Pb in LPE films is comparable [102, 172, 173]. The divalent Pb^{2+} ions have, however, detrimental effect on the PL properties of YSO/LSO:Ce systems. In some films any Ce^{3+} centers were not detected in the absorption or PL excitation spectra and related PL emission was not observed by direct excitation into ground 4f(Ce^{3+}) state at 3.45 eV (360 nm) [174]. The emission from these samples with maxima in blue ~2.8 eV and UV ~3.5 eV ranges were identified as Pb^{2+} origin [87, 173, 175]. However, under excitation by ionizing radiation (X-ray, e-beam) and/or photoexcitation in the absorption region above 4.2 eV, the typical 5d–4f(Ce) luminescence is excited even in films where Ce^{3+} centers are absent [174].

These contradictory results indicate that Ce^{3+} content was negligible in studied LPE films grown from PbO. This might be result of large amount of Pb^{2+} ions in YSO:Ce films resulting in changing cerium valency into tetravalent state, Ce^{4+}, due to charge compensation. Small tetravalent Ce^{4+} ions also contribute to effective lattice volume compensation [176].

The absorption spectra of several YSO:Ce epitaxial films and reference Czochralski grown SC are displayed in Fig. 5.30 left. The maxima at 360, 300, and 265 nm of YSO:Ce crystal come from 4f–5d transitions in Ce^{3+}. In YSO:Ce films only low energy Ce^{3+} related absorption band at 360 nm is discernible in the spectra and below 350 nm strong broad band absorption is observed in all films. This broad band absorption originates from charge transfer transitions from valence oxygen 2p(O^{2-}) band to empty metal 4f(Ce^{4+}) states. The

spectral peak located at 240–260 nm, which overlaps with charge transfer 2p–4f transitions, is observed in all LPE films and originates from Pb^{2+} centers ($^1S_0 - {}^3P_1$) [87, 128, 175].

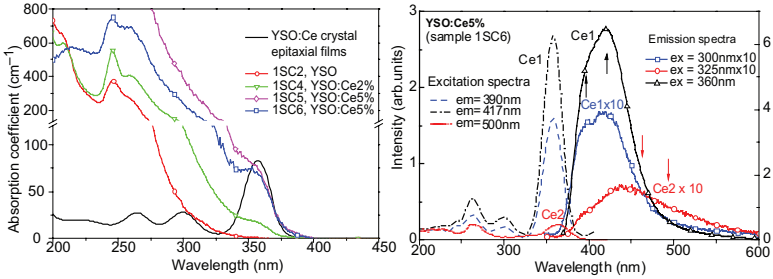

Figure 5.30 Left: Comparison of absorption coefficient spectra of YSO:Ce single crystal and epitaxial films grown from the PbO flux. Ce concentrations refer to the melt, note change of scale. Right: PL excitation and emission spectra of Ce1 and Ce2 centers in YSO:Ce epitaxial film, see also Ref. [9].

Nevertheless, in films grown using optimized LPE process the Ce^{3+} related luminescence is clearly observed, Fig. 5.30 right, in spite of significant amounts of Pb^{2+} and Ce^{4+} ions. Both the excitation and emission spectra of these films are in close correlation with those measured in YSO:Ce crystal [177–179] and the excitation spectra of films (Fig. 5.30 right) well correlate with the absorption spectrum of the reference SC (Fig. 5.30 left). Arrows in Fig. 5.30 right indicate Ce1 and Ce2 centers: emission doublet at 397 and 427 nm is ascribed to Ce1 center with 7-fold coordination and the wavelength tail (doublet at 460–500 nm) to Ce2 center with 6-fold coordination [180].

As mentioned above the luminescence can be excited by high energy excitation also in YSO:Ce films where content of trivalent Ce^{3+} is substantially reduced. This is due to the recombination of electrons coming from the conduction band with the Ce^{4+} centers and the two-photon excitation process, as proposed in Ref. [174]. The RL and CL spectra of LPE films and reference SC are shown in Fig. 5.31. The long-wavelength wings of the emission are notably red-shifted in comparison with the YSO:Ce single crystal. This is most likely caused by relative higher content of Ce^{3+} ions in Ce2 positions in films than in SC [22, 102]. The steady state emission efficiency is fairly high in LPE films grown under optimized conditions regardless

of reduced number of Ce^{3+} centers—integrated RL intensity is ~10× higher as compared to reference BGO crystal, see Fig. 5.31a. However, reported LY measured by alpha particle excitation was only about 25–40% value of LYSO:Ce SC [22], in optimized films reaches up to 70% [9]. Lower LY of LPE films is a consequence of quenching effect of Pb^{2+} ions on Ce^{3+} emission. This is demonstrated in Fig. 5.32 where comparison of PL decays of Ce1 centers is compared for LSO:Ce LPE film with sizable Pb impurity content and a SC counterpart. Significant nonlinearity of the initial part of the decay curve of LPE film indicates considerable energy transfer away from the Ce1 emission centers.

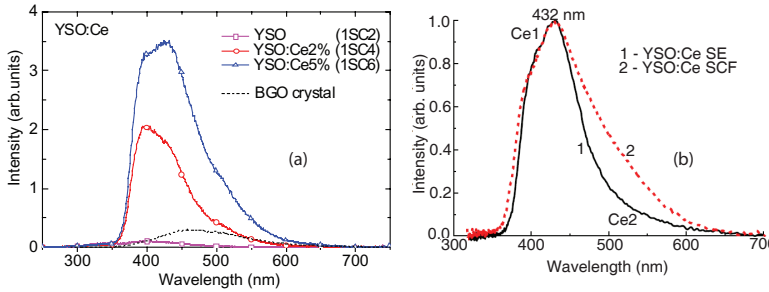

Figure 5.31 (a) X-ray excited RL spectra of YSO:Ce films with various Ce content [9]. BGO reference crystal is shown for comparison. (b) Normalized CL spectra of YSO:Ce film and single crystal SC. Reprinted from Ref. 22, Copyright 2013, with permission from Elsevier.

Important advantage of orthosilicates as compared to garnets is absence of shallow electron traps and consequential absence of slow components in the scintillation decay. Indeed, in pulsed height spectra the LY of YSO:Ce films is saturated within 0.5 μs [9].

Afterglow is substantially reduced (in ~2 orders of magnitude) in mixed LYSO:Ce and LGSO:Ce [181] systems usually co-doped by divalent Ca^{2+} or Mg^{2+} ions. Such co-doping in concentrations of tens of ppm has only marginal effect on the LY and decay kinetics.

The LY of LGSO:Ce films grown from PbO flux becomes significantly lower at increasing Gd in comparison with that of LSO:Ce films presumably due to the intensified quenching influence of Pb^{2+} impurity ions and increasing occupancy of Ce2 sites in the LGSO host [102].

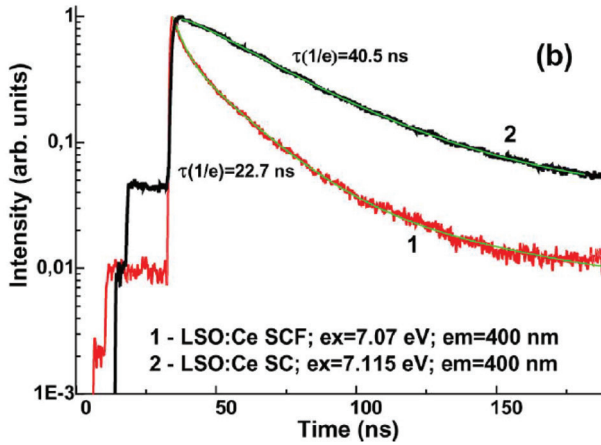

Figure 5.32 Comparison of LSO:Ce LPE film and single crystal (SC) decays (Ce1 centers) under excitation at the edge, 7.07–7.15 eV, multiexponential approximation of corresponding decay curves: 3.7+19+107 ns (LSO:Ce SCF) and 31.6+225 ns (LSO:Ce SC). Reprinted from Ref. 22, Copyright 2013, with permission from Elsevier.

5.4.3.2 Other dopants

Intense green emission is observed in Tb^{3+} doped YSO and LSO films grown from PbO flux [2, 25], Fig. 5.33. The lead Pb^{2+} impurity ions coming from the flux do not quench noticeably the 4f–4f (Tb^{3+}) emission (in contrast to Ce^{3+} emission in LSO/YSO:Ce mentioned above) and the emission is stable well above the RT, Fig. 5.33 left.

LSO:Tb films were used in high resolution X-ray microimaging detection screens in low and high dose beam lines of ESRF synchrotron [25, 100, 101, 182]. The thickness of films was between 2 and 30 μm and optimum efficiency was obtained for films with Tb concentration of 8–15% in the melt. In order to eliminate parasitic emission from standard LSO substrates, the best performance films were grown onto non-emitting YbSO substrates with suppressed afterglow [2, 183].

A bi-layer scintillator screen has been produced by the LPE process—Tb:LSO + LYSO:Ce double layer, 7 μm thick—with improved performance, ~1μm spatial resolution [25]. Double layer system enables combination most suitable activator ions for proposed application and prevents mutual quenching of dopants.

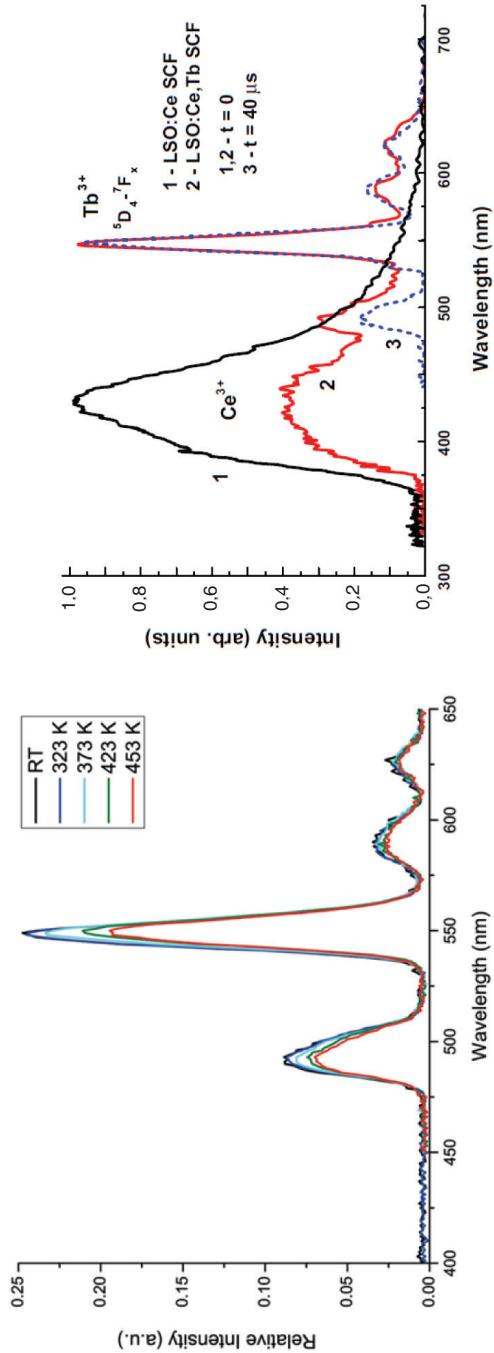

Figure 5.33 Left: X-ray excited RL spectrum of LSO:Tb at various temperatures and Tb content of 8%. Reproduced from Ref. 2, with permission of the International Union of Crystallography. Right: Time resolved normalized CL spectra of LSO:Ce (1) and LSO:Ce,Tb (2,3) films at delays (t = 0 (1,2) and 40 µs (3). Reprinted from Ref. 17, Copyright 2013, with permission from Elsevier.

Co-doped LSO:CeTb films were grown with the aim to increase the LY and/or for application in detection of complex events with different timing characteristics (ns × ms), Fig. 5.33b. Effective Ce → Tb energy transfer was observed, however, the LY under alpha excitation was only a fraction of LYSO:Ce or YAG:Ce reference single crystals [17, 99].

5.4.3.3 Concluding remarks

The results reported so far for the LPE grown orthosilicate demonstrate detrimental influence of Pb^{2+} contamination and lead-induced centers on the scintillation characteristics (LY and decay kinetics) of Ce^{3+} doped orthosilicates. Development of a lead-free flux for the growth of orthosilicate epitaxial films will be crucial for production fast, high performance Ce or Pr doped LYSO scintillators.

5.5 Applications of the LPE Films

5.5.1 Electron Detection in SEM

Epitaxial films of Ce-doped multicomponent garnet scintillator are especially perspective in the SEM detection units due to their high LY and low afterglow. Furthermore, the penetration depth of energetic electrons is typically only several micrometers and all the energy is deposited in the film. The practical impact of the scintillation properties on the quality of a SEM image is demonstrated in Fig. 5.34. When the YAG:Ce scintillator in the detector was replaced by epitaxial film of the multicomponent garnet GAGG:Ce scintillator with x_{Ga} = 2.7, the SEM image quality was obviously improved. This is consequence of higher electron–photon conversion efficiency of the GAGG:Ce scintillator and significantly reduced afterglow in single crystalline films as compared to the YAG:Ce single crystal. Such scintillator is suitable also for backscattered electron detectors where the high light yield of the scintillator is crucial.

5.5.2 X-ray Microimaging Screens

The efficiency of high-resolution pixel detectors for (hard) X-rays is important factor for X-ray imaging applications [2, 24–26, 100, 101]. The detector able to provide images with submicrometer spatial resolution used at ESRF synchrotron facility consists of a

scintillator screen (epitaxial film with thickness typically 5–20 μm), optical microscope and a digital camera, Fig. 5.35. The scintillator converts the X-rays into a visible light image which is detected by the camera. Due to the low absorption of X-rays in the scintillator, Fig. 5.10, films of high density and high effective atomic number are preferred. Image in Fig. 5.35 was obtained by means of 10 μm thick LSO:Tb scintillator film grown onto YbSO substrate. Improved spatial resolution < 1 μm was demonstrated using a double layer LSO:Tb/LYSO:Ce scintillator grown by LPE [25].

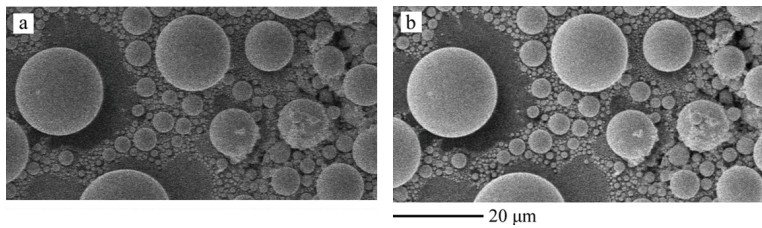

Figure 5.34 A SEM image of tin balls observed using the secondary electron detector with (a) commercial Czochralski grown YAG:Ce single crystal, and (b) GAGG:Ce multicomponent garnet epitaxial film grown from BaO flux. Images were recorded under the same conditions with e-beam energy of 10 keV and current of 57 pA. High scan speed with the dwell time (time per pixel) of 100 ns was used and the images were obtained by averaging of 3 consecutive scans. Reprinted from Ref. 10, Copyright 2016, with permission from Elsevier.

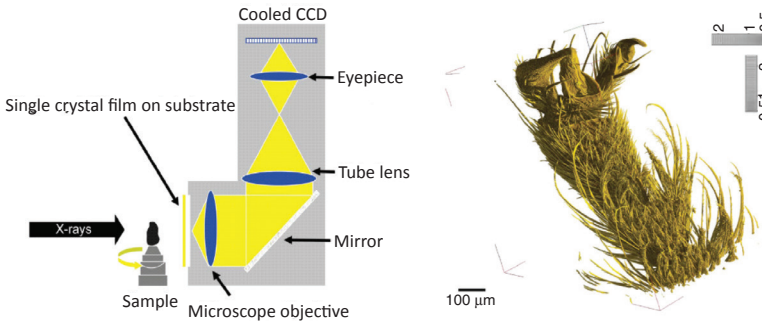

Figure 5.35 X-ray microtomography Left: Principle of an indirect high-resolution X-ray imaging system used in hard X-ray imaging in ESRF. Right: Rendering of a volume image acquired by synchrotron microtomography of a section of a honey bee tarsus. Reproduced from Ref. 2, with permission of the International Union of Crystallography.

5.5.3 Other Applications of Epitaxial Films: Waveguide Planar Lasers, Warm LEDs

Planar waveguides and channel planar lasers epitaxial films were demonstrated in number of rare earth doped garnets: Nd:YAG [105, 184], Tm:YAG [39, 105], Dy:YAG [185], Yb:YAG [186] Pr:YAG [187–189] and YbAG:Er [16, 190]. These waveguide garnet systems were grown from PbO flux, which provides the best surface morphology necessary for intended applications. Minor Pb contamination does not mean serious problem as in scintillators, since the devices are usually optically pumped in f states.

Phosphors for warm white LEDs are another prospective application. The emission wavelength can be properly red shifted by Gd substitution and required roughness of the surface is reached during the epitaxial growth, see Fig. 5.2b.

Acknowledgments

The authors are grateful to GACR, project No. P204/12/0805, for financial support of this work.

References

1. Nikl, M., Mares, J.A. et al. (2010), *IEEE Transactions on Nuclear Science,* **57**, pp. 1168–1174.
2. Douissard, P.A., Cecilia, A. et al. (2010), *Journal of Synchrotron Radiation,* **17**, pp. 571–583.
3. Zorenko, Y., Nikl, M. et al. (2009), *Physica Status Solidi a-Applications and Materials Science,* **206**, pp. 2586–2592.
4. Kucera, M., Nitsch, K. et al. (2010), *Journal of Crystal Growth,* **312**, pp. 1538–1545.
5. Kucera, M., Nitsch, K. et al. (2008), *IEEE Transactions on Nuclear Science,* **55**, pp. 1201–1205.
6. Nikl, M. (2005), *Physica Status Solidi a-Applied Research,* **202**, pp. 201–206.
7. Nikl, M., Vedda, A. et al. (2007), *Physical Review B,* **76**, pp. 195121.
8. Moszynski, M., Ludziejewski, T. et al. (1994), *Nuclear Instruments & Methods in Physics Research A,* **345**, pp. 461–467.

9. Kucera, M., Hanus, M. et al. (2015), unpublished results.
10. Bok, J., Lalinsky, O. et al. (2016), *Ultramicroscopy*, **163**, 1–5.
11. Prusa, P., Kucera, M. et al. (2015), *Crystal Growth & Design,* **15**, pp. 3715–3723.
12. Kučera, M., Nikl, M. et al. (2011), *Journal of Crystal Growth,* **318**, pp. 813–819.
13. Nikl, M., Mihokova, E. et al. (2005), *Physica Status Solidi B-Basic Solid State Physics,* **242**, pp. R119–R121.
14. Koch, A., Raven, C. et al. (1998), *Journal of the Optical Society of America a-Optics Image Science and Vision,* **15**, pp. 1940–1951.
15. Robertson, J.M., Vantol, M.W. et al. (1980), *Philips Journal of Research,* **35**, pp. 354–371.
16. Hlásek, T., Rubešová, K. et al. (2015), *Optical Materials,* **49**, pp. 46–50.
17. Zorenko, Y., Gorbenko, V. et al. (2013), *Radiation Measurements,* **56**, pp. 415–419.
18. Zorenko, Y., Gorbenko, V. et al. (2013), *Radiation Measurements,* **56**, pp. 159–162.
19. Martin, T. and Koch, A. (2006), *Journal of Synchrotron Radiation,* **13**, pp. 180–194.
20. Kucera, M., Nikl, M. et al. (2012), *IEEE Transactions on Nuclear Science,* **59**, pp. 2275–2280.
21. Kucera, M., Nitsch, K. et al. (2010), *Radiation Measurements,* **45**, pp. 449–452.
22. Zorenko, Y., Gorbenko, V. et al. (2013), *Radiation Measurements,* **56**, pp. 84–89.
23. Chewpraditkul, W., Swiderski, L. et al. (2009), *Physica Status Solidi a-Applications and Materials Science,* **206**, pp. 2599–2605.
24. Horodysky, P., Tous, J. et al. (2010), *Radiation Measurements,* **45**, pp. 628–630.
25. Martin, T., Douissard, P.A. et al. (2009), *IEEE Transactions on Nuclear Science,* **56**, pp. 1412–1418.
26. Tous, J., Blazek, K. et al. (2012), *Radiation Measurements,* **47**, pp. 311–314.
27. Nikl, M., Mares, J.A. et al. (2004), *Physica Status Solidi a-Applied Research,* **201**, pp. R41–R44.
28. Bruza, P., Fidler, V. et al. (2011), *Journal of Instrumentation,* **6**, pp. P09007–P09007.

29. Robertson, J.M. and Vantol, M.W. (1984), *Thin Solid Films,* **114**, pp. 221–240.
30. Zorenko, Y., Gorbenko, V. et al. (2005), *Journal of Luminescence,* **114**, pp. 85–94.
31. Winkler, G., *Magnetic garnets*. 1981, Braunschweig: Vieweg & Sons.
32. Robertson, J.M. (1978), *Journal of Crystal Growth,* **45**, pp. 233–242.
33. Blank, S.L. and Nielsen, J.W. (1972), *Journal of Crystal Growth,* **17**, pp. 302–311.
34. Ferrand, B., Chambaz, B. et al. (1999), *Optical Materials,* **11**, pp. 101–114.
35. Ferrand, B., Pelenc, D. et al. (1993), *Journal of Crystal Growth,* **128**, pp. 966–969.
36. Hanna, D.C., Large, A.C. et al. (1993), *Applied Physics Letters,* **63**, pp. 7–9.
37. Chartier, I., Ferrand, B. et al. (1992), *Optics Letters,* **17**, pp. 810–812.
38. Pelenc, D., Chambaz, B. et al. (1995), *Optics Communications,* **115**, pp. 491–497.
39. Rameix, A., Borel, C. et al. (1997), *Optics Communications,* **142**, pp. 239–243.
40. Sugimoto, N., Ohishi, Y. et al. (1995), *Applied Physics Letters,* **67**, pp. 582–584.
41. Prusa, P., Nikl, M. et al. (2009), *Physica Status Solidi a-Applications and Materials Science,* **206**, pp. 1494–1500.
42. Prusa, P., Cechak, T. et al. (2008), *Applied Physics Letters,* **92**.
43. Klemenz Rivenbark, C.F. (2010), Liquid phase epitaxy of advanced materials, in *Springer handbook of crystal growth*, Dhanarah, G. et al., Editors, Springer: Berlin. p. 1041–1068.
44. Capper, P. and Mauk, M. (2007), *Liquid Phase Epitaxy of Electronic, Optical and Optoelectronic Devices*, Chichester: J. Wiley.
45. Elwell, D. and Scheel, H.J. (2011), *Crystal Growth From High Temperature Solution,* 2 ed., London: Academic Press.
46. Tolksdorf, W. and Klages, C.-P. (1984), *Thin Solid Films,* **114**, pp. 33–43.
47. Giess, E.A. (1975), *Journal of Crystal Growth,* **31**, pp. 358–365.
48. Kucera, M., Nitsch, K. et al. (2003), *Physica Status Solidi a-Applied Research,* **198**, pp. 407–414.
49. Hiskes, R. (1974), *Journal of Crystal Growth,* **27**, pp. 287–298.

50. Suemune, Y. and Inoue, N. (1974), *Journal of Crystal Growth,* **24**, pp. 646–650.
51. Prusa, P., Mares, J.A. et al. (2010), *Optical Materials,* **32**, pp. 1360–1363.
52. Prusa, P., Kucera, M. et al. (2011), *Journal of Crystal Growth,* **318**, pp. 545–548.
53. Mares, J.A., Beitlerova, A. et al. (2007), *Radiation Measurements,* **42**, pp. 533–536.
54. Mares, J.A., Prusa, P. et al. (2010), *Radiation Measurements,* **45**, pp. 369–371.
55. Bonner, W.A., Lecraw, R.C. et al. (1978), *Journal of Applied Physics,* **49**, pp. 1871–1872.
56. Tamanoi, K., Nomoto, T. et al. (1991), *Japanese Journal of Applied Physics Part 1-Regular Papers Short Notes & Review Papers,* **30**, pp. 3516–3517.
57. Zorenko, Y., Gorbenko, V. et al. (2013), *Journal of Luminescence,* **141**, pp. 137–143.
58. Zorenko, Y., Gorbenko, V. et al. (2013), *Journal of Luminescence,* **134**, pp. 539–543.
59. Gorbenko, V., Krasnikov, A. et al. (2013), *Journal of Luminescence,* **134**, pp. 469–476.
60. Chani, V., Shimamura, K. et al. (1997), *Materials Science and Engineering,* **R20**, pp. 281–338.
61. Chani, V.I., Boulon, G. et al. (2010), *Japanese Journal of Applied Physics,* **49**, pp. 075601.
62. Chani, V. (2003), *Journal of Ceramic Processing Research,* **4**, pp. 67–70.
63. Kucera, M., Hanus, M. et al. (2014), *IEEE Transactions on Nuclear Science,* **61**, pp. 282–289.
64. Zorenko, Y., Gorbenko, V. et al. (2013), *Radiation Measurements,* **56**, pp. 150–154.
65. Robbins, D.J., Cockayne, B. et al. (1979), *Physical Review B,* **19**, pp. 1254–1269.
66. Petrosyan, A.G., Shirinyan, G.O. et al. (1999), *Journal of Crystal Growth,* **198**, pp. 492–496.
67. Leonyuk, N.I., Belokoneva, E.L. et al. (1999), *Journal of Crystal Growth,* **205**, pp. 361–367.
68. Cong, H.J., Zhang, H.J. et al. (2009), *Journal of Applied Crystallography,* **42**, pp. 284–294.
69. Gustafsson, T., Klintenberg, M. et al. (2001), *Acta Crystallographica Section C-Crystal Structure Communications,* **57**, pp. 668–669.

70. Zorenko, Y., Voloshinovskii, A. et al. (2007), *Physica Status Solidi (b),* **244**, pp. 2180–2189.
71. Przybylińska, H., Wittlin, A. et al. (2014), *Optical Materials,* **36**, pp. 1515–1519.
72. Kvapil, J., Manek, B. et al. (1981), *Journal of Crystal Growth,* **52**, pp. 542–545.
73. Ryskin, N.N., Dorenbos, P. et al. (1994), *Journal of Physics-Condensed Matter,* **6**, pp. 10423–10434.
74. Koschan, M., Yang, K. et al. (2012), *Journal of Crystal Growth,* **352**, pp. 133–136.
75. Nikl, M., Mares, J.A. et al. (2002), *Nuclear Instruments & Methods in Physics Research A,* **486**, pp. 250–253.
76. Stanek, C.R., Levy, M.R. et al. (2005), *Physica Status Solidi (b),* **242**, pp. R113–R115.
77. Nikl, M., Kamada, K. et al. (2014), *Crystal Growth & Design,* **14**, pp. 4827–4833.
78. Stanek, C.R., McClellan, K.J. et al. (2006), *Physica Status Solidi (b),* **243**, pp. R75–R77.
79. Stanek, C.R., McClellan, K.J. et al. (2006), *Journal of Applied Physics,* **99**, pp. 113518.
80. Stanek, C.R., McClellan, K.J. et al. (2007), *Nuclear Instruments and Methods in Physics Research A,* **579**, pp. 27–30.
81. Stanek, C.R., Levy, M.R. et al. (2008), *Nuclear Instruments and Methods in Physics Research B,* **266**, pp. 2657–2664.
82. Nikl, M., Yoshikawa, A. et al. (2013), *Progress in Crystal Growth and Characterization of Materials* **59**, pp. 47–72.
83. Stanek, C.R., Jiang, C. et al. (2013), *Physica Status Solidi B-Basic Solid State Physics,* **250**, pp. 244–248.
84. Zorenko, Y., Voloshinovskii, A. et al. (2004), *Radiation Measurements,* **38**, pp. 677–680.
85. Ashurov, M.K., Rakov, A.F. et al. (2001), *Solid State Communications,* **120**, pp. 491–494.
86. Kuklja, M.M. (2000), *Journal of Physics-Condensed Matter,* **12**, pp. 2953–2967.
87. Babin, V., Gorbenko, V. et al. (2013), *Radiation Measurements,* **56**, pp. 124–128.
88. Babin, V., Bichevin, V. et al. (2009), *Physica Status Solidi B-Basic Solid State Physics,* **246**, pp. 1318–1326.

89. Schauer, P. and Bok, J. (2013), *Nuclear Instruments & Methods in Physics Research B,* **308**, pp. 68–73.

90. Strocka, B., Holst, P. et al. (1978), *Philips Journal of Research,* **33**, pp. 186–202.

91. Bok, J. and Schauer, P. (2014), *Measurement Science & Technology,* **25**, pp. 075601.

92. Zorenko, Y., Gorbenko, V. et al. (2002), *Nuclear Instruments & Methods in Physics Research B,* **486**, pp. 309–314.

93. Yoshikawa, A., Yanagida, T. et al. (2012), *Ieee Transactions on Nuclear Science,* **59**, pp. 2286–2289.

94. D'Ambrosio, C. and Leutz, H. (2003), *Nuclear Instruments & Methods in Physics Research A,* **501**, pp. 463–498.

95. D'Ambrosio, C., Leutz, H. et al. (2003), *Nuclear Instruments & Methods in Physics Research A,* **497**, pp. 186–197.

96. Mares, J.A., Nikl, M. et al. (2003), *Nuclear Instruments & Methods in Physics Research A,* **498**, pp. 312–327.

97. Zorenko, Y., Gorbenko, V. et al. (2010), *Radiation Measurements,* **45**, pp. 444–448.

98. Zorenko, Y.V. and Gorbenko, V.I. (2009), *Physics of the Solid State,* **51**, pp. 1800–1808.

99. Zorenko, Y., Gorbenko, V. et al. (2012), *IEEE Transactions on Nuclear Science,* **59**, pp. 2260–2268.

100. Cecilia, A., Rack, A. et al. (2011), *Nuclear Instruments and Methods in Physics Research A,* **648, Supplement 1**, pp. S321–S323.

101. Cecilia, A., Rack, A. et al. (2011), *Nuclear Instruments and Methods in Physics Research A,* **633, Supplement 1**, pp. S292–S293.

102. Zorenko, Y., Gorbenko, V. et al. (2011), *Journal of Crystal Growth,* **337**, pp. 72–80.

103. Ehrentraut, D., Sato, H. et al. (2006), *Journal of Crystal Growth,* **287**, pp. 367–371.

104. Zorenko, Y., Gorbenko, V. et al. (2012), *Ieee Transactions on Nuclear Science,* **59**, pp. 2281–2285.

105. Szachowicz, M., Moretti, P. et al. (2007), *Applied Physics Letters,* **90**.

106. Nikl, M., Vedda, A. et al., (2010), Single-crystal scintillation materials, in *Springer Handbook of Crystal Growth,* Dhanarah, G. et al., Editors., pp. 1663–1700, Springer: Berlin.

107. Nikl, M. and Yoshikawa, A. (2015), *Advanced Optical Materials,* **3**, pp. 463–481.

108. Nikl, M. (2000), *Physica Status Solidi a-Applied Research,* **178**, pp. 595–620.
109. Nikl, M. (2006), *Measurement Science & Technology,* **17**, pp. R37–R54.
110. Nikl, M., Ogino, H. et al. (2005), *Physica Status Solidi a-Applied Research,* **202**, pp. R4–R6.
111. Nikl, M., Ogino, H. et al. (2005), *Chemical Physics Letters,* **410**, pp. 218–221.
112. Ogino, H., Yoshikawa, A. et al. (2006), *Journal of Crystal Growth,* **287**, pp. 335–338.
113. Pejchal, J., Nikl, M. et al. (2009), *Journal of Physics D-Applied Physics,* **42**.
114. Autrata, R., Schauer, P. et al. (1978), *Journal of Physics E-Scientific Instruments,* **11**, pp. 707–708.
115. Robertson, J.M. and Vantol, M.W. (1980), *Applied Physics Letters,* **37**, pp. 471–472.
116. Robertson, J.M., Vantol, M.W. et al. (1981), *Philips Journal of Research,* **36**, pp. 15–30.
117. Babin, V., Gorbenko, V. et al. (2010), *Radiation Measurements,* **45**, pp. 415–418.
118. Zorenko, Y., Gorbenko, V. et al. (2008), *Physica Status Solidi (b),* **245**, pp. 1618–1622.
119. Babin, V., Gorbenko, V. et al. (2007), *Journal of Luminescence,* **127**, pp. 384–390.
120. Onderisinova, Z., Kucera, M. et al. (2015), *Journal of Luminescence,* **167**, pp. 106–113.
121. Kucera, M., Onderisinova, Z. et al. (2016), *Journal of Luminescence*, **169**, pp. 674–677.
122. Bachmann, V., Ronda, C. et al. (2009), *Chemistry of Materials,* **21**, pp. 2077–2084.
123. Kamada, K., Endo, T. et al. (2011), *Crystal Growth & Design,* **11**, pp. 4484–4490.
124. Kamada, K., Yanagida, T. et al. (2011), *Journal of Physics D: Applied Physics,* **44**, pp. 505104.
125. Zorenko, Y., Zorenko, T. et al. (2014), *Journal of Luminescence,* **156**, pp. 102–107.
126. Zorenko, Y., Gorbenko, V. et al. (2015), *Materials Research Bulletin,* **64**, pp. 355–363.
127. Przybylinska, H., Ma, C.-G. et al. (2013), *Applied Physics Letters,* **102**, pp. 241112.

128. Scott, G.B. and Page, J.L. (1977), *Journal of Applied Physics,* **48**, pp. 1342–1349.

129. Tachiya, M. and Mozumder, A. (1974), *Chemical Physics Letters,* **28**, pp. 87–89.

130. Huntley, D.J. (2006), *Journal of Physics: Condensed Matter,* **18**, pp. 1359–1365.

131. Cherepy, N.J., Kuntz, J.D. et al. (2010), *Proceedings of SPIE - The International Society for Optical Engineering*.

132. Dorenbos, P. (2013), *Journal of Luminescence,* **134**, pp. 310–318.

133. Fasoli, M., Vedda, A. et al. (2011), *Physical Review B,* **84**, pp. 081102(R).

134. Kamada, K., Yanagida, T. et al. (2012), *Journal of Crystal Growth,* **352**, pp. 88–90.

135. Prusa, P., Kamada, K. et al. (2013), *Radiation Measurements*, pp. 62–66.

136. Kamada, K., Kurosawa, S. et al. (2014), *Optical Materials,* **36**, pp. 1942–1945.

137. Prusa, P., Kucera, M. et al. (2013), *Optical Materials,* **35**, pp. 2444–2448.

138. Zorenko, Y., Gorbenko, V. et al. (2014), *Journal of Crystal Growth,* **401**, pp. 532–536.

139. Kucera, M., Nikl, M. et al. (2013), *Physica Status Solidi-Rapid Research Letters,* **7**, pp. 571–574.

140. van Eijk, C.W.E., Dorenbos, P. et al. (1994), *IEEE Transactions on Nuclear Science,* **41**, pp. 738–741.

141. Dujardin, C., Pedrini, C. et al. (1997), *Journal of Physics-Condensed Matter,* **9**, pp. 5229–5243.

142. Ogino, H., Yoshikawa, A. et al. (2006), *Journal of Crystal Growth,* **292**, pp. 239–242.

143. Swiderski, L., Moszynski, M. et al. (2009), *Ieee Transactions on Nuclear Science,* **56**, pp. 2499–2505.

144. Yanagida, T., Sato, M. et al. (2011), *Optical Materials,* **33**, pp. 413–418.

145. Kamada, K., Yanagida, T. et al. (2012), *Journal of Crystal Growth,* **352**, pp. 91–94.

146. Gorbenko, V., Zorenko, Y. et al. (2010), *Radiation Measurements,* **45**, pp. 461–464.

147. Zorenko, Y., Gorbenko, V. et al. (2010), *IEEE Transactions on Nuclear Science,* **57**, pp. 1335–1342.

148. Nikl, M., Pejchal, J. et al. (2006), *Applied Physics Letters,* **88**.

149. Dujardin, C., Pedrini, C. et al. (1998), *Journal of Physics-Condensed Matter,* **10**, pp. 3061–3073.

150. Zhuravleva, M., Novoselov, A. et al. (2008), *Ieee Transactions on Nuclear Science,* **55**, pp. 1476–1479.

151. Yanagida, T., Kamada, K. et al. (2010), *Nuclear Instruments and Methods in Physics Research A,* **623**, pp. 1020–1023.

152. Autrata, R., Schauer, P. et al. (1983), *Scanning,* **5**, pp. 91–96.

153. Mares, J.A., Beitlerova, A. et al. (2004), *Radiation Measurements,* **38**, pp. 353–357.

154. Mares, J.A., Nikl, M. et al. (2005), *Nuclear Instruments & Methods in Physics Research A,* **537**, pp. 271–275.

155. Chewpraditkul, W., Phunpueok, A. et al. (2013), *Physica Status Solidi (A) Applications and Materials Science,* **210**, pp. 1903–1908.

156. Wojtowicz, A.J., Glodo, J. et al. (1998), *Journal of Luminescence,* **79**, pp. 275–291.

157. Laguta, V.V., Nikl, M. et al. (2009), *Physical Review B,* **80**, pp. 045114.

158. Trummer, J., Auffray, E. et al. (2005), *Nuclear Instruments & Methods in Physics Research A,* **551**, pp. 339–351.

159. Zorenko, Y., Gorbenko, V. et al. (2007), *Radiation Measurements,* **42**, pp. 528–532.

160. Weber, M.J. (1973), *Journal of Applied Physics,* **44**, pp. 3205–3208.

161. Babin, V., Gorbenko, V. et al. (2011), *Journal of Physics D: Applied Physics,* **44**, pp. 315402.

162. Douissard, P.A., Martin, T. et al. (2014), *IEEE Transactions on Nuclear Science,* **61**, pp. 433–438

163. Felsche, J. (1973), The crystal chemistry of the rare earth silicates, in *Structure and Bonding,* p. 99–197, Springer.

164. Chiriu, D., Faedda, N. et al. (2007), *Physical Review B,* **76**.

165. Aitasalo, T., Hölsä, J. et al. (2005), *Optical Materials,* **27**, pp. 1511–1515.

166. Aitasalo, T., Hölsä, J. et al. (2004), *Optical Materials,* **26**, pp. 107–112.

167. Thibault, F., Pelenc, D. et al. (2008), *Optical Materials,* **30**, pp. 1289–1296.

168. Dorenbos, P., van Eijk, C.W.E. et al. (1994), *Journal of Physics: Condensed Matter,* **6**, pp. 4167.

169. Nikl, M., Laguta, V.V. et al. (2008), *Physica Status Solidi B-Basic Solid State Physics,* **245**, pp. 1701–1722.

170. Blahuta, S., Bessiere, A. et al. (2011), *Materials,* **4**, pp. 1224–1237.

171. Blahuta, S., Bessiere, A. et al. (2013), *IEEE Transactions on Nuclear Science,* **60**, pp. 3134–3141.

172. Zorenko, Y., Nikl, M. et al. (2011), *Optical Materials,* **33**, pp. 846–852.

173. Zorenko, Y., Gorbenko, V. et al. (2012), *Optical Materials,* **34**, pp. 1969–1974.

174. Kärner, T., Laguta, V.V. et al. (2014), *Journal of Physics D: Applied Physics,* **47**, pp. 065303.

175. Gorbenko, V., Krasnikov, A. et al. (2012), *Journal of Physics D-Applied Physics,* **45**, pp. 355304.

176. Rotman, S.R., Tuller, H.L. et al. (1992), *Journal of Applied Physics,* **71**, pp. 1209–1214.

177. Jary, V., Nikl, M. et al. (2012), *IEEE Transactions on Nuclear Science,* **59**, pp. 2079–2084.

178. Jary, V., Nikl, M. et al. (2011), *Optical Materials,* **34**, pp. 428–432.

179. Chewpraditkul, W., Wanarak, C. et al. (2013), *Optical Materials,* **35**, pp. 1679–1684.

180. Feng, H., Jary, V. et al. (2010), *Journal of Applied Physics,* **108**, pp. 033519.

181. Jarý, V., Mihóková, E. et al. (2014), *Journal of Physics D: Applied Physics,* **47**, pp. 365304.

182. Douissard, P.A., Cecilia, A. et al. (2012), *Journal of Instrumentation,* **7**, pp. P09016–P09016.

183. Cecilia, A., Jary, V. et al. (2014), *Radiation Measurements,* **62**, pp. 28–34.

184. Gerhardt, R., Kleine-Borger, J. et al. (1999), *Applied Physics Letters,* **75**, pp. 1210–1212.

185. Klimczak, M., Malinowski, M. et al. (2009), *Journal of Luminescence,* **129**, pp. 1869–1873.

186. Malinowski, M., Kaczkan, M. et al. (2001), *Journal of Luminescence,* **94**, pp. 29–33.

187. Piramidowicz, R., Lawniczuk, K. et al. (2008), *Journal of Luminescence,* **128**, pp. 708–711.

188. Nakielska, M., Kosko, J. et al. (2008), *Optical Materials,* **30**, pp. 759–762.

189. Malinowski, M., Nakielska, M. et al. (2007), *Spectroscopy Letters,* **40**, pp. 271–292.

190. Hlásek, T., Rubešová, K. et al. (2015), *Journal of Luminescence,* **164**, pp. 90–93.

CRYSTAL GROWTH & DESIGN

Article

pubs.acs.org/crystal

Composition Tailoring in Ce-Doped Multicomponent Garnet Epitaxial Film Scintillators

Petr Prusa,*[,†,‡] Miroslav Kucera,[§] Jiri A. Mares,[†] Zuzana Onderisinova,[§] Martin Hanus,[§] Vladimir Babin,[†] Alena Beitlerova,[†] and Martin Nikl[†]

[†]Institute of Physics AS CR, Cukrovarnicka 10, 16253 Prague, Czech Republic

[‡]Faculty of Nuclear Sciences and Physical Engineering, Czech Technical University in Prague, Brehova 7, 11519 Prague 1, Czech Republic

[§]Faculty of Mathematics and Physics, Charles University, Ke Karlovu 5, 12116 Prague 2, Czech Republic

ABSTRACT: Bulk single crystals of multicomponent garnet scintillators $Lu_{3-x}Gd_xGa_y$-$Al_{5-y}O_{12}$:Ce exhibit much improved scintillation properties in optimized composition islands ($x = 2-3$, $y = 2-3$) compared to the simple $Lu_3Al_5O_{12}$:Ce one. Namely, a much higher light yield, less intense slow component in the scintillation response, and better energy resolution have been achieved. This work shows that comparable enhancement of the scintillation performance can be reached also in the case of epitaxial garnet films of similar composition though the nature of trapping states acting in the transfer stage of the scintillation mechanism may be different. This is the first time that excellent scintillation properties were reproduced in epitaxial films. $Lu_{3-x}Gd_xGa_yAl_{5-y}O_{12}$:Ce samples were grown by liquid phase epitaxy from $BaO-B_2O_3-BaF_2$ flux and quantitatively compared with top performance bulk crystals as concerns light yield, energy resolution, scintillation decay, and afterglow characteristics. Reported characteristics point to the potential of such thin film scintillators in high resolution two-dimensional imaging and particle beam diagnostics.

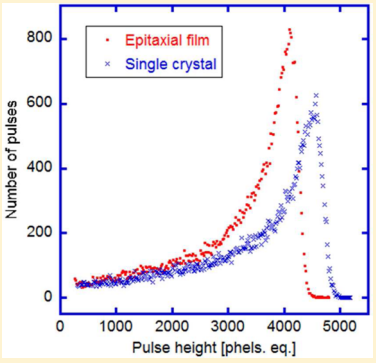

1. INTRODUCTION

Favorable scintillation characteristics of single crystal of $Y_3Al_5O_{12}$:Ce (YAG:Ce) were reported already in 1970s.[1] It is a material with very good light yield, fast scintillation response, and decent energy resolution, the properties of which have been instantaneously improved due to Czochralski growth technology optimization.[2−5] Additionally, it is non-hygroscopic, chemically stable, and has excellent optical and mechanical properties. Therefore, bulk crystals of YAG can be processed into very thin scintillating screens (down to 5 μm thickness) by cutting and polishing. These scintillating screens are used as electron detectors in electron microscopes for example[6,7] and can be applied in diagnostics of synchrotron beams or other particle accelerators as well.[8,9]

However, the YAG:Ce proton number is rather low, which makes high energy photon (hard X and γ rays) detection inefficient. In the effort to diminish such a disadvantage, the yttrium cation was replaced by lutetium and $Lu_3Al_5O_{12}$:Ce (LuAG:Ce) single crystals became of interest.[5,10−12] LuAG:Ce acquires a much higher proton number and offers quite high detection efficiency. LuAG:Ce bulk crystals can be processed into thin scintillation screens as well and can be used in 2D micro-radiography.[13−15]

Generally, the performance of bulk LuAG:Ce crystals grown from melt is negatively affected by shallow electron traps, usually attributed to LuAl antisite defects.[16,17] Antisite defects are produced due to high crystal growth temperature necessary for all melt growth techniques as Czochralski or Bridgman ones, and the presence of two cations of equal trivalent charge. The presence of antisite defects leads to intensification of slow scintillation components, decrease of light yield, and possibly to worsening of energy resolution.[18]

Recently, the "band-gap engineering" strategy was adopted for reducing the negative effects of shallow traps in bulk crystals grown from the melt.[19−27] Using the Ga admixture, it is possible to lower the bottom of the conduction band of LuAG. Although traps remain present in the material, they become buried in the conduction band. This approach strongly suppresses trapping effects which degrade the scintillation response. On the other hand, a reduced gap between the bottom of the conduction band and the $5d_1$ excited state of the Ce^{3+} luminescent center moves the onset of undesired excited state ionization to lower temperatures. Fortunately, this gap can be enlarged by the Gd admixture.

Recently, several studies reported much better scintillation properties of multicomponent $(Lu,Y,Gd)_3(Al,Ga)_5O_{12}$:Ce single crystals or ceramics in comparison with LuAG:Ce or YAG:Ce counterparts.[19−23,26−28] Very high light yield approaching 50 ph/keV, excellent energy resolution, and suppressed slower scintillation component were observed in bulk crystals.[28,29] In the latest studies the light yield approached the value of 58 000 photon/MeV in $Gd_3Ga_{2.7}Al_{2.3}O_{12}$:Ce

Received: March 5, 2015
Revised: June 17, 2015
Published: June 25, 2015

DOI: 10.1021/acs.cgd.5b00309
Cryst. Growth Des. 2015, 15, 3715−3723

composition, and the best energy resolution of 4.2%@662 keV was reached in $Gd_3Ga_{2.4}Al_{2.6}O_{12}$:Ce single crystals.[30] Moreover, a light yield of ceramic GAGG:Ce ($Gd_3(Al,Ga)_5O_{12}$) reached 70 ph/keV.[23] Consequently, this success has led to investigation of their possible application in space,[31] Compton cameras,[32] γ-ray spectrometry,[33] or nuclear medicine.[34,35]

For the above-mentioned two-dimensional (2D) imaging the production of a few micrometers thick screens by cutting and polishing is quite expensive, and for larger diameters above 5 cm it becomes technically very difficult. In any case, the minimum thickness is about 5 um. To lower manufacturing costs of screens and increase their dimensions, one can produce thin single crystalline films by the liquid phase epitaxy (LPE) method.[36−43] Moreover, LPE screens can be prepared even thinner compared to mechanically polished ones, which may further improve the 2D resolution in the images.

Applying the LPE manufacturing route, the film is grown onto an undoped substrate, usually produced from cheaper raw materials with lower purity grade. Additionally, it is possible to use heteroepitaxial growth; i.e., the substrate and the film have different dopant or even somewhat modified compositions: such phoswich solutions can resolve the individual components in mixed beams.[44,45]

The LuAG:Ce LPE grown scintillating films have been under development for approximately 15 years.[46,47] It was found that LPE grown films suffer much less from the presence of Lu_{Al} antisite defects.[16] Epitaxial garnet films are prepared from flux at temperatures almost 1000 K lower, so the antisite defects concentration is considerably reduced.[48] It results especially in the improvement of timing characteristics of these scintillators.[37]

On the other hand, epitaxial films can be contaminated by the ions coming from the used flux. Films grown from PbO-based flux contain Pb^{2+} ions, which act as quenching centers at room temperatures, thus lowering the light yield.[49,50] Optimization of growth conditions can diminish the negative effects of Pb^{2+} contamination, but their complete removal is impossible and their light yield under alpha excitation was at best comparable to bulk single crystals of YAG:Ce or LuAG:Ce,[18,51−55] i.e., approximately two times lower than light yield of recently discovered multicomponent garnet scintillators. However, the more recently used BaO-based flux does not contaminate the film and has a much lower negative effect on scintillation properties.[39,56] Unfortunately, high viscosity of this flux leads to production of pits and other macroscopic defects in the film.[57] Light yield is not severely affected, but an intense slow scintillation response component does exist.[51] Slow scintillation is most probably caused by trapping of charge carriers in shallow traps related to unspecified structural defects.

Very recently, the LPE method was adopted for production of multicomponent garnet films containing a significant amount of Gd and Ga.[58−63] This approach was inspired by the success of Gd−Ga balanced garnet bulk scintillators doped by Ce^{3+}. Despite much lower (if any) antisite defects concentration in epitaxial films, the Gd+Ga admixture may have a positive effect on scintillation properties of epitaxial garnet films as well given the fact that also deeper electron traps were diminished by Ga admixture in LuAG:Ce single crystals.[20] However, our first results were rather ambivalent.[58] Some improvement of light yield, energy resolution, and relative intensity of fast scintillation component was observed for $Gd_{1.50}Y_{1.44}Al_{5.05}O_{12}$:Ce sample grown from PbO-based flux. On the other hand, Ga containing samples performed slightly worse. Nonetheless, samples in our previous study contained only low concentrations of Ga and Gd, far from the optimal composition found for bulk crystals.

2. EXPERIMENTS AND METHODS

Therefore, this paper deals with preparation and characterization of high purity LPE-grown Ce-doped multicomponent garnet films containing a higher amount of Ga and Gd, closer to composition of the best performing garnet bulk crystals reported so far.

Ce^{3+}-doped epitaxial garnet films $(Lu,Gd)_3(Ga,Al)_5O_{12}$:Ce were grown in the Technology Laboratory of Charles University, Prague, by isothermal dipping liquid phase epitaxy from $BaO-B_2O_3-BaF_2$ flux onto Czochralski grown garnet substrates of 20 mm in diameter. The substrates were horizontally attached in the Pt holder, which rotated during growth at 120 rpm, and the rotation direction changed every 4 s. Resulting film thicknesses determined by weighing were in the range from 9.4 to 34.5 μm. Sample parameters are presented in Table 1.

Table 1. Composition of $Lu_{3-x}Gd_xGa_yAl_{5-y}O_{12}$:Ce Films (Determined by EPMA) and Reference Crystals, Substrates, Film Thickness, and Lattice Misfit $\Delta a = a_f - a_s$

sample	substrate	x	y	thickness [μm]	Δa [Å]
1LGB3	LuAG	0.14	0.00	17.9	0.006
1LGB4	LuAG	0.14	0.00	12.0	
2LGB2	LuAG	0.45	0.00	17.3	
2LGB4	LuAG	0.84	0.00	9.4	0.054
2LGB5	YAG	0.95	0.00	15.3	−0.031
3LGB1	YAG	1.15	0.81	22.0	
3LGB2	YAG	1.12	1.41	17.2	0.070
3LGB3	YAG	1.17	1.94	22.4	
4LGB1	YAG	1.62	2.02	34.5	0.117
4LGB2	YAG	2.08	2.10	23.3	
4LGB3	YAG	2.19	2.62	32.2	0.184
4LGB4	GGG	2.20	2.70	24.0	−0.183
4LGB5	YGG	2.19	2.69	11.9	−0.095
5LGB5	GGG	3.02	2.70	25.5	
5LGB6	YGG	3.02	2.69	21.9	
5LGB9	YGG	3.05	3.54	28.1	
L2G3	crystal	1.00	3.00		
L1G3	crystal	2.00	3.00		
L0G3	crystal	3.00	3.00		
L0G2.6	crystal	3.00	2.60		

Absorption spectra, photoluminescence excitation and emission spectra, X-ray excited radioluminescence spectra, and photoluminescence decay curves were measured for all of the samples. Absorption and photoluminescence spectra were measured using commercial spectrometers Specord 250 and Horiba JY Fluoromax 3. α particle excited scintillation decays and X-ray induced afterglow were measured for selected samples only. Radioluminescence spectra and photoluminescence decays were measured at custom-made spectrofluorometer 5000M, Horiba Jobin Yvon using an X-ray tube (10 kV, 50 mA) and nanoLED pulse excitation sources, respectively. X-ray tube is type DX-W 10×1-S 2400 W (tungsten) short anode powered by high voltage supply ISO−DEBYEFLEX 3003−60 kV. The crystallographic properties and lattice parameters of the films were studied using XRD on PANalytical X-ray high-resolution diffractometer, and composition was determined by electron probe microanalysis.

Photoelectron yield was measured using hybrid photomultiplier (HPMT) model DEP PPO 475B,[61] spectroscopy amplifier ORTEC model 672, and multichannel buffer ORTEC 927TM. Silicon grease was used for optical coupling of HPMT and samples. α-particles from ^{239}Pu (5.157 MeV) were used for excitation of film scintillation response, since films are too thin for effective high energy photon

DOI: 10.1021/acs.cgd.5b00309
Cryst. Growth Des. 2015, 15, 3715−3723

Table 2. Scintillation Characteristics of Epitaxial Films and Reference Crystals

sample	PhY_{Am} [a,f]	$PhY_{Cs,r}$ [a,f] ($PhY_{Cs,nr}$)	γ/α [b,f]	$fwhm_{\alpha(\gamma)}$ [c,f]	aftergl [%]	$A_{10/0.5}$ [%]	LY_{γ} [d,f]	LY_{α} [e,f]
1LGB3	139			15.1		208		1331
1LGB4	185			14.5		197		1779
2LGB2	163			12.8		302		1682
2LGB4	170			13.1		226		1827
2LGB5	180			12.4		283		1935
3LGB1	173			17.5		255		1849
3LGB2	432			10.6		192		4393
3LGB3	753			8.2	0.20	179		7351
4LGB1	826			9.2	0.09	133		8691
4LGB2	801			10.4	0.22	109		8749
4LGB3	733			12.7	0.25	108		7833
4LGB4	774			9.3	0.72	103		8276
4LGB5	797			7.4	0.96	104		8562
5LGB5	710			8.3	0.44	100		5922
5LGB6	771			12.2	1.00	100		6481
5LGB9	99			16.0		100		808
L2G3	383	3371(2642)	6.9	15.6 (17.0)		115	21300	3088
L1G3	387	3562(2632)	6.8	17.4 (12.9)		148	25800	3793
L0G3	883	7013(5099)	5.7	8.0 (5.8)		109	53800	9427
L0G2.6	884	5295(3663)	4.1	6.7 (5.4)		131	41100	9918

[a]Photoelectron yield measured under $\alpha(\gamma)$-particle excitation (nr - no reflector; r−with reflector) in phels/MeV. [b]Ratio of PhY (LY) under γ and α excitation. [c]Energy resolution measured under $\alpha(\gamma)$-particle excitation (no reflector) in [%]. [d]Light yield under γ −particle excitation in ph/MeV (with reflector). [e]Rough estimate of light yield ph./MeV. [f]1 μs amplifier shaping time.

interactions. The radioactive source was placed directly onto epitaxial film to minimize energy losses in air. All measurements were performed at room temperature. Energy resolution and photoelectron yield were obtained using Gaussian fit of peaks in the spectra.[52]

Photoelectron yield (PhY) rises with amplifier shaping time. In this article, we used parameter $A_{10/0.5}$ = PhY (10 μs)/PhY (0.5 μs) to quantify the increase, where PhY (t) means photoelectron yield measured using amplifier shaping time t. Higher $A_{10/0.5}$ reflects more intense slower component with decay constants a few microseconds long. An alternative quantification of the PhY dependence on shaping time can also be used.[52] This alternative is usable only if slow component is intense enough.

Furthermore, several Czochralski grown bulk crystal samples produced by the Yoshikawa group at Tohoku University, Sendai, Japan,[29,65] were used for reference purposes. The Ce concentration in these samples is few tenths of a percent, and their size is 5 × 5 × 1 mm with 5 × 5 faces polished. Their light and photoelectron yield were measured using α-particles from ^{239}Pu and γ radiation of ^{137}Cs (661.6 keV). See Tables 1 and 2 for composition and scintillation characteristics.

Small penetration range of α-particles (10 μm approximately) prohibits a reflector application, resulting in poorer and badly defined photon collection efficiency. Light yield was only roughly estimated due to this uncertainty.

The γ/α ratio of bulk crystals was determined. Measurement focused on reaching the same photon collection efficiency for both types of excitation; even the slightly reflecting dummy α source was used for measurement under γ excitation. Yet, there are differences—α-particles excite samples near the surface, while gamma particles in the whole volume. Also, collection efficiency is probably not the same for bulk crystals and epitaxial films due to an optical boundary substrate−film in epitaxial sample, which is not present in bulk crystals.

Epitaxial films with the highest photoelectron yield were selected for afterglow measurement. Additionally, substrate afterglow was measured as well. Substrate response was excited by X-ray tube (the same as for RL spectra measurement) operated at 40 kV, and film response was excited by the same tube operated at 10 kV. Lower voltage was used for films in order to avoid the substrate excitation as much as possible. It was calculated that even at 10 kV high voltage, a few percent of X-ray photons penetrates into the substrate. Afterglow was determined as a ratio of luminescence intensity during long X-ray excitation and luminescence intensity 3 ms after excitation cutoff. Excitation cutoff is executed after the photomultiplier current stabilization.

Scintillation decay curves were excited by α-particles from ^{241}Am and measured using photomultiplier type Hamamatsu R375 and Tektronix TDS3052C digital Phosphor Oscilloscope. Decay curves were decomposed to 2−3 exponential terms. Convolution of multiexponential function with instrumental response was fitted to experimental data using software SpectraSolve 3.01 PRO (1997 Ames Photonics, Inc.).

3. RESULTS AND DISCUSSION

3.1. Growth of Multicomponent Garnet Films by the LPE. Ce^{3+}-doped multicomponent garnet films were grown by isothermal dipping liquid phase epitaxy (LPE) onto Czochralski grown garnet substrates. The sample set covered a wide interval of compositions of $(Ce_zGd_xLu_{3-x-z})(Ga_yAl_{5-y})O_{12}$, where the Gd content x = 0.14−3 and Ga content y = 0−3.54, see Table 1. Cerium content in films slightly differs depending on the composition and lattice constant of films and was in the range z = 0.01−0.02. Sixteen samples were chosen for further characterization, Table 1.

Instead of PbO-B_2O_3 flux, a lead-free BaO-B_2O_3−BaF_2 flux (referred here as BaO flux) was used which has been proven as the best alternative in the preparation of efficient LPE scintillator films of the above-mentioned garnet compounds. The samples grown from this flux exhibit excellent purity compared to those grown from standard PbO flux; namely, they do not contain any Pb^{2+} ions, which severely quench Ce^{3+}-related emission.[49,50] The Ba^{2+} ions almost do not enter into the garnet lattice due to their large diameter (according to the GDMS analysis their concentrations is <5 ppm), and the concentration of other impurities depends only on purity of input raw materials. The growth temperatures were between 1040 and 1060 °C, and the growth rates were ∼0.1 μm/min. The details of the growth process from this flux were published elsewhere.[39,56]

DOI: 10.1021/acs.cgd.5b00309
Cryst. Growth Des. 2015, 15, 3715−3723

In order to cover a wide range of sample compositions, various substrates were used: LuAG ($Lu_3Al_5O_{12}$), YAG ($Y_3Al_5O_{12}$), YGG ($Y_3Ga_5O_{12}$), and GGG ($Gd_3Ga_5O_{12}$) with (111) and (100) crystallographic orientations. For each composition, a substrate with lattice constant which matches best the estimated lattice constant of the film was used.

All the films are single phase and single crystalline. Figure 1 shows a typical XRD diffraction of a $(GdLu)_3(GaAl)_5O_{12}$ film

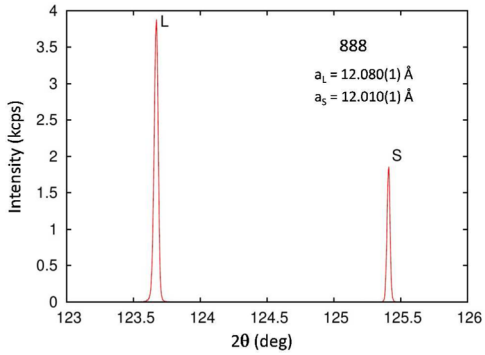

Figure 1. XRD profile of 888 diffraction of a 7 μm thick $(GdLu)_3(AlGa)_5O_{12}$:Ce film (L), grown from the BaO flux on (111) oriented YAG substrate (S); the film−substrate lattice mismatch is Δa = 0.07 Å (3LGB2).

grown from the BaO flux on YAG substrate. In spite of a relative large mismatch, $a_s - a_f$ = 0.07 Å, the film apparently exhibits high crystallographic quality with fwhm comparable to that of the YAG substrate.

While the films grown from the PbO flux have a smooth surface with excellent morphology, those grown from the BaO flux suffer from macroscopic defects, especially surface pits, due to higher viscosity and surface tension and more problematical homogenization of the BaO melt, cf. refs 39 and 57. However, these macroscopic defects do not influence the emission and scintillation properties except for light scattering on the rough surface of samples grown at larger lattice mismatch, $a_s - a_f >$ 0.05 Å, where the rms surface roughness can reach even hundreds of nanometers compared to several nanometers in homoepitaxial films.

A photograph of a garnet film grown on YAG substrate and microphotography of the surface is displayed in Figure 2.

3.2. Optical, Luminescence and Scintillation Characterization. All samples exhibited very similar excitation spectra, see Figure 3. Two most intense peaks are attributed to 4f-$5d_{1,2}$ Ce^{3+} transitions at about 440 and 345 nm, respectively (sample 4LGB2). With increasing Ga concentration 4f-$5d_1$ Ce^{3+} transition shifts to shorter wavelengths, and with increasing Gd concentration to longer wavelengths.[1] The weak sharp lines observed around 275 and 310 nm correspond to spin and parity forbidden 4f−4f transitions, $^8S \rightarrow {}^6I_J$ and $^8S \rightarrow {}^6P_J$, respectively, in the Gd^{3+} ions.[59] Films exhibit typical doublet emission originating from $5d_1$-4f transition of Ce^{3+} centered at 510−560 nm depending on Gd and Ga concentration. Shift acts in the same direction as that of 4f-$5d_1$ Ce^{3+} transition in excitation spectra.

Radioluminescence spectra of low Gd concentration samples exhibit intense $P_{7/2} \rightarrow {}^8S_{7/2}$ transition in Gd^{3+}, see Figure 4. This emission is extremely slow with millisecond decay times. Its intensity decreases with increasing Ce and Gd concentration and eventually is eliminated due to energy migration in Gd

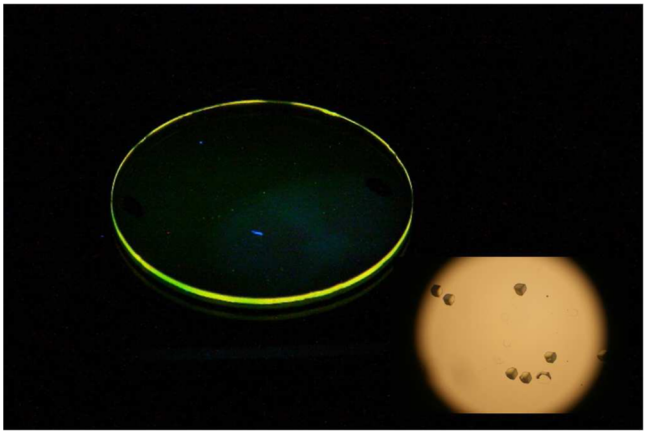

Figure 2. $(Gd,Lu)_3(Al,Ga)_5O_{12}$ epitaxial film grown on YAG substrate under ultraviolet illuminated at 355 nm. The green-yellow emission from the edges is due to the waveguide effect. In the inset, optical microscopy of the surface pits is shown (magnification 200×). The film−substrate lattice mismatch is <0.02 Å.

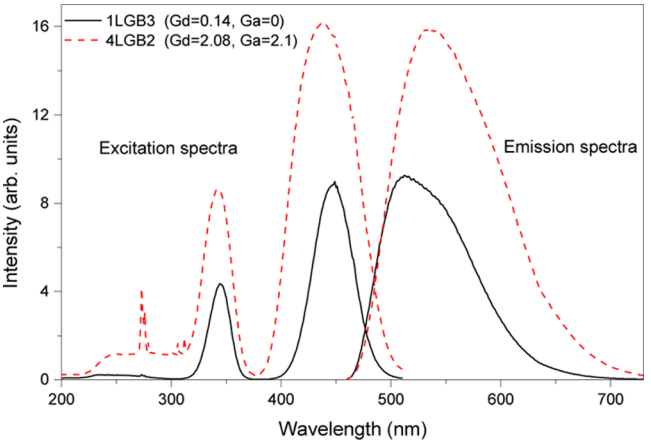

Figure 3. Emission and excitation spectra of samples 1LGB3 and 4LGB2 measured at room temperature at λ_{em} = 520 nm, λ_{ex} = 440 nm.

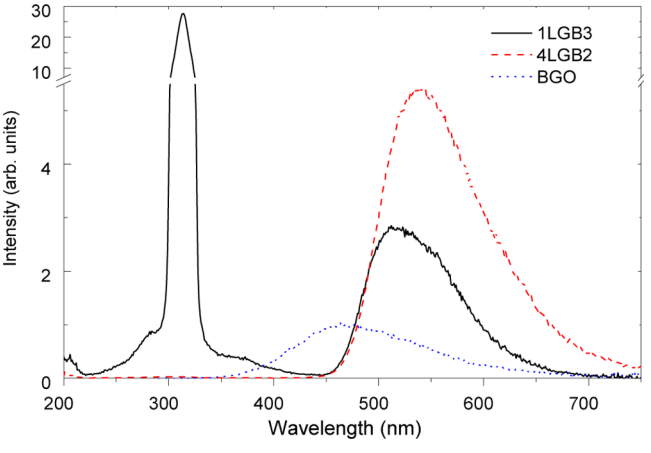

Figure 4. X-ray excited radioluminescence spectra, at 10 kV and 50 mA, of samples 1LGB3, 4LGB2, and BGO reference crystal.

sublattice and consequently enhanced energy transfer toward Ce^{3+} centers,[60,66] see also Figure 4.

5d-4f Ce^{3+} photoluminescence decay curves of Ce^{3+} center in samples having higher Gd concentration exhibit a decay time within 50−70 ns. Similar decay times were observed for α-

DOI: 10.1021/acs.cgd.5b00309
Cryst. Growth Des. 2015, 15, 3715−3723

particle excited decay, but a slower decay component was present as well, see Figure 5. This slower decay component

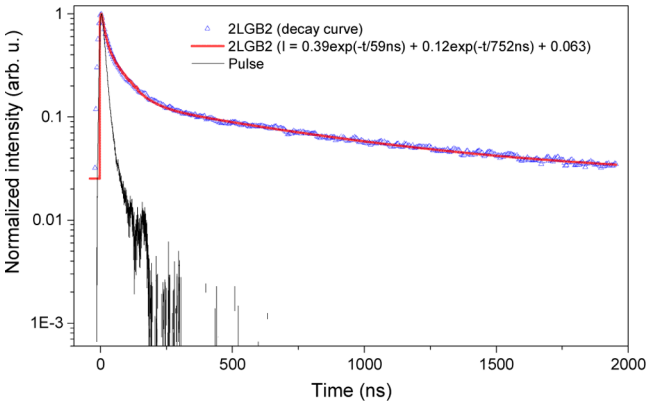

Figure 5. Spectrally unresolved α-excited decay curve of sample 2LGB2.

intensity decreases with increasing Gd and Ga concentration, Figure 6. Such behavior points to a diminishing effect of traps

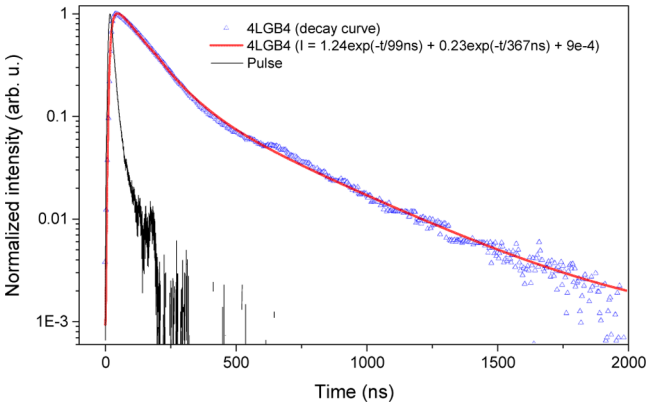

Figure 6. Spectrally unresolved α-excited scintillation decay curve of sample 4LGB4. An increase observed around 650 ns is an artifact caused by the PMT afterpulse effect.

in the scintillation process at higher Ga and Gd concentrations. This behavior slightly differs from data of ref 67 for Czochralski grown GAGG:Ce bulk crystals. The films exhibit faster scintillation decays (fast component having decay time 58−78 ns (all samples), slow component 622−714 ns (series 1LGB), 724−752 ns (2LGB), 643−744 ns (3LGB), 349−373 ns (4LGB), and less than 250 ns in 5LGB series) under α-particle excitation, while in the bulk crystal the decay time values are 145 and 764 ns.[67] It points to different influences of traps in the transport stage of the scintillation mechanism in films and crystals, although it is not possible to identify the nature of traps from the decay measurement.

Photoelectron yield measured under α-particle excitation of several epitaxial films exceeded 700 phels/MeV, two times even 800 phels/MeV, see Table 2. These are the highest values ever reached in garnet epitaxial films, exceeding at least two times those measured in our films prepared from the PbO flux[58,60] and LGGAG:Ce films from a recent study,[63] also grown using PbO flux. Moreover, it outperforms the best LuAG:Ce epitaxial films having PhY approximately 350 phels/MeV as well.[63] Clear dependence of photoelectron yield on sample composition is observed, see Figure 7. At low Ga concentration, the photoelectron yield values remain below 200 ph/MeV. In the

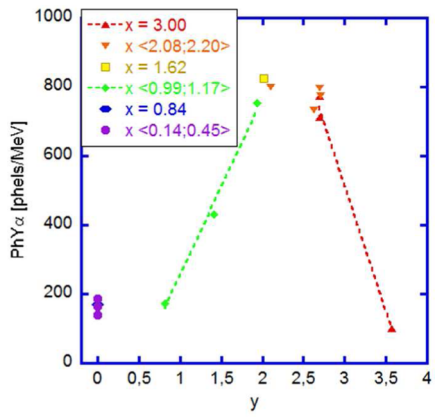

Figure 7. Dependence of α-excited photoelectron yield on sample composition for all $Lu_xGd_{3-x}Ga_yAl_{5-y}O_{12}$:Ce films. Lines are only to guide the eye in stressing the increase and decrease of PhY.

interval $0.81 < y < 2.0$, a sharp increase of photoelectron yield is observed, reaching the best value 826 phels/MeV at $y = 2.02$ of Ga (4LGB1). For $1.8 < y < 2.7$, the photoelectron yield remains almost independent of y. Finally, there is a huge drop of photoelectron yield at high Ga content, for $y = 2.98$ to 99 phels/MeV (5LGB9). These results are consistent with previous findings on bulk crystals.[19] In ref 63, the samples with $x = 1.5$ and 1.75 grown from PbO-based flux were measured. LY reaches its maximum at $y = 3.5$ in ref 63, compared to y values reported in our work here (2 to 3).The difference may result either from different x value or different flux used.

PhY = LY × QE × CE, where QE is photocathode quantum efficiency and CE denotes photon collection efficiency. PhY is directly measured quantity, but its value depends also on photomultiplier and measurement geometry; i.e., it is not a characteristic of the sole scintillator.

Therefore, LY is rather presented in the literature. However, knowledge of QE and CE is necessary for LY calculation. QE for emission spectra was calculated using RL spectra of all samples and QE(λ) for all wavelengths given by the HPMT producer. QE is in an interval 12.5−16.6% for LPE films and 12.9−15.8% for reference crystals. CE is considered close to unity usually. In our case, CE < 1 due to impossibility to use reflector. CE can be roughly estimated: $PhY_{nr} = LY \times QE \times CE_{nr} = QE \times CE_{nr} \times (PhY_r/(QE \times CE_r)) = CE_{nr} \times (PhY_r/CE_r)$. Index r denotes measurement with reflector, and nr without reflector, respectively. Assuming $CE_r = 1$, $CE_{nr} = PhY_{nr}/PhY_r$. PhY_r and PhY_{nr} values of reference crystals measured using gamma photons from ^{137}Cs are presented in Table 2. CE_{nr} estimates lie in the interval 0.69−0.78.

Experiment was designed in order to have same CE_{nr} under alpha and gamma excitation as well. Same measurement geometry was used in both cases. Also, a dummy alpha source was applied. Nonetheless, one must keep in mind that the CE_{nr} estimate is rough due to unavoidable differences among all measurements. Therefore, LY measured under alpha excitation is rough as well, unlike the quite precise PhY value. CE_{nr} for LY under alpha excitation is assumed to be the average of CE_{nr} values for crystals, i.e., 0.735.

DOI: 10.1021/acs.cgd.5b00309
Cryst. Growth Des. 2015, 15, 3715−3723

Gd concentration influence is not well traceable in our measurement as it increases simultaneously with Ga concentration in our sample set. At $y = 0$, there is a sample subset of $0.14 < x < 0.81$. No positive influence of Gd concentration is observed in the subset. At a higher x value around 1.15 (3LGB series), strong improvement of scintillation characteristics is observed. However, it should be most probably ascribed to increasing Ga content. For more detailed information on Gd concentration influence on scintillation properties in $Lu_{3-x}Gd_xAl_5O_{12}$:Ce, see ref 60. Gd and Ga concentration influence was studied in ref 68 as well, but results are somewhat different due to an additional influence of Pb^{2+} contamination.

Conduction band bottom position is given by the interplay of Gd and Ga concentration.[69] For sample 5LGB9, the conduction band bottom edge and Ce^{3+} $5d_1$ excited state are probably so close to each other that significant thermal ionization of excited state occurs, thus lowering the photoelectron yield significantly. According to ref 24, this shift of conduction band bottom starts when octahedral sites are completely occupied by Ga and Ga^{3+} ions begin to occupy tetrahedral sites also. On the other hand, another articles[69,70] conclude that difference in site occupation is negligible[70] or even that Ga prefers to occupy tetrahedral site,[71] like it does in isostructural $Y_3(Al,Ga)_5O_{12}$:Ce.[72,73]

Interestingly, reference GGAG:Ce Czochralski grown crystal photoelectron yield measured at the same conditions is only 7% higher than 4LGB1 photoelectron yield. Light yield of the same crystals measured with reflector under gamma excitation of ^{137}Cs is 53 800 ph/MeV.

Energy resolution (fwhm) is influenced mainly by photoelectron (light) yield value and material nonproportionality. In this study, nonproportionality could not be determined due to small film thickness. Correlation between fwhm and photoelectron yield is evident in our data, but is not very well pronounced. It is not possible to conclude whether this effect originates from differences in nonproportionality or inhomogeneity of the sample. However, nonproportionality may differ significantly among samples and influence energy resolution as it differs at bulk crystals,[30] see Table 2. Two crystals ($Gd_3Ga_{2.6}Al_{2.4}O_{12}$:Ce, $Gd_3Ga_3Al_2O_{12}$:Ce respectively) of the highest, almost the same photoelectron yield (884 phels/MeV, 883 phels/MeV respectively) exhibit different energy resolution (6.7%, 8.0% respectively). Crystal having better energy resolution shows a lower γ/α ratio (of photoelectron yields) 4.1 than the worse crystal having γ/α ratio equal to 5.8.

Since the α particle source is placed exactly on the surface of a film, not only lateral but also depth inhomogeneity may contribute to fwhm deterioration. Additionally, possible significant absorption of scintillation photons or different light collection efficiency from various places on film surface would lead to fwhm deterioration too. The best energy resolution among films is only slightly worse than best energy resolution among the reference samples, i.e., 7.4% (4LGB5) and 6.7% respectively, see Figure 8. Several other high yield films exhibited satisfactory fwhm values below 10% as well.

Measurement of slow scintillation component relative intensity, measured as $A_{10/0.5}$ parameter, is presented in Table 1. $A_{10/0.5}$ decreases as Ga and Gd content is increasing. $A_{10/0.5} >$ 190% for $y < 1.4$, $A_{10/0.5}$ falls rapidly then, until it reaches values 100−109% for higher Ga and Gd concentration. Obviously, reference crystals exhibit similar $A_{10/0.5}$ dependence on composition. Samples with very low parameter $A_{10/0.5}$ have high photoelectron yield and good energy resolution.

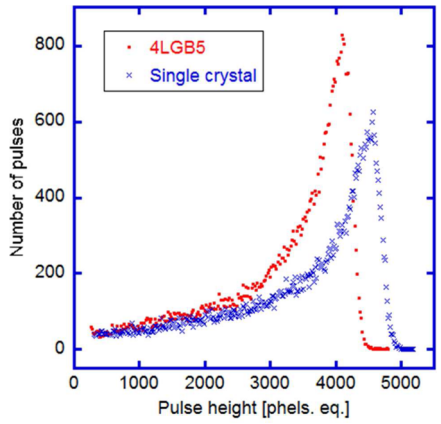

Figure 8. α-Excited pulse height spectrum of sample 4LGB5 (fwhm = 7.4%, PhY = 797 phels/MeV) and single crystal L0G2.6 (fwhm = 6.7% PhY = 884 phels/MeV). Amplifier shaping time = 1 μs, excited by ^{239}Pu.

Eight samples with the highest photoelectron yield were selected for afterglow measurement. Unfortunately, substrate excitation cannot be completely avoided even if low voltage (10 kV) on X-ray tube is used. Quite low percentage of X-ray beam energy is absorbed in the substrate compared to epitaxial film. On the other hand, the luminescence of substrate could be very persistent since there are no Ce luminescence centers in it. Therefore, we have measured substrate luminescence and afterglow as well. LuAG and YAG substrates exhibit relatively lower afterglow, 0.15% and 0.66%, respectively. YGG luminescence intensity remains on 10% of the original value at 3 ms after end of the pulse. GGG substrate luminescence is extremely persistent, it remains on 80% of the initial value even after 40 ms. On the other hand, YGG and GGG luminescence is not intense at all in absolute numbers (RL integral intensities in % of BGO are LuAG − 210%, YAG − 207%, YGG − 20%, GGG − 3%).

Thus, up to a small extent, the substrate response is contributing to the epitaxial film afterglow measurement. Two sets of measurements were obtained, with and without an edge filter which cut UV emission from substrate. Indeed, values measured with filter are comparatively lower. Unfortunately, substrate may still contribute to the afterglow signal even if filter is applied due to UV substrate emission reabsorption in the Ce^{3+} 4f-$5d_2$ absorption band.

The values of afterglow are in the range from 0.09% to 1.0% for filtered measurements, and 0.21% to 1.51% for nonfiltered measurements. It is interesting to note that afterglow values are highest for films on YGG substrate and lowest for films on YAG substrate (LuAG substrate not measured). There is a slight correlation between sample thickness and afterglow value (Pearson's correlation coefficient = −0.71), but between y (Tables 1 and 2) and afterglow value (0.74) as well. Considering the thickness, substrate afterglow and attenuation coefficient for X-rays, the substrate scintillation response is contributing most probably to film afterglow measurement and increases afterglow, indeed. Therefore, we conclude that film contribution in afterglow is even slightly lower than measured values, i.e., 0.1−0.2% for the best samples which is comparable with the afterglow of the best GGAG:Ce crystals reported in the literature.[74]

Discussing parameter $A_{10/0.5}$ (in correlation to scintillation decay) together with PhY, the trends become evident, see

DOI: 10.1021/acs.cgd.5b00309
Cryst. Growth Des. 2015, 15, 3715−3723

Figure 9. If no Ga is present, Gd concentration increase leads to an increase of PhY measured with shaping time 10 μs, but less

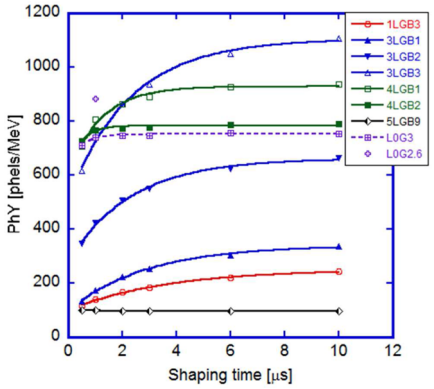

Figure 9. Shaping time dependence of PhY of selected samples.

significant increase of PhY is measured with 0.5 μs shaping time (compare 1LGB3 and 2LGB in Figure 9). At first, parameter $A_{10/0.5}$ and intensity of slow components in scintillation decay is increasing with increasing Gd concentration as well. If (Gd) x > 0.5 and (Ga) y = 0, the parameter $A_{10/0.5}$ does not increase significantly anymore. We hypothesize that Gd^{3+} emission and/or energy transfer from Gd^{3+} to Ce^{3+} contribute to the slow component of scintillation response.[57] At a higher Gd concentration, energy transfer through Gd sublattice become faster and more efficient, which leads to a decrease of parameter $A_{10/0.5}$ and an increase of PhY.

Substitution of Ga for Al in the range of Ga concentrations from 0.81 to 1.94 (samples 3LGBX) leads to decrease of $A_{10/0.5}$ parameter and substantial PhY increase, see Figure 9. Relative intensity of slow scintillation response component is decreasing, but absolute intensity of the same component is increasing. Tentatively, extremely slow decay components are suppressed in favor of components with decay times from tens of nanoseconds up to a few microseconds. Sample 3LGB3 exhibits the highest PhY at 10 μs shaping time, even higher than the best single crystals.

Sample 4LGB1 ((Gd) x = 1.62; (Ga) y = 2.02) exhibits the highest PhY at 1 μs shaping time and $A_{10/0.5}$ = 133%. If (Gd) x > 2 and (Ga) y > 2, PhY measured at 0.5 μs shaping time is approximately constant, but parameter $A_{10/0.5}$ is decreasing with increasing x and/or y. Gd emission is already quenched at (Gd) x > 2. Shallow traps influence is further decreasing with increasing y: even the components with μs decay times become suppressed.

Sample 5LGB9 ((Gd) x = 3.00; (Ga) y = 3.540) exhibits practically no slow scintillation response and very low PhY = 99 phels/MeV. Increasing Ga concentration leads to an increase of Stokes shift. Onset of thermal quenching is shifted to lower temperatures.[24] Additionally, a smaller gap between $5d_1$ Ce^{3+} excited state and conduction band bottom increases probability of excited state ionization,[75] which results in PhY loss.

4. CONCLUSIONS

Sixteen $(Lu,Gd)_3(Al,Ga)_5O_{12}$:Ce garnet films with a significant admixture of Ga and Gd cations prepared by liquid phase epitaxy from BaO-based flux have been measured. Compared to high quality bulk crystals with analogous composition, the best film samples exhibit similar values of α-excited photoelectron yield (film 4LGB1, 826 phels/MeV; bulk crystal L0G2.6, 884 phels/MeV) and similar energy resolution (sample 4LGB5, 7.4%; bulk crystal L0G2.6, 6.7%). To our best knowledge these are the highest light yield values ever obtained in garnet epitaxial films exceeding by at least two times the values previously reported for films prepared from PbO-based flux. Additionally, we determined the number of collected scintillation photons in an absolute way, unlike relative comparisons in many previous studies on epitaxial films.

Previously reported optimal composition of bulk crystals of multicomponent garnets, taking into account the photoelectron yield, energy resolution, and relative intensity of slow scintillation component, appears favorable also for the epitaxial films. The best films exhibit only a very small increase of pulse amplitude with amplifier shaping time. Furthermore, the measured afterglow of the film itself is very low, reaching the value around 0.1%, which is also comparable with that of the best bulk GGAG:Ce crystals reported so far.

Unlike in our previous study of samples grown from PbO-B_2O_3 flux, we observe significant improvement of scintillation performance in films at higher Ga ($1.8 < y < 2.7$) and Gd ($x > 1.5$) concentration when BaO-B_2O_3–BaF_2 flux is used. Increase in light yield accompanied by lower intensity of slow part of scintillation response components points to a more effective and faster energy transfer toward Ce^{3+} luminescence centers. The scintillation characteristics of epitaxial multicomponent garnet films grown from BaO-based flux are thus very similar to those obtained on high quality bulk crystals.

AUTHOR INFORMATION

Corresponding Author

*Tel.: +420 604 958 601. E-mail: petr.prusa@fjfi.cvut.cz.

Notes

The authors declare no competing financial interest.

ACKNOWLEDGMENTS

Financial support of Czech Science Foundation P204/12/0805 and RVO: 68407700 is gratefully acknowledged.

REFERENCES

(1) Autrata, R.; Schauer, P.; Kvapil, J.; Kvapil, J. *J. Phys. E: Sci. Instrum.* **1978**, *11*, 707.
(2) Moszyński, M.; Ludziejewski, T.; Wolski, D.; Klamra, W.; Norlin, L. O. *Nucl. Instrum. Methods Phys. Res., Sect. A* **1994**, *345*, 461–467.
(3) Mareš, J. A.; Nikl, M.; Beitlerová, A.; Horodyský, P.; Blažek, K.; Bartoš, K.; D'Ambrosio, C. *IEEE Trans. Nucl. Sci.* **2012**, *59*, 2120–2125.
(4) Yanagida, T.; Takahashi, H.; Ito, T.; Kasama, D.; Enoto, T.; Sato, M.; Hirakuri, S.; Kokubun, M.; Makishima, K.; Yanagitani, T.; Yagi, H.; Shigeta, T.; Ito, T. *IEEE Trans. Nucl. Sci.* **2005**, *52*, 1836–1841.
(5) van Eijk, C. W. E.; Andriessen, J.; Dorenbos, P.; Visser, R. *Nucl. Instrum. Methods Phys. Res., Sect. A* **1994**, *348*, 546–550.
(6) Autrata, R.; Hermann, R.; Müller, M. *Scanning* **1992**, *14*, 127–135.
(7) Lednický, F.; Coufalová, E.; Hromádková, J.; Delong, A.; Kolařík, V. *Polymer* **2000**, *41*, 4909–4914.
(8) Yang, B. *Beam Instrumentation Workshop 2002: Tenth Workshop*, May 6–9, 2002, Upton, NY; Vol. 648; AIP: Melville, NY, 2002; pp 59–78.
(9) van Garderen, E.; Boland, M.; LeBlanc, G.; Mountford, B.; Rhyder, A.; Starritt, A.; Walsh, A.; Zingre, K. *Proceedings of the 10th European Workshop on Beam Diagnostics and Instrumentation for Particle Accelerators* May 16–18, 2011, Hamburg, Germany; *MOPD007*; 2011; pp 47–49

DOI: 10.1021/acs.cgd.5b00309
Cryst. Growth Des. 2015, 15, 3715–3723

(10) Nikl, M.; Yoshikawa, A.; Kamada, K.; Nejezchleb, K.; Stanek, C. R.; Mareš, J. A.; Blažek, K. *Prog. Cryst. Growth Charact. Mater.* **2013**, *59*, 47−72.
(11) Petrosyan, A. G.; Ovanesyan, K. L.; Sargsyan, R. V.; Shirinyan, G. O.; Abler, D.; Auffray, E.; Lecoq, P.; Dujardin, C.; Pedrini, C. *J. Cryst. Growth* **2010**, *312*, 3136−3142.
(12) Chewpraditkul, W.; Swiderski, L.; Moszynski, M.; Szczesniak, T.; Syntfeld-Kazuch, A.; Wanarak, C.; Limsuwan, P. *Phys. Status Solidi A* **2009**, *206*, 2599−2605.
(13) Koch, A.; Raven, C.; Spanne, P.; Snigirev, A. *J. Opt. Soc. Am. A* **1998**, *15*, 1940−1951.
(14) Touš, J.; Blažek, K.; Nikl, M.; Mareš, J. A. *J. Phys.: Conf. Ser.* **2013**, *425*, 192017.
(15) Rack, A.; Garcıa-Moreno, F.; Baumbach, T.; Banhart, J. *J. Synchrotron Radiat.* **2009**, *432*, 432−434.
(16) Nikl, M.; Mihokova, E.; Pejchal, J.; Vedda, A.; Zorenko, Yu.; Nejezchleb, K. *Phys. Status Solidi B* **2005**, *242*, R119−R121.
(17) Stanek, C. R.; McClellan, K. J.; Levy, M. R.; Grimes, R. W. *Phys. Status Solidi B* **2006**, *243*, R75−R77.
(18) Průša, P.; Čechák, T.; Mareš, J. A.; Nikl, M.; Beitlerová, A.; Solovieva, N.; Zorenko, Yu.; Gorbenko, V. I.; Touš, J.; Blažek, K. *Appl. Phys. Lett.* **2008**, *92*, 041903.
(19) Kamada, K.; Endo, T.; Tsutsumi, K.; Yanagida, T.; Fujimoto, Y.; Fukabori, A.; Yoshikawa, A.; Pejchal, J.; Nikl, M. *Cryst. Growth Des.* **2011**, *11*, 4484−4490.
(20) Fasoli, M.; Vedda, A.; Nikl, M.; Jiang, C.; Uberuaga, B. P.; Andersson, D. A.; McClellan, K. J.; Stanek, C. R. *Phys. Rev. B: Condens. Matter Mater. Phys.* **2011**, *84*, 081102(R).
(21) Ogino, H.; Yoshikawa, A.; Nikl, M.; Mareš, J. A.; Shimoyama, J.; Kishio, K. *J. Cryst. Growth* **2009**, *311*, 908−911.
(22) Kamada, K.; Yanagida, T.; Pejchal, J.; Nikl, M.; Endo, T.; Tsutsumi, K.; Fujimoto, Y.; Fukabori, A.; Yoshikawa, A. *J. Phys. D: Appl. Phys.* **2011**, *44*, 505104.
(23) Yanagida, T.; Kamada, K.; Fujimoto, Y.; Yagi, H.; Yanagitani, T. *Opt. Mater.* **2013**, *35*, 2480−2485.
(24) Ogieglo, J. M.; Katelnikovas, A.; Zych, A.; Jüstel, T.; Meijerink, A.; Ronsa, C. R. *J. Phys. Chem. A* **2013**, *117*, 2479−2484.
(25) Dorenbos, P. *J. Lumin.* **2013**, *134*, 310−318.
(26) Seeley, Z. M.; Cherepy, N. J.; Payne, S. A. *J. Mater. Res.* **2014**, *29*, 2332−2337.
(27) Cherepy, N. J.; Kuntz, J. D.; Seeley, Z. M.; Fisher, S. E.; Drury, O. B.; Sturm, B. W.; Hurst, T. A.; Sanner, R. D.; Roberts, J. J.; Payne, S. A. *Proc. SPIE* **2010**, *7805*, 780501.
(28) Prusa, P.; Kamada, K.; Nikl, M.; Yoshikawa, A.; Mareš, J. A. *Radiat. Meas.* **2013**, *55*, 62−65.
(29) Kamada, K.; Yanagida, T.; Endo, T.; Tsutsumi, K.; Usuki, Y.; Nikl, M.; Fujimoto, Y.; Fukabori, A.; Yoshikawa, A. *J. Cryst. Growth* **2012**, *352*, 88−90.
(30) Kamada, K.; Kurosawa, S.; Prusa, P.; Nikl, M.; Kochurikin, V. V.; Endo, T.; Tsutsumi, K.; Sato, H.; Yokota, Y.; Sugiyama, K.; Yoshikawa, A. *Opt. Mater.* **2014**, *36*, 1942−1945.
(31) Sakano, M.; Nakamori, T.; Gunji, S. J.; Katagiri, J.; Kimura, S.; Otake, S.; Kitamura, H. *J. Instrum.* **2014**, *9*, P10003.
(32) Kataoka, J.; Kishimoto, A.; Nishiyama, T.; Fujita, T.; Takeuchi, K.; Kato, T.; Nakamori, T.; Ohsuka, S.; Nakamura, S.; Hirayanagi, M.; Adachi, S.; Uchiyama, T.; Yamamoto, K. *Nucl. Instrum. Methods Phys. Res., Sect. A* **2013**, *732*, 403−407.
(33) Iwanowska, J.; Swiderski, L.; Szczesniak, T.; Sibczynski, P.; Moszynski, M.; Grodzicka, M.; Kamada, K.; Tsutsumi, K.; Usuki, Y.; Yanagida, T.; Yoshikawa, A. *Nucl. Instrum. Methods Phys. Res., Sect. A* **2013**, *712*, 34−40.
(34) Yeom, J. Y.; Yamamoto, S.; Derenzo, S. E.; Spanoudaki, V. C.; Kamada, K.; Endo, T.; Levin, C. S. *IEEE Trans. Nucl. Sci.* **2013**, *60*, 988−992.
(35) Ferri, A.; Gola, A.; Serra, N.; Tarolli, A.; Zorzi, N.; Piemonte, C. *Phys. Med. Biol.* **2014**, *59*, 869−880.
(36) Robertson, J. M.; van Tol, M. W. *Thin Solid Films* **1984**, *114*, 221−240.
(37) Zorenko, Yu.; Gorbenko, V.; Konstankevych, I.; Voloshinovskii, A.; Stryganyuk, G.; Mikhailin, V.; Kolobanov, V.; Spassky, D. *J. Lumin.* **2005**, *114*, 85−94.
(38) Zorenko, Yu.; Gorbenko, V.; Mihokova, E.; Nikl, M.; Nejezchleb, K.; Vedda, A.; Kolobanov, V.; Spassky, D. *Radiat. Meas.* **2007**, *42*, 521−527.
(39) Kučera, M.; Nitsch, K.; Nikl, M.; Hanuš, M.; Daniš, S. *J. Cryst. Growth* **2010**, *312*, 1538−1545.
(40) Kučera, M.; Nikl, M.; Prusa, P.; Mareš, J. A.; Nitsch, K.; Hanuš, M.; Onderišinová, Z.; Kučerková, R. *J. Cryst. Growth* **2011**, *318*, 813−819.
(41) Martin, T.; Douissard, P.-A.; Seeley, Z.; Cherepy, N.; Payne, S.; Mathieu, E.; Schuladen, J. *IEEE Trans. Nucl. Sci.* **2012**, *59*, 2269−2274.
(42) Globus, M.; Grinyov, B.; Ratner, M.; Tarasov, V.; Lyubinskiy, V.; Zorenko, Yu.; Konstankevych, I. *Nuclear Sci. Symposium Conference Record* **2002**, *1*, 352−356.
(43) Horodyský, P.; Touš, J.; Blažek, K.; Nikl, M.; Zorenko, Yu.; Kučera, M. *Radiat. Meas.* **2010**, *45*, 628−630.
(44) Nagarkar, V. V.; Gaysinskiy, V.; Gelfandbein, V.; Miller, S.; Cool, S.; Kudrolli, H.; Bradford Barber, H.; Haston, K.; Kain, P. M.; Bora, V. *Nucl. Sci. Symposium Conference Record (NSS/MIC)* **2010**, 4−9.
(45) Kamada, K.; Kurosawa, S.; Yokota, Y.; Yanagida, T.; Nikl, M.; Yoshikawa, A. *Jpn. J. Appl. Phys.* **2014**, *53*, 04EH10.
(46) Zorenko, Yu.; Gorbenko, V.; Konstankevych, I.; Batentschuk, M. In *Proceedings of the Fifth International Conference on Inorganic Scintilators and Their Applications, SCINT'99*; Mikhailin, V., Ed.; M. V. Lomonosov Moscow State University: Moscow, 2000; pp 532−537.
(47) Zorenko, Yu.; Gorbenko, V.; Konstankevych, I.; Grinev, B.; Globus, M.; Batentschuk, M. *Semiconductor Physics, Quantum Electron. Optoelectron.* **2000**, *3*, 213−218.
(48) Przybylińska, H.; Wittlin, A.; Ma, C.-G.; Brik, M. G.; Kamińska, A.; Sybilski, P.; Zorenko, Yu.; Nikl, M.; Gorbenko, V.; Fedorov, A.; Kučera, M.; Suchocki, A. *Opt. Mater.* **2014**, *36*, 1515−1519.
(49) Babin, V.; Gorbenko, V.; Krasnikov, A.; Makhov, A.; Nikl, M.; Zazubovich, S.; Zorenko, Yu. *Radiat. Meas.* **2010**, *45*, 415−418.
(50) Babin, V.; Gorbenko, V.; Makhov, A.; Mareš, J. A.; Nikl, M.; Zazubovich, S.; Zorenko, Yu. *J. Lumin.* **2007**, *127*, 384−390.
(51) Průša, P.; Mareš, J. A.; Nikl, M.; Kučera, M.; Nitsch, K.; Hanuš, M. *Opt. Mater.* **2010**, *32*, 1360−1363.
(52) Průša, P.; Nikl, M.; Mareš, J. A.; Kučera, M.; Nitsch, K.; Beitlerová, A. *Phys. Status Solidi A* **2009**, *206*, 1494.
(53) Zorenko, Yu.; Gorbenko, V.; Savchyn, V.; Suchocki, A.; Wrzesinski, H.; Walczyk, K.; Fabisiak, K.; Bilski, P.; Twardak, A. *Opt. Mater.* **2014**, *36*, 1685−1687.
(54) Zorenko, Yu.; Gorbenko, V.; Savchyn, V.; Voznyak, T.; Sidletskiy, O.; Grinyov, B.; Nikl, M.; Mareš, J. A.; Martin, T.; Douissard, P.-A. *IEEE Trans. Nucl. Sci.* **2012**, *59*, 2260−2268.
(55) Zorenko, Yu.; Mareš, J. A.; Průša, P.; Nikl, M.; Gorbenko, V.; Savchyn, V.; Kučerková, R.; Nejezchleb, K. *Radiat. Meas.* **2010**, *45*, 389−391.
(56) Kučera, M.; Nitsch, K.; Kubová, M.; Solovieva, N.; Nikl, M.; Mareš, J. A. *IEEE Trans. Nucl. Sci.* **2008**, *55*, 1201−1205.
(57) Kučera, M.; Nitsch, K.; Nikl, M.; Hanuš, M. *Radiat. Meas.* **2010**, *45*, 449−452.
(58) Průša, P.; Kučera, M.; Mareš, J. A.; Hanuš, M.; Beitlerová, A.; Onderišinová, Z.; Nikl, M. *Opt. Mater.* **2013**, *35*, 2444−2448.
(59) Kučera, M.; Hanuš, M.; Nikl, M.; Onderišinová, Z. *Phys. Status Solidi RRL* **2013**, *7*, 571−574.
(60) Kučera, M.; Hanuš, M.; Onderišinová, Z.; Průša, P.; Beitlerová, A.; Nikl, M. *IEEE Trans. Nucl. Sci.* **2014**, *61*, 282−289.
(61) Zorenko, Yu.; Gorbenko, V.; Savchyn, V.; Batentschuk, M.; Osvet, A.; Brabec, C. *Radiat. Meas.* **2013**, *56*, 150−154.
(62) Zorenko, Yu.; Gorbenko, V.; Savchyn, V.; Zorenko, T.; Fedorov, A.; Sidletskiy, O. *J. Cryst. Growth* **2014**, *401*, 532−536.
(63) Zorenko, Yu; Gorbenko, V.; Vasylkiv, Ja.; Strzyżewski, T.; Fedorov, A.; Kučerková, R.; Mareš, J. A.; Nikl, M.; Bilski, P.; Twardak, A. *J. Lumin.* **2015**, DOI: 10.1016/j.jlumin.2014.11.040.

DOI: 10.1021/acs.cgd.5b00309
Cryst. Growth Des. 2015, 15, 3715−3723

(64) Kurosawa, S.; Shoji, Y.; Yokota, Y.; Kamada, K.; Chani, V. I.; Yoshikawa, A. *J. Cryst. Growth* **2014**, *393*, 134−137.
(65) D'Ambrosio, C.; Leutz, H. *Nucl. Instrum. Methods Phys. Res., Sect. A* **2003**, *501*, 463−498.
(66) Kucera, M.; Onderisinova, Z.; Bok, J.; Hanuš, M.; Schauer, P.; Nikl, M. *J. Lumin.* **2015**, DOI: 10.1016/j.jlumin.2015.1001.1034.
(67) Kobayashi, M.; Tamagawa, Y.; Tomita, S.; Yamamoto, A.; Ogawa, I.; Usuki, Y. *Nucl. Instrum. Methods Phys. Res., Sect. A* **2012**, *694*, 91−94.
(68) Zorenko, Yu.; Gorbenko, V.; Vasylkiv, Ja.; Zelenyj, A.; Fedorov, A.; Kučerková, R.; Mareš, J. A.; Nikl, M.; Bilski, P.; Twardak, A. *Mater. Res. Bull.* **2015**, *64*, 355−363.
(69) Xu, Y. N.; Ching, W. Y.; Brickeen, B. K. *Phys. Rev. B: Condens. Matter Mater. Phys.* **2000**, *61*, 1817.
(70) Wu, Y.; Meng, F.; Li, Q.; Koschan, M.; Melcher, C. L. *Phys. Rev. Appl.* **2014**, *2*, 004009.
(71) Stanek, C. R.; Jiang, C.; Yadav, S. K.; McClellan, K. J.; Uberuaga, B. P.; Andersson, D. A.; Nikl, M. *Phys. Status Solidi B* **2013**, *250*, 244−248.
(72) Marezio, D. M.; Remeika, J. P.; Dernier, P. D. *Acta Crystallogr., Sect. B: Struct. Crystallogr. Cryst. Chem.* **1968**, *24*, 1670.
(73) Nakatsuka, A.; Yoshiasa, A.; Yamanaka, T. *Acta Crystallogr., Sect. B: Struct. Sci.* **1999**, *55*, 266.
(74) Mihóková, E.; Vávrů, K.; Kamada, K.; Babin, V.; Yoshikawa, A.; Nikl, M. *Radiat. Meas.* **2013**, *56*, 98−101.
(75) Ueda, J.; Aishima, K.; Tanabe, S. *Opt. Mater.* **2013**, *35*, 1952−1957.

DOI: 10.1021/acs.cgd.5b00309
Cryst. Growth Des. 2015, 15, 3715−3723

Journal of Crystal Growth 410 (2015) 14–17

Contents lists available at ScienceDirect

Journal of Crystal Growth

journal homepage: www.elsevier.com/locate/jcrysgro

Growth of 2-inch size Ce:doped $Lu_2Gd_1Al_2Ga_3O_{12}$ single crystal by the Czochralski method and their scintillation properties

Kei Kamada [a,b,e,*], Akira Yoshikawa [a,b,c,e], Takanori Endo [d,e], Kousuke Tsutsumi [d,e], Yasuhiro Shoji [b,c,e], Shunsuke Kurosawa [c,e], Yuui Yokota [a,e], Petr Prusa [d,e], Martin Nikl [d,e]

[a] New Industry Creation Hatchery Center (NICHe), Tohoku University, 6-6-10 Aoba, Aramaki, Sendai 980-8579, Japan
[b] C&A Corporationy, 6-6-10 Aoba, Aramaki, Sendai 980-8579, Japan
[c] Institute for Material Research, Tohoku University, 2-1-1 Katahira, Sendai 980-8577, Japan
[d] Materials Research Laboratory, Furukawa Co. Ltd, 1-25-13, Kannondai, Tsukuba 305-0856, Japan
[e] Institute of Physics, AS CR, Cukrovarnická 10, 162 53 Prague, Czech Republic

ARTICLE INFO

Article history:
Received 21 May 2014
Received in revised form
24 September 2014
Accepted 2 October 2014
Communicated by: S. Uda
Available online 23 October 2014

Keywords:
A2. Single crystal growth
B1.Oxides
B2. Scintillator materials
B3. Scintillators

ABSTRACT

Ce 1% doped $Lu_2Gd_1Al_2Ga_3O_{12}$ (LGAGG) single crystals with a diameter of 50 mm and length of 150 mm were grown by the Czochralski (Cz) method using an RF heating system. The EPMA techniques is employed to check homogeniousity of chemical composition. Luminescence and scintillation properties were also evaluated. The grown LGAGG showed light yield of around 25,000 photon/MeV and energy resolution was 9.8%@662 keV. The scintillation decay time was 53.6 ns at room temperature.

1. Introduction

Scintillator materials combined with photodetectors are used to detect high-energy photons and particles in X-ray computed tomography (CT), positron emission tomography (PET) and other medical imaging techniques, high energy and nuclear physics detectors, and so on. In the last two decades, great effort was made to develop more efficient and faster scintillators in order to detect ionizing radiation. Recently developed Ce-activated materials show the best figure-of-merit given by a combination of stopping power, speed, and light yield [1–3]. The latest generation of Ce^{3+}-doped scintillators based on aluminum garnets (LuAG:Ce) show high intrinsic scintillation efficiency and light yield up to 26,000 photons/MeV [4,5]. However, their performance is always negatively influenced by shallow electron traps, which delay an energy transfer to Ce^{3+} emission centers and scintillation decay time contains a considerable amount of slow components [6]. After systematic study of $Lu_3Al_5O_{12}$-based single crystal scintillators (for the review see [7]), a new material concept was proposed, based on single crystal multicomponent $(Gd,RE)_3(Ga,Al)_5O_{12}$ host, RE=Lu, Y. Doped by Ce^{3+}, such a host lattice, with balanced combination of the admixed Gd and Ga (called as multi-component garnets) demonstrated very high light yield in both single crystal and ceramic materials [7–11]. In these reports, Ce:$(Lu_yGd_{1-y})_3(Ga_xAl_{1-x})_5O_{12}$ scintillator grown by μ–PD method were investigated and $Lu_2Gd_1Al_2Ga_3O_{12}$ showed light yield of about 21,000photon/MeV decay time of 46 ns and density of 7.13 g/cm^3[10].

In this report, Ce:$Lu_2Gd_1Al_2Ga_3O_{12}$ (Ce:LGAGG) single crystals were grown by the Czochralski (Cz) method. Segregation coefficients of Ce in grown crystals were investigated. Luminescence and scintillation properties such as light yield, nonproportionality, temperature dependence of light yield, and decay time were also investigated.

2. Experimental

2.1. Crystal growth procedure

A stoichiometric mixture of 4N CeO_2, Lu_2O_3, Gd_2O_3, β-Ga_2O_3, and α-Al_2O_3 powders (High Purity Chemicals Co.) was used as starting material. The Gd^{3+} site was partially substituted by Ce^{3+} according to the formula of $Ce_{0.03}Lu_2Gd_{0.97}Al_2Ga_{3.15}O_{12}$. Ce:LGAGG single crystals were grown by means of the Cz method using an RF heating system. Here, 3 mol% of β-Ga_2O_3 was added in excess to

* Corresponding author at: Tohoku University, Institute for Materials Research, New Industry Creation Hatchery Center (NICHe), 6-6-10 Aoba, Aramaki, Sendai, 980-8579 Japan. Tel.: +81 22 215 2214; fax: +81 22 215 2215.
E-mail address: kamada@imr.tohoku.ac.jp (K. Kamada).

http://dx.doi.org/10.1016/j.jcrysgro.2014.10.004
0022-0248/

compensate ignition loss. The rotation rate was 4–12 rpm and the growth rate was 1.0 mm/h. An automatic diameter control system using crystal weighing was applied to control the growth parameters. Crystals were grown from a 100 mm diameter Ir crucible under Ar with addition of 2% of O_2 atmosphere to prevent evaporation of gallium oxide. The seed crystal was a [1 0 0] oriented LuAG crystal. After the completion of the crystal growth, the crystal was removed from the melt and was gradually cooled down to room temperature. Plates of 5 mm × 5 mm × 1 mm were cut and polished for the purposes of the luminescence and gamma-ray response measurements, while the remaining rods were used for the structure and chemical composition analysis.

2.2. Characterization of obtained phase

Pieces of the grown crystals were crushed and ground into powder in a mortar. Powder X-ray diffraction analysis was carried out in the 2θ range of 15°–75° using RINT Ultima (RIGAKU) diffractometer. The CuKα X-ray source was used and the accelerating voltage and current were of 40 kV and 40 mA, respectively.

Quantitative chemical analysis of the grown crystals for the Al, Ga, Ce, Lu, and Gd content along the growth direction was performed using electron probe microanalysis (EPMA; JXA-8621MX, JEOL). So-called ZAF correction was used, where *Z* stands for atomic number, A for absorption correction factor, and F for fluorescence correction factor.

2.3. Luminescence and gamma-ray response measurement procedure

Absorption spectra were measured using the Shimadzu 3101PC spectrometer in the 190–800 nm range. Radioluminescence (RL) spectra and photoluminescence decays at room temperature (RT) were measured at custom made 5000 M model of Horiba Jobin Yvon spectrofluorometer using an X-ray tube (operated at 35 kV and 16 mA, Mo cathode) and the pulsed nanosecond hydrogen-filled flashlamp for the excitation (see [9–11] for further experimental details).

To determine the light yield, the energy spectra were collected under 662 keV γ-ray excitation (^{137}Cs source) by using an avaranche photodiode (APD, Hamamatsu, S8664-55). The 5×5 mm^2 face of the sample was coupled with the APD using silicone grease (OKEN, 6262A). The sample was covered by Teflon-tape. The signal was fed into a pre-amplifier (CP580K), shaping amplifier (CP 4417), pocket multichannel analyzer (MCA, Amptec 8000A), and finally to a personal computer. The bias for the APD was supplied by a power supplier (CP 6641). Because the APD was thermally sensitive, its temperature was controlled to be 20 ± 0.5 °C using a heat bath. Decay time was measured with a photomultiplier (PMT, Hamamatsu, H7600) with digital oscilloscope TDS3052 of Tektronix, Inc.

3. Result and discussion

3.1. The growth of Ce:LGAGG single crystal

Two-inch size $Lu_2Gd_1Al_2Ga_3O_{12}$ crystal with a diameter of 50 mm and length of 160 mm were grown. The grown crystals are shown in Fig. 1. The grown crystals are looked slightly cloudy because of the rough surface caused by gallium oxide evaporation or thermal etching. Metallic stripes on the crystal surfaces were identified as Ir deposit comes from oxidation of the crucible. Grown crystal was yellow transparent without incursion at the beginning part of the crystal; however, incursions were observed remarkably at the center position and tail part of the grown

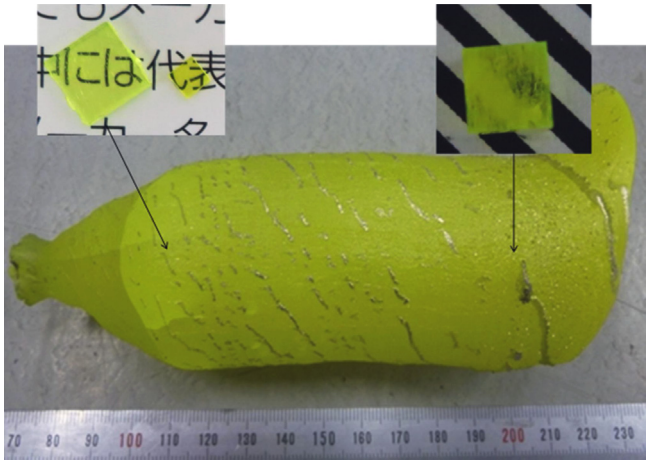

Fig. 1. Photographs of grown Ce:LGAGG crystals.

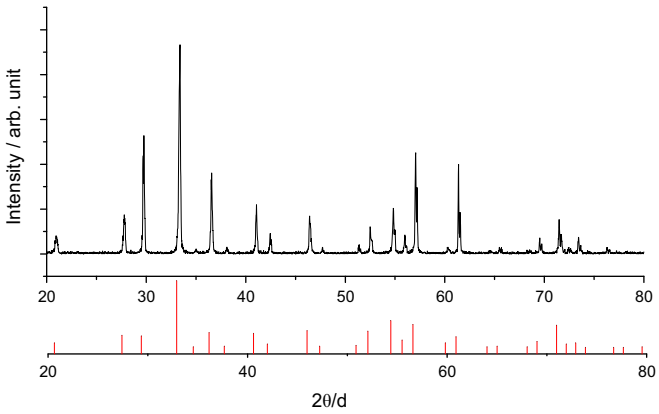

Fig. 2. Powder X-ray diffraction results of the end part of the grown crystal.

crystal. Powder X-ray diffraction was performed to identify crystal phase of the end part of the grown crystal.

Results of the powder X-ray diffraction are shown in Fig. 2. Obtained spectrum showed the single cubic garnet phase. A Q-mass analysis with vacuum chamber was performed to investigate the contents of the inclusions. Ar and O_2 gasses were detected using the Q-mass analysis and the incursions are guessed as gas bobbles from supersaturated melt. It is considered that bubble nucleation occurred at the center of concave melt/solid interface by constitutional undercooling,

The composition distributions of Lu, Ga, and Ce ions along the growth direction and radial direction are shown in Figs. 3 and 4. The solidification fractions (g) of the grown crystals were 0.37. Here g is described as follows:

$$g = \frac{(\text{mass of solidified part})}{(\text{total mass of starting raw material in the crucible})}$$

Segregation coefficients of Lu, Ga, and Ce were k_{eff}=1.12, 0.92, and 0.21, respectively. The composition distributions in the radial direction were almost homogeneous. The k_{eff} of Ce in $Lu_2Gd_1Al_2Ga_3O_{12}$ is much lower than that of $Gd_3Al_2Ga_3O_{12}$ (k_{eff}=0.36, [11]). These are in good agreement with difference between the ionic radii of Ce and host cations in dodecahedral site (Ce > Gd > Lu).

3.2. Luminescent characteristics

RL spectra of the grown Ce:LGAGG crystals are shown in Fig. 5. The 310 nm emission of Gd^{3+} 4f-4f, and 510 nm emission of Ce^{3+} 4f-5d transition were observed.

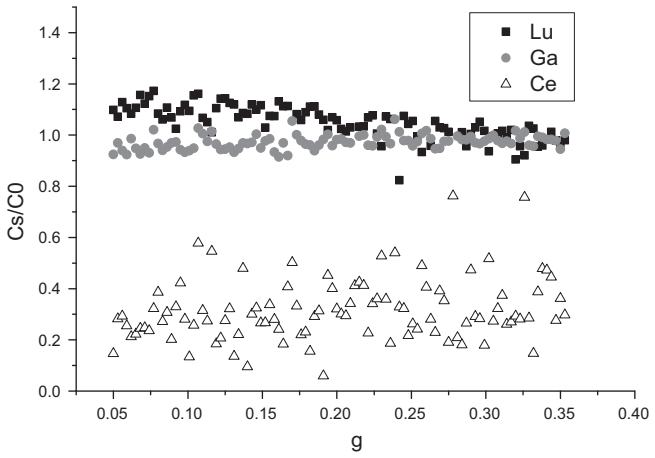

Fig. 3. The composition distribution of Lu, Ga, and Ce ions along the growth direction.

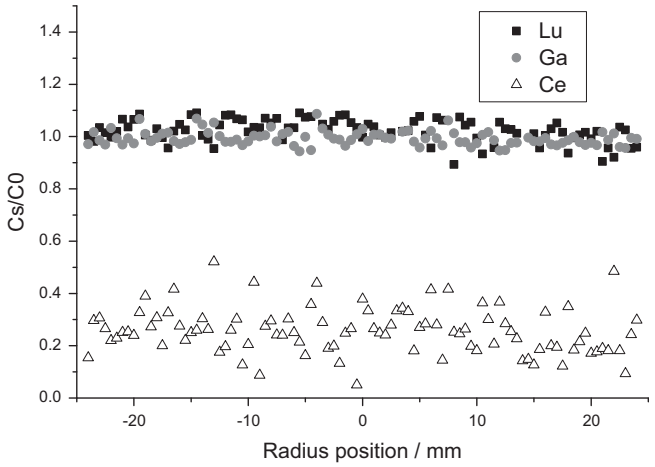

Fig. 4. The composition distribution of Lu, Ga, and Ce ions in the radial direction.

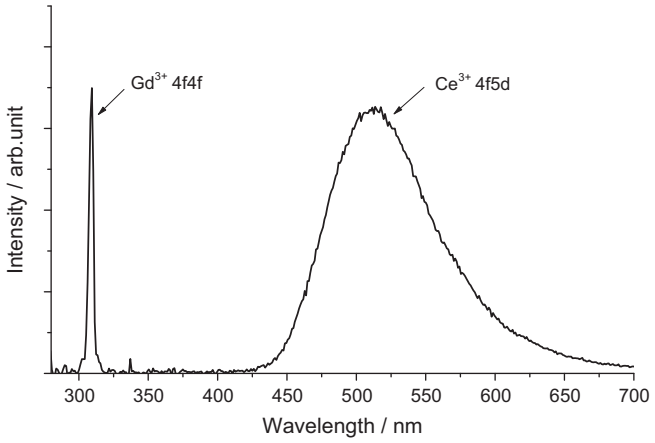

Fig. 5. RL spectra of grown Ce:LGAGG crystals.

3.3. Gamma-ray response

The typical energy spectra of Ce1%:GAGG excited by ^{137}Cs at room temperature and measured using the APD are shown in Fig. 6. The light yield of the sample was calibrated from the ^{55}Fe direct irradiation peak to APD. Such direct irradiation generates 5.9 keV/3.6 eV=1640 electron–hole pairs [11]. Based on this value, LY of Ce:LGAGG was calculated to be approximately 25,000 photons/MeV with correcting quantum efficiency (QE) of the APD, which was 80% at 510 nm. Energy resolution of the Ce 1%: GAGG sample was 9.8%@662 keV. The dependence of the light yield on the solidification fraction is shown in Fig. 7. Light yield was decreased with increasing solidification fraction and, at the same time, increasing Ga concentration (See Fig. 3). This tendency is good agreement with our previous reports [9,10]. Light yield of center position in radial direction is lower than that of edge position. It is guessed that the existence of light scattering center by the gas bobbles at center position affects degradation of light yield.

In Figs. 8 and 9, temperature dependences of the light output and dominant decay time of grown Ce:LGAGG and Ce1%$Gd_3Al_2Ga_3O_{12}$ (GAGG) sample produced by Furukawa were measured using the PMT (Hamamatsu R1288) and digital oscilloscope TD5032B excited by ^{137}Cs gamma-ray. Temperature dependence of prompt ns decay times also indicates that scintillation efficiency of Ce:LGAGG should not decrease until 70 °C. Ce:LGAGG showed the higher temperature stability of light output. These results are in good agreement with our previous report on Ce:$(Gd,Lu)_3(Al,Ga)_5O_{12}$ [10]. The Gd-rich sample has lower position of $5d_1$ level of Ce^{3+}, which secures sufficient separation of $5d_1$ level from the bottom of conduction band of the host. The onset of thermal quenching/ionization of Ce^{3+} center is certainly higher than in

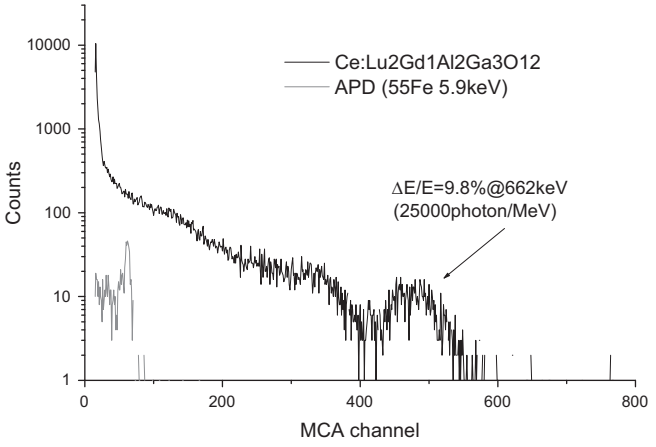

Fig. 6. Energy spectra of Pr:LGAGG crystal excited by a 662 keV gamma-ray source using the PMT at room temperature.

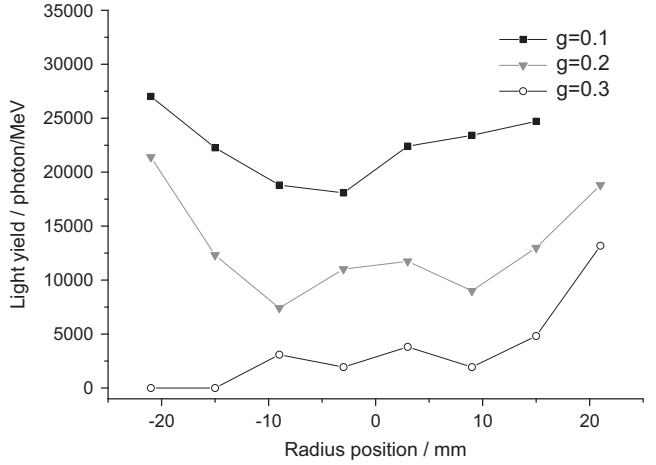

Fig. 7. Light yield variation in the grown crystal.

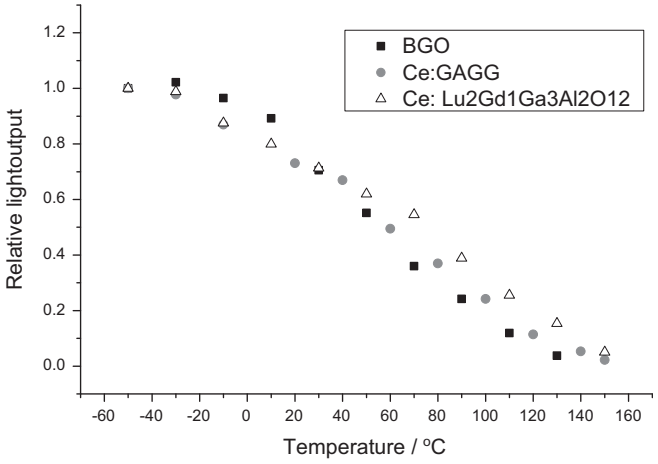

Fig. 8. Temperature dependence of relative light output measured by using the PMT excited by ^{137}Cs gamma-ray.

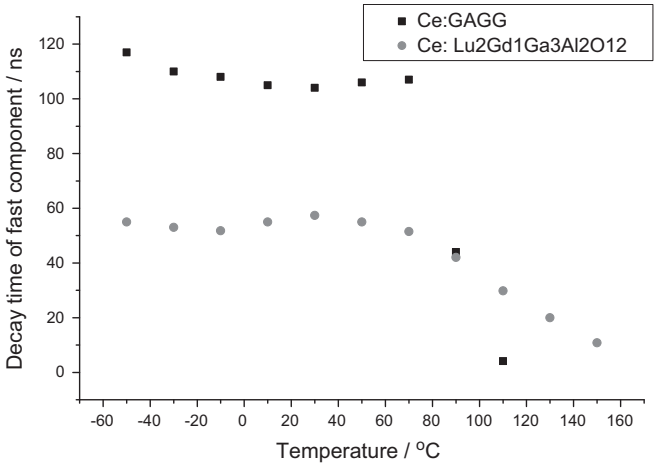

Fig. 9. Temperature dependence of decay time measured by using the PMT and digital oscilloscope excited by ^{137}Cs gamma-ray.

Gd-less samples and ensures effective scintillator functioning in room temperature applications. Increase of scintillation efficiency can be enabled also by the decrease of host band gap value, that is, the decrease of energy for creation of one electron–hole pair.

4. Conclusion

Ce 1%:$Lu_2Gd_1Al_2Ga_3O_{12}$ single crystal with a diameter of 50 mm and length of 160 mm was grown using the CZ method. Segregation coefficients of Lu, Ga, and Ce were k_{eff}= 1.12, 0.92 and 0.21, respectively. Temperature dependence of light yield and scintillation decay time were investigated in the grown crystals. The grown LGAGG showed light yield of around 25,000 photons/MeV and energy resolution was 9.8%@662 keV. The scintillation decay time was 53.6 ns at 20 °C.

Acknowledgements

This work is partially supported by (i) the funding program for next generation world-leading researchers (JSPS); (ii) Development of Systems and Technology for Advanced Measurement and Analysis, Japan Science and Technology Agency (JST); (iii) Adaptable & Seamless Technology Transfer Program through Target-driven R&D (A-STEP), JST; (iv) Japan Society for the Promotion of Science (JSPS) Grant-in-Aid for Exploratory Research (AY); (v) JSPS Research Fellowships for Young Scientists (S. Kurosawa); and (vi) the Health Labour Sciences Research Grant, The Ministry of Health Labour and Welfare. In addition, we thank the following persons for their support: Mr. Yoshihiro Nakamura in Institute of Multidisciplinary Research for Advanced Materials (IMRAM), Tohoku University and Mr. Hiroshi Uemura, Ms. Keiko Toguchi and Ms. Megumi Sasaki, Ms. Yumiko Saijo in IMR. Partial financial support from Czech MEYS, KONTAKT II no. 12150 project is also gratefully acknowledged.

References

[1] M. Nikl, A. Vedda,, V.V. Laguta, Single-crystal scintillation materials, in: G. Dhanaraj, K. Byrappa, V. Prasad, M. Dudley (Eds.), Springer Handbook of Crystal Growth, Springer Verlag, ISBN 978-3-540-74182-42010, pp. 1663–1700 (Chapter 50).
[2] B.D. Milbrath, A.J. Peurrung, M. Bliss, W.J. Weber, J. Mater. Res. 23 (No. 10) (2008) 2561–2581.
[3] M.J. Weber, Nucl. Instr. Meth. Phys. Res. A. 527 (2004) 9–14.
[4] C. Dujardin, C. Mancini, D. Amans, G. Ledoux, D. Abler, E. Auffray, P. Lecoq, D. Perrodin, A. Petrosyan, K.L. Ovanesyan, J. Appl. Phys. 108 (2010) 013510.
[5] J.A. Mares, M. Nikl, A. Beitlerova, P. Horodysky, K. Blazek, K. Bartos, C. D'Ambrosio, IEEE Trans. Nucl. Sci. 59 (2012) 2120.
[6] W. Chewpraditkul, L. Swiderski, M. Moszynski, T. Szczesniak, A. Syntfeld-Kazuch, C. Wanarak, P. Limsuwan, Phys. Stat. Sol. A 206 (2009) 2599.
[7] M. Nikl, A. Yoshikawa, K. Kamada, K. Nejezchleb, C.R. Stanek, J.A. Mares, et al., Progr. Cryst. Growth Charact. Mater. 59 (2013) 47.
[8] N.J. Cherepy, J.D. Kuntz, Z.M. Seeley, S.E. Fisher, O.B. Drury, B.W. Sturm, et. al., Transparent ceramic scintillators for gamma spectroscopy and radiography, in: A. Burger, L.A. Franks and R.B. James (Eds), Procedings SPIE on Hard X-Ray, Gamma-Ray, and Neutron Detector Physics XII, 2010, vol. 7805.
[9] K. Kamada, T. Yanagida, T. Endo, K. Tsutumi, Y. Fujimoto, A. Fukabori, et al., Cryst. Growth Des. 11 (2011) 4484.
[10] K. Kamada, T. Yanagida, J. Pejchal, M. Nikl, T. Endo, K. Tsutumi, et al., J. Phys. D: Appl. Phys 44 (2011) 505104.
[11] K. Kamada, T. Yanagida, J. Pejchal, M. Nikl, T. Endo, K. Tsutumi, et al., J. Cryst. Growth 352 (2012) 88–90.

Czochralski Growth and Scintillation Properties of $Ce : (Gd, Y, Lu)_3 (Al, Ga)_5O_{12}$ Single Crystals

Kei Kamada, Petr Prusa, Martin Nikl, Karel Blazek, Takanori Endo, Kousuke Tsutsumi, Shunsuke Kurosawa, Yuui Yokota, and Akira Yoshikawa

***Abstract*—1-inch size Ce1%:$Gd_2Lu_1Al_2Ga_3O_{12}$, $Gd_1Lu_2Al_2Ga_3O_{12}$, $Gd_1Y_2Al_{1.5}Ga_{3.5}O_{12}$ and $Lu_2Y_1Al_2Ga_3O_{12}$ were grown by the Czhocralski (Cz) method. The EPMA techniques is employed to check their chemical composition. Luminescence and scintillation properties were also evaluated. The Ce1%:$Gd_1Y_2Al_2Ga_3O_{12}$ sample showed the highest light yield of around 40 000 photon/MeV. The scintillation decay time was 46.6 ns(63%) and 157 ns(37%).**

***Index Terms*—Oxides, scintillator materials, scintillators, single crystal growth.**

I. Introduction

After a decade of R&D of the $Lu_3Al_5O_{12}$-based single crystal scintillators, new material concept was defined, based on multicomponent $(Gd, RE)_3$ $(Ga, Al)_5O_{12}$ host, $Re = Lu, Y$. Doped by Ce^{3+}, the Gd- and Ga rich host compositions showed amazingly high light yield up to almost 50 000 phot/MeV [1]–[7] which is the value exceeding by 30-40% the best LYSO:Ce materials ever seen. Thanks to the flexibility, cost-effective character and speed of micro-pulling-down method, such a combinatorial study could be done at a number of single crystal samples which is preferable with respect to attempts usually done with powders. Discovery of these ultra-efficient scintillators is based on several previous findings, namely: 1) scintillators based on aluminum garnets show high intrinsic scintillator efficiency, but their figure-of-merit is strongly degraded by shallow electron traps which delay an energy delivery to emission centers [89]; 2) the Ga-admixture into the aluminum garnet effectively diminishes the trapping effects mentioned in 1) [10], but at the same time, the bottom of the conduction band becomes close to the $5d_1$ level of Ce^{3+} which leads to the unwanted excited state ionization of emission centre and light yield decrease [11]; 3) the definition of strategy of the band-gap engineering in the family of aluminum-based garnets [12] and positioning of the $5d_1$ level by crystal field manipulation through the RE site symmetry [13]; 4) the simultaneous admixture of Gd and Ga into the YAG structure leads to dramatic LY increase in $Ce : (Gd\text{-}Y)_3$ $(Al\text{-}Ga)_5O_{12}$ ceramics [14].

In this report, $Ce : (Gd, Lu, Y)_3(Al, Ga)_5O_{12}$ single crystals were grown by the Czochralski (Cz) method. Segregation coefficients of Ce in grown crystals were investigated. Luminescence and scintillation properties such as light yield, non-proportionality, temperature dependence of light yield and decay time were also investigated.

II. Materials and Methods

1) Crystal Growth: Stoichiometric mixtures of 4 N CeO_2, Gd_2O_3, Y_2O_3, Lu_2O_3, β-Ga_2O_3 and α-Al_2O_3 powders (High Purity Chemicals Co.) were used as starting material. $Ce : (Gd, Lu, Y)_3(Al, Ga)_5O_{12}$ single crystals were grown by means of the Cz method using an RF heating system. The rotation rate was 4–12 rpm and the growth rate was 1.0 mm/h. An automatic diameter control system using crystal weighing was applied to control the growth parameters. Crystals were grown from a 50 mm diameter Ir crucible under Ar with adding 30% of CO_2 atmosphere to prevent evaporation of gallium oxide. The seed crystal was a [100] oriented LuAG crystal. After the completion of the crystal growth, the crystal was removed from the melt and was gradually cooled down to room temperature.

2) Gamma-Ray Response Measurement Procedure: Sample pieces with dimensions of $5 \times 5 \times 1 \times$ mm were cut from the grown single crystal; all surfaces were mechanically polished. Light yield measurement was performed by using an avalanche photodiode (APD) (Hamamatsu, S8664-55). The light yield (LY) of the sample was calibrated from the ^{55}Fe direct irradiation peak to APD.

Non-proportionality was determined by amplitude spectroscopy of scintillation response induced by gamma rays

Manuscript received May 24, 2013; revised July 30, 2013; accepted August 23, 2013. Date of publication January 09, 2014; date of current version February 06, 2014. This work was supported in part by the funding program for next generation world-leading researchers, JSPS, in part by Development of Systems and Technology for Advanced Measurement and Analysis, Japan Science and Technology Agency (JST), in part by Adaptable & Seamless Technology Transfer Program through Target-driven R&D (A-STEP), JST, in part by Japan Society for the Promotion of Science (JSPS) Grant-in-Aid for Exploratory Research (A.Y), in part by JSPS Research Fellowships for Young Scientists (S. Kurosawa), and in part by the Health Labour Sciences Research Grant, The Ministry of Health Labour and Welfare.

K. Kamada is with New Industry Creation Hatchery Center (NICHe), Tohoku University, Sendai, Miyagi 980-8579, Japan, and also with C&A Corporation, T-Biz, Sendai, Miyagi 980-8579, Japan (e-mail: kamada@imr.tohoku.ac.jp).

P. Prusa, M. Nikl and K. Blazek are with Institute of Physics, 162 53 Prague, Czech Republic.

T. Endo and K. Tsutsumii are with Materials Research Laboratory, Furukawa Co. Ltd., Tsukuba, 305-0856, Japan.

S. Kurosawa is with Institute for Material Research, Tohoku University, 980-8577 Sendai, Japan.

Y. Yokota is with New Industry Creation Hatchery Center (NICHe), Tohoku University, Sendai, Miyagi 980-8579, Japan.

A. Yoshikawa is with New Industry Creation Hatchery Center (NICHe) Tohoku University, Sendai, Miyagi 980-8579, Japan; with the C&A Corporation, T-Biz, Sendai, Miyagi 980-8579, Japan; and also with the Institute for Material Reseach, Tohoku University, 980-8577 Sendai, Japan.

Color versions of one or more of the figures in this paper are available online at http://ieeexplore.ieee.org.

Digital Object Identifier 10.1109/TNS.2013.2285613

(Mares *et al.*, 2007). Scintillation crystal is covered by teflon tape to ensure efficient light collection, and optically coupled to a hybrid photo-multiplier (HPMT) model DEP PPO 475B. Signal from HPMT is processed by spectroscopy amplifier ORTEC model 672 and multichannel-buffer ORTEC 927TM. Pulse height spectrum is displayed on a PC. Several gamma ray emitting radionuclide sources were used to induce a scintillation response: ^{137}Cs (661.6 keV), ^{22}Na (511 keV, 1274 keV), ^{241}Am (59.54 keV, 13.95 keV), ^{210}Pb (46.54 keV,10.84 keV), ^{109}Cd (88.04 keV, 22.16 keV), and ^{133}Ba (81.0 keV, 160.6 keV, 276.4 keV, 302.9 keV, 356.0 keV, and 383.9 keV) (Ekström and Firestone, 2004). Only selection of ^{133}Ba lines is presented for many samples due to non-negligible interference. A 1274 keV line of ^{22}Na is not presented because of experimental setup saturation. Radioactive source was placed at a distance of several mm from the sample, depending on detection efficiency and source activity. All measurements were performed at room temperature.

For measurements of temperature dependence of light yield and decay time, a photomultiplier tube (PMT Hamamatsu R1288) and digital oscilloscope TD5032B were used. Scintillator samples were attached to the PMT R1288 which was specially designed for the well logging application by Hamamatsu. The optical grease KF-96H (Shinetsu Sillicone) was used for optical coupling and the Teflon tape was used as a reflector to collect scintillation photons. The detector was installed in the heat bath (Isuzu HPCC-48-20), the maximum temperature of which was 150 °C and the temperature was stabilized within ±0.5°C. Through the 1 cm thick heat-resistant glass, gamma-photons from radioisotopes were exciting the sample. Once γ-photon from radioisotope was detected by the sample, signals were fed into preamplifier (ORTEC 113), shaping amplifier (ORTEC 572) with typically 2 μs shaping time, and Pocket MCA (Amptek). At the same time, we measured scintillation decay profiles by an oscilloscope (Tektronix TDS5034B). From room temperature (25 °C), data were obtained with 25 °C temperature steps up to 150 °C.

III. Results

1) Crystal growth: 1-inch size Ce1%:$Gd_2Lu_1Al_2Ga_3O_{12}$, $Gd_1Lu_2Al_2Ga_3O_{12}$, $Gd_1Y_2Al_2Ga_3O_{12}$ and $Lu_2Y_1Al_2Ga_3O_{12}$ crystals with a diameter of 25 mm and length of 70-120 mm were grown. The grown crystals are shown in Fig. 1. The grown crystals are looked slightly cloudy because of the rough surface caused by gallium oxide evaporation or thermal etching. Metallic stripes on the crystal surfaces were identified as Ir deposit comes from oxidation of the crucible.

Quantitative chemical analysis of the crystals for the Ce content along the growth direction was performed by electron probe microanalysis (EPMA; JXA-8621MX, JEOL). So-called ZAF correction was used, where Z stands for atomic number, A for absorption correction factor and F for fluorescence correction factor, respectively. The Ce distributions of Ce1%:$Gd_2Lu_1Al_2Ga_3O_{12}$, $Gd_3Al_2Ga_3O_{12}$, and $Lu_2Y_1Al_2Ga_3O_{12}$ along the growth direction are shown in Fig. 2. The solidification fractions (g) of the grown crystals were 0.9, 0.55 and 0.8 for Ce1%:$Gd_2Lu_1Al_2Ga_3O_{12}$, $Gd_3Al_2Ga_3O_{12}$, and $Lu_2Y_1Al_2Ga_3O_{12}$, respectively. Here g is described as follows:

$$\mathrm{g} = (\text{mass of solidified part})/(\text{total mass of starting raw material in the crucible}).$$

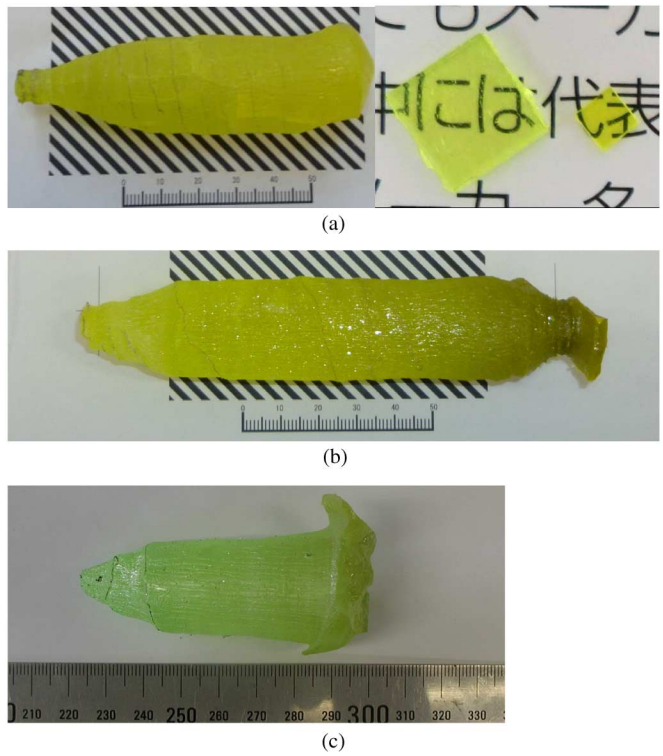

Fig. 1. Photographs of (a) $Gd_1Lu_2Al_2Ga_3O_{12}$ and a sample piece (b) $Gd_1Y_2Al_{1.5}Ga_{3.5}O_{12}$ and (c) $Gd_1Y_2Al_{1.5}Ga_{3.5}O_{12}$ single crystals grown by the Cz method.

Segregation coefficients of Ce were k_{eff} = 0.46, 0.26 and 0.10 in $Gd_3Al_2Ga_3O_{12}$, Ce1%:$Gd_2Lu_1Al_2Ga_3O_{12}$ and $Lu_2Y_1Al_2Ga_3O_{12}$, respectively. These are good agreement with that the ionic radii are Ce > Gd > Y > Lu.

2) Gamma-Ray Response: Table I shows scintillation properties of obtained samples and Ce1%:$Gd_3Al_2Ga_3O_{12}$ standard taken from 2-inch size single crystal. Smaller Gd concentration samples shows lower light yield, shorter decay time and shorter emission wavelength. Statistical occupancy in Gd site by the Lu and Y ions results in the emission band broadening. Compared to our previous report on $Ce:(Gd,Lu)_3(Al,Ga)_5O_{12}$ [1] and $Ce:(Gd,Y)_3(Al,Ga)_5O_{12}$ [2], higher light yield was obtained in the Cz grown crystals. Generally higher quality crystals can be obtained by the Cz method than that of m-PD method in the point view of lower defects such as strains and incursions, and higher homogeneity of Ce^{3+} and host composition in grown crystals [1]–[3].

An important characteristic of the Ce^{3+} luminescence center is temperature dependence of the nanosecond (prompt) decay: until the decay time value does not decrease with increasing temperature, the quantum efficiency of the center is close to one and scintillation efficiency is expected to be not decreasing as well. In Figs. 3 and 4, temperature dependences of the light output and dominant decay time were measured using the PMT

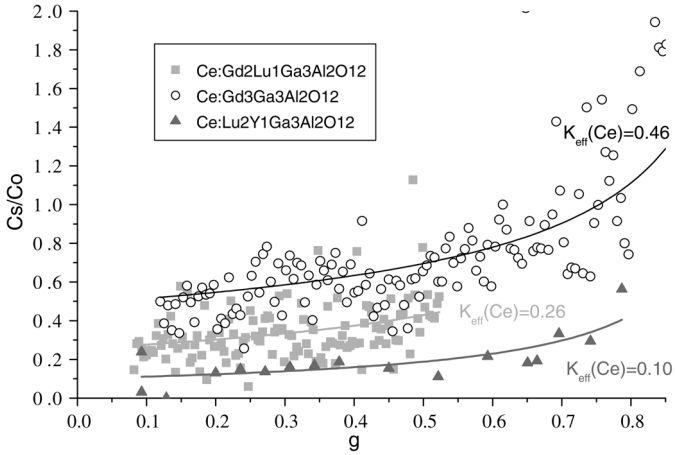

Fig. 2. Ce distributions of Ce1%:$Gd_2Lu_1Al_2Ga_3O_{12}$, $Gd_3Al_2Ga_3O_{12}$, and $Lu_2Y_1Al_2Ga_3O_{12}$ along the growth direction. Solid lines correspond to $Cs/C0 = k_{eff}(1\text{-}g)^{keff\text{-}1}$.

TABLE I
SCINTILLATION PROPERTIES OF THE SAMPLES

	Density /cm3	Emission wavelength /nm	Light yield (photon / MeV)	Decay time (ns)
Gd3Al2Ga3O12	6.65	520	46000	88ns(92%) 255ns(8%)
Lu2Gd1Ga3Al2O12	7.13	500	24000	50ns(61%) 104ns(39%)
Lu1Gd2Ga3Al2O12	6.89	510	35,000	83ns(26%) 710ns(74%)
Gd1Y2Ga3Al2O12	5.87	505	40,000	46.6ns(63%) 157ns(37%)
Lu2Y1Ga3Al2O12	6.69	490	28,000	39ns(14%) 235ns(86%)

(Hamamatsu R1288) and digital oscilloscope TD5032B excited by ^{137}Cs gamma-ray. Temperature dependence of prompt ns decay times also indicates that scintillation efficiency should not decrease until 20°C in any noticeable manner; the Gd_1Y_2 system will show the highest temperature of the onset of scintillation efficiency. These results are in good agreement with our previous report on Ce : $(Gd, Lu)_3(Al, Ga)_5O_{12}$ [1] and Ce : $(Gd, Y)_3(Al, Ga)_5O_{12}$ [2]. The Gd-rich samples have lower position of $5d_1$ level of Ce^{3+}, which secures sufficient separation of $5d_1$ level from the bottom of conduction band of the host. The onset of thermal quenching/ionization of Ce^{3+} center is certainly higher than in Gd-less samples and ensures effective scintillator functioning in room temperature applications. Increase of scintillation efficiency can be enabled also by the decrease of host band gap value, i.e., the decrease of energy for creation of one electron hole pair [14].

The dependence of relative light output on shaping time (normalized to 0.5 us value) for variously selected sample groups are shown in Fig. 5. The smallest increase of yield with shaping time is achieved for Ce : $Lu_2Gd_1Ga_3Al_2O_{12}$. It is in good agreement that Ce : $Lu_2Gd_1Ga_3Al_2O_{12}$ shows the smallest ratio of second decay component than that of others. The non-proportionality of the obtained samples is shown in Fig. 6. The

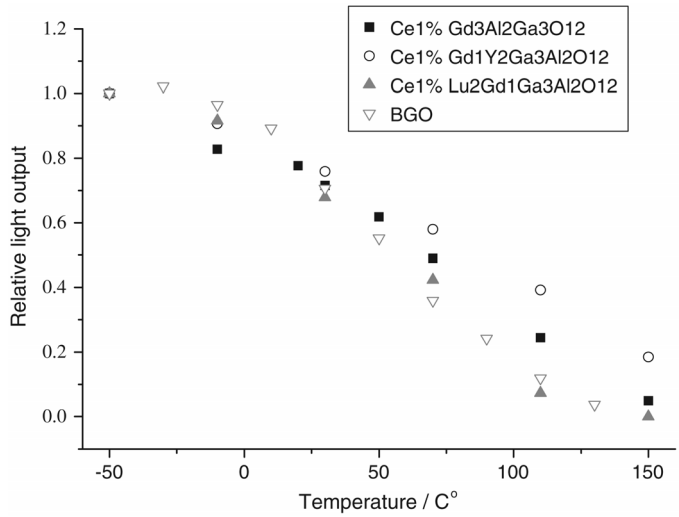

Fig. 3. Temperature dependence of relative light output measured by using the PMT excited by ^{137}Cs gamma-ray.

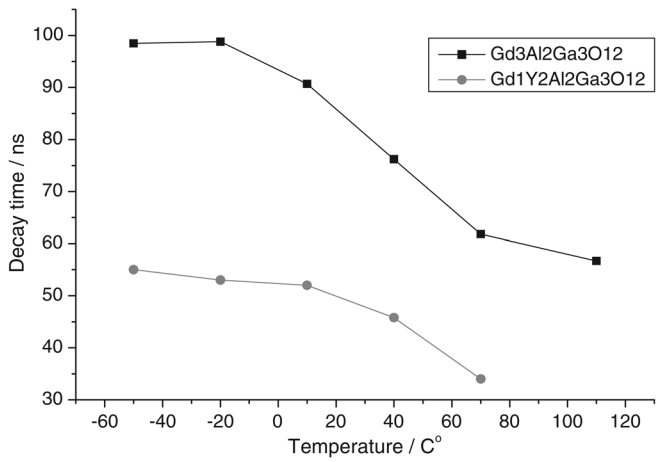

Fig. 4. Temperature dependence of decay time measured by using the PMT and digital oscilloscope excited by ^{137}Cs gamma-ray.

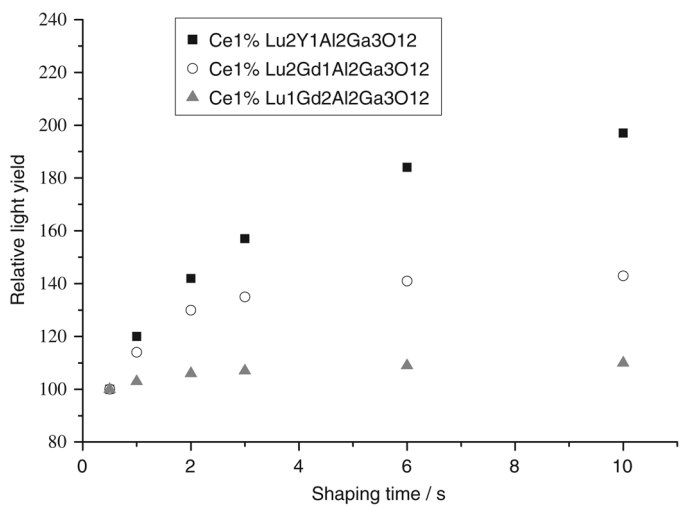

Fig. 5. Dependence of relative light out put on shaping time. Excitation by ^{137}Cs.

Ce : $Lu_2Y_1Ga_3Al_2O_{12}$ and Ce : $Lu_1Gd_2Ga_3Al_2O_{12}$ samples show better non-proportionality than that of the others.

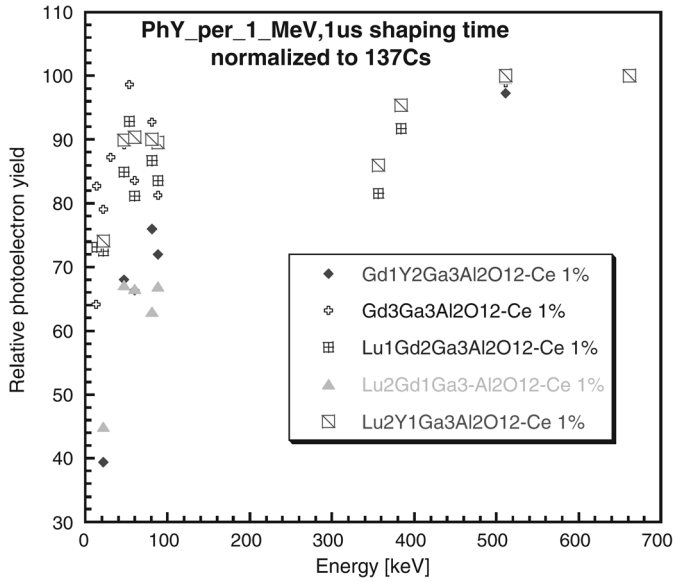

Fig. 6. Non-proportionality of the obtained samples.

IV. Conclusion

1-inch size Ce1%:$Gd_2Lu_1Al_2Ga_3O_{12}$, $Gd_1Lu_2Al_2Ga_3O_{12}$, $Gd_1Y_2Al_2Ga_3O_{12}$ and $Lu_2Y_1Al_2Ga_3O_{12}$ were grown by the Czhocralski (Cz) method. Segregation coefficients of Ce were $k_{eff} = 0.46$, 0.26 and 0.10 in Ce1%:$Gd_2Lu_1Al_2Ga_3O_{12}$, $Gd_3Al_2Ga_3O_{12}$, and $Lu_2Y_1Al_2Ga_3O_{12}$, respectively. These are in good agreement with the fact that the ionic radii are $Ce > Gd > Y > Lu$. Temperature dependence of light yield and scintillation decay time were investigated in the grown crystals. The Ce1%:$Gd_1Y_2Al_2Ga_3O_{12}$ shows the highest temperature stability and thermal quenching at the highest temperature among the grown crystals. The Ce1%:$Gd_1Y_2Al_2Ga_3O_{12}$ sample showed the highest light yield of around 40 000 photon/MeV. The scintillation decay time was 46.6 ns(63%) and 157 ns(37%).

Acknowledgment

The authors would like to thank the following persons for their support: Mr. Y. Nakamura in Institute of Multidisciplinary Research for Advanced Materials (IMRAM), Tohoku University and Mr. H. Uemura, Ms. K. Toguchi, Ms. M. Sasaki, and Ms. Y. Saijo in IMR.

References

[1] K. Kamada, T. Endo, K. Tsutumi, T. Yanagida, Y. Fujimoto, and A. Fukabori *et al.*, "Composition engineering in cerium-doped $(Lu, Gd)_3(Ga, Al)_5O_{12}$ single-crystal scintillators," *Cryst. Growth Design*, vol. 11, pp. 4484–4490, 2011.

[2] K. Kamada, T. Yanagida, J. Pejchal, M. Nikl, T. Endo, and K. Tsutumi *et al.*, "Scintillator-oriented combinatorial search in Ce-doped $(Y, Gd)_3(Ga, Al)_5O_{12}$ multicomponent garnet compounds," *J. Phys. D: Appl. Phys.*, vol. 44, pp. 505104–505111, 2011.

[3] K. Kamada, T. Yanagida, T. Endo, K. Tsutumi, Y. Usuki, and M. Nikl *et al.*, "2 inch diameter single crystal growth and scintillation properties of $Ce : Gd_3Al_2Ga_3O_{12}$," *J. Cryst. Growth*, vol. 352, pp. 88–90, 2012.

[4] K. Kamada, T. Yanagida, J. Pejchal, M. Nikl, T. Endo, and K. Tsutumi *et al.*, "Growth and scintillation properties of Pr doped $(Gd, Y)_3(Ga, Al)_5O_{12}$ single crystals," *IEEE Trans. Nucl. Sci.*, vol. 59, no. 5, pp. 2126–2129, 2012.

[5] K. Kamada, T. Yanagida, T. Endo, K. Tsutumi, M. Yoshino, and J. Kataoka *et al.*, "Large-size single crystal growth of $Pr : Lu_3Al_5O_{12}$ and its scintillation properties," *J. Cryst. Growth*, vol. 352, pp. 91–94, 2012.

[6] P. Prusa, K. Kamada, M. Nikl, A. Yoshikawa, and J. A. Mares, "Light yield of $(Lu, Y, Gd)_3Al_2Ga_3O_{12} : Ce$ garnets," *Radiat. Meas.*, to be published.

[7] M. Nikl, A. Vedda, M. Fasoli, I. Fontana, V. V. Laguta, and E. Mihokova *et al.*, "Shallow traps and radiative recombination processes in $Lu_3Al_5O_{12} : Ce$ single crystal scintillator," *Phys. Rev. B*, vol. 76, pp. 195121–195128, 2007.

[8] M. Nikl, "Energy transfer phenomena in the luminescence of wide band-gap scintillators," *Phys. Stat. Sol. (a)*, vol. 202, pp. 201–206, 2005.

[9] M. Nikl, J. Pejchal, E. Mihokova, J. A. Mares, H. Ogino, and A. Yoshikawa *et al.*, "Antisite defect-free $Lu_3(Ga_xAl_{1-x})_5O_{12} : Pr$ scintillator," *Appl. Phys. Lett.*, vol. 88, pp. 141916–14198, 2006.

[10] Y. Zorenko, "Mechanism of dissipation of the excitation energy in garnet oxides doped with rare-earth ions with 4f-5d transitions," *Opt. Spectroscopy*, vol. 88, pp. 551–553, 2000.

[11] M. Fasoli, A. Vedda, M. Nikl, C. Jiang, B. P. Uberuaga, and D. A. Andersson *et al.*, "Band-gap engineering for removing shallow traps in rare-earth $Lu_3Al_5O_{12}$ garnet scintillators using Ga^{3+} doping," *Phys. Rev. B*, vol. 84, pp. 081102–081107, 2011.

[12] J. L. Wu, G. Gundiah, and A. K. Cheetham, "Structure-property correlations in Ce-doped garnet phosphors for use in solid state lighting," *Chem. Phys. Lett.*, vol. 441, pp. 250–254, 2007.

[13] N. J. Cherepy, J. D. Kuntz, Z. M. Seeley, S. E. Fisher, O. B. Drury, and B. W. Sturm *et al.*, "Transparent ceramic scintillators for gamma spectroscopy and radiography," *Proc. SPIE*, vol. 7805, pp. 780501–780505, 2010.

[14] A. Lempicki, A. Wojtowicz, and E. Berman, "Fundamental limits of scintillator performance," *Nucl. Instrum. Meth. Phys. Res. A*, vol. 333, pp. 304–311, 1993.

Optical Materials 36 (2014) 1942–1945

Contents lists available at ScienceDirect

Optical Materials

journal homepage: www.elsevier.com/locate/optmat

Cz grown 2-in. size Ce:$Gd_3(Al,Ga)_5O_{12}$ single crystal; relationship between Al, Ga site occupancy and scintillation properties

Kei Kamada [a,b,*], Shunsuke Kurosawa [c], Petr Prusa [d], Martin Nikl [d], Vladimir V. Kochurikhin [b], Takanori Endo [e], Kousuke Tsutumi [e], Hiroki Sato [e], Yuui Yokota [a], Kazumasa Sugiyama [c], Akira Yoshikawa [a,b,c]

[a] Tohoku University, New Industry Creation Hatchery Center, 6-6-10 Aoba, Aramaki, Aoba-ku, Sendai, Miyagi 980-8579, Japan
[b] C&A Corporation, T-Biz, 6-6-10 Aoba, Aramaki, Aoba-ku, Sendai, Miyagi 980-8579, Japan
[c] Tohoku University, Institute for Material Reseach, 2-1-1 Katahira Aoba-ku, Sendai, Miyagi 980-8577, Japan
[d] Institute of Physics AS CR,16253 Prague, Czech Republic
[e] Materials Research Laboratory, Furukawa co. ltd, 1-25-13, Kannondai, Tsukuba 305-0856, Japan

ARTICLE INFO

Article history:
Available online 3 May 2014

Keywords:
Scintillator
Single crystal growth

ABSTRACT

2-in. size Ce 1%:$Gd_3(Al_{1-x}Ga_x)_5O_{12}$ (GAGG) single crystals with various Ga concentration of $x = 2$, 2.4, 2.7 and 3 were grown by the Czochralski (Cz) method. Light yield has maximum value of 58,000 photon/MeV at $x = 2.7$ Ga concentration. Energy resolution was improved with decreasing Ga concentration and $x = 2.4$ sample showed best energy resolution of 4.2%@662 keV. The dependence of scintillation properties on crystal structure and Al–Ga was discussed.

1. Introduction

Materials, which has garnet structure are promising candidates for scintillator applications, because of well-developed manufacturing technology as laser crystals. As it has optical transparency and has easy doping by rare-earth elements, it is considered for other applications, such as magneto-optics. After a decade of R&D of the $Lu_3Al_5O_{12}$-based single crystal scintillators, new material concept was defined, based on multicomponent $(Gd,RE)_3(Ga,Al)_5O_{12}$ host, Re = Lu, Y. Doped by Ce^{3+}, the Gd- and Ga rich host compositions showed amazingly high light yield up to almost 50,000 photon/MeV [1–8] which is the value exceeding by 30–40% the best LYSO:Ce materials ever seen. Recently, our group reported about Ce:$Gd_3Al_2Ga_3O_{12}$ (GAGG) single crystal and scintillation response of about ~90 ns at emission around 520 nm, prospective light yield of about 46,000 photon/MeV, and density of 6.63 g/cm^3 [2–4]. This multicomponent garnet Ce:$Gd_3(Ga,Al)_5O_{12}$ single crystals show very interesting features. The composition, which shows higher light yield, is not the same as that of higher energy resolution. Light yield and energy resolution has dependence on Al–Ga ratio. Moreover, when it crystallized, the initial phase has also strong dependence on Al–Ga ratio.

In this presentation, 2-in. size Ce 1%:$Gd_3(Al_{1-x}Ga_x)_5O_{12}$ (GAGG) single crystals with various Ga concentration of $x = 2$, 2.4, 2.7 and 3 were grown by the Czochralski (Cz) method using an RF heating system. Scintillation properties such as light yield and decay time were also evaluated. The dependence of scintillation properties on crystal structure and Al–Ga was discussed.

2. Experimental

2.1. Sample preparations

Stoichiometric mixtures of 4 N CeO_2, Gd_2O_3, β-Ga_2O_3 and α-Al_2O_3 powders (High Purity Chemicals Co.) were used as starting material. Nominally, Gd^{3+} site was substituted by Ce^{3+} according to the formula of $(Ce_{0.01}Gd_{0.99})_3Al_{5-x}Ga_xO_{12}$. Ce:GAGG ($x = 2$, 2.4, 2.7 and 3) single crystals were grown by means of the Cz method using an RF heating system. The rotation rate was 4–12 rpm and the growth rate was 1.0 mm/h. An automatic diameter control system using crystal weighing was applied to control the growth parameters. Crystals were grown from a 50 mm diameter Ir crucible under Ar with adding 30% of CO_2 atmosphere to prevent evaporation of gallium oxide. The seed crystal was a [100] oriented Ce:GAGG crystal. After the completion of the crystal growth, the crystal

* Corresponding author at: Tohoku University, New Industry Creation Hatchery Center, 6-6-10 Aoba, Aramaki, Aoba-ku, Sendai, Miyagi 980-8579, Japan. Tel.: +81 22 215 2214.
E-mail address: kamada@c-and-a.jp (K. Kamada).

http://dx.doi.org/10.1016/j.optmat.2014.04.001
0925-3467/

was removed from the melt and was gradually cooled down to room temperature.

2.2. Gamma-ray response measurement procedure

Light yield measurements were performed by using an avalanche photodiode (PD) (Hamamatsu, S8650) and APD (Hamamatsu S8664-55). Sample pieces with dimensions of 5 × 5 × 5 mm were cut from the grown single crystal, all surfaces were chemically polished. The samples were surrounded by $BaSO_4$ based reflector and optically coupled to the APD (Hamamatsu, S8664-55). The light yield (LY) of the sample was calibrated from the ^{55}Fe direct irradiation peak to APD. For the decay time measurement the same setup with a photomultiplier tube (PMT Hamamatsu R7600U-200 and digital oscilloscope TD5032B were used. Non-proportionality was determined by amplitude spectroscopy of scintillation response induced by gamma rays (Mares et al., 2007). Scintillation crystal is covered by teflon tape to ensure efficient light collection, and optically coupled to a hybrid photo-multiplier (HPMT) model DEP PPO 475B. Signal from HPMT is processed by spectroscopy amplifier ORTEC model 672 and multichannel-buffer ORTEC 927TM. Pulse height spectrum is displayed on a PC. Several gamma ray emitting radionuclide sources were used to induce a scintillation response: ^{137}Cs (661.6 keV), ^{22}Na (511 keV,1274 keV), ^{241}Am (59.54 keV, 13.95 keV), ^{210}Pb (46.54 keV,10.84 keV), ^{109}Cd (88.04 keV, 22.16 keV), and ^{133}Ba (81.0 keV,160.6 keV, 276.4 keV, 302.9 keV, 356.0 keV, and 383.9 keV)(Ekström and Firestone, 2004). Only selection of ^{133}Ba lines is presented for many samples due to non-negligible interference.1274 keV line of ^{22}Na is not presented because of experimental setup saturation.

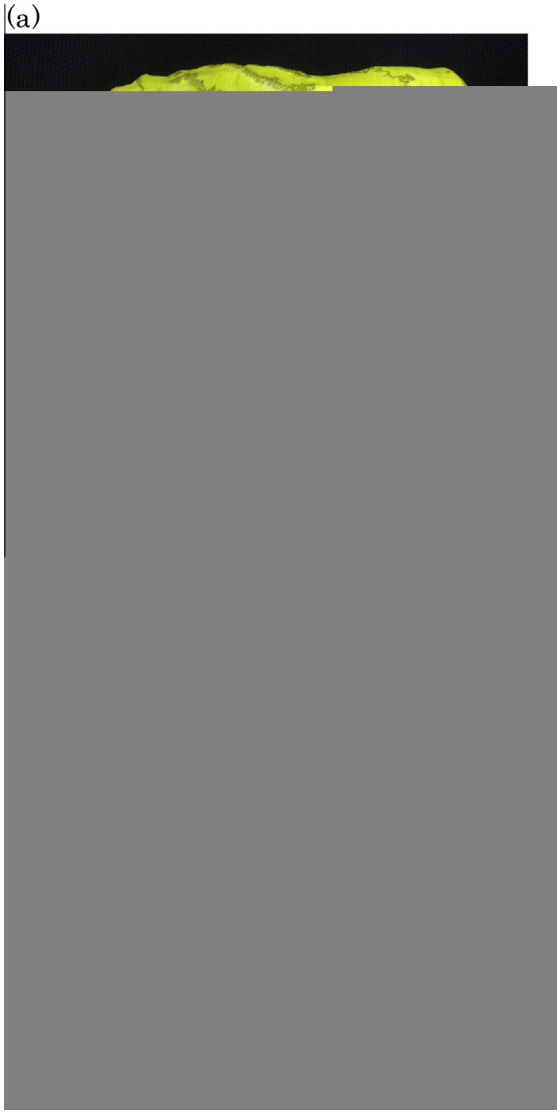

Fig. 1. Photographs of Ce:GAGG with Ga concentrations of x = (a) 2.0, (b) 2.4, (c) 2.7 and (d) 3.0.

3. Result and discussion

3.1. Crystal growth

Ce 1% doped GAGG (x = 2, 2.4, 2.7, and 3) crystals with a diameter of 50 mm and length of 80–120 mm were grown. The grown crystals looked slightly cloudy because of the rough surface caused by gallium oxide evaporation or thermal etching (see Fig. 1). Metallic stripes on the crystal surfaces were identified as Ir deposit comes from oxidation of the crucible. Powder X-ray diffraction (XRD) was performed to identify the phase of grown crystals. As shown in Fig. 2, beginning part of x = 2.0 and 2.4 had mixture phases of garnet and perovskite. This result is good agreement with previous report [9]. Single garnet phase appeared at the end part because of the increasing of Ga concentration due to Ga segregation. The crystals of x = 2.7 and 3 showed single garnet phase in whole crystals.

Quantitative chemical analysis of the crystals for the Ce content along the growth direction was performed by electron probe microanalysis (EPMA; JXA-8621MX, JEOL). So called ZAF correction was used, where Z stands for atomic number, A for absorption correction factor and F for fluorescence correction factor, respectively. The Ga distributions of Ce:GAGG (x = 2.4 and 2.7) along the growth direction are shown in Fig. 2. The solidification fractions (g) of the grown x = 2.4 and 2.7 crystals were 0.42 and 0.43, respectively. Here g is described as follows:

$$g = (\text{mass of solidified part})/(\text{total mass of starting raw material in the crucible})$$

Segregation coefficients of Ga were k_{eff} = 0.92 and 0.93 in x = 2.4 and 2.7 crystals. Secondary perovskite phase was observed in the part below Ga concentration of 2.3. This result is good agreement of previous reports [2,3,10].

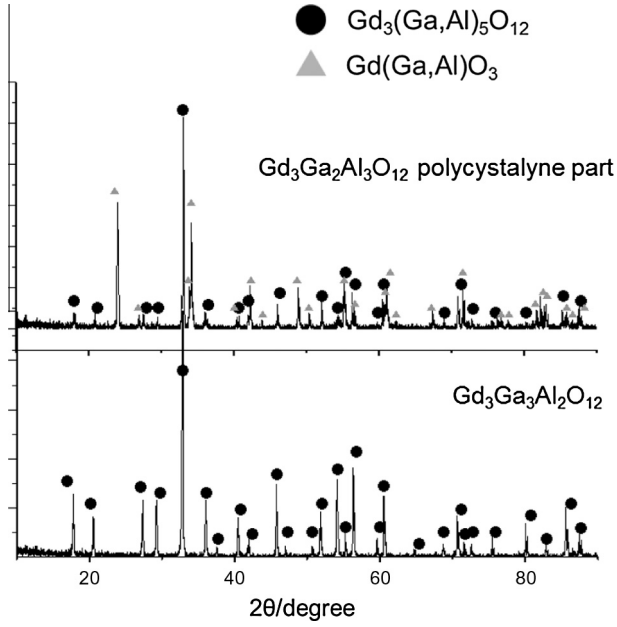

Fig. 2. Results of powder XRD on the grown x = 2.0 and x = 3.0 Ce:GAGG crystals.

3.2. Gamma-ray response

The typical energy spectra of Ce 1%:GAGG excited by ^{137}Cs at 19 °C and measured using the APD are shown in Fig. 3. The light yield (LY) of the samples were calibrated from the ^{55}Fe direct irradiation peak to the APD. Such direct irradiation generates 5.9 keV/3.6 eV = 1630 electron-hole pairs. After correcting the QE, which is at 80% at 520 nm, the total LY becomes ~58,000 photon/MeV in x = 2.7 crystal. Energy resolution of the x = 2.3 was 4.2%@662 keV. Fig. 4 shows decay curves of the samples. Decay time was accelerated with increasing Ga concentration. Table 1 shows relationship between Ga concentrations, light yield, energy resolution and decay time. Light yield has maximum value at x = 2.7 Ga concentration and energy resolution became better with decreasing Ga concentration. Non-proportionality of the samples are shown in Fig. 5. The x = 2.4 sample showed the best non-proportionality among the obtained samples. This is good agreement with the result of the best energy resolution in x = 2.4 sample.

3.3. Single crystal X-ray structure analysis

The garnet structure has a cubic symmetry (Ia3d) with the general chemical formula $C_3A_2D_3O_{12}$. The ions D are surrounded by a dodecahedron of eight O^{2-} ions, the ions A are surrounded by an octahedron of O^{2-} ions, and the ions D are surrounded by an O^{2-} tetrahedron as shown in Fig. 6. By ionic size considerations the doping RE ions predominantly enter in the dodecahedral C-sites while the D-elements enter in octahedral and/or tetrahedral sites of the garnet lattice. In case of GAGG the C species are Gd^{3+} ions, while both A and D species are randomly occupied by Ga^{3+} and Al^{3+} ions [2,3,10]. Here, ionic radii of Al^{3+} (IV), Al^{3+} (VI), Ga^{3+} (IV) and Ga^{3+} (VI) are 0.39, 0.54, 0.47 and 0.62 respectively (see Fig. 7).

Single crystals were cut from the ingots and then carefully shaped into tiny spheres with diameters of 130–160 μm using Bond's method [6]. Diffraction intensity data were collected using

Table 1
Scintillation properties of the samples.

Ga concentrations	Emission wavelength /(nm)	Light yield (photon/MeV)	Energy resolution / (%@662 keV)	Decay time (ns)
3	520	55,000	5.2	97 ns(80%) 353 ns(20%)
2.7	516	58,000	4.8	172 ns(88%) 1932 ns(12%)
2.4	510	46,000	4.2	138 ns(71%) 649 ns(2%)

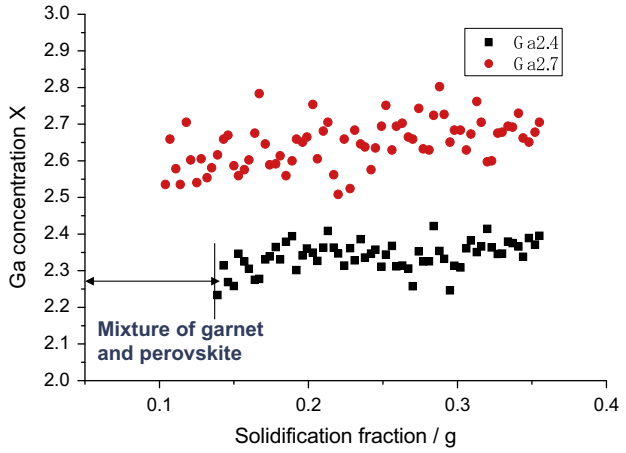

Fig. 3. Ga distributions of the grown x = 2.4 and 2.7 along the growth direction.

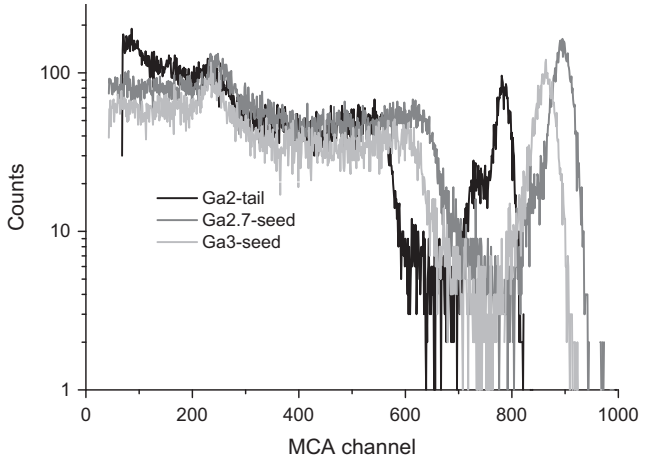

Fig. 4. Energy spectra of Ce 1%:GAGG samples excited by a 662 keV gamma-ray using the APD at 19 °C.

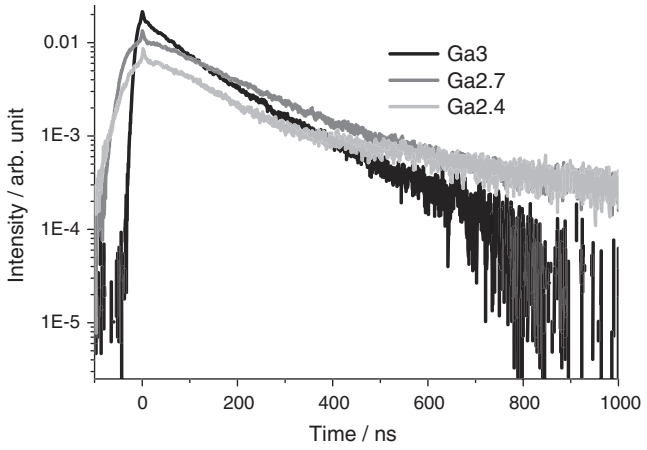

Fig. 5. Decay curves of Ce 1%:GAGG samples excited by a 662 keV gamma-ray using the PMT and digital oscilloscope.

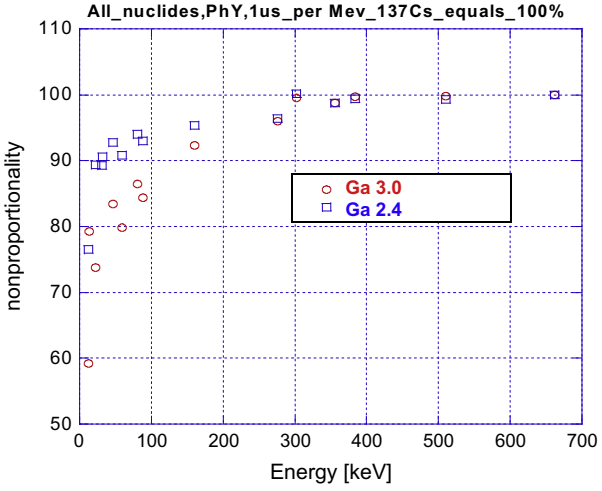

Fig. 6. Non-proportionality of the obtained samples.

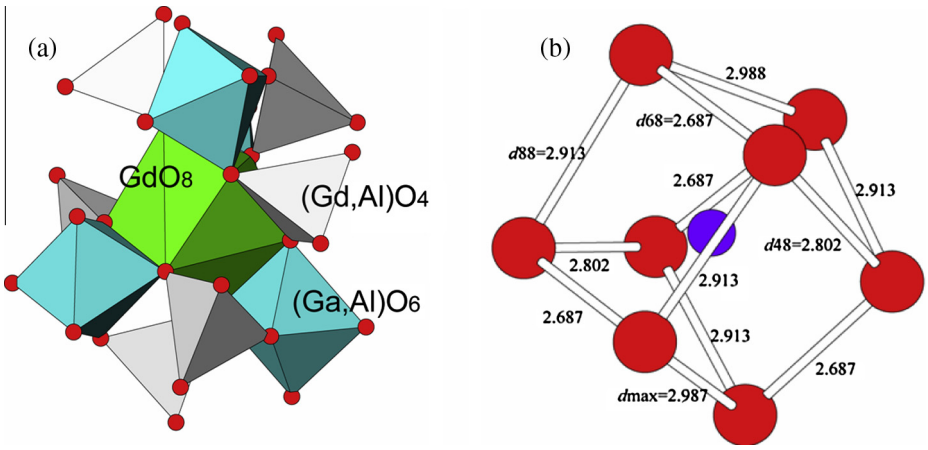

Fig. 7. (a) Schematic drawing of garnet structure of GAGG and (b) dodecahedral site.

Table 2
Interatomic distance (in Å) for $(Ce_{0.01}Gd_{0.99})_3Al_{5-x}Ga_xO_{12}$.

	Ga2.95	Ga2.65	Ga2.35	Ga2.05
Lattice constant	12.29509	12.28020	12.25216	12.24542
R factor	0.0252	0.0238	0.0233	0.0226
Dodecahedoron	2.364	2.362	2.357	2.361
	2.484	2.477	2.477	2.483
Dodecahedral_ave.	2.424	2.420	2.417	2.422
Octahedron	1.966	1.960	1.956	1.951
Tetrahedron	1.825	1.829	1.820	1.815
d68	2.687	2.675	2.676	2.677
d48	2.802	2.809	2.796	2.794
d88	2.913	2.907	2.909	2.927
d max	2.988	2.982	2.976	2.976
d ave.	2.832	2.826	2.824	2.830
Standard deviation	0.161	0.167	0.165	0.177

monochromated Mo Kα radiation ($\lambda = 0.71069$ Å) on a Rigaku AFC7R four-circle diffractometer: $h = 0 \rightarrow 22–23$, $k = 0 \rightarrow 16$, $l = 0 \rightarrow 22–23$; $2\theta_{max} = \sim 70°$; three standard reflections every 150 reflections (without intensity decay). After Lorenz and polarization corrections, absorption corrections for spherical samples were applied. The lattice constants recorded above were determined from 24 reflections with high 2θ values by the least-squares procedure. Experimental result and average distance between cation and anion in each sites in garnet structure. All R factors are well converging. Ga concentration was measured by EDX analysis in advance. As shown in Table 2, interatomic distance in tetrahedral site in Ga2.7 sample is specifically large while interatomic distance in octahedral site is gradually increase with increasing Ga concentration. Moreover, standard deviations of interatomic distances in dodecahedral site (d68, d48 and d88) showed particular value in Ga2.7. These results indicates particular occupancy of Ga^{3+} in octahedral and tetrahedral sites in Ga2.7. There are possibility that particular occupancy phenomena in Ga2.7 cause increase of its light yield. However, much more investigations and researches are necessary to explain the relationship between crystal structure and scintillation properties in Ce:GAGG.

4. Conclusion

Relationship between Ga concentration, light yield, energy resolution and crystal structure was discussed using the grown Ce 1%:$Gd_3(Al_{1-x}Ga_x)_5O_{12}$ (GAGG) single crystals with various Ga concentration of $x = 2$, 2.4, 2.7 and 3. Light yield has maximum value of 58,000 photon/MeV at $x = 2.7$ Ga concentration. Energy resolution was improved with decreasing Ga concentration and took the best value of 4.2%@662 keV at $x = 2.4$. Interatomic distance in tetrahedral site and standard deviation of anion bond length in dodecahedral site at Ga2.7 sample showed particular value compared to the other samples.

Acknowledgements

This work is partially supported by (i) the funding program for next generation world-leading researchers, JSPS, (ii) Development of Systems and Technology for Advanced Measurement and Analysis, Japan Science and Technology Agency (JST) (iii) Adaptable & Seamless Technology Transfer Program through Target-driven R&D (A-STEP), JST (iv) Japan Society for the Promotion of Science (JSPS) Grant-in-Aid for Exploratory Research (A.Y), (v) JSPS Research Fellowships for Young Scientists (S. Kurosawa) and (vi) the Health Labour Sciences Research Grant, The Ministry of Health Labour and Welfare. In addition, we would like to thank following persons for their support: Mr. Yoshihiro Nakamura in Institute of Multidisciplinary Research for Advanced Materials (IMRAM), Tohoku University and Mr. Hiroshi Uemura, Ms. Keiko Toguchi and Ms. Megumi Sasaki, Ms. Yuka Takeda in IMR.

References

[1] N.J. Cherepy, J.D. Kuntz, Z.M. Seeley, S.E. Fisher, O.B. Drury, B.W. Sturm, et al., Proc. SPIE 7805 (2010) 780501–780505.
[2] K. Kamada, T. Endo, K. Tsutumi, T. Yanagida, Y. Fujimoto, A. Fukabori, et al., Cryst. Growth Des. 11 (2011) 4484–4490.
[3] K. Kamada, T. Yanagida, J. Pejchal, M. Nikl, T. Endo, K. Tsutumi, et al., J. Phys. D: Appl. Phys. 44 (2011) 505104–505111.
[4] K. Kamada, T. Yanagida, T. Endo, K. Tsutumi, Y. Usuki, M. Nikl, et al., J. Cryst. Growth 352 (2012) 88–90.
[5] K. Kamada, T. Yanagida, J. Pejchal, M. Nikl, T. Endo, K. Tsutumi, et al., IEEE Trans. Nucl. Sci. 59 (5) (2012) 2126–2129.
[6] K. Kamada, T. Yanagida, T. Endo, K. Tsutumi, M. Yoshino, J. Kataoka, et al., J. Cryst. Growth 352 (2012) 91–94.
[7] P. Prusa, K. Kamada, M. Nikl, A. Yoshikawa, J.A. Mares, Radiation Measurements, in press, 2013, http://dx.doi.org/10.1016/j.radmeas.2013.01.055.
[8] M. Nikl, A. Vedda, M. Fasoli, I. Fontana, V.V. Laguta, E. Mihokova, et al., Phys. Rev. B 76 (2007) 195121–195128.
[9] H. Kimura, H. Maeda, M. Sato, J. Cryst. Growth 74 (January) (1986) 187–190.
[10] W.L. Bond, Rev. Sci. Instr. 22 (1951) 344.

Nuclear Instruments and Methods in Physics Research A 751 (2014) 1–5

Contents lists available at ScienceDirect

Nuclear Instruments and Methods in Physics Research A

journal homepage: www.elsevier.com/locate/nima

Scintillation properties of $Gd_3Al_2Ga_3O_{12}:Ce^{3+}$ single crystal scintillators

Ongsa Sakthong [a], Weerapong Chewpraditkul [a,*], Chalerm Wanarak [a], Kei Kamada [c], Akira Yoshikawa [b,c], Petr Prusa [d,e], Martin Nikl [e]

[a] Department of Physics, King Mongkut's University of Technology Thonburi, Bangkok 10140, Thailand
[b] Institute of Multidisciplinary Research for Advanced Materials, Tohoku University, 2-1-1 Katahira, Aoba-ku, Sendai 980-8577, Japan
[c] NICHe, Tohoku University, 6-6-10 Aoba, Aramaki, Aoba-ku, Miyagi, Sendai 980-8579, Japan
[d] Faculty of Nuclear Sciences and Physical Engineering, Czech Technical University in Prague, 11519 Prague, Czech Republic
[e] Institute of Physics, AS CR, Prague 16253, Czech Republic

ARTICLE INFO

Article history:
Received 29 July 2013
Received in revised form
11 February 2014
Accepted 8 March 2014
Available online 16 March 2014

Keywords:
Energy resolution
GAGG:Ce
Light yield
Photofraction
Scintillation detectors

ABSTRACT

The scintillation properties of $Gd_3Al_2Ga_3O_{12}:Ce^{3+}$ (GAGG:Ce) single crystals grown by the Czochralski method with 1 at% cerium in the melt were investigated and results were compared with so far published results in the literature. The light yield (LY) and energy resolution were measured using a XP5200B photomultiplier. Despite about twice higher LY for GAGG:Ce, the energy resolution is only slightly better than that of LuAG:Ce due to its worse intrinsic resolution and non-proportionality of LY. The LY dependences on the sample thickness and amplifier shaping time were measured. The estimated photofraction in pulse height spectra of 320 and 662 keV γ-rays and the total mass attenuation coefficient at 662 keV γ-rays were also determined and compared with the theoretical ones calculated using the WinXCom program.

1. Introduction

Single crystal scintillators are widely used for the detection of ionizing radiation in nuclear and high energy physics, modern medical imaging, space exploration, and industry. The fast and efficient $5d \rightarrow 4f$ luminescence of Ce^{3+} makes it a well-suited emission center in scintillator applications. As a result, new types of Ce-doped inorganic scintillators were intensively studied in the last two decades and some of them were successfully commercialized; for reviews see Refs. [1–4].

Oxide materials based on garnet structure are promising candidates for scintillator applications because of the well-mastered technology developed for laser hosts and easy doping by rare-earth elements. The Ce-doped $Lu_3Al_5O_{12}$ (LuAG:Ce) single crystal was shown to be a prospective scintillator material with a relatively high density of 6.7 g/cm^3 and a fast scintillation response of about 60–80 ns [5]. Due to technological improvements the reported light yield (LY) has gradually increased from about 14,000 up to 25,000 photons/MeV [6,7]. Scintillation performance of LuAG:Ce is strongly degraded by the presence of shallow electron traps which delay an energy delivery to the Ce^{3+} emission centers and give rise to intense slow components in the scintillation decay [8,9]. These traps were ascribed to the antisite Lu_{Al} defects in the LuAG host [10] which are typical defects in the garnet crystals grown from high temperature melt [11,12]. It has been reported that Ga admixture in LuAG host diminishes the energy trapping effects [13] and somewhat increased LY was obtained for Ga concentration up to 20 at% in $Lu_3(Al,Ga)_5O_{12}$:Ce [14]. Recently, $Gd_3Al_2Ga_3O_{12}$:Ce single crystal grown by the micro-pulling down method demonstrated high LY of 42,000 photons/MeV (ph/MeV) and energy resolution of 8.3% at 662 keV as measured with avalanche photodiode (APD) at room temperature [15]. An improvement of the scintillator performance was achieved in $Gd_3Al_2Ga_3O_{12}$:Ce single crystal grown by the Czochralski method which shows high LY of 46,000–50,600 ph/MeV and good energy resolution of 4.9–5.5% at 662 keV [16,17]. However, lower LY of about 33,000 ph/MeV and energy resolution of 6.1% at 662 keV were reported at the samples of the same composition by another group [18]. The composition of multicomponent garnet scintillators influences strongly the energy transfer processes and interaction of Ce^{3+} and Pr^{3+} emission centers with the host. Fundamental aspects of these processes became intensively studied and of abroad interest [19–22] and the research results in the field of garnet scintillators in the last decade have been recently summarized in a review paper [23].

In this paper we have investigated the scintillation properties of the latest generation of $Gd_3Al_2Ga_3O_{12}$:Ce (GAGG:Ce) single crystals grown by the Czochralski method. The measurements of

* Corresponding author. Tel.: +662 470 8944; fax: +662 470 8900.
E-mail address: weerapong.che@kmutt.ac.th (W. Chewpraditkul).

http://dx.doi.org/10.1016/j.nima.2014.03.011
0168-9002/

pulse height spectra were performed in order to evaluate LY, its non-proportionality and energy resolution. The LY dependences on the sample thickness and amplifier shaping time were measured. The estimated photofraction in pulse height spectra of 320 and 662 keV γ-rays and the total mass attenuation coefficient at 662 keV γ-rays were also determined and compared with the theoretical ones calculated using the WinXCom program.

2. Experimental

GAGG:Ce single crystals were produced in Materials Research Laboratory, Furukawa Co. Ltd. in Japan [16]. The crystals were grown by the Czochralski method with cerium concentration of 1 at% ($Ce_{0.03}Gd_{2.97}Ga_3Al_2O_{12}$) from Ir crucible under Ar with adding 1.5% of O_2 atmosphere. A stoichiometric mixture of high purity 4N CeO_2, Gd_2O_3, β-Ga_2O_3, and α-Al_2O_3 powders was used as starting materials. Polished plates of 1, 2 and 5 mm thickness cut from the parent sample were used for the measurements. The crystal density was 6.69 g/cm^3 determined by the Archimedes method.

Light yield measurements were performed under the excitation of 662 keV γ-rays from a ^{137}Cs source using a photomultiplier (PMT) based-setup described in Ref. [24]: the signal from a Photonis XP5200B PMT anode was sent to a CANBERRA 2005 preamplifier and then to a Tennelec TC243 spectroscopy amplifier. The PC-based multichannel analyzer (Tukan 8k MCA) was used to record the pulse height spectra. The photoelectron yield, expressed as a number of photoelectrons per MeV (phe/MeV) of energy deposited in the crystal, was determined by means of a single photoelectron method [24,25]. In this method the number of photoelectrons is measured by comparing the position of a full energy peak of γ-rays detected in the crystals with that of the single photoelectron peak from the photocathode. The measurements of LY non-proportionality and energy resolution were carried out for a series of X/γ-rays emitted by different radioactive sources in the energy range from 32.1 to 1274.5 keV.

The total mass attenuation coefficient at 662 keV γ-rays was determined using the good geometry arrangement of a source (15 mCi ^{137}Cs), absorber ($5\times5\times1$ mm^3 GAGG:Ce sample) and NaI:Tl detector. A narrow beam of γ-rays is defined by circular apertures (⌀4 mm) in the Pb-collimators of the source and detector, placed at a distance of 60 cm. All measurements were carried out at room temperature (RT).

3. Results and discussion

3.1. Light yield and energy resolution

Fig. 1 presents the pulse height spectra of γ-rays from ^{137}Cs (662 keV) source as measured at 4 μs shaping time for GAGG:Ce, LuAG:Ce and BGO crystals with the same size of $5\times5\times1$ mm^3, whereas the photoelectron yield and energy resolution values are summarized in Table 1. The photoelectron yield (phe/MeV) was recalculated to the LY (ph/MeV) using the average quantum efficiency $\overline{QE}$ of 18.5% for GAGG:Ce and LuAG:Ce and $\overline{QE}$ of 22% for BGO, based on the typical quantum efficiency characteristic of PMT provided by manufacturer and the emission spectrum of the crystals. Despite about twice higher LY for GAGG:Ce, its energy resolution is only slightly better than that of LuAG:Ce. It could be associated with its worse intrinsic resolution and non-proportionality of LY.

We also studied the dependence of LY on the sample thickness (h) for GAGG:Ce. The pulse height spectra of 662 keV γ-rays measured for the studied samples are shown in Fig. 2, whereas the values of LY and energy resolution are summarized in Table 2.

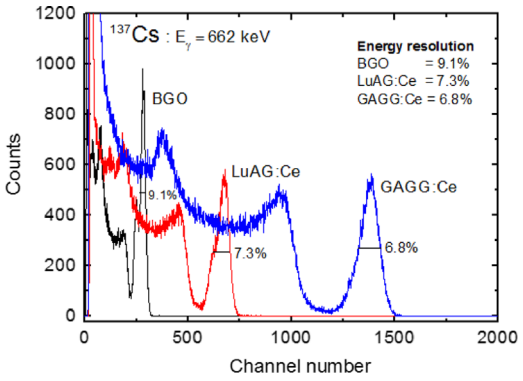

Fig. 1. Pulse height spectra of 662 keV γ-rays (^{137}Cs source) measured with GAGG:Ce, LuAG:Ce and BGO crystals with the same size of $5\times5\times1$ mm^3.

Table 1
Photoelectron yield, LY and energy resolution for GAGG:Ce, LuAG:Ce and BGO crystals with the same size of $5\times5\times1$ mm^3 measured at 4 μs shaping time.

Crystal	Photoelectron yield (phe/MeV)	LY (ph/MeV)	$\Delta E/E$ (%)
GAGG:Ce	8860 ± 440	47,900 ± 4800	6.8 ± 0.2
LuAG:Ce	4300 ± 220	23,200 ± 2300	7.3 ± 0.2
BGO	1860 ± 100	8450 ± 800	9.1 ± 0.3

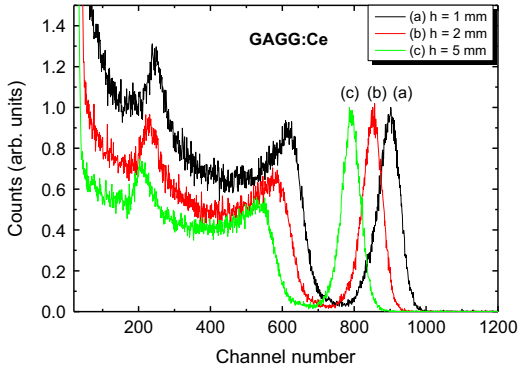

Fig. 2. Pulse height spectra of ^{137}Cs γ-rays measured for the GAGG:Ce samples with thickness (h) of 1, 2 and 5 mm.

The LY value of 47,900 ph/MeV (energy resolution of 6.8%) obtained in this work for a $5\times5\times1$ mm^3 GAGG:Ce sample is comparable to that of 46,000–50,600 ph/MeV (energy resolution of 4.9–7.3%) recently measured for the same size GAGG:Ce samples [16,17]. We note that the LY value of the studied GAGG:Ce decreases with thickness down to 42,100 ph/MeV (88% LY of 1 mm thick sample) for 5 mm thick sample, which is better than the value (85% LY of 1 mm thick sample) measured for 4.5 mm thick sample in Ref. [17]. It indicates that scintillation light loss due to self-absorption and photon scattering in the studied GAGG:Ce is smaller than that of the samples in Ref. [17]. This feature is of importance for maintaining high LY with increasing sample size. Despite a comparable photoelectron yield, the energy resolution of 6.8% obtained for a $5\times5\times1$ mm^3 sample is worse than that of 6.1% observed for a $10\times10\times5$ mm^3 GAGG:Ce sample in Ref. [18], which is due to a higher contribution of the intrinsic resolution (6.0% versus 5.2%) for the studied sample.

The energy resolution ($\Delta E/E$) of a full energy peak measured with a scintillator coupled to a PMT can be written as [26]

$$(\Delta E/E)^2 = (\delta_{sc})^2 + (\delta_p)^2 + (\delta_{st})^2 \quad (1)$$

Table 2
LY and energy resolution (at 662 keV) measured at 4 μs shaping time for studied GAGG:Ce samples with thickness of 1, 2 and 5 mm.

Sample size (mm^3)	LY (ph/MeV)	Relative LY (% of 1 mm)	$\Delta E/E$ (%)
$5\times5\times1$	47,900	100	6.8 ± 0.2
$5\times5\times2$	45,400	95	7.0 ± 0.2
$5\times5\times5$	42,100	88	7.3 ± 0.3

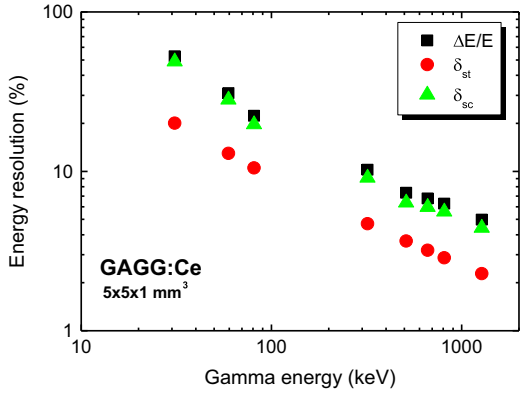

Fig. 3. Energy resolution and contributed factors versus energy of γ-rays for a $5\times5\times1$ mm^3 GAGG:Ce crystal.

where δ_{sc} is the intrinsic resolution of the crystal, δ_p is the transfer resolution and δ_{st} is the statistical contribution of PMT to the resolution.

The statistical uncertainty of the signal from the PMT can be described as

$$\delta_{st} = 2.355\times 1/N^{1/2}\times(1+\varepsilon)^{1/2} \quad (2)$$

where N is the number of the photoelectrons and ε is the variance of the electron multiplier gain, equal to 0.1 for an XP5200B PMT.

Overall energy resolution and PMT resolution can be determined experimentally. If δ_p is negligible, intrinsic resolution δ_{sc} of a crystal can be written as follows:

$$(\delta_{sc})^2 = (\Delta E/E)^2 - (\delta_{st})^2. \quad (3)$$

Fig. 3 presents the measured energy resolution versus energy of γ-rays for a $5\times5\times1$ mm^3 GAGG:Ce crystal. Other curves shown in Fig. 3 represent the PMT resolution (δ_{st}) and intrinsic resolution (δ_{sc}). Apparently, the energy resolution for the GAGG:Ce crystal is mainly contributed by the intrinsic resolution over whole energy range from 32 to 1274.5 keV, reflecting to its high LY. An analysis of the 662 keV energy resolution for GAGG:Ce compared to LuAG:Ce is presented in Table 3. Despite about twice higher LY for GAGG:Ce, its energy resolution is slightly better than that of LuAG:Ce, which is due to its worse intrinsic resolution δ_{sc}. Fig. 4 presents the non-proportionality characteristics of $5\times5\times1$ mm^3 GAGG:Ce and LuAG:Ce crystals. Over the energy range from 662 keV down to 32 keV, the LY non-proportionality for GAGG:Ce is ~20% which is worse than that of ~14% for LuAG:Ce, reflecting somewhat higher intrinsic resolution (see Table 3) as the non-proportionality of LY is a fundamental limitation to intrinsic resolution [27]. We note that the LY non-proportionality (20% at 32 keV) obtained for a studied $5\times5\times1$ mm^3 GAGG:Ce is comparable to those measured for $5\times5\times5$ mm^3 and $10\times10\times5$ mm^3 GAGG:Ce samples [18], and there is no sample size dependence.

In order to investigate the contribution of slow components in scintillation response for GAGG:Ce, the LY dependence on amplifier shaping time was measured under 662 keV γ-ray excitation and compared with LuAG:Ce. The result in Fig. 5 shows a lower

Table 3
Analysis of the 662 keV energy resolution for GAGG:Ce and LuAG:Ce crystals with the same size of $5\times5\times1$ mm^3. N is the number of photoelectrons measured at 662 keV.

Crystal	N	Energy resolution (%)		
		$\Delta E/E$	δ_{st}	δ_{sc}
GGAG:Ce	5860	6.8	3.1	6.0
LuAG:Ce	2850	7.3	4.4	5.8

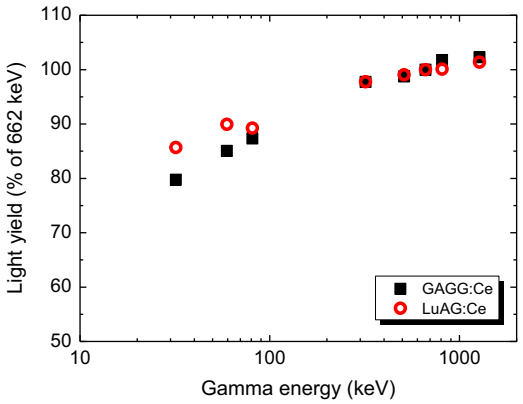

Fig. 4. Non-proportionality characteristics of $5\times5\times1$ mm^3 GAGG:Ce and LuAG:Ce crystals.

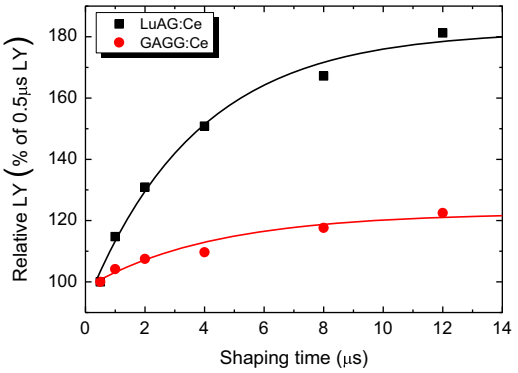

Fig. 5. Light yield dependence on amplifier shaping time normalized at 0.5 μs for GAGG:Ce and LuAG:Ce crystals. Solid lines are due to the model described in the text.

contribution of slow component in the scintillation response of GAGG:Ce with respect to LuAG:Ce. In the former material it confirms the diminished trapping effect due to intrinsic shallow electron traps and at the same time yet sufficient separation between the conduction band edge and $5d_1$ excited state of Ce^{3+} achieved due to the balanced admixture of Gd and Ga into aluminum garnet matrix [20,21,28].

Shaping time dependences of LY in Fig. 5 were approximated by the model of Prusa et al. in Ref. [29]. Based on a two-exponential approximation of scintillation decay the normalized LY(t) time dependence is expressed as

$$\mathrm{LY}(t) = m_1 - m_2\exp[-m_3 t] \quad (4)$$

where $m_{1,2,3}$ are parameters. Their physical meaning can be described as follows: m_1 is relative increase of LY for an infinite shaping time, relative fraction of the fast response part $K_{f/e}$ (t=0.5 μs) in the entire LY value ($t=\infty$) is obtained as $K_{f/e}=1-m_2/m_1$, and m_3 is proportional to the inverse decay time of

the slow component responsible for the LY(t) increase for increasing shaping time values. The values of $m_1=123\%$, $K_{f/e}=80\%$ and $1/m_3=4.2$ μs for GAGG:Ce and $m_1=182\%$, $K_{f/e}=50\%$ and $1/m_3=3.7$ μs for LuAG:Ce were obtained from Eq. (4) fitted to the data in Fig. 5, solid and dashed lines, respectively; for further evaluation details see Ref. [29]. This measurement supports higher content of fast component with contributed intensity of 85% and 47%, respectively, in the scintillation decay of GAGG:Ce [18] and LuAG:Ce [8,9]. $K_{f/e}$ value of 80% obtained for a studied GAGG:Ce is lower than those measured earlier for GAGG: 1% Ce [17].

3.2. Photofraction

The photofraction is defined as the ratio of counts under the full-energy peak to the total counts of the spectrum as measured at a specific γ-ray energy. Fig. 6 presents the pulse height spectra of γ-rays from ^{137}Cs (662 keV) and ^{51}Cr (320 keV) sources as measured with a $5\times5\times5$ mm^3 GAGG:Ce sample while the photofraction for all GAGG:Ce samples is presented in Table 4. The ratio of the cross-section for the photoelectric absorption to the total one calculated using the WinXCom program [30] is also given for a comparison. Note a higher photofraction as measured for the larger samples as expected due to a higher contribution from (multiple) Compton scattering and terminated by photoelectric absorption, leading to a full-energy peak in the pulse height spectrum, for the larger crystals. The higher photofraction for 320 keV γ-rays was also observed in the same trend with the cross-section ratio (σ-ratio) obtained from the WinXCom program. It is due to the increase of photoelectric absorption cross-section with decreasing energy of γ-rays.

3.3. Total mass attenuation coefficient

A parallel beam of monoenergetic γ-rays is attenuated in an absorber according to the Lambert–Beer law:

$$I(x)=I_0\exp(-\mu_m\rho x) \quad (5)$$

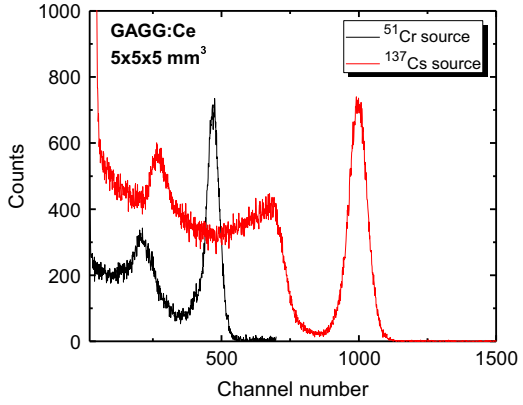

Fig. 6. Pulse height spectra of γ-rays from ^{137}Cs (662 keV) and ^{51}Cr (320 keV) sources as measured with a $5\times5\times5$ mm^3 GAGG:Ce crystal.

Table 4
Photofraction at 320 and 662 keV γ-rays for studied GAGG:Ce crystals.

Energy (keV)	Sample size (mm^3)	Photofraction (%)	σ-ratio (%)
320	$5\times5\times1$	33.4	40.8
	$5\times5\times2$	37.2	
	$5\times5\times5$	43.4	
662	$5\times5\times1$	10.74	12.97
	$5\times5\times2$	14.24	
	$5\times5\times5$	16.35	

Table 5
Mass attenuation coefficient at 320 and 662 keV γ-rays for GAGG:Ce crystal.

γ-energy (keV)	$(\mu_m)_{ex}$ (cm^2/g)	$(\mu_m)_{th}$ (cm^2/g)
320	n.m[a]	0.151
662	0.078	0.077

[a] not measured.

where I_0 and I are incident and transmitted intensities of γ-rays, respectively, μ_m is the mass attenuation coefficient, ρ is the density of the absorber, and x is the thickness of the absorber. The product $\mu_m\rho$ is called the linear attenuation coefficient. Theoretical values of the mass attenuation coefficient of mixture have been calculated using the WinXCom program [30]. Table 5 shows the experimental value $(\mu_m)_{ex}$ of the mass attenuation coefficient at 662 keV γ-rays for GAGG:Ce together with the theoretical ones $(\mu_m)_{th}$ calculated at 320 and 662 keV. The higher value $(\mu_m)_{th}$ for 320 keV was clearly seen in the same trend with the photofraction value (Table 4). It is mainly due to the increase of photoelectric absorption cross-section with decreasing energy of γ-rays.

4. Conclusion

The scintillation properties of the latest generation of $Gd_3Al_2Ga_3O_{12}$:Ce crystal grown by the Czochralski method were investigated. It shows a high LY value over 47,000 ph/MeV and a good energy resolution of 6.8% at 662 keV γ-rays, comparable to that of NaI(Tl). Dependence of the LY value on amplifier shaping time shows distinctly lower content of slower component (in the range of microseconds) in scintillation response compared to LuAG:Ce, which confirms the diminished trapping effect of shallow electron traps due to the balanced admixture of Gd and Ga into aluminum garnet matrix. These properties together with a high density of 6.69 g/cm^3, non-hygroscopic and intrinsic radioactivity-free host assure the capability of GAGG:Ce crystal for high energy γ-ray measurements and medical imaging applications. Further improvement of scintillation performance can be obtained by fine composition tuning in the range of $Gd_3Al_{2-3}Ga_{3-2}O_{12}$.

Acknowledgments

This work is supported by the NRU project of Thailand's Office of the Higher Education Commission and Czech GACR P204/12/0805 project. This work is partially supported by (i) Japan Society for the Promotion of Science (JSPS) Grant-in-Aid for Exploratory Research (AY), (ii) the Funding program for next generation world-leading researchers, JSPS, (iii) Development of Systems and Technology for Advanced Measurement and Analysis, Japan Science and Technology Agency (JST), (iv) Adaptable & Seamless Technology Transfer Program through Target-driven R&D (A-STEP) and JST, and (v) Supporting Industry program, Ministry of Economy, Trade and Industry (METI). Some part of this work was carried out under the collaboration program of Cooperative Research and Development Center for Advanced Materials, IMR, Tohoku University.

References

[1] C.W.E. van Eijk, Nucl. Instrum. Methods Phys. Res. A 460 (2001) 1.
[2] K.W. Kramer, P. Dorenbos, H.U. Gudel, C.W.E. van Eijk, J. Mater. Chem. 16 (2006) 2773.
[3] M. Nikl, Meas. Sci. Technol. 17 (2006) R37.

[4] P. Lecoq, A. Annenkov, A. Gektin, M. Korzhik, C. Pedrini, Inorganic Scintillators for Detector Systems, Springer, Dordrecht, The Netherlands, 2006.
[5] M. Nikl, E. Mihokova, J.A. Mares, A. Vedda, M. Martini, K. Nejezchleb, K. Blazek, Phys. Status Solidi B 181 (2000) R10.
[6] J.A. Mares, A. Beitlerova, M. Nikl, N. Solovieva, C. D'Ambrosio, K. Blazek, P. Maly, K. Nejezchleb, F. De Notaristefani, Radiat. Meas. 38 (2004) 353.
[7] C. Dujardin, C. Mancini, D. Amans, G. Ledoux, D. Abler, E. Auffray, P. Lecoq, D. Perrodin, A. Petrosyan, K.L. Ovanesyan, J. Appl. Phys. 108 (2000) 013510.
[8] M. Nikl, A. Vedda, M. Fasoli, I. Fontana, V.V. Laguta, E. Mihokova, J. Pejchal, J. Rosa, K. Nejezchleb, Phys. Rev. B 76 (2007) 195121.
[9] W. Chewpraditkul, L. Swiderski, M. Moszynski, T. Szczesniak, A. Syntfeld-Kazuch, C. Wanarak, P. Limsuwan, Phys. Status Solidi A 206 (2009) 2599.
[10] M. Nikl, E. Mihokova, J. Pejchal, A. Vedda, Y. Zorenko, Phys. Status Solidi B 242 (2005) R119.
[11] V. Lupei, A. Lupei, C. Tiseanu, S. Georgescu, C. Stoicescu, P.M. Nanau, Phys. Rev. B 51 (1995) 8.
[12] C.R. Stanek, K.J. McClellan, M.R. Levy, R.W. Grimes, Phys. Status Solidi B 243 (2006) R75.
[13] M. Nikl, J. Pejchal, E. Mihokova, J.A. Mares, H. Ogino, A. Yoshikawa, T. Fukuda, A. Vedda, C. D'Ambrosio, Appl. Phys. Lett. 88 (2006) 141916.
[14] H. Ogino, A. Yoshikawa, M. Nikl, J.A. Mares, J. Shimoyama, K. Kishio, J. Cryst. Growth 311 (2009) 908.
[15] K. Kamada, T. Yanagida, J. Pejchal, M. Nikl, T. Endo, K. Tsutumi, Y. Fujimoto, A. Fukabori, A. Yoshikawa, Cryst. Growth Des. 11 (2011) 4484.
[16] K. Kamada, T. Yanagida, T. Endo, et al., J. Cryst. Growth 352 (2012) 88.
[17] P. Prusa, K. Kamada, M. Nikl, A. Yoshikawa, J.A. Mares, Radiat. Meas. 56 (2013) 62.
[18] J. Iwanowska, L. Swiderski, T. Szczesniak, P. Sibczynski, M. Moszynski, M. Grodzicka, K. Kamada, K. Tsutsumi, Y. Usuki, T. Yanagida, A. Yoshikawa, Nucl. Instrum. Methods Phys. Res. A 712 (2013) 34.
[19] P. Dorenbos, J. Lumin. 134 (2013) 310.
[20] J.M. Ogiegło, A. Katelnikovas, A. Zych, T. Jüstel, A. Meijerink, C.R. Ronda, J. Phys. Chem. A 117 (2013) 2479.
[21] J. Ueda, K. Aishima, S. Tanabe, Opt. Mater. 35 (2013) 1952.
[22] Y. Wu, G. Ren, Opt. Mater. 35 (2013) 2146.
[23] M. Nikl, A. Yoshikawa, K. Kamada, K. Nejezchleb, C.R. Stanek, J.A. Mares, K. Blazek, Prog. Cryst. Growth Charact. Mater. 59 (2013) 47.
[24] M. Moszynski, M. Kapusta, M. Mayhugh, D. Wolski, S.O. Flyckt, IEEE Trans. Nucl. Sci. NS-44 (1997) 1052.
[25] M. Bertolaccini, S. Cova, C. Bussolatti, in: Proc. Nuclear Electronics Symp., Versailles, France, 1968.
[26] M. Moszynski, J. Zalipska, M. Balcerzyk, M. Kapusta, W. Mengeshe, J.D. Valentine, Nucl. Instrum. Methods Phys. Res. A 484 (2002) 259.
[27] P. Dorenbos, J.T.M. de Haas, C.W.E. van Eijk, IEEE Trans. Nucl. Sci. NS-42 (1995) 2190.
[28] M. Nikl, K. Kamada, S. Kurosawa, Y. Yokota, A. Yoshikawa, J. Pejchal, V. Babin, Phys. Status Solidi C 10 (2013) 172.
[29] P. Prusa, M. Nikl, J.A. Mares, M. Kucera, K. Nitsch, A. Beitlerova, Phys. Status Solidi A 206 (2009) 1494.
[30] L. Gerward, N. Guilbert, K.B. Jensen, H. Levring, Radiat. Phys. Chem. 71 (2004) 653.

Energy Transfer and Scintillation Properties of Ce^{3+} Doped $(LuYGd)_3(AlGa)_5O_{12}$ Multicomponent Garnets

Miroslav Kucera, Martin Hanus, Zuzana Onderisinova, Petr Prusa, Alena Beitlerova, and Martin Nikl

***Abstract*—Photoluminescence, X-ray excited radioluminescence and photoelectron yield characteristics were studied in multicomponent GdGaYAG:Ce and GdGaLuAG:Ce garnet films grown by liquid phase epitaxy. Nonradiative energy transfer from Gd^{3+} to activator Ce^{3+} ions was evidenced. At low Gd doping, $< 5\%$, two virtually independent emission centers coexist, which compete for intensity: Ce^{3+} with fast 5d-4f emission and Gd^{3+} with slow 4f-4f emission. At higher Gd concentrations, the Ce^{3+} emission retrieves intensity due to the energy transferred from Gd^{3+} donors. At Gd concentration $\sim 50\%$ and above, the Gd^{3+} emission is suppressed due to energy migration and transfer to Ce^{3+} centers. In these samples, the host emission is also completely quenched and the best scintillator performance is achieved. Contrary to melt-grown crystals, no positive role of Ga substitution was found in epitaxial films.**

***Index Terms*—Ce, energy transfer, garnet, Gd doping, liquid phase epitaxy, LuAG:Ce, luminescence, scintillator, YAG:Ce.**

I. Introduction

LUTETIUM and yttrium aluminum garnets (LuAG, YAG) doped by trivalent cerium ions Ce^{3+} are widely studied for scintillation application in detection of high energy particles, X-ray, and gamma radiation [1]–[4] and also as phosphors in lighting applications [5]. Although a promising light yield of 20–30 kPh/MeV and a relatively fast decay of 50–60 ns was reported in LuAG:Ce [6], its major disadvantage is occurrence of slow components in the scintillation decay, which degrade this compound where fast response is required, e.g., in medical applications [7]. The slow component in scintillation decay originates from shallow traps in energy gap identified as antisite defects Lu_{Al}[8], where lutetium ions occupy the aluminum octahedral positions. These defects are unavoidably present in LuAG or YAG single crystals grown at high temperatures from the melt. The Pr^{3+} doping of LuAG gives rise to even faster 5d–4f luminescence (18 ns decay time) in the UV part of the spectra at the 310 nm emission band. However, similarly to Ce-doped LuAG, the figure of merit of LuAG:Pr is degraded by the presence of shallow electron traps, which is responsible for delayed recombination [9], [10].

Recently, a new concept of Gd-Ga substituted YLuAG:Ce garnets was proposed [11], [12] as a promising way to settle the problem of shallow electron traps and to suppress the undesired slow light. The combined effect of Ga substitution, which decreases the band gap and thus eliminates the shallow traps [13], and Gd substitution, which increases the crystal field and shifts down the $5d(Ce^{3+})$ split states [14], protecting them from photoionization. For some of highly Gd-Ga substituted aluminum garnets, a substantial increase of the LY was reported, reaching 50–60 kPh/MeV [15].

In this work, we concentrate on the study of Gd and Ga doping of YAG:Ce and LuAG:Ce on the Ce^{3+} emission. We focused especially the following items, which were explored in detail:

- the energy transfer from Gd^{3+} to Ce^{3+};
- the effect of Gd and Ga substitution on emission, decay kinetic, and scintillation properties of YAG/LuAG:Ce^{3+} films;
- the dependence of the brightness (emission intensity) on the Gd content;
- optimal doping concentrations for the best emission and scintillation properties and quest for new material possibilities;
- scintillation properties – both the steady state (X-ray excited RL) and the photoelectron yield.

II. Samples

Single crystalline films of multicomponent $(GdYLu)_3(AlGa)_5O_{12}$:Ce garnets doped by trivalent Ce^{3+} ions were grown by the liquid phase epitaxy (LPE). Starting raw materials of 4–5N purity were used. Several sets of films with different compositions were prepared: reference samples YAG/LuAG:Ce, Gd-substituted samples GdYAG/GdLuAG:Ce with variable Gd content, or variable Ce content (at constant Gd content), and finally GdGaYAG/GdGaLuAG:Ce samples with high Gd content up to 100% and Ga content 0%–70%. All garnet films reported here were grown by the standard isothermal dipping technique either from $PbO–B_2O_3$ (PbO-flux) or from lead-free $BaO–B_2O_3–BaF_2$ flux (BaO-flux); the growth details were published elsewhere [16], [17]. The films were grown from a supercooled melt solution onto YAG, LuAG, or GGG ($Gd_3Ga_5O_{12}$) substrates

Manuscript received May 24, 2013; revised August 06, 2013; accepted August 06, 2013. Date of publication November 01, 2013; date of current version February 06, 2014. This work was supported by the Czech Science Foundation, project P204/12/0805.

M. Kucera, M. Hanus, and Z. Onderisinova are with Charles University, Faculty of Mathematics and Physics, 12116 Prague, Czech Republic (e-mail: kucera@karlov.mff.cuni.cz; hamatr@seznam.cz; zonderisin@gmail.com).

P. Prusa, A. Beitlerova, and M. Nikl are with the Institute of Physics, 16000 Prague, Czech Republic (e-mail: petr.prusa@fjfi.cvut.cz; beitler@fzu.cz; nikl@fzu.cz).

Color versions of one or more of the figures in this paper are available online at http://ieeexplore.ieee.org.

Digital Object Identifier 10.1109/TNS.2013.2281234

TABLE I
THICKNESS AND CONCENTRATION OF DOPANTS IN Gd AND Ga SUBSTITUTED YAG/LuAG:Ce EPITAXIAL GARNET FILMS

Sample No.	t [μm]	$x_{Ce}\times10^2$	y_{Gd}	z_{Ga}	Flux	Substrate
$(YGd)_3(AlGa)_5O_{12}$:Ce						
1YG2	15.3	0.23	0	0	PbO	YAG
1YG3	27.5	0.23	0.17	0	"	"
1YG4	14.8	0.20	0.30	0	"	"
1YG5	19.6	0.20	0.31	0.097	"	"
1YG7	16.1	0.33	0.44	0.19	"	"
1YGB3	15.7	0.41	0.19	0	BaO	"
1GA2	44	0.29	0.50	0	PbO	"
$(LuGd)_3(AlGa)_5O_{12}$:Ce						
12LBC1	12.3	0.20	0	0	BaO	LuAG
13LBC2	19.7	0.30	0	0	"	"
14LBC1	10.4	0.43	0.037	0	"	"
14LBC4	15.9	0.35	0.18	0.26	"	YAG
14LBC5	17.0	0.34	0.20	0.26	"	"
14LBC6	9.3	0.20	0.32	0.30	"	"
$(LuGd)_3Al_5O_{12}$:Ce						
1LGB1	17.5	0	0.050	0	BaO	LuAG
1LGB2	17.7	0.065	0.045	0	"	"
1LGB3	18.0	0.22	0.046	0	"	"
1LGB6	17.0	0.30	0.045	0	"	"
1LGB4	12.0	0.40	0.046	0	"	"
1LGB5	8.0	0.51	0.052	0	"	"
$Gd_3(AlGa)_5O_{12}$:Ce						
2GG3	16.6	0.25	1.0	0.34	PbO	GGG

t – film thickness, x_{Ce}, y_{Gd}, z_{Ga} – Ce, Gd, Ga concentrations in $(Ce_xGd_yR_{1-x-y})_3(Al_{1-z}Ga_z)_5O_{12}$ garnet films determined by the EPMA, where R = Y or Lu.

of (111) and (100) crystallographic orientations and 20 mm in diameter. The growth temperatures were in the range of 970 °C–1070 °C, supersaturation 5–70 K, and the growth rates 0.06–1.2 μm/min.

The PbO-flux provides films with high surface quality and excellent morphology, and films with large lattice mismatch up to 2% can be successively grown from this flux, as well. However, impurity ions (namely Pb^{2+} from the flux and Pt^{4+} from the crucible) inevitably enter into the garnet lattice. Higher concentration of these impurities would cause degradation of the scintillation yield. In the mastered LPE technique, the concentration of Pb and Pt ions can be suppressed below 10 and 30 ppm, respectively. The principal advantage of the BaO-flux is a negligible concentration of solvent ions in the garnet lattice (concentration of $Ba^{2+} < 2$ ppm according to the GDMS analysis) and its negligible chemical reactivity with platinum crucible.

III. PROPERTIES OF EPITAXIAL FILMS

A. Film Characterization

The basic parameters of films are summarized in Table I. Typical thickness of films measured by weighing was 10–20 μm, which is sufficient for characterization of scintillation properties. The composition of films shown in Table I was determined by the electron probe X-ray microanalysis (EPMA). Unless specifically mentioned, here reported concentrations of dopants, Ce, Gd, and Ga are referred to nominal concentrations in the garnet formula unit $(Ce_xGd_yY_{1-x-y})_3(Ga_zAl_{1-z})_5O_{12}$.

The segregation coefficients of Ce, Gd, and Ga ions were typically: $k_{Ce} \sim 0.01$–0.1, $k_{Gd} \sim 0.4$–1, $k_{Ga} \sim 0.6$–1.3, and they depend on the number of parameters, such as the type of used flux (PbO or BaO), composition of the melt, the supercooling, and the growth temperature.

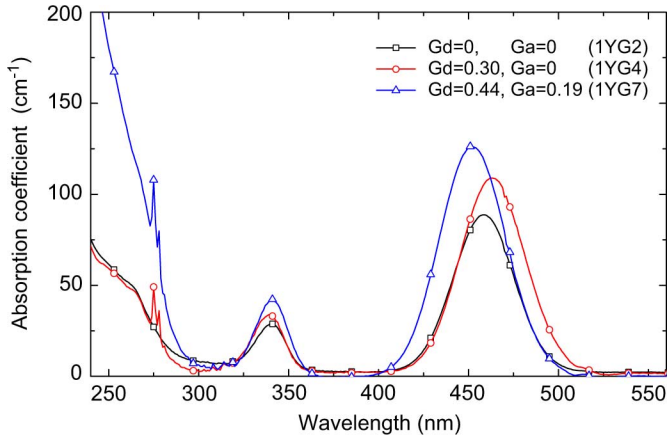

Fig. 1. The absorption coefficient of $(YGd)_3(AlGa)_5O_{12}$:Ce epitaxial films grown from the PbO flux. Concentrations of Gd and Ga are given in the legend, and concentration of Ce is proportional to the value of absorption coefficient at the ~ 460 nm maximum. A significant increase of absorption below 280 nm in the sample 1YG7 is a consequence of decreased band gap due to Ga substitution.

The crystallographic properties of films were studied by the X-ray diffraction. In all the films, the optical absorption and photoluminescence (PL) spectra were measured using commercial spectrophotometers Specord 200 and Fluoromax-3. The X-ray excited radioluminescence (RL) and the PL decay kinetics were measured at custom-made spectrofluorometer 5000M, Horiba JY using an X-ray tube (10 kV, 50 mA) and nanoLED pulse excitation sources, respectively. On selected samples, the photoelectron yield and energy resolution were determined by pulse height spectroscopy of scintillation response [18]. The alpha particles from the ^{239} Pu radioactive source (5.157 MeV) were used. The penetration depth of the alpha particles is of about 10 μm so that they deposit a major part of their energy in epitaxial films, and the substrate is not excited. The measurements were made at room temperature.

B. Optical Absorption and Photoluminescence

Optical transmission spectra were measured in the spectral range from the ultraviolet to the near infrared, 190–1100 nm. The films grown at low mismatch have high transparency $> 80\%$, close to the theoretical limit; however, those grown at large mismatch, $\Delta a = a_f - a_s \approx$ 0.05–0.25Å, where a_f and a_s are lattice parameters of the film and substrate, respectively, have dull surface, and they scatter light. The absorption spectra of typical Ce, Gd-Ga co-doped YAG films are displayed in Fig. 1. All samples exhibited very similar absorption spectra. Two dominant broad absorption bands at ~ 450 and 340 nm are attributed to the allowed electric dipole transitions in Ce^{3+} from $4f(^2F_J)$ multiplet to crystal field split $5d_{1,2}(^2D)$ excited states. Sharp absorption lines at 270 and 310 nm correspond to spin and parity forbidden 4f–4f transitions, $^8S_{7/2} \rightarrow {}^6I_J$ and ^6P_J, respectively, in the Gd^{3+} ions. The only effect of substitution of Ga for Al is a decrease of the band gap, due to 4s(Ga) states at the bottom of conduction band, and thus increased absorption in the UV spectral range below 280 nm, cf. sample YG7 in Fig. 1.

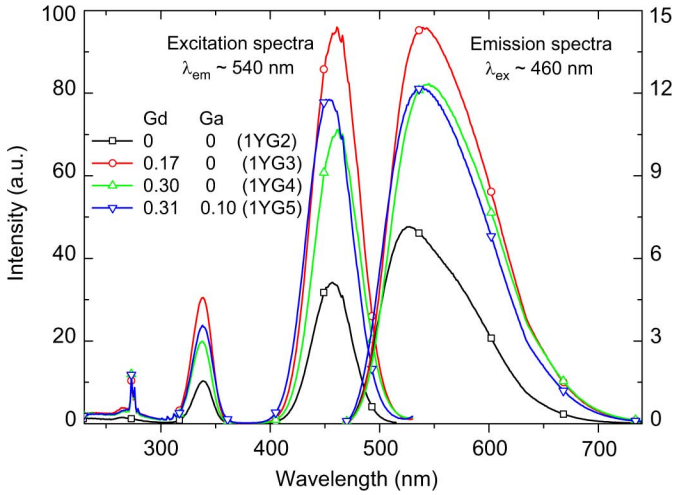

Fig. 2. The photoluminescence excitation and emission spectra (measured at maxima of emission or excitation peaks at ~ 540 and ~ 460 nm, respectively), of $(YGd)_3(AlGa)_5O_{12}$:Ce epitaxial films. Concentrations of Gd and Ga are given in the legend.

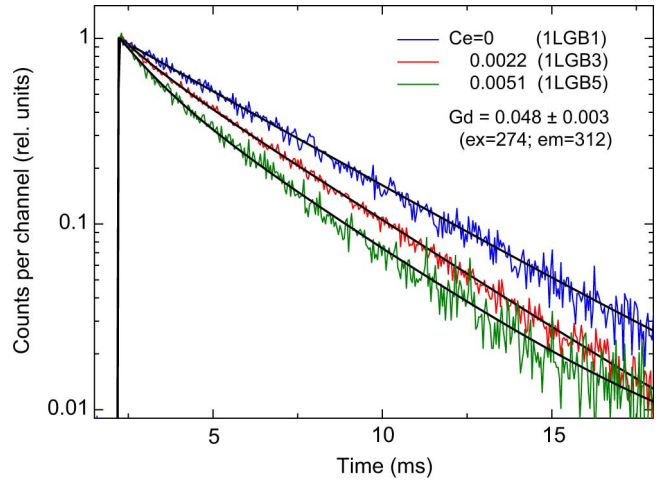

Fig. 3. PL decays measured at ^6P–^8S (4f, Gd) emission of $(GdLu)_3Al_5O_{12}$:Ce epitaxial films; the samples were excited at 274 nm and monitored at 312 nm. Gd concentration in films is 4.8 ± 0.3%, Ce concentration is shown in the legend. The solid lines are convolution of two-exponential decay function and the excitation pulse.

The PL excitation and emission spectra were measured in the spectral range from 200 to 750 nm with the spectral resolution of 0.5 –1 nm. The PL excitation and emission spectra of Ce, Gd substituted YAG samples are displayed in Fig. 2, the emission spectra were corrected for the apparatus spectral response.

The emission spectra were excited in the Ce $(5d_1)$ absorption maximum at ~ 460 nm. Observed emission doublet band with maximum around 520 nm is typical for $5d_1 \rightarrow 4f\,(^2F_{7/2,5/2})$ emission in Ce^{3+} ions. The position of this emission is sensitive to the local crystal field, i.e., material composition-its maximum moves from 510 nm in Ce:LuAG, to 525 nm in Ce:YAG, and towards 560 nm in heavily Gd substituted garnets. This red shift originates from increased crystal field splitting of 5d (Ce^{3+}) states due to Gd doping [14]. The Ga^{3+} substitution cause, on the contrary, the blue shift of the Ce^{3+} emission due to the decreased crystal field splitting of 5d states (increased symmetry of garnets).

The excitation spectra were monitored at the maximum of Ce^{3+} emission at ~ 540 nm . All spectra exhibit a close correlation with the absorption ones. Besides cerium related broadbands at 340 and 460 nm, we observed also sharp split peaks around 274 nm and a weak structure around 310 nm, which attracted our attention. Correlated to the absorption features in Fig. 1, these peaks originate from 4f–4f transitions in Gd^{3+}, and this suggests that Ce^{3+} emission is excited also by means of excitation of ^6I_J, $^6P_J(4f)$ multiplet states of Gd^{3+}. Such peaks in the PL excitation spectra were observed in all Gd-substituted samples. These observations point to possible energy transfer (ET) from Gd^{3+} to Ce^{3+} ions.

In subsequent parts of this work, we turn attention especially to the ET and its mechanism, to the role of mutual Ce/Gd concentrations on the emission properties, and to the role of Gd ions in scintillation properties.

C. Properties of GdLuAG/GdYAG:Ce Garnets at Low Gd Doping

The nonradiative energy transfer from the Gd^{3+} donor to Ce^{3+} acceptor ions in the Ce, Gd co-doped YAG and LuAG has been recently reported in our previous work [19]. This ET was supported by the observations that a) the Gd^{3+} absorption lines are fingerprinted in Ce^{3+} excitation spectrum (cf. Figs. 1 and 2), b) if Gd^{3+} ions are excited selectively, also Ce^{3+} emission is observed, and finally c) the decay time value of Gd^{3+} emission is significantly shortened in the presence of Ce^{3+} ions and the latter emission shows a millisecond decay component when excited via the Gd^{3+} absorption lines [19].

In Fig. 3, the initial parts of normalized Gd^{3+} decay curves are shown for samples with the same Gd content and different Ce content. With increasing cerium content, the $Gd^{3+}(^6P_J \rightarrow {}^8S_{7/2})$ decay time gradually decreases. Furthermore, the single-exponential Gd^{3+} decay was observed only in samples with the lowest Ce content, while it must be approximated by two exponentials (with additional short component) at higher Ce content. These facts suggested significant nonradiative energy transfer away from the Gd^{3+} ions due to the Ce^{3+} doping.

According to the Forster–Dexter model of the interaction mechanism [20], the efficiency of Gd^{3+}-to-Ce^{3+} transfer should be rather low because of a minor spectral overlap between the 4f (Gd^{3+}) emission line at 312 nm and $4f–5d_2(Ce^{3+})$ absorption bands (cf. Figs. 1 and 2). In such a case, the efficiency of the ET process can be improved by participation of lattice phonons.

The radioluminescence (RL) characteristics depend on the host-to-activator energy transfer mechanism, and it characterizes the steady state scintillation efficiency. The RL spectra were measured under X-ray excitation (10 kV, 50 mA) in the spectral range 200–800 nm. In spite of the low excitation voltage, the substrate was also partly excited. YAG and LuAG substrates exhibit significant host emission in the UV spectral range between 250 and 400 nm. The host emission comes from the structural defects, viz. antisite defects Lu_{Al} and Y_{Al}, where several percent of Lu or Y are placed in the Al octahedral sites. The host emission of the GGG substrate is negligible due to the quenching effect of the Gd sublattice.

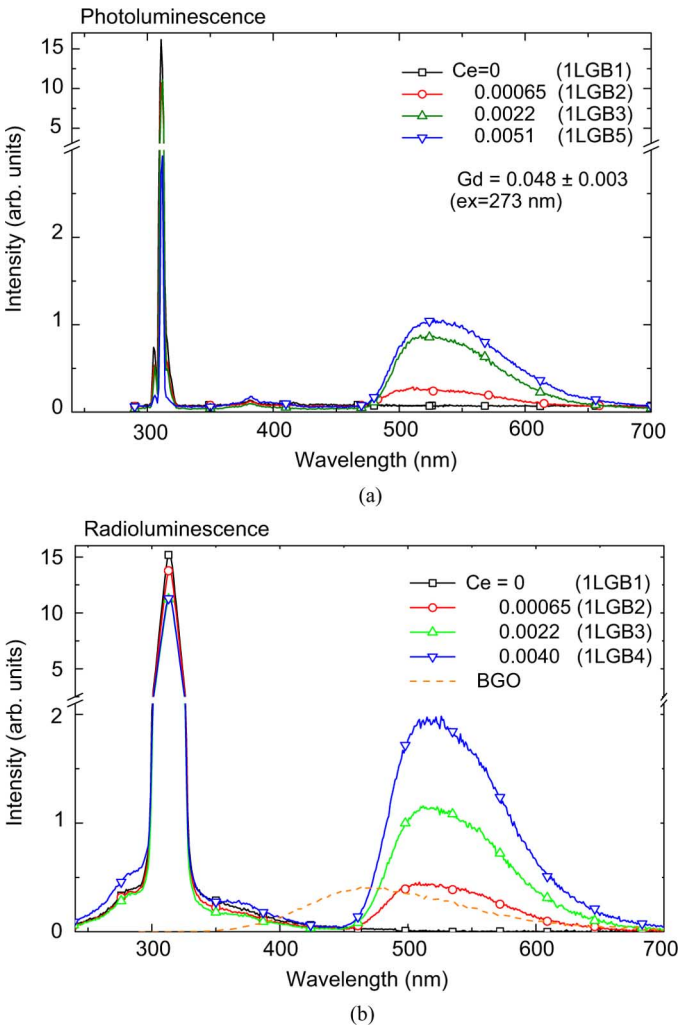

Fig. 4. (a) The PL spectra excited at 273 nm and (b) X-ray excited RL spectra of $(GdLu)_3Al_5O_{12}$:Ce epitaxial films grown on an LuAG substrate with variable Ce concentration (shown in the plot) and approximately constant Gd concentration, $4.8 \pm 0.3\%$. The PL and RL were measured with apparatus spectral resolution of 0.5 and 16 nm, respectively (i.e., the width of Gd emission in the RL spectra is significantly broadened).

In Fig. 4(a) and (b), the PL and RL spectra of GdLuAG:Ce samples (the same set of samples as that in Fig. 3) are displayed. The RL spectra were measured along with the reference BGO ($Bi_4Ge_3O_{12}$) single crystal and the spectra are mutually comparable in an absolute way. The samples have almost constant Gd content and variable Ce content as those shown in Fig. 3. We note that the RL was measured with a low spectral resolution of 16 nm, and thus the linewidth of the Gd emission at 312 nm in Fig. 4(b) is markedly overestimated (cf. with sharp 312 nm emission in the PL spectra).

The most striking feature of the PL spectra, which were excited at $^6I_J(Gd^{3+})$ multiplet, and the RL spectra in Fig. 4 is their very similar spectral development. Furthermore, the Ce^{3+} emission also appeared in the PL spectra—in other words, if Gd^{3+} ions are excited selectively, Ce^{3+} emission also appears. This suggests the above-mentioned ET from Gd^{3+} to Ce^{3+}, as discussed in detailed in[19]. However, the mutual comparison of relative amplitudes in the spectra in Fig. 4(a) and (b) indicates significantly higher participation of Ce-related emission in the RL spectra compared with the PL ones. We note that the weak emission peak at 380 nm observed in Fig. 4(a) of the PL spectra comes likely from an accidental Tb impurity ($^5D_3$–^7F_J transition) from the chemicals.

Nonetheless, it is evident that Gd^{3+} is a very efficient emission center, especially at the low concentrations used here. At increasing Ce content, however, the Gd emission gradually decreases, which is most striking especially in the PL spectra. This supports observation in the PL Gd^{3+} decay in Fig. 3.

In conclusion of this section, at low Gd doping, two virtually independent emission channels are observed, viz. the slow Gd^{3+} at 312 nm and fast Ce^{3+} around 520 nm. With increasing concentration of Ce^{3+} ions, the Gd^{3+} emission is markedly quenched due to the energy transfer from Gd^{3+} to Ce^{3+} ions.

D. Properties of GdLuAG/GdYAG:Ce Garnets at High Gd Doping

In heavily doped Gd multicomponent garnets, we explore in detail the effect of Gd concentration on the following:

— ^6P_J–$^8S_{7/2}(Gd^{3+})$ emission (and Gd concentration quenching);
— 5d–4f (Ce^{3+}) emission;
— scintillation properties.

First, we have to provide information concerning composition of studied multicomponent garnets: the GdAG garnet is thermodynamically unstable, and it does not exist as a single crystal. In order to stabilize the garnet structure, a part of Al atoms ($r_{VI} = 0.535$ Å-ionic radius in octahedral site [21]) should be replaced by those with larger ionic radius, such as Ga ($r_{VI} = 0.62$ Å) or Sc ($r_{VI} = 0.74$ Å) and the like, or a part of Gd ($r_{VIII} = 1.053$ Å) atoms in dodecahedral sites by those with smaller radius, such as Y ($r_{VIII} = 1.019$ Å) or Lu ($r_{VIII} = 0.977$ Å). Therefore, the samples here studied which have higher Gd content usually contain also Ga atoms, which are substituted for Al in tetrahedral and octahedral sites. We shall show in this work that Ga^{3+} ions have not any fundamental effect on emission and scintillation properties of the studied epitaxial films.

In Fig. 5(a)–(c), the decay curves of GdLuAG:Ce samples with varying Gd content are shown. Significant concentration quenching is observed: the ^6P_J–$^8S_{7/2}(Gd^{3+})$ decay time decreases from $\sim$ 6 ms at low Gd concentrations to submilisecond values above 15% of Gd. In Fig. 5(d), the main Gd decay component is shown as a function of Gd concentration. The Gd emission is almost completely quenched above $\sim 50\%$ of Gd in the dodecahedral sites [cf. also Fig. 7(b)]. Furthermore, the decays are multiexponential at higher Gd content indicating significant energy transfer away from the Gd sublattice. As we shall see below, the excitation energy captured by the Gd^{3+} ions is not lost but is effectively transferred to the Ce^{3+} centers.

On the other hand, the $5d_1$–$4f(Ce^{3+})$ decays are almost uninfluenced by the presence of Gd ions when directly excited into $5d_{1,2}$ states. As an example, in Fig. 6, the decay curves for a series of GdGaYAG:Ce samples with various Gd and Ga doping are shown. The decays were measured at $\lambda_{em} = 520$ nm under excitation in the $5d_2$ state of Ce^{3+} (339 nm). The decays are strictly single-exponential with decay time $\tau = 61$ ns, which is typical in aluminum garnet structures and corresponds exactly

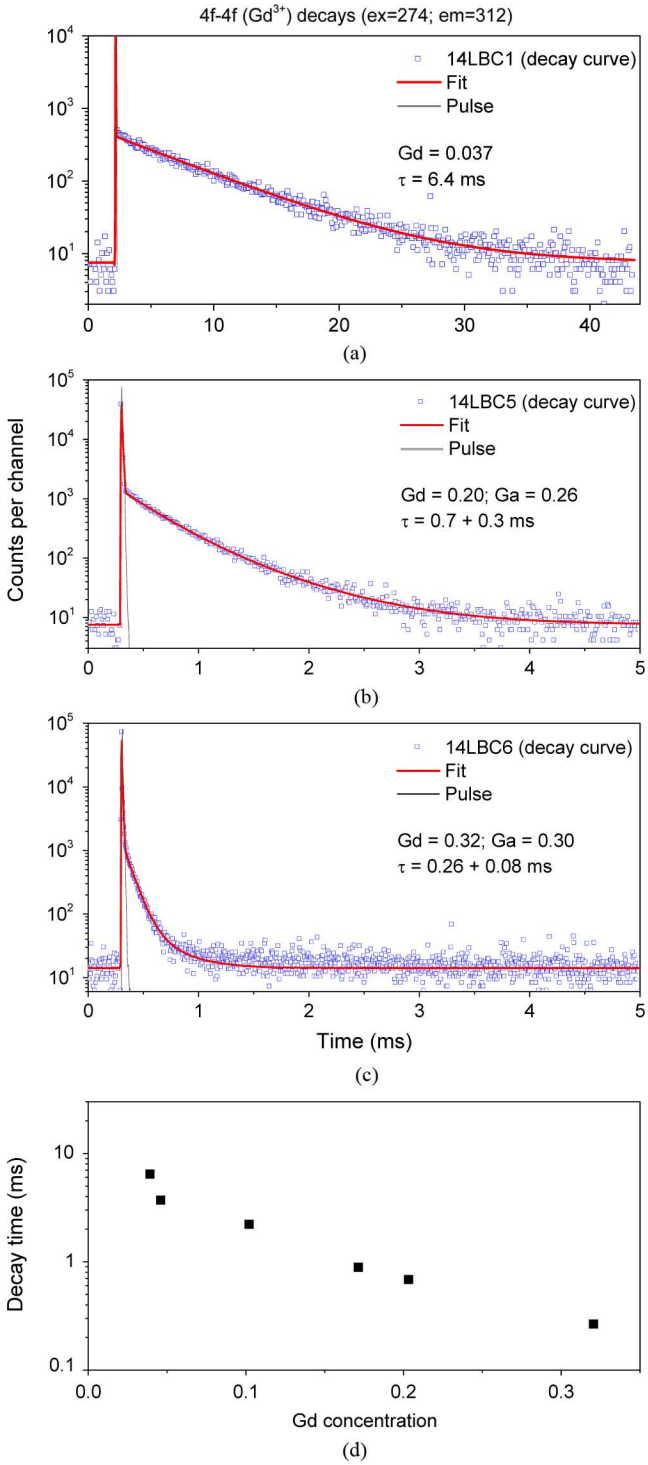

Fig. 5. (a)–(c) The 4f–4f (Gd^{3+}) decay curves of ^6P_J–$^8S_{7/2}$ emission measured at $\lambda_{cm} = 312$ nm and $\lambda_{ex} = 312$ nm in $(GdLuY)_3(AlGa)_5O_{12}$:Ce samples; the solid lines are convolution of instrumental response (pulse) with the decay function. Composition and decay times are shown in the legend. (d) Dependence of the main decay time on Gd concentration.

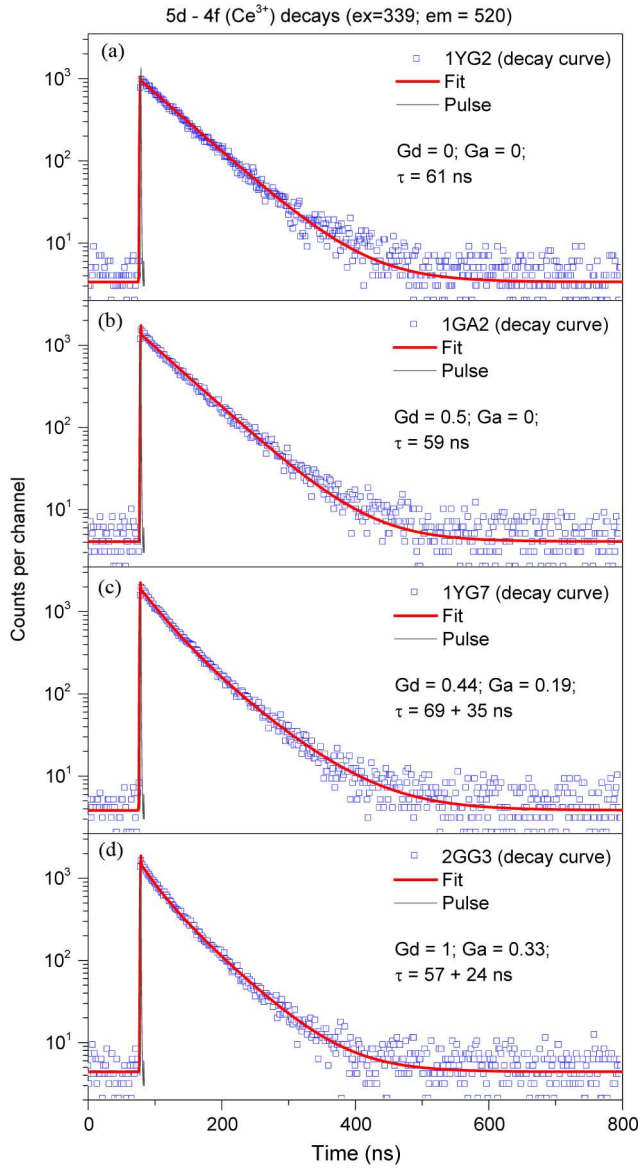

Fig. 6. The 5d–4f (Ce^{3+}) decays in $(GdY)_3(AlGa)_5O_{12}$:Ce samples and the effect of Gd and Ga substitution on the Ce^{3+} decay times. The decays were monitored at 520 nm and excited at 339 nm (5d2, Ce^{3+}). The solid lines are convolution of instrumental response (pulse) with the decay function. Concentrations of Gd and Ga and decay times are shown in the legend.

to the value observed pure YAG:Ce single crystals. The Gd substitution does not markedly affect the 5d(Ce) decay and negligible acceleration of Ce^{3+} decay to $\tau = 59$ ns was observed in highly concentrated $(Gd_{0.5}Y_{0.5})_3Al_5O_{12}$:Ce sample with Gd content of 50%. These observations give further support to our hypothesis that excitation energy, which is migrating over the Gd sublattice, is effectively transferred to the Ce^{3+} ions.

Recently, the Ga substitution for Al was adopted for eliminating the negative effects of shallow electron traps in garnet single crystals grown from the melt [12], [13]. Due to the admixture of 4s(Ga) states to the bottom of the conduction band, the band gap decreases, and the shallow traps are buried into the conduction band and thus effectively reduce the slow component in the scintillation response originating from these traps.

In order to verify this hypothesis in epitaxial garnet films several sets of Gd-Ga substituted YAG/LuAG:Ce samples were grown with various mutual concentrations of Ga and Gd. The concentration of Ga was varied in the range from 10 up to 75%. In samples with Ga content higher than 75%, the emission from

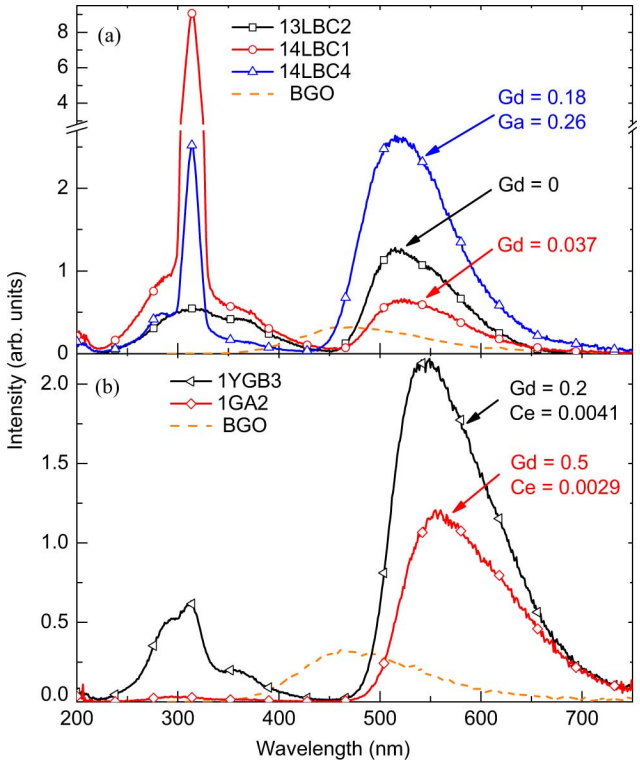

Fig. 7. X-ray excited radioluminesce spectra of $(GdLuY)_3(AlGa)_5O_{12}$:Ce. (a) Samples with low Gd concentration, $< 20\%$. (b) samples with high Gd concentration. The RL of BGO crystal is shown for comparison; note the change in y-axis scale in (a).

the Ce^{3+} centers was completely quenched (due to reduced band gap and consequent photoionization of 5d states).

In Fig. 6(c)–(d), the decay curves typical for of Ga substituted GdYAG:Ce samples are shown. The curves exhibit some deviation from the single-exponential decay: besides the main ~ 60 ns decay component also shorter one appears, which may point to some parasitic ET away from $5d_1$ level of Ce^{3+}. At low and medium Ga concentrations, $(Ga < 0.25)$, we did not observe any notable negative effect of the Ga admixture neither in the RL nor in the photoelectron yield. On other hand, any clear positive effect of Ga doping on the scintillation response was not also observed in the epitaxial films in contrast to single crystals. The most probable explanation is that the traps in the epitaxial films have different origin than in bulk single crystals. Namely, the number of antisite defects is considerably reduced in epitaxial films [22] due to much lower growth temperature of films. However, the new structural defects in films can be induced, owing to the growth on substrates with large lattice mismatch. The lattice constant of heavily Gd-Ga substituted films fits just in the middle of lattice parameters of available substrates, YAG (12.008 Å) and GGG (12.383 Å), and the mismatch amounts up to 2%. In order to explore the effect of Ga doping in more detail, new substrates with better lattice match are required.

E. Scintillation Properties

As we have seen above, at low Gd doping (i.e., when the distance between Ce and Gd ions is large), the emission is distributed between two independent Gd^{3+} and Ce^{3+} emitters, while at higher Gd content, the Gd^{3+} emission disappears due to concentration quenching.

In this section, we present the results of the measurements of the X-ray excited RL (steady state experiment) and the photoelectron yield (PhY). In the PhY experiments, the samples were excited by the alpha particles and measured at the shaping times between 0.5 and 10 μs. The aim of these experiments is to explore in detail the effect of Gd concentration on the Ce^{3+} related scintillation properties in the GdYAG/GdLuAG:Ce samples.

In Fig. 7, the RL spectra of samples with low and high Gd content are shown. The black curve in Fig. 7(a) represents the reference Gd-free LuAG:Ce sample. In this sample, two broad emission bands are observed—the first one centered at ~ 510 nm comes from Ce^{3+} $(5d \rightarrow 4f)$ centers, and the second one in the UV range between 250 and 400 nm comes from the host emission (most likely due to the exciton trapped on a structural defect). We note that the X-rays partly penetrate through the film into the substrate and thus the substrate also partially contributes to the host emission in the UV range.

Doping of the film with $\sim 4\%$ of Gd has a dramatic effect on the RL spectra. The Gd^{3+} 4f–4f emission line with maximum near 312 nm [red curve in Fig. 7(a)] appears, and simultaneously the intensity of the Ce^{3+} emission in the green–yellow spectral range is significantly reduced by a factor of ~ 2. The total integrated emission from the sample, however, stays roughly unchanged. These results support those in the PL spectra—the emission is divided between two centers, Ce^{3+} and Gd^{3+}.

At increasing Gd content to $\sim 20\%$ [the blue curve in Fig. 7(a)], we see very interesting behavior: the Ce^{3+} emission intensity considerably increases even above the value of the original Gd-undoped sample. Simultaneously, the Gd^{3+} related emission at 312 nm begins to be quenched. The integral RL intensity of the last sample is significantly higher. This confirms observations in the PL that the Gd substitution increases the green–yellow emission from the Ce^{3+} centers and supports the above presented concept that the energy captured by Gd sublattice is not lost but is transferred to Ce^{3+} ions.

In Fig. 7(b), the RL spectra of samples with higher Gd content are displayed. The Gd peak at 312 nm is considerably reduced, and at the Gd concentration of about of 50%, the Gd peak disappears completely. The beneficial effect of high Gd content is also almost complete quenching of the host emission in the UV spectral range. Since the host emission is associated with the delayed emission, the scintillation properties of such heavily Gd doped samples are expected to be improved.

Integration of the RL spectra makes it possible to assess the relative impact of the Ce-related emission to the total emission intensity over the UV-VIS spectral ranges. The result is shown in Fig. 8. The observed dependence supports the conclusions presented above.

The results obtained in steady state PL and RL measurements are fully supported by the photoelectron yield measurements. The PhY and energy resolution were determined by the pulse height spectroscopy of scintillation response described elsewhere [18]. The results, represented by the number of photoelectrons per MeV for shaping times 0.5–10 μs, are shown in Fig. 9. The alpha particles from ^{239}Pu radioactive source (5.157 MeV) were used. We note that PhY does not

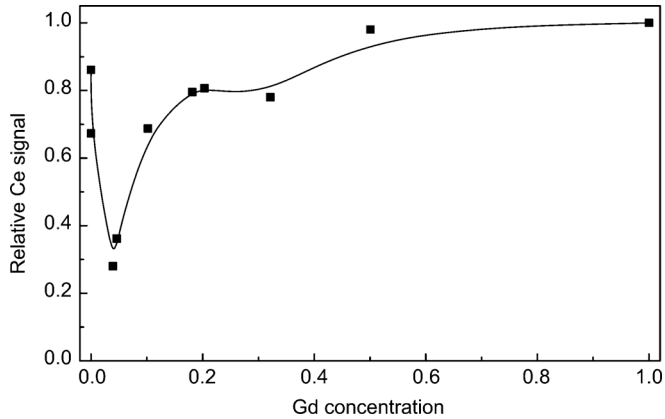

Fig. 8. Relative integrated Ce^{3+} contribution in the RL signal as a function of Gd concentration in of $(GdLuY)_3(AlGa)_5O_{12}$:Ce samples. The solid line is only guide for the naked eye.

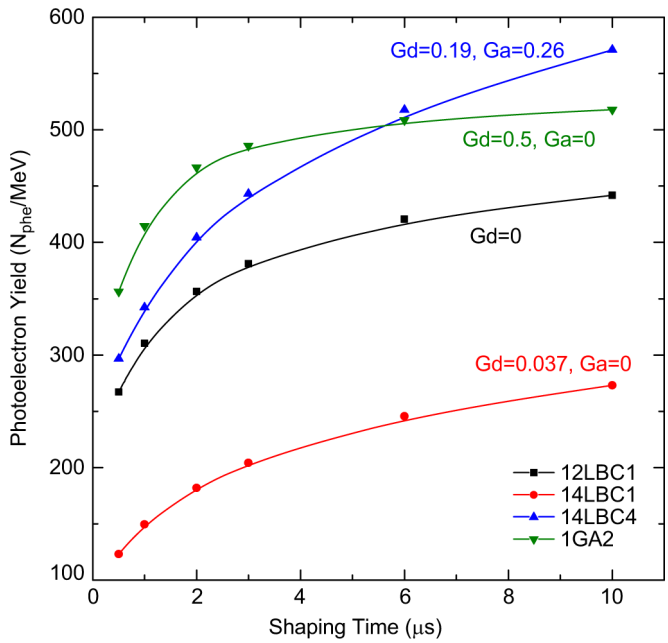

Fig. 9. Dependence of the photoelectron yield of $(GdLuY)_3(AlGa)_5O_{12}$:Ce samples on the shaping time. The PhY was measured under alpha particles excitation using radioactive source ^{239}Pu (5.157 MeV). The solid lines are normalized fits using [24, eq. (10)]. Concentrations of Gd and Ga are shown in the legend; see text for details.

probe contribution from the Gd^{3+} center due to its millisecond time response. Detailed analysis of the PhY, the role of fast and slow components, and energy resolution measured in Gd-Ga co-doped epitaxial films were published elsewhere [23]. Here, we present results concerning the role of the Gd concentration on scintillation response of the films.

The black curve in Fig. 9 represents the Gd-free LuAG:Ce sample. It is evident that slow components in the PhY play an important role; see [23] and [24]. Doping the film with $\sim 4\%$ of Gd considerably decreases the PhY (red curve in Fig. 9) at all shaping times—the number of detected photoelectrons decreased by a factor of ~ 2. On the contrary, a subsequent increase of the Gd concentration in samples to $\sim 20\%$ resulted in increase of the PhY signal (blue curve) significantly above that of Gd-free sample. However, the ratio of slow and fast components in the PhY remains more or less unchanged. Considerable improvement of scintillation properties was observed in sample $(Gd_{0.5}Y_{0.5})Al_5O_{12}$:Ce with 50% of Gd (green curve in Fig. 9). It is evident that the fast component within 1 μs shaping time increased markedly in this sample at the expense of slow components. This sample also exhibited the best energy resolution of 8%; for details, see [23]. The results of PhY measurements fully support presumptions formulated above and based on the RL and PL experiments.

IV. Conclusion

Summarizing the results, the non-radiative energy transfer from donor Gd^{3+} to activator Ce^{3+} ions was observed in Ce, Gd co-doped yttrium and lutetium aluminum garnets, GdYAG/GdLuAG:Ce. Because of a minor overlap of ^6P–$^8S(Gd^{3+})$ emission peak and ^2F_J–$5d_2(Ce^{3+})$ absorption spectral band, the transfer is presumably further mediated by lattice phonons. The ET is effective also at large Ce–Gd interionic distances. Doping of YAG/LuAG:Ce with several percent of Gd^{3+} ions leads to a considerable decrease by a factor of ~ 2 of both steady state RL intensity and scintillation response (photoelectron yield) compared with Gd-free YAG/LuAG:Ce samples. Namely, at low Gd content, the excitation energy is shared by two virtually independent and competing emission centers, Ce^{3+} and Gd^{3+}. At increasing Gd doping, the Ce^{3+} centers retrieve the intensity and the Gd^{3+} emission decreases and at Gd concentrations of $\sim 50\%$ and above, the Gd^{3+} emission is quenched. However, the excitation energy is not lost but it is effectively transferred from donor Gd^{3+} to acceptor Ce^{3+} ions. Another positive effect of high Gd substitution is complete suppression of slow emission of the garnet host in the UV spectral range between 250 and 400 nm, which comes usually from the structural defects. As a result, heavily Gd-doped GdYAG/GdLuAG:Ce epitaxial films have better scintillation performance, higher photoelectron yield, and superior energy resolution (under alpha particle excitation). Likewise, the fast component (within 1 μs shaping time) of the photoelectron yield was significantly higher compared to Gd-free samples. Furthermore, the 5d–4f (Ce^{3+}) PL decay was independent on the Gd concentration, and its decay time value was in the range 52–54 ns and 59–61 ns in GdLuAG:Ce and GdYAG:Ce, respectively. As an example, in $(Gd_{0.5}Y_{0.5})_3Al_5O_{12}$ sample more than 98% of the RL signal comes from the 5d–4f emission of Ce^{3+} ions, and energy resolution was 8%. These values indicate very efficient energy transport towards Ce^{3+} ions. We note that in contrast to melt-grown single crystals, no role of Ga substitution was found in epitaxial films, likely due to different origin of electron traps in films compared to single crystals.

References

[1] C. W. E. v. Eijk, "Inorganic-scintillator development," *Nucl. Instrum. Methods Phys. Res. A*, vol. 460, pp. 1–14, Mar. 2001.
[2] M. Nikl, "Scintillation detectors for X-rays," *Meas. Sci. Technol.*, vol. 17, pp. R37–R54, Apr. 2006.
[3] M. Nikl, A. Yoshikawa, K. Kamada, K. Nejezchleb, C. R. Stanek, J. A. Mares, and K. Blazek, "Develop. of LuAg-based scintillator crystals-a review," *Prog. Cryst. Growth Charact. Mater.*, vol. 59, pp. 47–72, 2013.

[4] W. Chewpraditkul, L. Swiderski, M. Moszynski, T. Szczesniak, A. Syntfeld-Kazuch, C. Wanarak, and P. Limsuwan, "Comparative studies of $Lu_3Al_5O_{12}$:Ce and $Y_3Al_5O_{12}$:Ce scintillators for gamma-ray detection," *Phys. Status Solidi A*, vol. 206, pp. 2599–2605, Nov. 2009.

[5] S. Ye, F. Xiao, Y. X. Pan, Y. Y. Ma, and Q. Y. Zhang, "Phosphors in phosphor-converted white light-emitting diodes recent advances in materials, techniques and properties," *Mater. Sci. Eng. R-Rep.*, vol. 71, pp. 1–34, Dec. 2010.

[6] A. G. Petrosyan, K. L. Ovanesyan, R. V. Sargsyan, G. O. Shirinyan, D. Abler, E. Auffray, P. Lecoq, C. Dujardin, and C. Pedrini, "Bridgman growth and site occupation in LuAg:Ce scintillator crystals," *J. Cryst. Growth*, vol. 312, pp. 3136–3142, Oct. 2010.

[7] C. W. E. v. Eijk, "Inorganic scintillators in medical imaging," *Phys. Med. Biol.*, vol. 47, pp. R85–R106, Apr. 2002.

[8] M. Nikl, A. Vedda, M. Fasoli, I. Fontana, V. V. Laguta, E. Mihokova, J. Pejchal, J. Rosa, and K. Nejezchleb, "Shallow traps and radiative recombination processes in $Lu_3Al_5O_{12}$:Ce single crystal scintillator," *Phys. Rev. B*, vol. 76, Nov. 2007.

[9] A. Yoshikawa, K. Kamada, F. Saito, H. Ogino, M. Itoh, T. Katagiri, D. Iri, and M. Fujita, "Energy transfer to Pr^{3+} ions in Pr:$Lu_3Al_5O_{12}$ (LuAG) single crystals," *IEEE Trans. Nucl. Sci.*, vol. 55, pp. 1372–1375, Jun. 2008.

[10] W. Drozdowski, P. Dorenbos, R. Drozdowska, A. J. J. Bos, N. R. J. Poolton, M. Tonelli, and M. Alshourbagy, "Effect of electron traps on scintillation of praseodymium activated $Lu_3Al_5O_{12}$," *IEEE Trans. Nucl. Sci.*, vol. 56, pp. 320–327, Feb. 2009.

[11] N. J. Cherepy, J. D. Kuntz, Z. M. Seeley, S. E. Fisher, O. B. Drury, B. W. Sturm, T. A. Hurst, R. D. Sanner, J. J. Roberts, and S. A. Payne, "Transparent ceramic scintillators for gamma spectroscopy and radiography," in *Proc. SPIE*, 2010, vol. 7805, pp. 780501–780501.

[12] K. Kamada, T. Endo, K. Tsutumi, T. Yanagida, Y. Fujimoto, A. Fukabori, A. Yoshikawa, J. Pejchal, and M. Nikl, "Composition engineering in cerium-doped $(Lu,Gd)_3(Ga,Al)_5O_{12}$ single-crystal scintillators," *Cryst. Growth Design*, vol. 11, pp. 4484–4490, 2011.

[13] M. Fasoli, A. Vedda, M. Nikl, C. Jiang, B. P. Uberuaga, D. A. Andersson, K. J. McClellan, and C. R. Stanek, "Band-gap eng.for removing shallow traps in rare-earth $Lu_3Al_5O_{12}$ garnet scintillators using Ga^{3+} doping," *Phys. Rev. B*, vol. 84, pp. 081102(R)–081102(R), 2011.

[14] J. L. Wu, G. Gundiah, and A. K. Cheetham, "Structure-property correlations in Ce-doped garnet phosphors for use in solid state lighting," *Chem. Phys. Lett.*, vol. 441, pp. 250–254, 2007.

[15] K. Kamada, T. Yanagida, T. Endo, K. Tsutumi, Y. Usuki, M. Nikl, Y. Fujimoto, A. Fukabori, and A. Yoshikawa, "2 inch diameter single crystal growth and scintillation properties of Ce:$Gd_3Al_2Ga_3O_{12}$," *J. Cryst. Growth*, vol. 352, pp. 88–90, Aug. 2012.

[16] M. Kucera, K. Nitsch, M. Kubova, N. Solovieva, M. Nikl, and J. A. Mares, "Ce-doped YAG and LuAG epitaxial films for scintillation detectors," *IEEE Trans. Nucl. Sci.*, vol. 55, pp. 1201–1205, Jun. 2008.

[17] M. Kucera, K. Nitsch, M. Nikl, M. Hanus, and S. Danis, "Growth and characterization of YAG and LuAG epitaxial films for scintillation applications," *J. Cryst. Growth*, vol. 312, pp. 1538–1545, Apr. 2010.

[18] J. A. Mares, P. Prusa, M. Nikl, K. Nitsch, A. Beitlerova, M. Kucera, M. Hanus, and Y. Zorenko, "Ce^{3+} -doped crystalline garnet films-scintillation characterization using alpha-particle excitation," *Adiation Meas.*, vol. 45, pp. 369–371, Mar.–Jul. 2010.

[19] M. Kucera, M. Nikl, M. Hanus, and Z. Onderisinova, "Gd^{3+} to Ce^{3+} energy transfer in multi-component GdLuAg and GdYAG garnet scintillators ," *Phys. Status Solidi RRL*, vol. 7, pp. 571–574, 2013.

[20] G. Blasse and B. C. Grabmaier, *Luminescent Materials*. Berlin, Germany: Springer-Verlag, 1994.

[21] R. D. Shannon, "Revised effective ionic radii and systematic studies of interatomic distances in halides and chalcogenides," *Acta Cryst. A*, vol. 32, pp. 751–767, 1976.

[22] M. Nikl, E. Mihokova, J. Pejchal, A. Vedda, Y. Zorenko, and K. Nejezchleb, "The antisite Lu-Al defect-related trap in $Lu_3Al_5O_{12}$:Ce single crystal," *Phys. Stat. Sol. B*, vol. 242, pp. R119–R121, Nov. 2005.

[23] P. Prusa, M. Kucera, M. Hanus, J. A. Mares, A. Beitlerova, Z. Onderisinova, and M. Nikl, "Scintillation properties of the Ce-doped multicomponent garnet epitaxial films," *Opt. Mater.*, vol. 35, pp. 2444–2448, Oct. 2013.

[24] P. Prusa, M. Nikl, J. A. Mares, M. Kucera, K. Nitsch, and A. Beitlerova, "The alpha-particle excited scintillation response of YAG:Ce thin films grown by liquid phase epitaxy," *Phys. Status Solidi A*, vol. 206, pp. 1494–1500, Jul. 2009.

Optical Materials 35 (2013) 2444–2448

Contents lists available at SciVerse ScienceDirect

Optical Materials

journal homepage: www.elsevier.com/locate/optmat

Scintillation properties of the Ce-doped multicomponent garnet epitaxial films

P. Prusa [a,b,*], M. Kucera [c], J.A. Mares [a], M. Hanus [c], A. Beitlerova [a], Z. Onderisinova [c], M. Nikl [a]

[a] Institute of Physics AS CR, Cukrovarnicka 10, 16253 Prague, Czech Republic
[b] Czech Technical University in Prague, Faculty of Nuclear Sciences and Physical Engineering, Brehova 7, 11519 Prague 1, Czech Republic
[c] Charles University, Faculty of Mathematics and Physics, Ke Karlovu 5, 12116 Prague 2, Czech Republic

ARTICLE INFO

Article history:
Received 28 May 2013
Received in revised form 26 June 2013
Accepted 28 June 2013
Available online 19 July 2013

Keywords:
Scintillator
Liquid phase epitaxy method
Photoelectron yield
Garnet
Ce^{3+}

ABSTRACT

$(Lu,Y,Gd)_3(Al,Ga)_5O_{12}$:Ce garnet scintillator single crystalline films were grown onto LuAG, YAG and GGG substrates by liquid phase epitaxy method. Absorption, radioluminescence spectra and photoluminescence excitation, emission spectra, and decay kinetics were measured. Photoelectron yield, its dependence on amplifier shaping time and energy resolution were determined to evaluate scintillation performance. Most of the samples exhibited strong UV emission caused by trapped excitons and/or Gd^{3+} 4f–4f transition. However, emission spectrum of the best performing $Gd_2YAl_5O_{12}$:Ce is dominated by the Ce^{3+} fast 5d–4f luminescence. This sample has outperformed photoelectron yield of all the garnet films studied so far.

1. Introduction

$Lu_3Al_5O_{12}$:Ce (LuAG:Ce) and some other Ce- or Pr-doped garnets represent interesting fast scintillation materials with excellent performance. They are chemically stable, non-hygroscopic and have excellent mechanical and optical properties [1–3]. Additionally, LuAG:Ce offers high detection efficiency for high energy photon radiation due to its high effective atomic number. These materials in bulk form are considered for various applications in high energy physics, medicine, industry and security fields [3,4]. Moreover, thin scintillation screens based on LuAG:Ce or YAG:Ce have been reported for microradiography imaging [5,6] or diagnostics of synchrotron or other radiation or particle beams [7].

Nowadays, garnet scintillation screens are usually fabricated from bulk crystals by cutting and polishing down to thickness of a few tens of μm [8]. Quality of these screens is very high, however, their cost is high as well and minimum thickness is of about 5 μm. To lower the production costs and improve 2D-resolution, the thin monocrystalline films prepared by liquid phase epitaxy (LPE) method could be an alternative [9–11]. LPE offers an easy possibility to prepare films only several μm thick, which can further improve the 2D-resolution in the images. The film is grown on the substrate, which may be produced from cheaper materials with lower purity grade. Additionally, it is possible to apply heteroepitaxial growth, i.e. to prepare LuAG:Ce film on undoped YAG substrate [9,11,12], thus avoiding the usage of more expensive Lu_2O_3 raw material. Finally, production of phoswich detectors with variously doped substrate and film can allow to resolve e.g. alpha particles and hard X- or gamma radiation in mixed beams [9,13].

The epitaxial growth may bring yet another advantage. Performance of bulk LuAG:Ce crystals grown from melt is negatively affected by shallow electron traps, usually attributed to Lu_{Al} antisite defects [14,15]. In LuAG bulk crystals, the antisite defects arise due to high temperature in the melt growth techniques (Czochralski or Bridgman methods), and presence of two cations of equal trivalent charge. Presence of antisite defects leads to creation of shallow electron traps, intensification of slow scintillation components, decrease of light yield and possibly also to worsening of energy resolution [16,17]. Epitaxial garnet films are prepared at temperatures almost 1000 K lower so that the antisite defects are not formed.

On the other hand, epitaxial films are contaminated by the ions coming from the used flux. Films grown from the PbO-based flux contains Pb^{2+} ions, which act as quenching centers at room temperatures [18]. Optimization of growth conditions can diminish the Pb^{2+} content, but it cannot be removed completely. In the BaO-based flux, there is no contaminant negatively affecting scintillation properties [12,19]. However, high viscosity of this flux leads to production of pits and other structural defects in the film. Light yield is not severely affected, but intense slow scintillation

* Corresponding author at: Institute of Physics AS CR, Cukrovarnicka 10, 16253 Prague, Czech Republic. Tel.: +420 604 958 601.
E-mail address: petr.prusa@fjfi.cvut.cz (P. Prusa).

0925-3467/$ - see front matter © 2013 Elsevier B.V. All rights reserved.
http://dx.doi.org/10.1016/j.optmat.2013.06.051

response component does exist. Slow scintillation is most probably caused by trapping of charge carriers in shallow traps related to unspecified structural defects.

Recently, the "band-gap engineering" strategy was adopted to reduce or even eliminate the shallow traps in bulk crystals grown from the melt [20–23]. Using the Ga admixture, it is possible to lower the bottom of conduction band of LuAG. Although the antisite defects remain in the material, related trap levels become buried in the conduction band. This approach strongly suppresses trapping effects which degrade the scintillation response. On the other hand, reduced gap between the bottom of conduction band and $5d_1$ excited state of Ce luminescent center moves the onset of undesired ionization to lower temperatures. However, this gap can be enlarged by the Gd admixture.

Several recent studies report much better scintillation properties of multicomponent $(Lu,Y,Gd)_3(Al,Ga)_5O_{12}$:Ce single crystals or ceramics in comparison with LuAG:Ce or YAG:Ce counterparts [22–25]. Very high light yield approaching 50 kPh/MeV [24,26], excellent energy resolution and suppressed slower scintillation component were observed. Properly balanced Gd&Ga admixture may have positive effect on scintillation properties of the epitaxial garnet films as well, even though the traps origin is different.

This paper is focused on the optimization of LuAG:Ce epitaxial films grown from BaO- and PbO-based fluxes. Additionally, we present preliminary results of scintillation properties measurement of epitaxial garnet films with the Gd and Ga admixture.

2. Experiments and methods

Several Ce^{3+} doped epitaxial garnet films were grown by the isothermal dipping LPE method onto undoped LuAG, YAG, and GGG ($Gd_3Ga_5O_{12}$) substrates of (111) and (100) crystallographic orientations using the $BaO–B_2O_3–BaF_2$ flux (further denoted as BaO-flux) or $PbO–B_2O_3$ flux (further denoted as PbO-flux). Nine samples were chosen for further characterization: first batch consisting of two LuYAG:Ce samples with no Gd, Ga admixture (samples LY1,2), second batch with five samples containing Lu, Y, Gd, Ga altogether (samples LGYG2-5 and LGY1), one sample $Gd_3(Al, Ga)_5O_{12}$:Ce (GG1), and finally one sample $(Gd,Y)_3Al_5O_{12}$ (GY1).

The substrate rotation was 120 rpm, the rotation direction changed every 4 s. The growth temperatures were between 960 and 1070 °C, supersaturation 10–40 K. Starting raw materials of 5 N purity were used. Resulting film thicknesses determined by weighing were in the range from 7 to 44 μm. Substrate material, its crystalographic orientation, film composition, and film thicknesses are presented in Table 1.

Absorption spectra, photoluminescence excitation and emission spectra, radioluminescence spectra, and photoluminescence decay curves were measured for all of the samples. Absorption and photoluminescence spectra were measured using commercial spectrometers Specord 250 and Horiba JY Fluoromax 3. Radioluminescence spectra and photoluminescence decays were measured at custom made spectrofluorometer 5000M, Horiba Jobin Yvon using an X-ray tube (10 kV, 50 mA) and nanoLED pulse excitation sources, respectively. The crystallographic properties and lattice parameters of the films were studied using XRD on PANalytical X-ray high-resolution diffractometer, composition was determined by electron beam microanalysis.

Photoelectron yield, slow component relative intensity and energy resolution were determined by pulse height spectroscopy of scintillation response [27]. Alpha particles from ^{239}Pu radioactive source (5.157 MeV) were used for excitation, since it is necessary that entire energy of most of the particles is deposited in epitaxial film which is only a few tens of μm thick.

Light yield was not calculated from photoelectron yield, because it is not possible to determine the light collection efficiency for our geometry of measurement. Since alpha particle penetration range is very small, radioisotope must be positioned directly onto the LPE film and any reflector utilization is impossible. Using a silicon grease, the sample is optically coupled from the other side to a hybrid photomultiplier (HPMT) [28] model DEP PPO 475B. Signal from HPMT is processed by spectroscopy amplifier ORTEC model 672 and multichannel buffer ORTEC 927TM. Pulse-height spectrum is displayed on PC. All measurements were performed at room temperature. Energy resolution and photoelectron yield was obtained using Gaussian fit of peaks in the spectra.

Measured photoelectron yield depends on the amplifier shaping time. If longer shaping time is used, more photons can contribute to the response and signal amplitude is rising. Amplifier model 672 enables shaping times of 0.5, 1, 2, 3, 6 and 10 μs (semi-Gaussian shaping). Obviously, the response increase is significant only for the samples with intense slow scintillation decay component in the range of microseconds. The components of significantly longer decay times do not contribute to the signal significantly. If a double-exponential decay approximation with fast component decay time of a few tens of ns is considered, light yield time dependence can be approximated by function $LY(t) = m_1 - m_2\exp(-m_3t)$, where m_i are parameters obtained by a fit. We have shown in an earlier paper [19] how these parameters can be used for calculation of the relative intensity of the fast fraction of the response $K_{f/e} = 1 - (m_2/m_1)$.

3. Results and discussion

All samples exhibited very similar absorption spectra with two intense peaks attributed to $4f–5d_{1,2}$ Ce^{3+} transitions at about 450 nm and 340 nm, respectively, see Fig. 1. The excitation within the dominating 445 nm absorption peak was used for the emission spectra measurement. All photoluminescence spectra show the $5d_1–4f$ Ce^{3+} transition with maximum around 530 nm, see Fig. 2, the position of which slightly fluctuates with the film composition. Excitation spectra for the Ce^{3+} emission are close to the absorption spectra, see Fig. 2, with some differences in the UV region below 250 nm, most probably due to competing parasitic absorption centers.

Table 1
Film compositions determined by EPMA, thicknesses, used fluxes, and substrate composition with its crystallographic orientation.

Sample	Substrate	Crystal orientation	Flux	Thickness (μm)	Composition
LY1	LuAG	111	BaO	12.3	$Lu_3Al_5O_{12}$:Ce
LY2	LuAG	111	BaO	19.7	$Lu_{2.43}Y_{0.57}Al_5O_{12}$:Ce
LGY1	LuAG	111	BaO	10.4	$Lu_{2.35}Y_{0.44}Gd_{0.12}Al_{5.06}O_{12}$:Ce
LGYG2	YAG	111	BaO	15.9	$Lu_{2.02}Y_{0.38}Gd_{0.55}Al_{3.74}Ga_{1.31}O_{12}$:Ce
LGYG3	YAG	111	BaO	17.0	$Lu_{1.98}Y_{0.37}Gd_{0.61}Al_{3.73}Ga_{1.31}O_{12}$:Ce
LGYG4	YAG	111	BaO	9.3	$Lu_{1.66}Y_{0.38}Gd_{0.96}Al_{3.48}Ga_{1.51}O_{12}$:Ce
LGYG5	YAG	111	BaO	7.0	$Lu_{1.45}Y_{0.42}Gd_{0.96}Al_{3.68}Ga_{1.48}O_{12}$:Ce
GG1	GGG	100	PbO	10.5	$Gd_{2.97}Ga_{1.19}Al_{3.83}O_{12}$:Ce
GY1	YAG	111	PbO	43.9	$Gd_{1.50}Y_{1.44}Al_{5.05}O_{12}$:Ce

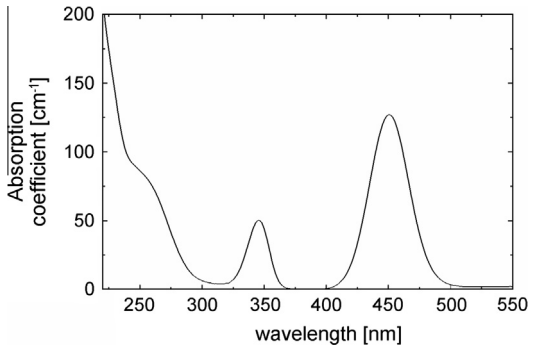

Fig. 1. Absorption spectrum of sample LY2 ($Lu_{2.43}Y_{0.57}Al_5O_{12}$:Ce).

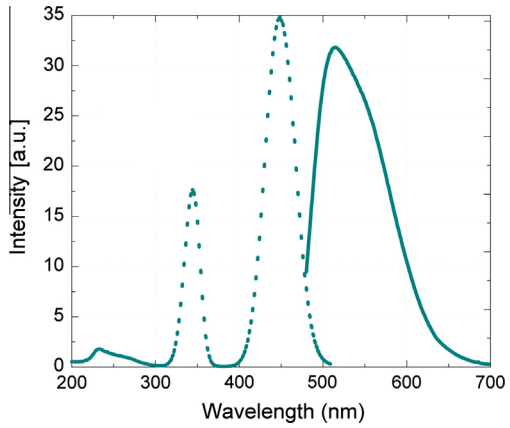

Fig. 2. Emission (excitation wavelength 445 nm, solid line) and excitation spectrum (emission wavelength 530 nm, dashed line) of sample LY2 ($Lu_{2.43}Y_{0.57}Al_5O_{12}$:Ce) measured at RT.

Radioluminescence spectra exhibit two main emission bands. The first one around 530 nm is due to the above mentioned Ce^{3+} $5d_1$–4f transition, the second one is in UV extending from approximately 240 nm to 400 nm. Broad-band UV emission is most probably due to trapped exciton and partially originate also from the substrate due to low thickness of films. Additionally, the Gd^{3+} 4f–4f emission line with the maximum at 315 nm (Fig. 3) appears in the Gd-containing films. Gd^{3+} emission line is very intense for samples LGYG2 and LGYG3 with low Gd content. Both UV emission bands, originating either from the host or from Gd^{3+} emission, are negligible in the GG1 and GY1 samples with high Gd content, see Fig. 3 and Table 2. Samples other than GG1 and GY1 emit from 20% to 34% of total light output (spectra integral) within 240–400 nm, except LGY1 sample which emits 78% of total light output in this spectral region. Light output (radioluminescence spectrum integral) of the Ce^{3+} $5d_1$–4f emission under X-ray excitation varies from 143% (LGY1) to 591% (LGYG2) of that of BGO reference sample, see Table 2 and Fig. 3.

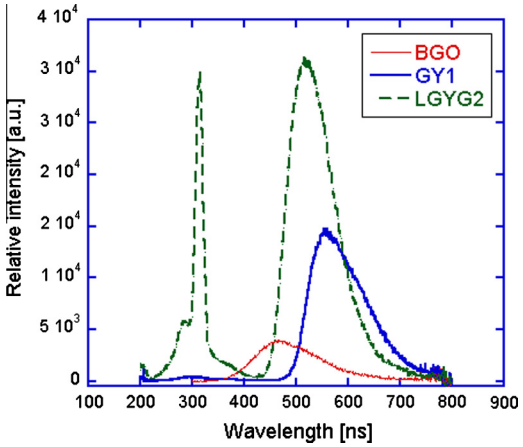

Fig. 3. Radioluminescence spectra of samples GY1 ($Gd_{1.50}Y_{1.44}Al_{5.05}O_{12}$:Ce), LGYG2 ($Lu_{2.02}Y_{0.38}Gd_{0.55}Al_{3.74}Ga_{1.31}O_{12}$:Ce), LGYG4 ($Lu_{1.66}Y_{0.38}Gd_{0.96}Al_{3.48}Ga_{1.51}O_{12}$:Ce) and reference BGO crystal.

Unlike Ce^{3+} 5d–4f transition, trapped exciton decay times and Gd^{3+} decay times are much longer. Therefore, UV luminescence is much more persistent, as observed by PL decay measurements for Gd^{3+} 4f–4f UV emission at 312 nm (Fig. 4a), and Ce^{3+} 5d–4f PL decay at 520 nm (Fig. 4b), both for sample LGYG3. Gd^{3+} 4f–4f transition is spin and parity forbidden. If Ce^{3+} $5d_1$ (sample LGYG3) state is excited directly, luminescence exhibits single exponential decay with decay constant of 54 ns for LGYG3 sample. In case of Gd^{3+} 4f–4f emission, decay is more complicated with several components having decay constants of the order of hundreds μs presumably due to the Gd concentration quenching. The situation is almost the same for all the Gd^{3+} containing samples with higher Gd content. Additionally, there is persistent excitonic luminescence present under X-ray (or α particle) excitation in all samples, except GG1 and GY1.

Photoelectron yield value (Table 2) of all samples except GG1 exceeds that of the best samples from PbO-flux (100 phel/MeV) in our previous studies [29]. Samples LY2, LGYG2 and GY1 outperform even the best previous sample from BaO-flux (314 phel/MeV). The best GY1 sample shows the value of 415 phel/MeV, see Table 2 and Fig. 5. On the other hand, sample GG1 exhibits low value of photoelectron yield 69 phel/MeV, unlike bulk crystals with similar composition [24]. It is important to note that used HPMT has quantum efficiency significantly higher for UV emission than for Ce^{3+} 5d–4f emission. Therefore, sample GY1 performance would be comparatively even better in the terms of (spectrally corrected) light yield.

Energy resolution (FWHM) is determined mainly by photoelectron (light) yield value and material non-proportionality. In this study, non-proportionality could not be determined, but correlation between FWHM and photoelectron yield is evident. Namely, the best GY1 sample exhibits FWHM value of 8.3%, the worst GG1 one of 47%. Samples LGYG4 and LGYG5 show a bit worse FWHM than expected considering light yield values of other samples. Unlike all other parameters, FWHM was only partially reproducible for all LGYG samples. FWHM varied from 10.5% to 15.0% for LGYG2 sample and from 10.7% to 16.2% for LGYG3 sample in several independent measurements. It can be possibly explained by

Table 2
Photoelectron yield and energy resolution measured under α particle excitation using 1 μs amplifier shaping time, $K_{f/e}$ value, $1/m_3$ parameter, radioluminescence intensity relative to BGO, and percentage of UV photons in radioluminescence spectra.

Sample	PhY/MeV (1 μs)	FWHM (%) (1 μs)	$K_{f/e}$ (%)	$1/m_3$ (ns)	RL (Ce/BGO)	RL (UV/BGO)
LY1	310	9.4	52.2	2261	160.9	82.5
LY2	376	11.0	60.8	2180	188.4	82.0
LGY1	150	19.3	36.4	3541	143.3	475.8
LGYG2	381	10.5	44.4	2348	591.4	153.0
LGYG3	335	10.7	41.5	3567	580.3	149.4
LGYG4	344	15.0	44.8	–	404.5	182.4
LGYG5	307	19.1	48.8	2370	343.0	138.2
GG1	69	47.0	96.7	3938	308.2	0.8
GY1	415	8.3	55.6	1273	289.4	5.6

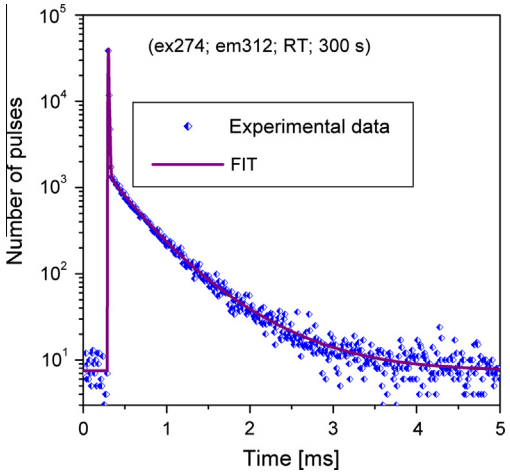

Fig. 4a. Decay curve of sample LGYG3 ($Lu_{1.98}Y_{0.37}Gd_{0.61}Al_{3.73}Ga_{1.31}O_{12}$:Ce). Excitation at 274 nm, emission at 312 nm. Solid line is convolution of instrumental response (pulse) with multi exponential function $I(t) = 124739\exp(-t/0.215\ \mu s) + 786\exp(-t/239\ \mu s) + 157\exp(-t/743\ \mu s) + 12.2$.

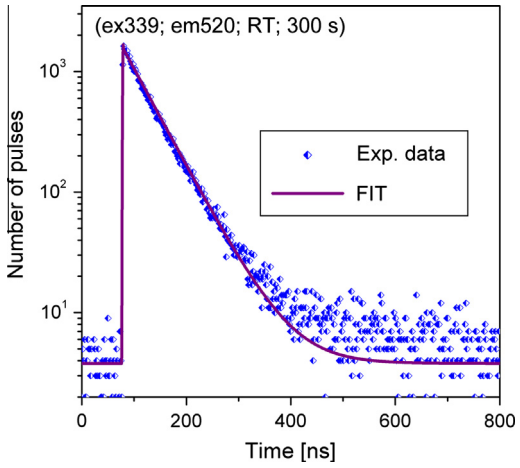

Fig. 4b. Decay curve of sample LGYG3 ($Lu_{1.98}Y_{0.37}Gd_{0.61}Al_{3.73}Ga_{1.31}O_{12}$:Ce). Excitation at 339 nm, emission at 520 nm. Solid line is convolution of instrumental response (pulse) with single exponential function $I(t) = 1556\exp(-t/54\ ns) + 4.05$.

non-uniformity of the films or varying influence of very slow component caused by different count rate.

Photoelectron yield time dependencies of selected samples are presented in Fig. 6. These dependencies were used for calculation of $K_{f/e}$ and $1/m_3$ parameters. $K_{f/e}$ is fast component relative intensity and $1/m_3$ is parameter proportional to slow scintillation component decay time, for the details, see Ref. [19]. Only sample GG1 exhibits very high $K_{f/e}$ parameter, i.e. 97%. Worst sample is the LGY1 with $K_{f/e}$ = 36% followed by LGYG samples (42–49%), and finally slightly better performing LY and GY samples (52–61%). Parameter $1/m_3$ is not very precisely measured, especially when $K_{f/e}$ approaches 100%, like for GG1 sample. However, it is still interesting to note that GY1 has the lowest $1/m_3$ parameter which indicates shorter decay time value of slower decay components. In the terms of $K_{f/e}$, the films grown in BaO-flux from the older studies are not outperformed.

The GY1 sample as shown the highest figure-of-merit due to highest photoelectron yield, best FWHM, shortest $1/m_3$ and average $K_{f/e}$ parameters. Its photoelectron yield is the highest among all the samples despite the fact that radioluminescence intensity (295% BGO) is more than 2× lower than that in the samples LGYG2 (744% BGO) and LGYG3 (730% BGO). Moreover, GY1 emits less than

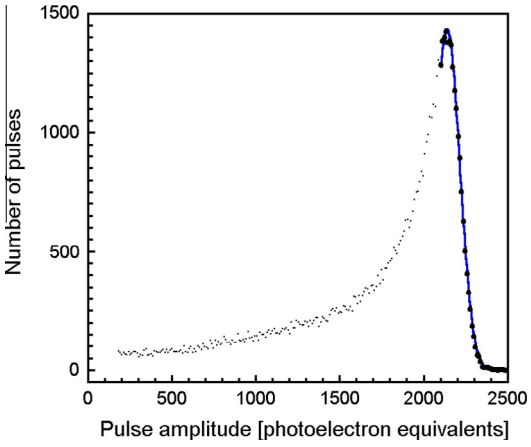

Fig. 5. Pulse height spectrum of sample GY1 ($Gd_{1.50}Y_{1.44}Al_{5.05}O_{12}$:Ce) scintillation response excited by ^{239}Pu α source, shaping time 1 μs, FWMH = 8.3%.

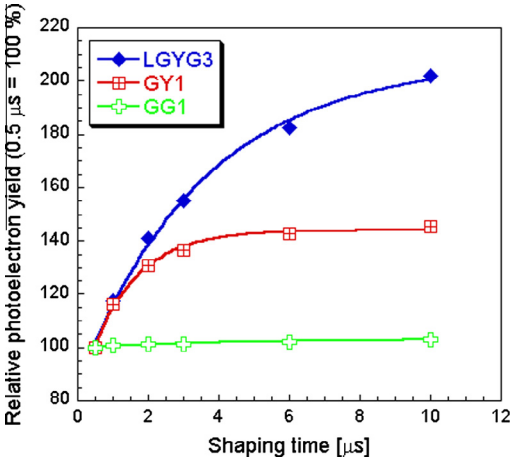

Fig. 6. Dependence of relative photoelectron yield of selected samples on amplifier shaping time.

2% of photons at wavelength region below 400 nm, i.e. the Ce^{3+} 5d–4f emission is absolutely dominating. Unlike photoelectron yield measurement, even very slow decay components contribute to the radioluminescence measurement due to its steady-state character. Apparently, much lower relative intensity of slow scintillation components is present in GY1 sample in comparison with the other samples.

Sample GG1 shows the lowest photoelectron yield and worst energy resolution. It exhibits parameter $K_{f/e}$ close to 100%, but radioluminescence intensity similar to sample GY1. High radioluminescence intensity excludes the Pb-contamination as a reason for low photoelectron yield. Thus, most of scintillation photons are emitted within very long times after excitation, hundreds μs or even later and do not contribute to the light yield signal. GG1 sample is less transparent compared to GY1 which is most probably due to the different growth conditions, and very high substrate-film lattice mismatch, which causes structural defects in the film [11]. Unfortunately, substrates with lower lattice mismatch are not available.

Lattice mismatch may be a problem for sample LGY1 grown on LuAG substrate and LGYG samples grown on YAG substrate as well. Among the BaO-flux-grown samples, LGY1 has lowest photoelectron yield, lowest $K_{f/e}$, worst energy resolution and highest relative intensity of UV emission. All these values indicate low efficiency and comparatively slow energy transfer to the Ce^{3+} luminescence centers. Migrating charge carriers can be trapped at the defects

caused possibly by the lattice mismatch. Thus, electron–hole recombination at Ce^{3+} center is prevented/delayed. Close to the defects, the electron–hole pairs may create trapped excitons, the decay of which is significantly slower as well [30].

LY1 and LY2 have significantly lower radioluminescence intensity, but almost the same photoelectron yield and slightly higher $K_{f/e}$ value than LGYG2-5, i.e. negative influence of defects seems less severe than for samples LGYG2-5. Lower concentration of the defect-related traps could be considered. Indeed, one defect formation mechanism, i.e. lattice mismatch, is minimized in the samples LY1 (homoepitaxial growth) and LY2 (almost homoepitaxial).

4. Conclusions

Measurement of nine epitaxial garnet films of different composition revealed the best performance of $Gd_{1.50}Y_{1.44}Al_{5.05}O_{12}$:Ce (sample GY1) scintillating film grown in PbO-flux. 98% of total light output is emitted by the 5d–4f Ce^{3+} emission, indicating very efficient energy transfer to Ce^{3+} centers. Photoelectron yield reached 415 phel/MeV and FWHM 8.4% under α particle excitation using amplifier shaping time of 1 μs. The GY1 sample thus outperformed all the Ce-doped garnet films studied by us in the past. Second PbO-flux grown sample GG1 ($Gd_3Ga_{2.4}Al_{2.6}O_{12}$:Ce) exhibits much worse scintillation characteristics, unlike bulk crystals of nearly the same composition. Very high film-substrate lattice mismatch and resulting worse structural quality may be partially responsible for such a result.

BaO-flux grown samples were performing slightly worse than sample GY1 in terms of photoelectron light yield, $K_{f/e}$ parameter, energy resolution and relative intensity of 5d–4f Ce^{3+} emission in radioluminescence spectra. Film-substrate lattice mismatch may also deteriorate performance in some of them. On the other hand, lattice mismatch of BaO-flux grown samples is not larger than that of GY1 sample. Therefore, film composition itself seems to be most important factor of better performance of GY1 sample.

Positive role of Ga admixture observed in bulk crystals was not found in the LPE grown films in this sample set. In bulk crystals the Ga admixture buries the traps attributed to antisite defects in conduction band and thus improves energy transfer to Ce^{3+} centers. However, traps in epitaxial films have different origin, structure and energy levels and film-substrate lattice mismatch, flux contamination and its viscosity are the most important factors influencing the performance of these thin film scintillators.

Acknowledgement

Financial support of Czech Science foundation Project No. P204/12/0805 and RVO: 68407700 is gratefully acknowledged.

References

[1] C.W.E. van Eijk, J. Andriessen, P. Dorenbos, R. Visser, Nucl. Instrum. Methods Phys. Res. A 348 (1994) 546–550.
[2] A.G. Petrosyan, K.L. Ovanesyan, R.V. Sargsyan, G.O. Shirinyan, D. Abler, E. Auffray, P. Lecoq, C. Dujardin, C. Pedrini, J. Cryst. Growth 312 (2010) 3136.
[3] M. Nikl, A. Yoshikawa, K. Kamada, K. Nejezchleb, C.R. Stanek, J.A. Mares, K. Blazek, Prog. Cryst. Growth Charact. Mater. (2013), http://dx.doi.org/10.1016/j.pcrysgrow.2013.02.001.
[4] C. Dujardin, C. Mancini, D. Amans, G. Ledoux, D. Abler, E. Auffray, P. Lecoq, D. Perrodin, A. Petrosyan, K.L. Ovanesyan, J. Appl. Phys. 108 (2010) 013510.
[5] J. Tous, K. Blazek, M. Nikl, J.A. Marea, J. Phys: Conf. Ser. 425 (2013) 192017.
[6] A. Koch, C. Raven, P. Spanne, A. Snigirev, J. Opt. Soc. Am. A 15 (1998) 1940–1951.
[7] P.-A. Douissard, A. Cecilia, T. Martin, V. Chevalier, M. Couchaud, T. Baumbach, K. Dupré, M. Kühbacher, A. Rack, J. Synchrotron Radiat. 17 (2010) 571.
[8] J. Tous, M. Horvath, L. Pina, K. Blazek, B. Sopko, Nucl. Instrum. Methods A 591 (2008) 264–267.
[9] Yu. Zorenko, V. Gorbenko, I. Konstankevych, A. Voloshinovskii, G. Struganyuk, V. Mikhailin, V. Kolobanov, D. Spassky, J. Lumin. 114 (2005) 85–94.
[10] Yu. Zorenko, V. Gorbenko, E. Mihokova, M. Nikl, K. Nejezchleb, A. Vedda, V. Kolobanov, D. Spassky, Radiat. Meas. 42 (2007) 521–527.
[11] M. Kučera, K. Nitsch, M. Nikl, M. Hanus, S. Danis, J. Cryst. Growth 312 (2010) 1538–1545.
[12] M. Kucera, M. Nikl, P. Prusa, J.A. Mares, K. Nitsch, M. Hanus, Z. Onderisinova, R. Kucerkova, J. Cryst. Growth 318 (2011) 813–819.
[13] M. Globus, B. Grinyov, M. Ratner, V. Tarasov, V. Lyubinskiy, Yu. Zorenko, I. Konstankevych, Nuclear Science Symposium Conference Record, 1, 2002, pp. 352–356.
[14] M. Nikl, E. Mihokova, J. Pejchal, A. Vedda, Yu. Zorenko, K. Nejezchleb, Phys. Status Solidi (b) 242 (2005) R119.
[15] C.R. Stanek, K.J. McClellan, M.R. Levy, R.W. Grimes, Phys. Status Solidi (b) 243 (2006) R75.
[16] P. Prusa, T. Cechak, J.A. Mares, M. Nikl, A. Beitlerova, N. Solovieva, Yu.V. Zorenko, V.I. Gorbenko, Appl. Phys. Lett. 92 (2008) 041903.
[17] W. Drozdowski, P. Dorenbos, R. Drozdowska, A.J.J. Bos, N.R.J. Poolton, M. Tonelli, M. Alshourbagy, IEEE Trans. Nucl. Sci. 56 (2009) 320–327.
[18] V. Babin, V. Gorbenko, A. Makhov, J.A. Mares, M. Nikl, S. Zazubovich, Yu. Zorenko, J. Lumin. 127 (2007) 384.
[19] P. Prusa, M. Nikl, J.A. Mares, M. Kucera, K. Nitsch, A. Beitlerova, Phys. Status Solidi (a) 206 (2009) 1494.
[20] M. Fasoli, A. Vedda, M. Nikl, C. Jiang, B.P. Uberuaga, D.A. Andersson, K.J. McClellan, C.R. Stanek, Phys. Rev. B 84 (2011) 081102(R).
[21] H. Ogino, A. Yoshikawa, M. Nikl, J.A. Mareš, J.-I. Shimoyama, K. Kishio, J. Cryst. Growth 311 (2009) 908–911.
[22] K. Kamada, T. Endo, K. Tsutsumi, T. Yanagida, Y. Fujimoto, A. Fukabori, A. Yoshikawa, J. Pejchal, M. Nikl, Cryst. Growth Des. 11 (2011) 4484–4490.
[23] K. Kamada, T. Yanagida, J. Pejchal, M. Nikl, T. Endo, K. Tsutsumi, Y. Fujimoto, A. Fukabori, A. Yoshikawa, J. Phys. D: Appl. Phys. 44 (2011) 505104.
[24] K. Kamada, T. Yanagida, T. Endo, K. Tsutsumi, Y. Usuki, M. Nikl, Y. Fujimoto, A. Fukabori, A. Yoshikawa, J. Cryst. Growth 352 (2012) 88–90.
[25] J. Kindem, R. Conwell, N.J. Cherepy, S.A. Payne, IEEE Nucl. Sci. Symposium Conference, Record NP5.S-94, 2011, pp. 1621–1623.
[26] P. Prusa, K. Kamada, M. Nikl, A. Yoshikawa, J.A. Mares, Radiat. Meas. (2013), http://dx.doi.org/10.1016/j.radmeas.2013.01.055.
[27] M. Moszynski, M. Kapusta, M. Mayhugh, D. Wolski, S.O. Flyckt, IEEE Trans. Nucl. Sci. 44 (1997) 1052–1061.
[28] C. D'Ambrosio, H. Leutz, Nucl. Instrum. Methods A 501 (2003) 463–498.
[29] P. Prusa, J.A. Mares, M. Nikl, M. Kucera, K. Nitsch, M. Hanus, Opt. Mater 32 (2010) 1360–1363.
[30] Yu. Zorenko, A. Voloshinovskii, I. Konstankevych, V. Kolobanov, V. Mikhailin, D. Spassky, Radiat. Meas. 38 (2004) 677–680.

Radiation Measurements 56 (2013) 62–65

Contents lists available at SciVerse ScienceDirect

Radiation Measurements

journal homepage: www.elsevier.com/locate/radmeas

Light yield of $(Lu, Y, Gd)_3Al_2Ga_3O_{12}$:Ce garnets

P. Prusa [a,*], K. Kamada [b], M. Nikl [a], A. Yoshikawa [c], J.A. Mares [a]

[a] Institute of Physics, Czech Academy of Sciences, Cukrovarnicka 10, 160 00 Praha, Czech Republic
[b] Materials Research Laboratory, Furukawa Co. Ltd., 1-25-13, Kannondai, Tsukuba 305-0856, Japan
[c] IMR, Tohoku University, Sendai 980-8577, Japan

HIGHLIGHTS

- Scintillation response of $(Gd,Y,Lu)_3(Ga,Al)_5O_{12}$:Ce garnets was studied.
- $Gd_3Al_2Ga_3O_{12}$:Ce has been found of best scintillation performance of garnets.
- Light yield & energy resolution reached 50 000 phot/MeV and 5.5%@662 keV, respectively.

ARTICLE INFO

Article history:
Received 22 October 2012
Received in revised form
11 January 2013
Accepted 21 January 2013

Keywords:
Scintillator
Garnet
Light yield
Hybrid photomultiplier

ABSTRACT

Two sets of Ce-doped multicomponent garnet scintillator samples were prepared using Czochralski method. Best performing sample from the first group was $Gd_3Al_2Ga_3O_{12}$ doped by 1% of Ce. Therefore, samples of $Gd_3Al_2Ga_3O_{12}$ with different thickness have been prepared for the second set. Light yield, its dependence on amplifier shaping time, energy resolution, and non-proportionality have been measured using hybrid photomultiplier. Best performing sample exhibits following parameters: light yield of 50 600 photons/MeV, energy resolution of 5.5%@662 keV, fast scintillation component intensity 91%, and good proportionality. Performance of other samples was negatively affected presumably either by ionization of $5d_1$ excited state of Ce^{3+} center or electron traps.

1. Introduction

$Lu_3Al_5O_{12}$:Ce (LuAG:Ce) (Moszynski et al., 1994; Nikl, 2006) and $Y_3Al_5O_{12}$:Ce (YAG:Ce) (Autrata et al., 1978; Nikl, 2006) garnets represent interesting fast scintillation materials with good light yield, they are chemically stable, non-hygroscopic and have excellent mechanical properties. Additionally, LuAG:Ce offers high detection efficiency due to high effective atomic number. However, performance of these materials is negatively affected by shallow traps, usually attributed to Lu_{Al} and Y_{Al} antisite defects (Nikl et al., 2005; Stanek et al., 2006), especially in LuAG:Ce. Presence of antisite defects leads to intensification of slow scintillation component, decrease of light yield and probably, also to deterioration of energy resolution.

Antisite defects are produced due to high preparation temperature. Therefore, shallow traps are unavoidable using melt growth, e.g. Czochralski, Bridgman or micro-pulling down methods. It is possible to suppress creation of traps using other methods, which enables growth at lower temperatures, e.g. liquid phase epitaxy (Nikl, 2006, 2005; Prusa et al., 2008; Zorenko et al., 2005) or ceramic (Mihóková et al., 2007; Cherepy et al., 2007). However, liquid phase epitaxy does not enable preparation of bulk scintillators and ceramic may exhibit scintillation properties inferior to bulk crystals.

Recently, the "band-gap engineering" approach was adopted for reducing or even eliminating the negative effects of shallow traps. Using the Ga admixture, it is possible to lower the bottom of conduction band (Fasoli et al., 2011; Nikl et al., 2008; Ogino et al., 2009). Although, antisite defects remain present in the scintillator, they become buried in the conduction band. This approach strongly suppresses trapping effects in scintillation response. On the other hand, reduced gap between the bottom of conduction band and $5d_1$ excited state of Ce luminescent center leads to undesired thermal ionization.

However, it is possible to widen this gap by Gd admixture (Kamada et al., 2011). In recent studies, micro-pulling down technique was adopted for preparation of a large number of samples with different composition (Kamada et al., 2011, 2011b, 2012).

* Corresponding author. Tel.: +420 604958601.
E-mail addresses: petr.prusa@centrum.cz, petr.prusa@fjfi.cvut.cz (P. Prusa).

1350-4487/$ – see front matter © 2013 Elsevier Ltd. All rights reserved.
http://dx.doi.org/10.1016/j.radmeas.2013.01.055

Among them, the best sample exhibits the light yield above 40 000 ph/MeV and very good energy resolution. Also, a slow scintillation component intensity was strongly reduced. This paper is focused on deeper study of scintillation response of such multi-component garnets.

2. Experiments and methods

Two sets of garnet single crystal scintillators were prepared. In both cases, 4N purity raw powder materials were used: CeO_2, Gd_2O_3, Y_2O_3, Lu_2O_3, β-Ga_2O_3, and α-Al_2O_3 (High Purity Chemicals Co.). First set of samples has different composition: $Gd_3Al_2Ga_3O_{12}$, $Y_2Gd_1Al_2Ga_3O_{12}$, $Lu_2Gd_1Al_2Ga_3O_{12}$, $Lu_2Y_1Al_2Ga_3O_{12}$, and $Lu_1Gd_2Al_2Ga_3O_{12}$, all samples doped by 1% of Ce. Two additional samples of $Gd_3Al_2Ga_3O_{12}$ were prepared, with 2% and 3% of Ce, From now on, these samples are designated as $1G_3C_{1\%}$, $1G_3C_{2\%}$, $1G_3C_{3\%}$, $1Y_2G_1C_{1\%}$, $1L_2G_1C_{1\%}$, $1L_2Y_1C_{1\%}$, and $1L_1G_2C_{1\%}$. All samples have been cut from 1 inch diameter Czochralski grown crystals, except for $1G_3C_{1\%}$ having 2 inch diameter. Dimensions are 5 × 5 × 1 mm, optically polished. For details see (Kamada et al., 2012).

The second set of samples was prepared from $Gd_3Al_2Ga_3O_{12}$:Ce1% crystal grown using Czochralski method, RF heating system, rotation rate 4–12 rpm and growth rate of 1 mm/h (Kamada et al., 2012). Sizes of samples were 5 × 5 × h mm, where h = 1, 2, 4.5 and 10 mm. These samples are further mentioned as $2G_3C_{1\%,1mm}$, $2G_3C_{1\%,2mm}$, $2G_3C_{1\%,4.5mm}$, and$2G_3C_{1\%,10mm}$.

Light yield, non-proportionality, slow component relative intensity and energy resolution were determined by amplitude spectroscopy of scintillation response induced by gamma rays (Mareš et al., 2007). Scintillation crystal is covered by teflon tape to ensure efficient light collection, and optically coupled to a hybrid photomultiplier (HPMT) model DEP PPO 475B. Signal from HPMT is processed by spectroscopy amplifier ORTEC model 672 and multichannel buffer ORTEC 927TM. Pulse-height spectrum is displayed on PC.

Several gamma ray emitting radionuclide sources were used to induce a scintillation response: ^{137}Cs (661.6 keV), ^{22}Na (511 keV, 1274 keV), ^{241}Am (59.54 keV, 13.95 keV), ^{210}Pb (46.54 keV, 10.84 keV), ^{109}Cd (88.04 keV, 22.16 keV), and ^{133}Ba (81.0 keV, 160.6 keV, 276.4 keV, 302.9 keV, 356.0 keV, and 383.9 keV) (Ekström and Firestone, 2004). Only selection of ^{133}Ba lines is presented for many samples due to non-negligible interference. 1274 keV line of ^{22}Na is not presented because of experimental setup saturation. Radioactive source was placed at a distance of several mm from the sample, depending on detection efficiency and source activity. All measurements were performed at room temperature.

Energy resolution and photoelectron yield was obtained using gaussian fit of peaks in the spectra. Light yield is obtained from photoelectron yield multiplied by HPMT photocathode quantum efficiency. This efficiency was calculated using radioluminescence spectra. Only the Ce^{3+} $5d_1$-4f emission was considered in quantum efficiency calculation.

Measured light yield is dependent on the amplifier shaping time. If longer shaping time is used, more photons contribute to the response, signal intensity is rising with longer shaping times. Used amplifier enables shaping times of 0.5, 1, 2, 3, 6 and 10 μs (semi-gaussian shaping). Therefore, the response increase is significant only for samples with intense slow scintillation decay component in the range of microseconds. Considering double-exponential decay approximation with fast component decay time of few tens of ns, light yield dependence can be fitted by function $LY(t) = m_1 - m_2\exp(-m_3 t)$, where m_i are parameters obtained by a fit (Prusa et al., 2009). Afterward, calculation of the relative intensity of the fast fraction of the response $K_{f/e}$ takes place: $K_{f/e} = 1 - (m_2/m_1)$ (Prusa et al., 2009).

3. Results

Light yield for reference shaping time $t = 1$ μs is given in Table 1. In the first set of samples, light yield is gradually increasing with rising Gd content and sample $1G_3C_{1\%}$ shows maximum value of 48 300 ± 3000 ph/MeV. Higher Ce concentration led to light yield decrease in $1G_3C_{2\%}$ and $1G_3C_{3\%}$ samples. Lowest light yield value was found in Gd-free sample $1L_2Y_1C_{1\%}$. Comparing samples $1Y_2Gd_1C_{1\%}$ and $1L_2Gd_1C_{1\%}$, light yield is more negatively affected by Lu than Y admixture. This conclusion is tentative due to small number of samples tested.

Second set of samples has confirmed good performance of $1G_3C_{1\%}$, 1 mm thick sample has shown the light yield of 50 600 ± 3500 ph/MeV. Its value decreased with thickness due to scintillation photons re-absorption and/or worse light collection, down to 41 100 ± 2800 ph/MeV for 10 mm thick sample, see Table 1 and Fig. 1 inset.

Light yield energy dependence, i.e. non-proportionality, was measured using amplifier shaping time $t = 1$ μs. For some of the samples, measurement error of light yield value for various gamma rays energies is comparable to differences between light yield values for the same energies. Therefore, non-proportionality dependencies are not very well pronounced. Exceptions to this rule are presented in Fig. 1. Ratio of light yield $LY_{22.16keV}/LY_{661.6keV}$ is given for all samples, see Table 1. Energy 661.6 keV was chosen because of its standard use in light yield measurement, energy 22.16 keV because it is below K absorption edge of Lu and Gd and non-proportionality is clearly significant for this energy.

$LY_{22.16}$keV/$LY_{661.6keV}$ is the lowest for $1G_3C_{2\%}$, i.e. 91%, followed by $1G_3C_{3\%}$, 86%, and $1G_3C_{1\%}$, 79%. Values for the whole second sample set are almost the same as for $1G_3C_{1\%}$, they vary from 78 to 81%. Samples $1L_2Y_1C_{1\%}$ and $1L_1G_2C_{1\%}$ reached intermediate values of 74% and 73%, respectively. Much lower values were found in samples $1Y_2Gd_1C_{1\%}$ and $1L_2Gd_1C_{1\%}$, 39% and 45%, respectively.

Energy resolution is given for shaping time $t = 1$ μs and energy of ^{137}Cs 661.6 keV, see Table 1. Most of the values for the first sample set are worse than 10%, only with sample $1G_3C_{1\%}$ showing more promising value of 7.3%. Generally, lower energy resolution corresponds to lower light yield. Worst FWHM was found for sample $1L_2Gd_1C_{1\%}$, namely 17.0%. Second set of samples produced by the optimized technology showed better results. FWHM is increasing with increasing thickness of samples, from 5.5% up to 7.3%.

Finally, shaping time dependencies of light yield have been measured using ^{137}Cs, see Fig. 2, $K_{f/e}$ values for all samples are given in Table 1. Clearly, all $Gd_3Al_2Ga_3O_{12}$ samples show the best $K_{f/e}$ values Only value for sample $1G_3C_{1\%}$ is below 90%. Two other samples ($1Y_2Gd_1C_{1\%}$ and $1L_2Gd_1C_{1\%}$) are comparable to $1G_3C_{1\%}$, having $K_{f/e}$ equal to 84%, 85% respectively. Last two samples

Table 1
Experimental values of light yield (LY), energy resolution (FWHM), ratio of light yields measured for 22 keV and 662 keV (giving information about non-proportionality), and relative contribution of fast scintillation component to response ($K_{f/e}$).

Sample	LY [ph/MeV]	FWHM [%]	LY_{22}/LY_{662} [%]	$K_{f/e}$ [%]
$1G_3C_{1\%}$	48 300	7.3	84	86
$1G_3C_{2\%}$	22 700	13.2	90	94
$1G_3C_{3\%}$	29 500	9.4	88	95
$1Y_2G_1C_{1\%}$	28 900	11.3	66	84
$1L_2G_1C_{1\%}$	25 800	12.9	81	58
$1L_2Y_1C_{1\%}$	21 300	17.0	67	85
$1L_1G_2C_{1\%}$	12 100	16.3	90	41
$2G_3C_{1\%,1mm}$	50 600	5.5	85	91
$2G_3C_{1\%,2mm}$	50 300	6.2	84	94
$2G_3C_{1\%,4.5mm}$	43 100	7.3	82	94
$2G_3C_{1\%,10mm}$	41 100	7.3	85	92

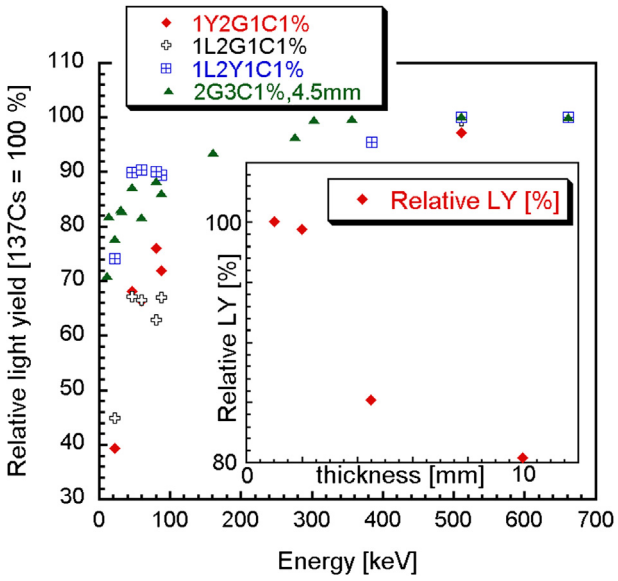

Fig. 1. Non-proportionality of four selected samples. Response for ^{137}Cs (661.6 keV) corresponds to 100%. Inset: Dependence of light yield of $Gd_3Al_2Ga_3O_{12}$:Ce on sample thickness. Light yield of 1 mm thick sample = 100%.

($1L_2Y_1C_{1\%}$ and $1L_1G_2C_{1\%}$) exhibit values of 41% and 58%. It is interesting to note, that for these four non-$Gd_3Al_2Ga_3O_{12}$ samples, worse $K_{f/e}$ value corresponds to better proportionality and vice versa.

4. Discussion

Samples $1G_3C_{1\%}$ plus the second set are the best performing in all respects. They seem to be optimized from the energy level structure point of view. Ga content ensures that traps arising from antisite defects are eliminated. Additionally, the Gd content ensures sufficient gap between $5d_1$ excited state of Ce^{3+} luminescence center and bottom of conduction band, thus preventing undesirable $5d_1$ ionization.

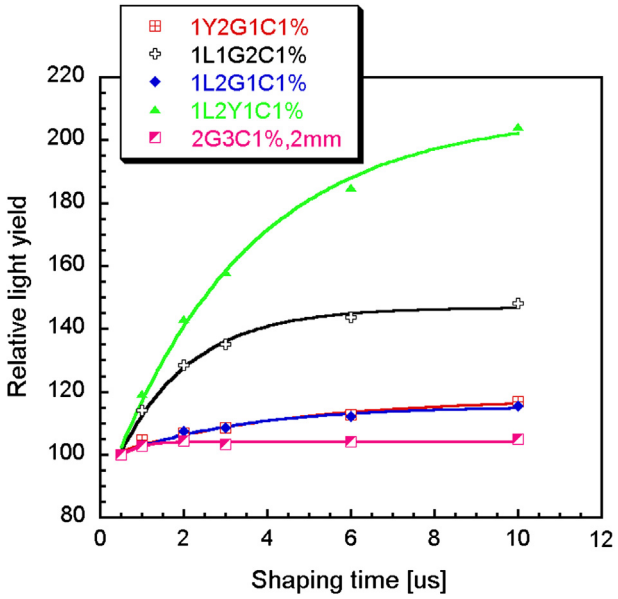

Fig. 2. Dependence of relative light yield on amplifier shaping time. Response for shaping time 0.5 μs corresponds to 100%.

Samples $1G_3C_{2\%}$ and $1G_3C_{3\%}$ exhibit lower light yield and energy resolution, but similar non-proportionality and time dependencies. Therefore, higher content of Ce leads to performance deterioration. It may be attributed either to Ce aggregate centers or defects created due to higher Ce concentration. Nonetheless, $1G_3C_{2\%}$ thermoluminescence intensity is rather low (Mihóková et al., 2013), so concentration quenching seems to be more probable explanation.

All samples with lower Gd content exhibit lower light yield. Generally, $5d_1$ excited states of Ce^{3+} luminescence center are closer to bottom of conduction band in these samples. Therefore, electrons at $5d_1$ excited state can probably reenter more easily the conduction band by (thermal) ionization. Ionized electrons can be partially lost or delayed for radiative recombination at Ce^{3+} centers.

The $5d_1$ excited state ionization explains differences between samples $Gd_3Ga_2Al_3O_{12}$ and samples with lower Gd concentration, but is not able to explain differences among non-$Gd_3Ga_2Al_3O_{12}$ samples. These samples differ significantly in non-proportionality and time dependencies. Further investigation is needed to explain these features.

Decrease of light yield in the second set of crystals is caused by decreasing light collection due to re-absorption of scintillation photons and worse light collection. Higher Stokes shift (Kamada et al., 2012) does give the advantage in $Gd_3Al_2Ga_3O_{12}$:Ce comparing to LuAG:Ce as for the former aspect. Scintillation response should be less dependent on thickness for thicker samples, since emission-absorption "overlap" region photons are almost completely absorbed in such samples. This response "stabilization" with thickness can be seen in inset of Fig. 1. However, it is not possible to precisely extrapolate dependence of light yield on thickness due to low number of samples and precision of the measurement.

Energy resolution is affected mainly by light yield. Non-proportionality and HPMT quantum efficiency play minor role in explanation of differences among samples, because these parameters are mostly very similar in given sets of crystals. There are two exceptions. Samples $1Y_2Gd_1C_{1\%}$ and $1L_2Gd_1C_{1\%}$ are suffering from worse non-proportionality and it is reflected in energy resolution as well. These two samples have significantly worse resolution than samples with almost the same light yield, e.g. samples $1G_3C_{2\%}$ and $1G_3C_{3\%}$ respectively. This is in agreement with (Valentine et al., 1998).

The sample with highest light yield and good proportionality, i.e. $2G_3C_{1\%,1mm}$, exhibits also best FWHM. This value is slightly worse than one reported in Kamada et al. (2012). However, the referred value was measured by photodiode, which has significantly higher quantum efficiency in the spectral region of $Gd_3Al_2Ga_3O_{12}$:Ce emission. This effect is well known for CsI:Tl scintillator having maximum emission wavelength around 550 nm. Reported FWHM for CsI:Tl coupled with silicon drift chamber based detector reaches 4.4% (Fiorini et al., 1997; Gacsón et al., 2008). It is significantly better than CsI:Tl coupled with photomultiplier. Additionally, $(Gd,Y)_3(Ga,Al)_5O_{12}$:Ce (GYGAG:Ce) scintillator exhibits very good energy resolution 4.0% coupled with photodiode (Kindem et al., 2011). It is possible, that $Gd_3Al_2Ga_3O_{12}$:Ce scintillator, having similar light yield as GYGAG:Ce, coupled with photodiode or other Si based detector will also reach better values in the future.

Worsening of energy resolution with sample thickness in second set of crystals may be partially attributed to decreasing light yield. However, light collection efficiency fluctuations may contribute to the explanation of this behavior as well. Light collection efficiency may be slightly different in different parts of the crystal, because of scintillation photon absorption demonstrated in inset of Fig. 1.

Light yield dependence on amplifier shaping time is most probably affected mainly by shallow traps. Measurement of both

the room temperature afterglow as well as thermoluminescence around room temperature (Mihóková et al., 2013) indicates that their higher concentration correlates with the higher intensity of slow scintillation components.

5. Conclusion

Measurement of two sets of garnet crystals with different composition have revealed that best performance was reached with $Gd_3Al_2Ga_3O_{12}$:Ce scintillator doped by 1% of Ce. Best sample has the light yield of 50 600 ph/Mev and energy resolution 5.5%. Light yield is decreasing with decreasing amount of Gd, especially if Gd is replaced by Lu. Also, non-proportionality and intensity of slow scintillation component are one of the lowest among samples in investigated set of crystals.

$Gd_3Al_2Ga_3O_{12}$:Ce scintillator is still affected by scintillation photon absorption. However, it is not a severe problem due to increasing Stokes shift in comparison with LuAG:Ce scintillator.

Performance of other samples may be negatively affected by traps, as indicated also by thermoluminescence measurement and ionization of excited $5d_1$ levels of Ce^{3+} luminescence centers. The light yield was lower than 30 000 ph/MeV and energy resolution worse than 9%.

$Gd_3Al_2Ga_3O_{12}$:Ce scintillator seems to be one of the best scintillators among garnets. Being a new material, it is still possible it will reach even better values of light yield and energy resolution, especially when coupled with photodiode or other Si-based detector instead of photomultiplier. Good properties of this scintillator produced by micro-pulling down method have been reported before, but Czochralski grown crystals are now also available.

Acknowledgment

This work was supported by Czech GACR P204/12/0805 and MSMT, KONTAKT LH12150 projects.

References

Autrata, R., Schauer, P., Kvapil, J., 1978. A single crystal of YAG – new fast scintillator in SEM. J. Phys. E: Sci. Instrum. 11, 707–708.

Cherepy, N.J., Kuntz, J.D., Tillotson, T.M., Speaks, D.T., Payne, S.A., Chai, B.H.T., Porter-Chapman, Y., Derenzo, S.E., 2007. Cerium-doped single crystal and transparent ceramic lutetium aluminum garnet scintillators. Nucl. Inst. Meth. A 579, 38–41.

Ekström, L.P., Firestone, R.B., 2004. WWW Table of Radioactive Isotopes. database version 2/28/99 from URL: http://ie.lbl.gov/toi/index.htm.

Fasoli, M., Vedda, A., Nikl, M., Jiang, C., Uberuaga, B.P., Andersson, D.A., McClellan, K.J., Stanek, C.R., 2011. Band-gap engineering for removing shallow traps in rare earth $Lu_3Al_5O_{12}$ garnet scintillators with Ga^{3+} doping. Phys. Rev. B 84, 081102(R).

Fiorini, C., Longoni, A., Perotti, F., Labanti, C., Lechner, P., Strüder, L., 1997. Gamma ray spectroscopy with CsI(Tl) scintillator coupled to silicon drift chamber. IEEE Trans. Nucl. Sci. 44, 2553–2560.

Gacsón, M., Álvarez-Pol, H., Benlliure, L., Casarejos, E., Cortina-Gil, D., Durán, I., 2008. Optimization of energy resolution obtained with CsI(Tl) crystals for the R3B calorimeter. IEEE Trans. Nucl. Sci. 55, 1259–1262.

Kamada, K., Endo, T., Tsutsumi, K., Yanagida, T., Fujimoto, Y., Fukabori, A., Yoshikawa, A., Pejchal, J., Nikl, M., 2011. Composition engineering in cerium-doped $(Lu, Gd)_3(Ga, Al)_5O_{12}$ single-crystal scintillators. Cryst. Growth Des. 11, 4484–4490.

Kamada, K., Yanagida, T., Pejchal, J., Nikl, M., Endo, T., Tsutsumi, K., Fujimoto, Y., Fukabori, A., Yoshikawa, A., 2011b. Scintillator-oriented combinatorial search in Ce-doped $(Y, Gd)_3(Ga, Al)_5O_{12}$ multicomponent garnet compounds. J. Phys. D Appl. Phys. 44, 505104.

Kamada, K., Yanagida, T., Endo, T., Tsutsumi, K., Usuki, Y., Nikl, M., Fujimoto, Y., Fukabori, A., Yoshikawa, A., 2012. 2 inch diameter single crystal growth and scintillation properties of Ce:$Gd_3Al_2Ga_3O_{12}$. J. Cryst. Growth 352, 88–90.

Kindem, J., Conwell, R., Cherepy, N.J., Payne, S.A., 2011. Performance comparison of small GYGAG(Ce) and CsI(Tl) scintillators with PIN detectors, IEEE Nucl. Sci. Symposium Conference Record NP5.S-94, 1621–1623.

Mareš, J.A., Beitlerová, A., Nikl, M., Solovieva, N., Nitsch, K., Kučera, M., Kubová, M., Gorbenko, V., Zorenko, Yu, 2007. Scintillation and optical properties of YAG:Ce films grown by liquid phase epitaxy. Radiat. Meas. 42, 533–536.

Mihóková, E., Nikl, M., Mareš, J.A., Beitlerová, A., Vedda, A., Nejezchleb, K., Blažek, K., D'Aambrosio, C., 2007. Luminescence and scintillation properties of YAG:Ce single crystal and optical ceramics. J. Lumin. 126, 77–80.

Mihóková, E., Vávrů, K., Kamada, K., Babin, V., Yoshikawa, A., Nikl, M., 2013. Deep trapping states in cerium doped $(Lu, Y, Gd)_3(Ga, Al)_5O_{12}$single crystal scintillators. Rad. Meas 56, 98–101.

Moszynski, M., Ludziewski, T., Wolski, D., Klamra, W., Norlin, L.O., 1994. Properties of the YAG:Ce scintillator. Nucl. Inst. Meth. A 345, 461–467.

Nikl, M., 2005. Energy transfer phenomena in the luminescence of wide band-gap scintillators. Phys. Stat. Sol. A 202, 201–206.

Nikl, M., 2006. Scintillation detectors for x-rays. Meas. Sci. Technol. 17, R37–R54.

Nikl, M., Mihóková, E., Pejchal, J., Vedda, A., Zorenko, Y., Nejezchleb, K., 2005. The antisite Lu_{Al} defect related trap in $Lu_3Al_5O_{12}$:Ce single crystal. Phys. Stat. Sol. B 242, R119–R121.

Nikl, M., Mihóková, E., Pejchal, J., Vedda, A., Fasoli, M., Fontana, I., Laguta, V.V., Babin, V., Nejezchleb, K., Yoshikawa, A., Ogino, H., Ren, G., 2008. Scintillator materials – achievements, opportunities, and puzzles. IEEE Trans. Nucl. Sci. 55, 1035–1041.

Ogino, H., Yoshikawa, A., Nikl, M., Mareš, J.A., Shimoyama, J.-I., Kishio, K., 2009. Growth and optical properties of $Lu_3(Ga, Al)_5O_{12}$ single crystals for scintillator application. J. Cryst. Growth 311, 908–911.

Průša, P., Čechák, T., Mareš,, J.A., Nikl, Beitlerová,, A., Solovieva, N., Zorenko, M., Yu., V., Gorbenko, V.I., Touš, J., Blažek, K., 2008. The α-particle excited scintillation response of the liquid phase epitaxy grown LuAG:Ce thin films. Appl. Phys. Let. 92, 041903.

Průša, P., Nikl, M., Mareš, J.A., Kučera, M., Nitsch, K., Beitlerová, A., 2009. The α-particle excited scintillation response of YAG:Ce thin films grown by liquid phase epitaxy. Phys. Stat. Sol. A 206, 1494–1500.

Stanek, C.R., McClellan, K.J., Levy, M.R., Grimes, R.W., 2006. Extrinsic defect structure of $RE_3Al_5O_{12}$ garnets. Phys. Stat. Sol. B 243, R75–R77.

Valentine, J.D., Rooney, B.D., Li, J., 1998. The light yield nonproportionality component of scintillator energy resolution. IEEE Trans. Nucl. Sci. 45, 512–517.

Zorenko, Y., Gorbenko, V., Konstankevych, I., Voloshinovskii, A., Struganyuk, G., Mikhailin, V., Kolobanov, V., Spassky, D., 2005. Single-crystalline films of Ce-doped YAG and LuAG phosphors: advantages over bulk crystals analogues. J. Lumin 114, 85–94.

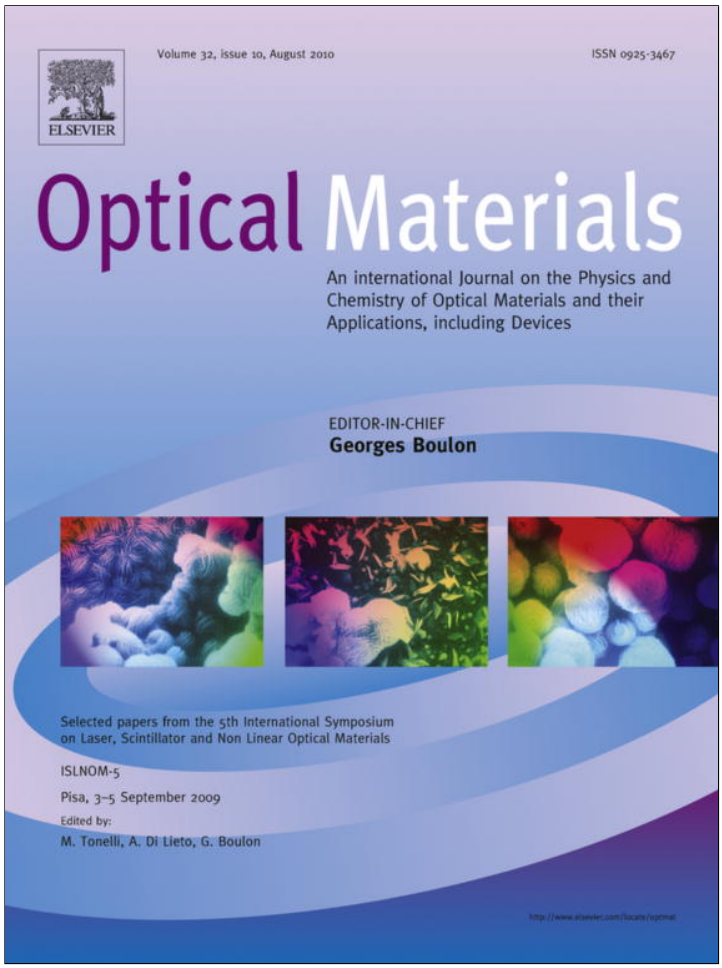

Optical Materials 32 (2010) 1360–1363

Contents lists available at ScienceDirect

Optical Materials

journal homepage: www.elsevier.com/locate/optmat

Scintillation properties of LuAG:Ce single crystalline films grown by LPE method

Petr Prusa [a,*], Jiri A. Mares [a], Martin Nikl [a], Miroslav Kucera [b], Karel Nitsch [a], Martin Hanus [b]

[a] Institute of Physics AS CR, Cukrovarnicka 10, 162 00 Prague, Czech Republic
[b] Charles University, Faculty of Mathematics and Physics, Ke Karlovu 5, 121 16 Prague 2, Czech Republic

ARTICLE INFO

Article history:
Received 31 October 2009
Received in revised form 9 April 2010
Accepted 22 April 2010
Available online 15 May 2010

Keywords:
LuAG:Ce
LPE method
Scintillation
Photoelectron yield

ABSTRACT

$Lu_3Al_5O_{12}$:Ce (LuAG:Ce) thin films were grown from the $PbO–B_2O_3$ (PB) and $BaO–B_2O_3–BaF_2$ (BBB) fluxes using the liquid phase epitaxy method (LPE). Photoelectron yield, its time dependence, and energy resolution were measured under α-particle excitation. A sample of the Czochralski grown bulk LuAG:Ce single crystal was measured as a reference. Photoelectron yield of the crystal was the best, followed by slightly inferior films grown from the BBB flux and still worse performing films grown from the PB flux. The samples grown from BBB flux and reference crystal exhibit the intense slow component in scintillation response. Relative energy resolution is indirectly proportional to photoelectron yield and varies from 9% to 28%. Obtained results are discussed taking into account the influence of the flux and technology used. Additionally, influence of α-particle energy deposition and substrate scintillation response are discussed.

1. Introduction

The Ce^{3+}-doped aluminum garnet scintillating crystals $Lu_3Al_5O_{12}$ (LuAG) and $Y_3Al_5O_{12}$ (YAG) belong to the family of high figure-of merit complex oxide scintillators [1–3]. Now, the Ce-doped LuAG and YAG few μm thin crystalline plates are used in high resolution 2-D imaging [4,5]. They can be prepared by mechanical processing of bulk crystals or liquid phase epitaxy (LPE) [6,7].

For good lateral resolution, the contrast, ability to record series of images within ms time range, high light yield (LY) and minimum afterglow are necessary [1]. The LY and luminescence decay can be affected by impurities and material-specific defects. E.g., Pb^{2+} contamination of LPE films grown from the PB flux is expected to result in non-radiative losses, because Pb^{2+} luminescence [8] is severely quenched at room temperature (RT).

On the other hand, slow decay components in the scintillation response were found less intense in films grown from PB flux with respect to LuAG:Ce single crystal [9]. Slower response of Czochralski grown LuAG:Ce crystals is caused by shallow electron traps [10,11] ascribed to the antisite defects (Lu^{3+} ion at octahedral Al^{3+} site) [12]. These defects arise in garnet lattice due to high growth temperature (~2000 °C), common for Czochralski or Bridgman techniques [13–15]. The LPE films are growing at much lower temperature (around 1000 °C). Consequently, negligible concentration of antisite defects should result in faster energy delivery to the Ce^{3+} centers.

Using other fluxes, e.g., BBB [16], it should be possible to avoid both Pb^{2+} contamination and antisite defects. Therefore, light yield and relative intensity of fast luminescence component could increase.

The aim of this work is to study scintillation response, N_{phels}/MeV photoelectron yield, its time dependence, and the energy resolution of LuAG:Ce films grown from the PB and BB fluxes and a Czochralski grown LuAG:Ce single crystal and to compare results obtained.

2. Experimental

The films were grown by the isothermal dipping liquid phase epitaxy onto a single crystalline LuAG (samples B-1 to B-8, P-1, P-2, and P-4) or YAG substrate (sample P-3) of (1 1 1) (samples B-1 to B-8, P-1, P-3, and P-4) or (1 1 0) (sample P-2) crystallographic orientation, 0.5 mm thickness and 20 mm in diameter. The films prepared from PB flux (samples P-1 to P-4) and BBB (samples B-1 to B-8) flux were grown under isothermal conditions at undercooling between 11.5 °C and 22 °C for growth from the PB flux, and between 20 °C and 80 °C from the BBB flux. The growth temperature was in the range of 1000–1025 °C for the PB flux, and 958.5–1060 °C for the BBB flux [17].

The thickness of the LPE films was determined by weighing and is in the range of 9.6–26.4 μm, and 4.4–15.1 μm for P-X samples and B-X samples respectively.

P-X films showed good lattice match film-substrate, and high quality surface, with exception of sample P-3 (YAG substrate). On the other hand, according to GDMS (glow-discharge mass

* Corresponding author. Tel.: +420 604958601.
E-mail address: petr.prusa@centrum.cz (P. Prusa).

0925-3467/$ - see front matter © 2010 Elsevier B.V. All rights reserved.
doi:10.1016/j.optmat.2010.04.010

spectrometry), the films contained hundreds ppm of Pt and tens ppm of Pb.

B-X films showed better luminescent properties than P-X films. Furthermore, due to higher segregation coefficient of Ce ions when using the BBB flux, higher Ce content can be achieved in films compared to the Czochralski grown single crystals. However, the growth and surface quality are negatively influenced by high viscosity and high surface tension of BBB flux. Namely, much higher number of dislocations is revealed. For all LPE films preparation the 5 N purity Y_2O_3, Al_2O_3 and CeO_2 raw powders were used.

A plate of LuAG:Ce single crystal of about 10 × 10 × 1 mm was cut and polished from parent boule crystal grown by the Czochralski method in reduction atmosphere from molybdenum crucible at Crytur Ltd., Turnov [5,10]. It served as reference sample and is noted as SC sample.

For substrates, the undoped LuAG and YAG plates were prepared in the same way. In some substrates the color centers in UV range were noted.

The N_{phels} yield, i.e., number of photoelectrons generated from the photocathode upon scintillating light exposure, was determined from the pulse height spectra. Three α-emitting radionuclides were used for scintillation response excitation: ^{241}Am (5.49 MeV) [18], ^{239}Pu (5.16 MeV) [19], and ^{244}Cm (5.80 MeV) [20]. The reference crystal was measured also under γ excitation of ^{137}Cs (661.6 keV) [21]. Dependence of N_{phels} on the shaping time t within 0.5–10 μs range and energy resolution (FWHM) was measured.

The experimental set-up for photoelectron yield and FWHM measurement consists of an HPMT (hybrid photomultiplier) model DEP PPO 475B, an ORTEC model 672 spectroscopy amplifier, a multichannel buffer ORTEC 927TM, and PC. This set-up works in pulse–height mode [22]. Measured samples were placed on HPMT, substrate in optical contact with HPMT window, film itself on the other (upper) side. Uncollimated radioactive sources were placed directly onto the LPE film surface, see Fig. 3 in Ref. [23], i.e., no energy loss in air occured. Because of the source, a reflector could not be used. Thus, the light collection efficiency was significantly lower than usual. All measurements were performed in air at RT. One set of measurement was performed with an edge filter (edge cca 460 nm) placed between the sample and HPMT window and the other one without such a filter.

Additionally, the photoluminescence decays were measured at RT under nanosecond pulsed flashlamp excitation and using time correlated single photon counting method, for other details and the evaluation of non-radiative losses, see Ref. [24].

2.1. Energy deposition of α-particle in thin films

Photoelectron yield (N_{phels}/MeV) is defined as number of photoelectrons (N_{phels}) emitted from photocathode per 1 MeV of absorbed energy E_{abs}, i.e., $N_{phels}/MeV = N_{phels}/E_{abs}$. Simple calculation of N_{phels}/MeV yield is possible when E_{abs} is equal to the energy of α-particle E_α, i.e., α-particle deposits energy only in the film. It is fulfilled for films with thickness greater than the penetration range of α-particles in LuAG (R_{LuAG}). Only one peak is present in spectrum in such a case [23].

Calculated R_{LuAG} for ^{239}Pu, ^{241}Am and ^{244}Cm sources are 9.4, 10.5 and 11.4 μm. Obviously, R_{LuAG} was greater than thickness (d) of some LPE films, see Table 1. Situation is explained in Fig. 3 in Ref. [23]. Since α-particles are emitted in all directions, it is possible that $\cos\theta < d/R_{LuAG}$, where θ is the penetration angle of α-particle. Then, the entire E_α is deposited in the LPE film. If $\cos\theta > d/R_{LuAG}$, particles pass through the LPE film into the substrate and deposits only part of E_α in the LPE film. Due to smaller light yield of undoped substrate [23], the response of particles penetrating into the substrate is lower. Therefore, two peaks are present in spectra if $R_{LuAG} > d$, see Fig 1. Peak 1 corresponds to particles depositing entire E_α in the LPE film, Peak 2 to particles passing through the LPE film into the substrate.

Table 1
Parameters of LuAG:Ce LPE films: thickness; Ce concentration (X in $Ce_XLu_{3-X}Al_5O_{12}$); $N_{\alpha,e}/N_{\alpha,d}$, number of α-particles depositing entire E_α in the LPE film to the number of detected particles; N_{phels}/MeV, photoelectron yield (number of photoelectrons per 1 MeV); $K_{f/e}$, relative intensity of the fast fraction (100% = entire response). FWHM was measured under ^{239}Pu excitation, other quantities under ^{241}Am excitation, and SC (γ) under ^{137}Cs excitation.

Sample	Thickness [μm]	$N_{\alpha,e}/N_{\alpha,d}$ [%]	N_{phels}/MeV	$K_{f/e}$ [%]	FWHM [%]	X
P-1	26.4	100	100.4	94	20.1	0.013
P-2	9.6	91	68.9	100	28.0	0.029
P-3	20.0	100	53.9	100	20.7	0.015
P-4	17.8	100	29.0	98	24.9	0.017
B-1	4.4	42	201.5	60	22.0	0.044
B-2	10.0	95	281.3	54	11.9	0.048
B-3	5.2	50	237.5	51	13.8	0.052
B-4	6.8	65	308.2	56	18.6	0.024
B-5	6.0	57	314.1	53	13.3	0.016
B-6	6.0	57	262.8	52	14.1	0.027
B-7	8.0	76	286.8	48	11.0	0.020
B-8	12.0	100	293.3	47	10.9	0.009
SC	~1000	100	389.0	53	9.0	0.009
SC (γ)	~1000	–	1524.0	49	11.9	0.009

$N_{\alpha,e}$ is the number of α-particles depositing entire E_α in the LPE film and $N_{\alpha,d}$ number of all detected α-particles entering the LPE film. It was shown in [23] that $N_{\alpha,e}/N_{\alpha,d} = d/R_{LuAG}$. Calculated percentage of α-particles depositing entire E_α in the film is in Table 1. The position and width of peak 1 in Fig. 1 was crucial for N_{phels} and FWHM evaluation. The distance between peak 1 and 2 should be large, and/or peak 2 small for simple evaluation. The α-particles passing through the LPE film also generated UV scintillation photons in the substrate [25]. Moreover, quantum efficiency of HPMT in the UV light region was cca 2× higher than that for scintillation photons from the LPE film [22]. Finally, the color centers in the substrates also contributed to scintillation response. As the contribution from substrate rose, the peaks were getting closer to each other which lead to peak overlap (Fig. 1 – red curve). It made the evaluation of N_{phels} very difficult. The overlap was a problem especially for longer shaping times, because of slow decay of the UV substrate luminescence [25].

A suitable filter between the sample and HPMT can diminish such a problem. The response of substrate decreased and peaks

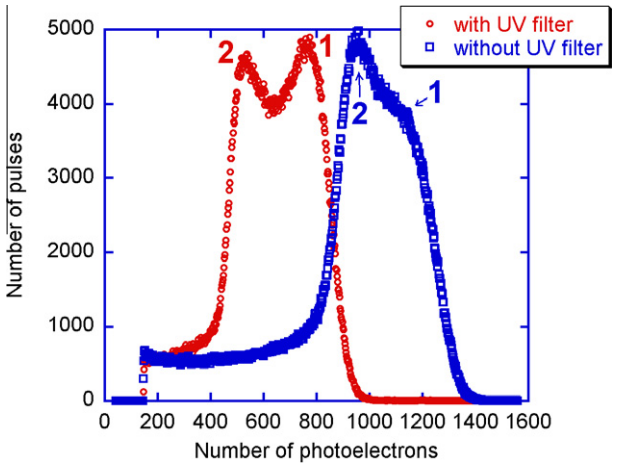

Fig. 1. Pulse height spectra of sample B-3, thickness 5.2 μm, shaping time 1 μs, source ^{241}Am measured with (red curve) and without (blue curve) UV filter (For interpretation of the references to colour in this figure legend, the reader is referred to the web version of this article).

were better separated (Fig. 1 – blue curve) even for t = 10 μs. N_{phels} decreased due to reflection losses at filter surfaces. According to experimental results, the decrease was ~25% and was almost the same for all the samples. Hence, time dependence of N_{phels} could be evaluated.

3. Results and discussion

The non-exponential photoluminescence decay indicated significant energy loss in samples P-X, i.e., quenching of luminescence, which was estimated (see [24] for details) of about 31% with respect to the ideal (single exponentially decaying) sample. Energy losses in B-X were smaller, of about 11% in average.

Values of N_{phels}/MeV for, 1 μs shaping and ^{241}Am excitation source measured without filter are given in Table 1 for all the samples. For other excitation sources, the results were the same within an experimental error. Comparison of γ-(^{137}Cs) and α-(^{241}Am) particle excitation of reference crystal (sample SC) showed much more significant difference arising from different stopping power of α-particles and electrons produced by γ-ray interaction: $N_{phels}/MeV_{SC,137Cs}$ = 1524 and $N_{phels}/MeV_{SC,241Am}$ = 389. The γ/α yield ratio is about 3.9 [9].

B-X samples showed the highest N_{phels}/MeV yield among the LPE-grown films. Even the worst film grown from BBB flux (B-1) had two times higher N_{phels}/MeV value than the best sample grown from the PB flux (P-1). However, reference LuAG:Ce crystal exhibited N_{phels}/MeV approximately 24% higher than the best sample grown from BBB flux (B-5).

The PB flux is the source of Pb^{2+} contamination, which quenches the scintillation response of P-X samples. The energy loss was bigger than that calculated from the luminescence decay kinetics, so that significant part of excitation energy never reached the Ce luminescence centers. Moreover, in B-X samples there was higher concentration of Ce due to higher segregation coefficient. Although the Pb contamination was negligible in B-X samples and Ce concentration was higher than in Czochralski grown crystal the B-X samples still exhibited lower value of N_{phels}/MeV with respect to SC. Defects in B-X samples may be responsible for such an effect.

As mentioned above, the fast scintillation decay is also required. Scintillation decay in LuAG:Ce can be treated as a sum of two exponential terms. The typical values of decay times are about 50–60 ns and 400–1000 ns for the faster and slower component, respectively [9,10,26]. Using t = 0.5–10 μs for the measurement of N_{phels} yield of such material, we scanned over the slower decay process (the fast component has decayed entirely within 500 ns). N_{phels} yield dependence on the shaping time should follow the dependence $N_{phels}(t) = m_1 - m_2\exp[-m_3 t]$ [9], where m_i are parameters obtained by a fit, see Fig. 2. Afterwards, calculation of the relative intensity of the fast fraction of the entire response $K_{f/e}$ takes place: $K_{f/e} = 1 - (m_2/m_1)$ [23].

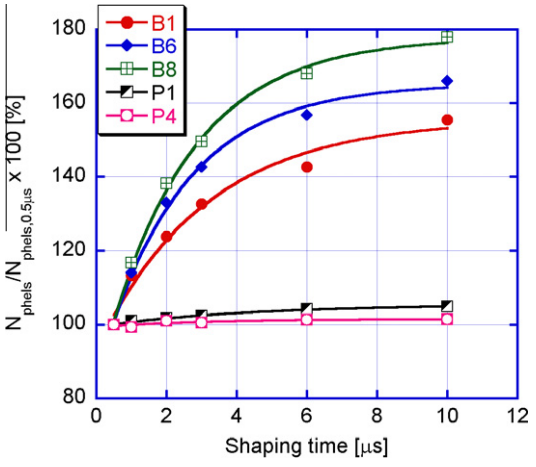

Fig. 2. Time dependence of N_{phels} photoelectron yield in the range 0.5–10 μs shaping time. Photoelectron yield is normalized to value measured at shaping time t = 0.5 μs. $K_{f/e}$ is the relative intensity of fast component of scintillation response.

$K_{f/e}$ values are presented in Table 1. $K_{f/e}$ varied from 47% to 60% for the samples B-X, 94–100% for the samples P-X flux, and equaled 53% for the sample SC. In the terms of $K_{f/e}$ value, the performance of samples B-X and SC was worse compared with the samples P-X. $K_{f/e}$ values of B-X samples and sample SC were almost the same.

Probably, at RT the delayed radiative electron–hole recombination was damped due to non-radiative traps created by Pb^{2+} centers, so less intense slow component of scintillation response was observed for samples P-X. However, the photoelectron yield decreased at the same time. In Czochralski grown crystals, the slowdown of decay process is caused by the shallow traps related to Lu_{Al} antisite defects, but these were not present in LPE films. Thus, slowdown of decay process in samples B-X was caused by other defects, created probably due to flux viscosity.

Parameter $1/m_3$ is directly proportional to decay time of slower component. No significant differences of parameter $1/m_3$ were observed among LPE films and sample SC.

Measured pulse height spectra were also used for the energy resolution evaluation by using the Gaussian fit to the peak-of-total-absorption band and evaluating full width at half maximum (FWHM). FWHM was generally decreasing with the increasing N_{phels}/MeV yield. Therefore, FWHM was the best for sample SC (9%), followed by the samples B-X (11–22%), films P-X exhibited the worst FWHM (20–28%), see Table 1.

4. Conclusions

Comparing the fluxes, it is obvious that the N_{phels}/MeV yield was better for samples B-X (BBB flux). However, even the best films grown from the BBB flux were still slightly worse compared to the SC sample. On the other hand, $K_{f/e}$ value was much higher for samples P-X (PB flux). Also, P-1, P-2 and P-4 samples had better surface morphology than the rest of the films. Surface morphology of sample P-3 was negatively affected by heteroepitaxial growth, for films grown from the BBB flux by high viscosity of this flux. $K_{f/e}$ value indicates that almost all scintillation photons were emitted within 0.5 μs for samples P-X. Comparable $K_{f/e}$ value was measured for Czochralski grown crystal and films grown from the BBB flux. FWHM values varied from 11% to 28% for LPE films, which was worse compared to Czochralski grown crystal (9%). FWHM was approximately indirectly proportional to N_{phels}. Because high $K_{f/e}$ value and low N_{phels}/MeV yield of P-X samples was probably due to Pb contamination, it may be possible to improve their performance by optimization of the Ce and Pb ratio in the films. The films grown from the BBB flux can become an alternative to Czochralski grown crystals, if their photoelectron yield is increased by about 30%.

Finally, this experimental study revealed and explained the shape of pulse height spectra measured with LPE films of very small thickness, where incomplete energy deposition of α-particle occurs, and substrate response is not negligible. These conditions make evaluation of the data difficult or impossible, but simple solution for this problem, i.e., usage of a suitable UV filter, was found.

Acknowledgment

This work was supported by the GA AS of the Czech Republic (Grant No. KAN300100802).

References

[1] M. Nikl, Meas. Sci. Technol. 17 (2006) R37.
[2] A. Lempicki, M.H. Randles, D. Wisniewski, M. Balcerzyk, C. Brecher, A.J. Wojtowicz, IEEE Trans. Nucl. Sci. 42 (1995) 280–284.
[3] M. Moszynski, T. Ludziejewski, D. Wolski, W. Klamra, L.O. Norlin, Nucl. Instrum. Methods Phys. Res. A 345 (1994) 461.
[4] T. Martin, J. Koch, J. Synch. Radiat. 13 (2006) 180.
[5] J. Tous, M. Horvath, L. Pina, K. Blazek, B. Sopko, Nucl. Instrum. Methods Phys. Res. A 591 (2008) 264.
[6] Y. Zorenko, Phys. Status Solidi. C 2 (2005) 375.
[7] J.M. Robertson, M.V. van Tool, J.P.H. Heynen, W.H. Smith, T. de Boer, Philips J. Res. 35 (1980) 354.
[8] V. Babin, V. Gorbenko, A. Makhov, J.A. Mares, M. Nikl, S. Zazubovich, Y. Zorenko, J. Lumin. 127 (2007) 384.
[9] P. Prusa, T. Cechak, J.A. Mares, M. Nikl, A. Beitlerova, N. Solovieva, Y. Zorenko, V. Gorbenko, Appl. Phys. Lett. 92 (2008) 041903.
[10] M. Nikl, Phys. Status Solidi. A 202 (2005) 201.
[11] M. Nikl, V.V. Laguta, A. Vedda, Phys. Status Solidi. A 204 (2007) 683.
[12] M. Nikl, E. Mihokova, J. Pejchal, A. Vedda, Y. Zorenko, K. Nejezchleb, Phys. Status Solidi. B 242 (2005) R119.
[13] M.K. Ashurov, Y.K. Voronko, V.V. Osiko, A.A. Sobol, M.I. Timoshechkin, Phys. Status Solidi. A 42 (1977) 101.
[14] M.M. Kuklja, J. Phys.: Condens. Matter 12 (2000) 2953.
[15] C.R. Stanek, K.J. McClellan, M.R. Levy, R.W. Grimes, Phys. Status Solidi. B 243 (2006) R75.
[16] M. Kucera, K. Nitsch, H. Stepankova, M. Marysko, P. Reiche, Phys. Status Solidi. A 198 (2003) 407.
[17] M. Kucera et al., J. Crystal Growth 312 (2010) 1538–1545.
[18] Y.A. Akovali, Nucl. Data Sheet 72 (1994) 191.
[19] M.R. Schmorak, Nucl. Data Sheet 66 (1992) 839.
[20] E.N. Shurshikov, Nucl. Data Sheet 49 (1986) 785.
[21] J.K. Tuli, Nucl. Data Sheet 72 (1994) 355.
[22] J.A. Mares, A. Beitlerova, M. Nikl, et al., Radiat. Meas. 42 (2007) 533.
[23] P. Prusa, M. Nikl, J.A. Mares, M. Kucera, K. Nitsch, A. Beitlerova, Phys. Status Solidi. A 206 (2009) 1377–1383.
[24] J. Ruzicka, D. Niznansky, M. Nikl, R. Kucerkova, C. Cannas, J. Mater. Res. 25 (2010) 229–234.
[25] V. Babin, K. Blazek, A. Krasnikov, K. Nejezchleb, M. Nikl, T. Savikhina, S. Zazubovich, Phys. Status Solidi. C 1 (2005) 97.
[26] M. Nikl, E. Mihokova, J.A. Mares, A. Vedda, C. D'Ambrosio, Phys. Status Solidi. B 181 (2000) R10;
R. Autrata, P. Schauer, Jos Kvapil, J. Kvapil, J. Phys. E 11 (1978) 707.

Early View publication on www.interscience.wiley.com
(issue and page numbers not yet assigned;
citable using Digital Object Identifier – **DOI**)

Phys. Status Solidi A, 1–7 (2009) / **DOI** 10.1002/pssa.200825050

physica status solidi a
www.pss-a.com
applications and materials science

The α-particle excited scintillation response of YAG:Ce thin films grown by liquid phase epitaxy

Petr Prusa[*,1,2], Martin Nikl[2], Jiri A. Mares[2], Miroslav Kucera[3], Karel Nitsch[2], and Alena Beitlerova[2]

[1] Faculty of Nuclear Sciences and Physical Engineering, Czech Technical University in Prague, Brehova 7, 11519 Prague, Czech Republic
[2] Institute of Physics AS CR, Cukrovarnicka 10, 16253 Prague, Czech Republic
[3] Faculty of Mathematics and Physics, Charles University, Ke Karlovu 5, 12116 Prague, Czech Republic

Received 30 January 2009, revised 9 March 2009, accepted 18 March 2009
Published online 7 May 2009

PACS 78.20.–e, 78.47.Cd, 78.60.–b, 81.15.Lm

* Corresponding author: e-mail petr.prusa@centrum.cz, Phone: +420 604 958 601

$Y_3Al_5O_{12}$:Ce (YAG:Ce) thin films were grown from PbO-, BaO-, and MoO_3-based fluxes using the liquid phase epitaxy (LPE) method. Photoelectron yield, its time dependence within 0.5–10 μs shaping time, and energy resolution of these samples were measured under α-particle excitation. For comparison a sample of the Czochralski grown bulk YAG:Ce single crystal was measured as well. Photoelectron yield values of samples grown from the BaO-based flux were found superior to other LPE films and comparable with that of the bulk single crystal. The same is valid also for the time dependence of photoelectron yield. Obtained results are discussed taking into account the influence of the flux and technology used. Additionally, α particle energy deposition in very thin films is modelled and discussed.

1 Introduction The Ce^{3+}-doped aluminium garnet scintillating crystals $Y_3Al_5O_{12}$ (YAG) and $Lu_3Al_5O_{12}$ (LuAG) belong to the family of high figure-of-merit complex oxide scintillators [1, 2]. Nowadays, the Ce-doped YAG and LuAG thin crystalline plates are used in high resolution X-ray 2D-imaging with resolution even in (sub)μm range [3, 4]. For such a resolution, a few μm thin scintillating plates are necessary and this is already difficult to obtain by mechanical processing, especially when larger dimensions above approx. 25 mm diameter are required. Therefore, other technologies, namely liquid phase epitaxy (LPE) method [5, 6], can also be used to prepare thin single crystalline films.

For good lateral resolution the contrast, ability to record series of images within ms time range, high photoelectron (light) yield, fast decay of luminescence, and minimum afterglow are necessary [1]. The light yield and luminescence decay can be negatively affected by impurities and material-specific defects. The light yield of LPE films grown from the standard PbO-based flux can be also considerably lower than that for crystals produced by the Czochralski or Bridgman techniques because of Pb^{2+} contamination and due to additional impurities coming from the flux. The Pb^{2+} luminescence has been described recently in the LuAG:Ce LPE films [7]. Since it is severely quenched at room temperature, the decrease of scintillation efficiency and nonradiative losses are expected due to the Pb contamination for both LuAG:Ce and YAG:Ce LPE films.

On the other hand, slow decay components in the scintillation response were found less intense in LPE films with respect to single crystals of LuAG:Ce [8]. It was shown that slower response of Czochralski-grown LuAG:Ce crystals is caused by shallow electron traps [9, 10] ascribed to the antisite defects (Lu^{3+} ion at the octahedral Al^{3+} site) [11]. These dominant structural defects arise in garnet lattice due to high growth temperature (~2000 °C), when Czochralski or Bridgman techniques are used [12–14]. The LPE method enables the growth of thin films at much lower temperature (around 1000 °C). Positive consequence of lower growth temperature is much lower content (if any) of antisite defects which results in

faster energy delivery to the Ce^{3+} centers in LuAG and possibly also in YAG, structures.

As mentioned above, using the PbO-based flux the LPE-grown aluminum garnet films can be manufactured cheaper than very thin plates cut from the Czochralski or Bridgman grown bulk crystals, but their light yield is lowered due to Pb^{2+} contamination. Using other fluxes, such as those based on MoO_3 [15] or BaO [16], quenching effect could be diminished and light yield increased accordingly. Thus, such LPE-grown films might have the overall scintillation efficiency comparable with Czochralski or Bridgman-grown aluminum garnet crystals and even faster scintillation response.

The aim of this study is to compare the scintillation response and other properties of YAG:Ce LPE films grown from the PbO-, BaO-, or MoO_3-based fluxes. Namely, their photoelectron yield (N_{ph}), its time dependence, and finally the energy resolution are systematically measured. A Czochralski grown YAG:Ce single crystal is used as a reference sample.

2 Experimental

2.1 Growth of YAG:Ce LPE films The LPE garnet films were grown by the isothermal dipping liquid phase epitaxy (LPE) onto single crystalline YAG substrate of (111) crystallographic orientation, 0.5 mm thickness and 20 mm in diameter. The films prepared from the PbO–B_2O_3 flux (samples P-1 to P-4) and BaO–B_2O_3–BaF_2 flux (samples B-1 to B-3) were grown under isothermal conditions from supercooled melts at undercooling between 3 °C and 60 °C. The growth temperature was in the range of 930–1080 °C. The films grown from the MoO_3–Li_2MoO_4 flux (samples M-1 to M-5) were grown isothermally by transfer of garnet nutrient through a temperature gradient. Details of LPE growth of garnet films from the PbO- and BaO-based fluxes were published elsewhere [17]. The thicknesses of the LPE films were determined by weighing and were in the range of 3–15 μm. Since the electron penetration depth in YAG host varies from 0.4 μm to 6 μm for energies of electron between 10 keV and 40 keV [18] (energy range of most electron microscopes), such thin LPE films may also be used as the detection element in the electron microscopy [19].

The LPE films grown from the PbO-based flux exhibited excellent crystallographic properties with good lattice match of film and substrate and high quality surface, Fig. 1a. However, the films contain mainly divalent and tetravalent Pb and Pt ions, respectively, and as a consequence, a variety of point defects can be created. It results in appearance of the slow decay component in the luminescence of Ce^{3+} centers [7] and additional absorption bands in the UV spectral region [20].

YAG:Ce LPE films with superior luminescent properties were obtained from the BaO-based flux. The photoluminescence decay curves do not indicate any energy transfer/loss or quenching of luminescence [17]. Furthermore, due to higher segregation coefficient of Ce ions in the BaO-based flux, higher Ce content can be achieved in films compared to the Czochralski grown single crystals. However, the growth and surface quality are negatively influenced by high viscosity and high surface tension of the BaO-based flux. Namely, much higher number of dislocations is revealed, Fig. 1b.

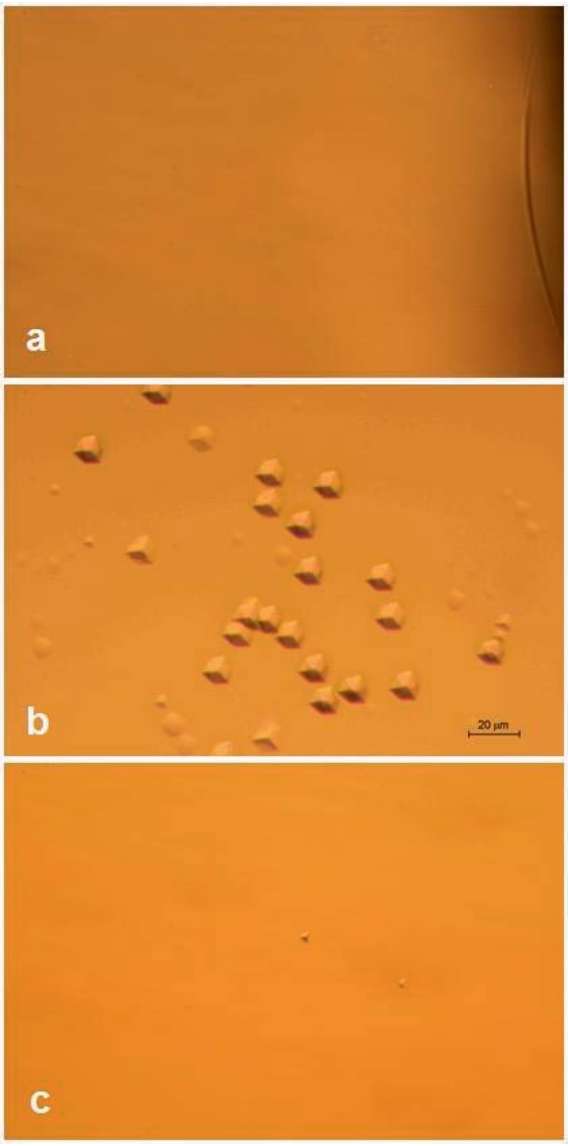

Figure 1 (online colour at: www.pss-a.com) Optical microscopy of the surface of Ce:YAG films grown on ⟨111⟩ oriented YAG substrate: (a) defect-free surface of a film grown from the PbO-based flux (the sample edge is shown on the right side of the picture for comparison), (b) surface pits originating from dislocations in ⟨111⟩ oriented YAG:Ce LPE film grown from the BaO-based flux, (c) isolated triangular pits in a film grown from the MoO_3-based flux.

The MoO_3-based flux has essentially zero volatility, low reactivity with the Pt crucible, and low viscosity. Excellent emission properties of LPE films and single-

exponential decay of 530 nm Ce^{3+} emission with 58 ns decay time were observed [21]. The surface morphology is comparable with films grown from the PbO flux, Fig. 1c. However, very small growth rate of 0.04–0.1 μm/min is achieved, which is at least ten times less with respect to PbO flux. Moreover, well-controlled temperature profile is required in growth process which makes this technological approach more demanding with respect to the other two fluxes described above.

YAG:Ce bulk single crystal used as a reference sample and undoped YAG single crystal for substrates were grown by Czochralski technique under reduction atmosphere from a molybdenum crucible in CRYTUR Ltd., Turnov [3, 9]. To obtain the reference crystal the plate of about 7 × 7 × 1 mm was cut from the parent YAG:Ce boule and polished up to an optical grade. The oriented substrates were cut from the parent boule and mechanico-chemically polished. For preparation of both the bulk crystals and LPE films the same 5N purity Y_2O_3 and 4N purity Al_2O_3 and CeO_2 raw powders were used.

2.2 The α-excited scintillation response of YAG:Ce LPE films The N_{ph} photoelectron yield, i.e. number of photoelectrons generated from the photocathode of the photomultiplier upon scintillating light exposure, was determined from the pulse height spectra. As the γ-ray excitation can't be used due to low thickness of LPE films, we use the α-particle excitation. Only the reference crystal was additionally measured also under γ excitation of ^{137}Cs (661.6 keV) [22]. Three α-emitting radionuclides were used: ^{241}Am (5.4856 MeV) [23], ^{239}Pu (5.1566 MeV) [24], and ^{244}Cm (5.8048 MeV) [25]. Dependence of N_{ph} yield and energy resolution on the shaping time was measured as well within 0.5–10 μs range.

The experimental set-up consists of an HPMT photomultiplier (model DEP PPO 475B), an ORTEC NIM model 672 spectroscopy amplifier, and a multichannel buffer in PC. This set-up works in pulse-height mode [26]. Radioactive source was placed directly onto sample surface to ensure minimum energy loss of α-particles in air. All measurements were performed at room temperature.

2.3 α-particle energy deposition in thin scintillation films Calculation of number of photoelectrons emitted per 1 MeV of absorbed energy requires that known amount of energy is absorbed in the scintillation film, i.e. entire energy of α-particle is absorbed. This requirement is fulfilled for scintillation films with thickness greater than the range of α-particles in YAG. Typical spectrum of such a film is displayed in Fig. 2.

The penetration range of α-particle in YAG R_{YAG} (cm) was calculated using the Eq. (1) [27]:

$$R_{YAG} = 2.3\times10^{-4}\frac{\sqrt{M_{eff,YAG}}}{\rho_{YAG}}R_{air}, \quad (1)$$

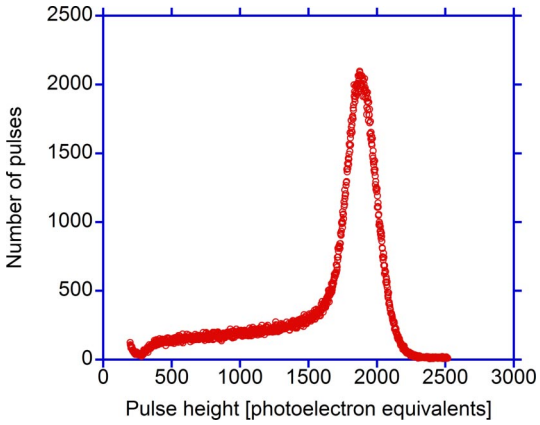

Figure 2 (online colour at: www.pss-a.com) Typical pulse height spectrum of YAG LPE film (sample P-1) excited with α-particles from ^{241}Am with thickness (d = 14.6 μm) greater than the α-particle range. Peak position and width determine N_{ph} yield and energy resolution, respectively.

where $M_{eff,YAG}$ is effective atomic mass of YAG, R_{air} is range of α-particle in air and ρ_{YAG} (kg cm^{-3}) is the density of YAG. The effective atomic mass can be found using the Eq. (2) [27]:

$$\frac{1}{\sqrt{M_{eff,YAG}}} = \sum_i \frac{\omega_i}{\sqrt{M_i}}, \quad (2)$$

where ω_i is the weight fraction of the i-th constituent and M_i is the atomic mass of the i-th constituent. Thus, $M_{eff,YAG}$ = 33.7.

Range of α-particle in air R_{air} (cm) can be found using the Eq. (3) [28]

$$R_{air} = 1.24E_\alpha - 2.62, \quad (3)$$

where E_α (MeV) is energy of α-particle.

Calculated ranges in YAG and air for ^{239}Pu, ^{241}Am and ^{244}Cm sources are presented in the Table 1. Obviously, R_{YAG} is greater than thickness (d) of some samples, see Table 2. However, if

$$\cos\theta < \frac{d}{R_{YAG}}, \quad (4)$$

where θ is the penetration angle of alpha particle, the entire energy of alpha particle is deposited. This case is displayed in Fig. 3.

Table 1 Range of α-particles of ^{239}Pu, ^{241}Am, and ^{244}Cm source in YAG (R_{YAG}) and in air (R_{air}), calculated using Eqs. (1)–(3).

material	^{239}Pu	^{241}Am	^{244}Cm
R_{YAG} (μm)	11.1	12.3	13.4
R_{air} (mm)	37.7	41.8	45.6

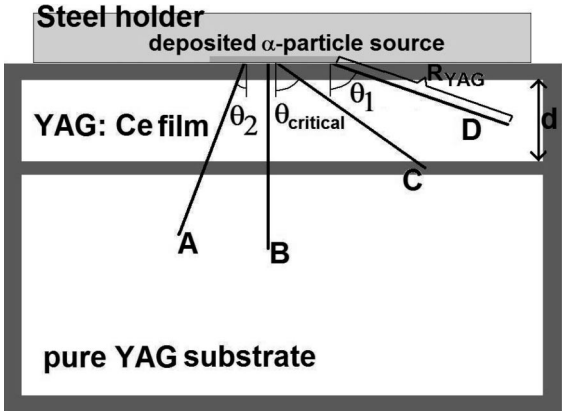

Figure 3 LPE film has a thickness (d) of about few μm, often lower than the penetration range of α-particles in YAG, i.e. R_{YAG}. In this case, some particles (particles A and B) penetrating under angle $\theta_2 < \theta_{critical}$ deposits only part of its energy in the LPE film. However, other particles (C and D) penetrating under the angle $\theta_1 \geq \theta_{critical}$, where $\theta_{critical} = \arccos(d/R_{YAG})$, deposits its entire energy in the scintillation film.

Number of α-particles depositing the entire energy in the film during the measurement, i.e. $N_{\alpha,e}$, is given by

$$N_{\alpha,e} = \frac{2\pi R_{YAG}^2 - (2\pi R_{YAG}(R_{YAG} - d))}{4\pi R_{YAG}^2} At = \frac{d}{2\pi R_{YAG}} At\,, \tag{5}$$

where A is activity of the radioactive source and t is time of measurement. Likewise, number of detected α-particles, i.e. number of particles emitted into the LPE film, $N_{\alpha,d}$,

$$N_{\alpha,d} = \frac{2\pi R_{YAG}^2}{4\pi R_{YAG}^2} At = \frac{1}{2} At\,, \tag{6}$$

and finally is given by:

$$\frac{N_{\alpha,e}}{N_{\alpha,d}} = \frac{d}{R_{YAG}} \times 100(\%)\,. \tag{7}$$

Equation (7) shows the ratio of α-particles depositing entire energy in the scintillation film to the number of detected α-particles. Calculated percentage of particles depositing entire energy displays Table 2. 26–31% of α-particles was fully absorbed in the thinnest sample M-3, which still was sufficient for N_{ph} and FWHM determination. Illustrative example of a typical pulse height spectrum for thin LPE film, which is sample M-4, is given in Fig. 4.

3 Results Values of N_{ph}/MeV for all samples, 1 μs shaping time and all excitation sources are given in Fig. 5. It is interesting to note that N_{ph}/MeV is the lowest for ^{239}Pu and the highest for ^{244}Cm for each shaping time and all the samples. Lower linear stopping power of higher energy α-particles leads to lower quenching due to excitation interactions in the ionization track. However, the magnitude of difference in response is quite small. Comparison of γ-(^{137}Cs) and α-(^{241}Am) particle excitation of reference crystal (RC) shows much more significant difference corresponding to big difference between stopping power of α-particle and secondary electron produced by γ-ray interaction: $N_{ph}/\mathrm{MeV}_{RC,137Cs} = 1849$ and $N_{ph}/\mathrm{MeV}_{RC,241Am} = 349$. The γ/α yield ratio is about 5.3 which is noticeably higher value with respect to LuAG:Ce where it was measured [8] about 3.9.

Table 2 Thickness of measured YAG:Ce LPE films, the percentage of detected α-particles depositing the whole energy $N_{\alpha,e}/N_{\alpha,d}$ for ^{239}Pu, ^{241}Am, and ^{244}Cm sources calculated using Eq. (7), relative Ce concentration, and relative FWHM measured using ^{239}Pu excitation source for 1 μs shaping time. The relative Ce concentrations $C_{Ce,rel}$ were determined relatively to the reference crystal (RC) from optical absorption measurement at wavelength 455 nm, i.e. $C_{Ce,rel}$ (RC) is defined as equal to 1, $C_{Ce,rel}$ (X) = $C_{Ce,rel}$ (RC) × α_X/α_{RC}, where $C_{Ce,rel}$ (RC) and $C_{Ce,rel}$ (X) are the relative Ce concentrations in the reference crystal and in the LPE film X, respectively. The α_X and α_{RC} are the absorption coefficients of reference crystal and LPE film X, respectively.

sample	thickness (μm)	$N_{\alpha,e}/N_{\alpha,d}$			α_X (cm^{-1})	$C_{Ce,rel}$(X) (rel.u.)	FWHM (%)
		^{239}Pu	^{241}Am	^{244}Cm			
P-1	14.6	100	100	100	70	0.9	10.0
P-2	8.0	72	65	59	35	0.4	10.3
P-3	12.8	100	100	95	120	1.5	18.4
P-4	12.2	100	99	91	80	1.0	48.4
B-1	4.4	40	36	33	280	3.5	10.9
B-2	7.0	63	57	52	240	3.0	9.6
B-3	5.6	51	46	42	270	3.4	10.2
M-1	4.0	36	33	30	22	0.3	13.9
M-2	13.6	100	100	100	47	0.6	23.3
M-3	3.3	30	27	25	26	0.3	12.6
M-4	4.7	43	39	35	30	0.4	8.9
M-5	3.5	31	28	26	unknown	unknown	9.8
RC	300.0	100	100	100	80	1.0	10.6

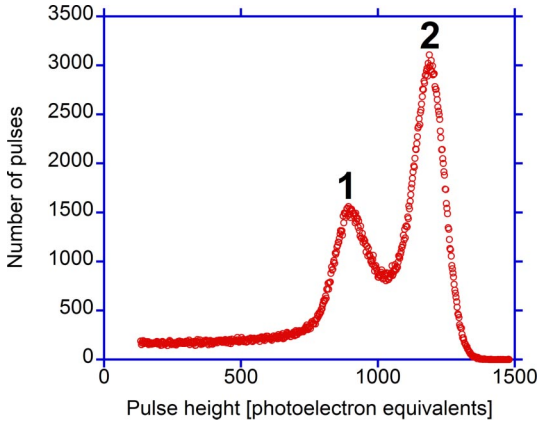

Figure 4 (online colour at: www.pss-a.com) Pulse height spectrum of YAG LPE film M-4 excited with α-particles from ^{241}Am. Thickness ($d = 4.7$ μm) of this film is smaller than penetration range of α-particle in YAG, i.e. R_{YAG}, which leads to creation of two peaks. Peak 1 is formed by particles crossing the scintillation film, peak 2 by particles depositing its entire energy $(N_{\alpha,e}/N_{\alpha,d})_{experimenat} = 0.57$.

The samples grown from the BaO-based flux show the lowest variability in N_{ph}/MeV, as well as the highest N_{ph} yield values. The M-5 sample has the highest N_{ph} yield value among the samples grown from the MoO_3-based flux and it is comparable even with the samples grown from the BaO-based flux. On the other hand, the worst N_{ph} yield among the MoO_3 flux group, sample M-2, exhibits about three times lower N_{ph} yield than M-5. Also samples grown from the PbO-based flux show significant differences. The best sample P-2 almost reaches the N_{ph} yield of the worst sample from BaO group (B-3), while the worst sample P-4 exhibits approximately four times lower N_{ph} yield.

Comparing fluxes in terms of α-particle excited N_{ph} yield, we can conclude that samples grown from the BaO-based flux were superior to the samples grown from the MoO_3-based flux, which were slightly superior to the samples grown from the PbO-based flux. Due to big scatter of N_{ph} yield of the samples grown from the MoO_3-based flux, however, they could appear as good as the samples grown from the BaO based flux, if technological parameters can be optimized further. Comparison of LPE films with the reference crystal shows that N_{ph} yield values of the best films (P-2, M-5, B-1, B-2, B-3) are approximately the same or even better than that of the reference crystal.

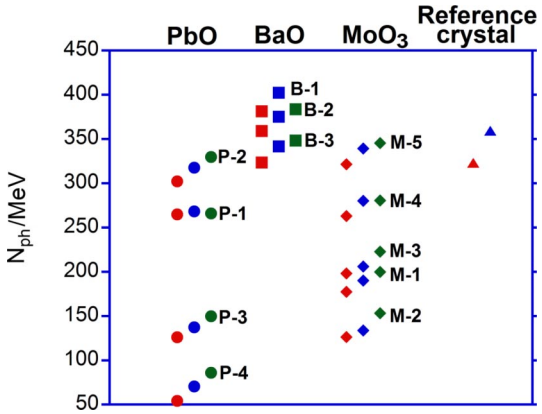

Figure 5 (online colour at: www.pss-a.com) N_{ph}/MeV of YAG LPE film samples grown from the PbO-based flux (circles), BaO-based flux (squares), MoO_3-based flux (diamonds), and Czochralski method grown reference crystal (triangles), excited with ^{239}Pu (red), ^{241}Am (blue), and ^{244}Cm (green), measured with 1 μs shaping time.

The PbO-based flux is the source of Pb^{2+} contamination, which quenches the scintillation response of samples grown from the PbO-based flux. However, it is not the case of samples grown from the MoO_3-based flux, which also exhibit lower N_{ph} yield than the samples grown from the BaO-based flux. LPE technology using MoO_3-based flux is apparently more demanding as for the growth process control. It is worth noting that better performance of the samples grown from the BaO-based flux could be partially caused by surface defects acting as "lightguides" conducting the scintillation photons out of the film towards the photocathode of HPMT.

As mentioned above, the fast scintillation decay is also required for high figure-of-merit scintillators. Scintillation decay in Ce-doped aluminum garnets can be treated as a sum of two exponential terms. In LuAG:Ce the typical values of the scintillation decay times are of about 50–60 ns and 400–1000 ns for the faster and slower components, respectively [8, 9, 29]. In YAG:Ce the situation is qualitatively similar, but slower scintillation components are less intense which is well observed in less pronounced time dependence of N_{ph} response [30]. Faster component is due to prompt electron–hole recombination at the Ce^{3+} centres, while the slower one is due to the delayed recombination process between traps and the same centres [31]. Using shaping times in the range 0.5–10 μs for the measurement of N_{ph} yield of such material, we scan over the slower decay process (as the fast component has decayed entirely within 500 ns). Two exponential approximation of the $I(t)$ decay intensity is given by

$$I(t) = A \times \exp[-t/\tau_1] + B \times \exp[-t/\tau_2], \quad (8)$$

where τ_1 and τ_2 are the decay times of the faster and slower scintillation components, A and B are proportional to intensity of fast and slow scintillation decay, and t is time ($t = 0$ is time of α-particle interaction). The expected time dependence of the light sum S (integral of $I(t)$ up to time t_0) for times $t_0 \gg \tau_1$ thus will be given by

$$S(t_0) = \int_0^{t_0} I(t)\,\mathrm{d}t = A\tau_1 + B\tau_2 - B\tau_2 \exp[-t_0/\tau_2], \quad (9)$$

and since $N_{ph} \sim S(t)$, the measured dependence of N_{ph} yield should thus follow the time dependence:

$$N_{ph}(t) = m_1 - m_2 \exp[-m_3 t], \quad (10)$$

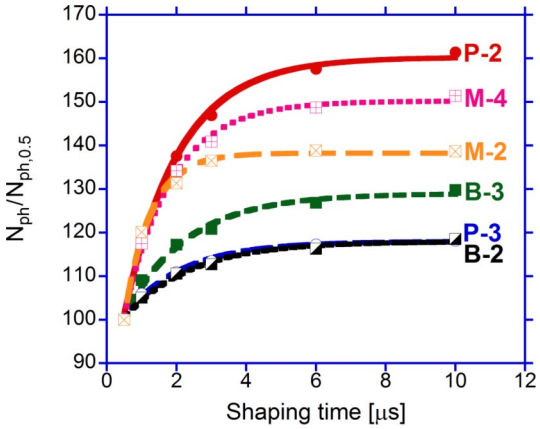

Figure 6 (online colour at: www.pss-a.com) $N_{ph,x}/N_{ph,0.5}$ of YAG:Ce LPE films measured under ^{241}Am α-particle excitation (^{241}Am). This dependence was fitted using Eq. (10). For clarity, only two samples from each flux group are shown. The reference crystal dependence is closely similar to that of B-2 and P-3 samples, see also Fig. 7.

where $m_{1,2,3}$ are constants related in an obvious way to the decay parameters in Eq. (9).

The measured data for the samples with the highest and the lowest parameter m_1 from each group and fits using the Eq. (10) are displayed in Fig. 6. The parameters m_1, m_2 and m_3 were obtained from the fit. The parameter m_1 can be written as:

$$m_1 = N_{\mathrm{ph,entire}}/N_{\mathrm{ph},0.5} \times 100\% , \tag{11}$$

where $N_{\mathrm{ph,entire}}$ is photoelectron yield extrapolated to infinite shaping time and $N_{\mathrm{ph},0.5}$ is the photoelectron yield measured at 0.5 μs shaping time. Thus for $t = 0$

$$m_1 - m_2 = N_{\mathrm{ph,fast}}/N_{\mathrm{ph},0.5} , \tag{12}$$

where $N_{\mathrm{ph,fast}}$ is a number of "instant" photoelectrons, i.e. photoelectrons emitted due to fast decay process. Afterwards, it is possible to calculate the relative intensity of the

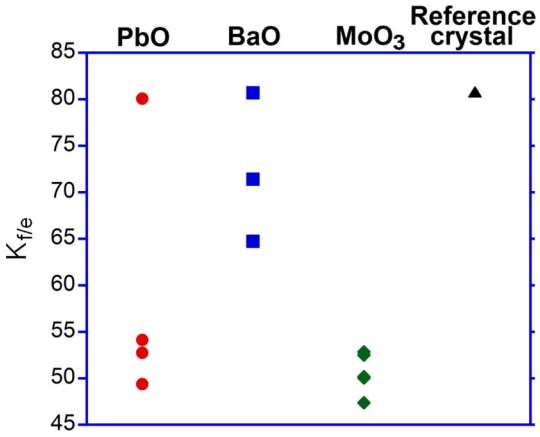

Figure 7 (online colour at: www.pss-a.com) $K_{f/e}$ value for all samples measured under ^{241}Am excitation.

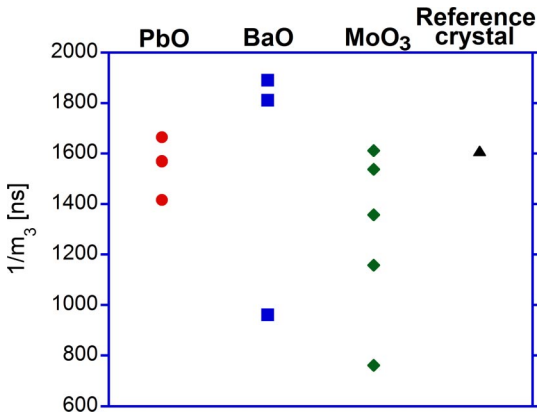

Figure 8 (online colour at: www.pss-a.com) Parameter $1/m_3$ of measured YAG:Ce LPE films and reference crystal.

fast fraction of the entire response $K_{f/e}$

$$K_{f/e} = \frac{N_{\mathrm{ph,fast}}}{N_{\mathrm{ph,entire}}} = \frac{m_1 - m_2}{m_1} = 1 - \frac{m_2}{m_1} . \tag{13}$$

$K_{f/e}$ values are presented in Fig. 7. $K_{f/e}$ values vary from 65% to 80% for the samples grown from the BaO-based flux, 49–80% for the samples grown from the PbO-based flux, and 47–53% for the samples grown from the MoO_3-based flux. For the reference crystal, $K_{f/e}$ value equals 81%. Performance of the MoO_3 samples is clearly worse compared with those BaO in the terms of $K_{f/e}$, while $K_{f/e}$ variations inside the PbO group cover very wide interval. The best LPE films (B-2, P-3) almost reach performance of the reference crystal in terms of $K_{f/e}$.

The slowdown of the decay process in the samples grown from the PbO- and MoO_3-based flux is probably caused by shallow traps related to the Pb contamination and other types of defects related to the technology of growth. These effects are not so significant for the reference crystal and the samples grown from the BaO-based flux.

Lower intensity (content) of slower component in scintillation response of the samples grown from the BaO-based flux might be also due to relatively higher concentration of cerium in them, see Table 2. It is supported by the observed decreasing content of slow components in the scintillation response of samples grown from the PbO-based flux with increasing cerium concentration.

Parameter $1/m_3$ is directly proportional to decay time of slower decay component, i.e. $\tau_2 \sim 1/m_3$. Unfortunately, $1/m_3$ parameter cannot be determined with high precision using our experimental set-up, standard deviation of parameter $m_3\sigma_{m3}$ varies from 6% to 20%, with one exception, sample M-3 where σ_{m3}(M-3) = 39%. No significant differences within experimental error of parameter $1/m_3$ between fluxes and the reference crystal were observed, see Fig. 8.

Measured pulse-height spectra were also used for the energy resolution evaluation by using the Gaussian fit to the peak-of-total-absorption band and evaluating full width

at half maximum (FWHM). Comparison among the fluxes gives the following result: FWHM generally decrease with the increasing N_{ph} yield. Table 2 shows FWHM of all YAG samples at shaping time 1 μs. No significant differences were observed among the fluxes, for the best samples FWHM equals 9–10%, which is slightly better than FWHM of the reference crystal (10.6%). This result is consistent with what we have found earlier at LuAG:Ce system [8].

4 Conclusions Comparing the fluxes, it is obvious that the N_{ph} yield is the best for the samples grown from the BaO-based flux, followed by the samples grown from the MoO_3-based flux and lastly the samples grown from the PbO-based flux. On the contrary, the surface morphology of the films is the worst for the BaO-based flux due to its high viscosity. The N_{ph} yields of samples B-1–B-3 are comparable or better even in comparison with the reference crystal grown by the Czochralski method. These samples also show the highest $K_{f/e}$ values comparable with the reference crystal again. FWHM values vary from 9% to 48% and are approximately indirectly proportional to the N_{ph} yield. For the best samples (P-1, P-2, M-4, M-5, B-2, and B-3) FWHM values are slightly better than FWHM of the reference crystal. While the lower N_{ph} yield and $K_{f/e}$ value of P-X samples is probably due to Pb contamination, for M-X samples it may be the non-optimized technology. If this technology is improved in the future, also MoO_3-based flux technology alongside with BaO-based flux may offer a way of production of good-performing LPE films, comparable even with Czochralski grown crystals.

Finally, this experimental study revealed and explained the shape of pulse height spectra measured with LPE films of very small thickness where incomplete energy deposition of α-particle occurs.

Acknowledgements Financial support of Czech GA AV KAN300100802, MSMT no. 1M06002, and MSM 6840770040 projects are gratefully acknowledged.

References

[1] M. Nikl, Meas. Sci. Technol. **17**, R37 (2006).
[2] M. Moszynski, T. Ludziejewski, D. Wolski, W. Klamra, and L. O. Norlin, Nucl. Instrum. Methods Phys. Res. A **345**, 461 (1994).
[3] J. Tous et al., Nucl. Instrum. Methods Phys. Res. A **591**, 264 (2008).
[4] T. Martin and A. Koch, J. Synch. Radiat. **13**, 180 (2006).
[5] Y. Zorenko, Phys. Status Solidi C **2**, 375 (2005).
[6] J. M. Robertson, M. V. van Tool, J. P. H. Heynen, W. H. Smits, and T. de Boer, Philips J. Res. **35**, 354 (1980).
[7] V. Babin, V. Gorbenko, A. Makhov, J. A. Mares, M. Nikl, S. Zazubovich, and Yu. Zorenko, J. Lumin. **127**, 384 (2007).
[8] P. Prusa, T. Cechak, J. A. Mares, M. Nikl, A. Beitlerova, N. Solovieva, Yu. V. Zorenko, and V. I. Gorbenko, Appl. Phys. Lett. **92**, 041903 (2008).
[9] M. Nikl, Phys. Status Solidi A **202**, 201 (2005).
[10] M. Nikl, V. V. Laguta, and A. Vedda, Phys. Status Solidi A **204**, 683 (2007).
[11] M. Nikl, E. Mihokova, J. Pejchal, A. Vedda, Yu. Zorenko, and K. Nejezchleb, Phys. Status Solidi B **242**, R119 (2005).
[12] M. Kh. Ashurov, Yu. K. Voronko, V. V. Osiko, A. A. Sobol, and M. I. Timoshechkin, Phys. Status Solidi A **42**, 101 (1977).
[13] M. M. Kuklja, J. Phys.: Condens. Matter **12**, 2953 (2000).
[14] C. R. Stanek, K. J. McClellan, M. R. Levy, and R. W. Grimes, Phys. Status Solidi B **243**, R75 (2006).
[15] W. A. Bonner, Mater. Res. Bull. **12**, 289 (1977).
[16] M. Kucera, K. Nitsch, H. Stepankova, M. Marysko, and P. Reiche, Phys. Status Solidi A **198**, 407 (2003).
[17] M. Kucera, K. Nitsch, M. Kubova, N. Solovieva, M. Nikl, and J. A. Mares, IEEE Trans. Nucl. Sci. **55**, 1201–1205 (2008).
[18] L. Katz and A. S. Penfold, Rev. Mod. Phys. **24**, 28 (1952).
[19] R. Autrata, P. Schauer, Jos. Kvapil, and J. Kvapil, J. Phys. E **11**, 707–708 (1978).
[20] G. B. Scott and J. L. Page, Appl. Phys. **48**, 1342 (1977).
[21] M. Kucera, K. Nitsch, M. Nikl, S. Danis, and M. Hanus, Growth and properties of epitaxial Ce-doped YAG and LuAG films for scintillators, ICDIM'08 Conference, Aracaju 2008, submitted for publication in J. Phys.: Conf. Ser.
[22] J. K. Tuli, Nucl. Data Sheet **72**, 355 (1994).
[23] Y. A. Akovali, Nucl. Data Sheet **72**, 191 (1994).
[24] M. R. Schmorak, Nucl. Data Sheet **66**, 839 (1992).
[25] E. N. Shurshikov, Nucl. Data Sheet **49**, 785 (1986).
[26] J. A. Mares, A. Beitlerova, M. Nikl et al., Radiat. Meas. **42**, 533 (2007).
[27] W. H. Bragg and R. Kleeman, Philos. Mag. **10**, 358 (1905).
[28] H. Cember, Introduction to Health Physics, 3rd ed. (McGraw-Hill, 1996), p. 132.
[29] M. Nikl, E. Mihokova, J. A. Mares, A. Vedda, M. Martini, K. Nejezchleb, and K. Blazek, Phys. Status Solidi B **181**, R10 (2000).
[30] J. A. Mares, M. Nikl, E. Mihokova, A. Beitlerova, A. Vedda, and C. D'Ambrosio, IEEE Trans. Nucl. Sci. **55**, 1142–1147 (2008).
[31] M. Nikl, A. Vedda, M. Fasoli, I. Fontana, V. V. Laguta, E. Mihokova, J. Pejchal, J. Rosa, and K. Nejezchleb, Phys. Rev. B **76**, 195121 (2007).

Radiation Measurements 45 (2010) 369–371

Contents lists available at ScienceDirect

Radiation Measurements

journal homepage: www.elsevier.com/locate/radmeas

Ce^{3+}-doped crystalline garnet films – scintillation characterization using α–particle excitation

Jiri A. Mares [a,*], Petr Prusa [a,c], Martin Nikl [a], Karel Nitsch [a], Alena Beitlerova [a], Miroslav Kucera [b], Martin Hanus [b], Yurij Zorenko [d]

[a] Institute of Physics, Academy of Sciences of the Czech Republic, Cukrovarnicka 10, 162 53 Prague 6, Czech Republic
[b] Charles University, Faculty of Mathematics and Physics, Ke Karlovu 5, 121 16 Prague 2, Czech Republic
[c] Faculty of Nuclear Sciences and Physical Engineering, Czech Technical University, Brehova 7, 115 19 Prague 1, Czech Republic
[d] Laboratory of Optoelectronic Materials, Department of Electronics, Ivan Franko National University of Lviv, 107 Gen. Tarnavskogo Str., Ukraine

ARTICLE INFO

Article history:
Received 17 August 2009
Received in revised form
29 October 2009
Accepted 13 December 2009

Keywords:
Ce^{3+}-doped garnet films
Scintillation
α-particle excitation

ABSTRACT

Scintillating properties of Ce^{3+}-doped (Lu,Y) aluminum garnet single crystalline films (SCF) were investigated. Thin SCF films of thickness between 1 and 30 μm were grown by a liquid phase epitaxy (LPE) method in various fluxes. The α-particle excitation (mainly 5.4857 MeV line of ^{241}Am) of pulse height spectra is used to measure scintillation response of SCF, especially peak of those α-rays which are totally absorbed in the films. Detailed studies and evaluation of scintillation measurements of large sets of Ce^{3+}-doped SCF (Lu,Y) aluminum garnets showed that at present time (i) YAG:Ce SCF have comparable scintillation properties as YAG:Ce single crystals, especially their N_{phels} photoelectron yields are the same while (ii) scintillation properties of LuAG:Ce SCF do not reach those of LuAG:Ce single crystal.

1. Introduction/scope

Ce^{3+}-doped (Lu,Y) aluminum garnet crystals belong to fast, with high or medium light yield, mechanically hard and chemically stable (non-hygroscopic) single crystal scintillators (Autrata et al., 1983; Moszynski et al., 1994; Zorenko, 2005; Nikl et al., 2009, 2000). Especially, $Lu_3Al_5O_{12}$:Ce crystal (LuAG:Ce) belongs to heavy scintillators due to its high density (6.67 g/cm^3) and high Z_{eff} = 59 (Nikl et al., 2009). New development in X-ray imaging applications of μm or even sub-μm resolution (Koch et al., 1998; Kucera et al., 2008; Nikl et al., 2009) needs very thin single crystalline plates or epitaxial layers or films of thickness a few tenths μm and down to 10 μm. Due to good mechanical and chemical properties of (Lu,Y) aluminum garnet single crystals (SC) it is possible to prepare SC plates of 30 μm thin but thinner plates must be coupled (glued) with glass base (Crytur Ltd, 2009).

Besides very thin SC plates from Czochralski grown crystals the another possibility to obtain very thin single crystalline layers (or films – SCF) is offered by a liquid phase epitaxial technology (LPE) (Robertson and van Tool, 1984; Koch et al., 1998; Kucera et al., 2008). The LPE technology allows to grow (Lu,Y) garnet films with much lower content of antisite defects compared with SC plates (Babin et al., 2007). SCF films are grown at much lower temperatures (around 1000 °C) than those of garnet SC where their melting points are around 1900 °C. Now, the LPE technology is being developed further and, different PbO-, BaO- and MoO_3-based fluxes are used (Kucera et al., 2008; Mares et al., 2007a; Prusa et al., 2009). The latest development also shows that other dopants can be used as e.g. Bi^{3+} (Zorenko et al., 2009).

This paper has two main goals: (i) presentation and description of the way of measurements and characterization of scintillation properties of SCF (Lu,Y) garnet films using α- particle excitation and (ii) to summarize and evaluate scintillation response of large sets of LuAG:Ce and YAG:Ce SCF films grown by LPE technology under different conditions, especially an influence of the flux composition (Kucera et al., 2008; Prusa et al., 2008).

2. Experimental

Scintillation characteristics and measurements of thin SCF of (Lu, Y) aluminum garnets are not possible using γ-ray lines excitation due to their small linear attenuation absorption (D'Ambrosio et al., 2000; Mares and D'Ambrosio, 2007). Energy of γ-ray lines is mainly deposited in the substrates (undoped LuAG or YAG SC) on which SCF are grown. The only possibility to measure scintillation response of the films (N_{phels} photoelectron yield, FWHM or N_{phels} yield time development (Mares et al., 2007a,b)) is to use that kind of excitation which fully deposit the energy in the films itself (Shimizu

* Corresponding author. .
E-mail address: amares@fzu.cz (J.A. Mares).

1350-4487/$ – see front matter © 2010 Elsevier Ltd. All rights reserved.
doi:10.1016/j.radmeas.2009.12.026

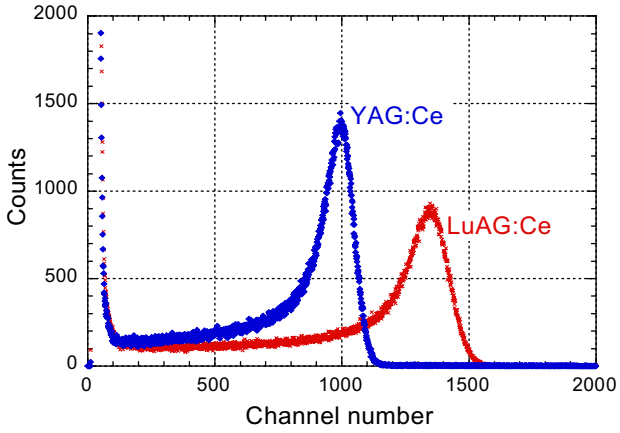

Fig. 1. Pulse height spectra of LuAG:Ce and YAG:Ce reference single crystals excited using α-particle excitation of 5.4857 MeV of ^{241}Am.

et al., 2005). Measured set-up consists of a HPMT (Hybrid Photo-Multiplier Tube), shaping amplifier ORTEC 672, MCB 927™ buffer and PC. This set-up is used in γ-ray excited measurements of the pulse height spectra (Mares et al., 2004). But for scintillation measurements of SCF we must use the α-particle excitation source, especially the energy line 5.4857 MeV of ^{241}Am. This α-particle source is put directly on surface of the films (Prusa et al., 2008, 2009).

The α-particle excited pulsed height spectra of Czochralski grown LuAG:Ce and YAG:Ce single crystals (Crytur Ltd, 2009) are presented in Fig. 1 (these spectra are used as the reference ones to those of measured SCF films). (Lu,Y)AG:Ce SCF have penetration range of α-particles between 9 and 13 μm (Prusa et al., 2009) and thickness of some of measured films is below the penetration range of α-particles. Fig. 2 presents pulse height spectrum of LuAG:Ce SCF of 5.2 μm thickness. This spectrum was decomposed into three Gaussians: (i) two clearly seen G2 and G3 peaks and (ii) less intense G1 one. G3 peak at channel number ~608 is due to total absorption of α-particles inside SCF while G2 one is due to α-rays moving perpendicularly to surface of SCF through (5.2 μm thickness) into substrate. Wide G3 peak is probably due to UV scintillation emission of the substrate.

Majority of measurements of LuAG:Ce SCF was carried out using optical cut-off filter ~480 nm and one example is shown in Fig. 3. An effect of optical filter influences shape of α-particle peaks compared if no filter is used because: (i) it decreases pulse height spectra

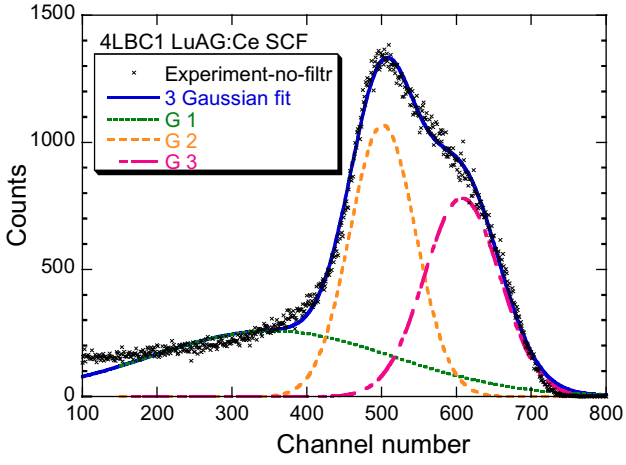

Fig. 2. Pulse height spectrum of LuAG:Ce SCF of 5.2 μm thickness prepared using BaO-based flux and its decomposition into three Gaussians (measured by 5.4857 MeV of ^{241}Am and 0.5 μs shaping time).

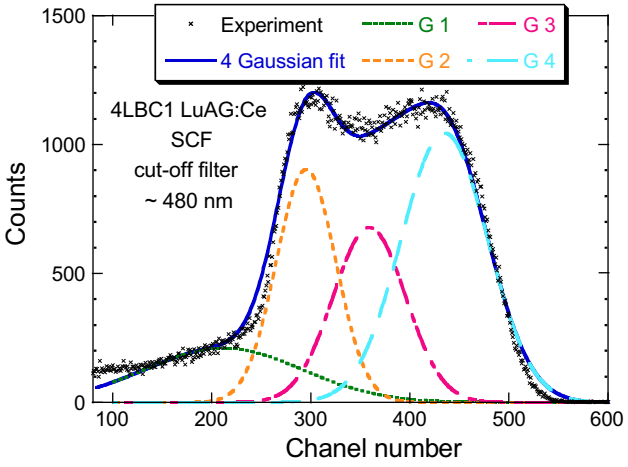

Fig. 3. Pulse height spectrum of LuAG:Ce SCF of 5.2 μm thickness prepared using BaO based flux measured with optical cut-off filter 480 nm and its decomposition into four Gaussians (measured by 5.4857 MeV of ^{241}Am and 0.5 μs shaping time).

intensity of about 25% and (ii) we only measure Ce^{3+} scintillation (emission) and not the UV one of the substrate (its intensity is much less compared that without filter use). The above given reasons (i) and (ii) allows more precise measurements of Ce^{3+} scintillation response (peak of penetrating α-particles) of (Lu,Y) aluminum garnet SCF. Pulse height spectrum in Fig. 3 was decomposed into four Gaussians G1–G4. Peaks G2 and G4 are due to α-particles moving either perpendicularly to film surface or in those directions where penetrate in films, respectively. G3 peak is due to those α-particles which move in directions between those of G2 and G4 peaks while G1 peak is probably due to weak rest of UV substrate emission. Now, we measure and compare properties of Ce^{3+}-doped (Lu,Y) aluminum garnet SCF using optical cut-off filter.

3. Results of measurements

In this paper we summarize our long term research of Ce^{3+}-doped SCF of (Lu,Y)AG (Mares et al., 2007a; Prusa et al., 2008, 2009). A few tens of both YAG:Ce and LuAG:Ce SCF samples were investigated. Majority of them was grown by us (Kucera and Nitsch) but some others were from Department of Electronics, Ivan Franko National University from Lviv, Ukraine (Zorenko, 2005; Zorenko et al., 2009). All SCF samples were grown by the LPE method at different temperatures (around 1000 °C) in three various fluxes: (i) $PbO–B_2O_3$, (ii) $BaO–B_2O_3$ and (iii) $MoO_3–Li_2MoO_4$. Parameters and basic scintillation properties of the best SCF or some others are given in Tables 1 and 2.

Now, the LPE technology allows to prepare well defined and good quality YAG:Ce SCF. Their N_{phels}/MeV photoelectron yields and FWHM (at 5.4857 MeV of ^{241}Am) are the same or even higher than those of YAG:Ce reference single crystal (see Table 1). The only deviation is higher time difference of N_{phels} yield in the shaping time

Table 1
Parameters and scintillation properties of YAG:Ce SCF and comparison with those of YAG:Ce single crystal measured at 1 μs shaping time under ^{241}Am 5.4857 MeV excitation (SC – single crystal, samples in rows 3 to 6 are SCF).

Sample	Thickness [μm]	N_{phels} per MeV (phels)	FWHM (%)	N_{phels} change 0.5–10 μs (%)	Flux based on
YAG:Ce SC	1 mm	349	11	~ 10	CZ grown
4C2	8	317.6	9.6	60	PbO
5YBC1	4.4	402.5	10.8	26.5	BaO
1MC13	3.5	372.2	9.5	47.5	MoO_3
N42-7	58	374.1	17.6	a few	PbO

Table 2
Parameters and scintillation properties of LuAG:Ce SCF and comparison with those of LuAG:Ce single crystal measured at 1 μs shaping time under 5.4857 MeV excitation of ^{241}Am (SC – single crystal, samples in rows 3 to 6 are SCF).

Sample	Thick-ness μm	N_{phels} per MeV (phels)	FWHM (%)	N_{phels} change 0.5–10 μs (%)	Flux based on
LuAG:Ce SC	1 mm	471	10.7	76	CZ grown
4LBC3	6	236	16.3 (^{239}Pu)	65.7	BaO
6Lu1	14.6	77	21	~ 5	PbO
LY6	17	228	10.5	20.8	PbO
LY16	27	152.6	17.6	6.8	PbO

range 0.5–10 μs. Some measured samples exhibit various defects or morphology deviations. Detailed YAG:Ce measurements of SCF (Prusa et al., 2009) showed that the best samples were grown using BaO-based flux.

Table 2 presents parameters and scintillation properties of Ce^{3+}-doped LuAG SCFs. Here, their scintillation properties do not reach those of LuAG:Ce single crystal. SCF N_{phels}/MeV yields of SCF are about one half of that of LuAG:Ce crystal. We measured two groups of LuAG:Ce SCF, one of them was prepared by us the second one is from Lviv (Zorenko, 2005). Some of LuAG:Ce SCF exhibit large N_{phels} time increase between 0.5 and 10 μs (around 70%) but thicker SCF have much less time difference (see Table 2). Again, the highest N_{phels} yield exhibit LuAG:Ce SCF grown from BaO-based flux.

4. Conclusions

Detailed research of large sets of Ce^{3+}-doped (Lu,Y)AG SCF was carried out using α-particle excitation. Scintillation properties of SCFs were evaluated from pulse height spectral bands arising from α-particles depositing their energy in the films (their paths are equal or larger than the penetration range). YAG:Ce SCF grown in different fluxes and conditions reached comparable scintillation properties, compared with their single crystal analogue. Further development is necessary however, in case of LuAG:Ce SCFs where their scintillation N_{phels}/MeV yield is in average about half of that of LuAG:Ce crystal.

Acknowledgments

Finantial support of The Czech Science Foundation project 202/08/0893 is gratefully acknowledged.

References

Autrata, R., Schauer, P., Kvapil, J., Kvapil, J., 1983. Cathodoluminescent efficiency of $Y_3Al_5O_{12}$ and $YalO_3$ single crystals in dependence on Ce^{3+} and other dopant concentrations. Cryst. Res. Technol. 18, 907–913.
Babin, V., Gorbenko, V., Makhov, A., Mares, J.A., Nikl, M., Zazubovich, S., Zorenko, Yu, 2007. Luminescence characteristics of Pb^{2+} centres in undoped and Ce^{3+}-doped $Lu_3Al_5O_{12}$ single-crystalline films and $Pb^{2+} \rightarrow Ce^{3+}$ energy transfer. J. Lumin. 127, 384–390.
Crytur Ltd., 2009. Booklets of Crytur or see www.crytur.com, Palackeho 175, 511 19 Turnov, Czech Republic.
D'Ambrosio, C., De Notaristefani, F., Leutz, H., Puertolas, D., Rosso, E., 2000. X-Ray detection with a scintillation YAP-window hybrid photomultiplier tube. IEEE. Trans. Nucl. Sci. 47, 6–10.
Koch, A., Raven, C., Spadne, P., Snigirev, A., 1998. X-ray imaging with submicrometer resolution employing transparent luminescent screens. J. Opt. Soc. Am. A. 15, 1940–1951.
Kucera, M., Nitsch, K., Kubova, M., Solovieva, N., Nikl, M., Mares, J.A., 2008. Ce-doped YAG and LuAG epitaxial films for scintillation detectors. IEEE. Trans. Nucl. Sci. 55, 1201–1205.
Mares, J.A., D'Ambrosio, C., 2007. Hybrid photomultipliers – their properties and application in scintillation studies. Opt. Mat. 30, 22–25.
Mares, J.A., Beitlerova, A., Nikl, M., Solovieva, N., D'Ambrosio, C., Blazek, K., Maly, P., Nejezchleb, K., De Notaristefani, F., 2004. Scintillation response of Ce-doped or intrinsic scintillating crystals in the range up to 1 MeV. Radiat. Meas. 38, 353–357.
Mares, J.A., Beitlerova, A., Nikl, M., Solovieva, N., Nitsch, K., Kucera, M., Kubova, M., Gorbenko, V., Zorenko, Yu, 2007a. Scintillation and optical properties of YAG: Ce films grown by liquid phase epitaxy. Radiat. Meas. 42, 533–536.
Mares, J.A., Beitlerova, A., Nikl, M., Vedda, A., D'Ambrosio, C., Blazek, K., Nejezchleb, K., 2007b. Time development of scintillating response in Ce-or Pr-doped crystals. Phys. Stat. Sol. (c) 4, 996–999.
Moszynski, M., Ludziejewski, T., Wolski, D., Klamra, W., Norlin, L.O., 1994. Properties of YAG: Ce scintillator. NIM Phys. Res. A 345, 461–467.
Nikl, M., Mihokova, A., Mares, J.A., Vedda, A., Martini, M., Nejezchleb, K., Blazek, K., 2000. Traps and timing characteristics of LuAG: Ce^{3+} scintillator. Phys. Stat. Sol. (a) 181, R10–R12.
Nikl, M., Tous, J., Mares, J.A., Prusa, P., Mihokova, E., Blazek, K., Vedda, A., Zorenko, Yu., Gorbenko, V., Babin, V., 2009. $Lu_3Al_5O_{12}$-based materials for high 2D-resoultion scintillation detectors. Proc. SPIE, Vol. 7310_7, pp. 731008-1–10.
Prusa, P., Cechak, T., Mares, J.A., Nikl, M., Beitlerova, A., Solovieva, N., Zorenko, Yu., Gorbenko, V.I., Tous, J., Blazek, K., 2008. The α-particle excited scintillation response of the liquid phase epitaxy grown LuAG: Ce thin films. Appl. Phys. Lett. 92, 041903-1-3.
Prusa, P., Nikl, M., Mares, J.A., Kucera, M., Nitsch, K., Beitlerova, A., 2009. The α-particle excited scintillation response of YAG: Ce thin films grown by liquid phase epitaxy. Phys. Stat. Sol. A 206, 1494–1500.
Robertson, J.M., van Tool, M.V., 1984. Cathodoluminescent garnet layers. Thin Solid Films 114, 221–240.
Shimizu, S., Suzuji, M., Koizumi, Y., Ishibashi, H., Kubota, S., 2005. Light output and decay curve of GSO: Ce under electron, proton, alpha particle and fission fragment excitations. NIM Phys. Res. A 537, 57–60.
Zorenko, Yu, 2005. Luminescence of isoelectronic impurities and antisite defects in garnets. Phys. Stat. Sol. 2, 375–379.
Zorenko, Yu., Mares, J.A., Kucerkova, R., Gorbenko, V., Savchyn, V., Voznyak, T., Nikl, M., Beitlerova, A., Jurek, K., 2009. Optical, luminescence and scintillation characteristics of Bi-doped LuAG and YAG single crystalline films. J. Phys. D: Appl. Phys. 42 (7), 075501.

$Lu_3Al_5O_{12}$-based materials for high 2D-resolution scintillation detectors

M. Nikl[a*], J. Tous[b], J.A. Mares[a], P. Prusa[a,c], E. Mihokova[a,d], K. Blazek[b], A. Vedda[d], Yu. Zorenko[e], V. Gorbenko[e], V. Babin[f]

[a] Institute of Physics AS CR, Cukrovarnicka 10, 162 53 Prague, Czech Republic

[b] CRYTUR Ltd. Palackeho 175, 511 19 Turnov, Czech Republic

[c] Faculty of Nuclear Sciences and Physical Engineering, Czech Technical University in Prague, Brehova 7, 11519 Prague, Czech Republic

[d] Dept. of Materials Science, University of Milano-Bicocca, Via Cozzi 53, 20125 Milan, Italy

[e] Ivan Franko National University of Lviv, 107 Gen. Tarnavsky str., 79017 Lviv, Ukraine

[f] Institute of Physics, University of Tartu, Riia 142, 51014 Tartu, Estonia

ABSTRACT

About 20 μm thick Ce-doped $Lu_3Al_5O_{12}$ thin films grown by Liquid Phase Epitaxy and thin plates of similar thickness prepared by mechanical cutting and polishing from Czochralski grown crystals are used in 2D-imaging experiment down to μm 2D-resolution. Their scintillation response is also measured under α-particle excitation and performance of film and bulk material is mutually compared. Furthermore, scintillation and thermoluminescence characteristics of UV emitting Sc-doped LuAG grown by Czochralski method are presented since this system is a candidate material for UV emission-based 2D sensors with improved diffraction limit with respect to the presently used Ce-doped aluminum garnets.

Keywords: Thin scintillator films, 2D imaging, Ce-doped $Lu_3Al_5O_{12}$ (LuAG), liquid phase epitaxy growth, thermoluminescence

* nikl@fzu.cz, ph. +420220318445; fax +420233343184

1. INTRODUCTION

Some inspection/imaging applications require thin (few μm – tens of μm) and large area (up to 50 mm diameter) single crystalline plate or film scintillators [1-3]. Coupled with position sensitive photodetectors (CCD) they enable 2D-imaging of tiny (hidden) objects down to sub-μm scale under x-ray or accelerated electron exposure. Controversial demands for high x-ray attenuation in the scintillator (requiring larger thickness) and excellent 2D-resolution (smallest possible plate/film thickness) call for using high density materials.

Ce^{3+} or Pr^{3+} doped and Lu-based compounds are under intense research as they can reach high density together with an excellent scintillation figure-of-merit [4,5]. $Lu_3Al_5O_{12}$:Ce (LuAG:Ce) has been reported recently as highly efficient scintillator material, the scintillation efficiency of which can reach up to 700 % of BGO under x-ray excitation [6,7]. LuAG host offers almost 50 % higher density (ρ=6.67 g/cm^3) and significantly larger effective atomic number Z_{eff}=59 with respect to YAG (ρ=4.6 g/cm^3, Z_{eff}=29). Bulk single crystals are grown by Czochralski technique from melt while single crystalline films are obtained by the Liquid Phase Epitaxy (LPE) method [8].

In this contribution we demonstrate the 2D-imaging ability of LuAG:Ce LPE-grown films and compare them with a Czochralski-grown plate of the same thickness (~20μm). Time dependence of scintillation response related to the delayed recombination phenomena, are discussed in the light of possible application in dynamic fluoroscopy imaging. Finally, we present technologically feasible modifications to obtain an UV-emitting material based on LuAG host by Sc doping which can lower the diffraction limit and enhance the 2D-resolution accordingly.

2. METHODOLOGY

Four single crystalline films (SCF) of (Lu-Y)AG:Ce grown by LPE from melt-solution based on PbO-B_2O_3 flux onto (110)-oriented YAG (quarter-moon of 20 mm diameter) and two LuAG:Ce plates of 20 μm thickness and 20 mm

Non-Intrusive Inspection Technologies II, edited by Brandon W. Blackburn, Proc. of SPIE
Vol. 7310, 731008 · © 2009 SPIE · CCC code: 0277-786X/09/$18 · doi: 10.1117/12.818358

diameter prepared from Czochralski grown bulk single crystals and glued on BK7 glass substrate were used in the imaging experiments, see Table 1 and Fig. 1. Furthermore, the 0.5wt% Sc-doped (in melt) bulk LuAG crystal was prepared and plate of about 7x7x1 mm and bulk of about 10x10x10 cm, all polished, were used for another spectroscopic experiments.

2D-imaging experiment is composed of microfocus X-ray source, sample holder and digital CCD camera with high 2D-resolution, see Fig. 2.

Sample acronym	Sample type	Film/plate material	Film/plate thickness [μm]	Substrate thickness [mm]	Scintillation efficiency [%]
Lu-6	LPE SCF	LuAG:Ce	17	0.5	70
Lu-9	LPE SCF	LuAG:Ce	29	0.5	67
Lu-11	LPE SCF	$Lu_{0.8}Y_{0.2}AG$:Ce	15	0.5	61
Lu-16	LPE SCF	$Lu_{0.6}Y_{0.4}AG$:Ce	27	0.5	62
Cz-2	Bulk Czochral	LuAG:Ce	20	3	100
Cz-3	Bulk Czochral	LuAG:Ce	20	3	92

Table 1. Characteristics of the samples used for the 2D imaging experiment.

Fig. 1 Visual appearance of LPE SCF samples Lu-6,9,11,16 after polishing-off the film from one side and 5 μm thickness from the other side. On the right the Cz-2 sample is displayed with the LuAG:Ce plate on the top surface.

Fig. 2 2D X-ray imaging experiment. X-ray source is on the left.

In the imaging experiment, a sample from Table 1. was placed on the sample holder with the active layer/plate towards the X-ray source. An imaged object was placed between X-ray source and the sample. During the X-ray exposition (500 ms) the luminescence image from the scintillator sample is collected by the CCD camera. Expositions without any object were made as well to compare both the scintillation efficiency and film/plate homogeneity of the samples.

Scintillation photoelectron yield and its dependence on shaping time of the detection electronics were also measured using modern HPMT-based detector, for the experimental details see [9]. Radioluminescence spectra and scintillation decays were measured at modified Spectrofluorometer 199S; thermally stimulated luminescence (TSL) glow curves and emission spectra below and above RT were measured by a home-made set-up [5-7]. Excitation spectra in VUV spectral region were measured using synchrotron radiation at Superlumi station, HASYLAB, DESY, Hamburg.

3. RESULTS AND DISCUSSION

3.1 Optical quality and scintillation efficiency of the samples prepared for 2D imaging

In Fig. 3 an optical image of one of the LPE SCF samples and that of Cz-3 is provided using an optical microscope. Samples were back-illuminated with UV light to induce Ce^{3+} luminescence. In SCF samples there are occasional incrustations and surface flaws which scatter the luminescence light out from the sample, i.e. they appear as bright spots. Plates prepared from Czochralski grown bulk crystals are very homogeneous and do not show any scattering effects.

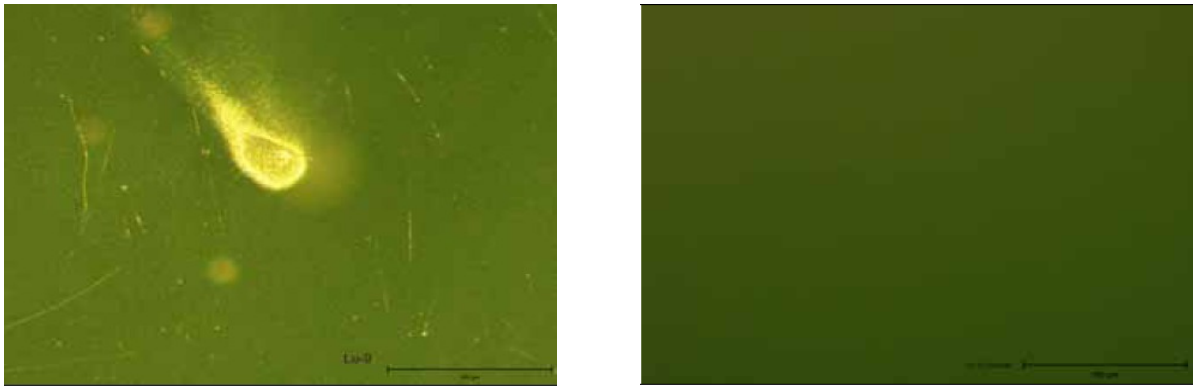

LPE SCF Sample Lu-9 Czochralski plate sample Cz-2

Fig. 3 Optical image of the samples back-illuminated with UV light. Magnification 57x.

In the case of X-ray excitation, the same effect is observed from the back side of the samples using the CCD camera: surface flaws in LPE-grown samples appear as bright spots, while Czochralski grown plate shows very homogeneous and spot-free image, Fig. 4.

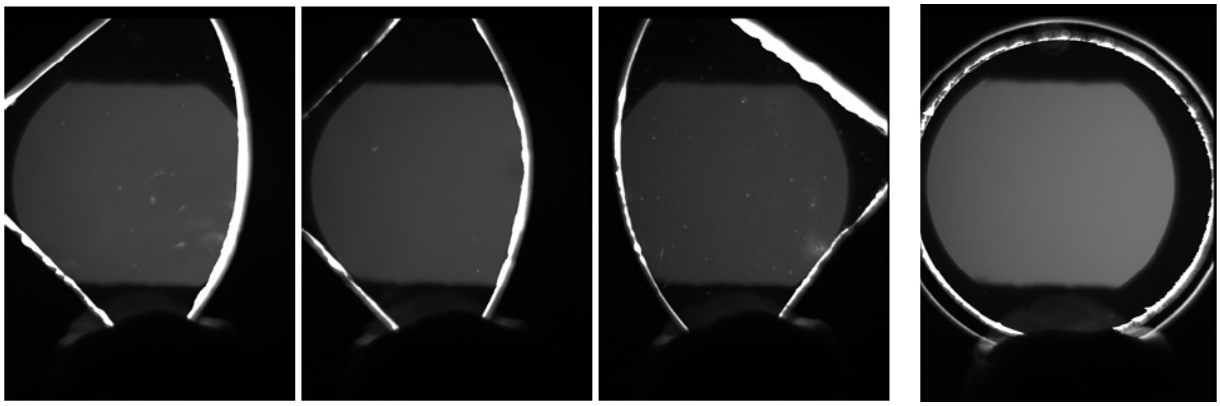

Sample **Lu-6** **Lu-9** **Lu-11** **Cz-2**

Fig. 4 CCD camera image of X-ray irradiated samples. Bright spots are due to the surface flaws.

In the measurement displayed in Fig. 4 also the integrated emission intensity from the sample was evaluated from an average of 25 times repeated expositions and was used to evaluate scintillation efficiency of the samples, which is given in Table 1. normalized with respect to Cz-2 sample. The best from LPE SCF samples showed about 70% efficiency with respect to that of Cz-2 one.

3.2 2D imaging experiment

To determine 2D resolution of the examined scintillation sensors the CCD camera was equipped with additional focusing and enlarging optics. The 8 μm thick golden wire grid, see Fig. 5, was placed in front of the sample towards the X-ray source.

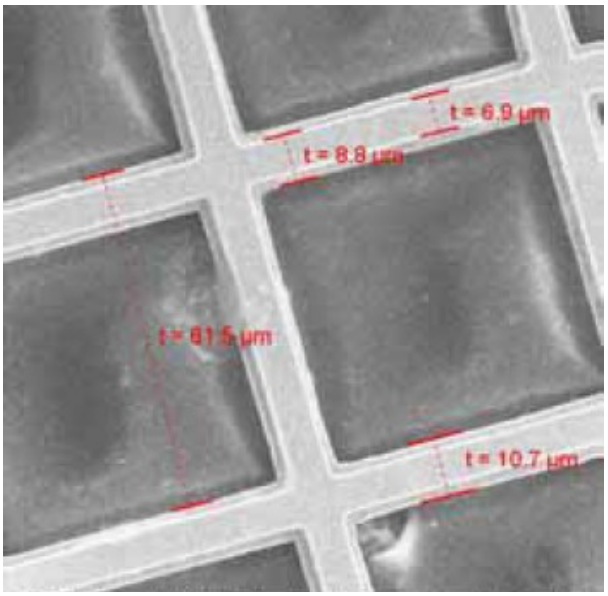

Fig. 5 SEM image of the golden wire grid. Thickness of wires is 8-11 μm.

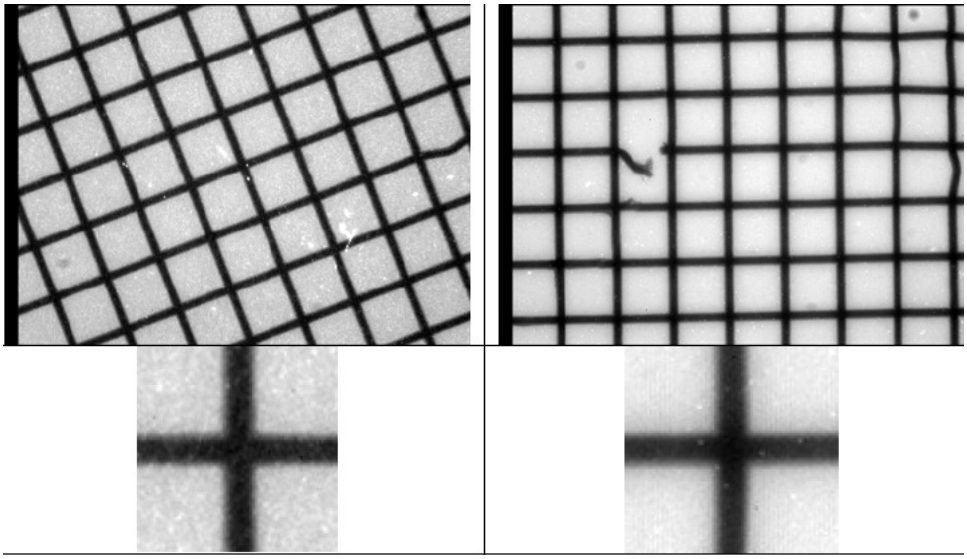

Fig. 6 The grid image obtained by Lu-6 sample screen (upper left) with the detail of wire crossing (lower left) and the same picture obtained by Cz-3 sample (right part of the figure)

The above mentioned flaws in LPE SCF sample degrade the image quality with respect to that obtained by Czochralski grown plates, but the 2D-resolution appears in both groups of the samples practically the same as can be seen from the detail of wire crossing in the bottom part of Fig. 6. The same 2D-resolution is also evidenced from the output signal dependence across the grid wire, Fig. 7 (X-axis in CCD chip pixels, 1 pixel=0.74 μm). Better signal-to-background ratio from CCD camera by factor 1.5 is achieved in Cz-3 sample due to its higher scintillation efficiency.

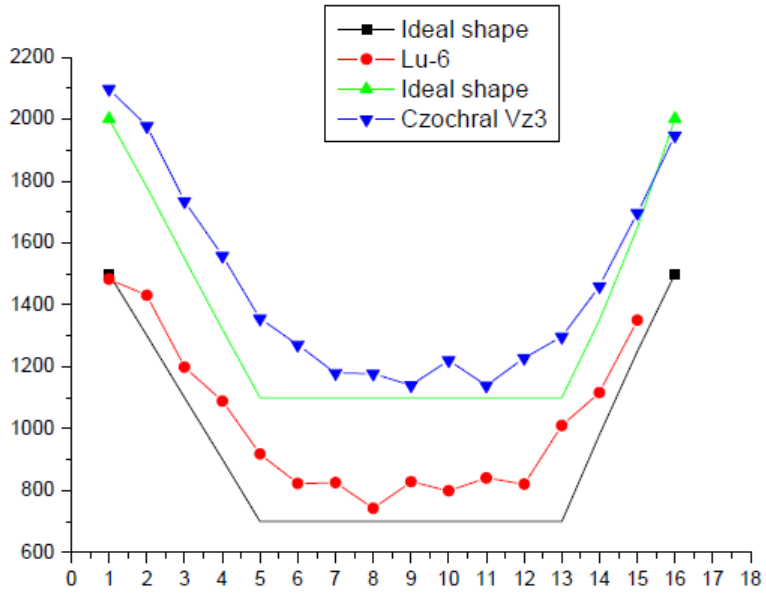

Fig. 7 Electrical output signal from CCD pixels across the grid wire. Theoretical shape of the signal is also given.

It is worth noting that in the case of LPE SCF samples the output luminescence signal could be "contaminated" by the intrinsic emission of undoped LuAG substrate due to penetrating X-irradiation which can worsen the 2D resolution in the image due to defocusing effects. However, this intrinsic luminescence occurs within 300-350 nm [10] and is thus mostly

absorbed by the glass focusing optics in front of CCD camera. Moreover, a CCD chip shows lower detection efficiency in this spectral region with respect to the green region of the spectra.

3.3 Photoelectron yield and its time dependence under α-particle excitation

Basic scintillation properties (scintillation response) as photoelectron or light yields ($N_{phels}(E)$ or LY(E), respectively), energy resolution (FWHM) and proportionality of the yields can be obtained from measurements of pulse height spectra of scintillating materials [11]. Recently, a new technique using hybrid photomultipliers (HPMT) is applied to measure scintillation response of Lu- or Y-based garnet compounds [12]. This technique allows to provide precise photoelectron calibration of the X- or γ-ray excited pulsed height spectra of scintillators [11-13]. Besides Ce^{3+} dopant also Pr^{3+} one was studied in LuAG or YAG and results are given in detail in [5,14]. Nowadays, LuAG:Ce crystals are characterized by (i) light yield around 15.000,- ph/MeV, (ii) energy resolution ~ 10 % at 662 keV and (iii) photoelectron yield proportional in the energy range 500-1300 keV. However, a deviation from proportionality (the decrease of about 30%) is observed in the energy range 500-10 keV.

Characterization of scintillation properties of SCF requires somewhat modified experiment in the scintillation response measurements. Due to small SCF thickness (from a few μm to 60 μm) it is not possible to use γ-ray excitation because of small γ-ray absorption in the SCF itself and prevalent energy deposit in the substrate. In such a case the emitted light would consist of that generated in the SCF film (Ce^{3+} emission) and the dominant UV emission coming from a thick substrate. The only possibility to characterize and compare SCF scintillation response is the use of α-ray excitation (e.g. 5.4857 MeV α-rays of ^{241}Am) [9]. According to detailed calculations, the penetration range of alpha-particles in LuAG and YAG crystals varies from 7 to 10 μm, respectively [15]. The α-rays excited scintillation response – pulse height spectra can be measured by the same set-up used for γ-ray excitation [11-13] using the α-ray sources (radioisotopes) placed directly onto the sample surface.

N_{phels} photoelectron yield (pulse height spectra) of LuAG:Ce and LuYAG:Ce SCF (samples Lu 6, 9, 11 and 16, see Fig. 1) were measured under ^{241}Am α-particle excitation (5.4857 MeV) in the shaping time range 0.5 – 10 μs together with two LuAG:Ce single crystals (SC 1 and 2 cut from the same parent boule as Cz-2 and Cz-3 samples above). Results of measurements are summarized in Fig. 8 and Table 2.

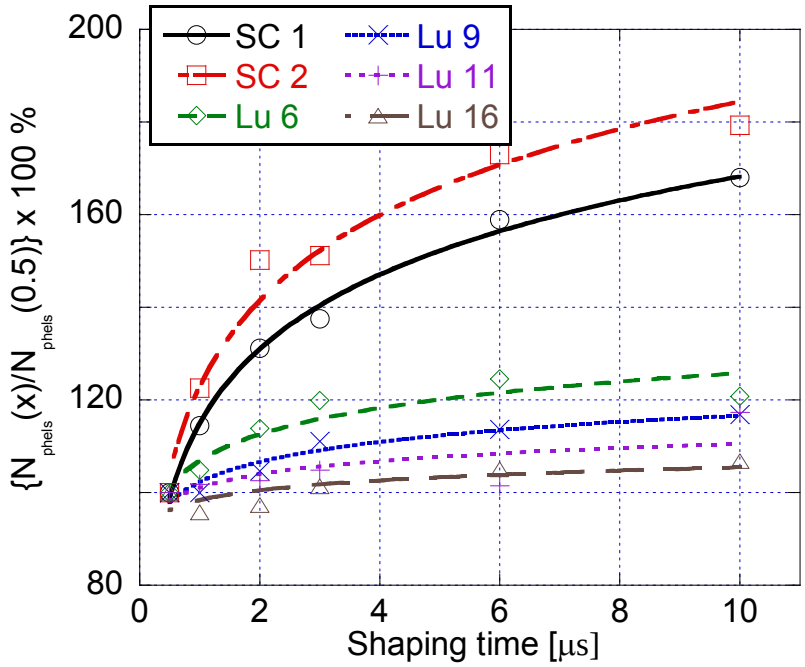

Fig. 8 The dependence of normalized photoelectron yield on the shaping time under α-rays excitation of ^{241}Am (energy 5.4857 MeV). The lines are logarithmic fits.

Sample acronym	Sample type Film/plate thickness	Film/plate material	N_{phels}/MeV (phels) under ^{241}Am at 1 μs shaping time	FWHM (%) at ^{241}Am at 1 μs shaping time	Difference N_{phels}/MeV (in %) between 0.5 and 10 μs shaping times
Lu-6	SCF (17 μm)	LuAG:Ce	1252	10.5	20.8
Lu-9	SCF (29 μm)	LuAG:Ce	1063	16.9	16.8
Lu-11	SCF (15 μm)	$Lu_{0.8}Y_{0.2}AG$:Ce	838	11.2	17.3
Lu-16	SCF (27 μm)	$Lu_{0.6}Y_{0.4}AG$:Ce	837	17.6	6.8
SC 1 (Cz-2)	Bulk (1 mm)	LuAG:Ce	2136	9.1	68
Sc 2 (Cz-3)	Bulk (1 mm)	LuAG:Ce	2026	8.9	79.3

Table 2 Scintillation response properties of measured LuAG:Ce, LuYAG:Ce SCF samples compared with those of CZ grown LuAG:Ce single crystals (N_{phels}/MeV photoelectron yield, FWHM and N_{phels}/MeV difference (in %) between 0.5 and 10 μs shaping times).

From Fig. 8 and Tab. 2 we can clearly see that Czochralski grown LuAG:Ce crystals exhibit much more slow components (about 60 %) than LuAG:Ce or LuYAG:Ce SCF samples, see also last column of Tab. 2. However, the photoelectron yield N_{phels}/MeV of LuAG:Ce crystals is distinctly higher than that of Ce-doped LuAG or LuYAG SCF samples.

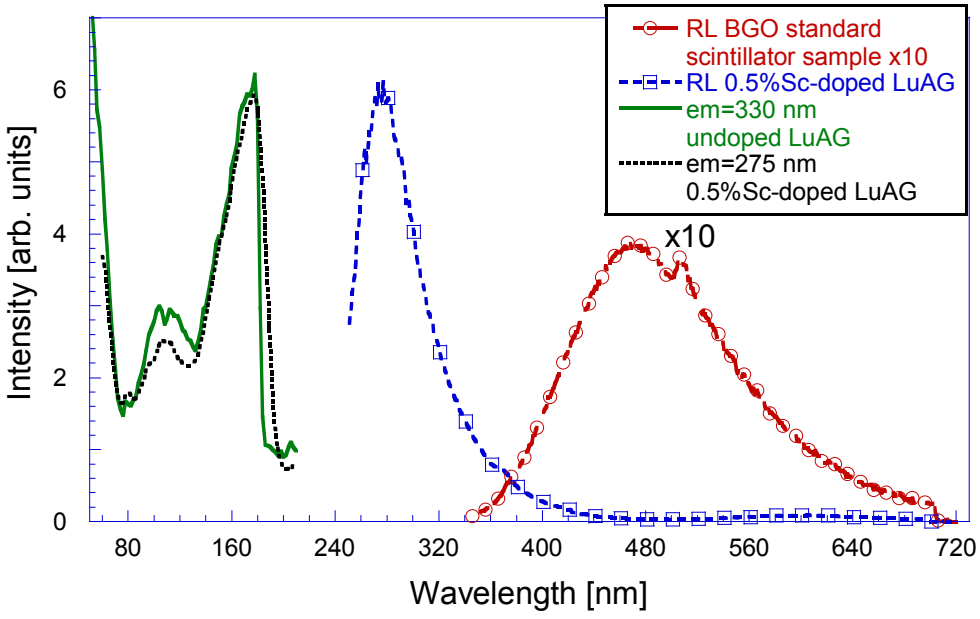

Fig. 9 Radioluminescence (RL) spectrum of 0.5%Sc-doped LuAG in absolute comparison with standard BGO scintillator sample. RT, excitation by X-ray tube, 40 kV, 15 mA. Excitation spectra of intrinsic luminescence of undoped LuAG (em=330nm) and that of Sc-related one (em=275 nm).#

3.4 UV emitting LuAG-based scintillators

It has been already mentioned in the literature that doping by isovalent ions of sufficiently different radius at Lu (Y) or Al site in aluminum garnets will result in appearance of UV emission bands [8,16-20]. The nature of such bands is usually interpreted in terms of localized (trapped) excitons around such substituted sites [18-20]. Scintillation characteristics of the Sc-doped LuAG single crystal [19] and SCF films [20] have been already reported in the literature. Radioluminescence spectrum of 0.5%Sc-doped LuAG is in Fig. 9. UV emission band shows the maximum at about 275 nm and an extended tail towards 400 nm can be interpreted as a residual intensity of the intrinsic undoped LuAG host emission in agreement with [19,20]. The 275 nm band is interpreted as a trapped exciton around the Sc-embedded site [19]. Excitation spectrum of the 275 nm emission closely follows that of the intrinsic 330 nm emission of undoped LuAG, see Fig. 9, which supports such an interpretation further. Scintillation decay reported in Fig. 10 is approximated by a two-exponential fit with the decay times of about 5 ns and 1330 ns, where the latter component contains more than 95% of the emitted scintillation light. TSL glow curve and spectra are provided in Fig. 11. It is interesting to note great similarity of the glow curve with those of undoped LuAG samples [21] where the glow curve was interpreted in terms of thermally induced liberation of holes from unspecified traps and their recombination with electrons localized elsewhere. In Fig. 11 b the band at 2 eV is the second order of the UV emission. The similarity of TSL and radioluminescence spectra in Fig. 9 and 11 suggests that electrons are localized around Sc ions sites and thermally liberated holes recombine with them. Due to the absence of intense TSL peaks above 130 K the afterglow of such a system at RT in millisecond time scale is expected to be rather low in accordance with the data provided in [19]. The growth of Sc-containing LPE films has been reported in [8], but the films were further codoped with Ce so that the dominant emission was that of Ce^{3+} in the green region of spectra. It is further expected that scintillation efficiency of such UV emitting $Lu_3(Al,Sc)_5O_{12}$ films will be decreased due to the use of PbO-based flux [22] so that other fluxes based e.g. on BaO would be necessary to reach good scintillation efficiency of such a UV emitting Sc-doped LuAG SCF. Due to the fact that the emission band of this system is peaking at 275 nm, it is expected that in the 2D-imaging application the diffraction limit can be decreased by almost a factor 2 with respect to the Ce-doped films used in the imaging experiment above.

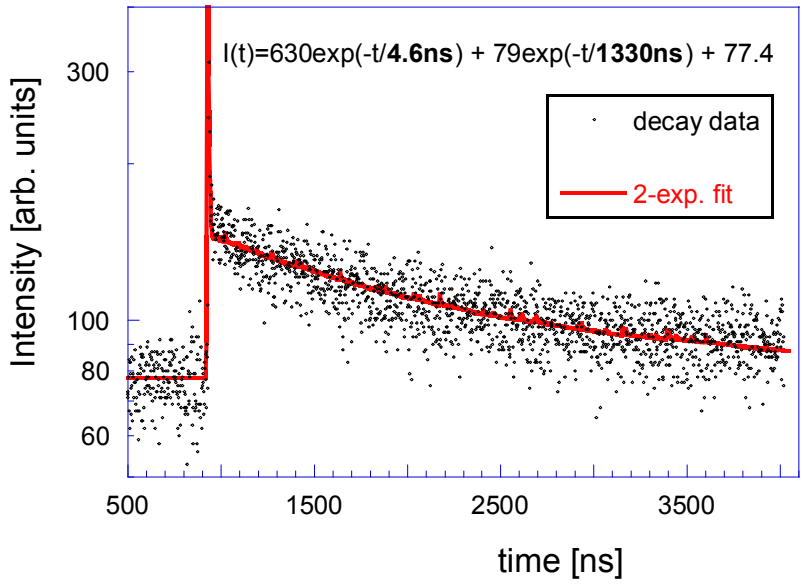

Fig. 10 Spectrally unresolved scintillation decay of 0.5%Sc-doped LuAG at RT. Excitation by ^{22}Na radioisotope (511 keV). The fit by solid line is the convolution of instrumental response and the function I(t) in the figure.

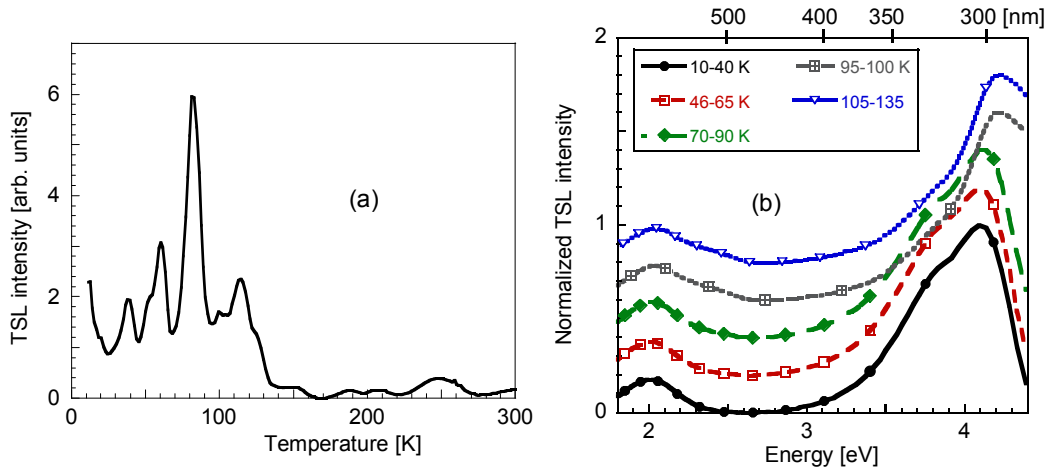

Fig. 11) TSL glow curve (obtained from integration of a wavelength resolved measurement in the 200-850 nm interval) after X- ray irrad iation at 10 K of 0 .5%Sc-doped LuA G,. b) TSL em ission sp ectra within the speci fied tem perature regions of the glow curve displayed in (a). Spectra are shifted on the ordinate scale for better clarity.

4. CONCLUSIONS

Using microfocused X-ray source and high resolution CCD camera with the appropriate focusing optics the 2D imaging with thin LPE films or plates (both about 20 μm thick) of LuAG:Ce single crystal can achieve sufficient contrast and the 2D resolution about 1 μm. Scintillation efficiency and photoelectron yield from present LPE films is somewhat inferior to those of single crystal plate of the same thickness made from Czochralski grown material. The deterioration of the former could be partially due to the use of PbO-based flux as already noted in the literature [23]. LuAG host offers a possibility to prepare an efficient UV emitting scintillation sensor with the emission peak at 275 nm when Sc doping is used at the level of 0.5%. 2D sensor based on such a material is expected to have the diffraction limit of about a factor of 2 lower with respect to presently used Ce-doped aluminum garnets.

Acknowledgement. This work was supported by the Czech GA AV KAN300100802 project. Support by the EC - Research Infrastructure Action under the FP6 "Structuring the European Research Area" Programme (through the Integrated Infrastructure Initiative "Integrating Activity on Synchrotron and Free Electron Laser Science i s acknowledged.

REFERENCES

[1] Koch, A., Raven, C., Spanne, P., and Snigirev, A., X-ray imaging with submicrometer resolution employing transparent luminescent screens *J. Opt. Soc. Am.* A 15, 1940-1951 (1998).

[2] Nikl, M., Scintillation detectors for X-rays. Meas. Sci. Technol. **17**, R37-R54 (2006).

[3] Tous, J., Horvath, M., Pina, L., Blazek, K. and Sopko, B., High-resolution application of YAG:Ce and LuAG:Ce imaging detectors with a CCD X-ray camera. Nucl. Instr. Meth. Phys. Research A 591 264-267 (2008).

[4] van Eijk, C. W. E., Andriessen, J., Dorenbos, P. and Visser, R., Ce^{3+} doped inorganic scintillators Nucl. Instr. Meth. Phys. Res.A 348 546-550 (1994).

[5] Pejchal, J., Nikl, M., Mihóková, E., Mareš, J.A., Yoshikawa, A., Ogino, H., Schillemat, K.M., Krasnikov, A., Vedda, A., Nejezchleb, K. and Múčka, V., Pr^{3+}-doped complex oxide single crystal scintillators. J. Phys. D: Appl. Phys. 42 055117 (2009) (10pp).

[6] Nikl, M., Mihokova, E., Mares, J.A., Vedda, A., Martini, M., Nejezchleb, K. And Blazek, K., Traps and timing characteristics of LuAG:Ce^{3+} scintillator. phys.stat.sol. (b) **181**, R10-R12 (2000).

[7] Nikl, M., Energy transfer phenomena in the luminescence of wide band-gap scintillators. phys. stat. sol. (a) 202, 201–206 (2005).
[8] Zorenko, Yu., Konstankevych, I., Globus, M., Grinyov, B. and Lyubinskiy, V., New scintillation detectors based on oxide single crystal films for biological microtomography. Nucl. Instr. Meth. Phys. Res.A 505, 93-96 (2003).
[9] Prusa, P., Cechak, T., Mares, J. A., Nikl, M., Beitlerova, A., Solovieva, N., Zorenko, Yu. V., Gorbenko, V. I. Tous, J., Blazek, K., The α-particle excited scintillation response of the LPE-grown LuAG:Ce thin films. Appl. Phys. Letters 92 041903 (2008) (3 pp)
[10] Nikl, M., Mares, J.A., Solovieva, N., Hybler, J., Voloshinovskii, A, Nejezchleb, K. and Blazek, K., Energy transfer to the Ce^{3+} centers in $Lu_3Al_5O_{12}$:Ce scintillator. Phys.stat.sol. (a) 201, R41-R44 (2004).
[11] Ambrosio, C. D' and Leutz, H., „Hybrid photon detectors," NIM Phys. Res. A 501, 463-498 (2003)
[12] Mares, J.A. and Ambrosio, C. D'., „Hybrid photomultipliers – their properties and application in scintillation studies," Opt. Mat. 30, 22-25 (2007)
[13] Mares, J.A., Beitlerova, A., Nikl, M., Solovieva, N., Ambrosio, C. D', Blazek, K.,P. Maly, P., Nejezchleb, K. and De Notaristefani, F., „Scintillation response of Ce-doped or intrinsic scintillating crystals in the range up to 1 MeV," Rad. Measur. 38, 353-357 (2004).
[14] Mares, J.A., Nikl, M., Blazek, K., Nejezchleb, K. and Ambrosio, C. D'. „Scintillation Characteristics and Development of Pr^{3+}, Ce^{3+}-Doped Lu-and Y-Aluminum Garnets" Proc. of the 8-th International Conference on Inorganic Scintillators and their Use in Scientific and Industrial Applications (SCINT'05), September 19-23, 2005, Alushta, Ukrajina, Kharkov, 138-141, (2006).
[15] Prusa, P., Nikl, M., Mares, J.A., Kucera, M., Nitsch, K. and Beitlerova A., The α-particle excited scintillation response of YAG:Ce thin films grown by liquid phase epitaxy, to be published in phys. stat. sol. (2009).
[16] Robertson, J.M. van Tol, M.V. and Smith, G., Philips J. Res. 36 15(1981).
[17] Valbis, Ya. A., Volzhenska, L. G., Dubov, Yu. G. Zorenko, Yu. V., Nazar, I. V. Patsagan, N. I., Luminescence centers in single crystalline compounds of yttrium-aluminium garnet doped by scandium isoelectronic impurity, Optics and Spectroscopy 63 1058-1063 (1987).
[18] Murk V and Yaroshevich N, Exciton and recombination processes in YAG crystals. J. Phys. Cond. Matter 7 5857-5864 (1995).
[19] Ryskin, N. N., Dorenbos, P., van Eijk, C. W. E. and Batygov, S. Kh., Scintillation properties of $Lu_3Al_{5-x}Sc_xO_{12}$ crystals. J. Phys. Cond. Matter 6 10423-10434 (1994).
[20] Yu. V. Zorenko, Luminescence of La^{3+} and Sc^{3+} Isoelectronic Impurities in $Lu_3Al_5O_{12}$ Single Crystalline Films Optics and Spectroscopy 100 572-580 (2006).
[21] Nikl, M., Vedda, A., Fasoli, M., Fontana, I., Laguta, V.V., Mihokova, E., Pejchal, J., Rosa, J. and Nejezchleb, K., Shallow traps and radiative recombination processes in $Lu_3Al_5O_{12}$:Ce single crystal scintillator. Phys. Rev. B 76, 195121 (2007).
[22] Zorenko, Yu., Gorbenko, V., Voznyak, T., Martin, T., Douissard, P. Mares, J. A. and Nikl, M., LuAG:Pr, LuAG:La and LuAP:Ce thin film scintillators for visualisation of X-ray images. Published in this SPIE volume.
[23] Babin, V., Gorbenko, V., Makhov, A., Mares, J. A., Nikl, M., Zazubovich, S. and Zorenko, Yu. Luminescence characteristics of Pb^{2+} centres in undoped and Ce^{3+}-doped $Lu_3Al_5O_{12}$ single-crystalline films and $Pb^{2+} \rightarrow Ce^{3+}$ energy transfer processes. J. Lumin. 127, 384-390 (2007)

The α-particle excited scintillation response of the liquid phase epitaxy grown LuAG:Ce thin films

P. Prusa[a] and T. Cechak
Faculty of Nuclear Sciences and Physical Engineering, Czech Technical University in Prague, Brehova 7, 11519 Prague, Czech Republic

J. A. Mares, M. Nikl, A. Beitlerova, and N. Solovieva
Institute of Physics AS CR, Cukrovarnicka 10, 16253 Prague, Czech Republic

Yu. V. Zorenko and V. I. Gorbenko
Laboratory of Optoelectronic Materials, Ivan Franko National University of Lviv, 107 Gen. Tarnavskyj Str., 79017 Lviv, Ukraine

J. Tous and K. Blazek
Crytur Ltd., Palackeho 175, 51101 Turnov, Czech Republic

(Received 21 November 2007; accepted 21 December 2007; published online 28 January 2008)

Liquid phase epitaxy grown $Lu_3Al_5O_{12}$:Ce (LuAG:Ce) 20 μm thick films and plate cut from the bulk Czochralski-grown LuAG:Ce crystal were prepared for comparison of photoelectron yield (PhY) and PhY dependence on shaping time (0.5–10 μs). ^{241}Am (α particles) was used for excitation. At the 0.5 μs shaping time, the best film shows comparable PhY with the bulk sample. PhY of bulk material increases noticeably more with shaping time than that of the films. Energy resolution of films is better. Influence of Pb^{2+} contamination in the films (from the flux) and antisite Lu_{Al} defect in bulk material is discussed. © *2008 American Institute of Physics*.
[DOI: 10.1063/1.2835458]

The Ce^{3+}-doped aluminum garnet scintillators $A_3Al_5O_{12}$, A=Y, Lu (YAG, LuAG) belong to a family of high performing complex oxide scintillators.[1,2] Decay times of scintillation response are degraded by an enhanced occurence of the delayed recombination processes in the melt-grown materials due to electron retrapping at shallow traps.[3,4] These traps were identified as due to the antisite (A^{3+} ion at the octahedral Al^{3+} site) defects,[5] which are dominant structural defects in garnet lattices[6–8] as an inevitable consequence of high melting temperature, when the Czochralski (CZ) or Bridgman technique is used. Apart from the bulk materials, their thin films are also of practical interest as can give rise to scintillation detectors with high two dimensional resolution down to even submicron scale, when coupled with suitable photodetector. Such resolution capability was demonstrated for YAG:Ce thin film,[9] where, however, due to low density and effective atomic number of YAG host only negligible percentage of incoming x-ray energy is effectively exploited. The growth and luminescence properties of LuAG:Ce films on YAG substrate have been recently reported.[10] Compared with YAG:Ce, LuAG:Ce appears much more suitable for this purpose due to elevated density and effective atomic number as well. Liquid phase epitaxy (LPE) method uses the $PbO-B_2O_3$ flux, which enables the film growth at much lower temperatures (around 1000 °C). Positive consequence of lower melting temperature is practical absence of the antisite defects, which results in faster energy delivery to the Ce^{3+} centers. However, Pb contamination was found in these films due to the flux used. Pb^{2+} luminescence has been described recently in the LPE-grown LuAG:Ce thin films.[11] As this emission is severely quenched at room temperature (RT), decrease of scintillation efficiency due to Pb contamination is expected.

The aim of this study is to compare the LPE-grown film and CZ-grown bulk LuAG:Ce scintillator for the amplitude and time dependence of their photoelectron yield and energy resolution as well. The achieved results confirm the positive impact of the absence of the antisite defects in the films on their scintillation characteristics.

The films of LuAG:Ce were grown by the LPE method using the solution (SL) based on $PbO-B_2O_3$ flux and (111) oriented YAG substrates of 20 mm diameter and 0.5 mm thickness.[10] The same raw materials (5*N* Lu_2O_3, 4*N* Al_2O_3, and CeO_2) were used also for the growth of the bulk sample described below. Typical film thickness was 25–30 μm. Five growth cycles were performed with slightly different temperature in the 915–930 °C range and the CeO_2 concentration in the SL of 7.5–10 mol %, resulting samples are further noted as Lu-*x* (*x*=2, 4, 5, 6, and 9). Due to the varying segregation coefficient of Ce^{3+} and Pb^{2+} ions with the SL temperature in the LPE-grown films, different Ce/Pb ratio can be obtained, which influences their scintillation efficiency. After an optical inspection in the microscope, the film was polished out from one substrate side (of visibly worse quality) also about 5 μm was removed from the other film side to get plane and flux-free surface. Also a plate of LuAG:Ce single crystal of about 10×10 mm^2 was cut from parent boule grown by the Czochralski method in reduction atmosphere at Crytur, Ltd. It was polished to the final thickness of about 0.5 mm. It will be further noted as SC-1 sample.

Scintillation response—photoelectron yield (PhY) of the samples was measured under the α-particle excitation from ^{241}Am radioisotope (5.4857 MeV) and the dependence of PhY and energy resolution on the shaping time (time gate)

[a]Electronic mail: petr.prusa@centrum.cz.

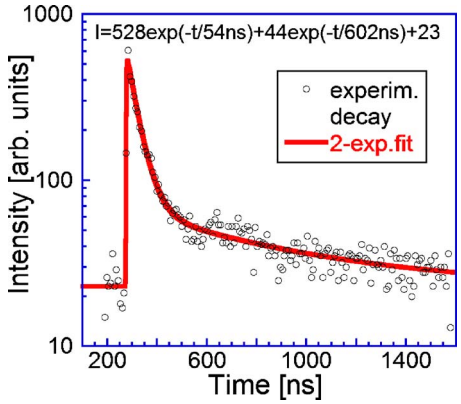

FIG. 1. (Color online) Spectrally unresolved scintillation decay of the SC-1 bulk LuAG:Ce sample (excitation by 511 keV photons from ^{22}Na radioisotope). Solid line is convolution of instrumental response (not in the figure) with the function $I(t)$ given in the figure.

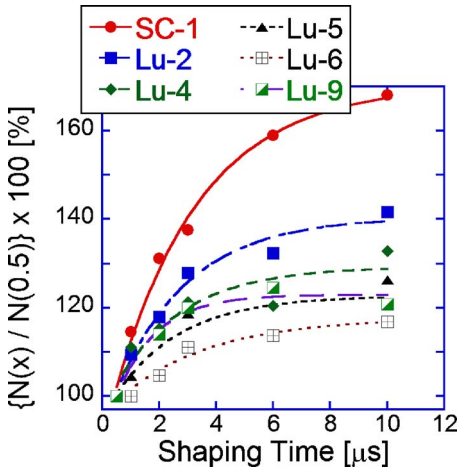

FIG. 2. (Color online) The dependence of normalized photoelectron yield on the shaping time duration, under excitation by ^{241}Am, α particles (E=5.4857 MeV). Solid lines are normalized fits using Eq. (3).

was measured as well within 0.5–10 μs. In LuAG:Ce, the penetration depth of such α particles was calculated of about 7 μm, i.e., complete energy deposition is achieved in 20 μm thick LPE-grown films. The experimental setup consisting of an HPMT photomultiplier, ORTEC electronic modules, and a multichannel plate in PC working in pulse-height mode was used.[12] For the reference, bulk SC-1 sample PhY was measured also under γ excitation (662 keV, ^{137}Cs). Scintillation decay of SC-1 was measured as well (511 keV, ^{22}Na). All measurements were performed at RT.

Scintillation decay obtained at SC-1 is presented in Fig. 1. It is approximated by the sum of two exponential terms. Typical values of the decay times of about 50–60 and 400–1000 ns are evaluated in the faster and slower component, respectively (see also Refs. 3, 4, and 13). Faster component is due to prompt electron-hole recombination at the Ce^{3+} centers, while the slower one is due to the delayed recombination process at the same centers.[14] Using shaping times over 0.5–10 μs in the measurement of PhY of such a material, we scan over the slower decay process (as the fast component has decayed entirely already within 500 ns). Using the mentioned two exponential approximation of the decay

$$I(t) = A \times \exp(-t/\tau_1) + B \times \exp(-t/\tau_2), \quad (1)$$

the expected time dependence of the light sum S [integral of $I(t)$ up to time t_0] for times $t_0 \gg \tau_1$ will, thus, be

$$S(t_0) = A\tau_1 + C\tau_2 - C\tau_2 \exp(-t_0/\tau_2) \quad (2)$$

and the measured dependence of photoelectron yield PhY should thus follow the time dependence

$$\mathrm{PhY}(t) = m_1 - m_2 \exp(-m_3 t), \quad (3)$$

where $m_{1,2,3}$ are constants related in an obvious way to the decay parameters in Eq. (2).

Time dependences of PhY(t) normalized to 100 at the shortest shaping time are in Fig. 2. Their approximations by Eq. (3) are given by solid lines and yield the parameter values as follows: m_1=170, 140, 129, 123, 118, and 123, m_2 =80.6, 48.0, 32.8, 27.6, 22.1, and 33.0, and m_3=0.329, 0.397, 0.421, 0.433, 0.313, and 0.715 for SC-1, Lu-2, Lu-4, Lu-5, Lu-6, and Lu-9 samples, respectively. There is clearly much higher relative increase of PhY with shaping time length in the case of bulk crystal sample with respect to LPE films. It is reflected in higher values of parameter m_2, which is proportional to the overall lightsum of the slower decay process.

Absolute value of PhY/MeV for selected shaping times are given in Table I. It is worth noting that for the SC-1 sample both α and γ excitation were accomplished and the former PhY values are typically 3.5–4 times lower with respect to the latter, which is a general phenomenon in scintillator materials.[15] Such a difference is explained by the dependence of PhY on the ionization density in the track of the excitation photon or particle. Higher ionization density results in the increasing interaction of excitations in the track and possible saturation of available emission centres which gives rise to additional nonradiative losses in the scintillator mechanism.

From the measured scintillation response, the energy resolution was also obtained by fitting the Gaussian function to the photopeak and evaluating full width at half maximum. Comparison among the film and bulk samples gave a very interesting result. Despite of equal or lower PhY in films with respect to the bulk samples the energy resolution in the former is clearly better (see Fig. 3).

The Lu_{Al} antisite defect (AD) in the melt-grown crystal creates a shallow electron trap, which effectively delays radiative recombination at Ce^{3+} ions.[5,14] Its absence in LPE-grown films is supported also by the observed suppression of

TABLE I. Values of PhY per MeV for the sample set and three different shaping times, excitation by α particles 5.4857 MeV, ^{241}Am. For the SC-1 LuAG:Ce single crystal the value under gamma excitation (662 keV, ^{137}Cs) is provided as well. Light yield N_{ph} (photons/MeV) can be calculated approximately as $N_{ph}=8\times N_{phels}$.

Sample	Shaping time (μs)		
	0.5	2	10
SC-1	340	446	571
Lu-2	338	398	478
Lu-4	293	338	389
Lu-5	291	300	367
Lu-6	194	203	226
Lu-9	218	248	263
SC-1 (γ)	1307	1775	2285

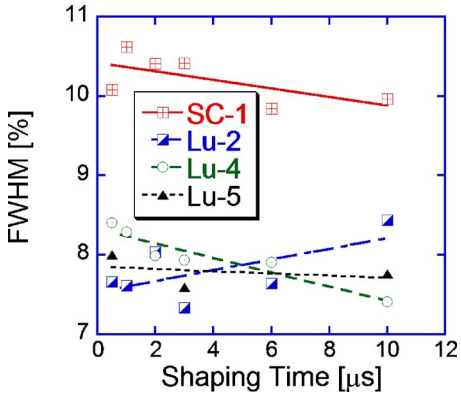

FIG. 3. (Color online) Dependence of the energy resolution (FWHM) on shaping time for the SC-1 bulk and Lu-2,4,5 LPE-grown film samples. The lines are only to guide the eyes.

AD-related emission both in YAG and LuAG films.[16] Faster emission decay in LPE garnet films at the band-to-band excitation has been reported already under synchrotron vacuum ultraviolet (VUV) excitation up to a few hundreds of nanoseconds and explained as due to the absence of Ce^{3+} excitation via the AD-based emission center as well as the absence of electron trapping at AD defects.[16] Consistently, time dependence also of PhY measured here up to the 10 μs shaping time shows the same trend in LPE samples, i.e., much less pronounced increase of PhY value with respect to the melt-grown bulk SC-1 sample. Unexpected improvement of the energy resolution in the films reported in Fig. 3 deserve another comment. It has been suggested that the energy resolution is affected by scintillator nonproportionality.[17] In the recent summary of achievements at this topic,[18] the degradation of energy resolution due to a cascade process occurring after a photoelectric interaction and due to particular features of exciton transport was discussed. The antisite defects in the aluminum garnet structure create effective localization sites for excitons. Thus, both the spectral and timing characteristics of the undoped material as well as the energy transport features to the Ce^{3+} emission centres are noticeably modified.[14,16] Reported results in Fig. 3 point to probable negative impact of these defects also on the energy resolution. This finding is consistent with recently reported dramatic improvement of the energy resolution in the bulk YAG:Ce after some of deep trapping states have been removed.[19]

Despite of the mentioned Pb-related nonradiative losses, the PhY value for the best film sample is equal to that of the bulk sample for the shortest shaping time. It further confirms the acceleration of energy transfer towards Ce^{3+} center in the films, which can balance the Pb-related energy losses. Thus, technology based on other flux which might not show such a negative impact,[20] can result in superior scintillation performance of LPE-grown films with respect to the bulk melt-grown aluminum garnets.

In conclusion, 20 μm thick LPE-grown films of Lu-AG:Ce appear competitive to their bulk analogs as for the scintillation response under α-particle excitation. Their photoelectron yield can reach the values of the bulk sample for the 0.5 μs shaping time. Furthermore, it shows in all the cases noticeably lower increase with enlarging shaping time up to 10 μs with respect to the bulk sample. It is explained by absence of specific shallow electron traps due to antisite Lu_{Al} defects in the LPE-grown films. Interestingly, despite of equal or even lower photoelectron yield the LPE-grown films show higher energy resolution with respect to the bulk sample, which points to dependence of energy resolution on the occurence of specific defects in the aluminum garnet structure.

Financial support of the Czech Science Foundation Grant No. 202/05/2471, INTAS Grant No. 04-78-7083, and Ministry of Education, Youth and Sports Grant No. MSM 6840770040 projects is gratefully acknowledged.

[1] M. Nikl, Meas. Sci. Technol. **17**, R37 (2006).
[2] M. Moszynski, T. Ludziejewski, D. Wolski, W. Klamra, and L. O. Norlin, Nucl. Instrum. Methods Phys. Res. A **345**, 461 (1994).
[3] M. Nikl, Phys. Status Solidi A **202**, 201 (2005).
[4] M. Nikl, V. V. Laguta, and A. Vedda, Phys. Status Solidi A **204**, 683 (2007).
[5] M. Nikl, E. Mihokova, J. Pejchal, A. Vedda, Yu. Zorenko, and K. Nejezchleb, Phys. Status Solidi B **242**, R119 (2005).
[6] M. Kh. Ashurov, Yu. K. Voronko, V. V. Osiko, A. A. Sobol, and M. I. Timoshechkin, Phys. Status Solidi A **42**, 101 (1977).
[7] M. M. Kuklja, J. Phys.: Condens. Matter **12**, 2953 (2000).
[8] C. R. Stanek, K. J. McClellan, M. R. Levy, and R. W. Grimes, Phys. Status Solidi B **243**, R75 (2006).
[9] A. Koch, C. Raven, P. Spanne, and A. Snigirev, J. Opt. Soc. Am. A **15**, 1940 (1998).
[10] Yu. Zorenko, V. Gorbenko, I. Konstankevych, B. Grinev, and M. Globus, Nucl. Instrum. Methods Phys. Res. A **486**, 309 (2002).
[11] V. Babin, V. Gorbenko, A. Makhov, J. A. Mares, M. Nikl, S. Zazubovich, and Yu. Zorenko, J. Lumin. **127**, 384 (2007).
[12] J. A. Mares, A. Beitlerova, M. Nikl, N. Solovieva, K. Nitsch, M. Kucera, M. Kubova, V. Gorbenko, and Yu. Zorenko, Radiat. Meas. **42**, 533 (2007).
[13] M. Nikl, E. Mihokova, J. A. Mares, A. Vedda, M. Martini, K. Nejezchleb, and K. Blazek, Phys. Status Solidi B **181**, R10 (2000).
[14] M. Nikl, A. Vedda, M. Fasoli, I. Fontana, V. V. Laguta, E. Mihokova, J. Pejchal, J. Rosa, and K. Nejezchleb, Phys. Rev. B **76**, 195121 (2007).
[15] R. B. Murray and A. Meyer, Phys. Rev. **122**, 815 (1961).
[16] Yu. Zorenko, V. Gorbenko, E. Mihokova, M. Nikl, K. Nejezchleb, A. Vedda, V. Kolobanov, and D. Spassky, Radiat. Meas. **42**, 521 (2007).
[17] J. D. Valentine and B. D. Rooney, Nucl. Instrum. Methods Phys. Res. A **353**, 37 (1994).
[18] W. W. Moses, S. A. Payne, G. Hull, and B. W. Reutter, "Scintillator non-proportionality," IEEE Trans. Nucl. Sci. (to be published).
[19] F. A. Selim, D. Solodovnikov, M. H. Weber, and K. G. Lynn, Appl. Phys. Lett. **91**, 104105 (2007).
[20] M. Kucera, K. Nitsch, M. Kubova, N. Solovieva, M. Nikl, and J. A. Mares, "Ce-doped YAG and LuAG epitaxial films for scintillation detectors," IEEE Trans. Nucl. Sci. (to be published).

Příloha 3 – Další publikační činnost autora v oboru výzkumu scintilátorů

PEJCHAL, J.; BÁRTA, J.; BABIN, B.; BEITLEROVÁ, A.; PRŮŠA, P.; KUČERKOVÁ, R.; PÁNEK, D.; PARKMAN, T.; GUGUSCHEV, C.; HAVLÁK, L.; ZEMENOVÁ, P.; KAMADA, K.; YOSHIKAWA, A.: Influence of Mg-codoping, non-stoichiometry and Ga-admixture on LuAG:Ce scintillation properties, *Optical Materials,* 2018, vol. 86, p. 213-232

PEJCHAL, J.; BURYI, M.; BABIN, V.; PRŮŠA, P.; BEITLEROVÁ, A.; BÁRTA, J.; HAVLÁK, L.; KAMADA, L.; YOSHIKAWA, A.; LAGUTA, V.; NIKL, M.; Luminescence and scintillation properties of Mg-codoped LuAG:Pr single crystals annealed in air, *Journal of Luminescence*, 2017, vol. 181, p. 277-285

MAREŠ, J.A.; BEITLEROVÁ, A.; PRŮŠA, P.; BLAŽEK, K.; HORODYSKÝ, P.; KAMADA, K.; YOSHIKAWA, A.; D'AMBROSIO, C.; NIKL, M.; Energy resolution studies of Ce- and Pr-doped aluminum and multicomponent garnets: The escape and photo-peaks, *Journal of Luminescence*, 2016, vol. 169, p. 701-705

JARÝ, V.; HAVLÁK, L.; BÁRTA, J.; MIHÓKOVÁ, E.; PRŮŠA, P.; NIKL, M.; Optical properties of Ce^{3+}-doped $KLuS_2$ phosphor, *Journal of Luminescence*, 2014, vol. 147, p. 196-201

CHEWPRADITKUL, W.; SHEN, Y.; CHEN, D.; YU, B.; PRŮŠA, P.; NIKL, M.; BEITLEROVÁ, A.; WANARAK, C.; Luminescence and scintillation of Ce^{3+}-doped high silica glass, *Optical Materials*, 2012, vol. 34, p. 1762-1766, **DOI:** 10.1016/j.optmat.2012.04.012

ZORENKO, Y.; GORBENKO, V.; SAVCHYN, V.; VOZNYAK, T.; GRINYOV, B.; SIDLETSKIY, O.; KURTSEV, D.; FEDOROV, A.; BAUMER, V.; NIKL, M.; MAREŠ, J.A.; BEITLEROVÁ, A.; PRŮŠA, P.; KUČERA, M.; Growth and Luminescent Properties of Lu2SiO5:Ce and (Lu1-xGdx)(2)SiO5:Ce Single Crystalline Films, *Journal of Crystal Growth*, 2011, vol. 337, iss. 1, p. 72-80

KUČERA, M.; NIKL, M.; PRŮŠA, P.; MAREŠ, J.A.; NITSCH, K.; HANUŠ, M.; ONDERIŠINOVÁ, Z.; KUČERKOVÁ, R.; Growth and emission properties of Sc, Pr, and Ce co-doped $Lu_3Al_5O_{12}$ epitaxial layers for scintillators, , *Journal of crystal growth*, 2011, vol. 318, p. 813-819

PRŮŠA, P.; KUČERA, M.; MAREŠ, J.A.; NIKL, M.; NITSCH, K.; HANUŠ, M.; ONDERIŠINOVÁ, Z.; ČECHÁK, T.; Scintillation properties of Sc, Pr, Ce- doped LuAG epitaxial garnet films, *Journal of crystal growth*, 2011, vol. 318, p. 545-548

ZORENKO, Y. MAREŠ, J.A.; PRŮŠA, P.; NIKL, M.; GORBENKO, V.; SAVCHYN, V.; KUČERKOVÁ, R.; NEJEZCHLEB, K.; Luminescence and scintillation characteristics of YAG:Ce single crystalline films and single crystals, *Radiation Measurements,* 2010, vol. 45, p. 389-391

Publikační činnost autora nesouvisející s tématikou výzkumu scintilátorů není uvedena. Jedná se o výsledky výzkumného projektu DIRAC, realizovaného v CERN. Příspěvek autora v těchto publikacích je relativně nízký.

Optical Materials 86 (2018) 213–232

Contents lists available at ScienceDirect

Optical Materials

journal homepage: www.elsevier.com/locate/optmat

Influence of Mg-codoping, non-stoichiometry and Ga-admixture on LuAG:Ce scintillation properties

J. Pejchal[a,*], J. Barta[a,b], V. Babin[a], A. Beitlerova[a], P. Prusa[a,b], R. Kucerkova[a], D. Panek[c], T. Parkman[c], C. Guguschev[d], L. Havlak[a], P. Zemenova[a], K. Kamada[e], A. Yoshikawa[e,f]

[a] Institute of Physics CAS, Cukrovarnicka 10, 16200, Prague, Czech Republic
[b] Faculty of Nuclear Sciences and Physical Engineering, Czech Technical University in Prague, Brehova 7, 11519, Prague, Czech Republic
[c] Faculty of Biomedical Engineering, Czech Technical University in Prague, Sitna Sq. 3105, Kladno, Czech Republic
[d] Leibniz-Institut für Kristallzüchtung, Max-Born-Str. 2, 12489, Berlin, Germany
[e] NICHe, Tohoku University, 6-6-10 Aoba, Aramaki, Aoba-ku, 980-8579, Sendai, Japan
[f] Institute for Materials Research, Tohoku University, 2-1-1 Katahira, Aoba-ku, 981-8577, Sendai, Japan

A B S T R A C T

This study focused on the influence of Mg codoping, non-stoichiometry and Ga-admixture on the scintillation and luminescence characteristics of Ce-doped lutetium-aluminum garnet crystals (LuAG), the stability of the Ce valence and the role of defects.

For the Ce-doped LuAG samples, codoping of Mg at a concentration around 300 ppm led to improvement of overall scintillation efficiency, which is in accordance with previous studies and can be attributed to an alternative scintillation mechanism involving Ce^{4+} stabilized by Mg^{2+}. Very significant improvement of the overall scintillation efficiency (almost a factor of 2) and exceptionally high light yield when compared to the stoichiometric sample was observed for the Ce0.2% Mg 300 ppm sample grown from the melt with 3 atomic % Al-rich nonstoichiometry. This was explained by enhanced energy transfer towards the Ce^{3+} luminescence center via defect levels induced by non-stoichiometry. The highest Mg concentration brings additional slow components to the scintillation decay.

Very similar trends were observed for the Ga-admixed LuGAG, but the defect luminescence was strongly suppressed. Suppression of this competitive luminescence channel led to further improvement of the overall scintillation efficiency. Interestingly, X-ray diffraction has shown that the crystals contain two or even three garnet phases with very close compositions.

1. Introduction

Scintillators are materials that convert the energy of ionizing radiation into photons of ultra-violet or visible light and are used for detection of ionizing radiation in various applications [1], such as security scanning, medical imaging [2], environmental monitoring, astronomy etc. The aluminum garnet-based scintillation materials have been intensively studied in the past decades due to their favorable properties, such as relatively easy crystal growth and mechanical, chemical and radiation stability. In the beginning the research focused mostly on the yttrium-aluminum garnet $Y_3Al_5O_{12}$ (YAG) [3] and its heavier analogue lutetium-aluminum garnet $Lu_3Al_5O_{12}$ (LuAG) [4]. Ce-doped LuAG showed fast Ce^{3+} 5d-4f emission around 510 nm; however, significant degradation of scintillation timing response has been already observed in the earliest studies [4]. This was ascribed to retrapping of electrons at shallow traps during their transport towards the luminescence center. It was found that the shallow electron traps are related to Lu_{Al} anti-site defects, when Lu^{3+} (or Y^{3+} in case of YAG) ion resides at the octahedral Al site. These defects are created also in other garnet crystals due to high temperatures during the crystal growth from the melt and their existence was confirmed by luminescence studies of 4f-4f emission of rare-earth-doped crystals [5,6]. Przyblinska et al. [7] also confirmed their presence in Czochralski-grown LuAG:Ce crystals with a determined concentration of about 0.5 atomic percent (at %, with respect to Al) using combination of infra-red spectroscopy and X-ray diffraction [7]. The Ce concentration in the concerned crystal was found to be 0.09 at % (with respect to Lu). Interestingly, Petrosyan et al. [8] demonstrated the directly proportional dependence of the Lu_{Al} concentration on Ce^{3+} content in the Bridgmann-grown crystals. For the undoped crystal, the Lu_{Al} concentration was determined to be 0.7 at % (with respect to Al), while for the highest Ce concentration (in the crystal) of 0.72 at % (with respect to Lu), the Lu_{Al} concentration was as high as 3 at % (with respect to Al). These observations are due to response of the lattice to incorporation of the very large Ce^{3+} cation. The electron paramagnetic resonance (EPR) spectroscopy revealed that some of the Ce^{3+} ions can also occupy the anti-site positions (octahedral Al sites), and that the Lu_{Al} defects are spatially correlated with Ce^{3+} ions occupying the dodecahedral sites [9]. Obviously, due to the

* Corresponding author.
E-mail address: pejchal@fzu.cz (J. Pejchal).

https://doi.org/10.1016/j.optmat.2018.10.015
Received 25 September 2018; Accepted 7 October 2018
Available online 15 October 2018
0925-3467/

Table 1
Summary of the nominal melt compositions formulas (index at the oxygen was rounded up to 12), dopant concentrations, non-stoichiometry and sample acronyms.

Nominal melt composition	Ce concentration (atomic %)	Mg concentration (atomic ppm)	Non-stoichiometry (atomic %)	Sample acronym
$Lu_{2.994}Ce_{0.006}Al_5O_{12}$	0.2	0	0	LuAG:Ce
$Lu_{2.994}Ce_{0.006}Al_{4.9985}Mg_{0.0015}O_{12}$	0.2	300	0	LuAG:CeMg300
$Lu_{2.994}Ce_{0.006}Al_{4.985}Mg_{0.015}O_{12}$	0.2	3000	0	LuAG:CeMg3000
$Lu_{2.964}Ce_{0.006}Al_{5.0285}Mg_{0.0015}O_{12}$	0.2	300	1	Lu2.97AG:CeMg300
$Lu_{2.904}Ce_{0.006}Al_{5.0885}Mg_{0.0015}O_{12}$	0.2	300	3	Lu2.91AG:CeMg300
$Lu_{2.904}Ce_{0.006}Al_{5.09}O_{12}$	0.2	0	3	Lu2.91AG:Ce
$Lu_{2.994}Ce_{0.006}Ga_3Al_2O_{12}$	0.2	0	0	LuGAG:Ce
$Lu_{2.994}Ce_{0.006}Ga_3Al_{1.9985}Mg_{0.0015}O_{12}$	0.2	300	0	LuGAG:CeMg300
$Lu_{2.994}Ce_{0.006}Ga_3Al_{1.9955}Mg_{0.0045}O_{12}$	0.2	900	0	LuGAG:CeMg900
$Lu_{2.994}Ce_{0.006}Ga_3Al_{1.985}Mg_{0.015}O_{12}$	0.2	3000	0	LuGAG:CeMg3000
$Lu_{2.964}Ce_{0.006}Ga_3Al_{2.0285}Mg_{0.0015}O_{12}$	0.2	300	1	Lu2.97GAG:CeMg300
$Lu_{2.904}Ce_{0.006}Ga_3Al_{2.0885}Mg_{0.0015}O_{12}$	0.2	300	3	Lu2.91GAG:CeMg300

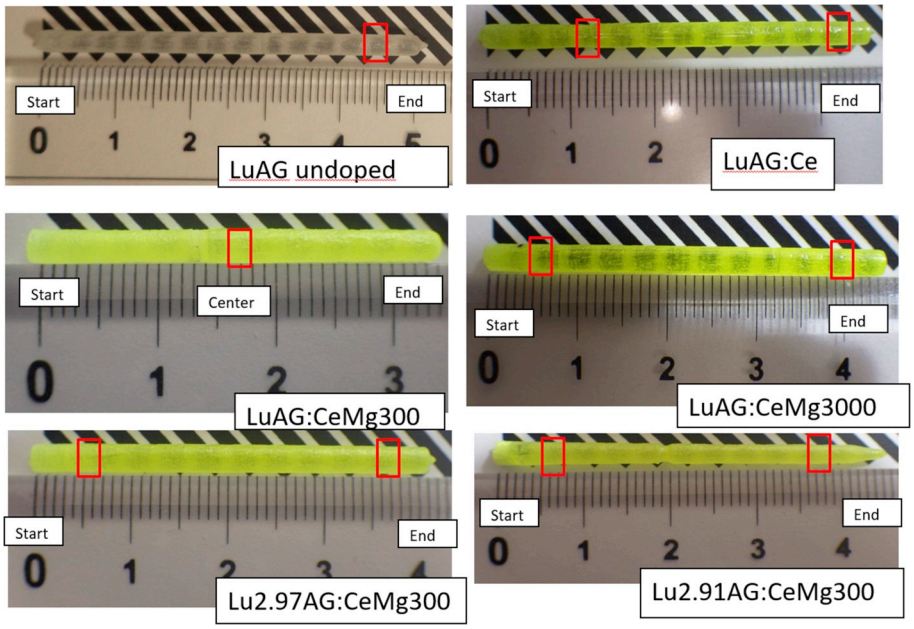

Fig. 1. The as-grown crystal rods based on LuAG. The red rectangles indicate the cut parts used for optical characterization. (For interpretation of the references to color in this figure legend, the reader is referred to the Web version of this article.)

larger radius of Y^{3+}, the Y_{Al} concentration in YAG is expected to be smaller with respect to that of Lu_{Al} in LuAG.

Discovering the influence of Lu_{Al} on the scintillation parameters, the subsequent research focused on improvement of the scintillation properties reducing the negative influence of anti-site defects.

For the Ce-doped LuAG (LuAG:Ce) it was found that the effect of the Lu_{Al} shallow traps can be greatly reduced by Ga-admixture while also suppressing the host emission related to exciton trapped at the Lu_{Al} [10]. Such an improvement consists in burying the shallow trap levels in the conduction band, whose edge shifts towards lower energies upon Ga admixture. The same was concluded in the earlier studies of the Pr-doped analogue [11]. On the other hand, the shift of the conduction band edge to the lower energies for the higher concentrations of Ga facilitates the 5d-excited state ionization of both Ce^{3+} and Pr^{3+} and resulting luminescence quenching. For the Ce-doped crystals this problem was solved by Gd-admixture, which shifts the Ce^{3+} 5d level to lower energies and increases its separation from the edge of the conduction band. In this way the highly-efficient multicomponent garnet scintillators have been developed [12].

Another way to reduce the negative influence of the anti-site defects can be stabilization of Ce^{4+} ion by divalent ion codoping. The positive effect of the Ce^{4+} consists in introduction of an alternative scintillation mechanism, where the Ce^{4+} directly competes with shallow electron traps including anti-site defects for electrons in the earliest stage of the scintillation process [13]. Such an approach was first found to work for the Ce-doped lutetium-yttrium-silicate (LYSO) scintillators [14] and was extended immediately to the LuAG:Ce and other garnet scintillation materials. Cerium can be promoted to its tetravalent state also by annealing in an oxidizing atmosphere. For more information see a broad overview of garnet-based scintillators in Ref. [15] and the references therein.

Since the Lu_{Al} defects are created due to the tendency of the matrix for an intrinsic (Lu-rich) non-stoichiometry [6], another solution of the problems related to the Lu_{Al} can be shifting the melt composition towards the Al-rich one. Not many papers have been devoted to the study of an intentional non-stoichiometry in LuAG so far. Positive effects of the Al-rich composition have been demonstrated both for the undoped LuAG single crystals [16] and optical ceramics [17]. Conversely, other group proposed positive effect of the Lu-rich non-stoichiometry on the scintillation properties of LuAG ceramics, but no reliable proof has been reported, though some positive effects on density and sintering process were found [18]. But the other works [16,17] confirmed negative effect of the Lu excess, which could be expected as the concentration of the Lu_{Al} would be increased due to the mentioned natural tendency of the melt to Lu-rich non-stoichiometry. Positive effect of the Al-rich non-stoichiometry on scintillation properties including scintillation decay time and energy resolution has been shown for YAG:Ce scintillator [19]. When considering the Al-rich non-stoichiometry in garnets, there

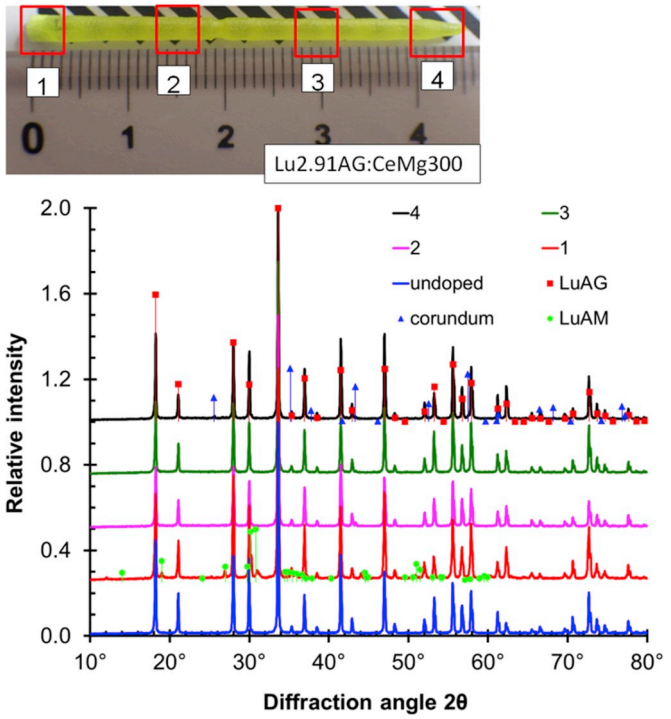

Fig. 2. XRD patterns of the selected parts of the Lu2.91AG:CeMg300 sample (see the photograph).

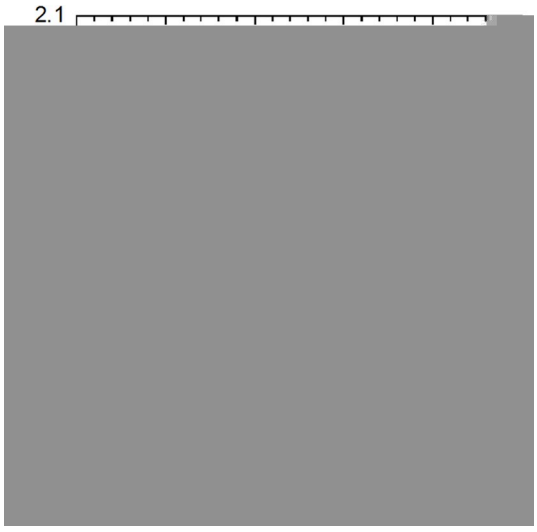

Fig. 3. Local composition of the Lu2.91AG:CeMg300 sample for different distances from the seed. (Ce and Mg was omitted for simplicity).

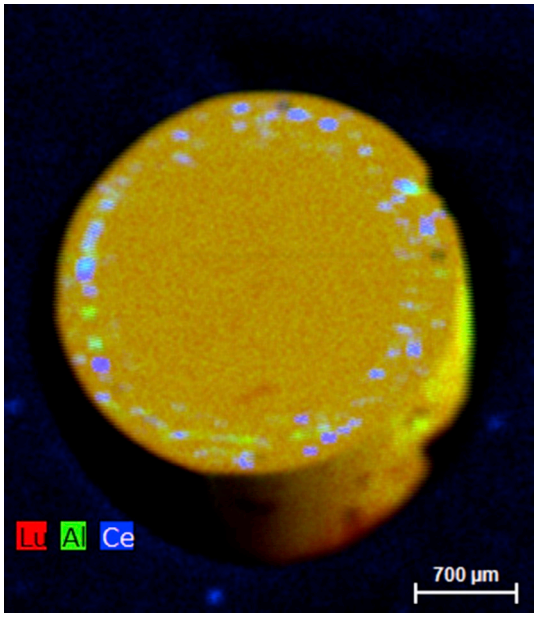

Fig. 4. µ-XRF element distribution map for Lu, Al and Ce measured for the cross-sectioned LuAG:Ce sample.

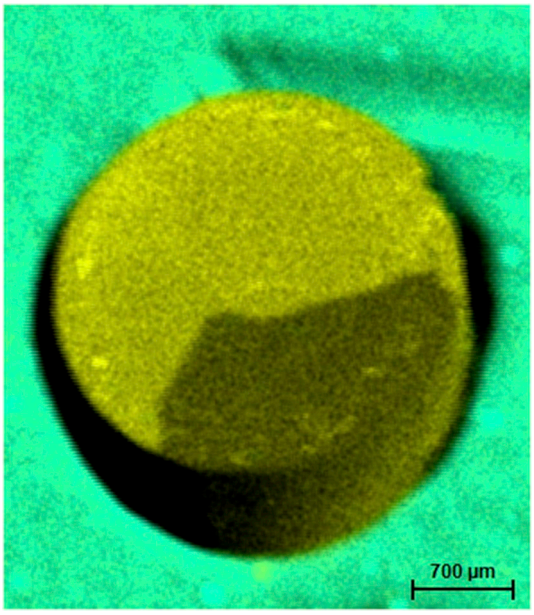

Fig. 5. EDLM results for the cross-sectioned LuAG:Ce sample.

is a question about the existence of the opposite anti-site defect in which Al would reside on the Lu (Y) site, i. e., Al_{Lu} (Al_Y). Theoretical calculations for the YAG crystal and their correlation with X-ray diffraction measurements [20] have revealed that formation energy of Al_Y defect would be the second lowest right after that for the Y_{Al} one. However, the calculated data and the X-ray measurements match only up to 0.2 mol% of Al_2O_3 excess. Above this concentration, other defects are most probably created, while surprisingly no Al_2O_3 inclusions have been observed [20]. Existence of the Al_{Lu} anti-site defect was also indirectly confirmed by EPR experiments as it increases the thermal stability of self-trapped hole in the garnet crystals [21]. There is also a question about the charge-trapping behavior of such a defect. Simulations based on the Density-functional theory [22] applied to YAG structure have suggested that such a defect would introduce a level slightly above the edge of the valence band, i. e., it would behave as a hole trap. Similar can be expected for the LuAG analogue.

Concerning the further improvement of the performance of LuAG-based scintillators, there is a question about interplay of the phenomena described above, i. e., Ga admixture, introduction of Ce^{4+} and non-stoichiometry. While Ce^{4+} would compete with the Lu_{Al} anti-site defects, Ga admixture and non-stoichiometry would reduce their trapping efficiency or concentration, respectively. Combination of these approaches is expected to improve the scintillation performance of the material.

The aim of this work is to study the influence of stoichiometry, Ga admixture and tetravalent Ce on LuAG scintillation characteristics, with the Ce^{4+} stabilized by Mg codoping. The influence of annealing of selected samples in air will be reported as well.

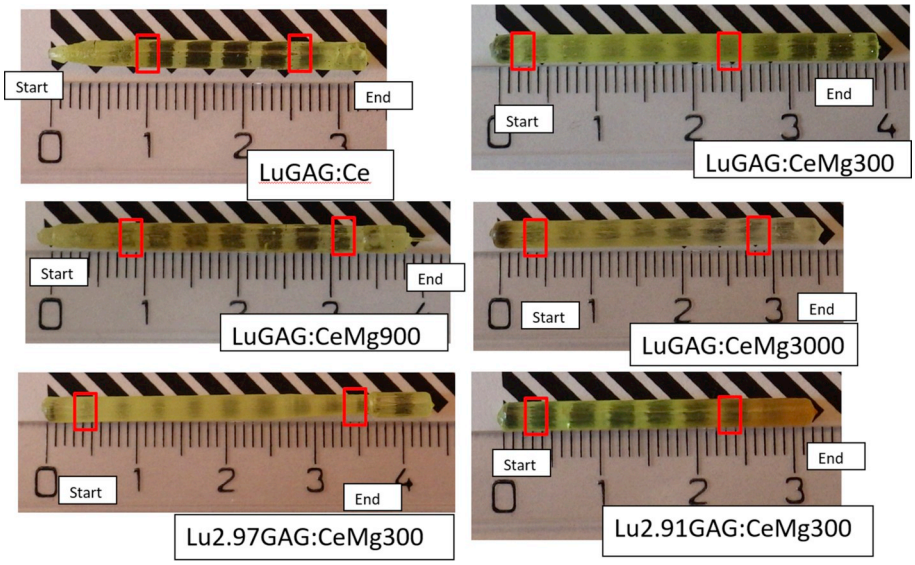

Fig. 6. The as-grown crystal rods based on LuGAG. The red rectangles indicate the cut parts used for optical characterization. (For interpretation of the references to color in this figure legend, the reader is referred to the Web version of this article.)

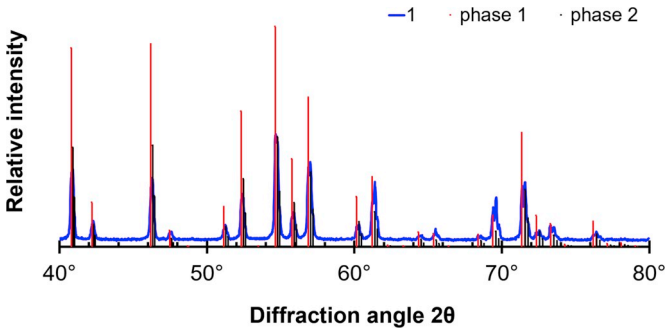

Fig. 7. XRD pattern of the selected part of the LuGAG:Ce 0.2% sample.

2. Materials and methods

The LuAG crystals were grown by micro-pulling-down method [23,24] with radiofrequency inductive heating. An iridium crucible with a die of 3 mm in diameter was used. The growth was performed under N_2 (4 N) atmosphere using < 100 > oriented LuAG single crystal as a seed. The pulling speed was around 0.07–0.1 mm/min. The starting materials were prepared by mixing 4 N purity Lu_2O_3, Al_2O_3 and CeO_2 powders. $MgCO_3$ of 4 N purity was added to the mixture for the Mg-codoped samples.

The growth was performed from slightly overheated melt to decrease its viscosity and increase wettability allowing the melt to spread over the whole diameter of the die. The hot-zone and afterheater were modified to keep a very steep vertical temperature gradient and mild radial gradient to improve the crystal quality. This means the hole diameter in the ceramic piedestal below the afterheater was increased and the afterheater was slightly shortened.

The LuAG:Ce samples with Ce concentration of 0.2 at % (with respect to Lu) were prepared. The Mg concentration was 0, 300 or 3000 atomic ppm (with respect to Al). We suppose that Ce substitutes for Lu and Mg substitutes for Al, even though Mg can be incorporated in all three kinds of sites available within the garnet structure [25]. Therefore, the Ce concentration is given with respect to Lu, while the Mg concentration is given with respect to Al. In addition, samples with 0.2 at % of Ce and 300 ppm Mg were prepared from the melt with 1 at % and 3 at % non-stoichiometry. The nominal composition of the starting material can be described using the following hypothetical formula, where x, y and n are related to Ce, Mg and off-stoichiometry,

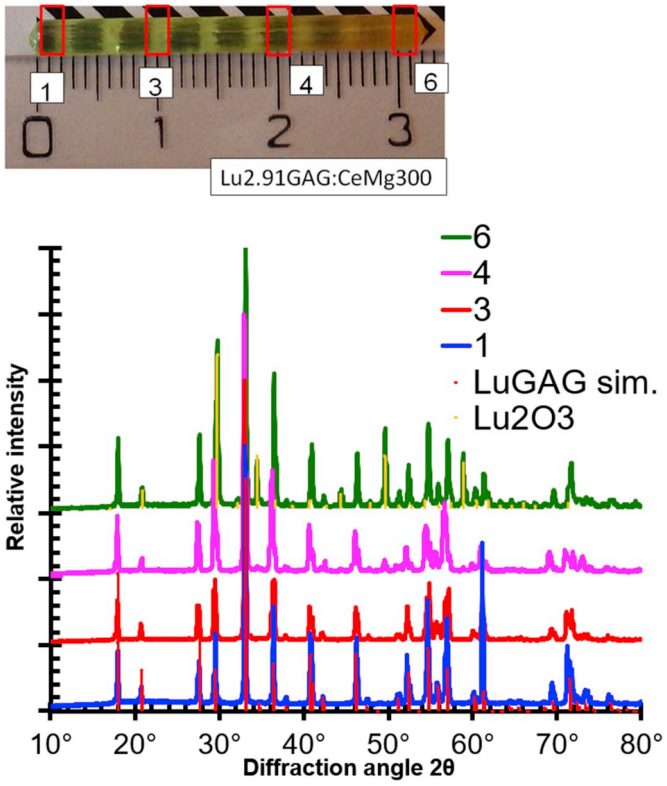

Fig. 8. XRD patterns of the selected parts of the Lu2.91GAG:CeMg300 sample (see the photograph).

respectively: $Lu_{3(1-n-x)}Ce_{3x}Al_{5(1+3n/5-y)}Mg_{5y}O_{(12+3x/2-5y/2)}$.

In the samples grown from the stoichiometric melt the nominal composition therefore corresponded to n = 0, while x = 0.002, y = 0, 0.0003, or 0.003. For the sample grown from the non-stoichiometric melt x = 0.002 and y = 0.0003 were used, while n = 0.01 or 0.03. One completely undoped crystal was also grown for comparison.

The Ga-admixed counterparts were also grown by the micro-pulling-down apparatus, using the same crucible and starting materials adding the 5 N Ga_2O_3. Due to better wettability, the < 100 > oriented YAG single crystal was used as a seed. The pulling speed was again

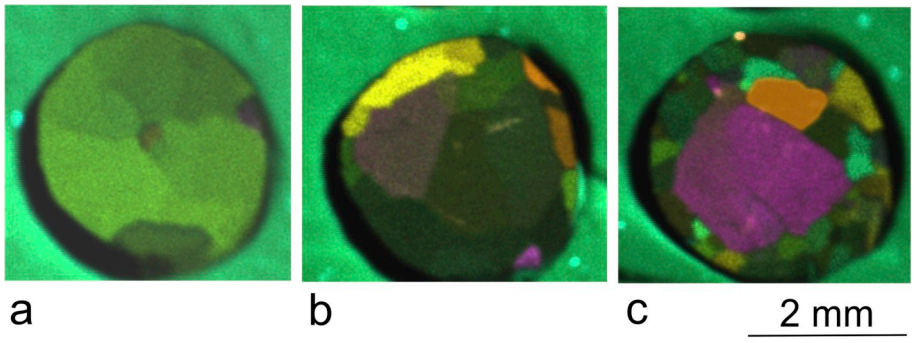

Fig. 9. EDLM results for selected LuGAG samples: (a) LuGAG:CeMg 300 (b) LuGAG:CeMg3000, (c) Lu2.91GAG:CeMg300.

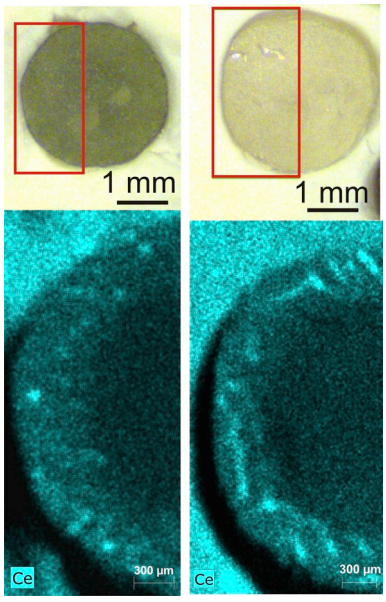

Fig. 10. µ-XRF element distribution maps for Ce measured on a cross-section of a LuGAG:CeMg300 sample (left) and on a LuGAG:CeMg3000 sample (right). The red boxes marked at the photographs indicate the measurement regions on the samples.

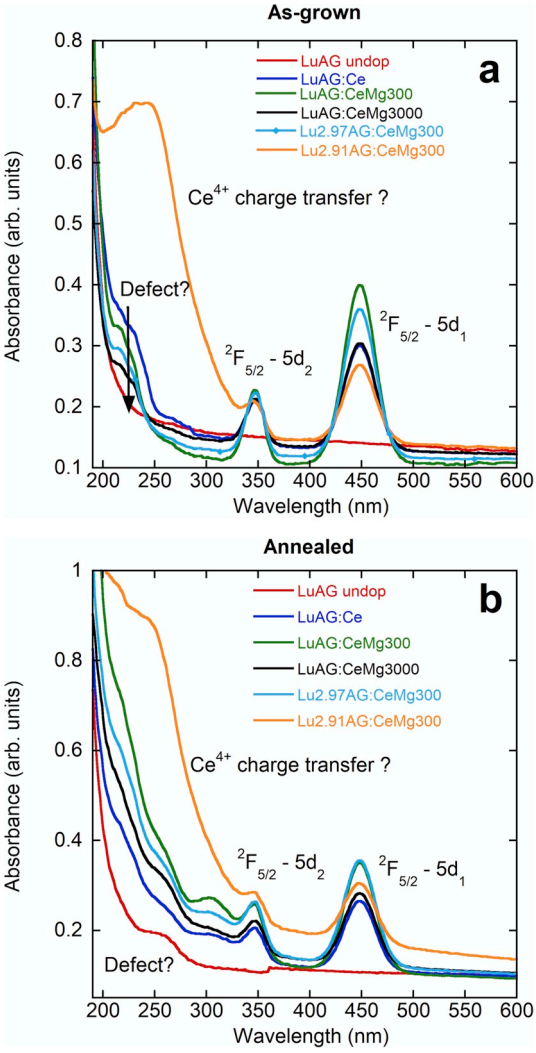

Fig. 11. Absorption spectra of the LuAG samples before (a) and after annealing (b).

0.07–0.1 mm/min. Excess of 1 mass % of Ga_2O_3 was added to compensate for Ga_2O_3 decomposition and subsequent evaporation. The Ar atmosphere was used to grow the $Lu_{2.91}Ga_3Al_{2.09}O_{12}$:Ce 0.2% Mg 300 ppm sample, while 1% O_2 was added in the growth of the other samples Three atoms of Al in the general formula were replaced by Ga (e.g. close to $Lu_3Al_2Ga_3O_{12}$ stoichiometry) and concentrations of Ce and Mg were the same as well as the Al excess in the LuAG crystals grown from the non-stoichiometric melt. Replacement of 3 Al by Ga was chosen as the earlier studies revealed that such a composition has still quite a high light yield among Ga-admixed LuAG (LuGAG) crystals while keeping fast scintillation response [26].

The composition can be again summarized with the analogous formula $Lu_{3(1-n-x)}Ce_{3x}Ga_3Al_{2(1+3n/2-5y/2)}Mg_{5y}O_{(12+3x/2-5y/2)}$. For the samples grown from stoichiometric melt n = 0, while x = 0.002, y = 0, 0.0003, 0.0009 and 0.003. For the samples grown from the non-stoichiometric melt x = 0.002 and y = 0.0003, while n = 0.01 or 0.03. The atomic % or atomic ppm will be again used for simplicity further in the text together with the nominal matrix composition. The samples will be marked further in the text using the acronyms summarized in Table 1 together with dopant concentrations and non-stoichiometry. For simplicity, the samples grown from the stoichiometric melt will be further denoted as "stoichiometric", while the term "non-stoichiometric" will be reserved for the samples grown from the non-stoichiometric melt.

The grown crystal rods had diameter of 3 mm and were from 35 to 45 mm in length. 1 mm thick circular samples were cut from approximately 1 cm from the seed part (marked as START) and 1 cm from the end part (marked as END) of the rod and mirror-polished for further optical characterization. The only exception is the LuAG:Ce0.2% Mg 300 ppm, where only the center part was chosen after visual examination of the crystal surface, where the start and end areas did not seem to be of sufficient quality. After characterization, the Ga-free samples were annealed in air for 12 h at a temperature of 1200 °C and investigated again.

The phase purity of the prepared crystals was examined by XRD

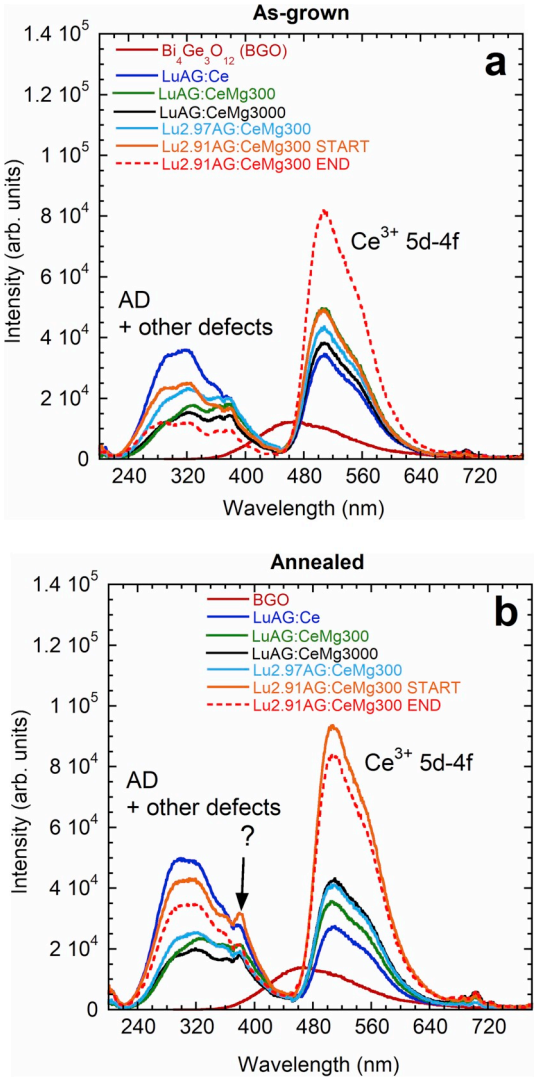

Fig. 12. RL spectra (under X-ray excitation) of the LuAG samples before (a) and after annealing (b).

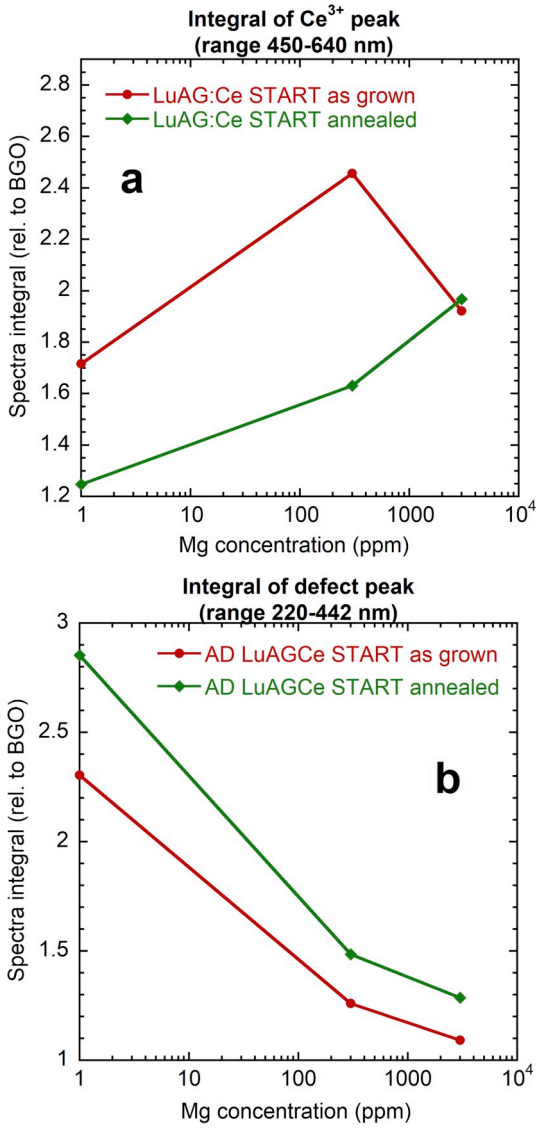

Fig. 13. Integrals of the RL spectra (under X-ray excitation) of the LuAG as-grown and annealed samples and their dependence on the Mg concentration: the Ce^{3+} emission peak (a) and the defect emission (b). Due to logarithmic scale on the x-axis, the Mg-free sample is represented as 1 ppm Mg.

analysis using the Rigaku MiniFlex 600 powder X-ray diffractometer equipped with Ni-filtered Cu X-ray tube (Cu-K$\alpha_{1,2}$ line; 40 kV, 15 mA) and NaI:Tl scintillation detector. Prior to the measurement, a selected part of the prepared crystal was grinded into a fine powder in an agate mortar and its diffraction pattern was then measured in continuous mode between 10° and 80° 2θ (scan rate 0.02°/min).

The X-ray fluorescence analysis (XRF) was performed using an X-ray fluorescence (XRF) analyzer Niton XL3t 900 GOLDD with Ag X-ray tube to investigate the elemental composition of the prepared crystals. For the XRF analysis, Lu-La (7.66 keV) and Ce-La (4.84 keV) fluorescent lines were used.

For selected samples, micro-X-ray fluorescence (μ-XRF) and energy-dispersive Laue mappings (EDLM) [27] were performed using a Bruker M4 Tornado apparatus to reveal element distributions at the crystal cross-sections and to evaluate the crystalline quality, respectively. The measurement system was equipped with an Rh X-ray source operated at 50 kV and 600 μA. Polycapillary X-ray optics were used to focus the non-polarized bremsstrahlung at the surface of the samples which results in a high spatial resolution of about 20 μm. Using a measurement time of 10 ms per point, the entire sample surfaces were scanned “on the fly” in small step distances (8–11 μm) and were cyclically repeated several times to increase count statistics, i.e. 6 to 10 passes of the scans were performed.

Luminescence measurements were performed by a modified spectrofluorometer (custom made 5000 M model, Horiba Jobin Yvon) equipped with TBX-04 photon counting detector (IBH Scotland). A deuterium steady-state lamp (Heraeus) was used for the excitation and emission spectra measurements. An X-ray tube operating at a voltage of 40 kV and 15 mA current with W anode (Seifert GmbH.) was used as an excitation source for the radioluminescence (RL) measurements. All the spectra were corrected for experimental distortions caused by the setup. The hydrogen nanosecond flashlamp or pulsed nanoLED source (IBH Scotland) were used for the luminescence decay measurements using the methods of time correlated single photon counting. Exponential fits of the decays were obtained by performing the convolution of the considered function with the instrumental response and a least-square sum fitting procedure (SpectraSolve software package from Ames Photonics). Thermally-stimulated luminescence measurements (TSL) and temperature dependent measurements were performed with the same apparatus using a cryostat. TSL glow curves were recorded with a heating rate of 6 K/min after irradiation of the samplein ultra-violet range at 13 or 77 K. The spectrally unresolved TSL signal was registered by a monochromator at zero order. For the measurements in wide

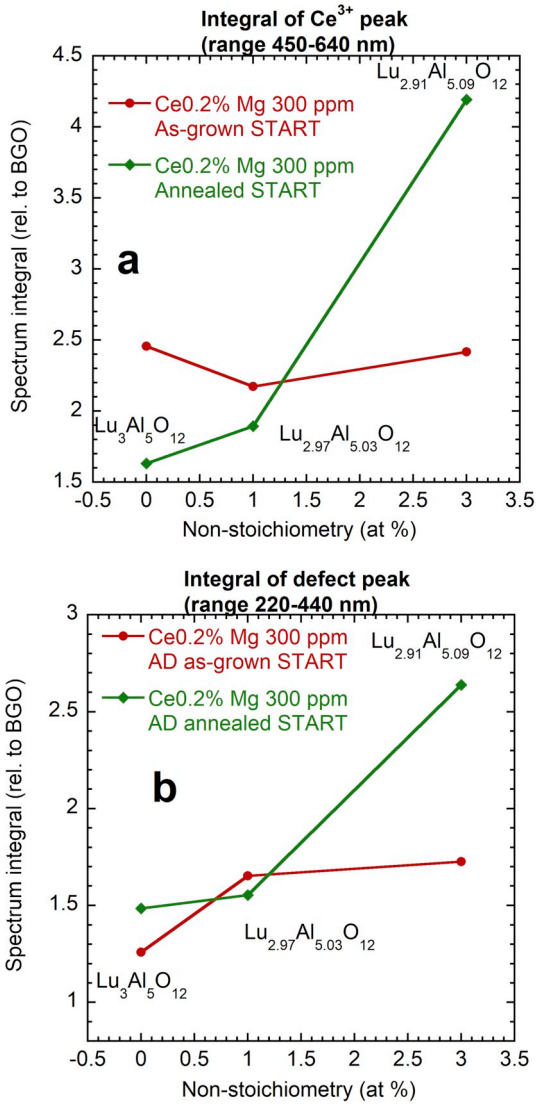

Fig. 14. Integrals of the RL spectra (under X-ray excitation) of the LuAG as-grown and annealed samples and their dependence on the sample stoichiometry: the Ce^{3+} emission peak (a) and the defect emission (b). The Mg concentration was 300 ppm in all the samples. The nominal matrix composition (omitting Ce and Mg dopants) is indicated for every point.

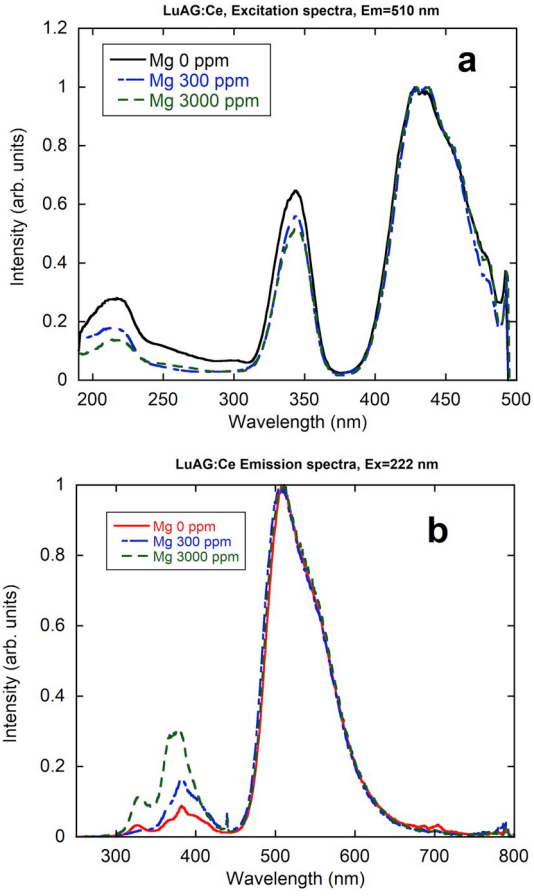

Fig. 15. Excitation spectra of the Ce^{3+} 510 nm emission for the as-grown LuAG:Ce stoichiometric samples with different Mg concentrations (a) and emission spectra under 222 nm excitation for the same samples (b).

temperature range, two cryostats were used: liquid nitrogen, for 77–800 K and closed cycle refrigerator, for 10–500 K (Janis).

For the scintillation light yield measurements, sample crystals were optically coupled with a hybrid photomultiplier (HPMT) DEP PPO 475B by silicon grease and wrapped in teflon tape used as a reflector (preliminary, $BaSO_4$ was used also for one sample, but the result was practically the same as for Teflon). The ^{137}Cs (661.6 keV) source was used for excitation and the amplifier shaping time was 6 μs The scintillation decay kinetics was measured with a fast photomultiplier and Tektronix TDS3052C digital Phosphor Oscilloscope under ^{137}Cs excitation. Scintillation decay data were evaluated by the SpectraSolve software as well. All the optical and scintillation measurements apart from TSL and temperature dependences were performed at room temperature (RT).

The scintillation decay under soft X-ray (SXR) excitation was performed using a nanosecond pulsed excitation source consisting of Ar plasma produced by short IR laser pulses (7 ns) in a gas puff target. The emitted radiation was filtered using a twin Ti filter of 0.4 μm thickness, which resulted in radiation with photon-energy of 350–450 eV and 4–5 ns duration. The light emitted from the sample further passed through a monochromator (Jobin Yvon H20) and was detected by a photomultiplier (Hamamatsu R7056). The signal was amplified by a *trans*-impedance amplifier (Analogue Devices AD847) and recorded by a digital oscilloscope (Agilent Infiniium DSO7104). For further details see Ref. [28]. The resulting curves were also corrected for the instrumental response using a deconvolution procedure in Matlab software.

3. Results and discussion

3.1. Characterization of the grown LuAG crystals

The as-grown LuAG-based crystal rods are shown in Fig. 1. The Ce-doped samples seem to be slightly opaque, but the opacity is just observed on the surface layer with the elevated concentration of the Ce dopant, which is a consequence of quite significant Ce segregation. The inner part of the crystals was transparent. The rectangles indicate the parts that were cut, polished and used for further optical characterization. The rest was used for XRD and XRF measurements.

The XRD diffraction patterns recorded, except for the most Lu2.91AG:CeMg300, were fully consistent with the ICDD PDF-2 record 01-73-1368 ($Lu_3Al_5O_{12}$) and showed some evidence of slight preferred orientation due to the grinding of the single-crystalline material. Regarding the mentioned non-stoichiometric Lu2.91AG:CeMg300 sample, we can see that the very beginning is strongly cracked and at the end the crystal narrowed to a conical shape. This sample has been measured by XRD and XRF more in detail. Other 4 parts were cut from the sample, as shown in the inset of Fig. 2. The parts were numbered from 1 (the beginning) to 4 (the end) and their XRD patterns are shown in Fig. 2 together with that for the undoped LuAG sample. The part 1

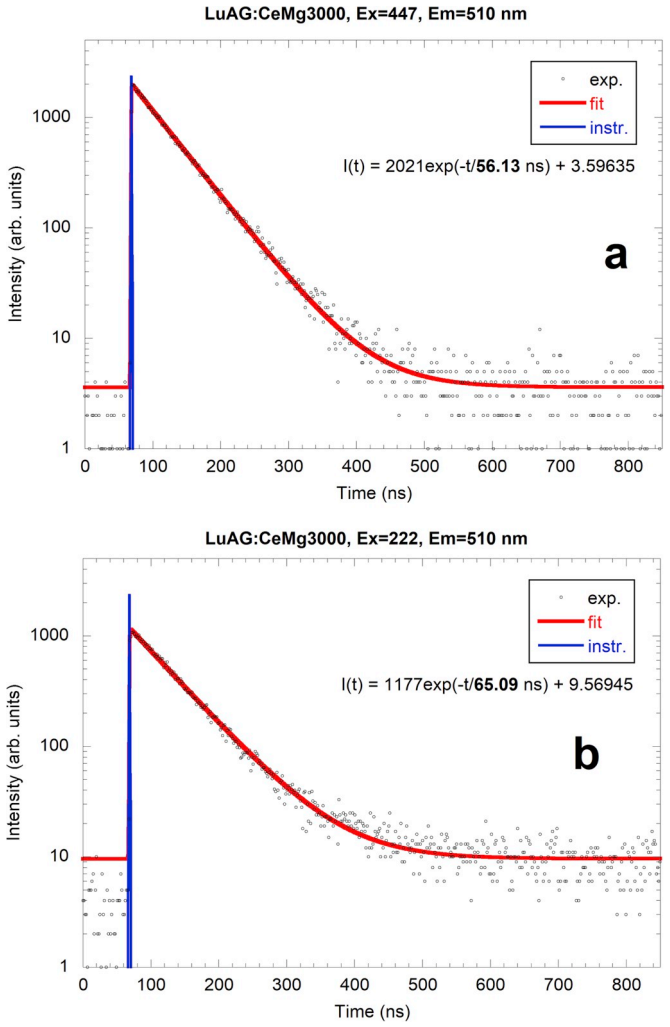

Fig. 16. Example of photoluminescence decay curves for the as-grown stoichiometric LuAG:CeMg3000 sample under 447 nm excitation directly into 4f-$5d_1$ Ce^{3+} transition (a) and under 222 nm excitation into a defect band (b).

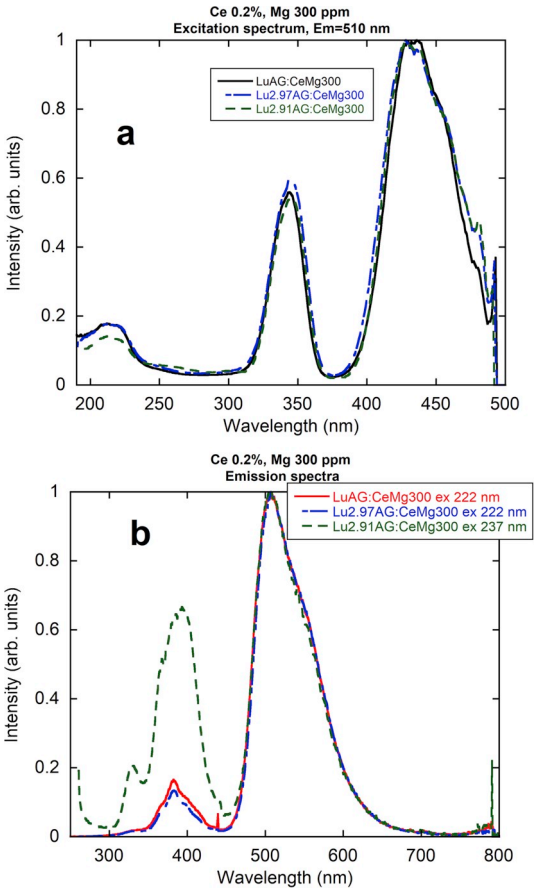

Fig. 17. Excitation spectra of the Ce^{3+} 510 nm emission for the as-grown CeMg300 samples with different stoichiometry (a) and emission spectra for the same samples (b); for the excitation wavelengths see the legend.

contains some fraction of Lu-rich monoclinic phase $Lu_4Al_2O_9$ (LuAM), which is probably the cause of the cracks. Part 2 and 3 still show the LuAG structure, not different from that of the regular undoped garnet. At the end when the growth became unstable, the crystal quite rapidly narrowed and finally disconnected leaving some part of the melt in the crucible. This was not observed for the growth of the other LuAG crystals, where all the melt was practically pulled out. The XRD pattern of the very end of the crystal (part 4) shows additional excessive Al_2O_3 phase, which means that the non-stoichiometry of the sample increased at the end enough so that the excessive alumina was already rejected by the crystal. This was also confirmed by the XRF measurement performed along the crystal rod. Before the XRD measurements, when the parts of the crystal had to be crushed into powders, selected surfaces of the cut parts were examined by the XRF. The results are shown in Fig. 3. The composition is the closest to the nominal one just in the very start of the crystal and then the Al/Lu molar ratio almost monotonously increases towards the end part, where it corresponds to the composition of approximately $Lu_{2.64}Al_{5.36}O_{12}$ (Ce and Mg were omitted for simplicity, as their concentrations are negligible with respect to the stoichiometry changes). Apparently, the garnet lattice seems to be able to adapt to a significant off-stoichiometry composition. There is a question what mechanism would stabilize the pure garnet phase, especially if one takes into account the mentioned calculations in Ref. [20], which allow the Al_{Lu} concentration to be below 0.2 mol %. It is also necessary to keep in mind that the XRF shows only the average composition over the selected cross-sections of the cut parts of the crystal. The radial distribution of the components and dopants can also play an important role (see μ-XRF results below). There is also another issue, which consists in considerably higher average Al concentration in the crystal when compared to the nominal one. One reason can be rejection of the Lu-rich LuAM phase at the very beginning of the crystal growth, but its amount seems to be still too small. Another reason might be that some excessive Lu could be in the melt which remained in the crucible after the growth and which could not be analyzed for technical reasons. Similar, but much less pronounced behavior without Al_2O_3 rejection was found also for the crystals grown from the stoichiometric melt. This would mean that in the beginning of the growth, the crystal tends to minimize the Al concentration, which then leads to increasing Al-rich non-stoichiometry towards the end of the crystal.

Regarding the Ce dopant incorporation, the average concentration measured over the cross-section by the XRF corresponded to the nominal one in all the selected samples. The Mg concentration could not be determined due to the low sensitivity of XRF for this element.

In Fig. 4 the μ-XRF mapping result shows the distribution of Lu, Al and Ce at the cross-section of the LuAG:Ce sample. It can be seen that even in the sample with the stoichiometric nominal composition, the Al and Ce concentration is somehow elevated at the narrow rim near the outer surface of the crystal. The increased Ce concentration was already observed in other garnet crystals before [26] and was explained by the very small segregation coefficient of Ce (around 0.1). So far we cannot explain the elevated Al concentration. We suppose such a significant radial distribution of the main components can take place in the non-stoichiometric sample as well. Since the rim contains closely spaced

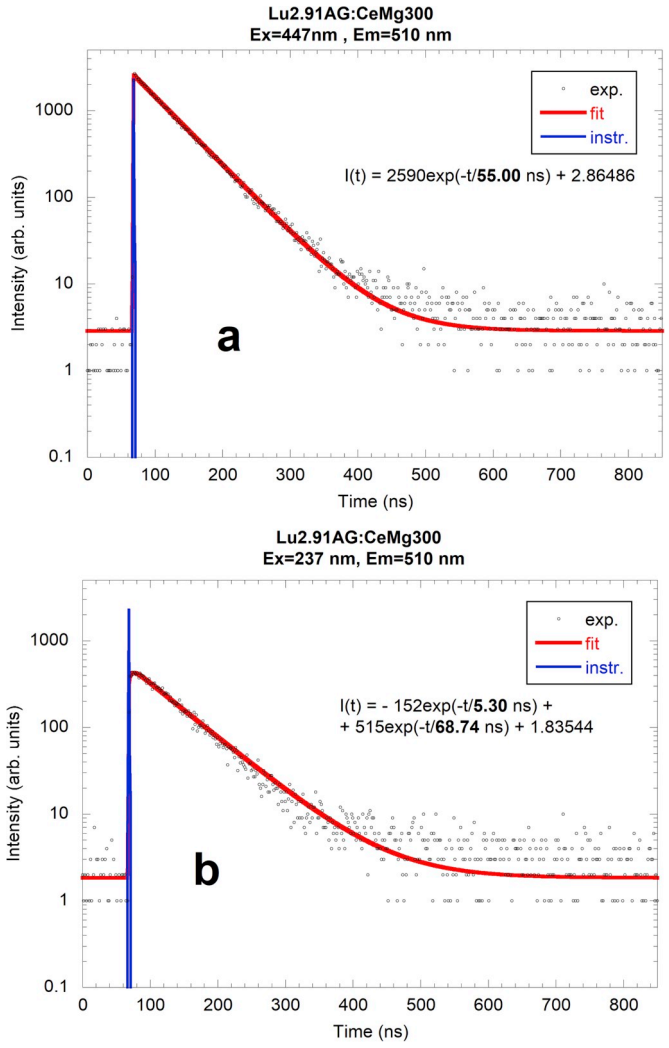

Fig. 18. Example of photoluminescence decay curves for the as-grown non-stoichiometric Lu2.91AG:CeMg300 sample under 447 nm excitation directly into 4f-5d$_1$ Ce^{3+} transition (a) and under 237 nm excitation into a defect band (b).

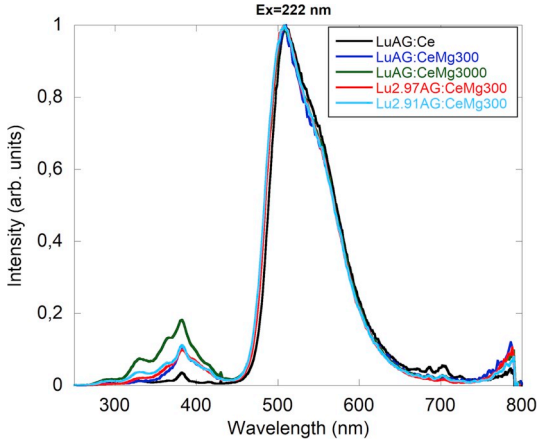

Fig. 19. Emission spectra of the annealed samples with different Mg concentrations and stoichiometry under 222 nm excitation.

posts with elevated Ce and Al concentrations, we can suppose creation of other phases, such as $CeAlO_3$ or Al_2O_3:Ce, but their concentrations are most probably below the detection limits of the used techniques.

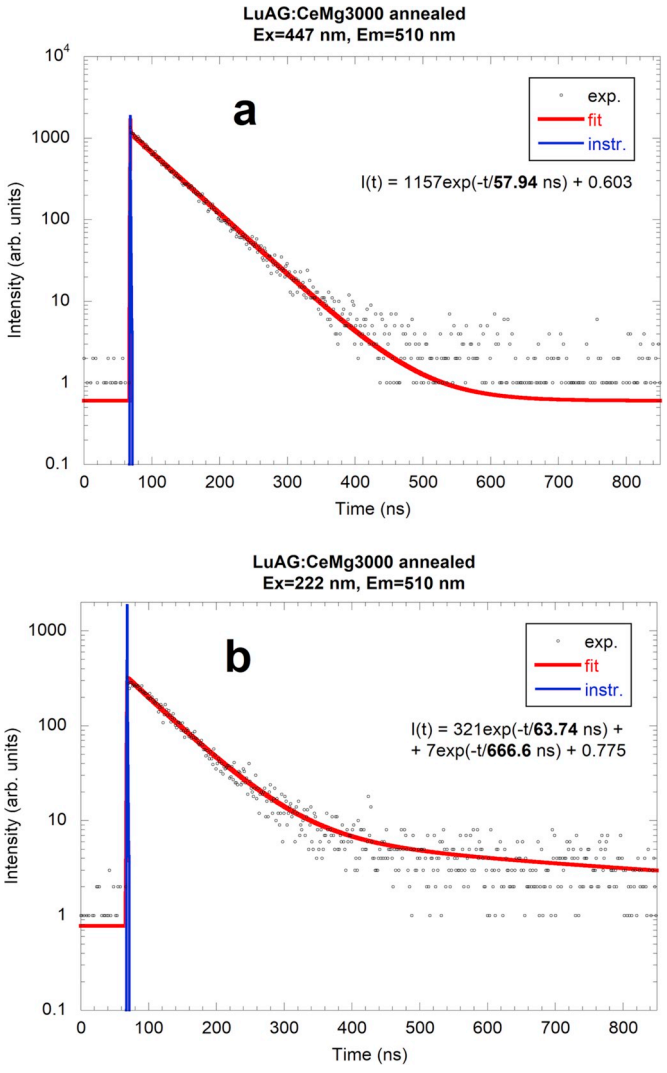

Fig. 20. Example of photoluminescence decay curves for the annealed stoichiometric LuAG:CeMg3000 sample under 447 nm excitation directly into 4f-5d$_1$ Ce^{3+} transition (a) and under 222 nm excitation into a defect band (b).

The EDLM of the LuAG:Ce sample is shown in Fig. 5. Two relatively large single crystalline sections can be observed.

3.2. Characterization of the grown LuGAG crystals

The as-grown LuGAG crystal rods are shown in Fig. 6. Their transparency is better when compared to the Ga-free counterparts in Fig. 1 and their color is a bit different due to change of the Ce^{3+} absorption spectra resulting from the change of crystal field upon Ga admixture, as will be discussed below in detail. It is worth emphasizing the much weaker coloration of the crystal with 3000 ppm Mg, especially in its end part. It can be explained by change of the Ce valence to the 4 + state for most of the Ce-atoms caused by Mg codoping, which seems more likely to occur in the Ga-containing matrix. The rectangles indicate the parts that were polished and used for further optical characterization and the rest was again used for XRD and XRF measurements.

The XRD diffraction patterns showed garnet structure for all the samples, however, splitting of the diffraction peaks in all the patterns was observed and was ascribed to presence of more (typically 2–3) garnet phases of very close compositions. See Fig. 7 for example of the XRD pattern for the LuGAG:Ce crystal, where two garnet phases were detected. Since the diffraction patterns of mixed LuGAG garnets diffraction patterns are not available in the ICDD database, the diffraction

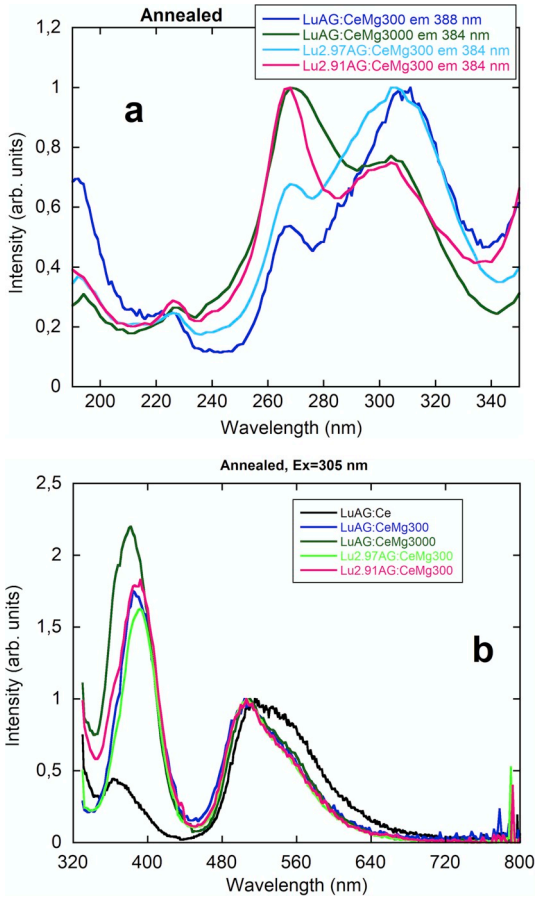

Fig. 21. Excitation spectra of the 380 nm emission peak for the annealed stoichiometric and non-stoichiometric samples.

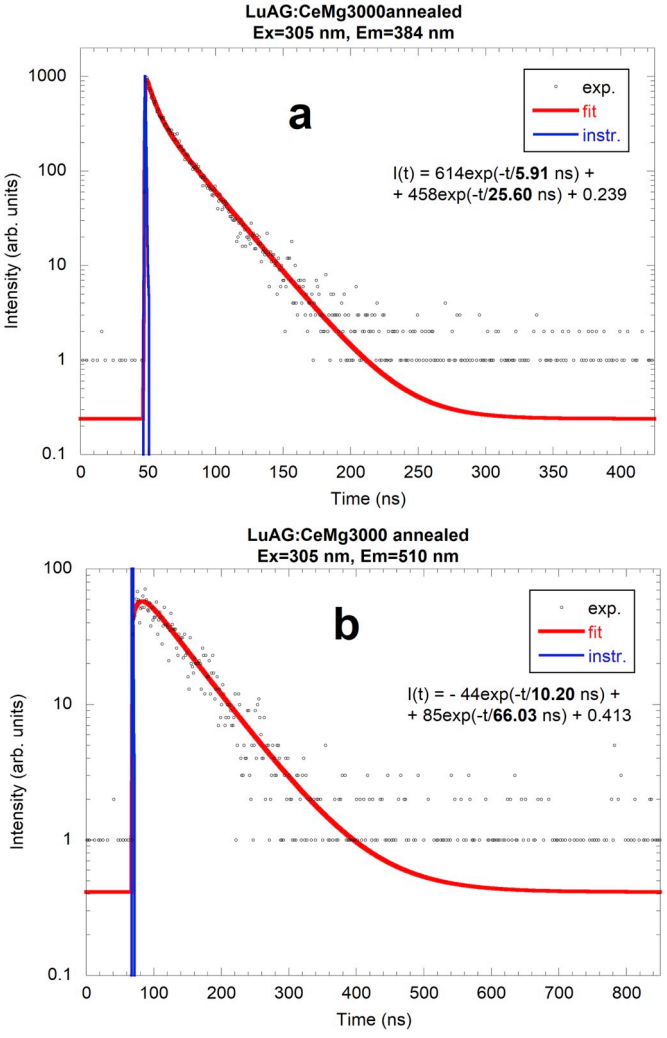

Fig. 22. Comparison of the decay curves of the 384 nm defect emission under 305 nm excitation (a) and decay curve for the Ce^{3+} 5d-4f emission under 305 nm excitation for the annealed stoichiometric LuAG:CeMg3000 sample (b).

data were compared to the LuAG pattern (ICDD PDF 01-73-1368) and $Lu_3Ga_5O_{12}$ one (LuGG, ICDD PDF 01-73-1372). The peaks of the measured patterns of the LuGAG crystals were observed between the diffraction peaks of the LuAG and LuGG, as can be expected. In ideal substitutional solid solutions, the lattice parameters, which determine the diffraction peak positions, depend linearly on the composition according to the Vegard's rule.

Based on the determined lattice parameters of the observed garnet phases, the approximate Ga content in each phase was calculated. However, the weight percentages of the different garnet phases could not be established precisely due to preferred orientation.

The non-stoichiometric Lu2.91GAG:CeMg300 was studied in more detail. As mentioned above, for this crystal the growth atmosphere contained only Ar practically without O_2 (negligible O_2 impurity only in the ppm range can be expected), therefore Ga-related species significantly evaporated during the growth. The XRD patterns of the selected parts are shown in Fig. 8 (see inset for indication of the cut parts). The diffraction peaks corresponding to garnet structure were found in all parts. The parts 1 and 3 contained two garnet phases with close compositions, while part 4 showed three phases. Two phases were found in the part from the very end together with excess of Lu_2O_3, which means that the melt composition became significantly Ga-poor at the end of the growth and excessive Lu was rejected by the crystal. Such a dramatic composition shift is most probably responsible for the different color of the end of the crystal. Traces of Lu_2O_3 were also already found in the part 4. The XRF analysis confirmed a significant loss of Ga due to the intense evaporation of the Ga-related species. Because of the gradual decrease of the Ga fraction, the end part of the crystal contained only 43% of Ga content relative to its start. Other crystals showed similar decrease of Ga content from start to end, albeit on a much smaller scale due to the protective effect of O_2. The EDLM measurements for selected samples (LuGAG:CeMg300, Mg3000 and Lu2.91GAG:CeMg300) showed quite large number of sub-grains and grains (Fig. 9a–c), especially for the sample grown from a non-stoichiometric melt (Fig. 9c). The μ-XRF mappings (not shown here) revealed, that the grains have slightly different compositions in dependence of their location at the cross section, i.e. the Ga concentration increases from the center towards the rim part while opposite trend is found for Al. This would be manifested in a XRD pattern as the above-mentioned splitting of the diffraction peaks.

Regarding the Ce distribution, a similar result as for the LuAG samples was obtained for the LuGAG:CeMg300 and Mg3000 samples, i.e. Ce is also concentrated at the outer rim of the crystal cross-sections (see Fig. 10). Several recent studies [30–32] have shown that the radial distribution of the dopant in the micro-pulling-down process is mainly determined by the distribution coefficient, the geometry of the crucible, the height of the molten zone and melt properties. Temperature profile and pulling speed play obviously a role as well [33]. Increased concentration of Ce at the YAG crystal rim was observed by Simura et al. [30] and explained by increased radial flow from the center of the die, where the capillary is positioned. Such an increased flow is caused by the significant difference between the diameters of the capillary and the die itself, whose shape determines the cross-section shape of the growing crystal. Since the melt layer is very thin and the melt is

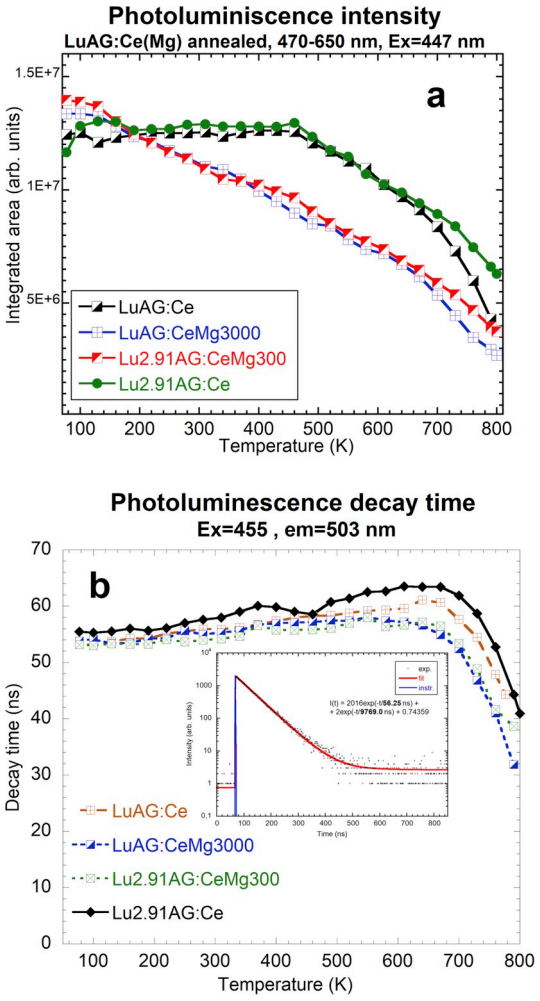

Fig. 23. Temperature dependence of the Ce^{3+} 5d-4f emission intensities (a) and corresponding decay times (b) for the selected annealed LuAG samples.

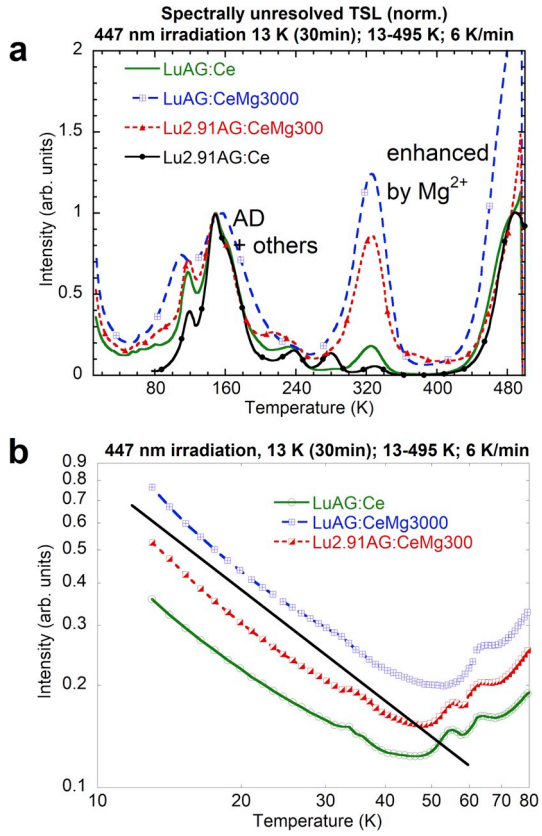

Fig. 24. TSL glow curves for the selected annealed LuAG samples after irradiation in the 4f-$5d_1$ absorption band of Ce^{3+} at 447 nm. The magnification of the low temperature part is on the right.

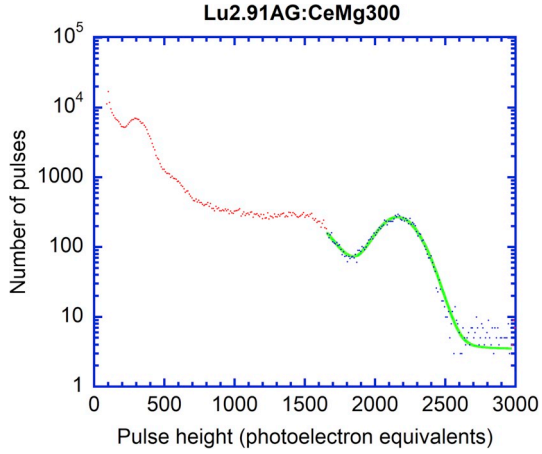

Fig. 25. An example of the pulse-height spectrum for the as-grown $Lu_{2.91}Al_{5.09}O_{12}$:Ce0.2% Mg 300 ppm under ^{137}Cs gamma ray excitation at 662 keV.

thermally stable (the temperature at the die is higher than the temperature at the solid-liquid interface), the injection of the melt to the melt layer is the leading transport mechanism. Turbulence can have influence as well [30]. During the flow, the dopant is incorporated into the crystal according to the distribution coefficient. Such a behavior was confirmed by theoretical modelling of the Ce distribution in YAG crystals [30,32]. Since out crystals are from the similar garnet family, it is very probable that our observations of the dopant distribution are determined by the phenomena described above. The calculation in Ref. [32] suggest that the dopant distribution in YAG:Ce system can be improved by increasing the number of capillaries or increasing the inclination angle of the die. Positive effect of the increase of the number of capillaries was experimentally verified in Ref. [29].

3.3. Luminescence and scintillation properties of the LuAG crystals

In this section, the luminescence and scintillation properties of the Ga-free LuAG crystals before and after annealing will be compared. The results will be shown only for the START parts of the crystals (see Fig. 1, or the CENTER part for the LuAG:CeMg300 sample) for simplicity. The results for the END parts showed some slight differences, but general trends and resulting conclusions have not changed. The results for the END parts will be shown only for some special cases.

The absorption spectra are shown in Fig. 11. The spectra for the as-grown samples (Fig. 11a) show the typical Ce^{3+} absorption bands at 448 and 347 nm ascribed to the 4f-$5d_1$ and 4f-$5d_2$ transitions, respectively. The unknown defect-related band around 220 nm decreases with increasing Mg concentration for the stoichiometric samples. The intense broad band observed at 240 nm only for the Lu2.91AG:CeMg300 might be ascribed to Ce^{4+} charge transfer (CT) transition. Such ascription can be supported by the slight decrease of the Ce^{3+} 4f-5d absorption features, as some part of the Ce^{3+} would be already transformed to Ce^{4+}. Similar absorption feature and its assignment to Ce^{4+} was observed also for $Gd_3Ga_3Al_2O_{12}$:Ce crystal, see Ref. [34]. However, our recently investigated nonstoichiometric Ce-free LuAG samples (not shown here) also showed a very similar absorption band. Therefore it can be also ascribed to some defect induced by the

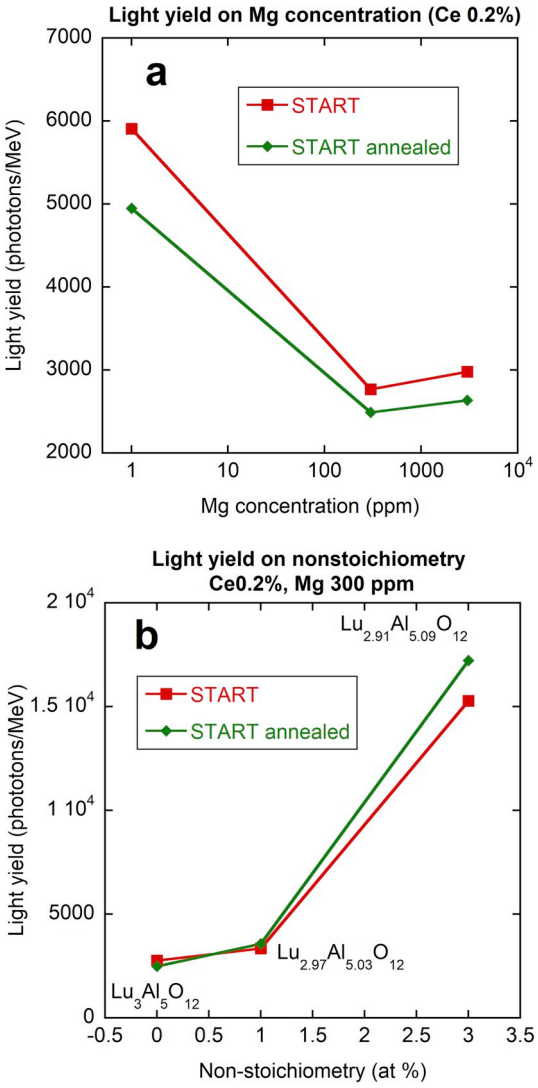

Fig. 26. Dependence s of the light yield on Mg concentration (a) and non-stoichiometry for constant Mg 300 ppm concentration (b) for the as-grown and annealed LuAG samples. The matrix compositions are again with omitted Ce and Mg concentrations.

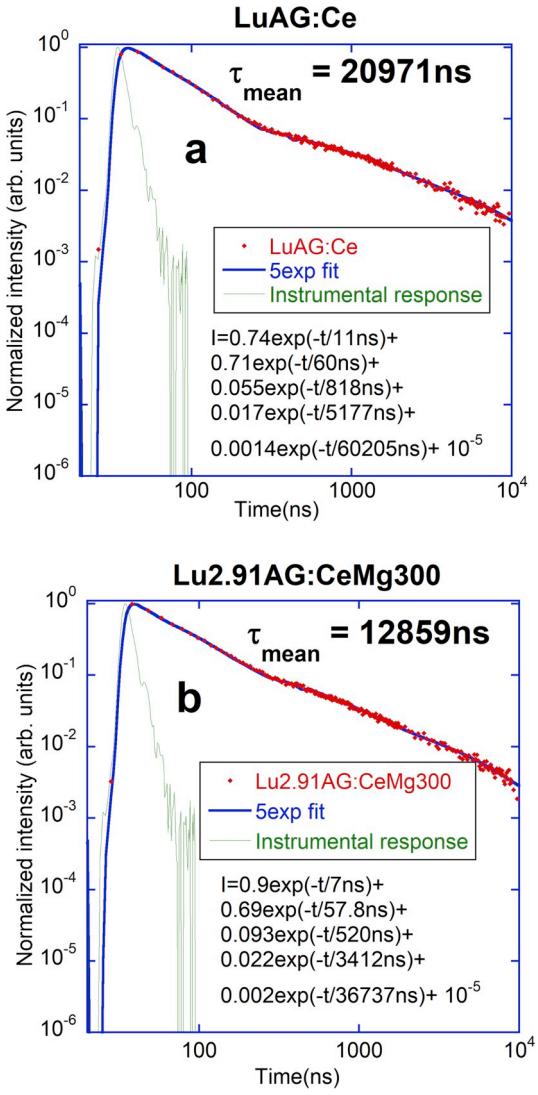

Fig. 27. The SXR-excited scintillation decay curves for the as-grown LuAG:Ce sample (a) and the Lu2.91AG:CeMg300 (b).

non-stoichiometry; a combination of both is also possible. After annealing in air, Ce^{3+} absorption bands decreased, as some part of the Ce^{3+} was probably oxidized to Ce^{4+} (Fig. 11b). Increase of the defect absorption bands below 300 nm can be observed and might be also obscured by the Ce^{4+} CT absorption. The 250 nm absorption feature appears also in the spectrum for the undoped sample.

The RL spectra under X-ray excitation for both as-grown and annealed samples are compared in Fig. 12 together with the spectrum of the $Bi_4Ge_3O_{12}$ (BGO) reference scintillator. The spectra consist of two main emission features: The Ce^{3+} 5d-4f band at 510 nm and defect luminescence band around 320 nm consisting of the emission of exciton trapped at the anti-site defect [35] and most probably also emission band related to some other defects. For the as-grown samples (Fig. 12a) the RL intensity does not show stable trend and seems to be generally higher for the Mg-codoped and nonstoichiometric samples. The END part of the Lu2.91AG:CeMg300 sample shows the highest RL intensity related to Ce^{3+} and the lowest defect luminescence, most probably due to lower Lu_{Al} defect concentration, which was reduced by higher Al content in the matrix.

Annealing generally leads to the decrease of the Ce^{3+} emission intensity, while the defect emission increases noticeably (Fig. 12b). This does not follow the results of recent studies [13], as one could expect increase of Ce^{4+} concentration and related improvements. Significant increase of the Ce^{3+} emission is observed only for the Lu2.91AG:CeMg300 sample. An unknown peak at 384 nm emerges in the spectra for the annealed samples and it will be shown later that this is due to the fast emission of a defect based on an oxygen vacancy. The structured weak feature around 700 nm was ascribed to the Cr^{3+} impurity.

In order to get a better insight in the trends of change of the RL features with composition, the Ce^{3+} luminescence and the defect luminescence peaks were integrated in the corresponding wavelength ranges and recalculated relatively to the integral of the radioluminscence spectrum of the BGO standard. The dependences of the integrals of the defect and Ce^{3+} RL peaks on Mg concentration for the as-grown and annealed stoichiometric samples are displayed in Fig. 13. The Ce^{3+} emission in the as-grown samples does not show a stable trend and is the most intense for the 300 ppm Mg (Fig. 13a). The Ce^{3+} intensity decreased by annealing for the un-codoped sample and the sample with the lowest Mg concentration. The intensity therefore grows almost linearly with Mg concentration for the annealed samples. Regarding the defect emission (Fig. 13b), its intensity steeply decreases with increasing Mg concentrations both for as-grown and annealed samples, while annealing brings a systematic increase of the defect emission for all the Mg concentrations. We can conclude that for the

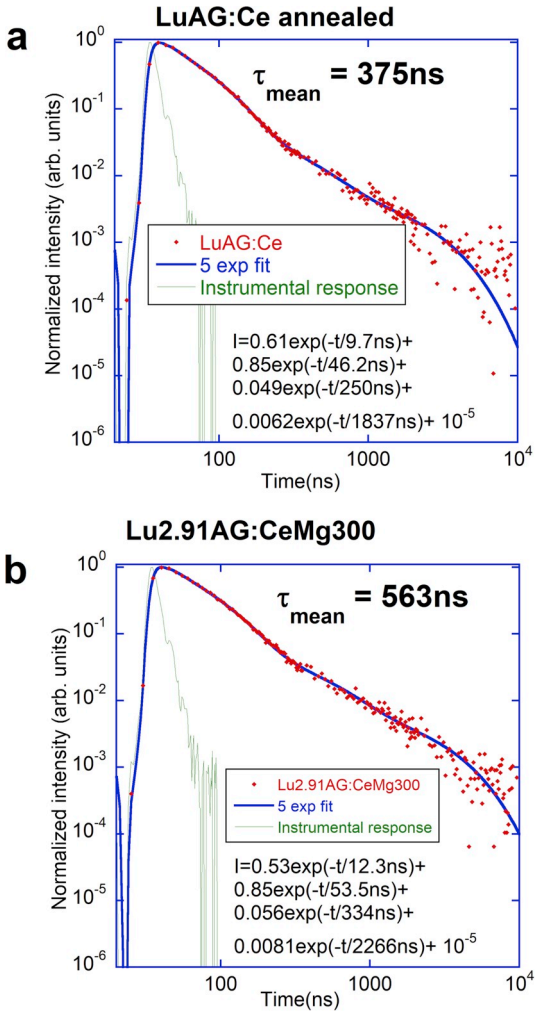

Fig. 28. The SXR-excited scintillation decay curves for the annealed LuAG:Ce sample (a) and the Lu2.91AG:CeMg300 (b).

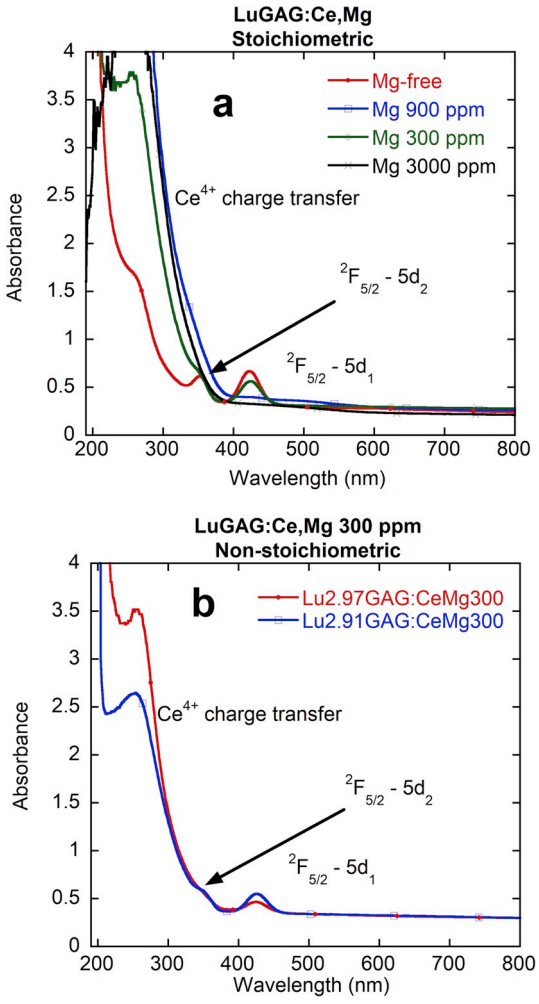

Fig. 29. Comparison of the absorption spectra of the as-grown LuGAG stoichiometric samples (a) and non-stoichiometric ones (b).

annealed samples the Mg codoping has a positive effect on the RL features, as it increases the Ce^{3+} emission and decreases the defect one. This can be due to the alternative scintillation mechanism involving Ce^{4+}.

Similar dependences of the Ce^{3+} and the defect RL integrals were constructed for samples with different non-stoichiometry and constant Mg concentration of 300 ppm, see Fig. 14. Such Mg content was chosen because the as-grown stoichiometric LuAG sample with 300 ppm Mg showed one of the highest Ce^{3+} emission intensities under X-ray excitation and positive effect of the 300 ppm Mg concentration was expected. The positive effect of lower Mg concentration of few hundreds (100–500) ppm on the LuAG:Ce scintillation properties was found also in other earlier studies [13].

For the as-grown LuAG samples, the Ce^{3+} emission does not show a clear trend with increasing non-stoichiometry. After annealing, the intensity decreases for the stoichiometric sample; however, with further increase of non-stoichiometry, it increases dramatically (Fig. 14a). The defect emission intensity for the as-grown samples increases only slightly with increasing non-stoichiometry (Fig. 14b). This would mean that some other defects can be introduced by non-stoichiometry or the efficiency of the energy transfer towards the concerned defects is improved. After annealing the increasing trends are again strongly amplified.

These results suggest that annealing further improves the RL efficiency of the non-stoichiometric LuAG:Ce crystals, but also modifies the defects in a way that their emission intensity increases as well. The defect-related features seem to be increased with increasing non-stoichiometry.

The normalized photoluminescence excitation spectra of the Ce^{3+} 5d-4f emission at 510 nm for the as-grown stoichiometric LuAG crystals are compared in Fig. 15a. They are composed of the typical Ce^{3+} 4f-$5d_1$ and 4f-$5d_2$ transitions around 345 nm and 440 nm, respectively, and a less intense band around 220 nm, whose relative intensity seems to decrease with increasing Mg concentration. This band is most probably identical with the obscured defect band observed in the absorption spectra in Fig. 11a. When excited by the 345 nm or 440 nm light, the samples show the typical Ce^{3+} 5d-4f emission band peaking around 510 nm, which corresponds to that in the RL spectra. The normalized photoluminescence emission spectra of the same samples under the 222 nm excitation, which corresponds to the defect absorption, are displayed in Fig. 15b. It consists of the dominant Ce^{3+} 5d-4f emission band at 510 nm and some defect emission between 320 and 370 nm, which most probably contributes to the long-wavelength part of the defect emission peak observed in the RL spectra. The increase of the relative intensity of the defect emission around 320 nm with increasing Mg concentration is clearly apparent (Fig. 15b). These results suggest that with increasing Mg concentration, the efficiency of the energy transfer from the defect absorbing at 220 nm towards Ce^{3+} decreases, while the transfer towards the defect emission around 320–370 nm becomes more efficient. This is a bit contradictory with the RL results (Figs. 12b and 13b), where the defect emission decreases with the increasing Mg concentration. This observation can be explained by an

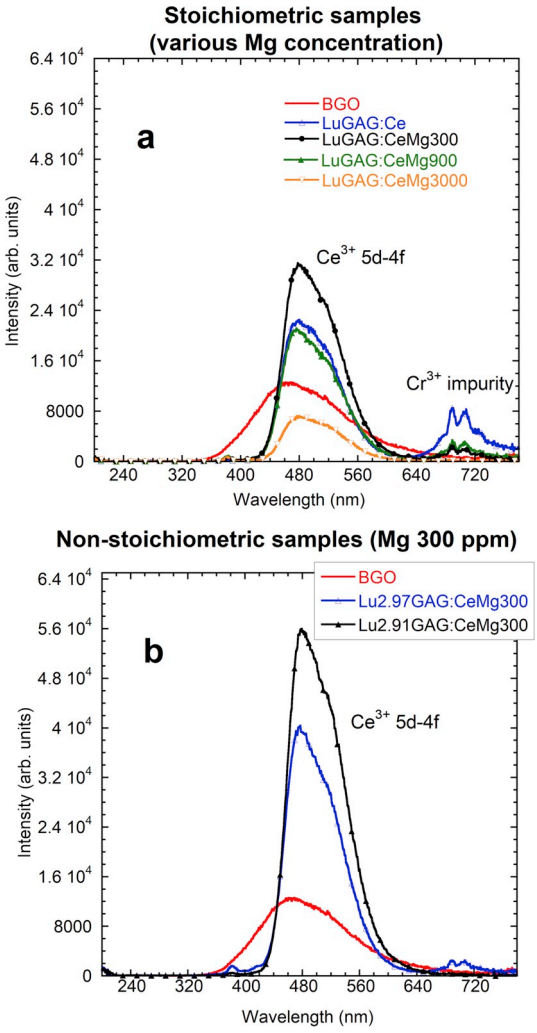

Fig. 30. Comparison of the RL spectra for the stoichiometric (a) and non-stoichiometric (b) LuGAG samples. (The spectra in both figures are comparable in an absolute scale).

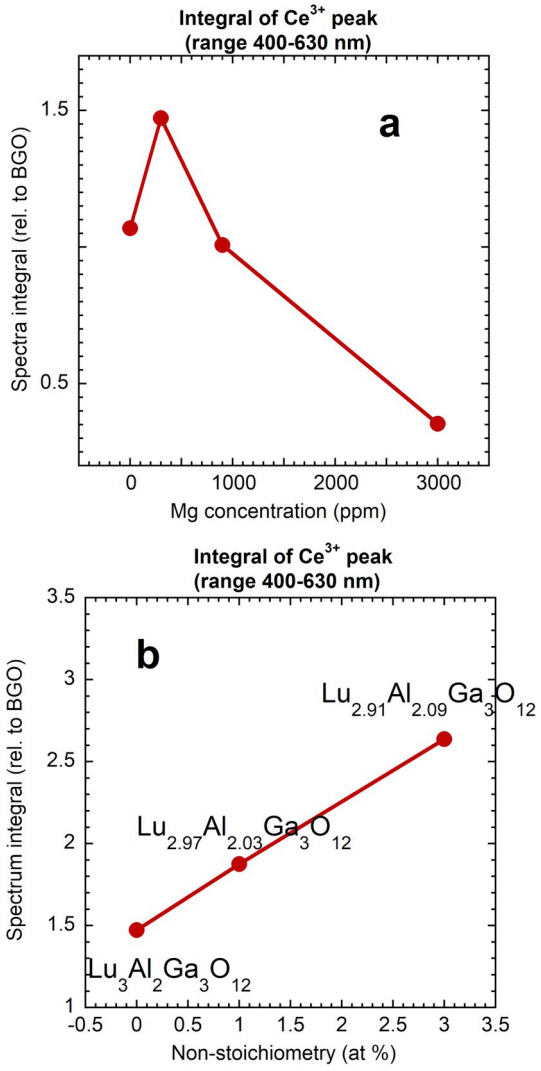

Fig. 31. Integrals of the RL spectra (under X-ray excitation) of the LuGAG as-grown samples and their dependence on the Mg concentration (a) and non-stoichiometry for the samples with constant Mg 300 ppm concentration (b). The matrix compositions are again with omitted Ce and Mg concentrations.

increase of Ce^{4+} content in the Mg-codoped crystals as the Ce^{4+} obviously cannot directly participate in the photoluminescence processes. The defects emitting at shorter wavelengths also play a role under the X-ray excitation. There is also a question if the 222 nm absorption/excitation peak is purely of a defect origin, or if some higher 5d level of Ce^{3+} is also partially involved, as was confirmed in YAG analogue by experiment and theoretical calculations [36].

The photoluminescence decay curves of the Ce^{3+} 5d-4f emission under direct excitation at 447 nm and excitation through the defect levels at 222 nm for the as-grown LuAG:CeMg3000 sample are shown in Fig. 16. The former decay curve is described by one single exponential component with a decay time of 56 ns, which is a value typical for Ce^{3+} 5d-4f luminescence in LuAG. When excited at 222 nm, this decay becomes clearly prolonged to 65 ns, which points to the change of energy transfer towards the Ce^{3+} and may be somehow related to the above-described changes of the photoluminescence excitation and emission spectra. Very similar results were obtained for the other two as-grown stoichiometric samples with 0 ppm and 300 ppm Mg. Further research would be needed to obtain clear conclusions.

Fig. 17a shows the analogous normalized excitation spectra for the Ce^{3+} 5d-4f emission at 510 nm for the as-grown samples with different stoichiometry and 300 ppm Mg concentration. They again consist of the Ce^{3+} bands at 345 and 440 nm and the defect band around 220 nm with very similar relative intensities. Normalized emission spectra for the excitation in the defect band are in Fig. 17b. The spectra for the stoichiometric LuAG:CeMg300 and the Lu2.97AG:CeMg300 are almost identical and similar to those for the stoichiometric samples, while in the spectrum for Lu2.91AG:CeMg300 the defect peak is very pronounced. Unlike the two other previous samples this one was excited by the 237 nm light, which corresponds to the absorption maximum found in the absorption spectrum in Fig. 11a. This would again mean that the band is not entirely related to the Ce^{4+} (excitation into the Ce^{4+} CT band would not lead to the Ce^{3+} emission) but to a defect (defects) and that the increased Al-rich non-stoichiometry increases the defect concentration or introduces new defects. This would explain the increase of the defect absorption and its shift to the shorter wavelengths (Fig. 11a). Such an increase of the defect concentration and their possible modification was already suggested by the RL measurements (Figs. 12 and 13). It is worth noting that the shape of the defect band in the photoluminescence spectra in Figs. 15b and 17b is obscured by the Ce^{3+} absorption bands around 345 and 440 nm, which is manifested by the dips at corresponding wavelengths. The consequence of such an overlap is that the Ce^{3+} levels are fed via the levels of the defects present in the material or introduced by non-stoichiometry.

Such a conclusion is further supported by the decay time measurements shown in Fig. 18, which show the comparison of the Ce^{3+} 5d-4f

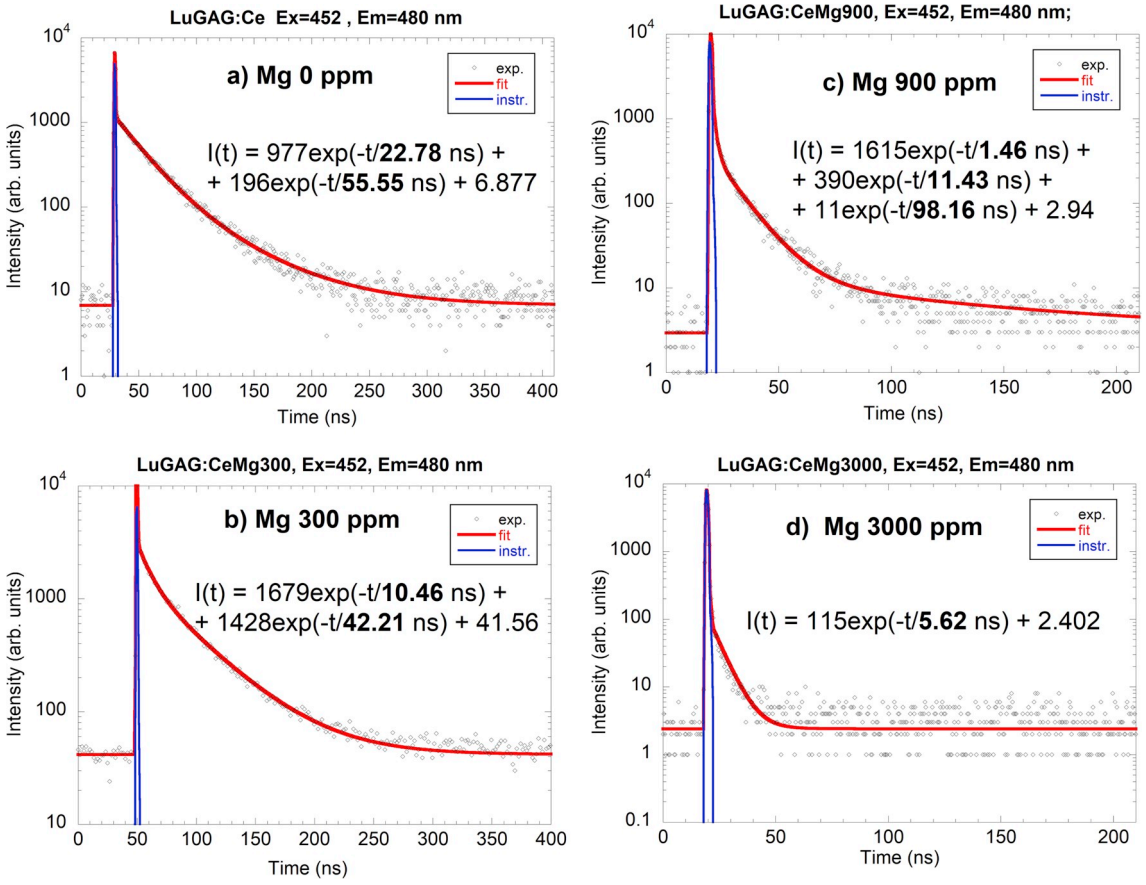

Fig. 32. Examples of the photoluminescence decay of the Ce^{3+} emission center under direct 4f-5d_1 excitation at 452 nm in the Mg-free stoichiometric LuGAG:Ce sample (a) and LuGAG:CeMg300 sample (b), LuGAG:CeMg900 sample (c) and LuGAG:CeMg3000 sample (d).

photoluminescence decay curves for the as-grown Lu2.91AG:CeMg300 sample under 447 nm excitation directly into 4f-5d_1 Ce^{3+} transition (a) and under 237 nm excitation into a defect band (b. While the former keeps the usual decay characteristics described by the single-exponential function with a decay time of 55 ns, the latter is composed of two exponential functions: one with prolonged decay time of 66 ns and another negative component with a rise time of 5 ns This is a clear evidence of an energy transfer towards the Ce^{3+} luminescence center.

Regarding the influence of annealing on the photoluminescence characteristics, the excitation spectra had very similar shape as for the as-grown samples, however, no clear trends were found. The normalized emission spectra for the annealed samples under the 222 nm excitation are compared in Fig. 19. The relative intensities of the defect PL emission again increase with the increasing Mg concentration and do not seem to significantly depend on the stoichiometry. No clear explanation can be so far given using the current data.

Examples of the photoluminescence decay curves for the annealed stoichiometric LuAG:Ce 0.2% Mg 3000 ppm sample under 447 nm excitation directly into 4f-5d_1 Ce^{3+} transition and under 222 nm excitation into a defect band are shown in Fig. 20. The slow component was observed in the latter one, which points to influence of annealing on the defect behavior and related energy transfer towards the Ce^{3+}. Changes were observed also for the other samples, but no systematic trends could be found again.

In the photoluminescence studies we have also focused on the unknown narrow peak observed in the RL spectra of the annealed samples around 380 nm in Fig. 12b. The excitation spectra of the 380 nm emission are compared in Fig. 21a for the annealed Mg-codoped samples. They consist of the bands around 305–310, 270, 225 nm and a shoulder around 200 nm. When excited under the 305 nm band, a spectrum containing the Ce^{3+} 510 nm emission and the dominating the 380 nm peak emerges, see Fig. 21b. It is also worth mentioning the defect emission spectra in Fig. 19, where the defect emission band is dominated by the 380 nm peak.

The decay curve of the 380 nm peak under 305 nm excitation for the annealed LuAG:CeMg3000 sample is described by two exponential components with decay times of 6 ns and 25 ns, which is unusually fast; see Fig. 22a. Very fast decay time of about 3 ns was found for the luminescence of F^+ center in LuAG at a similar emission wavelength of 390 nm [37]. The F^+ center was described in Ref. [37] as an oxygen vacancy with one captured electron, which is perturbed by the neighboring Lu_{Al} anti-site defect or another impurity ion on the Al^{3+} site. This would make sense since the higher Mg concentration could stabilize the oxygen vacancies even after annealing in the air. Similar decay characteristics of the 380 nm peak were observed also for the other samples. It seems that in our case the emission center related to oxygen vacancy can be perturbed also by more complex defects or other inhomogeneities in the samples, which can be expected for the crystals grown by the micro-pulling-down method. Decay curve of the Ce^{3+} 5d-4f emission under the 305 nm excitation (i.e. the excitation band of the defect related to oxygen vacancies) is shown in Fig. 22b and is described by the leading exponential component with decay time of 66 ns, which can be ascribed to the Ce^{3+}, and a negative component with a rise-time of 10 ns, which clearly evidences an energy transfer from this defect towards the Ce^{3+}. Since this defect emission is enhanced by the non-stoichiometry (see Fig. 12b), we can conclude that the defect related to oxygen vacancy is involved in the mechanism of improvement of the RL efficiency by non-stoichiometry. It might be, however, that other defects play role as well.

The temperature dependences of the Ce^{3+} 5d-4f emission intensities

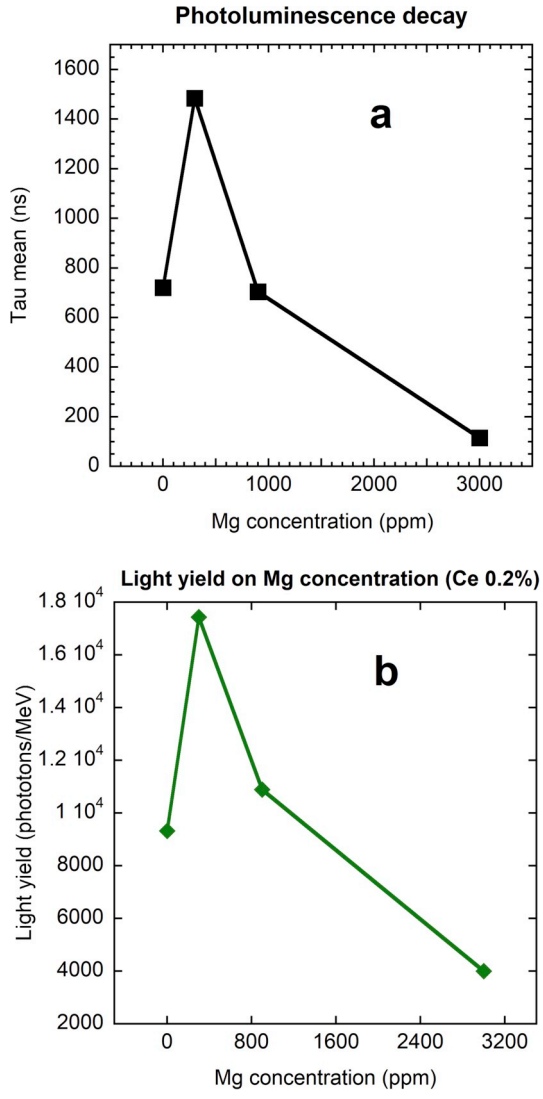

Fig. 33. Dependences of the photoluminescence mean decay time (a) and light yield (b) on Mg concentration for the stoichiometric LuGAG samples.

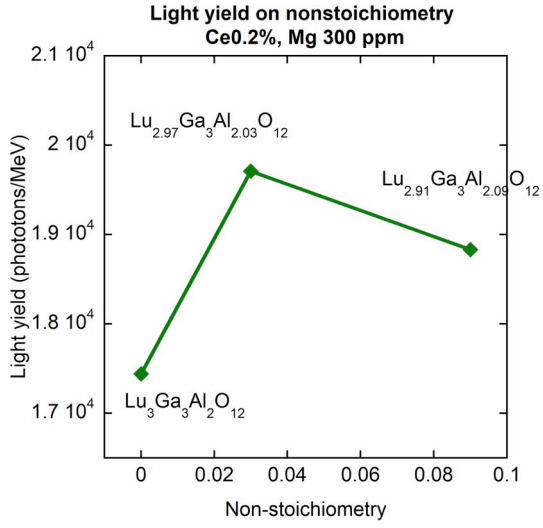

Fig. 34. Dependence of the light yield on non-stoichiometry for the LuGAG:Ce samples with Mg concentration of 300 ppm.

for the annealed LuAG:Ce, LuAG:CeMg3000, Lu2.91AG:CeMg300 and an additionally grown Mg-free Lu2.91AG:Ce are shown in Fig. 23a. The intensities for both the stoichiometric and non-stoichiometric Mg-free samples show the same trend, as they keep practically constant value and around 460K they start to decrease due to some quenching process. For the Mg-containing samples, such a phenomenon is observed at substantially lower temperatures around 150 K.

The temperature dependences of the corresponding decay times for the same annealed LuAG samples are depicted in Fig. 23b. All the 4 curves start to decrease around 670 K due to thermal quenching of the Ce^{3+} luminescence, i.e. at much higher temperatures than the luminescence intensity curves. This serious discrepancy between the behavior of the photoluminescence intensities and corresponding decay times can be explained by some unknown quenching process from the non-relaxed excited state of the Ce^{3+}, which cannot influence the decay time, but it influences the luminescence intensity. Such a quenching process is facilitated by Mg co-doping and is not influenced by stoichiometry, as can be inferred from Fig. 23.

The spectrally unresolved TSL glow curves for the same selected annealed samples (LuAG:Ce, LuAG:CeMg3000, Lu2.91AG:CeMg300 and Lu2.91AG:Ce) are compared in Fig. 24. The samples were irradiated at 13 K or 77 K by the UV light in broad wavelength range up to 450 nm thus involving 4f-5d and higher energy excitation, where electron can be released into conduction band. The features around 100–180 K can be ascribed to the release of electrons from the Lu_{Al} antisite defects. The peak around 320 K is apparently connected with Mg containing defect, moreover, its intensity strongly increases with the increase of Mg content. It might be that the glow peak is connected with the defects based on oxygen vacancies and some of them might be responsible for the above-described thermal quenching from the non-relaxed state. The initial parts of the curves measured from 13 K appear as straight lines in the log-log scale. This is a sign of tunneling process from the traps towards the luminescence centers. For more details about tunneling recombination in these crystals, see Ref. [38].

An example of the pulse-height spectrum for the as-grown Lu2.91AG:CeMg300 ppm under ^{137}Cs gamma ray excitation at 662 keV is shown in Fig. 25. The full absorption peak is clearly resolved, but very broad, which is most probably a consequence of inhomogeneities in the samples grown by the micro-pulling-down method. This results in an energy resolution of some 20–30%.

The light yield values were calculated for the as-grown and annealed single crystals and their dependences on Mg concentration and non-stoichiometry are plotted in Fig. 26.

For the stoichiometric samples the light yield generally decreases with increasing Mg concentration (Fig. 26a) with respect to Mg-free sample and is further degraded by annealing, which is in contradiction with recent observations for the samples grown by the micro-pulling-down method [13]. Since the scintillation light yield is not spectrally resolved and the defect emission around 320 nm has a relatively fast components with decay times of about several hundreds of ns or few μs [39], it still has a significant contribution in the light yield measurement, as the shaping time was 6 μs in our experiments (and only 1μs in Ref. [13]). Considering the data in Fig. 13b showing the significant decrease of the defect emission with increasing Mg concentration under X-ray excitation, the behavior of the light yield can be explained by this significant decrease of the defect emission, which contributes to the pulse-height spectrum.

On the other hand, the increasing non-stoichiometry for constant Mg 300 ppm concentration leads to significant increase of the light yield for both as-grown and annealed samples (Fig. 26b). Slight improvement with annealing can be observed only for the most non-stoichiometric sample. The light yield of the annealed Lu2.91AG:CeMg300 sample was as high as 17000 photons/MeV, which is a good

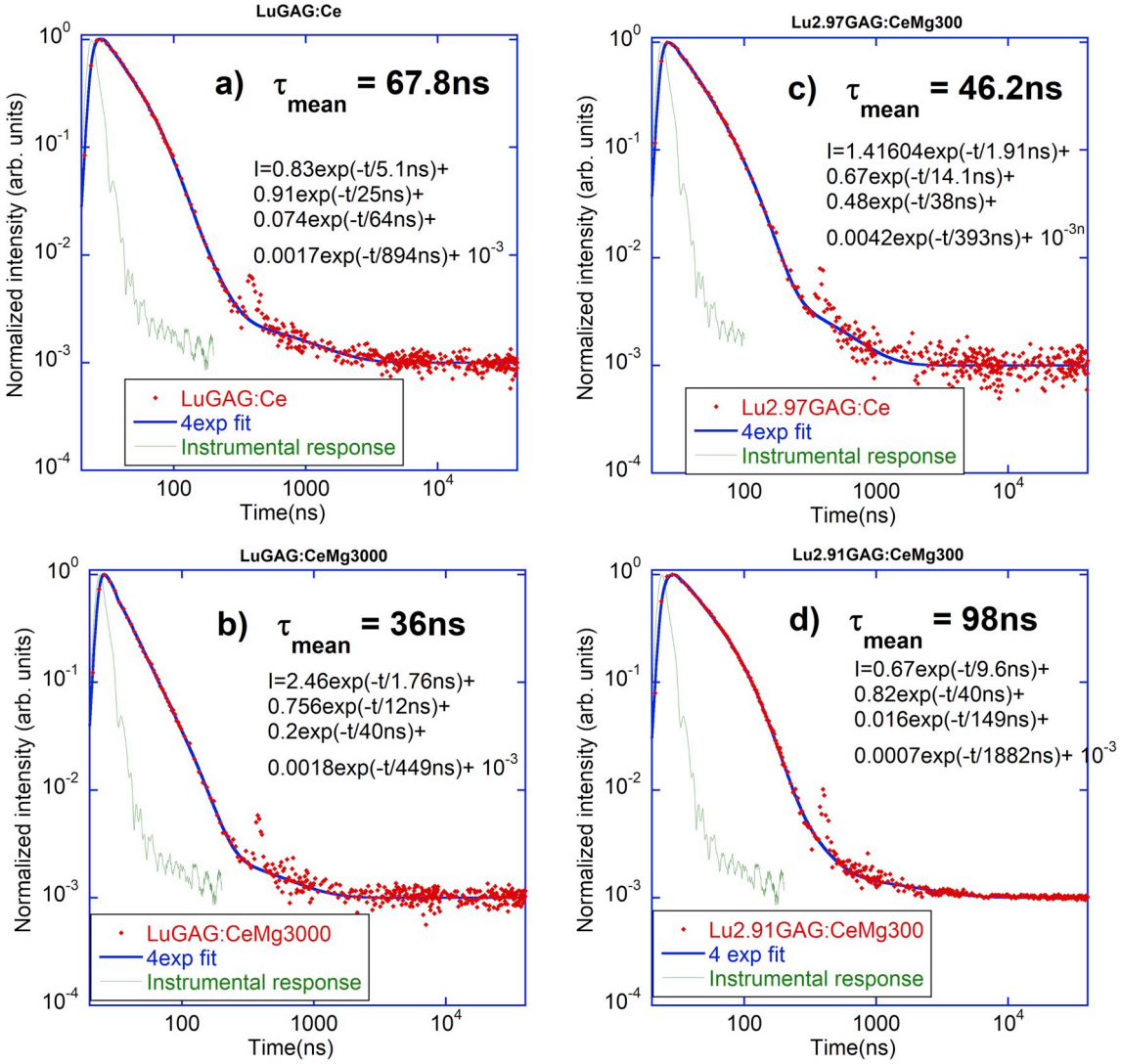

Fig. 35. The SXR-excited scintillation decay curves for the as-grown LuGAG:Ce sample (a), LuGAG:CeMg3000 (b), $Lu_{2.97}$GAG:CeMg300 (c), Lu2.91GAG:CeMg300 (d).

value for a crystal grown by the micro-pulling-down method. Such an observation can be explained by the above discussed increase of the fast defect emission especially for the non-stoichiometric samples, which contributes to the energy transfer towards the Ce^{3+} luminescence center.

The decay kinetics under excitation by ionizing radiation was checked using the SXR source in the wide time range of 10 μs Not very clear trends were found for the scintillation decay time measurements under ^{137}Cs gamma-ray excitation probably due to its much smaller time range and lower signal/noise ratio, when compared to the SXR experiments. The spectrally-unresolved selected scintillation decay curves under SXR excitation for the as-grown samples are shown in Fig. 27 for the LuAG:Ce (a) and Lu2.91AG:CeMg300 (b). In both curves, very fast components with a decay time of several ns can be observed and can be ascribed to the mentioned fast defect emission. The components with a decay time of around 60 ns most probably originate from the Ce^{3+} 5d-4f emission. The longer components can be related to processes connected with defects. Since the decay curves are complicated, the mean decay times were calculated as follows to obtain some overall decay characteristics:

$$\tau_{mean} = \frac{\sum_{i=1}^{n} A_i \tau_i^2}{\sum_{i=1}^{n} A_i \tau_i}$$

where A_i and τ_i are corresponding decay component amplitude and decay time, respectively. The τ_{mean} for LuAG:Ce was about 21000 ns (Fig. 27a), while for Lu2.91AG:CeMg300 it was significantly shorter, around 13000 ns (Fig. 27b). This would mean that the slowest components are suppressed in the non-stoichiometric as-grown sample, which cannot be explained with the currently available data. The τ_{mean} values for the as-grown stoichiometric sample with Mg 3000 ppm and the Lu2.91AG:CeMg300 sample were 21900 ns and 13000 ns, respectively. The positive effect of non-stoichiometry for the as-grown samples is therefore apparent.

On the other hand, annealing has brought significant acceleration of the SXR-excited decay curve in the considered long time range, see Fig. 28. The τ_{mean} for the LuAG:Ce was shortened to some 375 ns (Fig. 28a) and for Lu2.91AG:CeMg300 to 560 ns, which means acceleration of the overall decay time by almost 2 orders of magnitude, which is a consequence of improvement by annealing. After annealing the τ_{mean} for Lu2.91AG:CeMg300 remains slightly longer than for the LuAG:Ce, which would mean that annealing promotes creation of some other defects especially in the non-stoichiometric samples, as was observed in the RL measurements. The τ_{mean} for the annealed stoichiometric samples with 300 ppm and 3000 ppm was even shorter, 149 ns and 184 ns respectively. Further research would be needed to clarify these observations.

3.4. Luminescence and scintillation properties of the LuGAG crystals

This section will focus on the luminescence and scintillation properties of the as-grown LuGAG crystals. The results will be also shown only for the START parts of the crystals (see Fig. 6) for simplicity. The results for the END parts again showed some slight differences, but did not deviate from the general trends and the resulting conclusions.

Fig. 29 compares the absorption spectra of the as-grown LuGAG samples. The spectra show the Ce^{3+} absorption bands at 420 and 352 nm ascribed to the 4f-5d_1 and 4f-5d_2 transitions, respectively. The separation of these peaks is decreased and their positions are shifted towards slightly longer wavelength for the 4f-5d_2 and shorter wavelength for the 4f-5d_1 one when compared to those in LuAG. This is due to decrease of crystal field on the Lu^{3+} site and increased covalency between the Ga^{3+} and O^{2-} ions, which effectively removes O^{2-} outer electrons from around the Lu^{3+} site [15]. For the stoichiometric samples (Fig. 29a), some broad absorption feature occurs around 250 nm and its intensity strongly increases with Mg codoping in a way that it obscures the 4f-5d_2 absorption band. It can be ascribed to the Ce^{4+} absorption band, but also other defects may play a role in this absorption feature, as was sketched above for the LuAG crystals. It is necessary to notice that for higher Mg concentration (900 ppm, 3000 ppm) the Ce^{3+} 4f-5d absorption bands completely disappear, as all the Ce^{3+} ions would be transformed to the tetravalent form. This was also mentioned when discussing the appearance of the crystal with 3000 ppm Mg in Fig. 6. Such a radical change was not observed for the LuAG crystals, which suggests that Ga admixture increases the instability of the Ce^{3+} valence state and which further supports the ascription of the short-wavelength broad absorption feature to the Ce^{4+} CT transition. Such a phenomenon was observed also in other garnet crystals with varied Ga content [26] and was explained by an increased separation of the Fermi level from the Ce^{3+} 4f ground state. For the non-stoichiometric crystals (Fig. 29b) with Mg 300 ppm the same Ce^{3+} absorption peaks were observed. The feature around 250 nm seems to be slightly different with respect to the stoichiometric samples with more pronounced peak. Due to simultaneous increase of this band and decrease of the 4f-5d_1 Ce^{3+} absorption with increasing Al content, we can again ascribe it to the Ce^{4+} CT absorption, which in this case seems to be enhanced by the non-stoichiometry. On the other hand, it is necessary to mention that in the recent preliminary study of the Ce-free non-stoichiometric LuGAG samples (not shown here) very similar absorption feature was found. Therefore, the defect absorption becomes important in the non-stoichiometric samples. It may not be excluded that these defects are similar to those in LuAG counterparts discussed above.

The RL spectra under X-ray excitation for the as-grown samples are compared in Fig. 30. Unlike for the LuAG samples, the spectra consist only of the Ce^{3+} 5d-4f band at 480 nm, while the defect luminescence band completely disappeared upon Ga admixture, which was observed in the earlier studies [10]. For the stoichiometric samples (Fig. 30a), the LuGAGCeMg300 shows the highest RL intensity. Both non-stoichiometric crystals (Fig. 30b) outperform the stoichiometric ones in the RL intensity while it increases with increasing non-stoichiometry (Fig. 30a and b are mutually comparable). One can notice a very small sharp peak around 380 nm for the Lu2.97GAG:CeMg300 sample (Fig. 30b), which seems to be similar to the defect peak found for the Ga-free LuAG counterparts in Fig. 12b and which was finally ascribed to a very fast defect luminescence related to oxygen vacancies. Again, it seems that non-stoichiometry can support creation of such a defect, whose emission wavelength does not look to be affected by Ga-admixture. Some remains of the peak can be found also in the spectrum for the other non-stoichiometric LuGAG sample (Fig. 30b).

To have a better idea on the trends of the RL intensities with composition changes, integrals of the RL spectra were calculated and their dependences on the Mg concentration for stoichiometric samples (Fig. 31a) and on stoichiometry for constant Mg 300 ppm concentration (Fig. 31b) were created. For the stoichiometric samples the RL intensity reaches maximum for Mg 300 ppm and then decreases. A very interesting linear increase with increasing non-stoichiometry is evident from Fig. 31b.

To further study the influence of Mg, photoluminescence decay kinetics for the Ce^{3+} 5d-4f emission under direct excitation into the Ce^{3+} 4f-5d_1 band was measured for the stoichiometric samples with different Mg concentrations, see Fig. 32. Even for the Mg-free sample (Fig. 32a), the decay curve is not simple and consists of two exponential components: the fast one with decay time of 23 ns and the slower one with decay time of 56 ns Shortening of the Ce^{3+} decay time in LuGAG crystals was already observed in Ref. [10] due to lowering the separation of the Ce^{3+} 5d_1 state from the edge of the conduction band and resulting excited state ionization and decay time shortening. With addition of 300 ppm Mg, the ratio of the slower component increased and even some very slow component appeared, which was manifested as the increased background (Fig. 32b). With further increase of Mg concentration the decay curve became more complicated (Fig. 32c) and for 3000 ppm the decay became as short as 6 ns (Fig. 32d). To better observe the trend, the mean decay time was again calculated and plotted against the Mg concentration in Fig. 33a. The trend of the dependence is very similar to that of the dependence of the RL spectra integrals in Fig. 31a. Moreover, very similar behavior was found for the dependence of the light yield determined from the pulse-height spectra under ^{137}Cs 662 keV gamma ray excitation (Fig. 33b). It seems that Mg^{2+} modifies the deexcitation of Ce^{3+} luminescence center and this process is detrimental for the material behavior under excitation by ionizing radiation. Very similar dependence was also found for the mean scintillation decay time measured under the 662 keV excitation (not shown here). It is necessary to keep in mind that Mg^{2+} also reduces the Ce^{3+} concentration, as was observed in the absorption spectra (Fig. 29a), where no Ce^{3+} absorption features were found for the highest Mg concentrations. Further research is needed to clarify this behavior.

On the other hand no clear trend of the other luminescence or scintillation characteristics with non-stoichiometry was found, except for the RL intensity in Fig. 31b. Example of the dependence of the scintillation light yield for the LuGAG samples with constant Mg 300 ppm concentration on stoichiometry is shown in Fig. 34. The values for the stoichiometric LuGAG:CeMg300 and Lu2.97AG:CeMg300 samples are much higher than those for the Ga-free counterparts (see Fig. 26b). A slight decrease is observed for the highest non-stoichiometry (while keeping similar values for the Ga-free sample), probably due to some introduction of defects and related slow components, which could not affect the integral measurement in Fig. 31b.

The SXR-excited scintillation decays for the selected LuGAG samples are shown in Fig. 35. They are again rather complicated as for the LuAG counterparts and 4 exponential components were necessary to fit the decay curve. Again, some very fast components with decay times of the order of few ns can be observed and can be due to the fast luminescence of the defects. The component with decay time of few tens of ns can be ascribed to Ce^{3+} and can be further obscured by the other processes. The longer components can be due to some other defect-related processes. The τ_{mean} was again calculated for each curve to have some overall parameter characterizing the sample response. For the stoichiometric Mg-free LuGAG:Ce sample the τ_{mean} is 67.8 ns, which is much faster than for the Ga-free as-grown and even annealed counterpart (Figs. 27a and 28a). For the sample with Mg 3000 ppm the τ_{mean} gets as short as 36 ns, which might be due to fast processes related to oxygen vacancy defects induced by Mg codoping. For the slightly non-stoichiometric Lu2.97AG:CeMg300 it prolongs to 46 ns and with further increase of non-stoichiometry it is prolonged to almost 100 ns The mean decay time values are significantly shorter than those for the fastest annealed LuAG counterparts, which points to a very positive effect of Ga responsible for reducing the influence of defects.

The annealing experiments and subsequent study of the properties

are planned for the LuGAG samples. A much greater influence of annealing can be expected due to the above-mentioned decreased stability of the trivalent Ce^{3+} in Ga-admixed crystals.

4. Summary and conclusions

Stoichiometric LuAG:Ce crystals with various Mg concentration (0–3000 ppm) and non-stoichiometric Al-rich LuAG:Ce crystals with Mg 300 ppm were grown by micro-pulling-down method. XRD analysis confirmed the LuAG garnet structure, while for the most non-stoichiometric crystal the Al_2O_3 phase was detected at the end part, as during the growth the Al concentration increased along the crystal. Similar, but much smaller changes were observed for the other crystals. Increased Al and Ce concentrations were found in the cross-section in the rim near the surface.

Intense defect emission and Ce^{3+} 5d-4f emission were found in the RL spectra under X-ray excitation. For the as-grown samples, the Ce^{3+} emission was one of the most intense for low Mg concentration of 300 ppm. Defect emission and some defect absorption features systematically decreased with increasing Mg concentration. The Ce^{3+} emission did not show clear trend with increasing non-stoichiometry, while slight increase of the defect emission was observed, as the stoichiometry change might increase defect concentration. Annealing led to decrease of Ce^{3+} emission for lower Mg concentrations and clearly increasing trend with increasing Mg concentration was found. The defect emission intensity was systematically increased by annealing in all the stoichiometric samples while its decreasing trend with Mg concentration was conserved. Both Ce^{3+} and defect luminescence peaks clearly increased with increasing non-stoichiometry. Sharp emission peak with very fast luminescence component with decay time of several nanoseconds was found in the annealed samples and was enhanced by non-stoichiometry. Energy transfer from this defect towards Ce^{3+} was confirmed by photoluminescence measurement. This emission was ascribed to defects based on oxygen vacancies and seems responsible for improvement of luminescence and scintillation properties in the non-stoichiometric crystals.

The light yield at 662 keV gamma ray excitation decreased with increasing Mg concentration in the stoichiometric (both annealed and as-grown) samples due to decreasing contribution of the defect luminescence. Non-stoichiometry led to systematic pronounced light yield increase and the value for the annealed most non-stoichiometric Lu2.91AG:CeMg300 sample reached 17000 photons/MeV, which was 3 times higher that of the stoichiometric Mg-free LuAG:Ce crystal.

Annealing brought significant acceleration of scintillation decay in all the samples.

Improvement of luminescence and scintillation properties of the non-stoichiometric LuAG:Ce crystals is probably not related to reduction of Lu_{Al} anti-site defects, which was supposed and was not confirmed. The improvement consists in introduction of new energy transfer process towards Ce^{3+} via defect levels, whose creation is enhanced by non-stoichiometry and subsequent annealing. This process is in interplay with the alternative Ce^{4+} -related scintillation mechanism introduced by Mg-codoping and annealing which also brings improvement to the scintillation properties.

Ga-admixed LuGAG:Ce crystals were also successfully grown and XRD confirmed their garnet structure. However, existence of 2–3 garnet phases of very close compositions was observed. EDLM revealed the presence of sub-grains and grains in all the crystals. An increased Ce concentration in the rim of the cross-section was detected by μ-XRF measurement. The Ga concentration increased from the center towards the rim, while opposite trend was observed for Al.

For the Ga-admixed LuGAG:Ce crystals, the defect emission was almost completely suppressed and the stability of the Ce^{3+} valence was strongly decreased, which led to almost complete change of the Ce valence to the tetravalent state for higher Mg concentrations.

The RL intensity for the stoichiometric samples reached maximum for the 300 ppm Mg concentration and then systematically decreased. Same behavior was found for Ce^{3+} luminescence decay and light yield and was explained by introduction of some quenching process by Mg codoping. Increasing non-stoichiometry led to linear increase of the RL intensity, which was not observed for the light yield, which generally exceeded the values for the Ga-free counterparts. Scintillation decay was also significantly faster than for the Ga-free LuAG crystals. Influence of annealing on LuGAG crystals needs to be investigated.

Acknowledgments

The research in this article was supported by the Czech Science Foundation project no. 15-18300Y. Funding from the European Union's Horizon 2020 research and innovation program under the Marie Sklodowska-Curie grant agreement no. 644260 (Intelum) and bilateral AS CR-JSPS Joint Research Project are also gratefully acknowledged.

References

[1] M. Nikl, A. Yoshikawa, Recent R&D trends in inorganic single-crystal scintillator materials for radiation detection, Advanced Optical Materials 3 (2015) 463–481.
[2] P. Lecoq, Development of new scintillators for medical applications, Nucl. Instrum. Methods Phys. Res. 809 (2016) 130–139.
[3] M. Moszyński, T. Ludziejewski, D. Wolski, W. Klamra, L.O. Norlin, Properties of the YAG:Ce scintillator, Nucl. Instrum. Methods Phys. Res., Sect. A 345 (1994) 461–467.
[4] M. Nikl, E. Mihokova, J.A. Mares, A. Vedda, M. Martini, K. Nejezchleb, K. Blazek, Traps and timing characteristics of LuAG:Ce^{3+} scintillator, Phys. Status Solidi 181 (2000) R10–R12.
[5] V. Lupei, A. Lupei, C. Tiseanu, S. Georgescu, C. Stoicescu, P.M. Nanau, High-resolution optical spectroscopy of YAG:Nd: a test for structural and distribution models, Phys. Rev. B 51 (1995) 8–17.
[6] M.K. Ashurov, Y. Voronko, V.V. Osiko, A.A. Sobol, M.I. Timoshechkin, Spectroscopic study of stoichiometry deviation in crystals with garnet structure, Phys. Status Solidi 42 (1977) 101–110.
[7] H. Przybylińska, A. Wittlin, C.-G. Ma, M.G. Brik, A. Kamińska, P. Sybilski, Y. Zorenko, M. Nikl, V. Gorbenko, A. Fedorov, M. Kučera, A. Suchocki, Rare-earth antisites in lutetium aluminum garnets: influence on lattice parameter and Ce^{3+} multicenter structure, Opt. Mater. 36 (2014) 1515–1519.
[8] A.G. Petrosyan, K.L. Ovanesyan, R.V. Sargsyan, G.O. Shirinyan, D. Abler, E. Auffray, P. Lecoq, C. Dujardin, C. Pedrini, Bridgman growth and site occupation in LuAG:Ce scintillator crystals, J. Cryst. Growth 312 (2010) 3136–3142.
[9] V.V. Laguta, A.M. Slipenyuk, M.D. Glinchuk, I.P. Bykov, Y. Zorenko, M. Nikl, J. Rosa, K. Nejezchleb, Paramagnetic impurity defects in LuAG:Ce thick film scintillators, Radiat. Meas. 42 (2007) 835–838.
[10] H. Ogino, A. Yoshikawa, M. Nikl, J.A. Mares, J. Shimoyama, K. Kishio, Growth and optical properties of $Lu_3(Ga,Al)_5O_{12}$ single crystals for scintillator application, J. Cryst. Growth 311 (2009) 908–911.
[11] M. Nikl, J. Pejchal, E. Mihokova, J.A. Mares, H. Ogino, A. Yoshikawa, T. Fukuda, A. Vedda, C. D'Ambrosio, Antisite defect-free $Lu_3(Ga_xAl_{1-x})_5O_{12}$:Pr scintillator, Appl. Phys. Lett. 88 (2006) 141916.
[12] K. Kamada, T. Endo, K. Tsutumi, T. Yanagida, Y. Fujimoto, A. Fukabori, A. Yoshikawa, J. Pejchal, M. Nikl, Composition engineering in cerium-doped $(Lu,Gd)_3(Ga,Al)_5O_{12}$ single-crystal scintillators, Cryst. Growth Des. 11 (2011) 4484–4490.
[13] M. Nikl, K. Kamada, V. Babin, J. Pejchal, K. Pilarova, E. Mihokova, A. Beitlerova, K. Bartosiewicz, S. Kurosawa, A. Yoshikawa, Defect engineering in Ce-doped aluminum garnet single crystal scintillators, Cryst. Growth Des. 14 (2014) 4827–4833.
[14] S. Blahuta, A. Bessiere, B. Viana, P. Dorenbos, V. Ouspenski, Evidence and consequences of Ce^{4+} in LYSO:Ce,Ca and LYSO:Ce,Mg single crystals for medical imaging applications, IEEE Trans. Nucl. Sci. 60 (2013) 3134–3141.
[15] M. Nikl, A. Yoshikawa, K. Kamada, K. Nejezchleb, C.R. Stanek, J.A. Mares, K. Blazek, Development of LuAG-based scintillator crystals – a review, Prog. Cryst. Growth Char. Mater. 59 (2013) 47–72.
[16] K. Kamada, S. Kurosawa, Y. Yokota, J. Pejchal, M. Nikl, Y. Ohashi, A. Yoshikawa, Nonstochiometry of $Lu_3Al_5O_{12}$ single crystal and its effects of on luminescence and scintillation properties, J. Phys. Conf. 619 (2015) 012035.
[17] S. Liu, J.A. Mares, V. Babin, C. Hu, H. Kou, C. D'Ambrosio, J. Li, Y. Pan, M. Nikl, Composition and properties tailoring in Mg^{2+} codoped non-stoichiometric LuAG:Ce,Mg scintillation ceramics, J. Eur. Ceram. Soc. 37 (2016) 1689–1694.
[18] E.V. Tret'yak, G.P. Shevchenko, M.V. Korjik, Formation of high-density scintillation ceramic from LuAG:Ce + Lu_2O_3 powders obtained by co-precipitation method, Opt. Mater. 46 (2015) 596–600.
[19] D.T. Haven, P.T. Dickens, M.H. Weber, K.G. Lynn, Yttrium antisite reduction and improved photodiode performance in Ce doped $Y_3Al_5O_{12}$ by Czochralski growth in alumina rich melts, J. Appl. Phys. 114 (2013) 043102.
[20] A.P. Patel, M.R. Levy, R.W. Grimes, R.M. Gaume, R.S. Feigelson, K.J. McClellan, C.R. Stanek, Mechanisms of nonstoichiometry in $Y_3Al_5O_{12}$, Appl. Phys. Lett. 93 (2008) 191902.
[21] V.V. Laguta, M. Buryi, J. Pejchal, V. Babin, M. Nikl, Hole Self-trapping in the

$Y_3Al_5O_{12}$ and $Lu_3Al_5O_{12}$ Garnet Crystals, Appl. Phys. Rev. 10 (2018) 034058(1-10).
[22] A.B. Muñoz-García, E. Artacho, L. Seijo, Atomistic and electronic structure of antisite defects in yttrium aluminum garnet: density-functional study, Phys. Rev. B 80 (2009) 014105, https://doi.org/10.1103/PhysRevB.80.014105.
[23] A. Yoshikawa, M. Nikl, G. Boulon, T. Fukuda, Challenge and study for developing of novel single crystalline optical materials using micro-pulling-down method, Opt. Mater. 30 (2007) 6–10.
[24] A. Yoshikawa, V.I. Chani, Growth of optical crystals by the micro-pulling-down method, Mat. Res. Soc. Bull. 34 (2009) 266–270.
[25] D. Mateika, E. Volkel, J. Haisma, lattice-constant-adaptable crystallographics. II. Czochralski growth from multicomponent melts of homogeneous mixed-garnet crystals, J. Cryst. Growth 102 (1990) 994–1013.
[26] H. Yamaguchi, K. Kamada, J. Pejchal, S. Kurosawa, Y. Shoji, Y. Yokota, Y. Ohashi, A. Yoshikawa, Effects of Mg-codoping on luminescence and scintillation properties of Ce doped $Lu_3(Ga,Al)_5O_{12}$ single crystals, Opt. Mater. 65 (2017) 60–65, https://doi.org/10.1016/j.optmat.2016.08.030.
[27] C. Guguschev, R. Tagle, U. Juda, A. Kwasniewski, Microstructural investigations of $SrTiO_3$ single crystals and polysilicon using a powerful new X-ray diffraction surface mapping technique, J. Appl. Crystallogr. 48 (2015) 1883–1888, https://doi.org/10.1107/S1600576715019949.
[28] P. Bruza, V. Fidler, M. Nikl, Table-top instrumentation for time-resolved luminescence spectroscopy of solids excited by nanosecond pulse of soft X-ray source and/or UV laser, J. Instrum. 6 (2011) P009007(1–12).
[29] Y. Yokota, T. Kudo, V. Chani, Y. Ohashi, S. Kurosawa, K. Kamada, Z. Zeng, Y. Kawazoe, A. Yoshikawa, Improvement of dopant distribution in radial direction of single crystals grown by micro-pulling-down method, J. Cryst. Growth 474 (2017) 178–182, https://doi.org/10.1016/j.jcrysgro.2016.11.119.
[30] R. Simura, A. Yoshikawa, S. Uda, The radial distribution of dopant (Cr, Nd, Yb, or Ce) in yttrium aluminum garnet ($Y_3Al_5O_{12}$) single crystals grown by the micro-pulling-down method, J. Cryst. Growth 311 (2009) 4763–4769, https://doi.org/10.1016/j.jcrysgro.2009.07.012.
[31] D. Maier, D. Rhede, R. Bertram, D. Klimm, R. Fornari, Dopant segregations in oxide single-crystal fibers grown by the micro-pulling-down method, Opt. Mater. 30 (2007) 11–14, https://doi.org/10.1016/j.optmat.2006.10.023.
[32] Z. Zeng, L. Qiao, Y. Liu, Y. Yokota, Y. Kawazoe, A. Yoshikawa, Numerical study on the radial dopant distribution in micro-pulling-down crystal growth, J. Cryst. Growth 434 (2016) 110–115, https://doi.org/10.1016/j.jcrysgro.2015.10.029.
[33] C.W. Lan, S. Uda, T. Fukuda, Theoretical analysis of the micro-pulling-down process for Ge_xSi_{1-x} fiber crystal growth, J. Cryst. Growth 193 (1998) 552–562, https://doi.org/10.1016/S0022-0248(98)00527-2.
[34] Y. Wu, F. Meng, Q. Li, M. Koschan, C.L. Melcher, Role of Ce^{4+} in the scintillation mechanism of codoped $Gd_3Ga_3Al_2O_{12}$:Ce, Physical Review Applied 2 (2014) 044009.
[35] V. Babin, K. Blazek, A. Krasnikov, K. Nejezchleb, M. Nikl, T. Savikhina, S. Zazubovich, Luminescence of undoped LuAG and YAG crystals, Phys. Status Solidi 2 (2005) 97–100, https://doi.org/10.1002/pssc.200460120.
[36] P.A. Tanner, L. Fu, L. Ning, B.-M. Cheng, M.G. Brik, Soft synthesis and vacuum ultraviolet spectra of YAG:Ce^{3+} nanocrystals: reassignment of Ce^{3+} energy levels, J. Phys. Condens. Matter 19 (2007) 216213, https://doi.org/10.1088/0953-8984/19/21/216213.
[37] V. Babin, V.V. Laguta, A. Maaroos, A. Makhov, M. Nikl, S. Zazubovich, Luminescence of F^+-type centers in undoped $Lu_3Al_5O_{12}$ single crystals, Phys. Status Solidi 248 (2011) 239–242, https://doi.org/10.1002/pssb.201046245.
[38] E. Mihokova, V. Babin, J. Pejchal, V. Cuba, J. Barta, K. Popovich, L.S. Schulman, A. Yoshikawa, M. Nikl, Afterglow and quantum tunneling in Ce-doped lutetium aluminum garnet, IEEE Trans. Nucl. Sci. (2018), https://doi.org/10.1109/TNS.2018.2823582 1–1.
[39] M. Nikl, J.A. Mares, N. Solovieva, J. Hybler, A. Voloshinovskii, K. Nejezchleb, K. Blazek, Energy transfer to the Ce^{3+} centers in $Lu_3Al_5O_{12}$:Ce scintillator, Phys. Status Solidi 201 (2004) R41–R44, https://doi.org/10.1002/pssa.200409041.

Journal of Luminescence 181 (2017) 277–285

Contents lists available at ScienceDirect

Journal of Luminescence

journal homepage: www.elsevier.com/locate/jlumin

Full Length Article

Luminescence and scintillation properties of Mg-codoped LuAG:Pr single crystals annealed in air

Jan Pejchal [a,*], Maksym Buryi [a], Vladimir Babin [a], Petr Prusa [a,b], Alena Beitlerova [a], Jan Barta [a,b], Lubomir Havlak [a], Kei Kamada [c,d], Akira Yoshikawa [c,d], Valentin Laguta [a], Martin Nikl [a]

[a] Institute of Physics AS CR, Cukrovarnicka 10, Prague 6, 16200 Czech Republic
[b] Faculty of Nuclear Sciences and Physical Engineering, Czech Technical University in Prague, Brehova 7, Prague 1, 11519 Czech Republic
[c] Institute for Materials Research, Tohoku University, 2-1-1, Katahira, Aoba-ku, Sendai, Miyagi 980-8577, Japan
[d] New Industry Creation Hatchery Center, Tohoku University, 6-6-10 Aoba, Aramaki, Aoba-ku, Sendai, Miyagi 980-8579, Japan

ARTICLE INFO

Article history:
Received 24 May 2016
Received in revised form
8 September 2016
Accepted 9 September 2016
Available online 16 September 2016

Keywords:
Scintillation
Pr4+
Luminescence
Codoping
Lutetium–aluminum garnet

ABSTRACT

The influence of the Mg^{2+} codoping and annealing in the air on the scintillation and luminescence characteristics of Pr-doped lutetium-aluminum garnet crystals (LuAG) was studied to find a possible positive effect of Pr^{4+}. The overall scintillation efficiency under X-ray excitation of the annealed Pr-doped samples decreased with increasing Mg concentration. This was explained by increased overlap of the Pr^{3+} 5d-4f emission with the charge-transfer (CT) absorption band of the Pr^{4+} ion stabilized by Mg^{2+}. This absorption caused even greater decrease of the light yield, as the light is collected from the whole sample volume in the pulse-height spectrum measurement. Electron centers based on oxygen vacancies (F^{+} centers) which can have negative influence on scintillation mechanism were revealed by the electron paramagnetic resonance (EPR) experiments. The O^{-} hole center was detected as well and the temperature dependences of the EPR spectra showed that its thermal stability was decreased by Mg codoping. Negligible changes in the decay time of Pr^{3+} 5d-4f photoluminescence exclude the non-radiative energy transfer from relaxed $5d_1$ excited state of Pr^{3+} towards CT absorption transition of Pr^{4+} and suggest that simple reabsorption of the emitted light takes place. Unlike for the Ce-doped analogs, promoting the Pr^{3+} luminescence center to the tetravalent state by divalent ion co-doping and air annealing did not improve scintillation properties of Pr-doped LuAG.

1. Introduction

Inorganic scintillation single crystals have been employed in the ionizing radiation detection and related applications for several decades [1]. They are utilized in high-energy physics, environmental monitoring, geological survey and oil well logging or astronomy. Medical imaging and especially security scanning are the applications mostly stimulating the development of new scintillation materials due to increasing demands on their performance.

In several modern inorganic scintillators fast 5d-4f luminescence of Ce^{3+} has been employed to obtain the scintillation response of the order of several tens of ns with high efficiency (see [1] and references therein). Lutetium aluminum garnet ($Lu_3Al_5O_{12}$, LuAG) single crystal matrix appears as a very suitable host for the Ce^{3+} and other rare earth (RE) luminescence centers due to the Lu site where the RE^{3+} ion can be easily substituted, high density of 6.67 g/cm^3, high effective atomic number and mechanical and chemical and thermal resistance [2]. The first systematic studies started almost 2 decades ago [3]. Besides favorable scintillation properties, one of the main demerits of this material was presence of slow components in the scintillation decay caused by retrapping of electrons at the traps related to Lu_{Al} intrinsic anti-site defects (AD) [4], generally present also in some other aluminum garnets due to high crystal growth temperature [5]. This phenomenon caused serious deterioration of the light yield and timing performance. However, it is well known that the flexibility of the garnet matrix allows incorporation of other elements [6] and therefore the lattice constants, band-gap and other parameters such as depth and trapping efficiency of the AD-related traps can be easily tuned. This approach led to development of new slow-component-free and highly efficient Ce-doped scintillator based on the Gd, Ga-admixed multicomponent garnet [7]. Another recent approach to improve the scintillation performance is employing Ce^{4+}

* Corresponding author.
E-mail address: pejchal@fzu.cz (Jan Pejchal).

http://dx.doi.org/10.1016/j.jlumin.2016.09.025
0022-2313/

stabilized with divalent ion (Mg^{2+}, Ca^{2+}) codoping in the scintillation mechanism [2,8–10]. The Ce^{4+} can be regarded as Ce^{3+} with already captured hole, which is ready for an immediate capture of thermalized electron from the conduction band followed by forming the Ce^{3+} in an excited state. The stable Ce^{4+} center directly competes with shallow electron traps responsible for the slow decay components. The de-excitation of this temporary Ce^{3+} results in the usual Ce^{3+} emission which might show somewhat different emission characteristics regarding e.g. temperature stability [8,11]. Finally, a nonradiative hole capture from a nearby defect or valence band leads to the Ce^{4+} center regeneration [12,13]. This mechanism was reported to be responsible for improvement of scintillation properties of lutetium silicate crystals [8] and also LuAG:Ce optical ceramics, where Mg^{2+} was used as a sintering aid [9]. Another way to stabilize Ce in its tetravalent form in garnets is annealing in an oxidizing atmosphere [14]. The annealed crystals showed increased light yield and reduced proportion of the slow components in the scintillation decay. The suppression of the slow components is caused also by the reduction of concentration of deep traps related to oxygen vacancies.

Another suitable luminescence center is the Pr^{3+} ion. Some Pr-doped scintillators were briefly investigated in the past [15]. To obtain fast and high-energy-shifted 5d-4f emission of Pr^{3+} the crystal field of the host matrix should be strong enough to shift the lowest 5d-state well below the $^1S_0$ one to make the 5d-4f radiative transition possible. For details on these aspects of the Pr^{3+} luminescence, see for example [16]. High quality Pr-doped $Lu_3Al_5O_{12}$ (LuAG:Pr) was announced as a fast and efficient scintillator [17,18] and an attempt of its application in positron emission mammography has been already made [19]. Analogous problems with the retrapping at AD's were observed [17]. Similar attempt of composition engineering using Gd and Ga admixture failed in the case of Pr-doped multicomponent garnets due to overlap of the Pr^{3+} 5d-4f emission with the Gd^{3+} $^8S_{7/2} \rightarrow {}^6P_J$ transition and resulting energy back-transfer from the Pr^{3+} to the host [20]. There is a question if stabilizing Pr^{4+} by divalent ion codoping or annealing would improve the scintillation properties of garnet-based scintillators. Radiation hardness and some luminescence properties of Mg-codoped LuAG:Pr were studied recently and no positive influence was found mainly due to presence of Yb^{3+} and other impurities [21,22]. However, systematic study of scintillation properties of Mg-codoped LuAG:Pr is still missing. Thus the aim of this work is to investigate absorption, luminescence and scintillation properties of Mg-codoped and annealed LuAG:Pr for different concentrations of Mg codopant.

2. Materials and experimental methods

The crystals were grown by micro-pulling-down method [23,24] with radiofrequency inductive heating. An iridium crucible with a die of 3 mm in diameter was used. The growth was performed under N_2 (4N) atmosphere using $<111>$ oriented LuAG single crystal as a seed. The pulling speed was around 0.07–0.1 mm/min. The starting materials were prepared by mixing 4N purity Lu_2O_3, Al_2O_3 and Pr_6O_{11} powders. $MgCO_3$ of 4N purity was added to the mixture for the Mg-codoped samples.

The LuAG:Pr samples with Pr concentration of 0.2 atomic % were prepared. The Mg concentration was 0, 300 or 3000 atomic ppm. It is reasonable to suppose that Pr substitutes for Lu while Mg substitutes for Al, even though it can be incorporated in all the three kinds of sites available within the garnet structure [6]. Therefore the Pr concentration is given with respect to Lu, while the Mg concentration is given with respect to Al. Then we can specify the hypothetical formula of the grown crystal as $Lu_{3(1-x)}Pr_{3x}Al_{5(1-y)}Mg_{5y}O_{12}$, where $x=0.002$ and $y=0$, 0.0003 and 0.003. However, the atomic % or atomic ppm will be used for simplicity further in the text to specify the sample composition. One completely undoped crystal was also grown for comparison.

The crystal rods had diameter of 3 mm and were from 35 to 45 mm in length. 1 mm thick circular samples were cut from approximately 1 cm from the beginning (marked as START) and 1 cm from the end (marked as END) of the rod and mirror-polished for further optical characterization. The samples were annealed in air for 12 h at a temperature of 1200 °C.

The phase purity of prepared crystals was examined by XRD analysis using the Rigaku MiniFlex 600 powder X-ray diffractometer equipped with Ni-filtered Cu-K$\alpha_{1,2}$ line and NaI:Tl scintillation detector. Prior to the measurement, a selected part of the prepared crystal was grinded into a fine powder in an agate mortar and its diffraction pattern was then measured in continuous mode between 10° and 80° 2θ. The diffraction patterns recorded were fully consistent with the ICDD PDF-2 record 01-73-1368 ($Lu_3Al_5O_{12}$) and showed some evidence of slight preferred orientation due to the grinding of a single-crystalline material.

Luminescence measurements were performed by a modified spectrofluorometer (custom made 5000M model, Horiba Jobin Yvon) equipped with TBX-04 photon counting detector (IBH Scotland). A deuterium steady-state lamp was used for the excitation and emission spectra measurements. An X-ray tube operating at a voltage of 40 kV and 15 mA current with Mo anode (ISO-DEBYEFLEX 3003 Seifert Gmbh.) was used as an excitation source for the radioluminescence (RL) measurements. All the spectra were corrected for experimental distortions. The hydrogen nanosecond flashlamp or pulsed nanoLED source (IBH Scotland) were used for the luminescence decay measurements using the methods of time correlated single photon counting. Exponential fits of the decays were obtained by performing the convolution of the considered function with the instrumental response and a least-square sum fitting procedure (SpectraSolve software package from Ames Photonics Inc.). For the light yield measurements, sample crystals were optically coupled with a hybrid photomultiplier (HPMT) DEP PPO 475B. Samples were coupled to the HPMT by silicon grease and wrapped in teflon tape used as a reflector (preliminary, $BaSO_4$ was used also for one sample, but the result was practically the same as for Teflon). The ^{137}Cs (661.6 keV) source was used for excitation and the amplifier shaping time was 6 μs. The scintillation decay kinetics was measured with a fast photomultiplier and Tektronix TDS3052C digital Phosphor Oscilloscope under ^{137}Cs excitation. Scintillation decay data were evaluated by SpectraSolve as well. All the optical and scintillation measurements were performed at room temperature (RT).

The electron paramagnetic resonance (EPR) spectra were measured using the commercial Bruker X-/Q-band E580 FT/CW ELEXSYS spectrometer at X-band (microwave frequency 9.5 GHz) within the temperature range 10–296 K using an Oxford Instruments ESR900 continuous flow cryostat. As a source of X-ray irradiation the same ISO-DEBYEFLEX 3003 X-Ray equipment mentioned above was used. The X-ray tube 55 kV voltage and 30 mA current were kept during the samples irradiation at liquid nitrogen temperature (LNT).

3. Results and discussion

The absorption spectra of the Pr-doped samples are compared with the undoped one in the Fig. 1. Only the START parts from each sample were chosen, as the spectra of the END parts did not show any significant differences. For the Pr-doped Mg-free sample, the curve gradually goes up above the baseline between 300–600 nm and one can notice prominent relatively sharp peaks related to Pr^{3+} 4f-5d_1 and 4f-5d_2 transitions that appear at 285 and 240 nm,

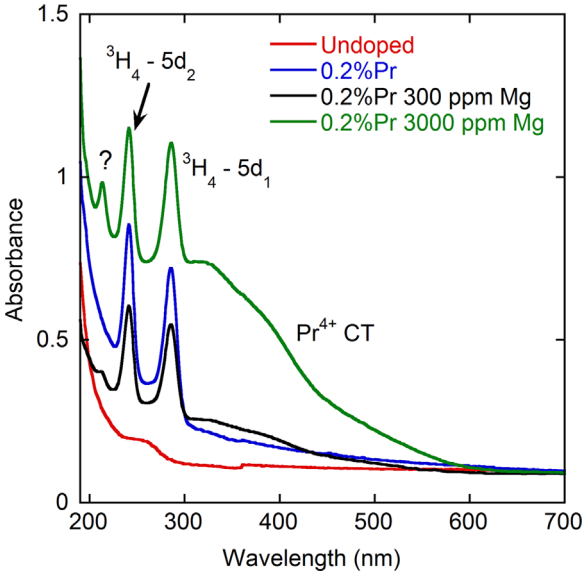

Fig. 1. Absorption spectra of the START parts of the annealed LuAG:Pr0.2% samples with 0, 300 and 3000 ppm of Mg codopant.

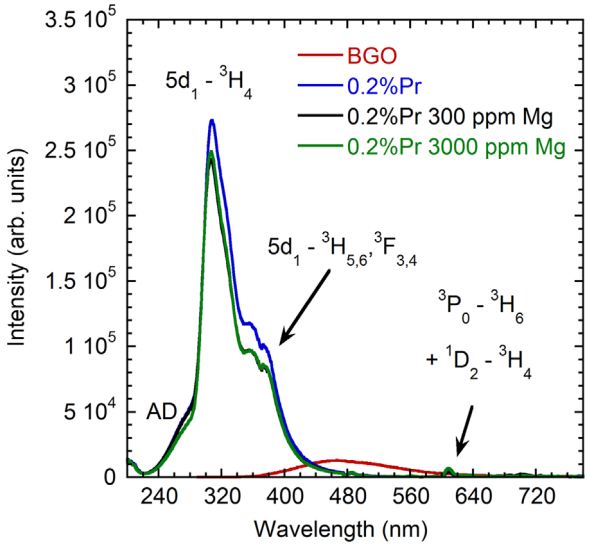

Fig. 2. Comparison of radioluminescence spectra of the START parts of the annealed LuAG:Pr0.2% samples with 0, 300 and 3000 ppm of Mg codopant.

respectively. This result corresponds to the observations in the literature (see [2] and references therein). The curve sharply increases below 200 nm which is most probably due to defect states modifying the band edge. For the sample codoped with 300 ppm Mg, the spectrum is very similar but the increase of the absorption between 300 and 600 nm is more pronounced. The absorption at the shortest wavelengths is significantly smaller. Concerning the sample codoped with 3000 ppm Mg, the absorption between 300 and 600 nm is very strong and obscures the features related to Pr^{3+} and band edge at the shorter wavelengths. The intensity of this absorption increases with increasing Mg concentration and it was ascribed to the charge-transfer (CT) transition of the Pr^{4+} ion, similarly as the analogous Ce^{4+} CT transition observed for Ce-doped scintillation materials codoped with divalent alkaline earth ions [8,10–13]. As can be expected, annealing causes the oxidation of Pr to its tetravalent state while the Mg^{2+} codoping enhances its stability. The effect is especially prominent for the sample with 3000 ppm Mg, which follows from the charge compensation of the divalent Mg^{2+} by Pr^{4+}. It is not excluded that some Pr^{4+} ions are already present in the Mg-codoped samples before annealing. Comparative study of the properties before and after annealing is under way and will be published elsewhere, as some peculiarities in the luminescence behavior can be observed. Considering that the onset of the Pr^{4+} CT transition is situated around 600 nm and that the Ce^{4+} CT absorption for the Ce doped scintillators has an onset around 340 nm, the difference of the onset positions corresponds to some 1.5 eV, which exactly matches the difference between 4f ground state energies of Ce^{3+} and Pr^{3+} [25] and provides further support for the ascription of the smooth absorption band below 600 nm. It is worth noting that in the spectra for both Mg-doped samples that a new sharp peak at 213 nm emerges after annealing. Its origin is unknown but might be related to simultaneous occurrence of Pr^{4+} and Mg^{2+}, as the Pr^{4+} CT absorption is present also in the Mg-free sample where the 213 nm peak is missing. It is most probably not related to f-states of Pr^{3+}, as it is absent in the photoluminescence excitation spectra of Pr^{3+} emission (see below). In the undoped sample, the absorption at 250 nm may be related to the iron impurity, which can change valence from 2+ to 3+ during annealing [26].

The comparison of the RL spectra of the studied samples under X-ray excitation with that for the $Bi_4Ge_3O_{12}$ (BGO) commercially used reference scintillator is in the Fig. 2. They are dominated by the 5d-4f emission peak at 308 nm (5d–$^3H_4$) and a shoulder around 360 nm caused by transitions from the 5d state to the higher 4 f levels ($^3H_{5,6}$, $^3F_{3,4}$). The shoulder at the short wavelength side of the 308 nm peak originates from host luminescence related to recombination of exciton at AD's. It is worth noting that its intensity is practically the same for both the Mg concentrations. Very weak 4f–4f transitions can be observed at longer wavelengths. The overall scintillation efficiency of all the samples is significantly higher than that of BGO scintillator and is slightly lower for the Mg-codoped samples. The cause can be an overlap of the Pr^{3+} 5d-4f emission peak with the broad absorption between 300 and 600 nm discussed above, which increases with increasing Mg concentration. Interestingly, the RL intensity for both Mg-codoped samples is practically the same. All the results shown here are again for the START parts. Only minimum differences were observed for the samples from the END parts.

The photoluminescence (PL) excitation spectrum of the 308 nm emission is shown in the Fig. 3a for the 300 ppm Mg Pr-doped LuAG sample (START). The dominant peaks at 280 and 235 nm corresponding to the 4f-5d transitions are already observed in the absorption spectra in the Fig. 1.

We guess that the slight shift to shorter wavelengths might be caused by an instrumental effect, as practically no changes can be observed for the 4f-5d peaks in the absorption spectra in the Fig. 1. The small peak below 200 nm is related to the defect states shaping the band edge. The 213 nm peak discussed above was not found at all, which again supports the idea that it is not related to Pr^{3+} ion. The same is valid for the excitation spectra of the other samples.

The comparison of the photoluminescence emission spectra for the same sample LuAG:Pr 0.2% Mg 300 ppm (START) under 200 nm and 285 nm excitation is in the Fig. 3b. Both spectra are again dominated by the Pr^{3+} 5d-4f luminescence and their shape is also comparable with the radioluminescence one (Fig. 2), but the host emission shoulder below 300 nm is obviously missing. For the spectrum excited under 200 nm (from valence band top to the defect levels near the bottom edge of the conduction band), the Pr^{3+} 4f–4f emission is quite apparent while it is almost missing in the spectrum excited under 285 nm. The pronounced 4f–4f emission can be related to the simultaneous excitation of the Pr^{3+} ion and some defect state from which an energy leak to the other

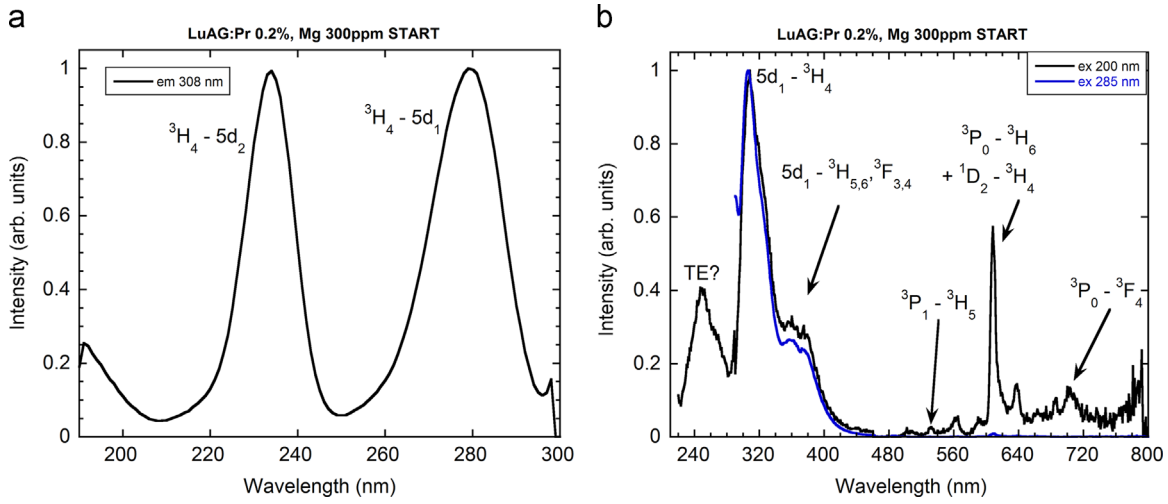

Fig. 3. a. photoluminescence excitation spectrum for the 308 nm emission for the LuAG:Pr 0.2% 300 ppm Mg sample. b Comparison of the photoluminescence spectra of the annealed Mg 300 ppm LuAG:Pr 0.2% sample (START) under 285 nm (direct 4f-5d excitation) and 200 nm (to the defect states below conduction band).

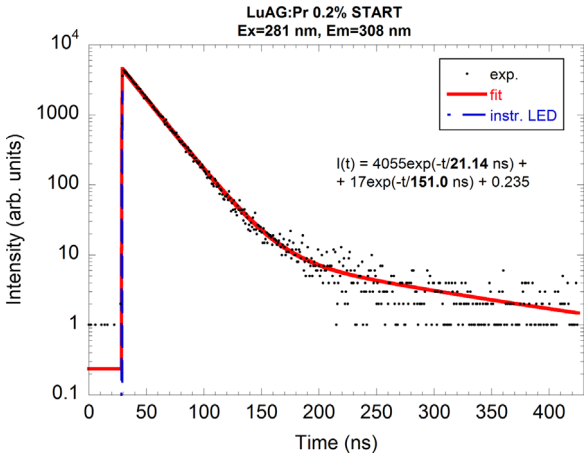

Fig. 4. Photoluminescence decay kinetics of the Pr^{3+} 5d-4f emission at 308 nm under 285 nm excitation (direct 4f-5d) for the annealed Mg-free LuAG:Pr 0.2% sample (START).

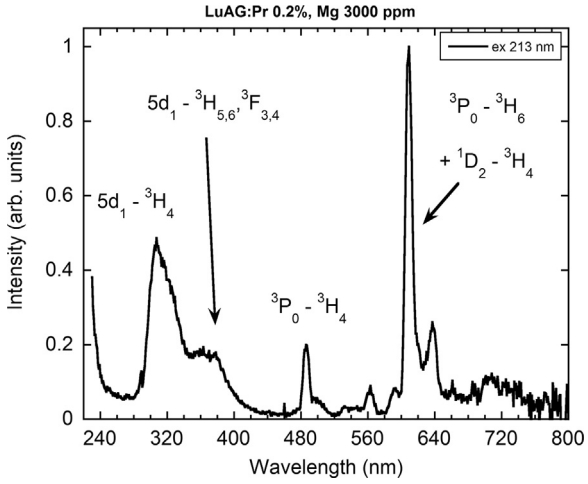

Fig. 5. Photoluminescence spectra of the annealed Mg 300 ppm LuAG:Pr 0.2% sample (START) under 213 nm excitation.

f-levels takes place. The assignment of the 4f–4f lines in the Fig. 3b was made according to [27].

It is worth mentioning that the shoulder related to the transitions from the 5d level to the higher 4f ones at 360 nm changes its relative intensity with respect to the dominant 5d-4f peak at 308 nm. It does not show any stable trend with the Mg concentration. Interestingly, the absorption of the F^+ center based on an oxygen vacancy in LuAG lies exactly in this spectral area [28]. Its creation might be modified by Mg codoping and annealing and it can influence the PL intensity in this region. Presence of an electron-like center (most probably the F^+ one) was proved by the EPR measurements below.

Another emission band emerged at 249 nm upon 200 nm excitation in the emission spectrum (Fig. 3b). This band can be related to an emission of some defect induced by annealing and stabilized by Mg^{2+} codopant. We should emphasize that this wavelength exactly corresponds with the emission of the low-temperature configuration of the AD- trapped exciton (TE) reported in [29]. It might be that this low-temperature trapped exciton configuration is stabilized by Mg co-doping. Note that the shape of this band might be further obscured by Pr^{3+} 4f-5d absorption bands at 245 and 280 nm. Due to this overlap an energy transfer from the defect levels to the 5d ones can take place, which can have an influence on the scintillation decay kinetics. As mentioned above, the intensity of the Pr^{3+} 4f–4f emission peaks in this spectrum are much more pronounced with respect to the spectrum under direct excitation at 285 nm. It seems that the levels related to the defect emitting at 249 nm can be responsible for the population of the Pr^{3+} 4f-levels. This effect is slightly more apparent also for the sample codoped with 3000 ppm Mg (not shown here).

The photoluminescence decay kinetics for the LuAG:Pr 0.2% Pr (START) under direct excitation to the 4f-$5d_1$ transition is in the Fig. 4 and is governed by a decay component with 21 ns decay time belonging to the 5d-4f Pr^{3+} emission. On the other hand, it seems that some slow component with a decay time around 200 ns emerges. Similar feature was observed for the other samples again. Concerning both of the Mg-codoped samples, the decay curve looked very similar and the leading decay time was shortened to around 19 ns. The decay curves under 200 nm excitation were very similar and followed the trends described for the direct excitation.

The observed very slight acceleration of the photoluminescence decay kinetics with increasing Mg concentration can be caused by a weak energy transfer from the excited Pr^{3+} $5d_1$ state towards the Pr^{4+} CT state, as there is the spectral overlap of the 5d-4f emission with the CT absorption, see above. Similar effect was observed for the samples from the END part.

The emission spectrum under excitation into the unknown absorption sharp band at 213 nm discussed above is in the Fig. 5. It

consists of the 5d-4f bands around 310 nm and the 4f–4f bands at longer wavelength, which are much more pronounced in this case. The $^3P_0$–$^3H_4$ transition at 488 nm is quite apparent and was not observed in the previously discussed emission spectra. It is interesting to note that even though the 5d-4f emission is excited at 213 nm, it is not found in the excitation spectrum of this emission. The 213 nm wavelength exactly corresponds with the position of the $^1S_0$ state of Pr^{3+}. If this peak is ascribed to the transition to this level, it should be seen in the excitation spectra as well, as one could expect a nonradiative energy transfer from this level to the 5d one. However, this is not true (Fig. 3a). The decay kinetics of the Pr^{3+} 5d-4f emission under 213 nm excitation is very similar as that in the Fig. 4, just the leading decay time is the shortest observed in all the experiments with the value of 17 ns (not shown here). Further research is necessary to clarify the origin of the 213 nm peak.

The scintillation light yield was determined from the pulse-height spectra under 667 keV gamma ray excitation from ^{137}Cs source. The example of such a spectrum is in the Fig. 6, where the fitted curve for the LuAG:Pr 0.2% END sample is displayed. The full-absorption peak is clearly observed, but it interferes with Lu escape peak at slightly lower energy. However, peaks are separated enough and escape peak area is approximately 6 times smaller than area of full-absorption peak. Therefore, the measurement precision is not affected significantly by Lu escape peak.

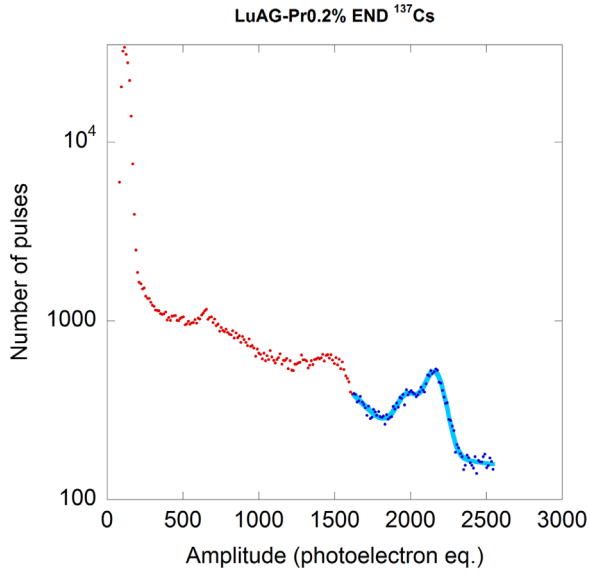

Fig. 6. Example fo the pulse-height spectrum for the LuAG:pr 0.2% END part under 662 keV gamma-ray excitation (^{137}Cs).

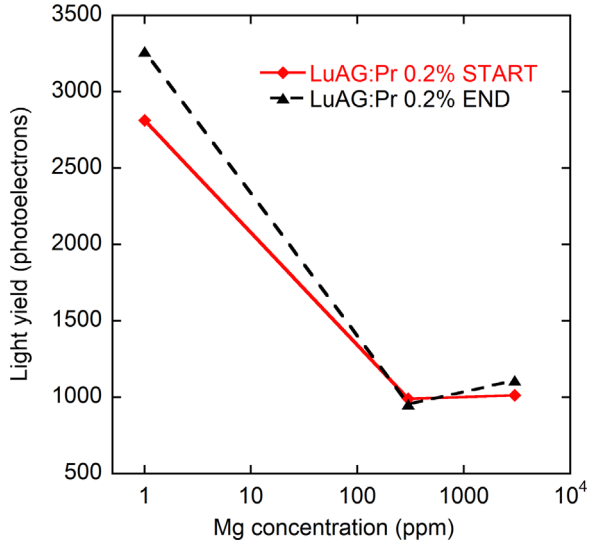

Fig. 7. Dependence of the light yield for the annealed LuAG:Pr0.2% samples on concentration of Mg codopant.

The light yield values for all the samples including START and END parts are summarized in the Fig. 7 (the 0 ppm concentration is indicated as 1 ppm to allow setting the logarithmic axis). A substantial decrease of the light yield with Mg codoping is observed for both parts of the Mg-codoped crystals. This decrease is the same for both START and END parts and seems to be independent on the Mg concentration similarly as radioluminescence intensities in the Fig. 2. On the other hand, the magnitude of the decrease of the light yield values for the samples with Mg 300 ppm and 3000 ppm with respect to the Mg-free one does not correspond to the decrease of the steady-state radioluminescence intensities (Fig. 2). This may be caused by much shorter penetration depth of X-ray excitation photons and reflection geometry used in RL measurement compared to all-the–volume excitation by 662 keV gamma photons and transmission geometry used in LY measurement. Slow components introduced by Mg-codoping or annealing through which the light is emitted outside the 6 μs shaping time window leading to the decrease of the light yield cannot be eventually excluded as well.

Decay kinetics under the gamma-ray excitation for the LuAG:Pr0.2% Mg 0 ppm and Mg 3000 ppm (START) is shown in the Figs. 8a and b. Fitting the curves with the sum of exponentials was complicated and often 4 or 5 components were necessary, which may be a consequence of the fact that the scintillation decay of the selected samples does not follow the usual exponential decay law. In the log-log scale (see Fig. 8) the course of the slower component following the fast exponential part is close to a straight line, which suggests that this part follows the inverse power law. Therefore the curves were fit with a sum of an exponential component and a power function according to the equation $I = A\exp(-t/tau) + a(b+ct)^{-p}$, where A, a, b,c and p are constants, tau stands for the decay constant and t is time. The inverse power decay course was described in the past [31] and observed in the Ce-doped LuAG scintillators [32]. It was ascribed to the tunneling of the electrons from the AD-related shallow traps towards adjacent Ce^{3+} with a trapped hole (which is Ce^{4+}). The usual values of the parameter p range between 0.9 and 1.5. For more details about tunneling-related luminescence processes see for example [30] and also references therein. It is reasonable to assume that the same phenomenon takes place in the Pr-doped analogs.

In the curves for both the Mg-free and the Mg 3000 ppm samples the fast exponential component has a decay time of 21.6 ns and 21 ns respectively and is ascribed to the 5d-4f luminescence of the Pr^{3+} center in the crystals. The almost negligible shortening can be again related to the energy transfer from the Pr^{3+} excited 5d state to the Pr^{4+} CT one. The slower component described with the power function is due to the mentioned tunneling of the electrons to from the AD-related traps and the parameter p has values of 0.73 and 0.82 for the Mg-free and Mg 3000 ppm sample respectively. These values ale slightly out of the range specified above, but it might be that there are other exponential components of small amplitude and substantially long decay time that may obscure the observed power decay kinetics. Taking into account that the value of p determines the slope of the power function in the log-log scale, it means that for the Mg-codoped sample the scintillation response is accelerated at the longer times when compared to the Mg-free sample.

Summarizing the influence of Mg codoping and annealing on luminescence and scintillation properties, we can state that it enhances the formation and stability of Pr^{4+} ion. This effect

increases with increasing Mg concentration. The Pr^{4+} CT band is responsible for reabsorption of the 5d-4f emission coming from Pr^{3+} ions. The Pr^{3+} ions can be either regular ones or the temporary ones created in an alternative scintillation mechanism, which would be analogous with the mechanism taking part in LuAG:Ce codoped with divalent ions and which is described in the introduction and treated in [2,8,10,11]. The nonradiative energy transfer from $5d_1$ relaxed excited state of Pr^{3+} towards CT state of Pr^{4+} is probably responsible for very slight photoluminescence (and also scintillation) decay shortening. However, as this process is almost negligible, a simple reabsorption of the 5d-4f emission by the CT transition is supposed to be the dominant process which leads to decrease of RL intensity and scintillation light yield for the Mg-codoped samples. Further studies are needed to explain the observed independence of this effect on Mg concentration. The decrease of the RL intensity upon Mg codoping is much smaller than the decrease of the scintillation light yield. It can be tentatively explained by different excitation energies and experiment geometries as mentioned above. Moreover, an introduction of very slow components by Mg-codoping, through which most of the scintillation light is emitted outside the corresponding time window in the light yield measurement cannot be excluded as well.

The selected samples were studied by EPR before and after X-ray irradiation at approximately 77 K. The samples were LuAG: Pr0.2% START and END, LuAG:Pr 0.2%, Mg 300 ppm START and END, and LuAG:Pr 0.2%, Mg 3000 ppm START and END. The EPR spectra measured at 40 K prior to an X-ray irradiation contained mostly resonance lines coming from Yb^{3+} ions, see for example the spectrum for the LuAG:Pr 0.2% START in the Fig. 9a. The Yb^{3+} was already described in LuAG [33] and in our samples it is

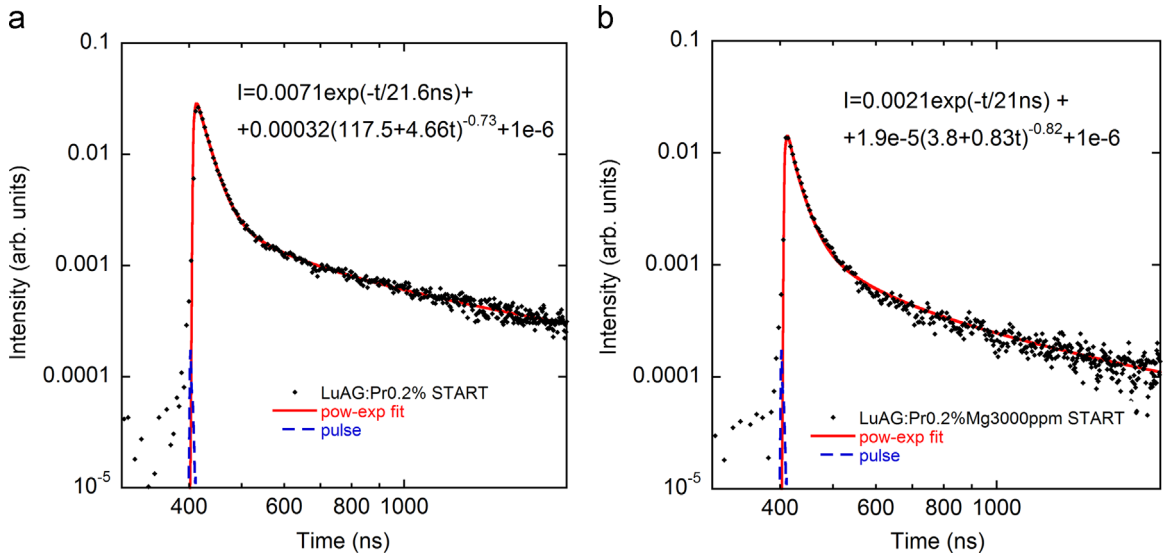

Fig. 8. Scintillation decay kinetics under gamma-ray excitation for the annealed LuAG:Pr0.2% START (a) and LuAG:Pr0.2% Mg 3000 ppm START (b).

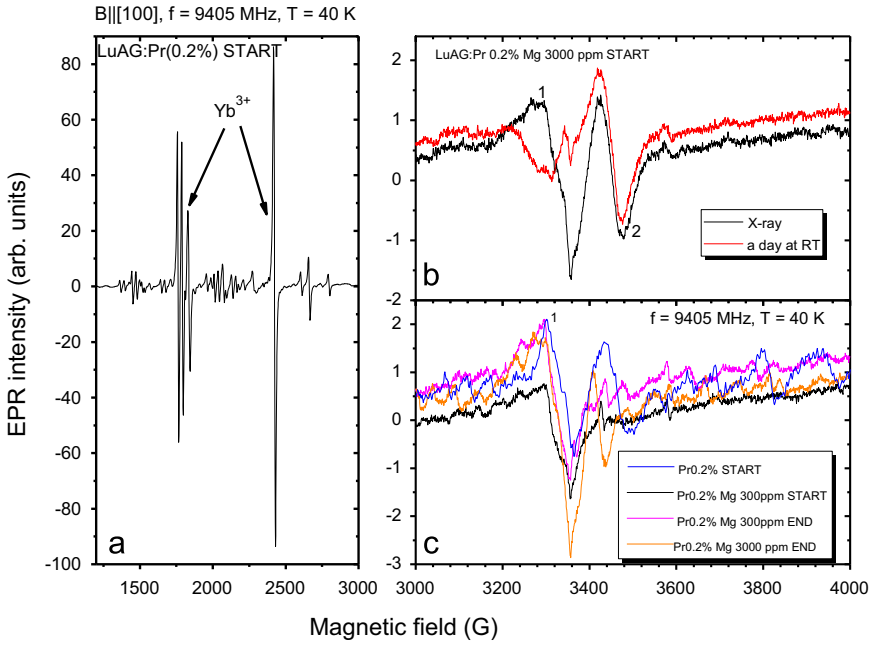

Fig. 9. EPR spectra measured at the orientation of the external magnetic field parallel with the $<100>$ axis for non-irradiated LuAG:Pr 0.2% START (a), X-ray irradiated LuAG:Pr 0.2%, Mg 3000 ppm START (b), LuAG:Pr 0.2% START, Pr0.2% Mg 300 ppm START and END, Pr0.2% Mg 3000 ppm END after X-ray irradiation. 1 and 2 mark the resonance lines coming from the hole- and electron-like centers, respectively.

obviously present as an accidental impurity. Moreover, there is also a number of lines of unknown origin (Fig. 9a) which could not be properly identified due to their low intensities. No Pr^{4+} resonance lines were found in the spectra at all. The Pr^{4+} spectral lines would be easy identified due to pronounced hyperfine structure produced by ^{141}Pr nucleus having 100% natural abundance and the nuclear spin 5/2. Therefore, either their position is out of the EPR spectrometer magnetic field range or the concentration of these ions is too low to be detectable. When the samples were exposed to the X-ray irradiation at liquid nitrogen temperature, new lines emerged in the spectra in the 3300–3450 G magnetic field range (see Fig. 9b and c), near *g* factor 2.

The resonance line marked as 1 in Fig. 9b and c was ascribed to the g-factor value $g \approx 2.026$ whereas the spectral position of the line marked as 2 is characterized by the $g \approx 1.949$. The g-factor value for the first one is common for the hole-like centers, namely O^- defects [34–40], since it is a bit higher than 2.0023, which is the value for a free electron. Remarkably, the position of the line 1 is almost independent on the orientation of the external magnetic field with respect to the $<100>$ crystallographic direction. The *g* factor of the paramagnetic center responsible for this line is thus almost isotropic. In principle, the O^- defects show very small or no anisotropy of the *g* factor, especially in cubic lattices [13,34–40]. The line 1 could be then ascribed to the O^- defect. The presence of O^- defect further supports the existence of the alternative scintillation mechanism similar to the Mg-codoped LuAG:Ce [2,10,11]. It involves the O^- center which releases a hole to regenerate the tetravalent luminescence ion in the final stage of the mechanism.

The line 2, which is observed only in the crystal with the highest Mg concentration, shows the isotropy of the *g* factor as well. Most probably, it belongs to the electron captured at an oxygen vacancy forming an F^+ center, since such centers similarly to the O^- ones show no or weak anisotropy of the *g* factor, see for example [34,41]. The intensity of this line does not change after heating of a sample up to RT and holding on at this temperature for 1 day (see Fig. 9b). Prompt heating of the sample up to approximately 420–450 K makes no effect as well. However, after keeping the sample for four days at RT, the center completely disappeared. F^+ centers can be very stable [40,41] surviving annealing even at the temperatures much higher than RT [40]. Moreover, it is possible that even after annealing in air not all the oxygen vacancies and related defects were removed in the Pr 0.2% Mg 3000 ppm (START) sample. It might be that the local lack of charge due to divalent Mg^{2+} codopant embedded at a trivalent site can stabilize the oxygen vacancies. Such an effect is expected to be significant especially in the samples with high Mg concentration, which is the case of this studied sample. However, such defects responsible for the line 2 were not detected in the END counterpart. Taking into account small or no differences in the luminescence and scintillation characteristics of both parts, such an observation is hard to explain so far and further study is necessary to clarify this discrepancy.

Due to similarity of the spectra measured in Pr0.2% START and END samples, the spectrum measured for the END sample was not shown in Fig. 9c.

It was found from the temperature dependences of the EPR signal that the O^- defects in the Pr only doped samples and those the Pr,Mg co-doped have different thermal stability, which was observed from measurements of the dependence of the intensity of the line 1 (Fig. 9b and c) on temperature for the LuAG:Pr0.2% START and END samples together with the Pr0.2% Mg 300 ppm START and Pr0.2% Mg 3000 ppm START. The corresponding dependences are shown in the Fig. 10 together with the fitted curves.

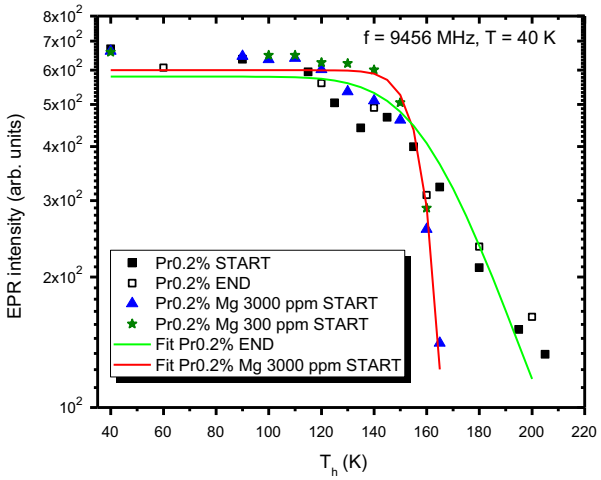

Fig. 10. Dependence of the O^- line EPR intensity on heating temperature T_h measured for the Pr0.2% START and END samples and Pr0.2% Mg 300 ppm START and Pr0.2% Mg 3000 ppm START samples at fixed temperature $T = 40$ K. Solid lines are the calculated dependences.

In this experiment the spectra were measured always at the reference temperature of 40 K but the sample was quickly heated up to the chosen temperature T_h and then promptly cooled down to the reference temperature, each time increasing T_h with the step of 10–15 K.

The Pr 0.2% START and END samples showed roughly the same temperature dependences of the O^- EPR intensity (Fig. 10). With Mg codoping the stability of the O^- center decreased and seems again almost independent on the Mg concentration as the dependences for the 300 ppm or 3000 ppm Mg^{2+} sample are quite similar especially at the highest temperatures.

The dependences shown in Fig. 10 have been fitted with the calculated curves according to the expressions 1 and 2 presented below. Each of them describes the hole trap kinetics (first order – Eq. 1, and second order – Eq. 2, respectively) which were adapted for the aims of the above described heating method mentioned in [42].

$$I_{i+1} = I_i \exp\left(-f_{01} t \exp\left[-E_{t1}/k_B T_i\right]\right), \quad i = 0, 1, \ldots, m, \tag{1}$$

$$I_{i+1} = \frac{I_i}{1 + \frac{I_i f_{02}}{P} \exp\left(-E_{t2}/k_B T_i\right)}, \quad i = 0, 1, \ldots, m, \tag{2}$$

Here the EPR intensity I_i [43], is proportional to the trapped holes concentration remaining after each heating cycle *i*; *P* is the coefficient which depends on the whole amount of traps in the crystal, and transition coefficients [42]. E_{t1} and E_{t2}, f_{01} and f_{02} are the trap depths and frequency factors for the first or second order kinetics, respectively. The parameters determined from the fit are: $E_{t1} = 0.338 \pm 0.005$ eV, $f_{01} = (1 \pm 0.5) \times 10^8$ s^{-1}; $E_{t2} = 0.105 \pm 0.005$ eV, $f_{02} = (1 \pm 0.5) \times 10^1$ s^{-1}.

The dependence in the Pr-only doped samples shows a very unusual course since it does not obey either of the kinetics separately but the combination of them. However, the second-order kinetics (Eq. 2) prevails. The f_{02} value obtained from fit does not have much physical sense since the frequency factor is mostly found within 10^6–10^{12} s^{-1} range [36,41,44,45]. The calculated trap depth E_{t2} is very big and considering the O^- to be a shallow trap, most probably we deal with some kind of thermally-assisted tunneling described for the Ce-doped analog in [30].

As mentioned above, the Mg codoping significantly decreases the stability of the centers and the kinetics becomes the first order one (Eq. 1) with the usual values of the trap depth and frequency factor.

When compared with the other observations [34–36,45], the relatively high thermal stability of the holes (see Fig. 10) in all the samples suggests that the holes must be stabilized by some imperfection nearby which can be further modified by Mg codoping. Correlated thermoluminescence experiments would bring deeper insight in the above described processes, but they will be published in the forthcoming more detailed comparative study of both the annealed and as-grown samples.

4. Conclusions

This study focuses on the influence of Mg codoping and annealing on luminescence and scintillation properties. Both Mg codoping and annealing lead to promotion of Pr to its tetravalent state and moreover the Mg codopant enhances its stability, which increases with increasing Mg concentration. The Pr^{4+} CT band is responsible for absorption of the 5d-4f emission coming from Pr^{3+} ions. A very slight photoluminescence (and also scintillation) decay acceleration may be caused by an almost negligible non-radiative energy transfer from the Pr^{3+} $5d_1$ level to the Pr^{4+} CT state. As this process is not significant, it means that the absorption by the CT state is responsible for the decrease of RL intensity and scintillation light yield for the Mg-codoped samples. Further studies are needed to explain the observed independence of this effect on Mg concentration. The decrease of the RL intensity upon Mg codoping is much smaller than the decrease of the scintillation light yield which can be tentatively explained by different excitation energies and geometries of radioluminescence and light yield measurements. This would imply that the absorption by the Pr^{4+} CT state might be hampered in thin films and thus positive effects of divalent ion codoping can be expected for Pr-doped garnet scintillators, which have faster response when compared to the Ce-doped counterparts.

The scintillation decay curves are composed of a fast component related to Pr^{3+} emission and a slower component described by a power function, which indicates a tunneling recombination process from the traps related to the anti-site defects. This was already observed in the Ce-doped analogs and therefore such an interpretation is plausible.

The EPR spectra measurements revealed presence of O^- centers in all the samples, which further supports the existence of the alternative scintillation mechanism in the Mg-codoped crystals. It involves the O^- center which releases a hole to regenerate the tetravalent luminescence ion in the final stage of the mechanism. The temperature dependence of the EPR spectra showed that Mg codoping significantly decreases the stability of this center. The EPR experiments revealed also presence of centers based on oxygen vacancies, most probably an F^+ centers, which are stable above room temperature. They were observed only in the crystal with the highest Mg concentration which would mean that in this case Mg on a trivalent site stabilizes the oxygen vacancies due to charge compensation and makes them resistant to annealing in air.

Acknowledgments

This work has been partially supported by

(i) Czech Science Foundation (GACR) 15-18300Y project,

(ii) Development of Systems and Technology for Advanced Measurement and Analysis (SENTAN), Japan Science and Technology Agency (JST),

(iii) Health Labor Sciences Research Grant, The Ministry of Health Labor and Welfare,

(iv) The New Energy and Industrial Technology Development Organization (NEDO),

(v) Supporting Industry program, Ministry of Economy, Trade and Industry (METI) and,

(vi) Association for the Progress of New Chemical Technology,

(vii) Japan Society for the Promotion of Science (JSPS).

(vii) Adaptable and Seamless Technology Transfer Program through Target-driven R&D (A-STEP), JST,

(ix) Ministry of Education, Youth and Sports of Czech Republic, projects SAFMAT LM2015088 and LO1409,

(x) European Union's Horizon 2020 research and innovation program under the Marie Sklodowska-Curie Grant agreement No. 644260 (Intelum).

In addition, we would like to thank following persons for their support: Tohoku University, and Mr. Hiroshi Uemura, Ms. Keiko Toguchi, Ms. Megumi Sasaki, Ms. Yuka Takeda and Ms. Kuniko Kawaguchi of IMR, Tohoku University.

References

[1] M. Nikl, A. Yoshikawa, Adv. Opt. Mater. 3 (2015) 463.
[2] M. Nikl, A. Yoshikawa, K. Kamada, K. Nejezchleb, C.R. Stanek, J.A. Mares, K. Blazek, Prog. Cryst. Growth Charact. Mater. 59 (2013) 47.
[3] M. Nikl, E. Mihokova, J.A. Mares, A. Vedda, M. Martini, K. Nejezchleb, K. Blazek, Phys. Status Solidi (b) 181 (2000) R10.
[4] M. Nikl, J.A. Mares, N. Solovieva, J. Hybler, A. Voloshinovskii, K. Nejezchleb, K. Blazek, Phys. Status Solidi A 201 (2004) R41.
[5] V. Lupei, A. Lupei, C. Tiseanu, S. Georgescu, C. Stoicescu, P.M. Nanau, Phys. Rev. B 51 (1995) 8.
[6] D. Mateika, E. Volkel, J. Haisma, J. Cryst. Growth 102 (1990) 994.
[7] K. Kamada, T. Yanagida, T. Endo, K. Tsutumi, Y. Fujimoto, A. Fukabori, A. Yoshikawa, J. Pejchal, M. Nikl, Cryst. Growth Des. 11 (2011) 4484.
[8] S. Blahuta, A. Bessiere, B. Viana, P. Dorenbos, V. Ouspenski, IEEE. Trans. Nucl. Sci. 60 (2013) 3134.
[9] S. Liu, X. Feng, Z. Zhou, M. Nikl, Y. Shi, Y. Pan, Phys. Status Solidi RRL 8 (2014) 105.
[10] M. Nikl, K. Kamada, V. Babin, J. Pejchal, K. Pilarova, E. Mihokova, A. Beitlerova, K. Bartosiewicz, S. Kurosawa, A. Yoshikawa, Cryst. Growth Des. 14 (2014) 4827.
[11] Y. Wu, F. Meng, Q. Li, M. Koschan, C.L. Melcher, Phys. Rev. Appl. 2 (2014) 044009.
[12] C. Hu, S. Liu, M. Fasoli, A. Vedda, M. Nikl, X. Feng, Y. Pan, Phys. Status Solidi RRL 9 (2015) 245.
[13] M. Nikl, V. Babin, J. Pejchal, V.V. Laguta, M. Buryi, J.A. Mares, K. Kamada, S. Kurosawa, A. Yoshikawa, D. Panek, P. Bruza, K. Mann, M. Müller, IEEE Trans. Nucl. Sci. 63 (2016) 433.
[14] M. Nikl, V. Babin, J.A. Mares, K. Kamada, S. Kurosawa, A. Yoshikawa, J. Tous, J. Houzvicka, K. Blazek, J. Lumin. 169 (2016) 539.
[15] C.W.E. van Eijk, P. Dorenbos, R. Visser, IEEE Trans. Nucl. Sci. 41 (1994) 738.
[16] A.M. Srivastava, J. Lumin. 169 (2016) 445.
[17] M. Nikl, H. Ogino, A. Krasnikov, A. Beitlerova, A. Yoshikawa, T. Fukuda, Phys. Stat. Sol. A 202 (2005) R4.
[18] H. Ogino, A. Yoshikawa, M. Nikl, K. Kamada, T. Fukuda, J. Cryst. Growth 292 (2006) 239.
[19] A. Yoshikawa, T. Yanagida, K. Kamada, Y. Yokota, J. Pejchal, A. Yamaji, Y. Usuki, S. Yamamoto, M. Miyake, K. Kumagai, K. Sasaki, T.R. dos Santos, M. Baba, M. Ito, M. Takeda, N. Ohuchi, M. Nikl, Opt. Mater. 32 (2010) 1294.
[20] V. Babin, M. Nikl, K. Kamada, A. Beitlerova, A. Yoshikawa, J. Phys. D: Appl. Phys. 46 (2013) 365303.
[21] M.V. Derdzyan, K.L. Ovanesyan, A.G. Petrosyan, A. Belsky, C. Dujardin, C. Pedrini, E. Auffray, P. Lecoq, M. Lucchini, K. Pauwels, J. Cryst. Growth 361 (2012) 212.
[22] A.G. Petrosyan, K.L. Ovanesyan, M.V. Derdzyan, I. Ghambaryan, G. Patton, F. Moretti, E. Auffray, P. Lecoq, M. Lucchini, K. Pauwels, C. Dujardin, J. Cryst. Growth 430 (2015) 46.
[23] A. Yoshikawa, M. Nikl, G. Boulon, T. Fukuda, Opt. Mater. 30 (2007) 6.
[24] A. Yoshikawa, V.I. Chani, Mat. Res. Soc. Bull. 34 (2009) 266.
[24] P. Dorenbos, J. Phys.: Condens. Matter 15 (2003) 8417.
[26] C.Y. Chen, G.J. Pogatshnik, Y. Chen, M.R. Kokta, Phys. Rev. B 38 (1988) 8555.
[27] A. Strzęp, W. Ryba-Romanowski, R. Lisiecki, P. Solarz, X. Xu, J. Di, J. Xu, J. Alloy. Compd. 550 (2013) 173.
[28] V. Babin, V.V. Laguta, A. Maaroos, A. Makhov, M. Nikl, S. Zazubovich, Phys. Status Solidi B 248 (2011) 239.
[29] V. Babin, K. Blazek, A. Krasnikov, K. Nejezchleb, M. Nikl, T. Savikhina, S. Zazubovich, Phys. Status Solidi (C) 2 (2005) 97.
[30] M. Nikl, A. Vedda, M. Fasoli, I. Fontana, V.V. Laguta, E. Mihokova, J. Pejchal, J. Rosa, K. Nejezchleb, Phys. Rev. B 76 (2007) 195121.
[31] M. Tachiya, A. Mozumder, Chem. Phys. Lett. 34 (1975) 77.
[32] D.J. Huntley, J. Phys.: Condens. Matter 18 (2006) 1359.

[33] V.V. Laguta, A.M. Slipenyuk, M.D. Glinchuk, M. Nikl, J. Rosa, A. Vedda, K. Nejezchleb, Opt. Mater. 30 (2007) 79.
[34] V.V. Laguta, M. Buryi, J. Rosa, D. Savchenko, J. Hybler, M. Nikl, S. Zazubovich, T. Kärner, C.R. Stanek, K.J. McClellan, Phys. Rev. B 90 (2014) 064104.
[35] M. Buryi, D.A. Spassky, J. Hybler, V.V. Laguta, M. Nikl, Opt. Mat. 47 (2015) 244.
[36] M. Buryi, P. Bohacek, K. Chernenko, A. Krasnikov, V.V. Laguta, E. Mihokova, M. Nikl, S. Zazubovich, Phys. Status Solidi B 253 (2016) 895.
[37] A. Watterich, L. Kovács, R. Würz, F. Schön, A. Hofstaetter, A. Scharmann, J. Phys.: Condens. Matter 13 (2001) 1595.
[38] S. Lenjer, O.F. Schirmer, H. Hesse, Phys. Rev. B 66 (2002) 165106.
[39] V.V. Laguta, M. Buryi, M. Nikl, J. Rosa, S. Zazubovich, Phys. Rev. B 83 (2011) 094123.
[40] D. Pan, G. Xu, L. Lu, Y. Yong, X. Wang, J. Wan, G. Wang, Appl. Phys. Lett. 89 (2006) 082510.
[41] W. Gellerman, F. Lüty, K.P. Koch, H. Welling, Opt. Commun. 35 (1980) 430.
[42] S.W.S. Mc Keever, Thermoluminescence of Solids, Cambridge University Press, 1985.
[43] A. Abragam, B. Bleaney, Electron Paramagnetic Resonance of Transition Ions, Clarendon Press, Oxford (1970), p. 560–568.
[44] G.F.J. Garlick, A.F. Gibson, Proc. Phys. Soc. 60 (1948) 574.
[45] V.V. Laguta, M. Nikl, A. Vedda, E. Mihokova, J. Rosa, K. Blazek, Phys. Rev. B 80 (2009) 045114.

Journal of Luminescence 169 (2016) 701–705

Contents lists available at ScienceDirect

Journal of Luminescence

journal homepage: www.elsevier.com/locate/jlumin

Energy resolution studies of Ce- and Pr-doped aluminum and multicomponent garnets: The escape and photo-peaks

J.A. Mares [a,*], A. Beitlerova [a], P. Prusa [a,b], K. Blazek [c], P. Horodysky [c], K. Kamada [d], A. Yoshikawa [d,e], C. D'Ambrosio [f], M. Nikl [a]

[a] Institute of Physics A S CR, Cukrovarnicka 10, 162 53 Prague 6, Czech Republic
[b] Faculty of Nuclear Sciences and Physical Engineering, Czech Technical University in Prague, Brehova 7, 115 19 Prague 1, Czech Republic
[c] Crytur Ltd., Palackeho 175, 511 01 Turnov, Czech Republic
[d] New Industry Creation Hatchery Center, Tohoku University, 6-6-10 Aoba, Aramaki, Aoba-ku, 980-8579 Sendai, Japan
[e] Institute for Material Research (IMR), Tohoku University, Sendai 980-8577, Japan
[f] CERN, PH-LHB Group, Geneva 23 CH1211, Switzerland

ARTICLE INFO

Article history:
Received 15 October 2014
Received in revised form
10 February 2015
Accepted 14 February 2015
Available online 20 February 2015

Keywords:
Multicomponent garnets
Energy resolution
Photo and escape peaks
Ce and Pr dopants
Pulse height spectra

ABSTRACT

The photopeak and escape peak processes were studied in heavy Ce^{3+}-doped LuAG and GGAG, Pr^{3+}-doped LuAG and undoped BGO scintillating crystals. Energy resolution measurements were performed with 511 keV photons of ^{22}Na radioisotope. In the pulse-height spectra the escape peaks were resolved clearly on thin samples (up to 3 mm). If sample thickness increases the escape peak cannot be resolved anymore (for thicknesses approx. above 5 mm, especially). Consequently, energy resolution increases by about 40% compared with that measured at 1 mm thick samples.

1. Introduction

Ce^{3+} or Pr^{3+}-doped yttrium aluminum garnet $Y_3Al_5O_{12}$ (YAG) or perovskite $YAlO_3$ (YAP) crystals were investigated from the late 1960s while their higher density Lu-based analogs comparatively later namely LuAG:Ce and LuAG:Pr from 1995 and 2004 year, respectively [1–10]. Recently the Ce^{3+}-doped $(Lu,Y,Gd)_3(Ga,Al)_5O_{12}$ multicomponent garnet scintillating crystals have been discovered which attracted considerable attention due to their ultrahigh light yield [11–14].

The garnet scintillators have been intensively studied in the last decade [15–21], see also related review [7]. Single and multicomponent garnet crystals are used in various applications as e.g. LuAG:Pr pixel array in Positron Emission Mamography [15], thin LuAG:Ce or YAG:Ce plates or even layers in X-ray microradiography of μm resolution [22,23] and generally in various imaging methods [7,15,24]. The latest scintillation studies have shown that the recently prepared Ce^{3+}-doped multicomponent garnets, such as $Gd_3Ga_3Al_2O_{12}$ (GGAG:Ce) reached very high light yield of around 50,000 ph/MeV and Energy Resolution (ER) of ≈5.5% at 662 keV [14]. Single component LuAG:Ce or LuAG:Pr garnets reached light yield up to 27,000 ph/MeV or 20,000 ph/MeV, respectively, and their energy resolutions at 511 keV or 662 keV are within 6–8% [6,10,16,21,25]; but in some samples energy resolution gets worse without light yield value decrease, e.g. in LuAG:Ce where ER∼10% [6]. The latest results presented by Drozdowski et al. [26] have shown that $(Lu_{0.75}Y_{0.25})_3AG$:Pr crystal can reach very high light yield ∼33,000 ph/MeV which is about 65% higher than the highest light yield of about 20,000 ph/MeV measured in LuAG:Pr crystal [10,19,20]. Detailed studies of LuAG:Pr or LuAG:Ce scintillation response show that their pulse height spectra consist of (i) a photopeak band and (ii) an escape peak band [10,19,27–29], especially if thin samples were studied (of thicknesses from ≈0.5 to 3 mm). The escape peak of LuAG:Pr and those observed in $Bi_4Ge_3O_{12}$ (BGO) and LuAG:Ce were explained to be due to KX-rays emission of Lu or Bi ion absorber, respectively, in the photoelectric absorption process to K electron shell of these ions [10,27,29]. Pulse height spectra of LuAG:Pr crystal have shown that the escape peak is placed at lower energy side of 551 or 662 keV photopeaks of around ∼53 keV (KX-rays energy of Lu should be 63.3 keV [27]). The presence of the escape peak is in a fact leakage channel in scintillation processes in crystals [27,29] and is observed mainly in heavy scintillators.

* Corresponding author.
E-mail address: amares@fzu.cz (J.A. Mares).

http://dx.doi.org/10.1016/j.jlumin.2015.02.023
0022-2313/

The main goal of this paper is to investigate in detail the energy resolutions of heavy scintillating crystals as Ce^{3+}- and Pr^{3+}-doped single or multicomponent garnets and also the BGO reference one with the aim to resolve the contributions from photopeak itself and associated escape peak. Pulse height spectra were measured on selected and well defined samples (rectangular plates or blocks and circular plates or cylinders of thickness between 1 and 10 mm). Using Gaussian decomposition the photopeak and the escape peak were separated in pulse height spectra, especially for 511 keV excitation by ^{22}Na radioisotope. Generally, it appears necessary to measure energy resolution characteristics of both thin and thick scintillating samples [28].

2. Experimental

Scintillation response studies were performed using experimental setup consisting of a hybrid photomultiplier (HPMT), measuring electronics and PC control [30]. The measurement accuracy of this setup is $\pm 5\%$. Using various radioisotopes for excitation the energy range of 8–1300 keV is covered; the details of measuring setup are described in [30]. Maestro program was used to evaluate Energy Resolution (ER) but for detailed evaluation of the photopeak and escape peak bands it was necessary to perform fits and decompositions using Gaussian curves. Here, we mainly measured pulse height spectra using radioisotope ^{22}Na at 511 keV or also ^{137}Cs 662 keV energy. Energy resolutions (ER) and FWHM were determined both for the photopeak and the escape peak bands. Given the proximity of both peaks it was necessary to carry out decomposition of the observed pulse height spectra. Energy resolution studies were carried out on well-defined single crystal samples: polished plates or cubes of thicknesses 1, 2, 4, 5 and 10 mm were prepared. All measured Ce^{3+}- or Pr^{3+}-doped LuAG, GGAG crystals and BGO reference one investigated were grown by the Czochralski method [6–8,11–13,16–18,31]. Samples were plates or cubes of rectangular shapes with cross-section of 5×5 mm^2 (or 7×7 mm^2) or circular shapes (cylinders) of 8 or 10 mm diameter. We used the same configuration as was used by Gierlik et al. in [32] to obtain the highest scintillation N_{phels} photoelectron yield. We carefully put reflection tapes (mainly teflon ones) on all sides of measured samples excluding only that in a direct contact with HPMT photocathode. We used optical couplant Dow Corning Q2-3067 to achieve good optical contact between samples and the HPMT photocathode. Teflon tapes are used as reflection ones for in the visible emitting BGO and Ce^{3+}-doped single or multicomponent garnets. For LuAG:Pr samples we used a $BaSO_4$ painting because it has higher reflectivity than teflon in the UV range around 310 nm where the Pr^{3+} emission is peaking [15]. The same measuring configuration was used for all samples with radioisotopes placed 2 mm above the center of samples.

3. Results and discussions

Detailed measurements of energy resolutions including their photo and escape peaks and relevant processes were carried out with single crystal samples of different thicknesses from 1 to 10 mm (for details see Section 2). Fig. 1 presents pulse height spectra of ^{22}Na 511 keV energy of LuAG:Pr single crystal samples of 1–2–5 and 10 mm thicknesses. With an exception of 10 mm thick LuAG:Pr sample all the other samples exhibit a peak at low energy side of their photopeak bands. Similar effect was observed in other LuAG:Ce, GGAG:Ce and BGO crystals measured. We carried out decomposition, fitting and evaluation of the observed photopeak spectra under 511 keV ^{22}Na excitation for all measurements. Especially, pulse height spectra of 1 mm thick samples are

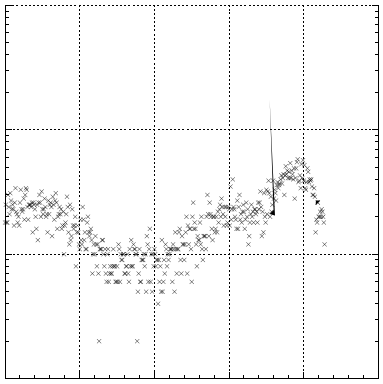

presented further in Figs. 2, 4, 6 and 8. Linear attenuation coefficients were calculated using relations from www.nist.gov/PhysRefData (X-Ray and Gamma-Ray Data) [33]. Table 1. presents ^{22}Na 511 keV energy resolution values for BGO, GGAG:Ce, LuAG:Ce and LuAG:Pr samples of different thickness (for 1 mm thin samples also ER's of ^{137}Cs 662 keV energy are given).

3.1. BGO crystal

BGO belongs to heavy scintillating crystals characterized by $\rho=7.13$ g/cm^3 and high $Z_{eff}=67.4$. Fig. 2 presents decomposition of pulse height spectrum of 1 mm thin BGO crystal where we can clearly resolve both the photopeak and escape peak. The less intense escape peak bands were also observed in 2 and 5 mm thick BGO samples. Detailed values of ER for all thicknesses of BGO samples are given in Table 1. At ^{22}Na 511 keV excitation the photopeak ER's increase between 1 and 10 mm BGO samples from 12% to 16.7% (by about 40%) and those of the escape peaks (for 1, 2 and 5 mm) from 15.7% to 21.7% (by about 38%). Ratio between amplitudes of the photo- and escape peaks increases from $\sim$2 to 6.3 times (from 1 to 5 mm thickness) and in 10 mm thick BGO no escape peak is observed. Observed energy difference between photo and escape peaks maxima are within 77.1 and 81.7 keV which is close to 90.53 keV energy of KX-rays of Bi (see Fig. 3 – linear attenuation calculations were performed according to expressions given in [33]).

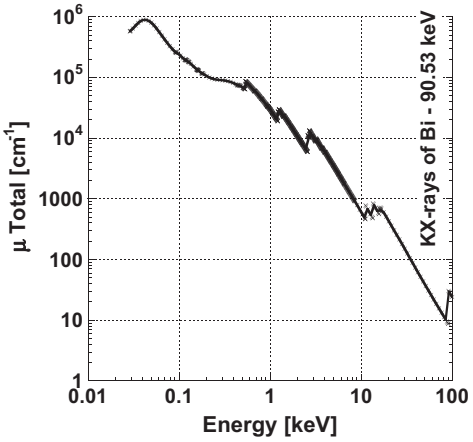

Fig. 3. Linear attenuation coefficient of BGO crystal calculated from X-Ray and Gamma-Ray Data [33].

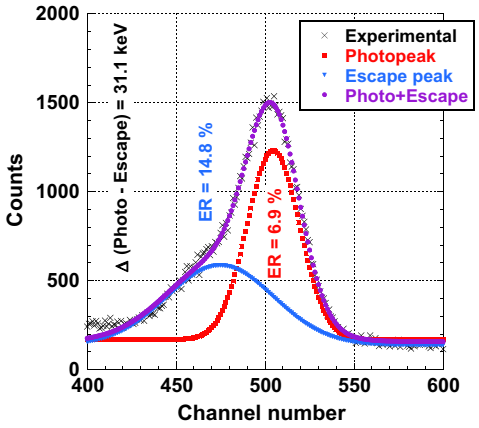

Fig. 4. Decomposition of pulse height spectrum of 1 mm thick GGAG:Ce crystal measured with 511 keV energy of ^{22}Na radioisotope at 1 μs shaping time.

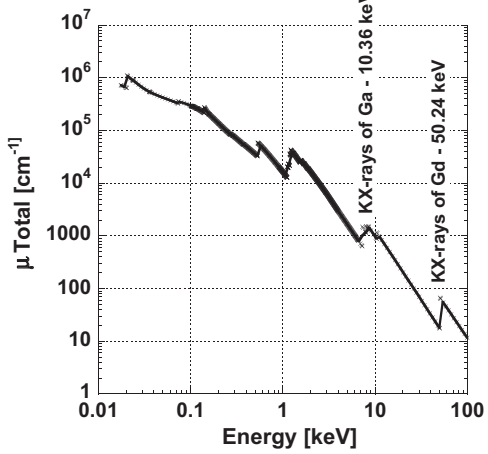

Fig. 5. Linear attenuation coefficient of GGAG crystal calculated from X-Ray and Gamma-Ray Data [33].

3.2. GGAG:Ce crystal

Multicomponent garnet crystal GGAG:Ce has recently been discovered. It is characterized by the highest L.Y. ≈ 50,000 ph/MeV [14] from group of garnet crystals. It is characterized by high density $\rho = 6.63$ g/cm^3 and rather high $Z_{eff} = 50.6$. So called "bandgap engineering" strategy was used in its development [11,12,14,28,31]. Fig. 4 represents decomposition of ^{22}Na 511 keV

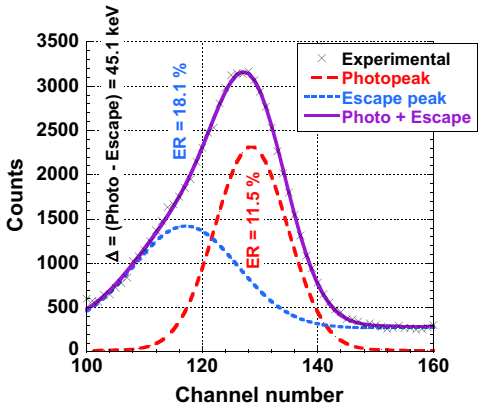

Fig. 6. Decomposition of pulse height spectrum of 1 mm thick LuAG:Ce crystal measured with 511 keV energy of ^{22}Na radioisotope at 1 μs shaping time.

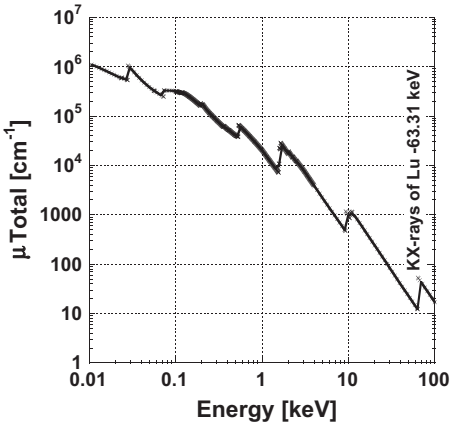

Fig. 7. Linear attenuation coefficient of LuAG crystal calculated from X-Ray and Gamma-Ray Data [33].

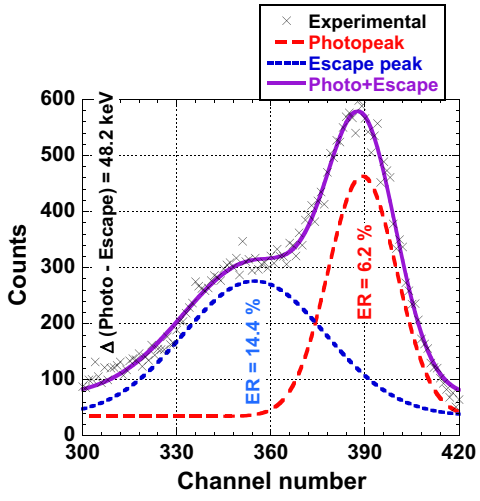

Fig. 8. Decomposition of pulse height spectrum of 1 mm thick LuAG:Pr crystal measured with 511 keV energy of ^{22}Na radioisotope at 1 μs shaping time.

energy of 1 mm thick GGAG:Ce sample. The escape peak is observed at low energy side of the photopeak band but it is not as strong as that of BGO one. Detailed values of ER for all measured thicknesses of GGAG:Ce samples are given in Table 1. At ^{22}Na 511 keV energy the photopeak ER increases between 1 and 10 mm from 6.2% to 8.7% (of about 40%) and the escape peak ER (for 1, 2 and 5 mm) are irregular ~18% to 27.3% from 1 and 2 mm thicknesses. Ratio between amplitudes of the photo and escape

Table 1
Energy resolutions of BGO, GGAG:Ce, LuAG:Ce and LuAG:Pr measured under ^{22}Na 511 keV and ^{137}Cs 662 keV. Photopeak and escape peak resolutions were measured for different sample thicknesses and shaping time 1 μs.

Crystal	Sample thickness [mm]	Photo-peak EN. RES. at 511 keV (%)	Escape peak EN. RES. at 511 keV (%)	Δ (Photo–escape) [keV]	Photo/escape (ratio of amplitudes)
BGO	1	11.9	15.7	77.1	1.9 ×
BGO	2	12.5	16.6	77.1	3.0 ×
BGO	5	14.6	21.7	81.7	6.3 ×
BGO	10	16.7	Not observed	–	–
BGO	1	10.7 at 662 keV	9.0 at 662 keV	81.2	2.3 ×
GGAG:Ce	1	6.9	14.8	31.1	2.1 ×
GGAG:Ce	2	7.2	10.2	40.4	4.3 ×
GGAG:Ce	5	8.2	27.3	27.3	8.2 ×
GGAG:Ce	10	8.7	Not observed	–	–
GGAG:Ce	1	7.3 at 662 keV	12.2 at 662 keV	30.1	2.1 ×
LuAG:Ce	1	11.5	18.1	45.1	1.6 ×
LuAG:Ce	2	10.7	19.6	43.9	3.5 ×
LuAG:Ce	4	12.3	Not observed	–	–
LuAG:Ce	10	8.7	Not observed	–	–
LuAG:Ce	1	8.3 at 662 keV	13.1 at 662 keV	47.3	1.4 ×
LuAG:Pr	1	6.2	14.4	48.2	2.1 ×
LuAG:Pr	2	5.9	7.1	51.4	3.6 ×
LuAG:Pr	5	6.6	9.5	51.8	4.9 ×
LuAG:Pr	10	8.4	Not observed	–	–
LuAG:Pr	1	At 662 keV 5.6	At 662 keV 15.5	47.6	1.2 ×

peaks from 1 to 5 mm increases from ~2 to 8.2 and at 10 mm thickness no escape peak is observed on GGAG:Ce. Observed energy difference between the photo- and escape peaks maxima is lying between 27.3 and 40.4 keV which is less than energy of KX-rays of Gd which is 50.4 keV (see Fig. 5 [33]). GGAG:Ce belongs to heavy scintillators and besides the Gd KX-rays (energy 50.4 keV) also the Ga KX-rays (energy 10.36 keV) can influence the escape peak (linear attenuation coefficients of GGAG crystal are presented in Fig. 5).

3.3. LuAG:Ce crystal

LuAG belongs to heavy scintillating crystals characterized by ρ=6.71 g/cm^3 and high Z_{eff}=58.7. Fig. 6 represents decomposition of pulse height spectrum under ^{22}Na 511 keV excitation of 1 mm thick LuAG:Ce crystal where we can resolve the photopeak and escape peak bands. The escape peak can also be observed in 2 mm thick sample but not in 4 mm thick one. Escape peak of this crystal is not as pronounced as that observed in BGO crystal. Detailed values of ER for all the thicknesses from 1 to 10 mm of LuAG:Ce samples are given in Table 1. At ^{22}Na 511 keV energy the photopeak ER changes irregularly between 1 and 10 mm from 8.7% to 12.3% (changes are of about 40%) and the escape peak ER's are ~18% or 19.6% for 1 and 2 mm thick samples. Ratio between amplitudes of the photo- and escape peaks from 1 to 2 mm thicknesses increases from ~1.6 to 3.5. At the 4 and 10 mm thickness no escape peaks are observed for LuAG:Ce. Observed energy difference between photo and escape peaks is between 43.9 and 47.3 keV which is rather lower than 63.3 keV energy of KX-rays of Lu (linear attenuation coefficients of LuAG are given in Fig. 7 [33]).

3.4. LuAG:Pr crystal

Fig. 8 represents decomposition of 511 keV energy of 1 mm thin LuAG:Pr crystal where we can clearly resolve the photopeak and escape peak (bands). The escape peak can be observed also in 2 and 5 mm thick samples. Detailed values of ER for all thicknesses of LuAG:Pr samples are given in Table 1. At 511 keV excitation the photopeak ER increases for 1 to 10 mm from 5.9% to 8.4% (of about 42%) and the escape peak ER's (for 1, 2 and 5 mm thick samples) are between 7.1% and 14.4%. Ratio between amplitudes of the photo and escape peaks from 1 to 5 mm decreases from ~2.1 to 4.9 and at 10 mm thickness no escape peak is observed in LuAG:Pr. Observed energy difference between photo and escape peaks is lying between 45.2 and 51.8 keV which is rather close to 63.3 keV energy of KX-rays of Lu (linear attenuation coefficients of LuAG are given in Fig. 7 [33]).

3.5. Escape peak processes in crystals investigated

All the investigated heavy and high Z_{eff} scintillating crystals (Ce^{3+}-doped LuAG and GGAG, Pr^{3+}-doped LuAG and the reference BGO crystal) exhibit (i) photopeak and escape peak bands (see Figs. 2, 4, 6 and 8 and Table 1) and (ii) both these bands develop with sample thickness. This is clearly shown under Gaussian decomposition of pulse height spectra in Figs. 2, 4, 6 and 8 because (i) ER's of photopeak and escape peak bands and (ii) photopeak/escape peak amplitude ratio change with sample thickness. The best ER of photopeak bands are between 6% to 8% with ^{22}Na 511 keV energy in GGAG:Ce and LuAG:Pr crystals. The photopeak ER's shows similar thickness dependence in both of them: if sample thickness increases (from 1 to 10 mm) the related photopeak ER increases by about 40%. This is surprising because GGAG:Ce and LuAG:Pr crystals exhibit different L.Y. values and that of GGAG:Ce is 2.5 times higher than that of LuAG:Pr (~50,000 ph/MeV and ~20,000 ph/MeV, respectively) [6,20]. In mixed $(Lu_{0.75}Y_{0.25})_3$AG:Pr the latest results have shown light yield ~33,000 ph/MeV [26].

Escape peak bands were observed in all measured heavy scintillating crystals investigated at low energy side of their photopeak bands. Process of escape peaks generation can be explained by arising X-ray radiation emitted by the heaviest lattice ions in crystals investigated, such as Lu, Gd or Bi immediately after photoelectric generation of their K electrons (photopeak in pulse height spectra). The escape processes arise immediately after the photoelectric generation processes because empty K electron sphere can be occupied by a free electron moving in the neighborhood and KX-rays radiation is generated [29]. KX-ray radiation that has arisen can be (i) either absorbed inside the crystal close to the original interaction site or (ii) can escape from the crystal if the interaction site is close to the sample surface. Escape peak bands are observed in thin samples (thickness between 1 to 3 mm and even 5 mm). Almost no escape peak bands are observed in 5 mm thicker samples and none in those of 10 mm thickness. If the sample thickness increases then for the same measuring configuration (radioisotopes are ≈ 2 mm above upper part of samples) the ratio between the whole sample surface area (for sample of square area 1 cm^2) and their volume is (i) 24 for 0.1 cm thick sample and (ii) 6 for 1 cm thick sample. Relatively significant part of KX-rays escapes from very thin samples while in thick samples KX-rays are absorbed inside the samples.

Escape peaks always appear on the low energy side of the photopeaks and the energy difference between their maxima is lower than *s* that calculated from linear attenuation spectra of

crystals (see Figs. 3, 5, and 7). The lowest energy mismatch was observed in BGO where the calculated KX-ray radiation should be 90.3 keV and the observed difference between the photopeak and the escape peak was between 77.1 and 81.7 keV which is only 10–15% smaller value (see Figs. 2 and 3 and Table 1). For other crystals larger differences between calculated KX-rays energies and measured ones were observed: the highest ones within 20–46% were observed in GGAG:Ce multicomponent garnet while in LuAG:Ce or LuAG:Pr these values are between 25–30% and 18–25%, respectively. The difference observed in BGO crystal is in a range of accuracy of measurements but in other crystals the difference is substantionally higher than accuracy of measurements. This difference can be explained due to processes occuring during transport of KX-ray photons in crystals, e.g. due to Compton or even coherent scattering [29,34]. Now, evaluation of these processes due to Monte Carlo method (detailed transport of photon including coherent scattering) are in progress [34].

4. Conclusions

Detailed energy resolution studies of various heavy scintillating crystals (see Table 1) showed that photopeak and escape peak energy resolution changes with sample thickness. They are influenced by sample thickness and probably by experiment configuration as well. Photopeak energy resolution under ^{22}Na 511 keV excitation is increasing by about 40% for thicknesses from 1 to 10 mm for BGO, GGAG:Ce, LuAG:Ce and LuAG:Pr. Escape peaks were clearly resolved in all measured samples for thicknesses below 3 mm. The escape peaks are positioned at low energy side of the photopeaks but measured energy difference between these peak maxima does not agree with calculated values of KX-rays emitted for Bi, Gd and Lu. This is probably due to the interaction before KX-rays escape from crystal – either they can excite other electrons (spheres L or M) or this KX-ray radiation can take part in Compton scattering. The escape X-rays are the pathway through which the absorbed energy leaves the crystals resulting in lower light yield measured in thin samples (up to 3 mm thickness).

Acknowledgements

Financial support of Czech Science Foundation Grant no. P204/12/0805 is gratefully acknowledged.

References

[1] R. Autrata, P. Schauer, Jos Kvapil, J. Kvapil, J. Phys. E 11 (1978) 707.
[2] M.J. Weber, J. Appl. Phys. 44 (1973) 3205.
[3] C.W.E. van Eijk, J. Adriessen, P. Dorenbos, Nucl. Intrum. Methods Phys. Res. A 348 (1994) 546.
[4] M. Moszynski, T. Ludziewski, D. Wolski, W. Klamra, L.O. Nordlin, Nucl. Intrum. Methods Phys. Res. A (1994) 461.
[5] P. Dorenbos, J. Phys.: Condens. Matter 15 (2003) 6249.
[6] J.A. Mares, M. Nikl, A. Beitlerova, K. Blazek, P. Horodysky, K. Nejezchleb, C. D'Ambrosio, Opt. Mater. 34 (2011) 424.
[7] M. Nikl, A. Yoshikawa, K. Kamada, K. Nejezchleb, C.R. Stanek, J.A. Mares, K. Blazek, Prog. Cryst. Growth Character. Mater. 59 (2013) 47.
[8] J.A. Mares, M. Nikl, A. Beitlerova, P. Horodysky, K. Blazek, K. Bartos, C. D'Ambrosio, IEEE Trans. Nucl. Sci. 59 (2012) 2120.
[9] L. Swidierski, M. Moszynski, A. Nassalski, A. Syntfeld-Kazuch, T. Szczesniak, K. Kamada, K. Tsutsumi, Y. Usuki, T. Yanagida, A. Yoshikawa, IEEE Trans. Nucl. Sci. 56 (2009) 934.
[10] K. Sreebunpeng, W. Chewpraditkul, M. Nikl, J.A. Mares, K. Nejezchleb, A. Phunpueok, C. Wanarak, Nucl. Instrum. Methods B 286 (2012) 85.
[11] K. Kamada, T. Yanagida, T. Endo, K. Tsutumi, Y. Fujimoto, A. Fukabori, A. Yoshikawa, J. Pejchal, M. Nikl, Cryst. Growth Des. 11 (2011) 4484.
[12] K. Kamada, T. Yanagida, J. Pejchal, M. Nikl, T. Endo, K. Tsutumi, Y. Fujimoto, A. Fukabori, A. Yoshikawa, J. Phys. D: Appl. Phys. 44 (2011) 505104.
[13] N.J. Cherepy, J.D. Kuntz, Z.M. Seeley, et al., Proc. SPIE 7805 (2010) 78050I.
[14] P. Prusa, K. Kamada, M. Nikl, A. Yoshikawa, J.A. Mares, Radiat. Meas. 56 (2013) 62.
[15] A. Yoshikawa, T. Yanagida, K. Kamada, Y. Yokota, J. Pejchal, A. Yamaji, Y. Usuki, S. Yamamoto, M. Miyaki, K. Kumagai, K. Sasaki, T.R. dos Santos, M. Baba, M. Ito, M. Takeda, N. Ohuchi, M. Nikl, Opt. Mater. 32 (2010) 1294.
[16] M.V. Derdzyan, K.L. Ovanesyan, A.G. Petrosyan, A. Belsky, C. Dujardin, C. Pedrini, E. Auffray, P. Lecoq, M. Lucchini, K. Pauwels, J. Cryst. Growth 361 (2012) 212.
[17] A.G. Petrosyan, K.L. Ovanesyan, R.V. Sargsyan, G.O. Shirinyan, D. Abler, E. Auffray, P. Lecoq, C. Dujardin, C. Pedrini, J. Cryst. Growth 312 (2010) 3136.
[18] H. Ogino, A. Yoshikawa, M. Nikl, K. Kamada, T. Fukuda, J. Cryst. Growth 292 (2006) 239.
[19] W. Drozdowski, P. Dorenbos, J.T.M. de Haas, R. Drozdowski, A. Owens, K. Kamada, K. Tsutsumi, Y. Usuki, T. Yanagida, A. Yoshikawa, IEEE Trans. Nucl. Sci. 55 (2008) 2420.
[20] K. Kamada, T. Yanagida, J. Pejchal, M. Nikl, T. Endo, K. Tsutumi, Y. Fujimoto, A. Fukabori, A. Yoshikawa, IEEE Trans. Nucl. Sci. 59 (2012) 2130.
[21] W. Drozdowski, P. Dorenbos, R. Drozdowski, A.J.J. Bos, N.R.J. Poolton, M. Tonelli, M. Alshourbagy, IEEE Trans. Nucl. Sci. 56 (2009) 320.
[22] K. Touš, M. Blazek, J.A. Nikl, Mares, J. Phys.: Conf. Ser. 425 (2013) 192017 1.
[23] Y. Zorenko, V. Gorbenko, T. Voznyak, T. Martin, P.-A. Douissard, J.A. Mares, M. Nikl, Proc. SPIE 7310 (2009) 731007-1–731007-8.
[24] F. Cindolo, C. D'Ambrosio, F. De Notaristefani, H. Leutz, D. Piedigrossi, D. Puertolas, E. Rosso, IEEE Trans. Nucl. Sci. 50 (2003) 126.
[25] C. Dujardin, C. Mancini, D. Amant, G. Ledoux, D. Adler, E. Auffray, K. Lebbou, A. Petrosyan, K.L. Ovanesyan, J. Appl. Phys. 108 (2010) 013510.
[26] W. Drozdowski, K. Brylew, A.J. Wojtowicz, J. Kisielewski, M. Swirkowicz, T. Lukasiewicz, J.T.M. de Haas, P. Dorenbos, Opt. Mater. Express 4 (2014) 1207.
[27] J.A. Mares, M. Nikl, A. Beitlerova, P. Horodysky, K. Blazek, P. Prusa, C. D´Ambrosio, Proceedings of Abstracts of LUMDETR2012 International Conference, Halle (Saale), Germany, September 10–14, 2012, p. X-ID-2150 (poster).
[28] H. Ogino, A. Yoshikawa, M. Nikl, A. Krasnikov, K. Kamada, T. Fukuda, J. Cryst. Growth 287 (2006) 335.
[29] G.F. Knoll, Radiation Detection and Measurements, 3rd edition,. Wiley, New York, 2000.
[30] J.A. Mares, C. D'Ambrosio, Opt. Mater. 30 (2007) 22.
[31] M. Fasoli, A. Vedda, M. Nikl, C. Jiang, B.P. Uberuaga, D.A. Andersson, K. J. McClellan, C.R. Stanek, Phys. Rev. B 84 (2011) 081102(R).
[32] M. Gierlik, M. Moszynski, A. Nassalki, A. Syntfeld-Kazuch, T. Szczesniak, L. Swidierski, IEEE Trans. Nucl. Sci. 54 (2007) 1367.
[33] X-Ray and Gamma-Ray Data, ⟨www.nist.gov/PhysRefData⟩.
[34] T. Vrba, Private communication and cooperation, Faculty of Nuclear Sciences and Physical Engineering, Czech Technical University in Prague, Brehova 7, 115 19 Prague 1, Czech Republic.

Journal of Luminescence 147 (2014) 196–201

Contents lists available at ScienceDirect

Journal of Luminescence

journal homepage: www.elsevier.com/locate/jlumin

Optical properties of Ce^{3+}-doped $KLuS_2$ phosphor

V. Jarý [a,b,*], L. Havlák [a], J. Bárta [b], E. Mihóková [a], P. Průša [a,b], M. Nikl [a]

[a] Institute of Physics, Academy of Sciences of the Czech Republic, Na Slovance 1999/2, Praha 8, Prague 18221, Czech Republic
[b] Faculty of Nuclear Sciences and Physical Engineering, Czech Technical University in Prague, Brehova 7, Praha 1, Prague 11519, Czech Republic

ARTICLE INFO

Article history:
Received 13 August 2013
Accepted 2 November 2013
Available online 11 November 2013

Keywords:
Inorganic scintillator
Ternary sulfide
Excited state dynamics
Thermally induced ionisation

ABSTRACT

$KLuS_2$ single crystals doped with trivalent cerium were synthesized in the form of crystalline hexagonal platelets. VUV/UV/VIS absorption and luminescence characteristics were measured in the broad temperature and concentration intervals. The band edge of $KLuS_2$ is found at 303 nm, Ce^{3+} 4f–5d excitation band at 490 nm and Ce^{3+} emission at 580 nm with the 35 ns decay time. Both thermal and concentration quenching of the Ce^{3+} emission are investigated. Phenomenological modeling and delayed recombination decays measurement are employed to understand the Ce^{3+} excited state dynamics. The application potential in X-ray phosphors is discussed.

1. Introduction

There are numerous works describing the optical properties of the Ce^{3+}-doped binary sulfides in the literature. $Lu_2S_3:Ce^{3+}$, very dense scintillator, shows the light yield of 25 000–30 000 ph/MeV, the decay time is rather short, i.e. 32 ns and the emission spectrum is peaking at 592 nm [1]. Luminescence properties of the $CdS:Ce^{3+}$ nanoparticles have been investigated in detail [2], and the effect of dopant concentration on the photoluminescence (PL) intensity has also been studied. Analogously, there are numerous papers dealing with the luminescence features of the $CaS:Ce^{3+}$ nanoparticles as well [3,4]. $CaS:Eu^{2+}$, Mn^{2+} and $CaS:Ce^{3+}$, Tb^{3+} synthesized by the flux method [5] were aimed to be used for cathode-ray tube display. It was also showed that $CaS:Eu^{2+}$, Tm^{3+}, Ce^{3+} can be used as an enhanced long persistent red phosphor [6] with a strong energy transfer from Ce^{3+} to Eu^{2+} found at a low doping concentration. A double insulated CaS:Ce thin-film electroluminescent (EL) device emitting a bright green EL due to the Ce^{3+} luminescent centre has been reported [7]. SrS doped by Ce^{3+} and co-doped by Pb^{2+} or Cl^-, Na^+ also gained attention mainly due to possibility of being used as thin films in electroluminescence devices [8–10]. Codoping of SrS:Ce by other RE^{3+} ions and their impact on the transient emission processes are discussed in [11]. The luminescence efficiency of SrS:Ce powders in the doping range from 0.01 at% to 1.0 at% was investigated by photoluminescence decay studies [12]. ZnS as a host for the Ce^{3+} emission centre was introduced [13] and the emission and excitation spectra of $ZnS:Ce^{3+}$,Tb^{3+} indicate that the Ce^{3+} sensitizes Tb^{3+}. Thin films of ZnS:Ce, which may be used in the electroluminescence devices, were also described [14,15] and novel Ce-doped $Zn_xSr_{1-x}S$ solid solutions were prepared as blue–green emitting phosphor thin films [16]. Luminescence spectra of Ce^{3+}-ion in $Ca_{1-x}Sr_xS$ solid solutions have been investigated as well [17]. A study of the photoluminescence of the undoped γ-La_2S_3 and γ-Ce_2S_3 and doped γ-[Na]Ce_2S_3 rare earth sulfides, performed comparatively under steady state and time resolved excitation and detection conditions, has also been reported [18].

Ce^{3+}-doped ternary sulfide designated for scintillation purposes are known as well, mainly those of the general formula $MeGa_2S_4$ (Me=Ca, Sr). Ce^{3+}-doped $CaGa_2S_4$ single crystals have been grown under various conditions by the horizontal Bridgman method using a travelling temperature gradient [19]. Ce^{3+} absorption band was observed at 3.2 eV. A novel monoclinic phase of impurity-doped $CaGa_2S_4$ was introduced as a high emission intensity phosphor [20]. $SrGa_2S_4$ provides a deep blue and saturated green emission when doped with Ce^{3+} and Eu^{2+}, respectively [21]. The behaviour and performances of respective electroluminescence devices are discussed in detail. Polarized photoluminescence (PL) spectra of $SrGa_2S_4$:Ce prepared by chemical vapor transport technique were measured and discussed in the framework of the crystal-field theory [22]. The Ce-doped $SrGa_2S_4$ films exhibit the characteristic photoluminescent emission occuring in the 445 nm region [23]. Green to yellowish green light emitting Ce^{3+}-doped barium zinc sulfide (Ba_2ZnS_3) phosphor powders have been synthesized by a double-crucible method [24]. The photoluminescence (PL) spectra show that the emission peaks located in the 502–532 nm range (under excitation at 422 nm) and in the 530–560 nm range (under excitation at 358 nm) depend on the Ce^{3+} concentration. $Ba_2ZnS_3:Ce^{3+}$ co-doped by Ag^+ ions emitting bluish to yellowish-green light [25]. Photoluminescence emission spectra and diffuse

* Corresponding author. Tel.: +420 220 318 510; fax: +420 233 343 184.
E-mail address: jary@fzu.cz (V. Jarý).

0022-2313/$ - see front matter © 2013 Elsevier B.V. All rights reserved.
http://dx.doi.org/10.1016/j.jlumin.2013.11.013

reflectance absorption spectra of phosphors composed of ternary sulfide hosts with the Th_3P_4, calcium ferrite, spinel, and thiogallate structure types each activated by Eu^{2+}, Ce^{3+}, Ho^{3+}, and Mn^{2+} were investigated [26]. Various sulfidic hosts potentially interesting for white LEDs phosphors were recently reviewed [27]. In particular, alkali earth sulfide phosphors doped with Eu^{2+} and Ce^{3+} gained attention in this field [28]. A review on the wavelengths of all five 4f–5d transitions of Ce^{3+} and systematic trends regarding the emission wavelength, maximum obtainable scintillation light output, gamma-ray energy resolution, and scintillation decay time of Ce^{3+} in about 150 different inorganic compounds, including sulfides, is presented in [29,30].

In addition to the recent activities in complex oxides [31] and lanthanide ions-activated orthoborate research [32] we started to study unexplored family of ternary sulfides. Optical properties of the Ce^{3+}-doped ternary sulfide of general formula $RbLnS_2$ (Ln=La, Gd, Lu) have been published for the first time only recently [33–35]. However, in such matrices, Ce^{3+} emission at room temperature is thermally heavily quenched. In this paper we report the luminescence characteristics of the Ce^{3+} center in $KLuS_2$ matrix which, to our best knowledge, have never been reported in the literature.

2. Experimental setup

$KLuS_2$:Ce crystals were prepared in an electric resistance furnace by the reaction of H_2S with a mixture of Lu_2O_3, x% Ce_2O_3 and excess of K_2CO_3. The reaction temperature reached 1000 °C and the hydrogen sulfide flow was applied for 90 min. Further technological details are reported in Ref. [33]. Structural properties of $KLuS_2$ compounds have been recently discussed [36].

Absorption spectra were measured using the UV/VIS Spectrophotometer Shimadzu UV-1601. Photoluminescence (PL) spectra and decay curves were measured by the custom made Spectrofluorometer 5000M, Horiba Jobin Yvon, using the steady state deuterium lamp (photoluminescence excitation (PLE) and emission (PL) spectra in the 190–500 nm and 200–800 nm spectral regions, respectively), Seifert X-ray tube (radioluminescence (RL) spectra within 200–800 nm), microsecond xenon-filled lamp and nanosecond pulsed LED diodes (PL decay curves) as the excitation sources. Spectra were corrected for instrumental effects and a convolution procedure was applied to the decay curves to determine true decay times (SpectraSolve software package, Ames Photonics). Room-temperature (RT) luminescence properties of $KLuS_2$:Ce crystalline platelets were studied without powdering of the samples. The Oxford Instruments liquid nitrogen bath cryostat was used to control the sample temperature in the 80–500 K temperature range. PLE spectra in VUV–UV region were measured at Superlumi station, HASYLAB, DESY, Hamburg.

Light yield and energy resolution were determined by the pulse height spectroscopy of scintillation response [37], using the HPMT (Hybrid Photomultiplier) [38] model DEP PPO 475B, spectroscopy amplifier ORTEC model 672 (shaping time t=1 μs) and multichannel buffer ORTEC 927TM. Low energy γ-ray from ^{57}Co (122 keV) and ^{241}Am (59.5 keV) were used for excitation. The sample was optically coupled to HPMT using a silicon grease. Higher γ-ray energies could not be used, since samples were very thin (approximately 0.1 mm). All measurements were performed at room temperature. Energy resolution and photoelectron yield were obtained from the Gaussian fit of the photopeak in the pulse-height spectra.

3. Results and discussion

X-ray excited emission spectra of $KLuS_2$ doped by different concentrations of trivalent cerium are shown in Fig. 1a. They all feature a broad band with a maximum at about 580–620 nm which we assign to the Ce^{3+} 5d–4f fully allowed transition, based also upon similarity to $RbLuS_2$:Ce [35]. Extended low energy part of the spectrum might be shaped by unspecified perturbed Ce^{3+} centers. With increasing Ce^{3+} concentration above 0.5%, the spectra are getting broader and low energy shifted. There is another band peaking at around 450 nm whose origin remains unclear. It might be connected to the $KLuS_2$ host [39]. A spectrum of the 0.05% sample recorded at 77 K, see the inset of Fig. 1b, shows the characteristic well-resolved doublet of the Ce^{3+} ground state ($5d_1 \rightarrow {}^2F_{5/2}$ at 580 nm and $5d_1 \rightarrow {}^2F_{7/2}$ at 664 nm). The energy separation of two emissions of about 2180 cm^{-1}, matches the value of about 2000 cm^{-1} known from many other hosts. With increasing temperature the doublet becomes unresolved due to thermalization of ground state levels. The integral of each spectrum (in the eV–W/eV coordinates) was related to that of the BGO ($Bi_4Ge_3O_{12}$) powder standard sample obtained under identical experimental conditions. The results are displayed in Fig. 1b. Starting from very low Ce concentration, the Ce 0.002% sample still shows 350% of the BGO integral. Between 0.002% and 2.5%, 350–590% of BGO intensity is obtained. For a heavily doped 6% sample, the RL intensity sharply decreases, but still shows 290% of the BGO integral. Observed decrease for the highest concentration is probably due to the onset of concentration quenching also evidenced in the photoluminescence decay in Fig. 4. In comparison, the Eu^{2+} emission in the $KLuS_2$ is completely quenched for Eu 2% concentration at RT [36]. There is a correlation between the RL intensity and reduction of the decay curve integrals for the highest Ce concentration (cf. Fig. 1b). For above-mentioned applications, the interval of Ce concentrations between 0.1% and 2% appears to be the most suitable.

RT absorption (2.5% sample), PL and PLE spectra (0.05% and 0.5% samples) of the Ce^{3+}-doped $KLuS_2$ are presented in Fig. 2a and b, details are listed in the legends. Both absorption and PLE spectra feature the $KLuS_2$ band edge situated at about 300–310 nm at RT (Fig. 2a) and 290–300 nm at 10 K (Fig. 2b). These values are high-energy shifted with respect to $RbLnS_2$ [33–35] and in a good agreement with Ref. [36]. Another band at around 496 nm is ascribed to the Ce^{3+} 4f–$5d_1$ transition. PLE spectra in the 440–500 nm region (see Fig. 2a) are, however, partially distorted due to a very weak excitation source (deuterium steady state lamp) and strong correction curve influence. Ce^{3+} 4f–$5d_1$ transition is fully allowed and offers an efficient excitation in the blue spectral region. The hint of another excitation band at around 400 nm (see Fig. 2a) in the PLE spectra is noted and could be connected to a host lattice defect [39]. PLE spectra in the VUV spectral part (see Fig. 2b) are dominated by a broad band in the 160–240 nm region, which might reflect the density of states in the valence band, and the onset of the multiplication of electronic excitation ($>2E_g$) below 150 nm [40]. PL spectra, under excitation in both the band edge and Ce^{3+} 4f–5d band regions, and RL spectra coincide (for given temperatures) and exhibit broad intense Ce^{3+} $5d_1$–4f emission peaking at 580 nm. From the position of the lowest 4f–$5d_1$ absorption band (at 496 nm, see Fig. 2a) and emission maximum (580 nm) one can estimate the Stokes Shift of 360 meV.

Experimental determination of the $KLuS_2$:Ce scintillation light yield (LY) was quite difficult due to small size, especially the thickness, of the sample which makes its wrapping difficult. Consequently, the light collection efficiency is questionable and obtained values surely underestimate true LY. Given the relatively low energy of gamma sources, its value can be further influenced by non-proportionality effect [41]. Under gamma excitation of ^{57}Co and ^{241}Am, the measured LY value of the 0.5% Ce sample is 23 800 ph/MeV and 22 300 ph/MeV, respectively, see Fig. 3. For the sample 0.05% Ce, LY value of 20 300 ph/MeV was measured. Despite values for the 0.5% Ce sample, it is premature to make statements on non-proportionality having light yield values only

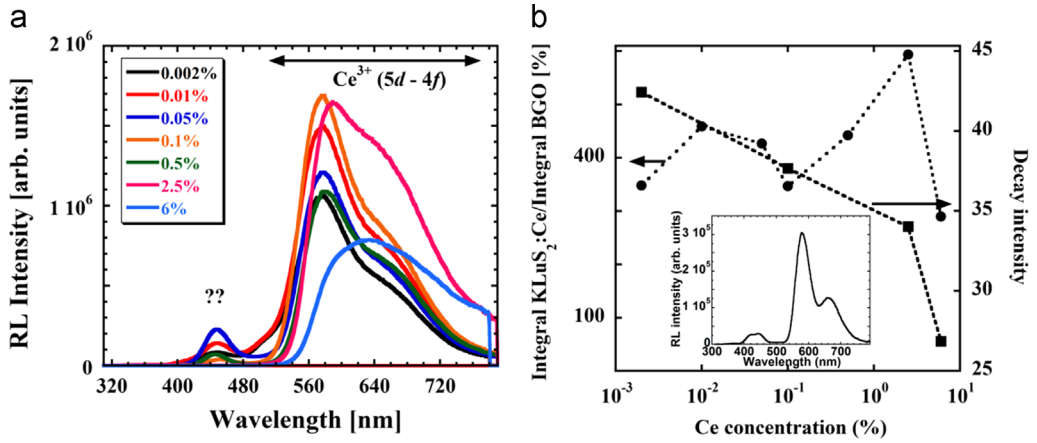

Fig. 1. In (a), X-ray excited emission spectra (40 kV, 15 mA) of the $KLuS_2:Ce^{3+}$ with different concentrations of Ce^{3+} at RT. The spectrum at 77 K for the Ce^{3+}concentration 0.05% is shown in the inset of (b). In (b), concentration dependence of the Ce^{3+} radioluminescence intensity in $KLuS_2$ (full circles) and concentration dependence of the normalized decay curves integrals (full squares).

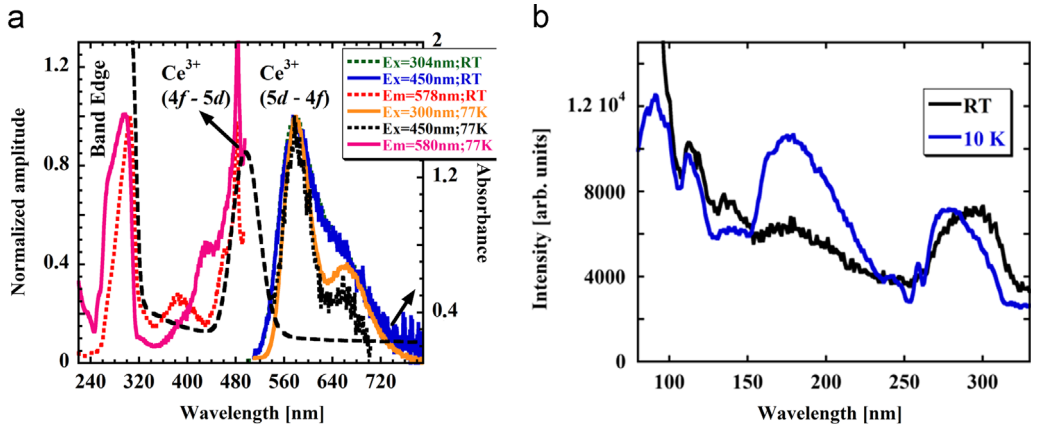

Fig. 2. (a) RT Absorption (black dashed line, 2.5% Ce), PLE (red dotted line for 578 nm emission at RT, 0.05% Ce; pink solid line for 580 nm emission at 77 K, 0.05% Ce) and PL (blue solid line under 450 nm excitation at RT, 0.05% Ce; orange solid line under 300 nm excitation at 77 K, 0.05%; green dotted line under 304 nm excitation at RT; black dotted line under 450 nm excitation at 77 K) spectra of $KLuS_2:Ce$; (b) PLE spectra of $KLuS_2:Ce$ (0.5%) for the 570 nm emission recorded at 10 K and RT using synchrotron radiation. (For interpretation of the references to color in this figure legend, the reader is referred to the web version of this article.)

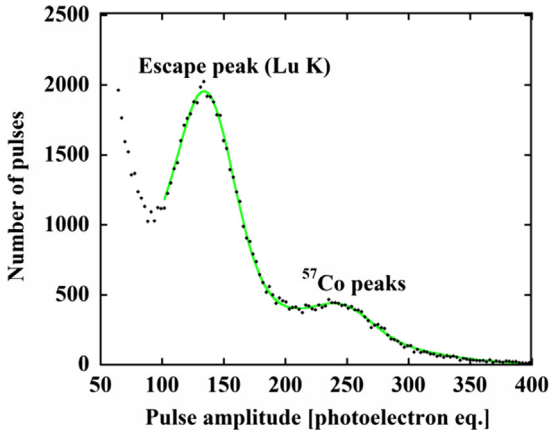

Fig. 3. Pulse height spectrum of ^{57}Co (0.5% sample) measured by $KLuS_2:Ce$. Gaussians with the second order polynomial background was fit to a part of the spectrum. 247 photoelectrons were collected at energy 122 keV, i.e. (PhY) photoelectron yield=2025 phels/MeV. Quantum efficiency (QE) is 8.52%, LY=PhY/QE=23 800 ph/MeV.

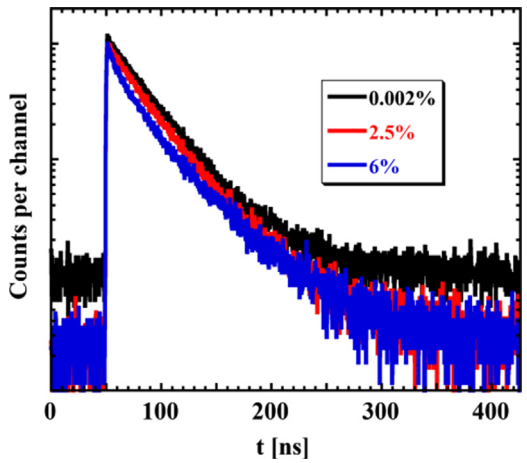

Fig. 4. Normalized RT PL decay curves related to the Ce^{3+} 5d–4f transition (λ_{ex}=490 nm, λ_{em}=580 nm) in $KLuS_2$ for various Ce^{3+} content.

for two different energies measured with precision of approximately 5–10%.

Measured LY is only slightly dependent on the amplifier shaping time, i.e. LY (t=10 μs)/LY (t=0.5 μs)=1.05 which is much less than e.g. in LuAG:Ce where this value is typically 1.7 [42]. Therefore, slow components in the scintillation response of $KLuS_2$:Ce with decay times on the order of units to tens of μs are very weak. However, this measurement is insensitive to much slower (hundreds of μs or more) components in the scintillation response.

Energy resolution for the peak with energy 122 keV (^{57}Co) and 59.5 keV (^{241}Am) is 20 ± 4% and 29 ± 4%, respectively. The value is negatively affected by combination of the low HPMT quantum efficiency, low excitation energy and moderate LY. However, there is a space for improvement by using semiconductor photon detector that is more sensitive for longer wavelength photons.

RT PL decay curves related to the Ce^{3+} 5d–4f transition (λ_{ex}=490 nm, λ_{em}=580 nm) in $KLuS_2$ for different Ce^{3+} content were recorded (Fig. 4) in order to investigate the occurrence of concentration quenching. Decay curve for the Ce 0.002% is strictly single-exponential with the RT decay times of 34.9 ns which is in a good agreement with the expected value of fully-allowed Ce^{3+} 5d–4f transitions. In contrast, the decay of Ce2.5% sample becomes distorted. It can be approximated by a double-exponential function with decay times of about 30.1 ns and 88.5 ns, where the shorter component indicates the onset of concentration quenching. Slower tail may indicate the presence of excited state ionization, see below. Finally, the decay curve of the Ce6% sample is even more distorted. Interestingly, its signal-to-background ratio improves which may be related to processes of the excited state ionization of Ce^{3+} centers as well. Furthermore, the decay curves shown in Fig. 4 were normalized and integrated. The obtained integrated values were plotted as a function of the Ce^{3+} concentration in Fig. 1b and were discussed above.

To further study a thermal stability of the Ce^{3+} emission centre in this ternary sulfide host, the temperature dependence of the Ce^{3+} 5d–4f decay times for two different Ce^{3+} concentrations (0.05% and 0.5%) was investigated between 77 K and 497 K. Decay curves are single exponentials within 77–347 K and 77–257 K for the 0.05%Ce and 0.5%Ce concentrations, respectively. Above these temperatures, a slower tail appears in the decay curve. The decay must be then approximated by the sum of two exponential terms $I(t)=A_1\exp[-t/T_1]+A_2\exp[-t/T_2]+$background. The relative weight (lightsum) of both fast and slow components is calculated as $I_i=A_iT_i/(A_1T_1+A_2T_2)$, i=1,2 and displayed in Fig. 5. The slow decay component (T_2) is probably due to thermally induced ionisation of the Ce^{3+} excited state (see below). It can be concluded that the onset of the ns decay time shortening (concerning the fast component) is at about 320 K for the 0.05% sample and 280 K for the 0.5% sample and decay times change from 41.4 ns at 77 K to 0.29 ns at 497 K (for the 0.05% sample) and from 40.8 ns at 77 K to 6.0 ns at 490 K (for the 0.5% sample). We note that the radiative decay time at 77 K is equal for both Ce^{3+} concentrations. However, the decay time decrease is much more dramatic for the 0.05% sample (more than two orders of magnitude) compared to the 0.5% sample. Taking into account this discrepancy and the presence of the slower component at higher temperatures, one can conclude that another dynamic process is possibly at work, most probably thermally induced ionization of the Ce^{3+} 5d excited state (see below). We also mention that the relative light sum of the slow component is increasing significantly with increasing temperature while that of the fast component is, at the same time, decreasing for both Ce concentrations. It means that the amount of the emission light released in slower component is increasing with increasing temperature.

We approximated the temperature dependence of the fast component decay time for both the 0.05% and 0.5% samples by a simple barrier model described by Eq. (1),

$$(\tau_{\text{observed}})^{-1}=(\tau_{\text{radiative}})^{-1}+K_x\times\exp(-E_x/kT) \quad (1)$$

where τ_{observed}, $\tau_{\text{radiative}}$, K_x, E_x, k, and T represent the PL decay time measured at temperature T, the low temperature limit of the PL decay time, frequency factor, energy barrier height, Boltzmann constant and absolute temperature, respectively. The parameters of the best fit of Eq. (1) to experimental data are $K_x=9\times10^{13}$ s^{-1}, E_x=480 meV for the 0.05% sample and $K_x=1.7\times10^{11}$ s^{-1}, E_x=280 meV for the 0.5% sample. Such different values of the energy barrier and frequency factor again indicate that the decay time shortening is maybe not only due to classical temperature quenching to the ground state but there can be a contribution of another process. In case of mentioned Ce^{3+} excited state thermal ionization, higher Ce^{3+} concentration can enable more effective and fast return of electrons thermally promoted to the conduction band back to an ionized Ce^{4+} centre. Such a trend can effectively slow down the decay in submicrosecond time scale at the highest temperatures.

To further investigate the nature of decay times shortening at higher temperatures we performed the measurement of the temperature dependence of the delayed recombination (DR) decays integrated in the extended time window. This measurement consists in the decay monitoring under the same excitation and emission wavelengths as in Figs. 4 and 5, but using the xenon-filled microsecond flashlamp excitation and multichannel scaling mode detection in the extended time window (44 ms). Under such conditions a prompt nanosecond Ce^{3+} decay is accumulated in the first few channels and the delayed recombination decay (produced by charge carriers that were thermally ionized and later returned back to the emission centre) can be easily investigated (for details concerning the method, see Ref. [43]).

Fig. 6 illustrates the temperature dependence of the normalized (at the lowest temperature) DR integrals related to Ce^{3+} centre in $KLuS_2$ host, for two different Ce^{3+} concentrations (0.05% and 0.5%). Before integrating the decay curves a few data points with the highest intensity at the very beginning of the decay (containing

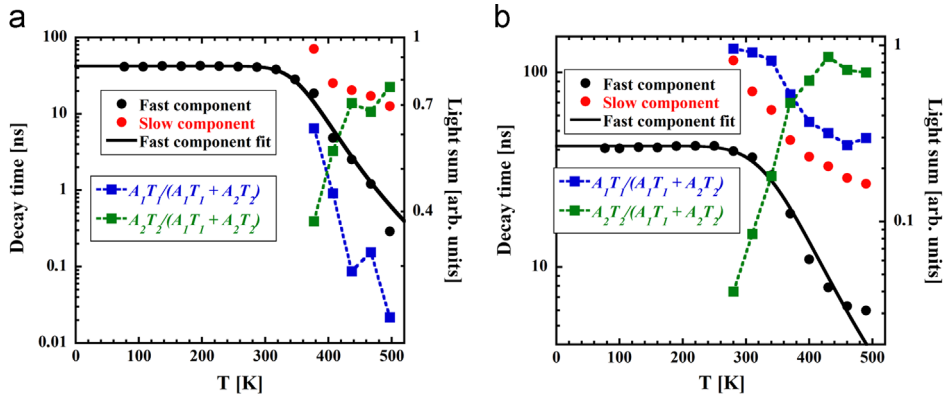

Fig. 5. Temperature dependence of the ns decay time for the (a) $KLuS_2$:Ce 0.05% sample (λ_{ex}=490 nm, λ_{em}=580 nm) and (b) $KLuS_2$:Ce 0.5% (λ_{ex}=490 nm, λ_{em}=600 nm); black full circles are the fast component data, red full circles are the slow component data, blue full squares stand for the light sum of the fast component and green full squares the light sum of the slow component, black solid line is the fit of the phenomenological model (see the text) to the ns decay time data. (For interpretation of the references to color in this figure legend, the reader is referred to the web version of this article.)

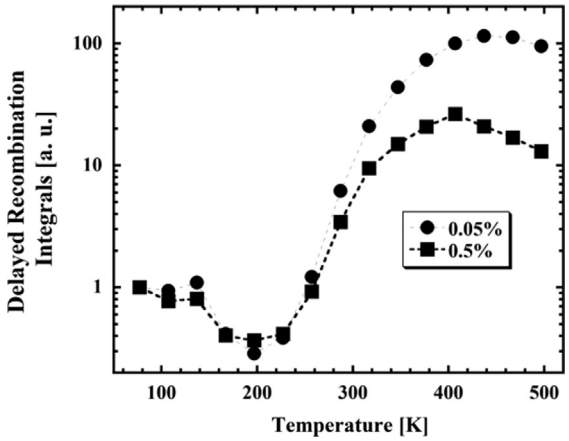

Fig. 6. Temperature dependence of normalized (at the lowest temperature) delayed recombination integrals (ex=490 nm, em=580 nm) for $KLuS_2$:Ce (0.05% – full circles, 0.5% – full squares).

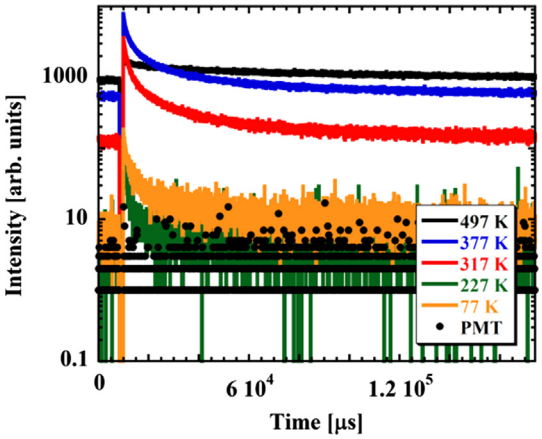

Fig. 7. Examples of delayed recombination decays connected to $KLuS_2$:Ce (0.05%), (λ_{ex}=490 nm, λ_{em}=580 nm) at different temperatures.

prompt nanosecond Ce^{3+} luminescence) were omitted. As demonstrated in Fig. 6 there is, indeed, a rapid increase of the DR integrals between 200 K and 400 K (0.5%), 450 K (0.05%). We ascribe it to a process in which electron escapes from the Ce^{3+} $5d_1$ excited state to the conduction band from where it can return at later times and radiatively recombine with the hole, giving rise to the delayed recombination luminescence. The behavior of the delayed recombination integrals between 400 K and 500 K can be due to shaping of the DR temperature dependence by the presence of traps [44,45]. Interestingly, the relative maximum value of the DR integrals for the 0.05% sample (at around 450 K) is by one order of magnitude higher than that of the 0.5% sample (at around 400 K). As the experimental conditions were identical and both dependences are normalized, it means that more delayed light is produced in the measurement window (44 ms) in the sample containing lower Ce^{3+} concentration. This observation is consistent with the hypothesis given above that at higher Ce concentration there is enhanced return of electrons from conduction band/traps towards ionized Ce^{4+} centers in the submicrosecond time scale. Consequently, the evaluated decay times become longer and evaluated quenching barrier obtained from the decays in Fig. 5 can be altered in the sample with the higher concentration of Ce. On the other hand combined results reported in Figs. 4 and 5 clearly indicate that shortening of the nanosecond decay times between 300 K and 500 K is due to thermal ionization rather than the classical thermal quenching. We also note that delayed recombination integrals show a non-zero value even at the lowest temperatures, which has been explained by quantum tunneling between luminescence center and a nearby defect state [46].

As an example, several delayed decay curves, recorded at different temperatures, are shown in Fig. 7 (λ_{ex}=490 nm, λ_{em}=580 nm). Because of minimized dead-times between the 44 ms long measurement windows, even delayed recombination processes of much longer decay times (up to the time of measurement which is typically 10 min) provide the signal which is visible in the "background" of the decay curve before the rising edge of the ms decay, i.e. the actual measurement window in this experiment is extremely extended, from a few tens of μs up to about 10 min. Ns decay time values, however, begin to shorten at higher temperatures compared to delayed recombination integrals increase. This seeming discrepancy might be due to the difference in monitoring the onset of decay times shortening and the onset of delayed recombination increase. While the former is monitored as the change with respect to its maximum value, the latter is monitored as the change with respect to its minimum value. As a result, the latter can become more sensitive in the overall dynamic range. Better understanding of the DR behavior would require an independent study of characteristics of the traps involved in the delayed recombination process as mentioned above.

4. Conclusions

In this study we present the Ce^{3+}-doped $KLuS_2$ single crystalline material as novel, potentially interesting X-ray phosphor. By the inorganic reaction in an electric resistance furnace we prepared the optically transparent single crystal samples about 0.1 mm thick with a cross-section area up to a few square mm, consisting of the single $KLuS_2$ phase. The absorption and PLE spectra show the $KLuS_2$ band edge at 303 nm and Ce^{3+} 4f–$5d_1$ absorption band peaking at 490 nm. Both X-ray and PL excitation provide the broad Ce^{3+} emission peaking at 580 nm with the shoulder at 660 nm due to Ce^{3+} 5d–4f transition. At room temperature, the photoluminescence decay time of the Ce^{3+} center is about 35 ns. The Stokes shift value of 360 meV is evaluated. Concentration dependence study reveals the onset of concentration quenching around 0.5 mol% of Ce^{3+} and the highest emission intensity under X-ray excitation is reached for the sample containing 0.1% of cerium.

Moderate light yield value of the $KLuS_2$:Ce0.5% was measured (under gamma excitation) of about 23 800 ph/MeV and almost no slower components were found in scintillation response within 0.5–10 μs shaping time interval.

A phenomenological model is employed to describe the Ce^{3+} excited state dynamics and explain ns decay times reduction with increasing temperature. The parameters of the best fit of Eq. (1) to experimental data are $K_x=9\times10^{13}$ s^{-1}, E_x=480 meV for the 0.05% sample and $K_x=1.7\times10^{11}$ s^{-1}, E_x=280 meV for the 0.5% sample. The former value set is probably more relevant in the quantitative description of the processes occurring in the $5d_1$ excited state of Ce^{3+} in $KLuS_2$ host where the dominant influence is due to thermally induced ionization of the Ce^{3+} excited state. It is supported by additional measurements and evaluation of the delayed recombination decay curves.

Elevated effective atomic number (Z_{eff}=59), efficient energy transfer from the host to Ce^{3+} centers and lower band gap, relative to oxide-based materials, are intrinsic advantages of the Ce^{3+}-doped $KLuS_2$ and make this material prospective for applications for fast X-ray phosphors, especially when semiconductor detectors would be used. All studied samples also show reasonable long-term stability and negligible moisture sensitivity.

Acknowledgment

Financial support of Czech TACR TA01011017 project and RVO: 68407700 are gratefully acknowledged.

References

[1] J.C. Van´t Spijker, P. Dorenbos, C.P. Allier, C.W.E. Van Eijk, A.R.H.F. Ettema, G. Huber, Nucl. Instrum. Methods Phys. Res., Sect. B 134 (1998) 304.
[2] L. Saravanan, A. Pandurangan, R. Jayavel, Mater. Lett. 66 (2012) 343.
[3] G. Sharma, P. Chawla, S.P. Lochab, N. Singh, Radiat. Eff. Defects Solids 164 (2009) 763.
[4] V. Kumar, S.S. Pitale, V. Mishra, I.M. Nagpure, M.M. Biggs, O.M. Ntwaeaborwa, H.C. Swart, J. Alloys Compd. 492 (2010) L8.
[5] M. Pham-Thi, J. Alloys Compd. 225 (1995) 547.
[6] D. Jia, ECS Trans. 2 (2007) 1.
[7] V. Shanker, S. Tanaka, M. Shiiki, H. Deguchi, H. Kobayashi, H. Sasakura, Appl. Phys. Lett. 45 (1984) 960.
[8] T.A. Oberacker, G. Schlotterbeck, G. Bilger, H.W.D. Braunger; Schock, J. Appl. Phys. 80 (1996) 3526.
[9] S. Tanaka, J. Lumin. 40–41 (1988) 20.
[10] B. Huettl, U. Troppenz, K.O. Velthaus, C.R. Ronda, R.H. Mauch, J. Appl. Phys. 78 (1995) 7282.
[11] S. Okamoto, E. Nakazawa, Jpn. J. Appl. Phys. 34 (1995) 521.
[12] B. Huttl, G.O. Muller, R. Mach, C. Fouassier, P. Benalloul, Adv. Mater. Opt. Electron. 3 (1994) 131.
[13] C.L. Deng, K.H. Qiu, J. Chengdu Inst. Technol. 30 (2003) 409.
[14] S. Tanaka, H. Kobayashi, M. Shiiki, T. Kunou, V. Shanker, H. Sasakura, J. Lumin. 31–32 (1984) 945.
[15] M. Tammenmaa, M. Leskelä, T. Koskinen, L. Niinistö, J. Less-Common Met. 126 (1986) 209.
[16] S.T. Lee, M. Kitagawa, K. Ichino, H. Kobayashi, Appl. Surf. Sci. 100–101 (1996) 656.
[17] O. Krachni, L. Guerbous, L. Louail, Mod. Phys. Lett. B 20 (2006) 1405.
[18] R. Mauricot, J. Dexpert-Ghys, M. Evain, J. Lumin. 69 (1996) 41.
[19] C. Hidaka, T.. Takizawa, J. Cryst. Growth 237–239 (2002) 2009.
[20] A. Suzuki, T. Takizawa, C. Hidaka, N. Shigetaka, I. Kitajima, Acta Crystallogr., Sect. E: Struct. Rep. Online 68 (2012) i42.
[21] P. Bénalloul, C. Barthou, J. Benoit, J. Alloys Compd. 275–277 (1998) 709.
[22] K. Tanaka, T. Ohgoh, K. Kimura, H. Yamamoto, K. Shinagawa, K. Sato, Jpn. J. Appl. Phys. 34 (1995) L1651.
[23] O.N. Djazovski, T. Mikami, K. Ohmi, S. Tanaka, H. Kobayashi, J. Electrochem. Soc. 144 (1997) 2159.
[24] Y.F. Lin, Y.H. Chang, B.S. Tsai, J. Alloys Compd. 377 (2004) 277.
[25] Y.F. Lin, Y.H. Chang, B.S. Tsai, J. Electrochem. Soc. 152 (2005) G698.
[26] M.M. Yuta, W.B. White, J. Electrochem. Soc. 139 (1992) 2347.
[27] P.F. Smet, A.B. Parmentier, D. Poelman, J. Electrochem. Soc. 158 (2011) R37.
[28] D. Jia, X.J. Wang, Opt. Mater. 30 (2007) 375.
[29] P. Dorenbos, J. Lumin. 135 (2013) 93.
[30] P. Dorenbos, Nucl. Instrum. Methods Phys. Res., Sect. A 486 (2002) 208.
[31] J.M. Ogieglo, A. Katelnikovas, A. Zych, T. Jűstel, A. Meijerink, C.R. Ronda, J. Phys. Chem. A 117 (2013) 2479.
[32] Y. Wu, G. Ren, M. Nikl, D. Ding, J. Wang, S. Shang, F. Yang, S. Pan, J. Phys. Chem. A 115 (2011) 13821.
[33] L. Havlák, V. Jarý, M. Nikl, P. Boháček, J. Bárta, Acta Mater. 59 (2011) 6219.
[34] V. Jarý, L. Havlák, J. Bárta, E. Mihóková, M. Nikl, Opt. Mater. 35 (2013) 1226.
[35] V. Jarý, L. Havlák, J. Bárta, M. Nikl, Phys. Status Solidi RRL 6 (2012) 95.
[36] V. Jarý, L. Havlák, J. Bárta, E. Mihóková, M. Nikl, Chem. Phys. Lett. 574 (2013) 61.
[37] M. Moszynski, M. Kapusta, M. Mayhugh, D. Wolski, S.O. Flyck, IEEE Trans. Nucl. Sci. 44 (1997) 1052.
[38] C. D'Ambrosio, H. Leutz, Nucl. Inst. Meth. A 501 (2003) 463.
[39] V. Jarý, L. Havlák, J. Bárta, E. Mihóková, M. Nikl, IEEE Trans. Nucl. Sci. (2013).
[40] J. Becker, J.Y. Gesland, N.Yu. Kirikova, J.C. Krupa, V.N. Makhov, M. Runne, M. Queffelec, T.V. Uvarova, G. Zimmerer, J. Alloys Compd. 275–277 (1998) 205.
[41] G. Bizarri, W.W. Moses, J. Singh, A.N. Vasil´ev, R.T. Williams, J. Appl. Phys. 105 (2009) 044507.
[42] P. Průša, T. Čechák, J.A. Mareš, M. Nikl, A. Beitlerová, N. Solovieva, Yu.V. Zorenko, V.I. Gorbenko, J. Touš, K. Blažek, Appl. Phys. Lett. 92 (2008) 041903.
[43] J. Pejchal, M. Nikl, E. Mihóková, J.A. Mareš, A Yoshikawa, H. Ogino, K.M. Schillemat, A. Krasnikov, A. Vedda, K. Nejezchleb, V. Múčka, J. Phys. D: Appl. Phys. 42 (2009) 055117.
[44] M. Fasoli, A. Vedda, E. Mihókova, M. Nikl, Phys. Rev. B: Condens. Matter 85 (2012) 085127.
[45] E. Mihóková, M. Nikl, L.S. Schulman, V. Jarý, Phys. Status Solidi RRL 7 (2013) 228.
[46] E. Mihóková, L.S. Schulman, V. Jarý, Z. Dočekalová, M. Nikl, Chem. Phys. Lett. 578 (2013) 66.

Optical Materials 34 (2012) 1762–1766

Contents lists available at SciVerse ScienceDirect

Optical Materials

journal homepage: www.elsevier.com/locate/optmat

Luminescence and scintillation of Ce^{3+}-doped high silica glass

Weerapong Chewpraditkul [a,*], Yinglong Shen [b], Danping Chen [b,*], Bingkun Yu [c], Petr Prusa [d], Martin Nikl [d], Alena Beitlerova [d], Chalerm Wanarak [a]

[a] Department of Physics, King Mongkut's University of Technology Thonburi, Bangkok 10140, Thailand
[b] Shanghai Institute of Optics and Fine Mechanics, CAS, Shanghai 201800, PR China
[c] Department of Physics, Shanghai University, Shanghai 201800, PR China
[d] Institute of Physics, AS CR, Prague 16253, Czech Republic

ARTICLE INFO

Article history:
Received 13 January 2012
Received in revised form 17 April 2012
Accepted 18 April 2012
Available online 16 May 2012

Keywords:
Ce^{3+}
Luminescence
Porous materials
Scintillation
Photoluminescence decay

ABSTRACT

Ce^{3+}-doped high silica glass was prepared by impregnation of Ce ions into a porous silica glass followed by high temperature sintering in a CO reducing atmosphere. The characteristic emission of Ce^{3+} 5d → 4f transition peaking around 375 nm is observed in its luminescence spectra under UV and X-ray excitation. Its photoluminescence decay is governed by several tens of nanoseconds decay time. Its integral scintillation efficiency is comparable to that of a $Bi_4Ge_3O_{12}$ (BGO) crystal under X-ray excitation. Scintillation light yield under gamma and alpha excitation was measured and compared with that of BGO.

1. Introduction

Silica glass is an attractive host material used for studying the luminescent properties of rare-earth and transition metal ions because it has good optical and mechanical properties as well as good chemical durability. Scintillating glasses can be used for the detection of X-rays, γ-rays and neutrons [1–3]. They are cheaper and easier to fabricate with respect to single crystal materials, but they suffer from inefficient energy transfer and concentration quenching resulting in low light yield. The concentration quenching is closely related to the phenomenon of phase separation, which occurs mainly during glass melting [4]. Solubility of rare-earth (RE) ions is low in silica glass prepared by direct high-temperature melting of RE compounds and raw materials of glass, and easily leads to segregation or phase separation even at low concentration.

In order to suppress concentration quenching of emission ions to obtain intense luminescence glass, our group have developed a novel method based on fabrication and sintering technique for uniform distribution of RE ions in high silica glass host [5–7]. In contrast to the direct introduction of RE ions into silica glasses by high-temperature melting, a three-step process was employed including preparation of a porous silica glass, adsorption of RE ions and high-temperature sintering in a reducing atmosphere. With very large specific surface area and uniform distribution of the pore channels of the obtained porous glass, the RE dopants can be adsorbed and distributed uniformly in the glass host. After sintering, the dense nonporous glass was obtained with uniform distribution of RE ions, bound to non-bridging oxygen (NBO) in the form of RE–O–Si or RE–O–Al in the glass host. Very intense luminescence emissions were observed in the leached, sintered high silica glasses impregnated with Tb^{3+} [8,9] and Eu^{2+} [3,10,11] ions under UV excitation. It showed that this novel method can uniformly distribute the RE dopants in the glass host without clusters occurring in the form of RE–O–RE bonds. Clustering facilitates energy migration among RE ions resulting in luminescence quenching due to the interaction between the emission ions. It confirmed the success in solving the mentioned problem of concentration quenching of emission ions.

The 5d → 4f emission of Ce^{3+} occurs usually at shorter wavelength range than that of Eu^{2+} when both ions are at same host lattice site. Moreover, the fully allowed luminescence transition of Ce^{3+} is faster than that of Eu^{2+}. This feature makes the Ce^{3+}-doped inorganic materials good candidates for fast scintillators [12]. In this paper, we prepared Ce^{3+}-doped high silica glass by impregnation of Ce ions into a porous silica glass followed by high temperature sintering in a CO reducing atmosphere and investigated its luminescence characteristics under UV and X-ray excitation. In order to evaluate its potential in scintillation applications, the integral scintillation efficiency and scintillation light yield (LY) were also determined.

* Corresponding authors. Tel.: +66 2470 8944; fax: +66 2470 8900.
E-mail addresses: weerapong.che@kmutt.ac.th (W. Chewpraditkul), d-chen@mail.siom.ac.cn (D. Chen).

0925-3467/$ - see front matter © 2012 Elsevier B.V. All rights reserved.
http://dx.doi.org/10.1016/j.optmat.2012.04.012

2. Experimental

The porous glass was obtained by leaching the alkaliborate phase from phase-separated alkali - borosilicate glass in hot acid solution [5–7]. Reagent-grade chemicals SiO_2, H_3BO_3, Na_2CO_3, $CaCO_3$, and $Al(OH)_3$ were used as starting materials in a solid-state reaction to produce an initial glass. The initial glass with the composition (in wt.%) $51.8SiO_2{\cdot}33.3B_2O_3{\cdot}2.6Al_2O_3{\cdot}4.0CaO{\cdot}8.3Na_2O$ was melted in a platinum crucible at 1400 °C for 4 h. The melt was then poured onto a preheated stainless steel plate and pressed to a thickness of about 2 mm by another plate. Phase separation of alkaliborate and silicate phases was performed at 590 °C for 40 h. The obtained phase-separated glass was cut to pieces and polished with dimension of about $8 \times 8 \times 1$ mm^3, followed by leaching in hot (90 °C) 1 N HNO_3 acid solution for 48 h. After washing with distilled water and drying, then porous glasses were obtained. The obtained porous glass contains over 96% of SiO_2 [5,6] and is therefore called high silica glass. The pores smaller than 12 nm were distributed uniformly in the silica network and occupied about 40% volume of glass. The porous glasses were immersed in the 0.03 M solution of $Ce(NO_3)_3{\cdot}6H_2O$ for 1 h and dried at room temperature (RT) and then sintered at 1100 °C in a CO reducing atmosphere for 2 h to obtain nonporous glasses. The obtained Ce glasses are colorless and transparent with the density of 2.2 g/cm^3 determined by Archimedes method. Intense violet–blue emission was visibly observed for the Ce glass sample under excitation with 254-nm UV light from a mercury lamp, as shown in Fig. 1. The homogeneous luminescence of Ce glass sample together with a high quantum efficiency of about 80% [6] confirming the uniform distribution of the Ce^{3+} ions in the glass host, thus reducing the Ce^{3+} clusters that lowers fluorescence yield. However, the small inhomogeneity of the Ce^{3+} sites in the host glass was noted, which was reflected in minor luminescence characteristics variation (up to 10–15% relative change) of different samples prepared from the same parent glass.

Excitation and emission spectra in the UV/visible region were recorded on a Hitachi F-2500 fluorescence spectrophotometer equipped with a 150 W xenon lamp source. Absorption spectrum in the UV/visible region was recorded on a Shimadzu UV-3101PC absorption spectrometer. Radioluminescence (RL) spectra and photoluminescence (PL) decays were obtained using the custom made 5000 M fluorometer, Horiba Jobin Yvon, equipped with X-ray tube (steady-state tube, 40 kV, Mo anode) and pulsed (ns) coaxial H_2 – flashlamp as excitation sources, for details see Ref. [13]. RL spectra were corrected for the wavelength dependence of the photodetector quantum efficiency as well as of the monochromator transmission. The integrated RL spectra measured at the samples of the same size and same experimental conditions provide a good relative estimate of scintillation efficiency of our glass sample compared to commercial $Bi_4Ge_3O_{12}$ (BGO) scintillation crystal used as a reference. LY measurements were performed under the excitation of 662 keV γ-rays from a ^{137}Cs source using a photomultiplier (PMT)-based setup described in [14]: The signal from the PMT anode was passed to a Canberra 2005 preamplifier and then to a Tennelec TC243 spectroscopy amplifier set at 4 μs shaping time constant. The PC-based multichannel analyzer (Tukan 8 k MCA) was used to record the pulse height spectrum. BGO and CeF_3 scintillation crystals with size of $8 \times 8 \times 1$ mm^3 were used as a reference. Furthermore, LY measurement was also performed under the excitation of 5.1566 MeV alpha particles from a ^{239}Pu source and a setup with hybrid photomultiplier (HPMT) [15]. All the measurements were carried out at RT.

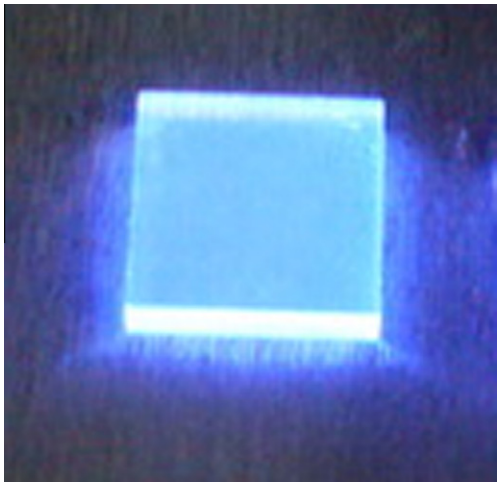

Fig. 1. Photograph of Ce^{3+}-doped silica glass sample under 254-nm UV excitation.

3. Results and discussion

3.1. Photoluminescence of Ce^{3+}-doped silica glass

Fig. 2 presents the absorption (curve a), excitation (curves b and c) and emission (curve d) spectra at RT for the Ce^{3+}-doped silica glass sintered in a reducing (CO) atmosphere. In the absorption and excitation spectra, a broad band peaking at approximately 300 nm can be attributed to the absorption due to the $4f \rightarrow 5d$ transitions of Ce^{3+} ions. The higher lying absorption band with an absorption edge around 240 nm is not reflected in the excitation spectrum for the Ce^{3+} emission, so that it might be related to the glass–host absorption. Alternatively, the higher lying 5d states of Ce^{3+} might be situated in the host conduction band and the excitation into them leads rather to the excited Ce^{3+} ionization followed by its nonradiative return to ground state.

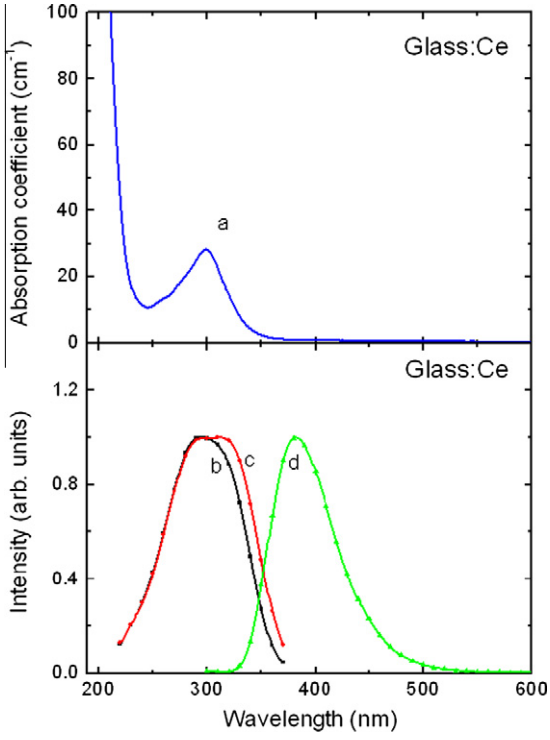

Fig. 2. Absorption (a), excitation (λ_{em} = 380 nm for curve b and λ_{em} = 420 nm for curve c) and emission (λ_{ex} = 295 nm, curve d) spectra of Ce^{3+}-doped silica glass sintered in a reducing (CO) atmosphere as measured at RT.

Characteristic broad emission band of Ce^{3+} is peaking around 375 nm under 295 nm excitation (curve d), but it is worth to note that the band is inhomogeneously broadened as its excitation spectrum shows small low energy shift when emission wavelength is set longer (curve c). This is rather typical situation of Ce^{3+} center in glassy environment, in which the change in the short distance order and eventual defects nearby will shift position of $5d_1$ level and/ or change its relaxation pathway. Usually, the emission of Ce^{3+} ions occurs as a doublet band due to transitions from the relaxed lowest 5d excited state to the spin–orbit split 4f ground states ($^2F_{5/2}$, $^2F_{7/2}$). At RT, these two bands merge into an asymmetric broad band because of the large spatial extension of the 5d wavefunction and its interaction with lattice vibrations.

The PL decay curves of the Ce^{3+}-doped silica glass measured at RT are shown in Fig. 3. Each decay curve can be well fitted with a double-exponential equation, $I(t) = \Sigma A_i \exp(-t/\tau_i) + \text{background}$, $i = 1,2$, where $I(t)$ is the luminescence intensity, A stands for the amplitude, t for the time and τ for the decay time constant of the exponential component. The PL decay at 370 nm under excitation at 290 nm (Fig. 3a) yields the decay times $\tau_1 = 49.6$ ns and $\tau_2 = 147$ ns with respective component intensities $I_i = (A_i\tau_i)/(\Sigma A_i\tau_i)$, namely, $I_1 = 93\%$ and $I_2 = 7\%$, respectively. The PL decay at longer wavelength of 440 nm under excitation with 320 nm (Fig. 3b) yields the decay times $\tau_1 = 67.7$ ns and $\tau_2 = 255$ ns with respective component intensities $I_1 = 95\%$ and $I_2 = 5\%$, respectively. Increasing decay time value at longer emission wavelength is consistent with the above mentioned inhomogeneous broadening of Ce^{3+} emission band, indicating non-equivalent Ce^{3+} centers due to defects nearby, glassy host environment or similar reasons. While τ_1 decay times are typical for the $5d_1 \rightarrow 4f$ radiative transition of Ce^{3+} [16] there is no immediate explanation of longer τ_2 ones though respective component amplitude is very small.

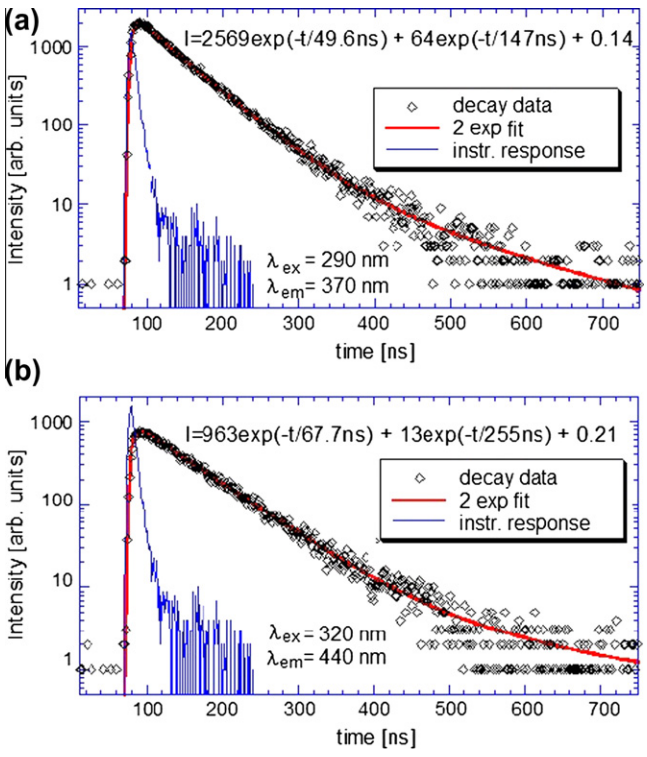

Fig. 3. PL decay curves of the Ce^{3+}-doped silica glass as measured at RT [(a) $\lambda_{ex} = 290$ nm, $\lambda_{em} = 370$ nm and (b) $\lambda_{ex} = 320$ nm, $\lambda_{em} = 440$ nm]. The solid lines are the convolution of the instrumental response and the function $I(t)$ given in the figures.

Somewhat non-exponential decay of Ce^{3+} center in Fig. 3 and varying τ_1 values with emission wavelength are worth a comment. Similar phenomena can be noticed in the silica glasses doped with Ce^{3+} ions [17,18] and Eu^{2+} ions [3]: the 5d excited state of both Ce^{3+} and Eu^{2+} is sensitive to symmetry, short-range order and crystal field strength at a given site of host glass. Due to glass matrix, the dopant is embedded at a number of slightly non-equivalent sites, the emission band broadens inhomogeneously and the decay time value varies as well. Nevertheless, the decay non-exponentiality is rather small (note quite low I_2 intensity of the decay component associated with longer τ_2 decay times) and observed shift in the excitation spectra as well which means that the inhomogeneity of the Ce^{3+} sites is rather small.

3.2. Radioluminescence of Ce^{3+}-doped silica glass

RL spectra of a Ce^{3+}-doped silica glass and a BGO reference crystal recorded at RT are shown in Fig. 4. The Ce glass shows a broad emission band peaking around 375 nm due to the $5d_1 \rightarrow 4f$ transitions of Ce^{3+}. Note a nearly coinciding position and shape for PL and RL spectra (Figs. 2 and 4) of Ce glass. This result further confirms rather small inhomogeneity of the Ce^{3+} sites in the host glass. The Ce glass and BGO crystal are the same size and the measurements were performed in the same experimental conditions, so that the spectra can be compared in an absolute way. The integral scintillation efficiency (integral of RL spectra) of the Ce glass is about 105% of that of the BGO crystal, determined from the ratio of its integrated RL intensity to that of the BGO reference sample.

LY measurements were performed by measuring pulse height spectra of 662 keV γ-rays from a ^{137}Cs source. The sample was coupled by silicone grease to the Photonis XP5200B PMT and covered with several layers of Teflon tape in a configuration of a reflective umbrella for better light collection. Fig. 5 presents the pulse height spectra of 662 keV γ-rays from a ^{137}Cs source as measured with Ce glass, CeF_3 and BGO crystals, but with lower amplification gain factor of 0.18 for BGO.

The intensity in a scintillation pulse (x-axis), expressed as a number of photoelectrons released from the PMT photocathode, was obtained by relating the position of a photopeak of 662 keV γ-rays detected in the BGO or CeF_3 crystals with that of the single photoelectron peak from the PMT photocathode [14,19]. We obtained photoelectron yield of 1850 and 260 photoelectrons/MeV (phe/MeV) for BGO and CeF_3 crystals, respectively. By taking into account the quantum efficiency (QE) of the PMT for the BGO (21% at peak emission 480 nm) and CeF_3 (6% at peak emission 290 nm), we estimated the LY of 8810 and 4330 photons/MeV

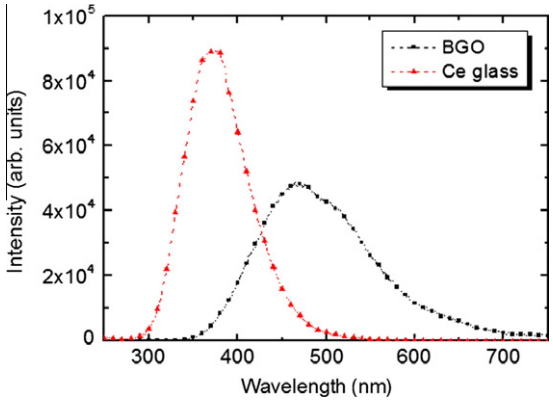

Fig. 4. RL spectra (X-ray excitation: 40 kV, 15 mA) of Ce^{3+}-doped silica glass and BGO crystal as measured at RT. The spectra are mutually comparable in an absolute way.

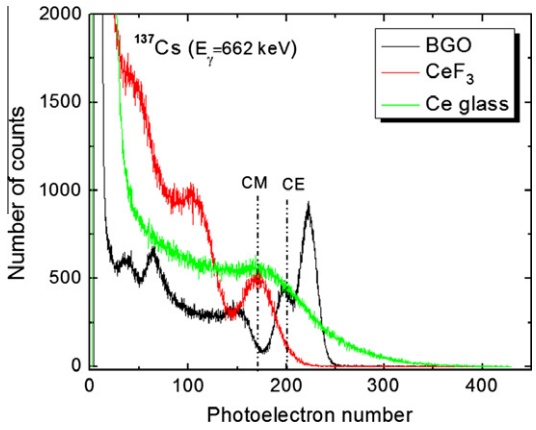

Fig. 5. Pulse height spectra of 662 keV γ-rays from a ^{137}Cs source as measured with Ce glass, CeF_3 and BGO (with a lower gain factor of 0.18) crystals.

(ph/MeV), respectively, for BGO and CeF_3 crystals which goes perfectly well with the earlier reported values [12,20]. Unfortunately, Ce glass shows only the Compton continuum (CC) with the absence of 662 keV photopeak in the pulse height spectrum. This is due to low density and effective atomic number of the glass matrix. However, we can estimate the LY of Ce glass using the position of Compton edge (CE), which corresponds to a maximum energy of Compton electron (E_e = 477 keV), in the pulse height spectrum of 662 keV γ-rays. It must be noted that exact position of CE in the CC is not located at the same position with Compton maximum (CM) but it slightly shifts to higher energy shoulder [21]. A rough estimate of the CE position for a low density glass scintillator can be obtained by assuming a value of 0.8 [21] for a fraction of CM at which CE crosses the CC spectrum (see Fig. 5). We estimated the photoelectron yield of 420 phe/MeV (at E_e = 477 keV). This value corresponds to the LY of 1410 ph/MeV by taking into account a QE of 30% for the PMT at peak emission (375 nm) of the Ce glass. In spite of comparable integral scintillation efficiency under X-ray irradiation ($E_x \leqslant 40$ keV), the scintillation LY of the Ce glass is much lower, i.e. about 16% of that of BGO crystal (as measured at integrating time of 4 μs) under excitation with high energy (662 keV) γ-rays from a ^{137}Cs source.

We further completed LY measurement using the 5.1566 MeV alpha particles from a ^{239}Pu source. Though LY under alpha excitation is typically several times lower with respect to the gamma-excited one due to high energy density in the ionization track, short attenuation path of the order of 10 μm assures total energy absorption even in thin sample of low density. In Fig. 6 the full energy peak in pulse height spectra of the 5.1566 MeV alpha particles as measured with BGO crystal (a) and Ce glass (b) is shown with *x*-axis calibrated in number of photoelectrons. We obtained photoelectron yield of 148 and 78 phe/MeV for BGO and Ce glass, respectively. By taking into account the QE of the HPMT for the BGO (16% at peak emission 480 nm) and Ce glass (24% at peak emission 375 nm), we estimated the LY of 920, and 320 ph/MeV, respectively, for BGO and Ce glass. It is interesting to note relatively higher LY of Ce glass with respect to BGO in case of alpha excitation which points to comparatively lower energy losses in the ionization track of the former material.

Due to clearly obtained full energy peak of the 5.1566 MeV alpha particles as measured with Ce glass, LY dependence on shaping time could be measured and compared with BGO which gives an indication about the presence of slower components in scintillation response, as shown in Fig. 7. Assuming double exponential decay (for simplicity), normalized LY dependence on shaping time was fitted using function: $LY = m_1 - m_2 \exp(-m_3 t)$,

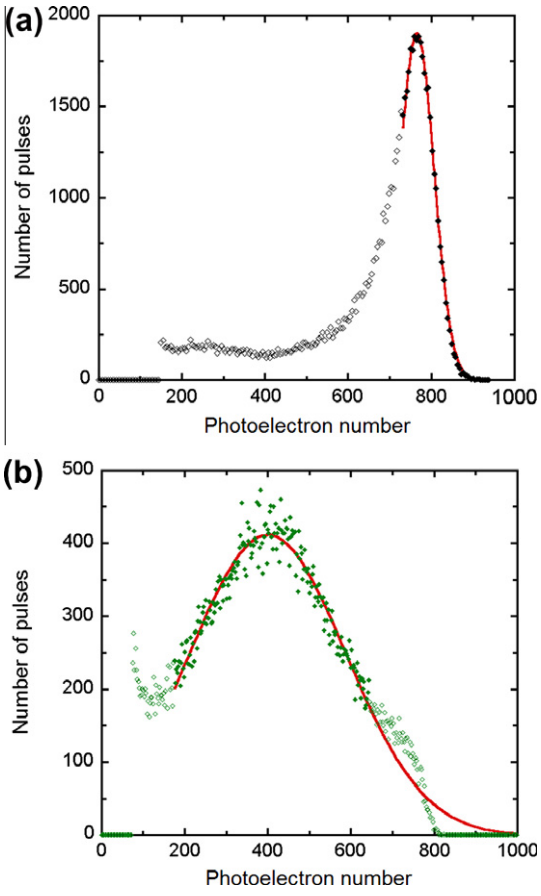

Fig. 6. Pulse height spectra of 5.1566 MeV alpha particles from a ^{239}Pu source as measured with BGO crystal (a) and Ce glass (b). The experimental data indicated by solid symbols and the Gaussian function fit by solid line to determine the peak positions.

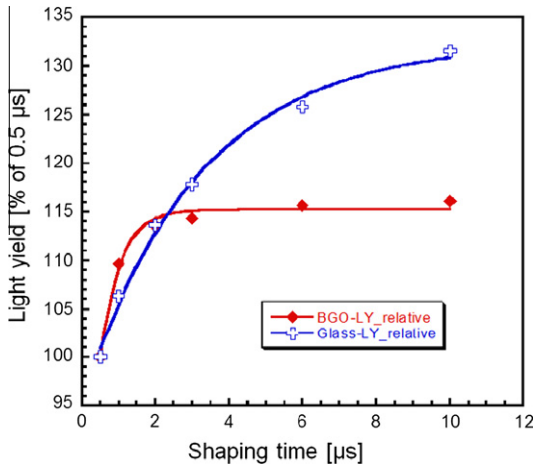

Fig. 7. Dependence of normalized photoelectron yield on the shaping time duration under excitation with 5.1566 MeV alpha particles from a ^{239}Pu source as measured for BGO crystal and Ce glass.

where m_i are fitting parameters. m_1 represents the relative increase of scintillation response with respect to response of shaping time τ = 0.5 μs. Additionally, $1/m_3$ is time constant of slow response component, i.e. reflects the speed of response saturation [22]. While the LY dependence of BGO is mainly due to its relatively long PL decay time (300 ns), m_1(BGO) = 115% ± 1%,

Table 1
Photoelectron yield and light yield for Ce^{3+}-doped silica glass, CeF_3 and BGO crystals as measured using ^{137}Cs (^{239}Pu) source.

Scintillator	Photoelectron yield (phe/MeV)	Light yield (ph/MeV)
BGO	1850 ± 90 (148 ± 10)	8810 ± 880 (920 ± 90)
CeF_3	260 ± 10	4330 ± 430
Ce glass	420 ± 20 (78 ± 6)	1410 ± 140 (320 ± 30)

$1/m_3$(BGO) = 550 ± 90 ns, in case of the Ce glass it is mainly coming from timing characteristics in the transport stage of scintillation mechanism as the PL decay time of Ce^{3+} is much shorter (50–70 ns, see Fig. 3), m_1(glass) = 132% ± 2%, $1/m_3$(glass) = 3180 ± 450 ns. Taken together, this effect and short-range order of glass matrix indicate that energy transfer efficiency of scintillating glasses is much lower with respect to single crystal materials, thus reducing scintillation LY of the Ce glass. The results summarizing the photoelectron yield and LY measured for Ce^{3+}-doped glass, CeF_3 and BGO crystals are presented in Table 1.

4. Conclusions

The Ce^{3+}-doped high silica glass with small inhomogeneity of Ce sites and high radioluminescence intensity was successfully prepared by impregnation of $Ce(NO_3)_3$ solution into a porous silica glass and sintered at high temperature in a CO reducing atmosphere. It exhibits an intense violet–blue emission of Ce^{3+} ions peaking around 375 nm under UV and X-ray excitation with a fast luminescence decay time of about 50 ns. Moreover, it shows a high integral scintillation efficiency under X-ray irradiation comparable to that of the BGO crystal while the LY of about 16% and 35% of that of the BGO is obtained under excitation with 662 keV γ-rays and 5.1566 MeV alpha particles, respectively. Dependence of light yield on shaping time shows under the double exponential approximation a slower component with a 3.2 μs scintillation decay time due to energy transfer from the glass matrix to Ce^{3+} activator. In terms of the overall scintillation efficiency, this Ce^{3+}-doped silica glass prepared by such a unique technology appears to be clearly superior than the Ce^{3+}-doped traditional melt glass [23]. It seems worthwhile to enhance the scintillation efficiency further, e.g. by optimizing the concentrations of Ce^{3+} and Gd^{3+} co-doping in the silica glass, which employs the efficient energy transfer from Gd^{3+} to Ce^{3+}. It could be useful for developing new UV and X-ray sensors or phosphors.

Acknowledgements

This work is financially supported by the NRCT–NSFC project (NSFC Nos. 60878043 and 50911140475), the TICA-MOST project (No. 19-502J) and the NRU project of Thailand's Office of the Higher Education Commission. Partial support of Czech MSMT KONTAKT II Grant LH12185 is also gratefully acknowledged.

References

[1] G. Zanella, R. Zannoni, R. Dall'Igna, P. Polato, M. Bettinelli, Nucl. Instrum. Methods Phys. Res. A 359 (1995) 547.
[2] M. Nikl, K. Nitsch, E. Mihokova, N. Solovieva, J.A. Mares, P. Fabeni, G.P. Pazzi, M. Martini, A. Vedda, S. Baccaro, Appl. Phys. Lett. 77 (2000) 2159.
[3] W. Chewpraditkul, D. Chen, B. Yu, Q. Zhang, Y. Shen, M. Nikl, R. Kucerkova, A. Beitlerova, C. Wanarak, A. Phunpueok, Phys. Status Solidi RRL 5 (2011) 40.
[4] V. McGahay, M. Tomozawa, J. Non-Cryst. Solids 159 (1993) 246.
[5] J. Xia, D. Chen, J. Qiu, C. Zhu, Opt. Lett. 30 (2005) 47.
[6] D. Chen, H. Miyoshi, T. Akai, T. Yazawa, Appl. Phys. Lett. 86 (2005) 231908.
[7] W. Liu, D. Chen, H. Miyoshi, K. Kadono, T. Akai, Chem. Lett. 34 (2005) 1176.
[8] W. Liu, D. Chen, H. Miyoshi, K. Kadono, T. Akai, J. Non-Cryst. Solids 352 (2006) 2969.
[9] W. Liu, D. Chen, T. Akai, Mater. Chem. Phys. 109 (2008) 257.
[10] D. Chen, L. Yang, M. Peng, C. Wang, N. Da, Y. Qiao, Q. Zhou, C. Zhu, T. Akai, J. Rare Earths 24 (2006) 191.
[11] Q. Zhang, X. Liu, Y. Qiao, B. Qian, G. Dong, J. Ruan, Q. Zhou, J. Qiu, D. Chen, Opt. Mater. 32 (2010) 427.
[12] C.W.E. van Eijk, J. Andriessen, P. Dorenbos, R. Visser, Nucl. Instrum. Methods Phys. Res. A 348 (1994) 546.
[13] H. Feng, V. Jary, E. Mihokova, D. Ding, M. Nikl, G. Ren, H. Li, S. Pan, A. Beitlerova, R. Kucerkova, J. Appl. Phys. 108 (2010) 033519.
[14] M. Moszynski, M. Kapusta, M. Mayhugh, D. Wolski, S.O. Flyckt, IEEE Trans. Nucl. Sci. 44 (1997) 1052.
[15] J.A. Mares, A. Beitlerova, M. Nikl, N. Solovieva, K. Nitsch, M. Kucera, M. Kubova, V. Gorbenko, Y. Zorenko, Rad. Meas. 42 (2007) 533.
[16] G. Blasse, B.C. Grabmaier, Luminescent Materials, Springer, Berlin, Germany, 1994. p. 46.
[17] A. Vedda, N. Chiodini, D. Di Martino, M. Fasoli, S. Keffer, A. Lauria, M. Martini, F. Moretti, G. Spinolo, M. Nikl, N. Solovieva, G. Brambilla, Appl. Phys. Lett. 85 (2004) 6356.
[18] A. Vedda, N. Chiodini, D. Di Martino, M. Fasoli, F. Morazzoni, F. Moretti, R. Scotti, G. Spinolo, A. Baraldi, R. Capelletti, M. Mazzera, M. Nikl, Chem. Mater. 18 (2006) 6178.
[19] M. Bertolaccini, S. Cova, C. Bussolatti, A technique for absolute measurement of the effective photoelectron per keV yield in scintillation counters, in: Proc. Nuclear Electronics Symp., Versailles, France, 1968.
[20] M. Moszynski, T. Ludziejewski, D. Wolski, W. Klamra b, L.O. Norlin, Nucl. Instrum. Methods Phys. Res. A 345 (1994) 461.
[21] L. Swiderski, M. Moszynski, W. Czarnacki, J. Iwanowska, A. Syntfeld-Kazuch, T. Szczesniak, G. Pausch, C. Plettner, K. Roemer, Rad. Meas. 45 (2011) 605.
[22] P. Prusa, M. Nikl, J.A. Mares, M. Kucera, K. Nitsch, A. Beitlerova, Phys. Status Solidi A 206 (2009) 1494.
[23] W. Chewpraditkul, H. Xe, D. Chen, Y. Shen, Q. Zhang, B. Yu, M. Nikl, R. Kucerkova, A. Beitlerova, C. Wanarak, A. Phunpueok, Phys. Status Solidi A 208 (2011) 2830.

Journal of Crystal Growth 337 (2011) 72–80

Contents lists available at SciVerse ScienceDirect

Journal of Crystal Growth

journal homepage: www.elsevier.com/locate/jcrysgro

Growth and luminescent properties of Lu_2SiO_5:Ce and $(Lu_{1-x}Gd_x)_2SiO_5$:Ce single crystalline films

Yu. Zorenko [a,b,*], V. Gorbenko [b], V. Savchyn [b], T. Voznyak [b], B. Grinyov [c], O. Sidletskiy [c], D. Kurtsev [c], A. Fedorov [c], V. Baumer [c], M. Nikl [d], J.A. Mares [d], A. Beitlerova [d], P. Prusa [d], M. Kucera [e]

[a] Institute of Physics, Kazimierz Wielki University in Bydgoszcz, Weyssenhoffa sq., 11, Bydgoszcz 85-090, Poland
[b] Laboratory of Optoelectronic Materials (LOM), Department of Electronics of Ivan Franko National University of Lviv, Gen. Tarnavskyj str. 107, Lviv 70017, Ukraine
[c] Institute for Scintillation Materials, National Academy of Sciences of Ukraine, Lenina pr. 60, Kharkiv 61001, Ukraine
[d] Institute of Physics Academy of Sciences of Czech Republic, 10 Cukrovarnicka str. 10, 162 53 Prague, Czech Republic
[e] Charles University, Faculty of Mathematics and Physics, Ke Karlovu 5, 12116 Prague 2, Czech Republic

ARTICLE INFO

Article history:
Received 20 June 2011
Received in revised form
27 September 2011
Accepted 1 October 2011
Communicated by A. Ohtomo
Available online 10 October 2011

Keywords:
A1. Luminescence
A1. Single crystalline films
A3. Liquid phase epitaxy
B3. Scintillators
B1. Orthosilicates
A1. Ce^{3+} dopant

ABSTRACT

Single crystalline films (SCF) of Lu_2SiO_5:Ce (LSO:Ce), $(Lu_{1-x}Gd_x)_2SiO_5$:Ce (LGSO:Ce) and LGSO:Ce,Tb orthosilicates with thickness of 2.5–21 μm were crystallized by liquid phase epitaxy method onto undoped LSO substrates from melt-solution based on $PbO–B_2O_3$ flux. The concentration of Gd was varied in the range of $x=0.2–0.7$ formula units (f.u.). In the case of LGSO:Ce SCF growth we do not use any additional doping for reducing the misfit between the SCF and substrate lattices. The luminescence and scintillation properties of LSO:Ce, LGSO:Ce and LGSO:Ce,Tb SCFs were mutually compared and confronted with the performance of reference LSO:Ce and LYSO:Ce crystals. With increasing Gd content the luminescence spectrum of LGSO:Ce SCF is gradually red-shifted with respect to that of LSO:Ce SCF. The LY of $(Lu_{1-x}Gd_x)$SO:Ce SCF becomes lower in comparison with that for LSO:Ce SC at increasing Gd content in the range of $x=0.2–0.7$ f.u. The peculiarities of luminescence properties of LSO:Ce and LGSO:Ce SCFs in comparison with crystal analogs are explained by the different distribution of Ce^{3+} over Lu1 and Lu2 positions of LSO host and by the influence of Pb^{2+} contamination coming from the flux used for the film growth.

1. Introduction

The liquid phase epitaxy (LPE) is a beneficial method for the development of different luminescent materials based on single crystalline films (SCF) of oxide compounds (garnets, perovskites, silicates, tungstates and sapphire) [1]. The SCF of mentioned compounds activated by RE ions and other dopants can be applied as laser media [1], cathodoluminescent screens [2,3], α- and β-scintillators [4,5], screens for visualization of X-ray images [6–12] and "white LED" phosphors [13].

The single crystals (SC) of Lu_2SiO_5:Ce (LSO:Ce) are under development for about two decades [14,15] and became excellent scintillators to be applied in Positron Emission Tomography (PET) [16]. To improve the scintillation properties of LSO:Ce crystals, degraded by presence of the oxygen vacancies acting as electron trapping centers [17,18], the Gd-admixed $(Lu_{1-x}Gd_x)_2SiO_5$:Ce (LGSO:Ce) [19,20] and Y-admixed $(LuY)_2SiO_5$:Ce SC scintillators [21,22] were also developed. The increase of the distance between Ce^{3+} ions as emission centers and oxygen vacancies as trapping center in LGSO:Ce and LYSO:Ce SCs might be one of the reasons of the observed significant decrease of the content of slow components in scintillation decay of the latter crystals with respect to LSO:Ce SC [17–22].

The Lu_2SiO_5 orthosilicate host has significantly higher density ($\rho=7.4$ g/cm^3) and effective atomic number ($Z_{eff}=66$) [7,8,16] as compared to commonly used $Y_3Al_5O_{12}$ and $Lu_3Al_5O_{12}$ garnets ($\rho=4.6$ and 6.7 g/cm^3, $Z_{eff}=29$ and 61, respectively) so that it appears advantageous for producing SCFs scintillators [7,8,12]. Therefore, this matrix attracts special attention as an excellent host for preparation of SCF scintillators emitting in the blue range [23–25].

Recently, the growth of LSO:Ce SCF scintillators onto LSO substrates by LPE method were briefly reported by us [23]. The growth of LSO:Tb, LSO:Tb,Ce and LYSO:Ce SCFs was also reported in [24,25]. Test of these SCF screens for visualization of X-ray image was also made [24,25]. The result of work [23,24] shows that the LSO:Tb SCF screens have excellent spatial resolution of X-ray image up to 0.8 FWHM. Co-doping of LSO:Tb SCF with Ce^{3+} ions is also very efficient and leads to an increase of the conversion

* Corresponding author at: Institute of Physics, Kazimierz Wielki University in Bydgoszcz, Weyssenhoffa sq., 11, Bydgoszcz 85-090, Poland.
E-mail address: zorenko@ukw.edu.pl (Yu. Zorenko).

0022-0248/$ - see front matter © 2011 Elsevier B.V. All rights reserved.
doi:10.1016/j.jcrysgro.2011.10.003

ability of LSO:Tb,Ce screens as compared to LSO:Tb SCF [25]. The double epitaxial structures consisting of LYSO:Ce and LSO:Tb films were also prepared by LPE method with the emission extending over the blue and green ranges [25].

It is known from the growth of bulk LSO:Ce SC that due to the relatively large ionic radius, the Ce^{3+} ions are localized preferably (up to 95%) in the 7-fold coordinated by oxygen ions Lu1 positions and to a much lesser extent in the smaller, 6-fold coordinated by oxygen ions Lu2 position of LSO lattice [26,27] (further noted as Ce(Lu1) and Ce(Lu2) centers, respectively). The Gd^{3+} and Y^{3+} ions incorporation change the Ce^{3+} relative distribution over Lu1 and Lu2 positions and leads to the respective changes in the emission spectra of LGSO:Ce and LYSO:Ce crystals [19,20]. Therefore, it appears interesting to compare the distribution of Ce^{3+} ions over the Lu1 and Lu2 positions of LSO host in LSO:Ce and LGSO:Ce SCF grown by LPE method at significantly lower ($\sim$1000 °C) temperatures with that in their SC counterparts grown at much high-temperatures by Czochralski methods.

In this work, we study the growth processes of Ce^{3+} doped LSO and LGSO SCF by LPE method. The main attention is paid to the possibility of growth of the $(Lu_{1-x}Gd_x)_2SiO_5$:Ce SCFs with different Gd content in range of $x=0.2$–0.7 by LPE method *on the substrates prepared from undoped LSO crystals*. We further studied the luminescent and scintillation properties of LSO:Ce and LGSO:Ce SCF and compared them with the properties of reference bulk LSO:Ce and LYSO:Ce SCs grown by Czochralski method. We expect that Ce-doped orthosilicates can provide larger light yield (LY) with respect to previously studied SCF systems.

2. Growth of LSO:Ce, LGSO:Ce and LSO:Ce,Tb SCF

One set of nominally undoped LSO SCF (**a** series), five sets of LSO:Ce (**b** series), five sets of LGSO:Ce SCFs (**c** and **d** series) and two sets of LGSO:Ce,Tb SCF (**e** series) with dimensions of 0.5×0.5 cm^2 and thickness between 2.5 and 21 μm (see Tables 1 and 2) were grown at LOM, Lviv University using the LPE method from super-cooled melt-solution (MS) based on $PbO:B_2O_3$ (12:1 mol/mole) flux onto undoped LSO substrates, prepared in ISMA, Kharkiv. The orientation of LSO substrates for the growth of LSO:Ce and LGSO:Ce SCF was arbitrarily chosen along (22-3) plane with the deviation of about 2° (Table 3).

Table 1
The growth conditions of LSO:Ce SCF (h—SCF thickness, f_g—SCF growth rate, T_g—temperature of SCF growth) as well as the LY of LSO:Ce SCFs in comparison with reference LSO:Ce and LYSO:Ce SC samples under excitation by α-particles of ^{241}Am sources (5.5 MeV), measured with the shaping time of 3.0 μs; n.m.—samples not measured.

Samples content	Samples number	CeO_2 conent in MS, mol%	Ce/Pb content in SCF, at%	Lu/Si ratio in MS	h	f_g, μm/min	T_g, °C	LY RL, %
Lu_2SiO_5 SCF	a2	–	0.04	2:01	2.5 μm	0.035	1015	–
	a6	–			5.5 μm	0.06	1005	–
Lu_2SiO_5:Ce SCF	b7	5		2:01	8.2 μm	0.041	1005	35
	b8				6.7 μm	0.035	1010	78
Lu_2SiO_5:Ce SCF	b9	10	0.043/0.018	2:01	5.9 μm	0.02	1015	87
	b10		0.047/0.033		10 μm	0.05	1005	60
Lu_2SiO_5:Ce SCF	b11	20		2:01	5.5 μm	0.024	1015	110
	b12				5.4 μm	0.03	1005	87
Lu_2SiO_5:Ce SCF	b13	14		2:03	21 μm	0.12	1015	n.m.
	b14				12.8 μm	0.07	1025	112
	b15				16 μm	0.09	1020	45
Lu_2SiO_5:Ce SCF	b16	14		3:07	7.6 μm	0.042	1030	145
Lu_2SiO_5:Ce SC	20-08		0.2/–		0.6 mm		2030	100
$(LuY)_2SiO_5$:Ce SC	R		n.m.		0.5 mm		~2000	282

Table 2
The growth conditions and LY of LGSO:Ce SCF (similarly to Table 1).

Samples content	Samples number	CeO_2/Tb_4O_7 content in MS, mole%	Gd/Ce(Tb)/Pb content in SCF, at%	Lu/Si ratio in MS	h	f_p, μm/min	T_g, °C	LYRL, %
$(Lu_{0.3}Gd_{0.7})_2SiO_5$:Ce, SCF	c1	1.5/–	12.46/0.025/0.045	3:07	3.5 μm	0.034	1003	50
	c3				2.8 μm	0.065	987	
	c4				3.2 μm	0.045	998	
$(Lu_{0.5}Gd_{0.5})_2SiO_5$:Ce, SCF	d1	1.5/–	10.23/0.08/0.105	3:07	10 μm	0.055	990	57
	d2				12 μm	0.045	995	
	d3				6.5 μm	0.04	998	
$(Lu_{0.5}Gd_{0.5})_2SiO_5$:Ce, SCF	d4	15/–	11.8/0.16/0.105	3:07	5.3 μm	0.024	1000	67
	d5				4.7 μm	0.038	994	
$(Lu_{0.6}Gd_{0.4})_2SiO_5$:Ce, SCF	d6	15/–	9.24/0.07/0.07	3:07	2.5 μm	0.07	997	77
	d8				5.4 μm	0.09	998	
$(Lu_{0.8}Gd_{0.2})_2SiO_5$:Ce, SCF	d10	15/–	5.47/0.045/0.22	3:07	8 μm	0.09	993	87
	d12				11.5 μm	0.023	1003	
$(Lu_{0.8}Gd_{0.2})_2SiO_5$:Ce, Tb SCF	e13	15/1.5	5.49/0.04/(0.93)/0.39	3:07	8.9 μm	0.07	994	
	e14				4.5 μm	0.12	988	68
	e15				4.5 μm	0.18	982	
$(Lu_{0.8}Gd_{0.2})_2SiO_5$:Ce, Tb SCF	e16	15/1.5		3:07	12.5 μm	0.06	995	
	e17				~2.0 μm	0.02	1000	48
	e18				4.8 μm	0.11	989	
Lu_2SiO_5:Ce, SC	20-08	~0.2	0.2		0.6 mm			100

Half-width of the substrate (22-3) reflection was obtained using double crystal spectrometer with Si (400) monochromator and evaluated to 0.026°.

For the growth of $(Lu_{1-x}Gd_x)_2SiO_5$ SCF, the Gd_2O_3 oxide was added in MS in concentrations, corresponding to calculated values $x=0.2$, 0.4, 0.5 and 0.7 formula units (f.u.). It is important to note that for the growth of these SCFs we do not use any additional doping to decrease significant lattice mismatch (from 0.55 up to 1.36%) between the LSO substrate and $(Lu_{1-x}Gd_x)_2SiO_5$ SCFs when changing the Gd_2O_3 concentration in MS from $x=0.2$ to $x=0.7$ (see Table 1). For explanation of that antiviral growth phenomenon we tentatively suggest that the crystallization of LGSO SCFs onto LSO substrates at such significant mismatch is enabled due to the formation of a transition layer (TL) onto SCF-substrate interface where the difference between the lattice constants of LGSO and LSO host can be gradually eliminated. Recently, we observed the formation of such type TL at quasi-hetero-epitaxial growth of SCF of TbAG garnet [10] and TbAP perovskite [28] onto YAG and YAP substrates at misfit of about 0.7% and 1.4%, respectively. Specifically, for both SCFs, the content of TL presents the solid-state solutions between the material of substrate and mentioned SCFs [28].

Table 3
XRD analyses structure of LSO substrate and two LGSO:Ce SCFs (2θ—reflection angle, d—distance between the lattice planes, M—misfit between the lattice constants of SCF and substrate).

2θ	d, Å	Comment	hkl	M, %
Substrate				
37.779	2.378		22-3	
80.7104	1.1895	Kα1	44-6	
80.9476	1.1896	Kα2	44-6	
$(Lu_{0.8}Gd_{0.2})_2SiO_5$ d10, 8.0 μm				
37.576	2.391	sub+SCF	22-3	0.55
80.2076	1.1957	Kα1 SCF	44-6	
80.4355	1.1958	Kα2 SCF	44-6	
80.7428	1.1891	Kα1 sub	44-6	
80.9649	1.1894	Kα2 sub	44-6	
$(Lu_{0.3}Gd_{0.7})_2SiO_5$ c1, 3.5 μm				
37.2717	2.410	SCF	22-3	1.36
37.7714	2.379	Substrate	22-3	
79.4173	1.2056	Kα1 SCF	44-6	
79.6432	1.2057	Kα2 SCF	44-6	
80.7424	1.1891	Kα1 sub	44-6	
80.9703	1.1893	Kα2 sub	44-6	

2.1. Structural characterization of LSO and LGSO SCF samples

The XRD pattern (Cu Kα radiation) of LGSO:Ce d10 and c1 SCF samples grown by LPE onto LSO substrate shows that both films have the single crystalline structure (Fig. 1), indices of the reflections are denoted assuming C2/c space group. The growth plane of SCFs is exactly the same as substrate plane (22-3) (Fig. 1). Misfit of lattice constants of SCF and substrate is equal to 0.55% and 1.36%, respectively (Table 1). Due to such large misfit, the FWHM of SCF-related peaks in Fig. 1 is slightly larger then that for substrate. Subsequently, the surface roughness of LGSO:Ce c1 SCF sample, measured by 2D profile-meter ZYGO (Fig. 2c), is relatively large (~190 nm).

It is important to note that the XRD analyzes of $(Lu_{1-x}Gd_x)SO$ SCF samples in whole range of Gd^{3+} concentration up to $x=0.7$ f.u. show that all SCFs have C2/c crystalline structure (Fig. 1, Table 1), e.g., the same crystalline structure as the LSO and YSO hosts [19,20]. Due to closer ionic radii of Gd^{3+} and Y^{3+} ions (0.94 Å and 0.9 Å in 6-fold coordination) [29], we suppose that the $(Lu_{1-x}Gd_x)SO$ SCF in principle *can be also grown onto significantly cheaper YSO substrates* with same as LSO crystalline structure.

We have studied also the film surface morphology and surface profiles using the polarized optical microscopy in reflection and transmission modes and by means of interferometric surface profiler ZYGO. The $(Lu_{1-x}Gd_x)_2SiO_5$:Ce SCF samples grown from the PbO-based flux show good structural and optical quality (Fig. 2). The surface of the $(Lu_{0.3}Gd_{0.7})_2SiO_5$:Ce c3 SCF sample, observed in optical microscope is shown in Fig. 2a and b. The main part of mirror-like surface is from structural defects. Only two types of surface defects, such as pits and scratches, are observed on the surface of in the LGSO SCF. The surface pits are the most frequent ones which are well visible in transmission mode. They are rather deep, ranging from several hundreds of nm up to several microns and they can also penetrate through all the film down to the substrate. In the latter case the pits can originate from the defects existing in the substrate, e.g. from structure imperfections like dislocations, point mechanical defects in substrate surface, or contamination of the substrate surface before the growth. Other frequent defects, which we have observed in LGSO SCF, are scratches that arise as a result of polishing process of the substrate. It worth to note, that we have not observed any inclusions of isolated crystallites of silicate or other phases on the surface of LGSO SCF.

Another important source of surface defects is the after-growth imperfections, when the PbO-based flux cannot be completely removed from the film surface at the end of the growth process,

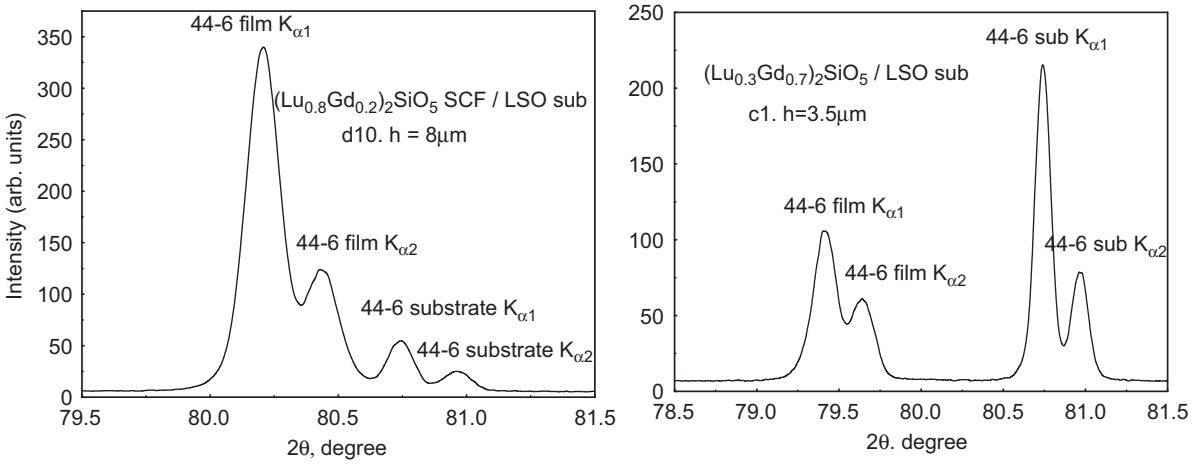

Fig. 1. XRD pattern of LGSO:Ce SCF d10 and c1 SCF grown by LPE onto LSO substrate. The difference between peak positions for SCF and substrate is proportional to misfit SCF-substrate.

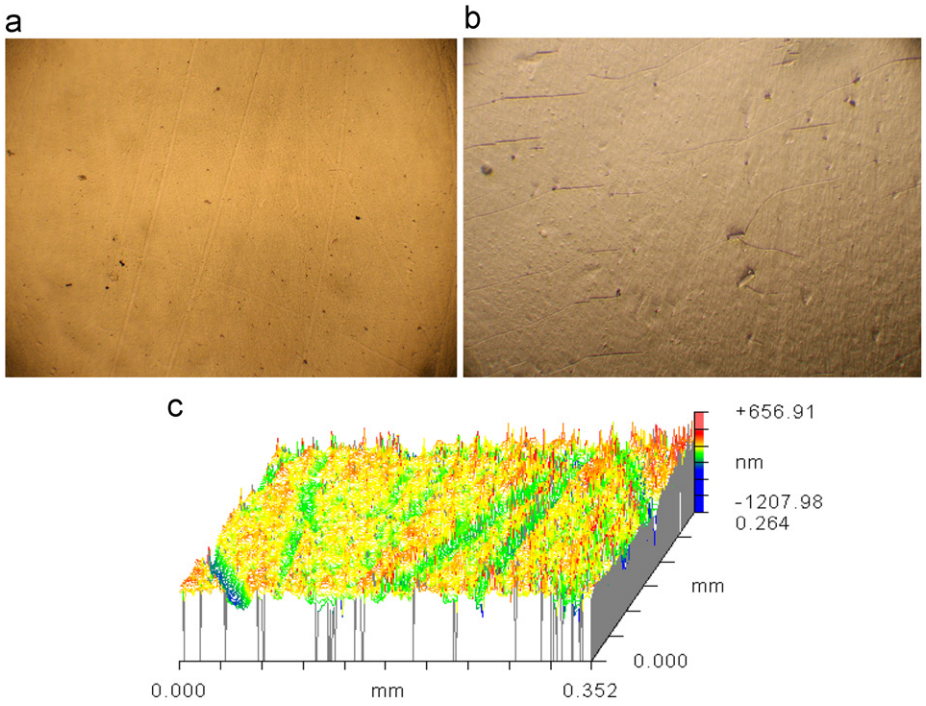

Fig. 2. Optical microscope image with magnification 40 × of surface of $(Lu_{0.3}Gd_{0.7})_2SiO_5$:Ce c3 SCF sample with thickness of 2.8 μm in the transmission (a) and reflection (b) regime; (c) surface profile of same samples measured by means of interferometric surface profiler ZYGO. The surface roughness is about 190 nm.

when the sample is removed from the melt-solution. The growth can thus continue under undefined conditions from the rests of the melt on the sample surface. The non-uniform, rough and undulating surface of the film, Fig. 2c, originates mostly from these particular after-growth processes.

2.2. Dopant content in LSO and LGSO SCF

We used the equimolar ratio (2Lu/Si) of crystal-forming components in melt-solution (MS) for the growth of LSO:Ce SCF (samples b7–b12). Apart from that, the non-equimolar ratio's 2Lu:3Si and 3Lu:7Si were also used for growth LSO:Ce SCF (samples b13–b15 and b16, respectively, Table 1) and LGSO:Ce SCF (all samples, Table 2). We noted *better condition of LPE growth of LSO-based SCFs with non-equimolar Lu/Si ratio*: it resulted in larger growth rate; better structural perfection and higher LY of radioluminescence of SCF samples (see Table 1).

The concentration of crystal-forming components with respect to the total content of melt-solution was 5.2–6.9 mol%. These values determine different temperatures of saturation of respective melt-solutions T_S=1025–1040 °C as well as the ranges of SCF growth temperature T_g=982–1015 °C, see Tables 1 and 2. The SCF growth rate was in 0.02–0.18 μm/min range (Tables 1 and 2). The growth rate decreases when the temperature of SCF growth increases and vice versa (Tables 1 and 2).

The concentration of CeO_2 activated oxide ions in MS was equal to 5, 10 and 20 mol% for the growth of LSO:Ce SCF (see Table 1) and 1.5 and 15 mol% for the growth of LGSO:Ce SCF (see Table 2). The Tb_4O_7 doping in concentration of 1.5 and 15 mol% was used for the growth of SCF with nominal content in MS $(Lu_{0.8}Gd_{0.2})_2SiO_5$:Ce,Tb (Table 2). From microanalyses of the content of several LSO:Ce, LGSO:Ce and LSO:Ce,Tb SCFs performed using JEOL JXA-8612 MX electron microscope, we estimated the segregation coefficient of Ce^{3+} and Tb^{3+} ions in these SCF of about 0.0045 and 0.62, respectively. The segregation coefficient of Gd^{3+} ions decrease from 1.2 up to 0.48 at the relative change of the Gd concentration x in LSO host from 0.8 to 0.3 f.u. (Table 2). Such significant difference in the segregation coefficients of mentioned ions is due to respective difference in the ionic radii of Ce^{3+} (1.01 Å), Gd^{3+} (0.94 Å) and Tb^{3+} (0.92 Å) ions in six-fold coordination in comparison with radius of Lu^{3+} ions (0.86 Å) in Lu1 positions of LSO host [29].

It is important to note that the concentration of Ce^{3+}, Gd^{3+} and Tb^{3+} ions as well as Pb^{2+} flux related impurity in LSO and LSO:Ce SCFs are determined not only by the content of activating oxides in MS but also strongly influenced by the SCF growth temperature: when the growth temperature decreases, the concentrations of activator and Pb ions increase and vice versa. At the same time, the RE dopants and Pb^{2+} ions incorporation in LSO:Ce SCF show different rate of dependence on SCF growth temperature. Specifically, the LSO:Ce b9 SCF, grown from MS with 10 mol% CeO_2 concentration at higher (1015 °C) temperature, has the content of Lu_2SiO_5:Ce(0.043 at%),Pb(0.018 at%) while the LSO:Ce b10 SCF grown from the same MS at lower (1005 °C) temperature has the content of Lu_2SiO_5:Ce (0.047 at%), Pb(0.033 at%). Thus, the value of the Ce/Pb ratio in LSO:Ce SCF increases with increasing the growth temperature. However, even in LSO:Ce SCF grown at high temperatures, the value of Ce/Pb ratio is only ~1.5–2.5. For comparison, the Ce/Pb ratio in the best samples of garnet YAG:Ce and LuAG:Ce SCF is above 15. Therefore, the segregation coefficient of lead ions is about one order higher for homo-epitaxial growth of LSO SCF onto LSO substrates then in the case of growth of YAG and LuAG SCF onto YAG substrates [27,28]. It is important to note that we suppose here that the distribution of the Pb^{2+} ions over Lu1 and Lu2 positions in LSO host is similar to the distribution of Ce^{3+} ions due to their large ionic radius [29].

3. Experimental technique for optical measurements

The absorption spectra of LSO:Ce and LGSO:Ce SCF and SC were measured using UV/VIS/ NIR spectrophotometer Shimadzu UV-310 PC in the wavelength range 190–1200 nm at 300 K.

The CL spectra and LY of CL of LSO-based SCF were measured at 300 K with a set-up based on a DMR-4 monochromator and a FEU-106 PMT under pulsed e-beam excitation (9 KeV, 100 μA) with pulse duration of 2 μs and a frequency of 3–30 Hz. Emission spectra were corrected for the spectral dependence of the detection part.

The scintillation LY of LSO:Ce SCFs was measured at 300 K using a detector based on hybrid PMT (DEP PPO 475B type) with maximum sensitivity in the range 200–400 nm under excitation by ^{241}Am sources (5.5 MeV α-particles). Energy spectra were measured with time gate of 3.0 μs. In case when the thickness of LSO:Ce and LGSO:Ce SCFs (Tables 1 and 2) was smaller than the calculation penetration depth of α-particles in studied materials (Table 4) we estimate the LY values of the SCF using the comparison of the scintillation response of the SCF and the substrate. Nevertheless, for most of the SCF samples in Tables 1 and 2 the film thickness is comparable with the penetration depth and LY value can be taken as the characteristics of the film itself.

The LY of LSO and LSO:Ce SCFs were also compared with those of reference LSO:Ce and LYSO:Ce bulk SC scintillators, manufactured in ISC, Ukraine and SIC Shanghai, respectively. Under gamma excitation (662 keV, ^{137}Cs) the light yield of reference LSO:Ce and LYSO:Ce SC was 7380 and 16,560 ph/MeV, respectively.

Table 4
Full α-particle penetration range of LSO, GSO and YSO [30]. Penetration ranges of mixed LYSO and LGSO are lying between those of pure LSO–YSO or LSO–GSO, respectively.

Parameters of α-energy line (MeV)	Penetration range (μm)		
	LSO (ρ=7.5 g/cm^3)	**GSO** (ρ=6.7 g/cm^3)	**YSO** (ρ=4.54 g/cm^3)
^{244}Cm, 5.805	12.6	13.2	15.0
^{241}Am, 5.4857	11.5	12.0	13.7
^{239}Pu, 5.1566	**10.4**	**10.9**	12.4

4. Experimental results

4.1. Absorption spectra

Absorption spectra at 300 K of LSO, LSO:Ce, LGSO:Ce and LGSO:Ce,Tb SCFs in comparison with the absorption spectra of undoped LSO SC substrate and reference LSO:Ce and GSO:Ce SCs are shown in Fig. 3. Contrary to LSO SC substrate, where no absorption in the spectral range above 210 nm was detected, the characteristic feature of absorption spectra of all LSO-based SCF is the existence of the intensive band peaked at 258–262 nm, the

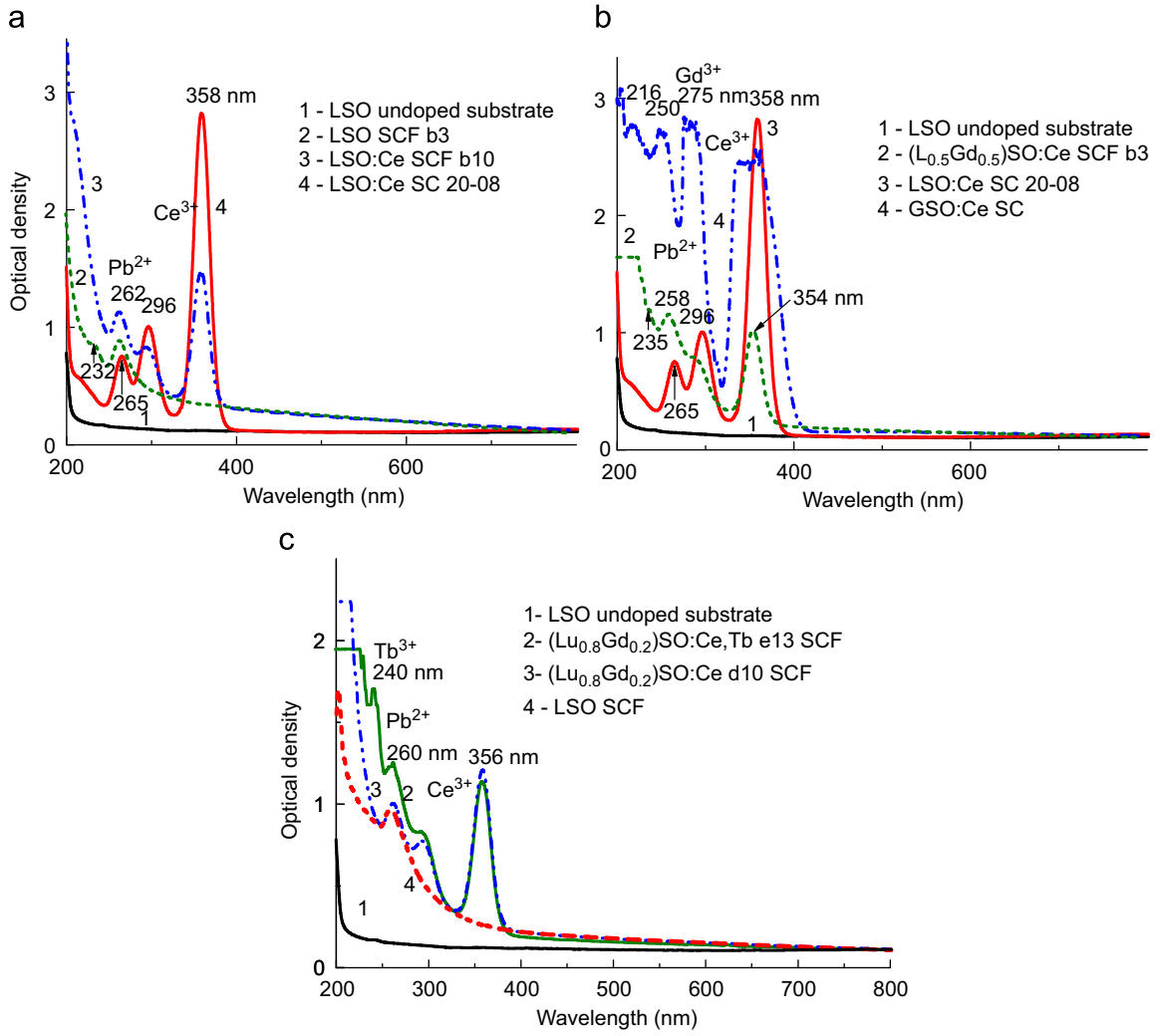

Fig. 3. (a) Absorption spectra at 300 K of undoped LSO substrate (1), LSO SCF (2), LSO:Ce SCF (3) and reference LSO:Ce SC (4); (b) absorption spectra at 300 K of undoped LSO substrate (1), ($Lu_{0.5}Gd_{0.5}$)SO:Ce SCF (2) and reference GSO:Ce SC (3) and LSO:Ce SC (4); (c) absorption spectra of LGSO:Ce,Tb SCF (1) in comparison with the absorption spectra of LSO:Ce SCF (2) and LSO SCF (3). T=300 K.

weaker band at ~230 nm as well as the strong band peaked at <200 nm. The intensity of these bands increases with decreasing the SCF growth temperature, e.g., the Pb^{2+} content in SCFs, and vice versa. Therefore, the mentioned bands can be caused by the absorption of Pb^{2+} flux-related impurity. Specifically, by the analogy with absorption of Pb^{2+} ions in SCF of garnet compounds [31,32], the band peaked at 262, 230 and <200 nm corresponds to $^1S_0 \rightarrow {}^3P_1$, $^3P_2$ and $^1P_1$ transition of Pb^{2+} ions (A, B and C band), respectively. The latter band can be overlapped also with the broad band in the same spectral range related to the charge transfer transition (CTT) between the Pb^{2+} ions and bottom of LSO conduction band. We note that the continuous background "absorption" of LSO and LSO:Ce SCF samples throughout the whole spectrum up to 800 nm is caused by light scattering effects on the rough surface of SCF.

The absorption spectra of LSO:Ce SCF (Fig. 3a, curve 3) and reference LSO:Ce SC (curve 4) show the same structure of the Ce-related absorption bands caused by the 4f–5d transition of Ce^{3+} ions. Specifically, the bands peaked at 265, 296 and 358 nm can be corresponds to 4f ($^2F_{5/2}$)→5d ($^3T_{2g}$ and ^2E) transitions of Ce^{3+} ions in Lu1 positions of LSO host [26,27]. The low intensity of these bands in SCF is due to significantly lower SCF thickness with respect to the thickness of LSO crystals.

The absorption spectrum at 300 K of Ce^{3+} doped $(Lu_{1-x}Gd_x)SO$ SCF in comparison with the spectra of undoped LSO SC substrate and reference GSO:Ce and LSO:Ce SCs is shown in Fig. 3b. The position of absorption bands of Ce^{3+} ions in the spectra of $(Lu_{0.5}Gd_{0.5})SO$:Ce SCF (Fig. 3b, curve 2) is slightly shifted with respect to absorption spectra of LSO:Ce SC and SCF (curve 1) and notable transformed with respect to the spectrum of GSO:Ce SC (curve 4). Namely, the Ce^{3+} related bands in the absorption spectrum of $(Lu_{0.5}Gd_{0.5})SO$:Ce SCF sample are situated between the same bands in the spectra of GSO:Ce and LSO:Ce SC but close to the spectrum of the latter sample. This also indicates that $(Lu_{1-x}Gd_x)SO$ SCF has the same (C2/c) as the LSO crystalline structure. Taking into account this fact, the mentioned shift of absorption spectra can be caused by (i) the redistribution of Ce^{3+} ions over Lu1 and Lu2 cations position with 7-fold and 6-fold coordination by oxygen ligands caused by Gd^{3+} ions incorporation [19,20], (ii) the change of the crystal field strength in the Lu1 and Lu2 positions inducing by the substitution of smaller Lu^{3+} cations by large Gd^{3+} ions. Similarly to LSO:Ce SCF, the absorption spectra of LGSO:Ce SCF also contain the bands peaked at 258 and 235 nm, related to $^1S_0 \rightarrow {}^1P_1$, $^2P_1$ transition of Pb^{2+} flux impurity. The intensive band in the absorption spectrum GSO:Ce SC peaked at 275 nm and bump in the same spectral range in $(Lu_{1-x}Gd_x)SO$ SCF are due to $^8S_{7/2} \rightarrow {}^6P_{7/2-3/2}$ transition of Gd^{3+} cations.

The absorption spectrum at 300 K of Tb^{3+} doped $(Lu_{0.2}Gd_{0.8})$-SO:Ce SCF in comparison with the spectra of undoped LSO SC substrate and LSO SCF and LSO:Ce SCF samples is shown in Fig. 3c. Apart the Ce^{3+} related absorption bands peaked at 356 and 294 nm and Pb^{2+} related band peaked at 256–262 nm and 232–235 nm, the absorption spectrum of $(Lu_{0.2}Gd_{0.8})SO$:Ce,Tb SCF also includes the strong band peaked at 260 nm, related to spin-allowed 4f–5d transition of Tb^{3+} ions (Fig. 3c, curve 2).

4.2. Luminescent properties of Ce-doped Lu_2SiO_5 SCF

The CL spectra of LSO:Ce SCFs, grown with different CeO_2 content in MS are shown in Fig. 4 in comparison with the CL spectra of a reference LSO:Ce crystal. The dominant doublet emission band peaked in the 395–425 nm range in the spectra of both the LSO:Ce SCF and SC is mainly caused by the luminescence of Ce(Lu1) centers in the LSO host. At the same time, the emission spectra of LSO:Ce SCF (curves 2–4) show higher intensity in the long-wavelength range with respect to the spectrum of SC analog (curve 1) where Ce(Lu2) centers can emit [15,26,27], see arrows. The low-intensity bands peaked at 348 and 438 corresponds to luminescence of Pb^{2+} in Lu1 and Lu2 position, respectively. The intensity of these bands strongly increases with decreasing the temperature of SCF growth, i.e. with Pb^{2+} concentration in SCF (Fig. 4, curve 2).

As one can see from Fig. 4b, the CL spectra of LSO:Ce SCF in comparison with SC analog show lower intensity of emission in the band peaked at 3.06 eV (406 nm), related to the luminescence of Ce(Lu1) centers, and larger intensity of emission in the band peaked at 2.68 eV (462 nm) related to luminescence of Ce(Lu2) centers in LSO host. We also note that the ratio of Ce^{3+} ions in the Lu1/Lu2 position notably increases as the Ce^{3+} content in LSO:Ce SCF increases from 5 to 10 mol% (Fig. 3a, curves 2 and 3, respectively) and then does not change at further increase of the CeO_2 content to 20 mol% (Fig. 3a, curves 3 and 4, respectively).

4.3. Luminescent properties and LY of Ce-doped $(LuGd)_2SiO_5$ SCF

The CL spectra of LGSO:Ce SCFs, grown with different Gd content in $x=0.2$–0.7 f.u. range are shown in Fig. 5 in comparison

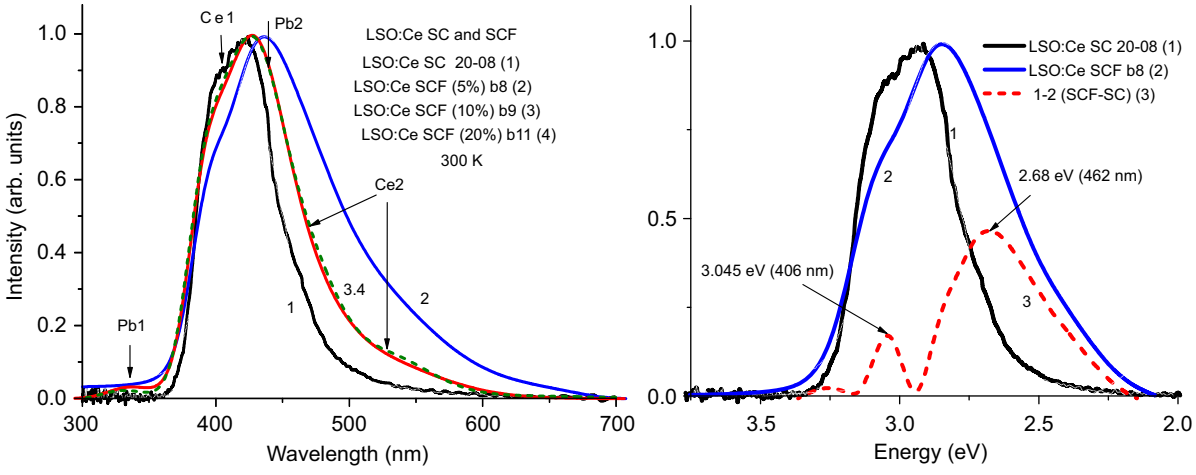

Fig. 4. (a) normalized (on the maximum of the main peak) CL spectra of LSO:Ce SCF (2–4) grown at CeO_2 content in MS of 5 mol% (2), 10 mol% (3) and 20 mol% (4) in comparison with CL spectrum of LSO:Ce SC (1); (b) difference curve (curve 3) between the normalized CL spectra of LSO:Ce (20 mol%) SCF (curve 1) and SC (curve 2). $T=300$ K.

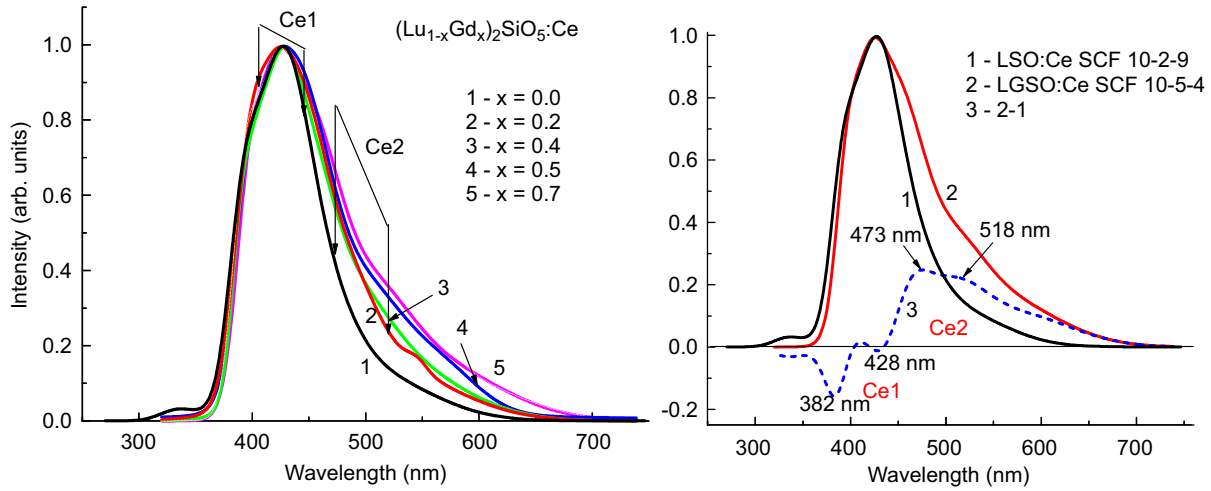

Fig. 5. (a) normalized CL spectra (at 300 K) of Lu_2SiO_5:Ce SCF (1) and $(Lu_{1-x}Gd_x)_2SiO_5$:Ce SCF (2–5) grown with different Gd content $x=0.2$ (2), 0.4 (3), 0.5 (4) and 0.7 (5) f.u.; (b) difference (3) between the CL spectra of Lu_2SiO_5O:Ce (1) and $(Lu_{0.5}Gd_{0.5})_2SiO_5$:Ce (2) SCFs at 300 K. The local extremes in the difference curve indicate the positions of Ce1 and Ce2 bands in LSO:Ce host.

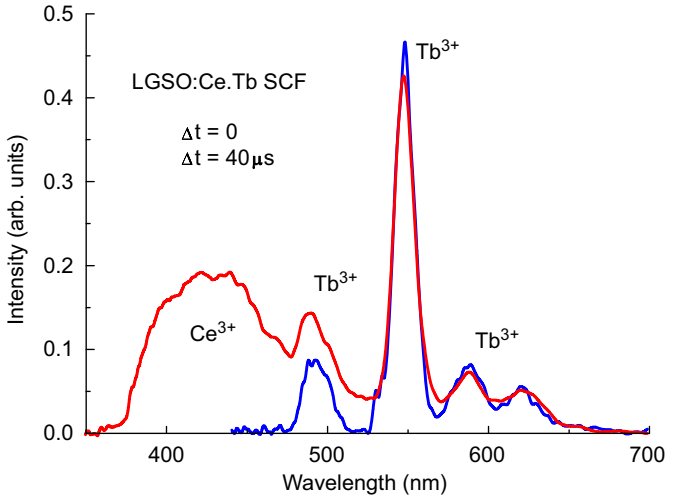

Fig. 6. CL spectra of LuGdSO:Ce,Tb SCF at $\Delta t=0$ and delay signal after $\Delta t=40$ μs.

with the CL spectra of a LSO:Ce SCF sample. The dominant doublet emission band peaked in the 395–425 nm range in the spectra of all LGSO:Ce and LSO:Ce SCF and SC is caused by the luminescence of Ce(Lu1) centers. At the same time, the emission spectra of LGSO:Ce SCF (curves 2–5) are notably red shifted with respect to the spectrum of the LSO:Ce SCF samples (curve 1).

As one can see from Fig. 5b, the CL spectra of $(Lu_{0.5}Gd_{0.5})_2SiO_5$:Ce SCF (curve 2) in comparison with LSO:Ce SCF (curve 1) show lower intensity of emission in the band peaked at 382 and 428 nm, related to the luminescence of Ce(Lu1) centers, and larger intensity of emission in the bands peaked at 473 and 518 nm related to luminescence of Ce(Lu2) centers in LSO host. Therefore, the ratio of Ce^{3+} ions in the Lu2 /Lu1 position steeply increases as the Gd^{3+} content in LGSO:Ce SCF increases from $x=0.2$ to 0.7. Most probably, this is first reason why the LY of $(Lu_{1-x}Gd_x)$SO:Ce SCF steeply decrease down to 50% of that of LSO:Ce SC with increasing the Gd content in the range of $x=$ 0.2–0.7 f.u. (see Table 3). The second reason for lower LY of LGSO:Ce SCF can be connected with relatively large segregation coefficient of Pb^{2+} flux impurity in these SCF with larger-then-LSO lattice constant in comparison with the conditions of LPE growth of LSO:Ce SCF onto the same undoped LSO substrate.

4.4. Luminescent properties of Tb-doped $(LuGd)_2SiO_5$ SCF

The CL spectra of $(Lu_{0.8}Gd_{0.2})_2SiO_5$:Ce,Tb SCF present the superposition of fast Ce^{3+} luminescence and slow Tb^{3+} ($^5D_4$–^7F_x) emission in the visible range (Fig. 5). Green Tb^{3+} luminescence is dominating in the CL spectra of $(Lu_{0.8}Gd_{0.2})_2SiO_5$:Ce,Tb SCF recorded with the delay time of 40 μs with respect to the excitation electron pulse.

In comparison with the CL spectra of LSO:Ce SCF (Fig. 5), the intensity of Ce^{3+} luminescence in LSO:Ce,Tb SCF (Fig. 6) is strongly decreased. Most probably, the effective $Ce^{3+}\rightarrow Tb^{3+}$ energy transfer is realized in LGSO:Ce,Tb SCF due to the overlap of Ce1 emission and $^5D_3$–$^7F_6$ around 380 nm, but this assumption needs the additional experimental confirmation. The Tb^{3+} co-doping also leads to strong decrease of scintillation LY of LSO:Ce,Tb SCF (see Table 2).

5. LY of LSO:Ce and LGSO:Ce SCF

The LY of RL of LSO:Ce SCFs grown with the different content of CeO_2 activating oxide in MS in 5–20 mol% range under excitation by α-particles of ^{241}Am sources (5.5 MeV) is presented in Table 2. The LY of these SCF increases with increasing of CeO_2 content up to 20 mol%. Meanwhile, the LY of LSO:Ce SCF strongly depends on SCF growth temperature T_g: when the growth temperature decreases, it also decreases and vice versa (see Table 1). Such a dependence of LY(T_g) reflects the respective change of the value of Ce/Pb ions ratio in SCF due to different dependence of the segregation coefficient of Ce^{3+} and Pb^{2+} ions on the growth temperature. The LY of the best LSO:Ce SCF samples grown from MS with 2Lu/Si equal-molar ratios reach the value of 87% in comparison with the reference LSO:Ce crystal (Table 1). Using the non-equal-molar Lu/Si ratios in MS enables to increase the LY of LSO:Ce SCF approximately up to ~145% with respect to reference LSO:Ce crystal (Table 1) presumably due to increasing of the segregation of Ce^{3+} ions in these SCF. This assumption is in the agreement with some increasing of the intensity Ce^{3+} related bands in the absorption spectra of these films (not shown in Fig. 1a). We note that the reference LSO:Ce SC shows rather low LY with respect to high quality LYSO:Ce crystal, see Section 3.

It is worth to note that the important feature of LPE growth of LSO-based SCF at low (~1000 °C) temperatures in air is the

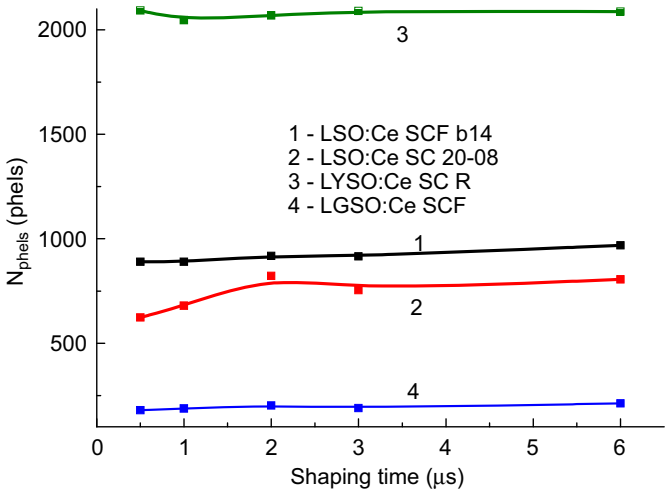

Fig. 7. Dependence of LY N_{phels} on shaping time for LSO:Ce SCF a14 (1) and LGSO:Ce SCF d12 (4) in comparison with LSO:Ce (20-08) SC (2) and LYSO:Ce (R) SC (3).

significantly lower content of oxygen vacancies in comparison with SC analogs, grown at high (~2030 °C) temperature and inert atmosphere. It is well known, that the oxygen vacancies are most easily created at non-bounded chains between Lu1 and Lu2 positions of LSO host [27,33] and they are responsible for large afterglow of LSO:Ce crystals and decrease of their scintillation LY [17,19–21]. Therefore, we expect that in the case of elimination or strong decreasing the influence of Pb^{2+} flux impurity on the luminescence of Ce^{3+} ions in LSO:Ce SCF, one could possess even better scintillation properties in comparison with SC counterparts.

This conclusion is strongly supported by the comparison of the dependence of LY of LSO:Ce SCF, LGSO:Ce SCF and LSO:Ce and LYSO:Ce SC counterparts on the shaping time under excitation of the mentioned samples by α-particles of ^{241}Am sources (Fig. 6). Due to presumably large content of oxygen vacancies in LSO:Ce SC, its LY notably increases with increasing the shaping time of LY measurement (Fig. 6, curve 2). Such dependence in LSO:Ce and LGSO:Ce SCF is more flat (curves 1,4), similar to that in high quality LYSO:Ce SC (curve 3) where the influence of the oxygen vacancies on scintillation processes is strongly diminished [17–22].

At the same time, the LY even in the best LSO:Ce and LGSO:Ce SCF samples is significantly lower than that for LYSO:Ce crystal (Table 2). The lower LY of LSO:Ce and LGdSO:Ce SCF with respect to LY of LYSO:Ce SC is caused by the strong quenching influence of Pb^{2+} centers on the Ce^{3+} luminescence in these SCF. Therefore, future development of LSO:Ce and LGdSO:Ce SCF scintillators by LPE methods strongly demands the usage of the lead-free fluxes for their crystallization. The most known is the BaO-based flux [34–37]. We successfully used this flux for producing the SCF scintillators based on YAG [34,35], LuAG [36] and YAP [37] compounds and it will be used also for preparation of silicate SCF in our future work (Fig. 7).

6. Conclusions

The single crystalline films (SCF) of Ce^{3+}-doped Lu_2SiO_5 (LSO:Ce) and $(Lu_xGd_{1-x})_2SiO_5$ (LGSO:Ce, $x=0.2–0.7$ formula units) orthosilicates with a thickness of 2.5–21 μm were successfully crystallized by the liquid phase epitaxy (LPE) method onto undoped LSO substrates from melt-solution based on $PbO–B_2O_3$ flux. In case of LGSO:Ce SCF growth we do not use any additional doping to reduce the significant misfit (up to 1.36% for $(Lu_{0.3}Gd_{0.7})_2SiO_5$) between the SCF and substrate lattice constants. Better conditions for LPE growth of LSO-based SCFs were obtained with non-equimolar silicon-rich Lu/Si ratio in melt solution.

The luminescent properties of LSO:Ce and LGSO:Ce SCFs grown from melt-solution with CeO_2 content in 5–20 mol % range were compared with LSO:Ce single crystal (SC). We found that the luminescence of LSO:Ce SCF caused by the $5d_1–4f$ radiative transition of Ce^{3+} ions is red-shifted in comparison with LSO:Ce crystal. This shift can be caused by different relative occupancy of Lu1 and Lu2 sites of LSO host by Ce^{3+} ions in the case of SCF and SC crystallization due to very different temperatures for crystals (2100 °C) and films (~1000 °C) growth. We also found that the luminescence spectrum of $(Lu_xGd_{1-x})_2SiO_5$ SCF is systematically red-shifted with respect to spectrum of LSO:Ce SCF with increasing the Gd content in range of $x=0.2–0.7$ formula units. Such a red shits of the emission spectra of LGSO:Ce SCF is also accompanied with more then twice decrease of their LY for $(Lu_{0.3}Gd_{0.7})$-SO:Ce SCF in comparison with the LY of LSO:Ce SCF. Red shift of the CL spectra of LGSO:Ce is caused by increasing occupancy of Lu2 sites by Ce^{3+} ions in LGSO host.

The light yield (LY) of LSO:Ce SCF reaches value of 145% of that of a LSO:Ce crystal under excitation by α–particles of Pu^{239} sources (5.15 MeV) but only ~25–50% of LY of high-quality reference LYSO:Ce crystal. Lower LY of LSO:Ce and LGSO:Ce SCFs with respect to LYSO:Ce SC reference crystal is presumably due to the quenching influence of Pb^{2+} impurity in SCF on the luminescence of Ce^{3+} ions. Therefore, the usage of the lead-free fluxes are strongly needed for crystallization by LPE methods of LSO:Ce and LGdSO:Ce SCF scintillators to increase their LY. Nevertheless, it seems plausible that the LSO:Ce and LGSO:Ce SCFs, after the optimization of their growth conditions, can be used as scintillating screens for ionizing radiation monitoring and 2D X-ray microimaging.

Acknowledgements

The work was supported by SL-28F (Ukraine), GACR 202/08/0893 (Czech Republik) and NATO CBP.NUKR.CLG 984305 projects.

References

[1] B. Ferrand, B. Chambaz, M. Couchaud, Optical Materials 11 (1999) 101.
[2] M. Robertson, M.V. van Tol, Thin Solid Films 114 (1984) 1.
[3] Z.D. Hrytskiv, Y. Zorenko, V. Gorbenko, A.D. Pedan, V.I. Shkliarskyi, Radiation Measurements 42 (2007) 933.
[4] Yu V. Zorenko, S.S. Novosad, M.V. Pashkovskii, A.B. Lyskovich, V.G. Savitskii, M.M. Batenchuk, P.S. Malyutenkov, N.I. Patsagan, I.V. Nazar, V.I. Gorbenko, Journal of Applied Spectroscopy 52 (1990) 645.
[5] M. Globus, B. Grinyov, M. Ratner, V. Tarasov, V. Lyubinskiy, Y. Vydai, A. Ananenko, Y. Zorenko, V. Gorbenko, I. Konstankevych, IEEE Transactions on Nuclear Science 51 (2004) 1297.
[6] A. Koch, C. Raven, P. Spanne, A. Snigirev, Journal of Optical Society of America A 15 (1998) 1940.
[7] A. Koch, F. Peyrin, P. Heurtier, B. Chambaz, B. Ferrand, W. Ludwig, M. Couchaud, Proceedings of SPIE 3659 (1999) 170.
[8] T. Martin, A. Koch, Journal of Synchrotron Radiation 13 (2006) 180.
[9] Yu Zorenko, V. Gorbenko, I. Konstankevych, B. Grinev, M. Globus, Nuclear Instruments and Methods in Physics Research A 486 (2002) 309.
[10] Yu Zorenko, V. Gorbenko, I. Konstankevych, A. Voloshinovskii, G. Stryganyuk, V. Mikhailin, V. Kolobanov, D. Spassky, Journal of Luminescence 114 (2005) 85.
[11] Y. Zorenko, V. Gorbenko, E. Mihokova, M. Nikl, K. Nejezchleb, A. Vedda, V. Kolobanov, D. Spassky, Radiation Measurements 42 (2007) 521.
[12] Yu Zorenko, V. Gorbenko, M. Nikl, J.A. Mares, T. Martin, P.-A. Douissard, IEEE Transactions on Nuclear Science 57 (2010) 1335.
[13] Y. Zorenko, V. Gorbenko, T. Voznyak, M. Batentschuk, A. Osvet, A. Winnacker, Journal of Luminescence 128 (2008) 652.
[14] C.L. Melcher, R.A. Manente, C.A. Peterson, J.S. Schweizer, Journal of Crystal Growth 128 (1993) 1001.
[15] H. Suzuki, T.A. Tombrello, C.L. Melcher, J.S. Schweizer, Nuclear Instruments and Methods in Physics Research A 320 (1992) 263.
[16] W.W. Moses, Nuclear Instruments and Methods in Physics Research A 471 (2001) 209.
[17] R. Visser, C.L. Melcher, J.S. Schweitzer, H. Suzuki, T.A. Tombrello, IEEE Transactions on Nuclear Science 41 (1994) 689.

[18] A. Vedda, M. Nikl, M. Fasoli, E. Mihokova, J. Pejchal, M. Dusek, G. Ren, C.R. Stanek, K.J. McClellan, D.D. Byler, Physical Review B 78 (2008) 195123.
[19] O.Ts Sidletskiy, V.G. Bondar, B.V. Grinyov, D.A. Kurtsev, et al., Functional Materials 16 (2009) 67.
[20] O. Sidletskiy, V. Bondar, B. Grinyov, D. Kurtsev, V. Baumer, K. Belikov, K. Katrunov, N. Starzhinsky, O. Tarasenko, V. Tarasov, O. Zelenskaya, Journal of Crystal Growth 312 (2010) 601.
[21] G. Ren, L. Qin, S. Lu, H. Li, Nuclear Instruments and Methods in Physics Research A 531 (2004) 560.
[22] D.W. Cooke, K.J. McClellan, B.L. Bennett, J.M. Roper, M.T. Whittaker, R.E. Muenchausen, R.C. Sze, Journal of Applied Physics 88 (2000) 7360.
[23] Yu Zorenko, V. Gorbenko, V. Savchyn, T. Voznyak, I. Solsky, B. Grynyov, O. Sidletskiy, A. Fedorov, M. Nikl, Optical Materials 33 (6) (2011) 846–8522011 33 (6) (2011) 846–852.
[24] A. Rack, S. Zabler, B.R. Muellerb, H. Riesemeier, G. Weidemann, A. Lange, J. Goebbels, M. Hentschelb, W. Goerner, Nuclear Instruments and Methods in Physics Research A 586 (2008) 327.
[25] T. Martin, P.-A. Douissard, M. Couchaud, A. Cecilia, T. Baumbach, K. Dupré, A. Rack, IEEE Transaction on Nuclear Science 56 (2009) 1412.
[26] L. Pidol, O. Guillot-Noël, A. Kahn-Harari, B. Viana, D. Pelenc, D. Gourier, Journal of Physics and Chemistry of Solids 67 (2006) 643.
[27] G. Dominiak-Dzik, W. Ryba-Romanowski, R. Lisiecki, P. Solarz, M. Berkowski, Applied Physics B 99 (2010) 285.
[28] Yu. Zorenko, V. Gorbenko, T. Voznyak, M. Batentschuk, A. Osvet, A. Winnacker, Physics Status Solidi (a) 207 (2010) 967.
[29] http://abulafia.mt.ic.ac.uk/shannon/radius.php.
[30] P. Prusa, M. Nikl, J.A. Mares, M. Kucera, K. Nitsch, A. Beitlerova, Physics Status Solidi A 206 (2009) 1377.
[31] V. Babin, V. Gorbenko, A. Makhov, J.A. Mares, M. Nikl, S. Zazubovich, Yu Zorenko, Journal of Luminescence 127 (2007) 384.
[32] V. Babin, V. Bichevin, V. Gorbenko, A. Makhov, E. Mihokova, M. Nikl, A. Vedda, S. Zazubovich, Yu Zorenko, Physics Status Solidi V. B 246 (2009) 1318.
[33] Liu Bo, Qi Zeming, Gu Mu, Liu Xiaolin, Huang Shiming, Ni Chen, Journal of Physics: Condensed Matter 19 (2007) 436215.
[34] J.A. Mares, A. Beitlerova, M. Nikl, N. Solovieva, K. Nitsch, M. Kucera, M. Kubova, V. Gorbenko, Y. Zorenko, Radiation Measurements 42 (2007) 533.
[35] Yu Zorenko, J.A. Mares, P. Prusa, M. Nikl, V. Gorbenko, V. Savchyn, R. Kucerkova, K. Nejezchleb, Radiation Measurements 45 (2010) 389.
[36] M. Kučera, K. Nitsch, M. Kubová, N. Solovieva, M. Nikl, J.A. Mareš, IEEE Transaction on Nuclear Science 55 (2008) 1201.
[37] Y. Zorenko, M. Nikl, J.A. Mares, V. Gorbenko, V. Savchyn, T. Voznyak, M. Kucera, A. Beitlerova, R. Kucerkova, A. Fedorov, Physics Status Solidi A 206 (2009) 2586.

Journal of Crystal Growth 318 (2011) 813–819

Contents lists available at ScienceDirect

Journal of Crystal Growth

journal homepage: www.elsevier.com/locate/jcrysgro

Growth and emission properties of Sc, Pr, and Ce co-doped $Lu_3Al_5O_{12}$ epitaxial layers for scintillators

M. Kučera [a,*], M. Nikl [b], P. Průša [b], J.A. Mareš [b], K. Nitsch [b], M. Hanuš [a], Z. Onderišinová [a], R. Kučerková [b]

[a] Charles University, Faculty of Mathematics and Physics, Ke Karlovu 5, 12116 Prague 2, Czech Republic
[b] Institute of Physics, Academy of Sciences CR, Cukrovarnická 10, 16000 Prague 6, Czech Republic

ARTICLE INFO

Available online 2 December 2010

Keywords:
A1. Luminescence
A3. Liquid phase epitaxy
B1. Garnets
B1. LuAG
B1. Sc, Pr doping
B2. Scintillator materials

ABSTRACT

The effect of Sc, Pr, and Ce co-doping on the emission and scintillation properties of lutetium aluminum epitaxial garnet layers, $Lu_3Al_5O_{12}$ (LuAG), was studied. The Sc and Pr co-doped garnets with optimized dopant content provide in many aspects better emission and scintillation response compared to those without Sc co-doping. Energy transfer from sensitizer Sc^{3+} to activator Pr^{3+} ions was observed for small Sc doping levels, which consequently resulted in increased radioluminescence intensity and photoelectron yield. At higher Sc content above 3 at%, however, the Pr^{3+} emission was partly quenched. Considerable suppression of slow components and notable increase of fast components in the photoelectron yield was the most remarkable effect of the Sc co-doping in PrSc:LuAG.

1. Introduction

Ce- or Pr-doped $Lu_3Al_5O_{12}$ (LuAG) garnets are prospective scintillation crystals due to their rather high density, 6.7 g/cm^3, high effective atomic number, $Z_{eff} \approx 60$, and high light yield [1,2]. Pr^{3+}-doped aluminum garnets or perovskites exhibit broad emission in the ultraviolet spectral range and very fast luminescence in the nanosecond time range. This is due to the facts that the lowest ^2D crystal field split states of the 5d configuration lie at lower energy than $^1S_0(4f^2)$ state, the 5d states are well separated from the highest $^3P(4f^2)$ states and thus the nonradiative transitions from relaxed 5d states are weak. Under high energy excitation of Pr-doped LuAG or YAG, a broad emission band is observed in the ultraviolet spectral range between 300 and 400 nm, which originates from parity allowed interconfigurational 5d–4f transitions. Due to high intensity and short decay time ~20 ns of this emission, these garnet systems are potential candidates in fast scintillation applications [3].

Doping of YAG or LuAG with isovalent Sc^{3+} ions, which occupy preferably the aluminum octahedral sites, induces an intense broad emission band near 275 nm in photoluminescence (PL) or radioluminescence (RL) spectra [4]. The Sc^{3+} ions have closed shell configuration and do not show any radiative transitions in the visible and UV spectral regions. However, they induce defects in the garnet lattice due to different ionic radii of Sc^{3+} (r_{VI}=74.5 pm) and Al^{3+} (r_{VI}=53.5 pm) ions. This emission, which has decay time of 600 ns, originates from recombination of an exciton located near the Sc defect [4]. The lowest absorption band of 4f–5d, allowing transition of Pr^{3+} ions, is located at 280 nm and coincides with the Sc emission. This leads us to an idea of possible energy transfer from Sc^{3+} sensitizer to Pr^{3+} activator ions. Therefore co-doping of garnets with Sc^{3+} ions may additionally increase the emission output from the Pr^{3+} ions via excitation energy transfer to Pr due to good spectral overlap of both Sc-emission and Pr-absorption spectral bands. A solitary attempt with Sc co-doping was made only for a fixed Sc concentration of 1 at% but any positive effect on the RL spectra was not reported [5].

The goal of this work is to study the effect of Sc co-doping on emission properties of Pr^{3+} ions for a wide range of Sc concentrations, from 0.025 to 10 at% (related to LuAG molecule), in order to find out optimal Sc and Pr doping providing maximal light yield (LY). We have studied in detail the PL, RL properties, and the photoelectron yield, N_{phe}, excited by alpha particles. Several samples were co-doped also with Ce^{3+} ions, which have an intense emission in the green spectral range and cascade energy transfer Sc – Pr – Ce was tested with the aim to increase additionally the total light output from the garnet samples.

2. Growth of ScPrCe:LuAG epitaxial layers

The single crystalline epitaxial garnet layers with various contents of Sc, Pr, and Ce ions were grown by liquid phase epitaxy. The samples were grown from the flux at temperatures around ~1000 °C, which are much lower compared to the Czochralski grown garnet crystals, i.e. ~2000 °C. Positive effect of lower growth temperatures is also lower content of some typical intrinsic defects in epitaxial layers compared to

* Corresponding author. Tel.: +420 221911329.
E-mail address: kucera@karlov.mff.cuni.cz (M. Kučera).

0022-0248/$ - see front matter © 2010 Elsevier B.V. All rights reserved.
doi:10.1016/j.jcrysgro.2010.11.140

single crystals [6,7], e.g. antisite Lu_{Al} defects, where the Lu ions occupy octahedral Al sites. Such defects form recombination centers or shallow traps for electrons in the energy gap and induce a slow component in the scintillation decay [8]. On the other hand, various impurities can enter the garnet lattice from the flux, which may have negative impact on the emission and scintillation properties. Thus carefully selected flux was of primary importance.

2.1. Liquid phase epitaxy

The epitaxial garnet films were grown by the isothermal dipping liquid phase epitaxy from the flux onto the Czochralski grown LuAG or YAG substrates of (1 1 1) crystallographic orientation and 20 mm in diameter. Most of layers were grown onto LuAG substrates, but layers with higher Sc content, >3 at%, were grown onto YAG substrates, which match better the lattice constant, and layers with the highest Sc concentration, $\sim$10 at%, were grown on (1 0 0) oriented $Ca_3Ga_2Ge_3O_{12}$ garnet substrates. The samples were grown from the Pt crucible by dipping the substrate into supercooled melt at a constant supercooling, which was kept in the range of 10–30 K. All the epitaxial layers were grown under nearly the same growth conditions, i.e. growth temperature, supercooling, growth rate, and the solvent composition, in order to rule out the effect of growth conditions on the sample properties. The growth temperatures, T_G, were between 1000 and 1030 °C. Starting raw materials of 5 N purity were used. The thicknesses of studied films determined by weighing were between 6 and 18 μm, most of films have the thickness of around 10 μm.

Several sets of undoped, Sc-doped, Pr-doped, ScPr co-doped, and ScPrCe co-doped LuAG films were grown. In the technology process we thoroughly considered the flux to be used for growing epitaxial layers. The layers grown from routinely used $PbO–B_2O_3$ flux exhibited increased absorption in the ultraviolet spectral range due to the impurity Pb^{2+} and Pt^{4+} ions coming from the flux, which cannot be eliminated. The allowed s–p (Pb) transitions observed near 260 nm practically make impossible to obtain efficient photoemission in the UV spectral range below 300 nm. Furthermore, the UV emission in oxides grown from PbO is more or less quenched [9] and the light yield of Pr-doped garnet and perovskite is strongly reduced in 70–80% [10,11], due to the presence of impurity Pb^{2+} ions coming from the melt.

Because of these problems, the epitaxial layers reported here were grown from a lead-free $BaO–B_2O_3–BaF_2$ flux recently developed for producing aluminum garnets [12,13]. Basic advantage of BaO-based flux, compared to the routinely used $PbO–B_2O_3$ flux, is its possibility to obtain scintillators with efficient UV emission down to 220 nm. Divalent Ba^{2+} ions practically do not enter into the garnet lattice due to their large ionic radius (according to the GDMS analysis the content of Ba ions in layers was below 5 ppm) and their influence on the photoemission or light yield was insignificant. Likewise the presence of isovalent boron B^{3+} impurity ions does not influence negatively the emission and scintillation properties, even though their concentration in layers grown from the BaO flux can attain up to several hundreds ppm. The BaO flux does not attack the Pt crucible and films with superior luminescent properties were obtained from this flux. Content of garnet-forming oxides in the melt was 20–22 mol%. The segregation coefficients of both Ce and Pr ions attain values of only $\sim$0.05 and they depend on supercooling. Thus huge excess of Pr or Ce activator ions in the flux was necessary. The content of both of these ions in layers depends significantly both on melt composition and on supercooling. The dopant concentration in layers can be tailored by a factor 2–3 by adjusting the T_G, i.e. supercooling [13]. In contrast to the PbO flux, any notable increase of undesirable impurities with increase in supercooling was not observed. On the other hand, the BaO flux is relatively viscous, which causes problems with removal of all the flux from the sample surface after finishing the growth process. As a consequence, it is rather difficult to grow layers with defect free high quality surface [14].

The crystallographic properties of the epitaxial layers were studied using XRD on PANalytical high-resolution X-ray diffractometer. The epitaxial films have virtually the same crystallographic properties as the substrates. Observed half-width 12 ang. s of 444 diffraction peak of homoepitaxially grown layers (i.e. doped LuAG layers on LuAG substrates) were comparable to those of the substrates (10 ang. s) giving evidence of high crystallographic quality of the film. Lattice constants determined by the XRD increase with increase in Sc content. Comparison of measured and calculated lattice parameters according to Ref. [15] with chemical analysis of layers shows that Sc ions occupy primarily octahedral positions.

The composition of layers was determined by electron–probe microanalysis, concentrations of activator ions (Pr, Ce), which are very low, were measured by the GDMS analysis (glow discharge mass spectrometry). The results for selected samples and their basic parameters are presented in Table 1. The Sc content in layers was in the range of 0.025–10 at%, the Pr content from 0.0012 to 0.024 at%. Finally Ce was doped into ScPr:LuAG films in concentrations up to 0.015 at%. Unlike activator Pr and Ce ions, which were doped into the garnet lattice in concentrations of the order of several hundreds ppm, the scandium atoms were substituted also in rather higher concentrations up to 10 at%, which corresponds to hypothetical formula $Lu_3Sc_2Al_3O_{12}$. However, for the highest

Table 1
Properties of Sc:LuAG, Sc,Pr:LuAG, and Sc,Pr,Ce:LuAG epitaxial layers and comparison with Pr:LuAG Czochralski grown crystals.

Sample	No.	Thickness (μm)	Sc content (at%)	Pr content (10^{-3} at%)	N_{phe} (1 μs) (MeV)
ScPr:LuAG	1LB1	18.1	–	–	
ScPr:LuAG	1LBS3	11.6	0.025	9.1	427
ScPr:LuAG	1LBS7	5.5	1.8	9.1	354
ScPr:LuAG	1LBS8	6.9	3.95	9.1	244
ScPr:LuAG	1LBS10	5	10	9.1	278
ScPr:LuAG	3LBS2	6.3	0.6	1.2	935
ScPr:LuAG	3LBS4	11.7	0.6	4.4	630
Sc:LuAG	4LBS2	5.7	0.14	–	591
Sc:LuAG	4LBS5	7	1.83	–	327
ScPr:LuAG	5LBS4	9.1	2.9	4.8	419
ScPrCe:LuAG	5LBS6	10.9	2.9	4.8+7.3 Ce	278
ScPr:LuAG	6LBS4	10.7	1.2	5.2	680
Pr:LuAG	7LBS4	14.9	–	23.7	516
Pr:LuAG crystal	8846/1	1 mm	–	10.5	848
Pr:LuAG crystal	8849/1	1 mm	–	17	963

Sc concentration the growth was rather unstable, the optical quality of layers strongly decreased.

3. Emission and scintillation properties

The optical properties were studied using the optical absorption, photoluminescence, and radioluminescence spectroscopy in the spectral range from ultraviolet to the near infrared. The PL decay was measured by the single photon counting method under excitation of nanosecond hydrogen flash lamp. The scintillation properties, photoelectron yield, were studied under alpha particles excitation. All the measurements were made at room temperature.

3.1. Optical absorption

Optical absorption of epitaxial layers was measured in the spectral range 190–1100 nm from the ultraviolet to the near infrared. Absorption coefficient of ScPrCe:LuAG layers for two selected Sc doping levels, 0.6 and 2.9 at%, and varying Pr and Ce content from 0 to 0.008 at% is shown in Fig. 1.

Optical transparency of all epitaxial layers grown from the BaO flux is high and any impurity related absorption was not observed at wavelength above 230 nm. The broad intense spectral bands at 240 and 282 nm come from parity allowed 4f–5d (Pr^{3+}) transitions to the two lowest crystal field split 5d(^{2}D) states. The f–f (Pr^{3+}) parity forbidden transitions were not noticeable in the absorption spectra due to low doping and low thickness of layers. Allowed 4f→5d transitions coming from Ce^{3+} ions were observed at 345 and 445 nm. Doping with isoelectronic Sc^{3+} ions does not induce any new features in the absorption spectra. A slight increase in absorption coefficient apparent below 230 nm presumably comes from certain decrease in the band gap of LuAG due to Sc doping or due to possible unidentified impurities coming from the flux. The Sc doping has no apparent effect on the absorption related to the allowed 4f–5d transitions of rare earth ions, Pr or Ce.

3.2. Photoluminescence (PL)

The excitation and emission spectra of the PL were measured in the spectral range 200–850 nm. The garnet layers doped with Pr^{3+} ions show intense ultraviolet photoluminescence between 290 and 450 nm corresponding to transitions from 5d states to 4f(^{3}H$_J$, ^{3}F$_J$) manifolds (Fig. 2a). This emission has principal maximum at 308 nm and its position practically does not depend on Sc co-doping (Fig. 2b and c). Narrow intraconfigurational 4f–4f(Pr^{3+}) transitions from ^{3}P and ^{1}D terms to ^{3}H$_J$ ground states, observed

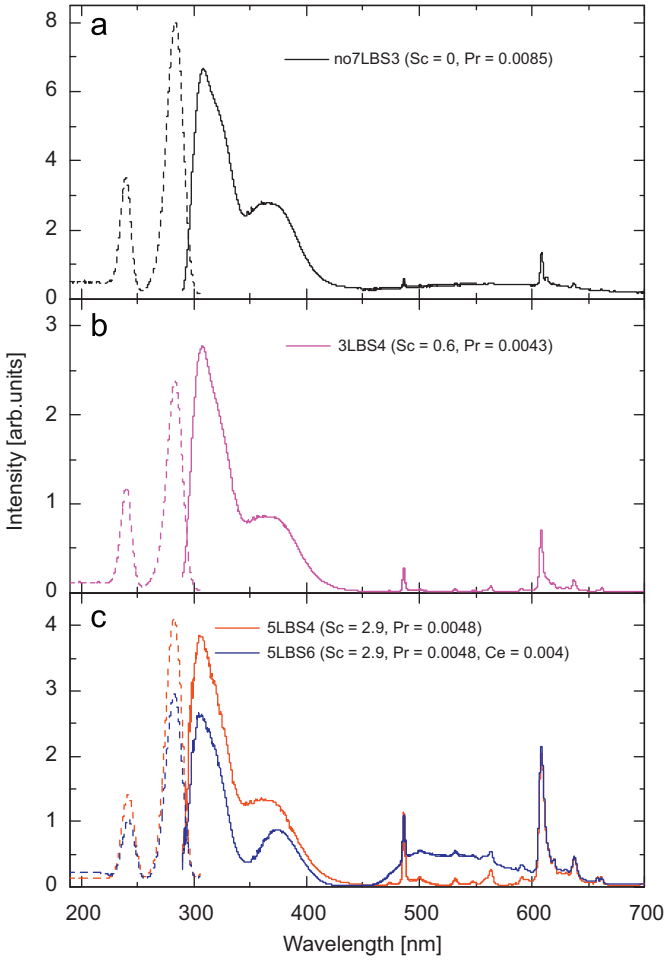

Fig. 2. Photoluminescence excitation (for emission at 308 nm) and emission (excited at 282 nm) spectra of ScPrCe-doped LuAG epitaxial layers. Concentrations of individual dopants in layers are shown in figures. For details, see text.

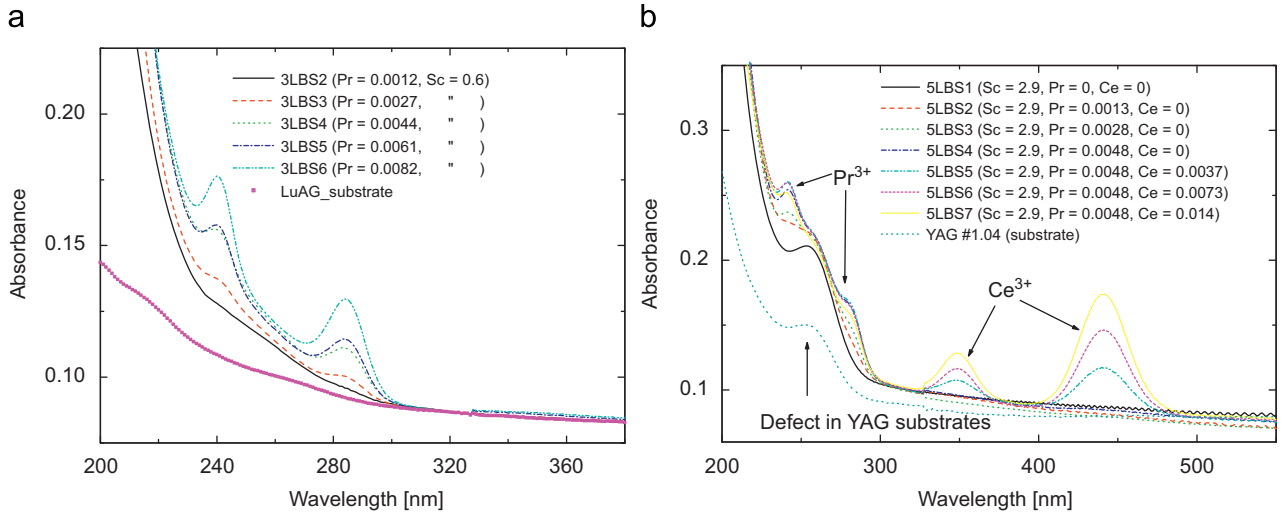

Fig. 1. Absorbance of ScPr co-doped LuAG epitaxial layers. (a) with 0.6 at% of Sc and Pr content specified in the legend grown on LuAG substrates and (b) ScPrCe:LuAG layers with 2.9 at% of Sc grown on YAG substrates. Samples doped with Ce exhibit maxima at 345 and 445 nm. The absorption band at 260 nm comes from the defect centers in YAG substrates. The results were not corrected for reflection.

near 480 and 615 nm, are very weak. Almost all the emissions in Pr:LuAG (i.e. without Sc co-doping) are located in the UV spectral range between 300 and 400 nm. Integral intensity of all f–f peaks reaches $<4\%$ compared to that of 5d–4f spectral band. The broad 5d(Pr^{3+}) bands in the excitation spectra at 240 and 282 nm are closely related to the absorption ones. All the PL features of Pr:LuAG are practically identical to those observed in single crystal counterparts [16–18].

The PL spectra of ScPr and ScPrCe co-doped LuAG films are shown in Fig. 2b and c, respectively. Any Sc related emission was not observed in the PL spectra (note that PL was excited at energies below the band gap). However, at higher Sc doping levels, the most striking feature observed in the PL spectra is significant increase in PL intensities of forbidden f–f transitions, both at 480 and 615 nm. This increase in f–f intensities is accompanied by the decrease in intensity of allowed 5d–4f emission. Fig. 3 shows the ratio of f–f integral PL intensities to d–f ones: linear dependence is observed up to the highest Sc content, 10 at%, where this ratio is about an order of magnitude higher than Sc-undoped samples—almost one third of emission then comes from the forbidden f–f transitions in this sample. The mechanism of the transfer of energy towards ^3P and ^1D terms is not obvious, but presumably nonradiative transitions from 5d states to these terms may play a crucial role.

Additional Ce^{3+} co-doping, ScPrCe:LuAG samples, however, decreases the PL of Pr^{3+} ions (Fig. 2c). Broad 5d→4f emission from the Ce^{3+} ions observed between 480 and 650 nm is relatively weak. Substantial energy transfer from Sc or Pr to Ce ions is not obvious and, on the contrary, quenching of 5d(Pr^{3+}) emission due to Ce doping is rather observed.

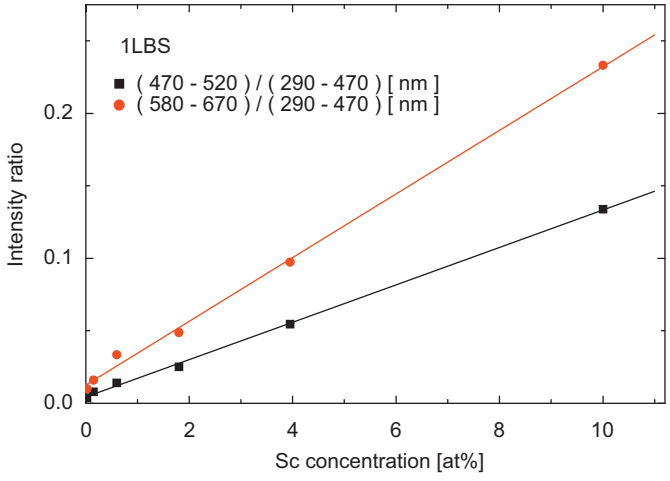

Fig. 3. Dependence of the ratio of integral intensities of f–f photoemissions centered at 470–520 nm ($^3P\rightarrow{}^3H$) and at 580–670 nm ($^1D\rightarrow{}^3H$), respectively, to 5d–4f (^3H,^3F) emission at 290–470 nm on Sc concentration.

3.3. Decay kinetics of PL

In order to obtain more detailed information on the role of impurities in the PL emission of epitaxial garnet films, the 5d–4f decay kinetics from both Pr^{3+} and Ce^{3+} ions were measured. The decay curves are shown in Fig. 4. The samples were excited either at 282 or 340 nm and 5d emissions of Pr^{3+} or Ce^{3+} ions were collected at 320 and 520 nm, respectively. The deconvolution of the decay curves enabled to determine individual contributions in the PL decay. The detailed inspection shows two components for Pr^{3+} 5d emission at 320 nm with a dominant 18 ns component and two orders of magnitude weaker ~80–100 ns component. This slow component was also observed in Pr-undoped layer and it originates likely from the host lattice or from substrate that contains small amount of color centers. These centers have absorption near 280 nm and they are also excited. Only one 55 ns component was observed for Ce^{3+} 5d emission at 520 nm. The obtained values of decay times for both Pr^{3+} and Ce^{3+} ions are in close relation with those reported for the high quality Czochralski single crystals [16]. We can conclude that in layers grown from a lead-free BaO flux, the PL decay curves do not indicate any notable loss of energy from Pr^{3+} or Ce^{3+} ions due to possible flux-related impurities.

3.4. Radioluminescence (RL)

The radioluminescence of layers was measured under X-ray excitation (10 kV, 50 mA) in the spectral range 200–670 nm. All measured RL spectra were compared with reference BGO single crystal ($Bi_4Ge_3O_{12}$), which enabled the mutual comparison of samples and estimate the X-ray yield. The RL spectra of Sc-doped LuAG are displayed in Fig. 5. The spectra of Sc-doped LuAG support the results of Ref. [4]. The Sc^{3+} emission is maximum at 265 nm for the lowest Sc doping, 0.13 at%, and it moves to 290 nm for 2.9 at% of Sc. This intensive emission originates from radiative recombination of an exciton situated near the Sc defect. The shift of the peak may be connected with Sc occupation of both octahedral and dodecahedral sites at high doping levels.

The RL spectra of ScPr and ScPrCe co-doped LuAG layers are displayed in Fig. 6. The integral RL intensity of these spectra is an order of magnitude higher than that of BGO reference single crystal. Comparing the RL spectra with those of LuAG doped either only by

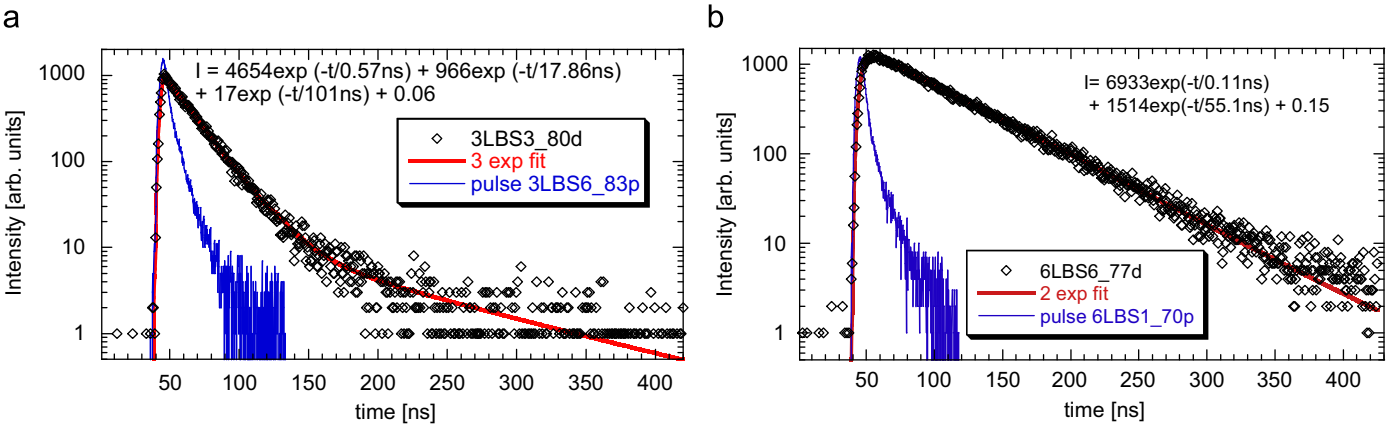

Fig. 4. Photoluminescence decay curves of ScPr- and ScPrCe-doped LuAG epitaxial layers measured at (a) Pr^{3+}(5d–4f) emission, $\lambda_{em}=320$ nm and $\lambda_{exc}=282$ nm and (b) Ce^{3+}(5d–4f) emission, $\lambda_{em}=520$ nm and $\lambda_{exc}=349$ nm. The solid line is convolution of the fitting curve $I(t)$ with the instrumental response.

Sc or only by Pr ions, we can easily identify the main contributions from individual ions. The principal Sc^{3+}- and Pr^{3+}-related peaks are situated at 280 and 308 nm, respectively, and they are marked by arrows in Fig. 6. Detailed inspection of the spectra shows that the integral RL intensity of ScPr:LuAG samples increases with Sc content in 60–80% for Sc doping in the range 1.2–2.9 at%. Furthermore, the relative intensity of Sc peak at 280 nm does not increase in proportion to the Sc concentration. While for low Sc content we observe a proportional increase in RL intensity, Fig. 6a, for higher Sc content > 2 at% contribution from this ion decreases (Fig. 6a and b). The most remarkable feature of Sc doping is connected with the Pr emission: we observed significant increase in intensity of the Pr^{3+} peak at 308 nm with increase in Sc content while the Pr content almost does not change (Fig. 6a). This notable dependency observed for relatively high Sc concentrations up to 3 at% can be explained by the transfer of the excitation energy from sensitizer Sc^{3+} to activator Pr^{3+} ions. For heavily Sc-doped samples above > 3 at%, however, the RL intensity of 5d–4f emission band in the UV spectral range decreases, Fig. 6b, presumably due to concentration quenching and nonradiative transfer of energy to ^3P and ^1D terms, see Fig. 3. For 10 at% of Sc the RL intensity in the UV range is drastically reduced.

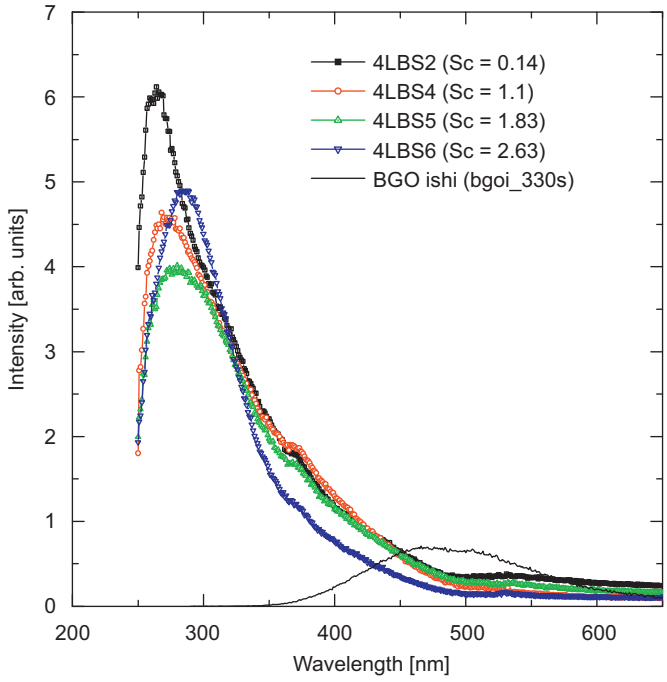

Fig. 5. Radioluminescence spectra of Sc-doped LuAG epitaxial layers. The RL of reference BGO crystal is also shown. Concentrations of Sc, in at%, are shown in the legend.

The RL spectra support the observations in the PL ones: the f–f emissions at 480 and 615 nm are also significantly amplified compared to d–f emission due to Sc doping. Additional doping with Ce^{3+} ions in ScPrCe:LuAG, however, significantly decreases the RL intensity of Pr^{3+} ions. The green 5d–4f emission from the Ce^{3+} ions observed between 500 and 600 nm is relatively weak compared to Ce:LuAG crystal. We did not observe any energy transfer to Ce^{3+} ions and, on the contrary, quenching of Pr^{3+} emission due to Ce doping was rather observed (Fig. 6b).

3.5. Scintillation properties

Scintillation properties of Sc:LuAG, ScPr:LuAG, and ScPrCe:LuAG epitaxial layers were studied under alpha particle excitation (mainly using ^{239}Pu alpha particle source of energy 5.16 MeV). Experimental set-up was described elsewhere [19,20]. This method uses hybrid photon detection and it consists of HPMT (S20 cathode sensitivity) and electronics for pulse height spectra measurements [19,21].

The largest photoelectron yield, N_{phe}, was observed for ScPr:LuAG samples containing low Sc or Pr concentrations, 0.6 at%, of Sc. In the best samples the observed photoelectron yield was even higher as compared to the Czochralski grown Pr:LuAG single crystals (Fig. 7a and Table 1). However, at higher Sc concentrations the N_{phe} yield significantly decreases.

The most remarkable effect of the Sc substitution is related to relative fraction of slow and fast components in the N_{phe} yield.

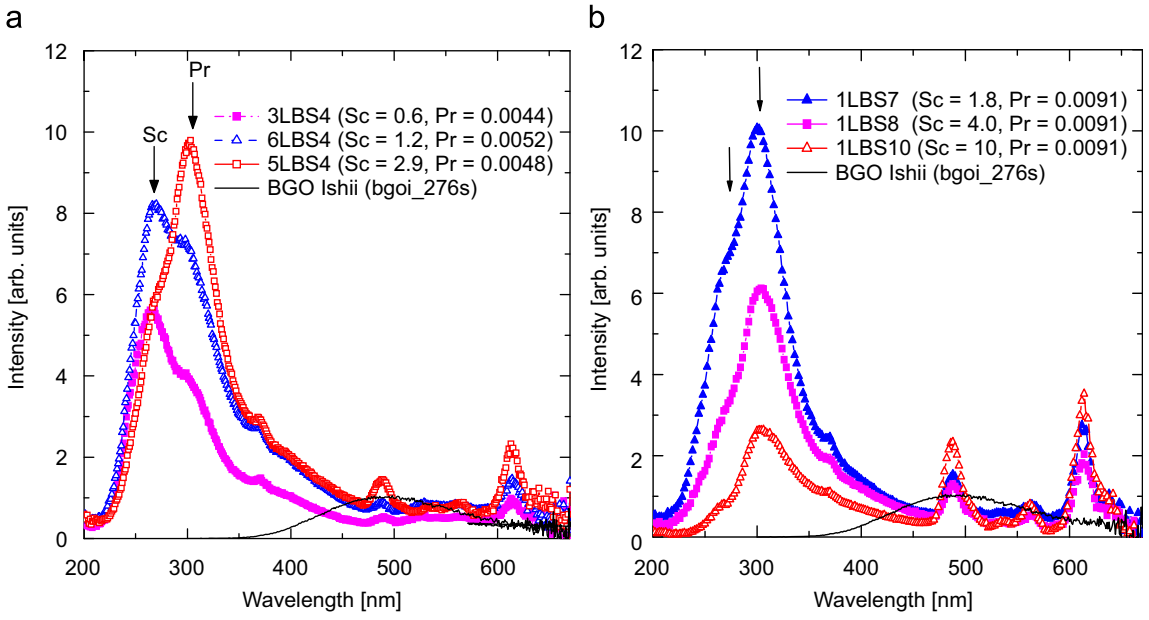

Fig. 6. Radioluminescence of ScPr co-doped LuAG epitaxial layers: (a) samples with low and medium Sc concentration and (b) heavily Sc-doped samples. Concentrations of Sc and Pr, in at%, are shown in the legend, Pr content is approximately the same in individual panels. Arrows indicate respective contributions originating from Sc^{3+} and Pr^{3+} ions. The spectrum of BGO crystal is shown for comparison.

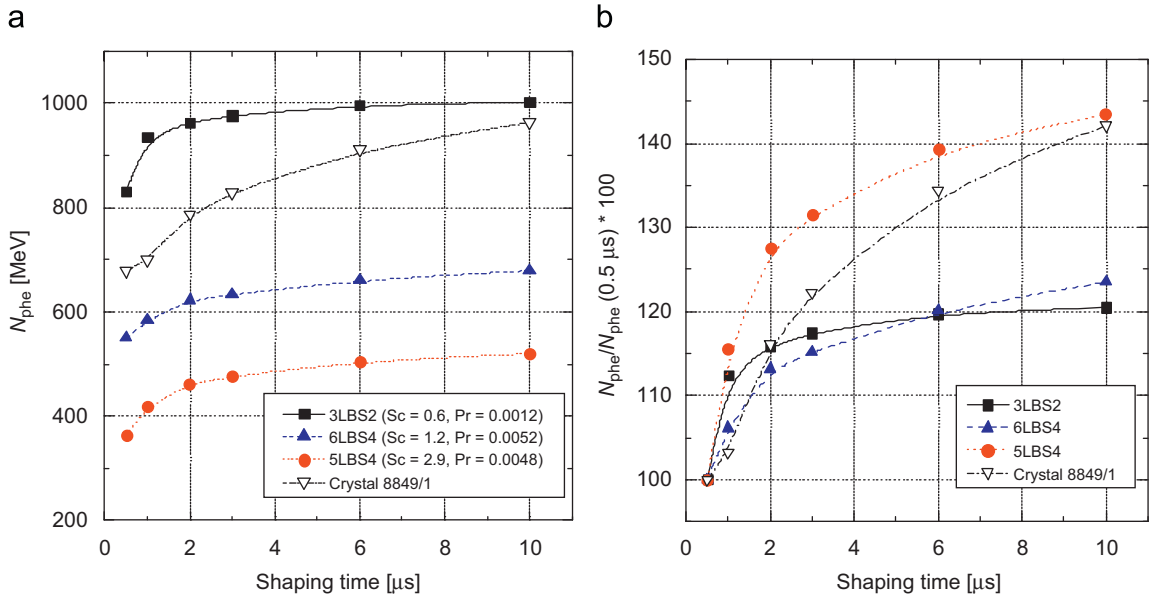

Fig. 7. (a) Photoelectron yield N_{phe} per 1 MeV at different shaping times under alpha particles (^{239}Pu) excitation of ScPr:LuAG epitaxial layers, concentrations of Sc and Pr, in at%, are shown in the legend. (b) N_{phe} normalized to the shortest shaping time of 0.5 μs for the same samples. Reference Czochralski grown single crystal Pr:LuAG, sample 8849/1 is also shown for comparison.

The slow components are strongly suppressed and, on the contrary, the intensity of fast components increases in layers compared to the Czochralski Pr:LuAG single crystals. The time dependence of the photoelectron yield in shaping time range 0.5–10 μs, Fig. 7b, shows that ScPr:LuAG epitaxial layers have substantially smaller N_{phe} time difference than Pr:LuAG single crystals—the relative N_{phe} increase is only ~18% and ~23% at Sc contents 0.6 and 1.2 at%, respectively. In contrast, N_{phe} increases in 40–60% in Pr:LuAG single crystals and it is still far from saturation even at 10 μs shaping time (Fig. 7b). This means that ScPr:LuAG epitaxial layers have smaller content of slow components and values of N_{phe} at the shortest shaping time of 0.5 μs indicate relative increase of fast components in layers compared to single crystals. The slow components come from delayed recombination and according to Ref. [6,8] they originate from antisite Lu_{Al} defects in single crystals and related shallow electron traps. We can speculate that Sc substitution into the octahedral sites effectively suppresses the Lu_{Al} antisite defects, which have favorable effect on scintillation decay. However, at higher Sc concentrations, > 1.2 at%, the fraction of slow components in layers again increases and for 2.9 at% of Sc the slow components form ~45% of N_{phe} signal, which is comparable to the Czochralski grown single crystals. Detailed discussion of scintillation properties of ScPr co-doped LuAG is reported in Ref. [22].

The energy resolution (FWHM), as determined from N_{phe}, of epitaxial layers and single crystals was comparable—the FWHM values were about 10% or even a bit less. Again, ScPr:LuAG samples of low Sc and Pr concentration, which also have the highest N_{phe}, exhibit somewhat better FWHM, ~8%. However, the FWHM increases with increase in Sc content and for heavily doped layers (> 2.5 at% of Sc) it is ~20%.

The Ce^{3+} co-doping leads to the decrease in N_{phe} even more and thus Ce doping is likely useless. This is in correlation with the RL spectra and supports the observation that the Ce co-doping does not improve the scintillation properties of ScPr-doped LuAG but rather effectively quenches emission from the Pr^{3+} ions.

4. Conclusions

The LuAG epitaxial layers doped with optimized concentrations of Sc and Pr ions and grown from the $BaO–B_2O_3–BaF_2$ flux have competitive radioluminescence and scintillation properties with the Czochralski grown single crystals. The maximum integral radioluminescence was observed for samples with moderate Sc concentrations, 1.2–2.9 at%, and it was 60–80% higher compared to samples without Sc co-doping. This is due to the combined contribution of Sc and Pr ions in the RL spectra and apparent energy transfer from Sc^{3+} to Pr^{3+} activator ions. However, at higher Sc concentrations, > 3 at%, both the PL and RL intensities are rapidly reduced and emission is partly quenched. The observed PL decay time of 5d–4f transitions of Pr^{3+} ions was ~18 ns and it was independent of Sc content in the layers, which indicates that there is not any notable energy loss due to Sc co-doping.

The best photoelectron yield N_{phe} measured under alpha particle excitation was obtained, in contrast to the RL results, for relatively low Sc concentrations, ~0.6 at%. Considerable suppression of slow components in the photoelectron yield is the most remarkable effect of Sc co-doping. Furthermore, the fast components are notably higher in layers compared to the Czochralski grown crystals. However, at higher Sc concentrations, about > 1 at%, N_{phe} started to decrease, the slow components increased, and also energy resolution became worse. An increase of slow component in photoelectron yield with increase in Sc content can be tentatively explained by new stable electron traps, which were induced by the presence of Sc ions and which would delay radiative recombination at Pr^{3+} ions. They may have similar origin as relatively deep traps which were found in ScCe co-doped bulk crystals [23,24]. While at low Sc concentrations the radiative recombination of an exciton trapped on Sc impurity and fast energy transfer to nearby Pr^{3+} ions is a dominant process, at higher Sc concentrations likely electron trapping around Sc defect may become dominant and slow components are relatively more intense. Thus the defects induced at high Sc doping are likely the main reason for reduced improvement. Certain discrepancy between RL results (which indicate increased light yield at rather high Sc content, up to 3 at%) and N_{phe} results (increased yield was observed only at low Sc content < 1 at%) can be explained by the fact that RL is a steady state measurement, which takes into account all slow components while the largest shaping time of N_{phe} was 10 μs.

In conclusion, Sc^{3+} and Pr^{3+} co-doped LuAG crystals with optimized dopant content can provide in many aspects better scintillation response compared to Pr:LuAG samples without Sc co-doping.

Acknowledgments

The supports of the Grant Agency AS CR, no. KAN300100802, Czech Science Foundation, no. 202/08/0893, Ministry of Education CR, research plans MSM0021620834 and 1M06002, are gratefully acknowledged.

References

[1] W. Drozdowski, T. Lukasiewicz, A.J. Wojtowicz, D. Wisniewski, J. Kisielewski, J. Cryst. Growth 275 (2005) e709.
[2] L. Swiderski, M. Moszynski, et al., IEEE Trans. Nucl. Sci. 56 (2009) 2499.
[3] C.W.E. van Eijk, P. Dorenbos, R. Visser, IEEE Trans. Nucl. Sci. 41 (1994) 738.
[4] N.N. Ryshkin, et al., J. Phys.: Condens. Matter 7 (1995) 5857.
[5] P. Dorenbos, et al., Proceedings of the SCINT 2005, Alushta, Crimea, Ukraine, 2005 (Gektin, Grinyov, Ukraine, 2006), pp. 365–367.
[6] Y. Zorenko, V. Gorbenko, I. Konstankevych, A. Voloshinovskii, G. Stryganyuk, V. Mikhailin, V. Kolobanov, D. Spassky, J. Lumin. 114 (2005) 85.
[7] M. Nikl, E. Mihóková, J. Pejchal, A. Vedda, Y. Zorenko, K. Nejezchleb, Phys. Status Solidi (b) 242 (2005) R119.
[8] M. Nikl, A. Vedda, M. Fasoli, I. Fontana, V. Laguta, E. Mihokova, J. Pejchal, J. Rosa, K. Nejezchleb, Phys. Rev. B 76 (2007) 195121.
[9] V. Babin, V. Gorbenko, A. Makhov, J.A. Mares, M. Nikl, S. Zazubovich, Y. Zorenko, J. Lumin. 127 (2007) 384.
[10] Y. Zorenko, et al., Radiat. Meas. 45 (2010) 444.
[11] V. Grobenko, et al., Radiat. Meas. 45 (2010) 461.
[12] M. Kučera, K. Nitsch, M. Kubová, N. Solovieva, M. Nikl, J.A. Mareš, IEEE Trans. Nucl. Sci. 55 (2008) 1201.
[13] M. Kucera, K. Nitsch, M. Nikl, M. Hanus, S. Danis, J. Cryst. Growth 312 (2010) 1538.
[14] M. Kucera, K. Nitsch, M. Nikl, M. Hanus, Radiat. Meas. 45 (2010) 449.
[15] B. Strocka, P. Holst, W. Tolksdorf, Philips J. Res. 33 (1978) 186.
[16] J. Pejchal, et al., J. Phys. D: Appl. Phys. 42 (2009) 055117.
[17] M. Nikl, H. Ogino, A. Krasnikov, A. Beitlerova, A. Yoshikawa, T. Fukuda, Phys. Status Solidi (a) 202 (2005) R4.
[18] H. Ogino, A. Yoshikawa, M. Nikl, A. Krasnikov, K. Kamada, T. Fukuda, J. Cryst. Growth 287 (2006) 335.
[19] J.A. Mares, P. Prusa, M. Nikl, A. Beitlerova, et al., Radiat. Meas. 45 (2010) 369.
[20] P. Prusa, T. Cechak, J.A. Mares, M. Nikl, et al., Appl. Phys. Lett. 92 (2008) 041903.
[21] C. D'Ambrosio, H. Leutz, Nucl. Instr. Methods Phys. Res. A 501 (2003) 463.
[22] P. Prusa, M. Kucera, J.A. Mares, M. Nikl, K. Nitsch, M. Hanus, Z. Onderisinova, T. Cechak, J. Cryst. Growth, this issue, doi:10.1016/j.jcrysgro.2010.10.046.
[23] J.A. Mares, et al., Phys. Status Solidi (c) 4 (2007) 996.
[24] J.A. Mares, A. Beitlerova, M. Nikl, K. Blazek, et al., Proceedings of the SCINT'05, September 19–23, 2005, Alushta, Ukraine, Kharkov, 2006, p. 138.

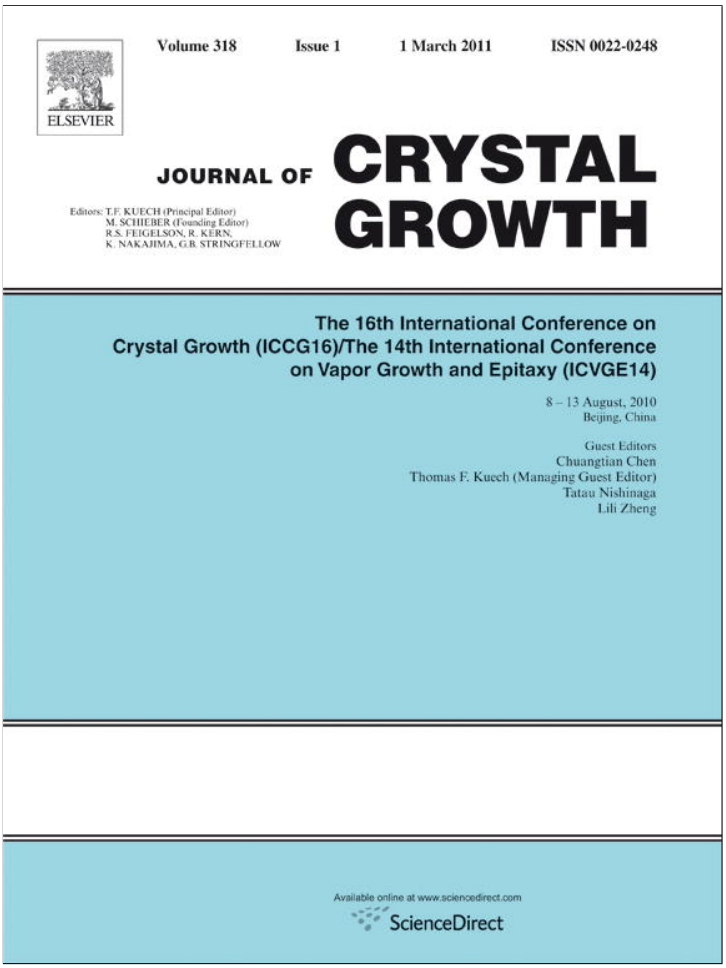

Journal of Crystal Growth 318 (2011) 545–548

Contents lists available at ScienceDirect

Journal of Crystal Growth

journal homepage: www.elsevier.com/locate/jcrysgro

Scintillation properties of Sc-, Pr-, and Ce-doped LuAG epitaxial garnet films

P. Prusa [a,*], M. Kucera [b], J.A. Mares [a], M. Nikl [a], K. Nitsch [a], M. Hanus [b], Z. Onderisinova [b], T. Cechak [c]

[a] Institute of Physics v.v.i., AS CR, Cukrovarnicka 10, CZ 16200 Prague, Czech Republic
[b] Charles University, Faculty of Mathematics & Physics, Ke Karlovu 5, CZ 12116 Prague, Czech Republic
[c] Faculty of Nuclear Engineering and Physical Sciences, Czech Technical University, Brehova 7, CZ 115 19, Prague, Czech Republic

ARTICLE INFO

Available online 23 October 2010

Keywords:
A1. Energy resolution
A1. Photoelectron yield
A3. Liquid phase epitaxy
B1. LuAG:Pr
B1. Sc codoped material
B2. Scintillator materials

ABSTRACT

$Lu_3Al_5O_{12}$ (LuAG) films were grown from the $BaO–B_2O_3–BaF_2$ flux on LuAG and YAG substrates using the liquid phase epitaxy method (LPE). They were doped with Pr^{3+}, Sc^{3+}, and eventually still with Ce^{3+} ions. Photoelectron yield, its time dependence, and energy resolution were measured under α-particle excitation. A sample of the Czochralski-grown bulk LuAG:Pr single crystal was measured as a reference. The best performing epitaxial films had low Sc^{3+} concentration and appeared comparable or superior to the Czochralski-grown crystal in terms of photoelectron yield and relative intensity of the fast component of scintillation response. High concentration of Sc^{3+} ions results in slowdown of response and lower photoelectron yield. Some samples with lower photoelectron yield than that of the Czochralski-grown crystal did exhibit better energy resolution.

1. Introduction

Pr^{3+} [1,2] and Ce^{3+} [3–5] doped lutetium aluminum garnet scintillators (LuAG–$Lu_3Al_5O_{12}$) with the emission peaks at about 310 and 510 nm, respectively, due to fast allowed $5d_1$–4f transitions, belong to a family of high performance complex oxide scintillators. Nowadays, LuAG thin crystalline films coupled with a CCD chip are used in the field of 2D radiography with high 2D resolution, even in submicrometer scale [6]. Usually, detector screens for this application are prepared from the Czochralski-grown bulk crystals by cutting and polishing to obtain very thin disc. However, this process is time consuming and expensive. Liquid phase epitaxy (LPE) method offers a cheaper alternative to manufacture such an element [7]. Since the reasonable efficiency of CCD chips reached the UV region, it is also possible to use Pr^{3+} doped LuAG for 2D radiography. Shorter wavelength of LuAG:Pr scintillation photons in comparison with LuAG:Ce promises better 2D spatial resolution.

For good lateral resolution, the contrast, ability to record series of images within millisecond time range, high light yield (LY) and minimum afterglow are necessary [3]. The LY and luminescence decay can be affected by impurities and/or material-specific defects.

Pr^{3+} center offers high quantum efficiency and fast response (20 ns decay time) in the 310 nm emission band in LUAG host [8,9]. However, slow scintillation component exists due to retrapping migrating electrons at shallow electron traps [10,11]. The Pr^{3+}–Sc^{3+} codoping may speed up the scintillation response, because Sc^{3+} ions could simplify the excitation energy migration towards Pr^{3+} centres due to good overlap of the Sc-related emission (Sc-trapped exciton) at around 275 nm with the 4f–$5d_1$ absorption band of Pr^{3+} center [7,12].

LPE method may lead to lower amount of slow component in the scintillation response with respect to LuAG:Pr single crystal. Lower amount of slow scintillation component was already observed in LuAG:Ce epitaxial films [13,14]. Slower response of the Czochralski-grown LuAG:Ce crystals is caused by shallow electron traps [15,16] ascribed to the Lu_{Al} antisite defects (Lu^{3+} ion at octahedral Al^{3+} site) [17]. These defects arise in garnet lattice due to high growth temperature from the melt (~2000 °C), using the Czochralski or Bridgman techniques [18–20]. The LPE films are prepared from flux at much lower temperature (around 1000 °C). Consequently, negligible concentration of antisite defects should result in faster energy delivery to the Ce^{3+} centres. The behavior of LuAG:Pr should be similar [10].

The aim of this work is to study scintillation response, N_{phels} photoelectron yield, its time dependence, and the energy resolution of LuAG:Pr films grown by the LPE method and a Czochralski-grown LuAG:Pr single crystal. Moreover, Sc^{3+} and Ce^{3+} codoping influence on scintillation response was studied in order to optimize the concentration of Pr and Sc in the melt in terms of scintillation performance.

2. Experimental

Six batches of epitaxial films with approximately 6 samples in every batch were prepared. Most of the films were selected to be used in this study. The films were grown by the isothermal dipping

* Corresponding author. Tel.: +420 604 958 601.
E-mail address: petr.prusa@centrum.cz (P. Prusa).

0022-0248/$ - see front matter © 2010 Elsevier B.V. All rights reserved.
doi:10.1016/j.jcrysgro.2010.10.046

liquid phase epitaxy onto a single crystalline LuAG or YAG substrate of (1 1 1) crystallographic orientation, 0.5 mm in thickness, and 20 mm in diameter. The epitaxial films were grown using recently developed $BaO–B_2O_3–BaF_2$ flux [21]. This flux is especially suitable for the growth of UV (down to 200 nm) emitting scintillation films, such as the Pr-doped LuAG. $BaO–B_2O_3–BaF_2$ flux was preferred over traditional $PbO–B_2O_3$ flux because of the Pb^{2+} contamination from the latter flux quenching the scintillation response [13,22].

For high concentration of Sc in the film, the lattice constant of LuAG:Pr,Sc becomes significantly larger than the lattice constant of LuAG substrate. In this case, YAG substrate is preferable due to bigger lattice constant. In this way, the growth of LuAG:Pr,Sc with high concentration of Sc is possible. Samples with Sc concentration higher than 1.5 at% were grown on YAG substrate, others on LuAG substrate (see Table 1).

The growth temperature of epitaxial films was in the range 997–1030 °C. The thickness of the LPE films was determined by weighing and is in the range 5.5–14.0 μm. The amount of Sc, Pr, and Ce in the melt was varied (see Table 1). We assume approximately the same concentration of Sc in the film as in the melt, and 18 times lower concentration of Pr and Ce in the film than in the melt. Segregation coefficient calculations are based on glow discharge mass spectrometry (GDMS) analysis of one sample and may vary from sample to sample by a small factor.

The growth and surface quality of all samples was negatively influenced by high viscosity and high surface tension of the flux, namely, high number of dislocations was revealed. Samples grown on YAG substrates suffered from heteroepitaxial growth, their surfaces were cracked with the exceptions of samples 1LBS8, 2LBS3, and 2LBS4. The 5 N purity Lu_2O_3 and Al_2O_3 and 4 N purity Pr_6O_{11}, CeO_2, and Sc_2O_3 raw powders were used. The preparation and morphology of samples are given in more detail in [23].

For substrates, plates of LuAG and YAG single crystals of about $\varnothing\ 20\times0.5\ mm^2$ were cut from parent boule crystals grown by the Czochralski method in reduction atmosphere from molybdenum crucible at Crytur, Ltd., Turnov. They were further mechanico-chemically polished.

The single crystal of LuAG:Pr (0.31 w% of Pr in the crystal) was grown analogously to Ce-doped and undoped LuAG's mentioned above [14]. The 1 mm thick plate of 10 mm diameter was cut from the crystal boule and polished up to an optical grade. It served as a reference sample and is noted as SC sample.

The N_{phels} yield, i.e. number of photoelectrons generated from the photocathode on scintillating light exposure, was determined from the pulse height spectra. The α-emitting radionuclide, ^{239}Pu (5.16 MeV) [24], was used for scintillation response excitation. The reference crystal was also measured under γ excitation of ^{137}Cs (661.6 keV) and $3172N_{phels}$/MeV photoelectron yield at 1 μs shaping time was obtained. Dependence of N_{phels} on the shaping time t in 0.5–10 μs range was measured. Energy resolution (FWHM) was evaluated by the Gaussian fit of the peak in spectrum. Photoelectron yield N_{phels}/MeV was calculated as $N_{phels}/MeV = N_{phels}/E_\alpha$, where E_α is energy of α-particle.

The experimental set-up, in detail described in Ref. [25], consists of a hybrid photomultiplier (HPMT) model DEP PPO 475B, an ORTEC model 672 spectroscopy amplifier, a multichannel buffer ORTEC 927TM, and a PC. This set-up works in pulse height mode. Radioactive source was placed directly onto the sample surface. All measurements were performed at RT. Small number of samples has thickness lower than the penetration depth of α-particle in LuAG (10.2 μm). However, it has been shown that it is possible to measure photoelectron yield even under this circumstance [26,13].

Table 1
Scintillating parameters, relative amount (in at%) of Sc, Pr, and Ce in the melt and thickness of LuAG:Pr,Sc,Ce epitaxial films; all quantities were measured under ^{239}Pu excitation and SC (γ) under ^{137}Cs excitation; N_{phels}/MeV photoelectron yield and energy resolution FWHM measured with shaping time $\tau=1$ μs, N_{phels}/MeV with $\tau=0.5$ μs, with exception of SC (γ): $\tau=1$ μs. Last column S indicates substrate (L=LuAG and Y=YAG).

Sample	Sc	Pr	Ce	Thickness (μm)	N_{phels}/MeV	$K_{f/e}$ (%)	FWHM (%)	S
1LBS1	0.025	0.000	0.000	14.0	293	69	14.0	L
1LBS2	0.025	0.083	0.000	12.1	376	67	9.4	L
1LBS3	0.025	0.165	0.000	11.6	387	66	8.2	L
1LBS4	0.15	0.165	0.000	12.1	389	74	10.3	L
1LBS5	0.60	0.165	0.000	8.2	395	76	12.2	L
1LBS7	1.80	0.165	0.000	5.5	316	66	28.1	Y
1LBS8	3.95	0.165	0.000	6.9	214	58	12.0	Y
2LBS2	2.75	0.044	0.000	10.5	323	57	12.2	Y
2LBS3	2.85	0.150	0.000	11.9	262	59	18.2	Y
2LBS4	2.80	0.375	0.000	10.4	196	63	16.4	Y
3LBS2	0.60	0.023	0.000	6.3	832	73	8.0	L
3LBS3	0.60	0.050	0.000	8.5	620	76	8.3	L
3LBS4	0.60	0.080	0.000	11.7	576	78	9.8	L
3LBS5	0.60	0.111	0.000	9.9	554	79	9.7	L
3LBS6	0.60	0.149	0.000	11.2	465	79	10.5	L
4LBS2	0.14	0.000	0.000	5.7	529	74	10.6	L
4LBS3	0.50	0.000	0.000	7.8	528	77	10.0	L
4LBS6	2.63	0.000	0.000	6.7	403	64	29.7	Y
5LBS1	2.88	0.000	0.000	10.5	338	58	18.6	Y
5LBS2	2.88	0.024	0.000	11.8	360	57	14.0	Y
5LBS3	2.88	0.051	0.000	11.0	363	60	14.8	Y
5LBS4	2.88	0.087	0.000	12.3	362	61	15.6	Y
5LBS5	2.88	0.087	0.068	11.9	322	64	18.8	Y
5LBS6	2.88	0.087	0.134	10.9	245	64	27.5	Y
5LBS7	2.88	0.087	0.263	10.2	193	68	17.8	Y
6LBS1	1.20	0.000	0.000	7.0	648	75	13.3	L
6LBS2	1.20	0.026	0.000	11.2	652	77	12.1	L
6LBS3	1.20	0.056	0.000	9.9	543	76	17.6	L
6LBS4	1.20	0.095	0.000	10.7	550	77	14.0	L
6LBS5	1.20	0.095	0.038	10.5	601	78	15.3	L
6LBS6	1.20	0.095	0.086	10.8	601	79	9.6	L
SC	–	–	–	~1000	678	64	10.7	
–	SC (γ)	–	–	–	~1000	3172	–	–
–								

3. Results and discussion

The values of N_{phels}/MeV for 0.5 μs shaping time are given in Table 1 for all the samples. Samples with higher Sc^{3+} concentration were grown on YAG substrates. They suffered with a large number of cracks and bad surface quality also due to heteroepitaxial growth.

Fig. 1 displays dependences of N_{phels}/MeV ($\tau=0.5$ μs) on Sc concentration in the melt for three fixed concentrations of Pr. At first, N_{phels} rises, but at some point, it starts to decrease. The maximum seems to shift to lower Pr concentration with increase in Sc concentration. For fixed Sc concentration, the dependence of N_{phels}/MeV on Pr concentration is similar (see Fig. 2).

Probably, the electrons are trapped around Sc^{3+} while Pr^{3+} ion serves as a hole trap [7]. Thus, separation of charges may occur and their recombination at Pr^{3+} luminescent center is delayed or even prevented. On the other hand, maxima in Fig. 1 indicate that some energy is transferred to the Pr^{3+} luminescent centres. However, the trapping of electron near Sc^{3+} ion dominates in samples with higher Sc concentration.

Samples codoped by Ce^{3+} ions with Pr concentration of 0.087 and Sc concentration of 2.88 show a decrease in N_{phels} yield with increase in Ce^{3+} concentration. However, it is a question whether light yield is also lowered. The quantum efficiency of HPMT photocathode in the region of Ce^{3+} emission is smaller by factor 1.5–1.8 with respect to a 250–400 nm region, where the emission of Ce-free sample is placed. In fact, the Ce^{3+} codoped samples with Pr concentration of 0.095 and Sc concentration of 1.20 exhibit N_{phels} increase in comparison with sample free from Ce^{3+} ions.

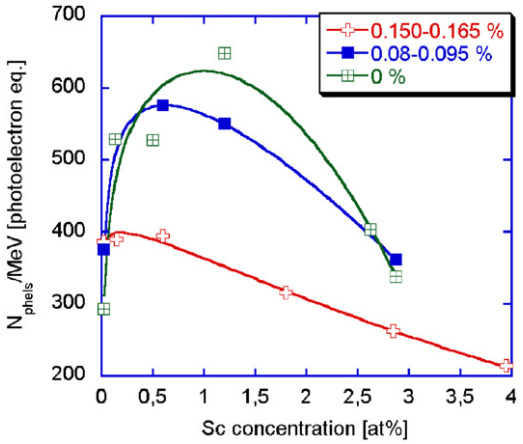

Fig. 1. Dependence of N_{phels} photoelectron yield on Sc concentration in the melt for three different Pr concentrations in the melt. The lines are only to guide the eyes.

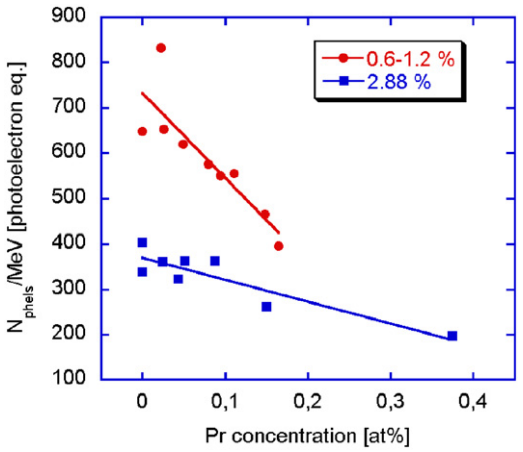

Fig. 2. Dependence of N_{phels} photoelectron yield on Pr concentration in the melt for two different Sc concentrations in the melt. The lines are only to guide the eyes.

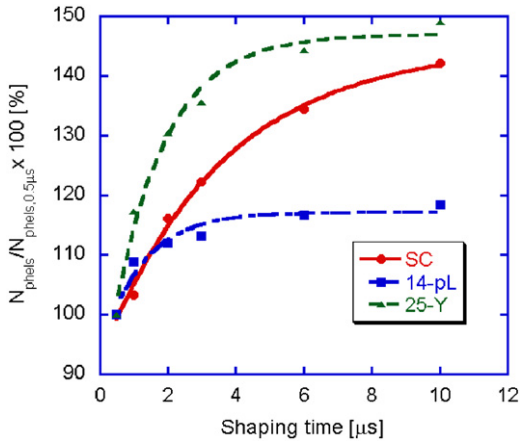

Fig. 3. Time dependence of N_{phels} photoelectron yield in the range 0.5–10 μs shaping time. Photoelectron yield is normalized to the value measured at shaping time $\tau=0.5$ μs. $K_{f/e}$ is the relative intensity of fast component of scintillation response. Fastest and slowest samples among epitaxial films together with SC sample are presented.

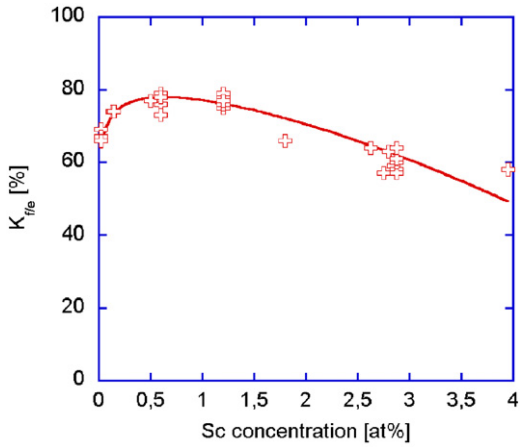

Fig. 4. Dependence of $K_{f/e}$ value on Sc concentration in the melt. The line is only to guide the eyes.

Some epitaxial films exhibit higher (or comparable) N_{phels} as SC sample. Comparison of γ-(^{137}Cs) and α-(^{239}Pu) particle excitation of reference crystal (sample SC) showed significant difference arising from different stopping power of α-particles and electrons produced by γ-ray interaction: $N_{phels}/MeV_{SC,137Cs}=3172$ and $N_{phels}/MeV_{SC,241Am}=700$. The γ/α yield ratio is about 4.5.

Scintillation decay in LuAG:Pr can be treated as a sum of two exponential terms. The typical values of decay times are of about 20 ns for the dominating faster component [9] and of hundreds of nanoseconds for slower component. Using $t=0.5$–10 μs for the measurement of N_{phels} yield of such material, we scanned over the slower decay process (the fast component has decayed entirely in 500 ns). N_{phels} yield dependence on the shaping time should follow the dependence $N_{phels}(t)=m_1-m_2\exp[-m_3t]$, where m_i are parameters obtained by a fit (see Fig. 3). Afterwards, we calculate the relative intensity of the fast fraction of the entire response $K_{f/e}$ as $K_{f/e}=1-(m_2/m_1)$.

The $K_{f/e}$ values are presented in Table 1. $K_{f/e}$ is dependent on Sc concentration (see Fig. 4). As N_{phels}, $K_{f/e}$ exhibits maximum for one Sc concentration. Fortunately, fastest samples also exhibit higher N_{phels}. The values of $K_{f/e}$ of three samples with highest N_{phels} are equal to 73%, 75%, and 77%. These are significantly higher than $K_{f/e}$ of the SC sample (64%).

In the Czochralski-grown crystals, the slowing down of decay process was caused by the shallow traps related to Lu_{Al} antisite defects, but these were not present in LPE films. Thus, the slow component of scintillation response of many epitaxial films had lower relative intensity. At low Sc concentration, Sc-trapped exciton formation is probably dominant and its energy is rapidly transferred to a nearby Pr^{3+} center. However, the electron trapping around Sc becomes a dominant process at higher Sc concentration. Thus, the slow component of scintillation response becomes relatively more intense. It is in agreement with the N_{phels} behavior.

The response of Ce^{3+} codoped samples was probably fastened a little by additional radiative recombination channel at Ce^{3+} ion. This effect was observed for samples with Pr concentration of 0.087 and Sc concentration of 2.88, as well as for samples with Pr concentration of 0.095 and Sc concentration of 1.20.

Parameter $1/m_3$ is directly proportional to decay time of slower component. Interestingly, $1/m_3$ also exhibits the dependence on dopants concentration (see Fig. 5). Also, the decay of slow component is faster for all epitaxial films (from 863 to 2226 ns) than for sample SC (3612 ns). The slow component of scintillation decay of LuAG:Ce is normally approximated by two (or more) exponentials [27]. In the present case, having only six values of photoelectron yield is not reasonable. Parameter $1/m_3$ reflects an average decay time. If $1/m_3$ decreases, faster decay processes become more significant in the time scale above 500 ns. In case of LuAG:Sc,Pr,Ce system it is most probably the Sc-trapped exciton with decay time above 610 ns [28]. Since the

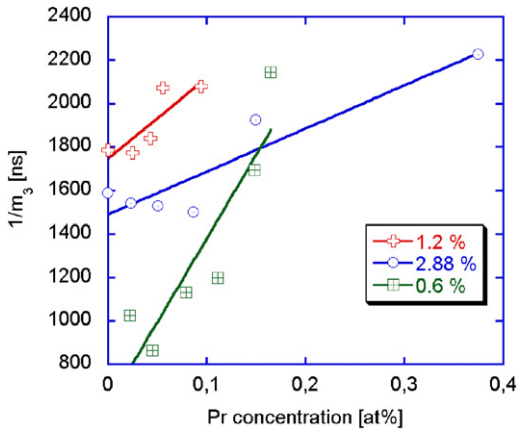

Fig. 5. Dependence of $1/m_3$ parameter on Pr concentration in the melt for three different concentrations of Sc in the melt. $1/m_3$ is directly proportional to decay time of the scintillation response slow component. The lines are only to guide the eyes.

decay of Pr^{3+} center itself is fast, rise in $1/m_3$ with Pr concentration points rather to different processes (e.g. the separation of charges around Sc and Pr ions) responsible for the delay of radiative recombination. Slower components in SC sample are related with delayed recombination caused by the presence of shallow trap levels in the band gap. Detailed analysis of this problem is beyond the scope of this paper.

Measured pulse height spectra were also used for the evaluation of energy resolution. FWHM generally decreases with the increase in N_{phels} yield. Consequently, it was best for sample 3LBS2 and worst for samples with high Sc concentration. However, FWHM of few epitaxial films was better or comparable to sample SC although they exhibited lower N_{phels} yield (see Table 1).

Such an improvement for an epitaxial film prepared by the LPE method has been already reported [13]. It has been suggested that the scintillator intrinsic energy resolution is affected by the scintillator nonproportionality [29]. The degradation of energy resolution is introduced due to a cascade process occurring after the energy of ionizing particle is transferred to secondary electron and due to particular features of exciton transport. Recent reports [30–32], together with FWHM and N_{phels} values in Table 1, point to probable negative impact of defects and related trapping levels on the energy resolution.

4. Conclusions

The N_{phels} yield depends on both Sc and Pr concentrations. Epitaxial films with lower Sc^{3+} ions concentration of 0.6% and Pr^{3+} concentration below or equal to 0.05% were comparable or even superior to the Czochralski-grown crystal in all the studied parameters. Also, the higher concentration of Sc^{3+} leads to worse $K_{f/e}$ value, which gives the relative intensity of the fast scintillation component. FWHM was negatively affected by the high Sc^{3+} concentration as well. Therefore, we conclude that relative Sc concentration of 2.8 at% in the melt is very high for LuAG:Pr,Sc epitaxial films growth. The worst surface morphology was observed for samples grown on YAG substrate due to high flux viscosity, heteroepitaxial growth, and possible mismatch of lattice constants between the substrate and the film. Bad surface morphology usually does not affect negatively scintillation performance of epitaxial films, as observed in [26], but is unwanted in microradiography applications.

The LPE method proved to be superior for production of LuAG based scintillators compared to the Czochralski method in terms of relative intensity of the fast scintillation component. This effect is presumably due to the absence of Lu_{Al} antisite defects in epitaxial films, introduced into the bulk crystals because of high temperature of growth.

Codoping of Sc^{3+} and Pr^{3+} appears a suitable way of preparing high figure-of-merit scintillating films, even though results were not as good as expected and optimum concentrations are rather critical. Ce^{3+} codoping appears useless.

Better energy resolution of samples with lower N_{phels} with respect to SC sample was obtained. This improvement may also be related to the absence of antisite defects in epitaxial films.

Acknowledgment

The support of the Grant Agency of the AS CR KAN300100802, MSMT no. 1M06002, and Czech Science foundation no. 202/08/0893 projects is gratefully acknowledged.

References

[1] M. Nikl, H. Ogino, A. Krasnikov, A. Beitlerova, A. Yoshikawa, T. Fukuda, Phys. Status Solidi A 202 (2005) R4.
[2] J.A. Mares, A.Beitlerova, M. Nikl, K. Blazek, K. Nejezchleb, C. D'Ambrosio, Proceedings of the 8th International Conference on Inorganic Scintillators and their Use in Scientific and Industrial Applications, National Academy of Sciences of Ukraine, Alushta, Crimea, Ukraine, 19–23 September 2005, pp. 138–141.
[3] M. Nikl, Meas. Sci. Technol. 17 (2006) R37.
[4] C. Dujardin, C. Mancini, D. Amans, G. Ledoux, D. Abler, E. Auffray, P. Lecoq, D. Perrodin, A. Petrosyan, K.L. Ovanesyan, J. Appl, Physics 108 (2010) 013510.
[5] M Nikl, E Mihokova, J.A Mares, A Vedda, M Martini, K Nejezchleb, K Blazek, Phys. Status Solidi (b) 181 (2000) R10–R12.
[6] J. Tous, K. Blazek, L. Pina, B. Sopko, Radiat. Meas. 42 (2007) 925.
[7] M. Nikl, J. Tous, J.A. Mares, P. Prusa, E. Mihokova, K. Blazek, A. Vedda, Yu. Zorenko, V. Gorbenko, Proceedings of the SPIE 7310 (2009)731008-731008-10.
[8] J. Pejchal, et al., J. Phys. D: Appl. Phys. 42 (2009) 055117.
[9] J.A. Mares, A. Beitlerova, M. Nikl, A. Vedda, C. D'Ambrosio, K. Blazek, K. Nejezchleb, Phys. Status Solidi C 4 (2007) 996.
[10] M. Nikl, J. Pejchal, E. Mihokova, J.A. Mares, H. Ogino, A. Yoshikawa, T. Fukuda, A. Vedda, C. D'Ambrosio, Appl. Phys. Lett. 88 (2006) 141916.
[11] L. Swiderski, M. Moszynski, A. Nassalski, A. Syntfeld-Kazuch, T. Szczesniak, K. Kamada, K. Tsutsumi, Y. Usuki, T. Yanagida, A. Yoshikawa, W. Chewpraditkul, M. Pomorski, IEEE Trans. Nucl. Sci. 56 (2009) 2499–2505.
[12] P. Dorenbos, et al., Proceedings of the SCINT1995 Conference, 1995 pp. 364–367.
[13] P. Prusa, T. Cechak, J.A. Mares, M. Nikl, A. Beitlerova, N. Solovieva, Yu.V. Zorenko, V.I. Gorbenko, J. Tous, K. Blazek, Appl. Phys. Lett. 92 (2007) 041903.
[14] P. Prusa, J.A. Mares, M. Nikl, M Kucera, K. Nitsch, M Hanus, J. Opt. Mat. doi:10.1016/j.optmat.2010.04.010.
[15] M. Nikl, Phys. Status Solidi A 202 (2005) 201.
[16] M. Nikl, A. Vedda, M. Fasoli, I. Fontana, V.V. Laguta, E. Mihokova, J. Pejchal, J. Rosa, K. Nejezchleb, Phys. Rev. B 76 (2007) 195121.
[17] M. Nikl, E. Mihokova, J. Pejchal, A. Vedda, Y. Zorenko, K. Nejezchleb, Phys. Status Solidi B 242 (2005) R119.
[18] M.K. Ashurov, Y.K. Voronko, V.V. Osiko, A.A. Sobol, M.I. Timoshechkin, Phys. Status Solidi A 42 (1977) 101.
[19] M.M. Kuklja, J. Phys.: Condens. Matter 12 (2000) 2953.
[20] C.R. Stanek, K.J. McClellan, M.R Levy, R.W. Grimes, Phys. Status Solidi B 243 (2006) R75.
[21] M. Kučera, et al., IEEE Trans. Nucl. Sci. 55 (2008) 1201.
[22] V. Babin, V. Gorbenko, A. Makhov, J.A. Mares, M. Nikl, S. Zazubovich, Yu. Zorenko, J. Lumin. 127 (2007) 384.
[23] M. Kucera, K. Nitsch, M. Nikl, M. Hanus, S. Danis, J. Cryst. Growth 312 (2010) 1538–1545.
[24] M.R. Schmorak, Nucl. Data Sheet 66 (1992) 839.
[25] J.A. Mares, P. Prusa, M. Nikl, K. Nitsch, A. Beitlerova, M. Kucera, M. Hanus, Yu. Zorenko, Radiat. Meas. doi:10.1016/j.radmeas.2009.12.026.
[26] P Prusa, M. Nikl, J.A. Mares, M. Kucera, K. Nitsch, A. Beitlerova, Phys. Status Solidi A 206 (2009) 1494.
[27] W. Chewpraditkul, L. Swiderski, M. Moszynski, T. Szczesniak, A. Syntfeld-Kazuch, C. Waranak, P. Limsuwan, Phys. Status Solidi A 206 (2009) 2599–2605.
[28] N.N. Ryskin, P. Dorenbos, C.W.E. van Eijk, S.Kh. Batygov, J. Phys.: Condens. Matter 6 (1994) 10423–10434.
[29] J.D. Valentine, B.D. Rooney, Nucl. Instr. Meth. Phys. Res. A 353 (1994) 37.
[30] W.W. Moses, S.A. Payne, W.-S. Choong, G. Hull, B.W. Reutter, IEEE Trans. Nucl. Sci. 55 (2008) 10.
[31] G. Bizarri, W.W. Moses, J. Singh, A.N. Vasil'ev, R.T. Williams, J. Lumin. 129 (2009) 1790.
[32] F.A. Selim, D. Solodovnikov, M.H. Weber, K.G. Lynn, Appl. Phys. Lett. 91 (2007) 104105.

Radiation Measurements 45 (2010) 389–391

Contents lists available at ScienceDirect

Radiation Measurements

journal homepage: www.elsevier.com/locate/radmeas

Luminescence and scintillation characteristics of YAG:Ce single crystalline films and single crystals

Yu. Zorenko [a], J.A. Mares [b], P. Prusa [b,c], M. Nikl [b,*], V. Gorbenko [a], V. Savchyn [a], R. Kucerkova [b], K. Nejezchleb [d]

[a] Electronics Department of Ivan Franko National University of Lviv, Gen. Tarnavskogo str., 107, 79017 Lviv, Ukraine
[b] Institute of Physics AS CR, Cukrovarnicka 10, Prague, Czech Republic
[c] FNSPE, Czech Technical Universit, Brehova 7, Prague, Czech Republic
[d] CRYTUR Ltd., Palackeho 175, Turnov, Czech Republic

ARTICLE INFO

Article history:
Received 17 August 2009
Accepted 17 September 2009

Keywords:
YAG:Ce scintillator
LPE technology
Luminescence
Photoelectron yield

ABSTRACT

The detailed comparative analysis of luminescent and scintillation properties of the single crystalline films (SCF) of YAG:Ce garnet grown from melt-solutions based on the traditional PbO-based and novel BaO-based fluxes, and of a YAG:Ce bulk single crystal grown from the melt by the Czochralski method, was performed in this work. Using the ^{241}Am (α-particle, 5.49 MeV) excitation we show that scintillation yield and energy resolution of the optimized YAG:Ce SCF is fully comparable with that of the YAG:Ce single crystal analogue.

1. Introduction

Ce^{3+}-doped single crystals (SC) and single crystalline films (SCF) of $Y_3Al_5O_{12}$ (YAG) and $Lu_3Al_5O_{12}$ (LuAG) garnets are considered for fast scintillator applications. The YAG:Ce and LuAG:Ce SC are characterized by large (up to 0.2 and 0.6 at.%, respectively) content of Y_{Al} and Lu_{Al} antisite defects (AD) (Ashurov et al., 1977). The AD presence is the consequence of high-temperature (~2000 °C) growth of bulk SC of these garnets from melt by the Czochralski or Bridgman methods and energetically favourable creation of such defects (Kuklja, 2000; Stanek et al., 2006). The Y_{Al} and Lu_{Al} ADs in YAG:Ce and LuAG:Ce SC play the role of emission centers in UV range (Zorenko et al., 2007a) and trapping centers (Nikl et al., 2005). These centers participate in the excitation of the Ce^{3+} luminescence and are responsible for large amount of slow components in scintillation decay of YAG:Ce and LuAG:Ce SCs (Nikl, 2005; Zorenko et al., 2007b). Due to low temperature of growth by the liquid phase epitaxy (LPE) method, the YAG:Ce and LuAG:Ce SCFs can in principle possess better scintillation properties as compared with the corresponding SC due to the absence of Y_{Al} or Lu_{Al} ADs. However, the SCF grown from the PbO-based flux are contaminated by lead ions which negatively influence their light yield (LY) and timing characteristics (Babin et al., 2007).

Recently, the detailed comparative analysis of scintillation properties of LuAG:Ce SC and SCF was performed (Prusa et al., 2008) and positive influence of the novel BaO-based flux on scintillation characteristics of the Ce-doped YAG and LuAG SCFs was reported (Kucera et al., 2008). In this work, the luminescence and scintillation properties of the YAG:Ce SCF grown by LPE from PbO- and BaO-based fluxes and bulk YAG:Ce SC grown by Czochralski method were compared.

2. Samples and experimental methods

The YAG:Ce SC was grown in Crytur Ltd (Czech Republic) by Czochralski method from the melt in oxygen-free reduction atmosphere. The YAG:Ce SCF with a thickness of 13–55 μm were grown in University of Lviv (Ukraine) by LPE method on YAG substrates from melt-solution (MS) based on $PbO–B_2O_3$ and $BaO–B_2O_3–BaF_2$ fluxes (labeled later as YAG:Ce (PbO) and YAG:Ce (BaO) SCF, respectively) at temperatures within 960–1025 °C. The growth conditions of these SCF are presented in Table 1. A SCF growth rate of 0.48–1.33 μm/min in the case of using the PbO-based flux was significantly larger with respect to that of 0.045–0.075 μm/min in the case of using the BaO-based flux (Table 1).

The Ce content in YAG:Ce SCF was determined using SEM JEOL 6420 equipped by a JXA-8612 MX setup. For the YAG:Ce (PbO) SCF, grown from MS with CeO_2 content of 6.2 and 10 mole %, the Ce concentration in SCF was 0.032 and 0.073 at.% (C3 and 42-7 samples, respectively, Table 2). Thus, the segregation coefficient of

* Corresponding author.
E-mail address: nikl@fzu.cz (M. Nikl).

1350-4487/$ – see front matter © 2009 Elsevier Ltd. All rights reserved.
doi:10.1016/j.radmeas.2009.09.009

Table 1
Conditions of growth of YAG:Ce SCF by LPE method from the $PbO–B_2O_3$ and $BaO–BaF_2–B_2O_3$ fluxes.

Molar ratios in melt-solution	$PbO–B_2O_3$	$BaO–BaF_2–B_2O_3$
$BaCO_3/BaF_2/B_2O_3$		0.4/0.4/0.2
PbO/B_2O_3	12	
$R_2 = [Y_2O_3]/[Al_2O_3]$	0.28	0.49
$R_3 = \Sigma R_2O_3/[BaCO_3 + BaF_2 + B_2O_3]$	0.028	0.143
$R_4 = [CeO_2]/[\Sigma R_2O_3]$	0.062–0.1	0.053–0.1
Temperature of growth, T_g, °C	960–1000	950–1025
Velocity of substrate rotation ω, rev/min	100	100
SCF growth rate f_p, μm/min	0.4–1.5	0.045–0.075
SCF thickness, μm	13–55	3.5–9.0

Ce ions is 0.004–0.007. The Ce concentration in YAG:Ce (BaO) SCFs, grown from MS with CeO_2 content of 5.2 mole % (Ba5 sample) and 10 mol.% (B10 and B12 samples) was equal or even below of the detecting limit of our apparatus (≥0.01 at. %). Thus, the segregation coefficient of Ce ions in the case of using the BaO-based flux does not exceed the values of 0.001–0.002 which is in contradiction with the results (Kucera et al., 2008), where higher Ce segregation coefficient was found in both YAG and LuAG SCF grown from BaO-based flux. The reason of such a contradictory result is not clear and deserves further studies.

The content of Ce and Pb flux dopants in the SCF is also strongly influenced by the growth temperature T_g and increase with decreasing T_g value and vice versa (Kucera et al., 2008). Therefore, we have used relatively high temperatures above 950 °C (Table 1) for growth of YAG:Ce (PbO) SCF. The content of Pb ions in such SCF usually appeared below the detection limit of the apparatus, but in some SCF, grown at low temperatures, namely C3 sample, was of about 0.01 at. %.

The CL spectra were measured at 300 and 80 K with the setup based on a DMR-4A monochromator and a FEU-106 PMT under the pulsed e-beam (9 keV, 100 μA) excitation (duration of pulse 2 μs, repetition frequency 3–30 Hz). The decay kinetics of the Ce^{3+} luminescence was measured using the Spectro-fluorometer 199S (Edinburgh Instrument) equipped by TBX-04 PMT detection module (IBH Scotland) under excitation by the M-5000 ns coaxial hydrogen-filled flashlamp. The N_{phels} photoelectron yield was measured using Hybrid DEP PPO 475B PMT under excitation by α-particles of ^{241}Am (5.5 MeV) and ^{239}Pu (5.15 MeV) sources with shaping times of 0.5–10 μs.

3. Results and discussion

The CL spectra of YAG:Ce SC and SCF at RT are shown in Fig. 1a. Apart from the intensive Ce^{3+} luminescence in the 2.75–1.75 eV range with maximum at 2.235 eV, the CL spectra of YAG:Ce SC contain the low-intensity UV emission band arising due to the AD presence (Fig. 1, curve 1). This band in RT range presents a superposition of the luminescence of excitons localized around Y_{Al} AD and the luminescence of Y_{Al} AD in the bands peaked at 4.14 and 3.75 eV, respectively. The shape of the latter emission band is

Table 2
Scintillation properties of YAG:Ce SCF in comparison with YAG:Ce SC under excitation by α-particles of ^{241}Am (5.49 MeV eV) source.

Samples	SCF thickness (μm)	FWHM FW(1/5) (%)	N_{phels} yield per MeV (phels)	N_{phels} (SCF) to N_{phel} (SC)
YAG:Ce (PbO) 42-7	58	**11.5** (**15.4**)	386.8	**111.1**
YAG:Ce (PbO) C3	55	18.5 (29.1)	100.3	28.8
YAG:Ce (BaO) Ba5	2.5	15.3 (22.9)	202.3	58.1
YAG:Ce (BaO) Ba12	1.56	30.9 (42.2)	126.2	36.2
YAG:Ce SC	1 mm	**11** (**17.2**)	348.2	**100**

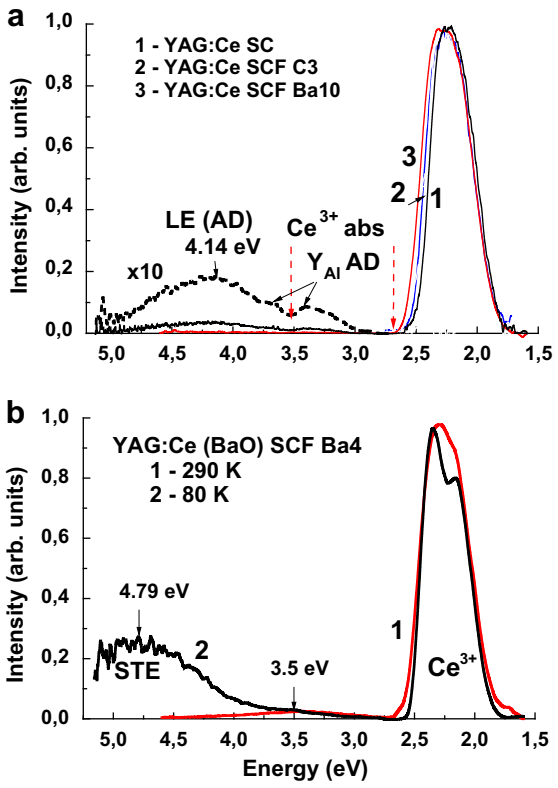

Fig. 1. (a) – CL spectra of YAG:Ce SC (1), YAG:Ce (PbO) (2) and YAG:Ce (BaO) (3) SCF at 300 K. The part of spectra of YAG:Ce SC in the UV range is multiplied by a factor of 10. Position of the Ce^{3+} absorption band is marked; (b) – CL spectra of YAG:Ce (BaO) SCF at 80 K (1) and 300 K (2).

strongly distorted by the Ce^{3+} absorption bands peaked at 3.52 eV. Opposed to YAG:Ce SC, the emission bands related to Y_{Al} AD are diminished in the CL spectra of YAG:Ce (PbO) and YAG:Ce (BaO) SCFs due to the absence of Y_{Al} AD and only Ce^{3+} luminescence is observed (Fig. 1, curves 2 and 3). The different positions of the onset of the Ce^{3+} emission band in CL spectra of YAG:Ce SC and both SCFs (Fig. 1a, curves 1–3) are caused by varying reabsorption of Ce^{3+} luminescence by the Ce^{3+} absorption band peaked at 2.69 eV.

The CL spectra of YAG:Ce (PbO) and YAG:Ce (BaO) SCF at 80 K show the emission of self-trapped excitons (STE) in the band peaked at 4.79 eV (Fig. 2b). In CL spectra of YAG:Ce (BaO) SCF the

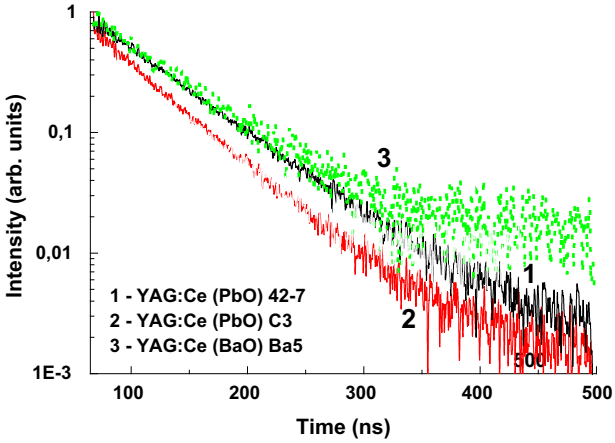

Fig. 2. Decay kinetics of the Ce^{3+} luminescence in YAG:Ce (PbO) (1, 2) and YAG:Ce (BaO) (3) SCF at 530 nm under excitation at 340 nm and at RT.

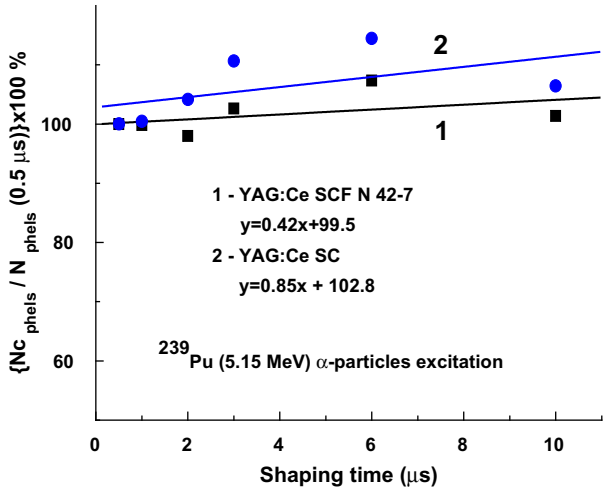

Fig. 3. Dependence of LY of YAG:Ce SCF (1) and YAG:Ce SC (2) on the shaping time of registration of scintillation response under excitation by α-particles of Am^{241} (5.49 MeV) sources.

additional low intensity band peaked at 3.5 eV is present. The origin of this band is not clear and might be connected with the formation of some defects of YAG host during the SCF growth from BaO-based flux.

The decay kinetics of the Ce^{3+} emission in YAG:Ce (PbO) and YAG:Ce (BaO) SCFs under excitation in the Ce^{3+} absorption band at 340 nm is shown in Fig. 3. The decay of the Ce^{3+} emission in YAG:Ce (PbO) SCF with small (below 0.01 at. %) lead content is a single-exponential with the decay time of 65 ns which is close to that in YAG:Ce SC. Increasing the lead content in SCF accelerates the decay of the Ce^{3+} emission in YAG:Ce (PbO) SCF (Fig. 3, curve 3 for C3 sample) which can be caused by the energy transfer from the Ce^{3+} ions to Pb^{2+}-based complex centers (Babin et al., 2009). The decay of the Ce^{3+} luminescence in YAG:Ce (BaO) SCF is close to the single-exponential course within one decade but may contain another slower components, the origin of which is not understood and has not been observed in another YAG:Ce (BaO) SCF samples in (Kucera et al., 2008).

The detailed studies of scintillation response under α-particle excitation by ^{241}Am (5.49 MeV) and ^{239}Pu (5.15 MeV) sources showed that N_{phels} LY of the best YAG:Ce (PbO) SCF (42-7 sample) is even slightly exceeding that of YAG:Ce SC sample (Table 2). Their energy resolutions are similar (~11%) under ^{241}Am (5.49 MeV) excitation (Table 2). The increasing lead content in YAG:Ce SCF (C3 sample) leads to the significant N_{phels} decrease and energy resolution deterioration (Table 2).

The dependence of N_{phels} on the shaping time of registration of scintillation response of the best YAG:Ce (PbO) SCF (42-7 sample) and reference YAG:Ce SC is shown in Fig. 3. In the latter sample the N_{phels} LY increases in the 0.5–10 μs time range by about of 8.5% while for YAG:Ce SCF this value is at least two time lower (~4.2%). The latter observation points to lower content of shallow electron traps in the YAG:Ce SCF with respect to YAG:Ce SC due to absence of the ADs as trapping centers in SCF scintillators (Nikl et al., 2005; Nikl, 2005). Thus, the PbO-based flux can be successfully applied for producing the YAG:Ce SCF scintillators with comparable or even better scintillation properties than those of the SC analogues.

N_{phels} of the best YAG:Ce (BaO) SCF (B5 sample) achieves the values of about 60% in comparison with YAG:Ce SC with energy resolution of about 15.3% (Table 2). The lower values of LY and energy resolution are caused by low (≥0.01 at.%) Ce concentration and small thickness in these SCFs. Considerably better scintillation performance of YAG:Ce (BaO) SCF with higher Ce content were reported very recently (Prusa et al., 2009) though the problem of bad surface morphology and high dislocation density remains unsolved so that there is certainly the room for further BaO-based flux technology optimization.

4. Conclusions

Detailed comparison of the luminescent and scintillation properties of the YAG:Ce SCF grown by LPE from the PbO- and BaO-based fluxes and a bulk YAG:Ce SC grown from the melt by Czochralski method, was made. Apart the common Ce^{3+} luminescence in the visible range, the emission spectra of YAG:Ce SC at RT under high-energy electron excitation show also the complex emission band in UV range arising due to Y_{Al} antisite defect presence, which is absent in LPE-grown SCF.

N_{phels} photoelectron yield of the optimized YAG:Ce SCF, grown from the PbO-based flux, is slightly superior to that of YAG:Ce SC. The energy resolution of these SC and SCF samples is the same (~11%) under ^{241}Am (5.49 MeV) α-particle excitation. Therefore, the PbO-based flux can be successfully applied to manufacturing the YAG:Ce SCF scintillators with comparable scintillation figure-of-merit with respect to the SC analogues. N_{phels} of the best YAG:Ce SCF samples, grown from BaO-based flux, is about 60% of that of YAG:Ce SC, and energy resolution is of about 15.3%. Inferior performance is presumably caused by too low Ce^{3+} concentration in these SCF samples. The fundamental problem of the BaO-based flux is also very high viscosity and surface tension as well as rather low SCF growth rate in comparison with the growth from PbO-based flux.

Acknowledgments

This research was supported by Czech Science Foundation (project 202/08/0893) and MES of Ukraine (project SL-28 F).

References

Ashurov, M., Voronko, Yu., Osiko, V., Solol, A., 1977. Spectroscopic investigation of structural disordering of garnet crystals with rare-earth dopants. Phys. Stat. Sol. (a) 42, 101–110.

Babin, V., Gorbenko, V., Makhov, A., Mares, J.A., Nikl, M., Zazubovich, S., Zorenko, Yu, 2007. Luminescence characteristics of Pb^{2+} centers in undoped and Ce^{3+}doped Lu3Al5O12 single crystalline films and $Pb^{2+} \rightarrow Ce^{3+}$ energy transfer processes. J. Luminescence 127, 384–390.

Babin, V., Bichevin, V., Gorbenko, V., Makhov, A., Mihokova, E., Nikl, M., Vedda, A., Zazubovich, S., Zorenko, Y., 2009. Luminescence of dimer lead centers in aluminium perovskites and garnets. Phys. Stat. Sol. (b) 246, 1318–1326.

Kucera, M., Nitsch, K., Kubová, M., Solovieva, N., Nikl, M., Mares, J.A., 2008. Ce-doped YAG and LuAG epitaxial films for scintillation detectors. IEEE Trans. Nucl. Sci. 55, 1201–1205.

Kuklja, M.M., 2000. Defects in yttrium aluminium perovskite and garnet crystals: atomistic study. J. Phys. Condens. Matter. 12, 2953–2967.

Nikl, M., Mihokova, E., Pejchal, J., Vedda, A., Zorenko, Yu, 2005. The antisite LuAl defect-related trap in Lu3Al5O12:Ce single crystal. Phys. Stat. Sol. (b) 242, R119–R121.

Nikl, M., 2005. Energy transfer phenomena in the luminescence of wide band-gap scintillators. Phys. Stat. Sol. (a) 202, 201–206.

Prusa, P., Cechak, T., Mares, J.A., Nikl, M., Zorenko, Y., Gorbenko, V., Tous, J., Blazek, K., 2008. The α-particle excited scintillation response of the liquid phase epitaxy grown LuAG: Ce thin films. Appl. Phys. Lett. 92, 041903.

Prusa, P., Nikl, M., Mares, J.A., Kucera, M., Nitsch, K., Beitlerova, A., 2009. The α-particle excited scintillation response of YAG: Ce thin films grown by liquid phase epitaxy. Phys. Stat. Sol. (a) 206, 1494–1500.

Stanek, C.R., McClellan, K.J., Levy, M.R., Grimes, R.W., 2006. Extrinsic defect structure of RE3Al5O12 garnets. Phys. Stat. Sol. (b) 243, R75–R77.

Zorenko, Yu., Voloshinovskii, A., Savchyn, V., Vozniak, T., Nikl, M., Nejezchleb, K., Mikhailin, V., Kolobanov, V., Spassky, D., 2007a. Exciton and antisite defect-related luminescence in Lu3Al5O12 and Y3Al5O12 garnets. Phys. Stat. Sol. (b) 244, 2180–2189.

Zorenko, Y., Gorbenko, V., Konstankevych, I., Voznjak, T., Savchyn, V., Nikl, M., Mares, J.A., Nejezchleb, K., Mikhailin, V., Kolobanov, V., Spassky, D., 2007b. Single crystalline film scintillators based on Ce- and Pr-doped aluminium garnets. Radiat. Meas. 42, 528–532.

Poděkování

Úplným závěrem chci vyslovit poděkování všem spoluautorům vědeckých publikací, na nichž jsem se podílel, jmenovitě vedoucímu Oddělení optických materiálů Fyzikálního ústavu AV ČR, Doc. Ing. Martinu Niklovi, CSc. Děkuji též za podporu kolegů z Katedry dozimetrie a aplikace ionizujícího záření. Jenom díky nim jsem nalezl čas a motivaci k napsání této práce. Za kvalitu této práce nicméně nesu zodpovědnost já sám.